

THE UNIVERSITY OF CHICAGO

COBALTS AND PYRROLE-MANCY: UTILIZING COOPERATIVE STRATEGIES FOR  
SUSTAINABLE CATALYSIS

A DISSERTATION SUBMITTED TO  
THE FACULTY OF THE DIVISION OF THE PHYSICAL SCIENCES  
IN CANDIDACY FOR THE DEGREE OF  
DOCTOR OF PHILOSOPHY

DEPARTMENT OF CHEMISTRY

BY

SOPHIE WHITMEYER ANFEROV

CHICAGO, ILLINOIS

AUGUST 2024

© Copyright 2024 Anferov

For Sasha, Miso and you, for reading. Thank you.

The truth, however ugly in itself, is always curious and beautiful to seekers after it.

Agatha Christie

# Table of Contents

List of Figures .....	viii
List of Tables .....	xii
List of Schemes.....	xiii
Acknowledgments.....	xiv
Abstract.....	1
Preface: Metals, Ligands, and Something Close to First Principles .....	3
Chapter I: Introduction to Metal-Ligand Cooperativity.....	7
Chapter II: Cobalt-Catalyzed Hydrogenation Reactions Enabled by Ligand-Based Storage of Dihydrogen .....	25
Introduction.....	25
Results and Discussion .....	28
Synthesis and Characterization of 1.....	29
Synthesis and Characterization of 2.....	30
Generation and Characterization of 3 .....	33
Hydrogenation Catalysis.....	35
Computational Analysis.....	38
Conclusions.....	41
Experimental Section.....	41
General Methods .....	41
Co( <sup>t</sup> Bu,TolDHP)Cl (1).....	43
Co( <sup>t</sup> Bu,TolDHP)OTf (2).....	43
Reactivity with H <sub>2</sub> .....	44
References.....	45
Chapter III: A cobalt adduct of an N-hydroxy-piperidinium cation .....	44
Introduction.....	44
Results and discussion .....	46
Synthesis and characterization of 1.....	46
Mechanism of Formation of 1.....	48
Reactivity of 1.....	50
Conclusions.....	51
Experimental Section.....	51
General Methods.....	52

Co( <sup>t</sup> Bu,TolDHP)(TEMPOH <sub>2</sub> <sup>+</sup> )(OTf) (1).....	52
Co( <sup>t</sup> Bu,TolDHP)OH(3).....	53
References.....	54
<b>Chapter IV: Selective Cobalt Mediated Formation of Hydrogen Peroxide from Water Under Mild Conditions Via Ligand Redox Non-Innocence.....</b>	<b>57</b>
Introduction.....	57
Results and Discussion .....	59
<i>Synthesis and Characterization of 2</i> .....	59
<i>Stoichiometric Hydrogen Peroxide Production from Water</i> .....	61
<i>Mechanistic Interrogation</i> .....	62
<i>Catalytic Hydrogen Peroxide Production from Water</i> .....	68
<i>Conclusion</i> .....	71
Experimental Section.....	72
General Methods.....	72
<i>Electrochemical experiment</i> .....	73
( <sup>t</sup> Bu, TolDHP)Co (2).....	73
Reoxidation of ( <sup>t</sup> Bu, TolDHP)Co (2) to ( <sup>t</sup> Bu, TolDHP)CoOTf (1-OTf) .....	74
Biphasic reaction of ( <sup>t</sup> Bu, TolDHP)CoCl (1) to ( <sup>t</sup> Bu, TolDHP)Co(MeCN) (2-MeCN).....	75
References.....	76
<b>Chapter V: Tunable Olefin Isomerization via In-Situ Modification of a H-atom Storing Ligand</b>	<b>80</b>
Introduction.....	80
Results and Discussion .....	83
<i>Thermodynamic Alkene Transpositions</i> .....	83
<i>Catalyst Characterization</i> .....	88
Methods .....	92
<i>Reactivity with Boranes</i> .....	94
<i>Preparation of IR samples of 2-BPin</i> .....	94
<i>Thin film on ATR IR</i> .....	94
<b>Chapter VI: Synthesis of a Potassium Capped Terminal Oxido.....</b>	<b>99</b>
<b>Chapter VII: Conclusions and Future Outlook.....</b>	<b>110</b>
<b>Appendices: Supplementary Informations and Unpublished Work .....</b>	<b>112</b>
Appendix I: Chapter II Supplementary Information.....	112
References.....	166
Appendix II: Chapter III Supplementary Information .....	168

References.....	190
Appendix III: Chapter IV Supplementary Information.....	192
References.....	248
Appendix IV: Chapter V Supplementary Information.....	249
Appendix V: Chapter VI Supplementary Information.....	325
Appendix VI: Unpublished Work: Variable Temperature, Ligand-Promoted Metal-Ligand Spin Tautomerism .....	347
Introduction.....	347
Synthesis and Characterization of <sup><i>t</i></sup> Bu,TolDHPCoOTf-MeCN.....	348
References.....	352
Appendix VII: Unpublished Work: Oh the Crystals You'll Grow, Oh the Reactions You'll See .....	354
Appendix VIII: Unpublished Work: Charging into Something New .....	358
References.....	361

## List of Figures

### Chapter I:

- Figure 1. Overview of strategies to store both H<sup>+</sup> and e<sup>-</sup> on ligand scaffolds. A. Advantages of combining different strategies. B. Selected reactions and applications. C. Ligand scaffolds capable of H-atom or H<sub>2</sub> storage. .... 8
- Figure 2. Selected examples where ancillary ligands can store A) H-atoms [1-4], B) H<sub>2</sub> across an extended conjugated system [5-8], and C) H<sub>2</sub> across a double bond [9-12]. .... 10
- Figure 3. Overview showing the strength of metal-ligand cooperativity in leveraging electrochemistry for electrosynthesis in both reductive and oxidative reactivity. Some commonly catalyzed reactions are shown as examples. .... 14
- Figure 4. CV of (<sup>t</sup>Bu,<sup>Tol</sup>DHP)Ni ([Ni], 1 mM) with added benzoic acid (10 mM), and with 1-octyne (10 mM) showing suppression of HER current upon the addition of substrate. 0.1 M TBAPF<sub>6</sub> in MeCN, 100 mV s<sup>-1</sup>. (adapted with permission). .... 16
- Figure 5. (A) Comparison between alcohol oxidation overpotentials. (B) Mechanism for Cu/bpy/TEMPO alcohol oxidation catalysis. Reproduced from ref. 22 with permission from the Royal Society of Chemistry. .... 19

### Chapter II:

- Figure 1. Existing Co-based hydrogenation catalysts or active species<sup>12ce,15a; 14abde</sup> and the current system highlighting ligand-based H<sub>2</sub> storage. .... 25
- Figure 2. SXRD Structures (from left to right) of 1 and 2. All displacement ellipsoids shown at 50% and hydrogens omitted for clarity. .... 27
- Figure 3. Perpendicular mode X-band EPR spectrum from top to bottom of 15 mM solutions of 2 and 3 at 15.9 K in toluene and 20 K in toluene respectively. Simulation shown in black lines for each. Simulation parameters for: 2: g = 2.01, 2.11, 2.61; Co-A = +56.5, +89.0, +75.6 MHz; N-A = +12.1, +5.9, +11.2 MHz. 3: g = 2.02, 2.10, 2.56; Co-A = +54.8, +61.0, +66.8 MHz, N-A = +23.1, +24.5, -14.1 MHz. Experimental conditions: microwave frequency 9.6304 GHz, microwave power 0.2 mW. The full and simulated spectra are shown in the SI (Appendix I: Figure S21-S27, Table S1). .... 29
- Figure 4. Thin Film IR spectrum of 3 and 3-D<sub>2</sub> with difference spectrum inset. .... 32

### Chapter III:

- Figure 1. SXRD Structures (from left to right) of 1, 1 rotated to see the hydrogen-bonding interaction, and 3. All displacement ellipsoids shown at 50% and hydrogens omitted for clarity, with the exception of O-H/N-H protons which are shown with a ball-and-stick model. .... 46
- Figure 2. Thin Film IR spectrum of 1 (black) and (<sup>t</sup>Bu,<sup>Tol</sup>DHP)CoOTf (gray) with shaded area indicating O-H/N-H stretches. .... 48

### Chapter IV:

Figure 1. Single-crystal structure of (<sup>t</sup>Bu,<sup>Tol</sup>DHP)Co (2). Selected bond lengths (Å): Co–N1/N5: 1.796(2), 1.847(2); Co–N3: 1.821(2); N1–N2/N4–N5: 1.323(2), 1.318(2); Co–(C1–H): 1.770(2); N2–C5/N4–C10: 1.343(3), 1.336(3); C5–C6/C9–C10: 1.403(3), 1.402(3); C6–C7/C8–C9: 1.436(3), 1.433(3); C7–C8: 1.353(3). Selected bond angles (°): N1–Co–N5: 172.33(8); N3–Co–(C1–H): 162.15(8)..... 59

Figure 2. UV-vis of 0.094 mM 1-OH reacting with acetonitrile under pseudo-first order conditions in diethyl ether at 2 °C. A) Traces taken during the first 2500 seconds of the reaction, with an inset showing a first-order fit to the absorbance at 560 nm. B) Traces taken from 2500 to 7700 seconds, with an inset showing a second-order fit to the absorbance at 560 nm. Details on fitting and parameters are provided in the SI. .... 65

Figure 3. A) Current enhancement observed in the presence of 1, H<sub>2</sub>O, and 2,6-lutidine (1 mM 1, 320 mM H<sub>2</sub>O, and 160 mM 2,6-lutidine in acetonitrile with 0.1 M NBu<sub>4</sub>PF<sub>6</sub>). B) Theoretical yield (black) and experimental yield (red) determined via NaI assay in micromoles of H<sub>2</sub>O<sub>2</sub> plotted against time (seconds)..... 68

#### Chapter V:

Figure 1: Alkene isomerization overview. A: Natural products accessible via 1- to 2- alkene isomerization. B: Co-based olefin isomerization catalysts in the literature. C: This work—reversible and selective olefin isomerization by an in-situ generated catalyst. .... 81

Figure 2: a) In-situ EPR of 1 + NaBArF<sub>4</sub> with fit in red. Experimental conditions: 15 K, MW freq. 9.639, MW power. 2.0 mW. Simulation parameters: g<sub>1,2,3</sub> = 2.02, 2.12, 2.58; <sup>59</sup>Co A<sub>1,2,3</sub> = +56.2, +73.6, +108.5 MHz; <sup>14</sup>N A<sub>1,2,3</sub> = +73.5, +12.7, +172.4 MHz. b) In-situ EPR of 1 + NaBArF<sub>4</sub> + HBpin. Experimental conditions: 127 K, MW freq. 9.639, MW power. 2.0 mW. Simulation parameters: g<sub>1,2,3</sub> = 2.04, 2.16, 2.33; <sup>59</sup>Co A<sub>1,2,3</sub> = +73.9, +72.9, +234.5 MHz, <sup>14</sup>N A<sub>1,2,3</sub> = +20.3, +16.1, -10.4 MHz. c) IR spectra of 1 + NaBArF<sub>4</sub> + HBpin (black) with simulations of a ligand borylated complex (red) and a hydrogenated complex (blue). Signals for HBpin shown with \* ..... 88

Figure 3. DFT computed energies and pathway for isomerization. Energies shown in kcal/mol, and all energies shown are free energies. .... 90

#### Chapter VI:

Figure 1. (A) SXRD structure of 1. A) One half of the dimeric unit with the full DHP ligand. B) A side view focusing on the O<sub>2</sub>K<sub>2</sub> core with peripheral groups omitted. C) A top view showing the stacked interactions with the K cations with peripheral groups omitted. Co (pink), N (blue), C (grey), O (red), K (violet). Ellipsoids at 50% and hydrogens omitted for clarity..... 100

Table 1. Selected bond lengths (Å) and angles (°) of (1) and related complexes..... 101

Figure 2. X-band EPR spectrum (black) and simulated spectrum (red) of a 15 mM solution of 1 (dimer) in toluene at 25 K. Conditions: MW frequency, 9.63 GHz; MW power, 2.0 mW. Simulation parameters: g<sub>x,y,z</sub> = 2.143 2.015 1.983; <sup>59</sup>Co A<sub>x,y,z</sub> = 37.85 7.06 22.66 MHz; <sup>14</sup>N A<sub>x,y,z</sub> = 85.39, 87.94, 22.66 MHz; HStrain<sub>x,y,z</sub> = 41.7975, 32.2248, 100. .... 105

#### Appendix VII:

Figure 1. Synthesis of Complexes Discussed in this Section .....	348
Figure 2. Complex 1-MeCN at 100 K and Complex 1-MeCN at 298 K .....	348
Figure 3. Complex 1-MeCN (left) at 15.9 K and Complex 1 (right) at 15.9 K. 1-MeCN: $g = 2.0585, 2.0788, 2.1315$ ; Co-A = +15.9328, +9.9042, 57.2366 MHz, N-A = +58.4688, +19.2988, +30.0000 MHz. 1: $g = 2.0598, 2.0766, 2.1739$ ; Co-A = +10.8252, +22.5562, +5.6313 MHz; N-A = +31.5100, -8.0770, +30.9039 MHz. microwave frequency 9.6304 GHz, microwave power 0.2 mW .....	350
Figure 4. A) Integrated Variable Temperature EPR Spectra (16 K-22 K); B) 297 K to 173 K (black to red), individual scans at each temperature in 1 MeCN: 10 2-methyl THF, scan speed 1200 nm/min. C) Variable Temperature Evans Method in 1 CD <sub>3</sub> CN: 10 d <sub>8</sub> -toluene—358 K to 238 K. D) and E) Complex 1-MeCN at 297 K and 173 K respectively, from B) .....	351
Appendix VIII:	
Figure 1. Attempts to make a new ligand! BF <sub>3</sub> Catalysis on the hydrazine condensation went wrong! [ <sup>Tol,2,6-Chloro-phenyl</sup> DHP]B, B (tan), N (blue), C (gray), Cl (dark green). C-H-atoms were omitted for clarity. ....	354
Figure 2. Breaking up is hard to do—trying to cleave out the boron with salts. [ <sup>Tol,2,6-Chloro-phenyl</sup> DHP]BF <sub>3</sub> K, B (tan), F (light green), K (purple) N (blue), C (gray), Cl (dark green). C-H-atoms were omitted for clarity. ....	354
Figure 3. Cobalt chloride complex reacted with <i>tert</i> -butyl isocyanide. [ <sup><i>t</i>Bu,Tol</sup> DHP]CoCl(CN <sup><i>t</i>Bu</sup> ), Co (pink), N (blue), C (gray), Cl (dark green). C-H-atoms were omitted for clarity. ....	354
Figure 4. Cobalt chloride complex forms this upon reactivity with oxygen—probably some kind of disproportionation reaction. [ <sup><i>t</i>Bu,Tol</sup> DHP]CoCl <sub>2</sub> , Co (pink), N (blue), C (gray), Cl (dark green). C-H-atoms were omitted for clarity. ....	354
Figure 5. Neutral cobalt complex with benzyl amine bound. [ <sup><i>t</i>Bu,Tol</sup> DHP]Co(NH <sub>2</sub> Bz), Co (pink), N (blue), C (gray). C-H-atoms were omitted for clarity. ....	355
Figure 6. Oxo or Hydroxide bridged dimer—formed from potassium oxide cobalt complex attempt for a cyclic voltammogram in NBu <sub>4</sub> PF <sub>6</sub> electrolyte. [ <sup><i>t</i>Bu,Tol</sup> DHP]CoO(H?)Co[ <sup><i>t</i>Bu,Tol</sup> DHP](NBu <sub>4</sub> ), Co (pink), N (blue), C (gray), O (red). C-H-atoms were omitted for clarity. ....	355
Figure 7. Cobalt triflate complex reacted with <i>tert</i> -butyl isocyanide. [ <sup><i>t</i>Bu,Tol</sup> DHP]CoOTf(CN <sup><i>t</i>Bu</sup> ), Co (pink), N (blue), C (gray), Cl (dark green), O (red), S (gold), F (light green). C-H-atoms were omitted for clarity. ....	355
Figure 8. Cobalt neutral complex reacted with tetrabutyl ammonium acetate. [ <sup><i>t</i>Bu,Tol</sup> DHP]CoOAc(NBu <sub>4</sub> ), Co (pink), N (blue), C (gray), O (red). C-H-atoms were omitted for clarity. ....	356
Figure 9. Manganese-metallated pyridine adduct. [ <sup><i>t</i>Bu,Tol</sup> DHP]Mn(Py), Mn (purple), N (blue), C (gray). C-H-atoms were omitted for clarity. ....	356

Figure 10. Complex formed from reduction of chloride complex with cobaltacene in the presence of hydroquinone/benzoquinone. [<sup>t</sup>Bu,<sup>Tol</sup>DHP]CoOPhOC[<sup>t</sup>Bu,<sup>Tol</sup>DHP], Co (pink), N (blue), C (gray), O (red). C-H-atoms were omitted for clarity. .... 356

Figure 11. Cobalt homoleptic complex with phenyl analog of ligand—from an attempt to metallate! [<sup>Ph</sup>,<sup>Tol</sup>DHP-H<sub>2</sub>]Co[<sup>Ph</sup>,<sup>Tol</sup>DHP-H], Co (pink), N (blue), C (gray). C-H-atoms were omitted for clarity..... 357

Figure 12. Water soluble pentacene from collaboration with L. E. McNamara and the Maurer group. [Pentacene-(S-C<sub>4</sub>H<sub>8</sub>CO<sub>2</sub>)<sub>2</sub>]KCl(MeOH)<sub>n</sub>, K (purple), S (gold), C (gray), O (red), Cl (dark green). C-H-atoms were omitted for clarity..... 357

#### Appendix VIII:

Figure 1. Ru and Fe analogs with two neutral bipyridine ligands and a single 4,4-BF<sub>3</sub>-bipyridine. .... 358

Figure 2. Metallations to form Ru and Fe analogs with one bipyridine ligand and two 4,4-BF<sub>3</sub>-bipyridines..... 359

Figure 3. Compared UV-Vis Spectra of differently substituted Ru (A) and Fe (B) analogs. Excitingly, the Ru spectrum changes shape dramatically and there is a shoulder at 600 nm in the Fe spectra that suggests potentially we are observing the triplet iron complex..... 360

## List of Tables

### Chapter II:

Table 1. Selected bond lengths (Å) and angles (°) of 1, 2, and related Ni complexes ..... 28

Table 2. Hydrogenation Substrate Scope with 2..... 35

### Chapter V:

Table 1: Thermal olefin isomerization with 1 at different catalyst loadings. .... 83

Table 2. Contra-thermodynamic and switchable catalysis, with standard conditions as 2.5 mol% 1, 2.5 mol% borane., 2.5 mol% NaBAr<sup>F</sup><sub>4</sub> with 476 long-pass filtered sun-simulator lamp for 18 hours in C<sub>6</sub>D<sub>6</sub> ..... 84

Table 3. Variations on added borane. .... 86

### Chapter VI:

Table 1. Selected bond lengths (Å) and angles (°) of (1) and related complexes..... 101

### Appendix VI:

Table 1. Selected bond lengths of 1, 1-MeCN, and related complexes (Å) ..... 349

# List of Schemes

## Chapter I:

Scheme 1. Reductive electrocatalytic transformations enabled by catalysts with ligand-based H-storage. Isolable (D) and transient (A, B, C) intermediate structures from the proposed catalytic cycles are depicted to highlight the properties of each ligand. .... 15

Scheme 2. Organometallic Complexes with H-atom Storing Ligands Utilized in Metal-Cooperative Oxidative Electrocatalysis. Isolable (A, B) intermediate structures, as well as one transition state (A), from the proposed catalytic cycles are depicted to highlight the properties of each ligand..... 17

## Chapter II:

Scheme 1. Synthesis of <sup>t</sup>Bu,TolDHP complexes of Co and hydrogenation reactivity..... 26

Scheme 2. Mechanism for the synthesis of 3 as well as for the hydrogenations of olefins (1-hexene used as model substrate)

## Chapter III:

Scheme 1. Oxidation and protonation states of TEMPO up to a full equivalent of dihydrogen..... 44

Scheme 2. Synthesis of 1 and proposed decomposition ..... 45

Scheme 3. Proposed mechanism of the formation of 1..... 50

## Chapter IV:

Scheme 2. Proposed mechanism for the molecular and catalytic generation of H<sub>2</sub>O<sub>2</sub> from the reaction between Co(<sup>t</sup>Bu,TolDHP) complexes and H<sub>2</sub>O. All energies shown in kcal/mol. .... 63

## Chapter V:

Figure 3. DFT computed energies and pathway for isomerization..... 90

## Chapter VI:

Scheme 1. Top: Examples of previously reported metal oxides stabilized by hydrogen bonding or Lewis acid interactions. Bottom: Synthesis of 1 from [<sup>t</sup>Bu,TolDHP]CoOH. .... 99

## Acknowledgments

I have had an incredible experience studying inorganic chemistry during the last decade or so at the University of North Carolina at Charlotte (UNCC), the California Institute of Technology (Caltech) and the University of Chicago (UChicago). Although I cannot thank everyone who has inspired and helped me, I would like to thank a few people in particular.

I would first like to acknowledge Prof. Daniel Rabinovich (UNCC---now UNC Greensboro) for welcoming me into his lab and imparting valuable synthetic knowledge to me. He encouraged me to pursue research and reach out to professors, and his scientific insight, mentorship, and kindness have allowed me to thrive in the new scientific environment. Of all the PIs I've had, DR's thoughtfulness and giving nature set him apart. I'm so grateful to him for instilling in me an appreciation of stamps and a passion for organometallic chemistry. I would also like to thank his graduate students, especially Casey Oian and Lizeth Hernandez, for being my friends and mentors, as well as the other members of that group during 2014-2015.

Next, I would like to thank and acknowledge Prof. Theodor Agapie who allowed me to conduct research in the cluster subgroup since my second quarter as an undergraduate at Caltech. Working with Theo, I have learned not only how to refine my synthetic skills, but also how to think like a scientist. His mentorship has shaped me more than any other professor as a chemist, and he has always been encouraging and responsive to the projects I have chosen to pursue and the work I have done on them. The SURF office at Caltech has also been a truly important resource for me to pursue scientific research both with Theo (summer 2016/2017) and summer 2018 with Professor John Anderson at UChicago.

I would also like to thank Dr. Christopher Reed for mentoring me and providing a rigorous training. His time and efforts have really been valuable to me. I would also like to thank the other members

(present and past) of the cluster subgroup: Charlie Arnett, Heui Beom (HB) Lee, Dr. Zhiji Han, Dr. Gwen Bailey, Alexandra Barth, Anna Scott, Angela Shiau, Kurtis Carsch, Dr. Graham de Ruiter, Diamond Thomas, Paige Gannon, and Till Schmidt Raentsch. Also from the group, I would like to thank Gavin Heim, Ruomeng Wan, and Dr. Nathaniel Hirscher. I would similarly like to thank Mona Shahgholi, Dave VanderVelde, Mike Takase, and Larry Henling. Professor Harry Gray, and Professor Jonas Peters also deserve acknowledgement for their mentorship and excitement about chemistry.

In my time at UChicago, I have received help and support for countless individuals, too many to ever name by name or thank sufficiently. To the entire physical sciences community—physicists, chemists, facility managers and more—I am eternally grateful. A few honorable mentions go out to, first, my secondary boss—Dr. Alexander Filatov, who has nurtured and grown a passion for crystallography within me. I look forward to every crystal I run, and I have very much appreciated Alex introducing me to the greater crystallography community—at Northwestern, during our UChicago diffractometer’s time of troubles, and at ACA, where Alex’s name never fails to get a positive reaction from anyone who knows him. His advice, friendliness and generosity with his time and efforts are unmatched, and I will miss having such an amazing mentor a text away. Second, I want to thank Dr. Josh Kurutz, who has allowed me to test the limits of his facilities on many occasions (probably to his great chagrin). Despite this, I’ve had a great time over the years running into him in the NMR labs and chatting about his relentless automation of the NMR facility and our former times at Caltech. Also honorable mentions to a number of other members of the department go to Russell Kielawa in the Snyder lab; for having wonderful crystals and just being so easy and pleasant to collaborate with (even if my samples aren’t enantio-enriched); Patrick Kelly in the Levin lab; for making me first strive to be a better teacher and then also a better

scientist by being so undeniably excellent himself; and Di Wang in the Talapin lab; for always being quick to reply to hare-brained ideas and try MXene experiments. I appreciate them and rest of the synthetic cadre I entered with: Shinyoung Choi, Allison Brink, Manish Gupta, and Rui Zhang. We're so close, guys!

I would also like to thank my committee—John Anderson (more later), Guangbin Dong—who hopefully will be happy I did some more organic chemistry later in my degree, and Mark Levin—who is not only delightful himself, but has a delightful group to match. In all seriousness, I appreciate their time, feedback, and careful consideration of my work, and I am deeply grateful to be able to present this labor of love to them.

The Anderson lab has been a wonderful community to do science in as well. I would not be writing this today without their love and support, and certainly not without their expertise and many talents. To all those who have contributed to my experience, both those who graduated or left during my time—Kate Jesse, Andrew McNeece, Vennela Mannava, Norman Zhao, Noah Horwitz, Ethan Hill, Shutian Jiang, Airi Kawamura, Jiaze Xie, Jorge Martinez, Omar Salinas, Andrew Ritchhart, Emory Apodaca, Joel Gardner, Eyob Tewelde, Remi Dado, Daniel Bourland—and those who remain—Lauren McNamara, Maia Czaikowski, Joe Scott, Alexandra Krupinski, Chen-Yu Lien, Shilin Zeng, Nathan Lopez, Ningxin Jiang, Alex Tascher, Lei Wang, Patrick Crossland, Ashley Zhu—I am deeply appreciative.

Some special notes-- Norman Zhao was my first desk mate, and his calm and slightly cynical approach to lab definitely eased the first-year transition. Noah Horwitz rebuilt the vacuum pump I still use for my Schlenk line with me my first year, and I still think of his generosity and helpfulness every time I use it. Ethan Hill let me in every morning I locked myself out and was surprisingly gracious about being wrong on how to thaw frozen J-Young tubes. Jorge Martinez is a blast, who

nevertheless likes very bad tasting pumpkin beers. Joe Scott is also a delight to have in lab (so funny, such good taste in music), and I would've loved to have more time with him during my degree.

My former undergrads—Emory Apodaca and Daniel Bourland—I loved teaching. I think one of my great degree regrets is that I was never able to pass on the love I have for organometallic chemistry like it was passed to me. I still really appreciated the chance to try, and I appreciated the enthusiasm and hard work both of these undergraduates demonstrated. For Alex Krupinski, the first year graduate student I have been working together with this year, I would like to extend my apologies for the quality of instruction she is receiving from me and also my gratitude that she is listening to it. I do my best to still give her things to laugh at, even if some of them are me. In the same vein of things, Elizabeth Filatov, who is as bright as she is patient, has been a delight to mentor for the last month or so, and I can't wait to have more time to devote to mentorship after the writing of this thesis.

I would like to finish by mentioning a few individuals in particular who have deeply enriched my time in the group. First, Andrew McNeece, for being my very first mentor in the group, and showing me how much more relaxed life in a lab could be. Second, Kate Jesse, one of my favorite people in the world, who—whether working side-by-side in a glovebox or zooming down a ski slope—never fails to make me laugh. Third, Vennela Mannava, who tolerated and then added to the puns in my life, and who is both brilliant in her work and in her wordplay. Fourth, Maia Czaikowski—who is better than me in every way, and probably would be doing a better job writing all of this than I plan to do. Last, but not least, Lauren McNamara. A better desk partner could never be found—Lauren inspires me both to do and to not do chemistry, making me both excited to play and to do work. All of these individuals have inspired me to try and not try hare-brained

ideas, and many of them have worked (hence the graduation), and to them goes all the credit and all my love.

Professor Anderson has also been great. Anything I say here will make him too smug, so I just want to say—10/10. He has put up with a lot.

Finally, I would like to thank a number of people outside of the lab who have helped me survive the last few years and throughout my life in general. My parents and brother have been there for me my entire career, from encouraging me to reach out and join my first lab in high school to supporting my decision to attend Caltech and after, graduate school at UChicago. My father especially, I know I can always reach out for insight, advice or anything at all. I also have truly delightful in-laws, who despite their regrettable inclination for physics, always demonstrate interest in my convoluted explanations of my research. My mother-in-law, Svetlana Monroe, in particular has been incredibly warm, welcoming, and supportive, and I can't believe how lucky I am to have married into such a family. My final family member, my cat, Miso, has also been a pillar of support (purrar of support) throughout this experience, and she has brightened every day, early in the morning, making sure I wake up on time to go to work.

It takes truly great friends to keep in touch year after year from other sides of the country or even the world, and I have been incredibly lucky to have multiple friends who have cared enough to try. Particularly, I would like to acknowledge Allison Tang—a brilliant scientist in her own right—who is about as sweet and kind as it is possible for a person to be. I look forward every week to hanging out over the phone and catching some fish (inevitably). I would further like to thank Annika Bowers, Jessica Motzkus, and Kelly Telljohann, for being my friends over the years or listening to me talk about chemistry or just keeping me sane. Annika shows me her rats and sends me her amazing musical talents. She is also responsible for showing me a number of very fun

movies (one of which is referenced later), and she inspires me to make my life into an adventure. Jessica (Jessi) is a true-blue friend. She always gives and gives, and I hope that she feels that same energy being given back. I'm really looking forward to being on the same continent as her for a few years! Kelly Telljohann has been such a surprise gift in my life. When I left North Carolina, we (and Jessi) both put the appreciable effort into keeping in texting-contact over the years, which was suddenly and wonderfully brought back to real world contact when she moved to Chicago. Since then, she has been my bridesmaid, Chicago neighborhood exploring buddy, and baking co-experimentalist! Some friendships really do last more than a lifetime.

Lastly and most importantly, I want to thank Sasha Anferov for being my best friend and my other half. His time, brilliance and support have enabled me to stay excited and passionate about waking up every day and looking forward to spending it with him (and in lab).

Truly, I could not have completed this degree without him.

## Abstract

Metal-ligand cooperativity is ubiquitous throughout both biological and chemical catalysis, but often goes unattributed or underutilized in organic catalysis. Practically, utilizing every resource available and not discriminating metal vs. ligand is a powerful strategy to getting more tunability as well as more efficiency in any kind of chemical transformation, and nature, and an ever-increasing number of chemists, realizes this. By building in this biomimetic strategy, first row metals can also be enhanced past their native one-electron preferences, opening the door to multi-proton, multi-electron chemistry. In particular, hydrogen transfer chemistry is important due to its wide variety of applications in industrial processes and pharmaceutical development. For this reason, there has been extensive research into catalyst design for reactions involving hydrogen transfer reactivity. Homogenous catalysts are attractive for studies due to the relative ease of their characterization. However, any reaction that involves the movement of protons and electrons, even in a redox-neutral fashion, can benefit from a multifunctional ligand. In these studies, a 2,5-dihydrizonopyrrole ( $^{t\text{Bu,Tol}}\text{DHP}$ ) ligand scaffold, which has previously been shown to store a full  $\text{H}_2$  equivalent (in addition to any redox-capabilities of the metal center), was utilized in complexes with Co, and with these complexes alone, I show the diversity of reactivity, enhanced and altered selectivity, and broad applicability afforded by ligands as complex as the metals they bind.

*In Chapter I*, I discuss the precedence for proton and electron storing ligands in catalysis, and the distinct benefits of coupling their advantages with the catalytic powerhouse of Co metal-centers in particular.

*In Chapter II*, I discuss a  $^{t\text{Bu,Tol}}\text{DHP}$  complex with Co, where an  $\text{H}_2$  equivalent can be stored on the ligand periphery and can be leveraged for mild, catalytic olefin hydrogenations. Computational and reaction analysis suggests ligand hydrogenation proceeds by  $\text{H}_2$  association followed by H-H scission, with radical intermediates playing a prominent role in driving turnover. This complex is an unusual example where a synthetic system can mimic biology's ability to mediate  $\text{H}_2$  transfer via secondary coordination sphere-based processes.

*In Chapter III*, I discuss the synthesis of a previously unobserved oxidation state of TEMPO (another proton and electron storing ligand) bound to a metal center, Co. This complex is stabilized by the  $^{t\text{Bu,Tol}}\text{DHP}$  ligand electronic rearrangement, and a putative Co(I) complex. IBO analysis reveals an initial proton transfer from a free TEMPOH to a bound TEMPOH species, followed by rapid electron transfer to the metal center from a dissociated TEMPO $\cdot$ . This demonstrates a previously unproposed, but clearly possible, intermediate in TEMPO dehydrogenative reactivity, which is facilitated by our similarly bifunctional ligand scaffold.

*In Chapter IV*, I discuss the oxidative reactivity of these  $^{t\text{Bu,Tol}}\text{DHP}$ Co complexes with  $\text{H}_2\text{O}$ . Upon addition of  $\text{H}_2\text{O}$  to these complexes, both  $\text{H}_2\text{O}_2$  and the reduced  $^{t\text{Bu,Tol}}\text{DHP}$ Co complex are detectable as the major products. This chemistry can be rendered catalytic with oxidative potential, and I observed selective  $\text{H}_2\text{O}_2$  production in all cases, with no  $\text{O}_2$  observed. This unusual selectivity is engendered by the redox-stabilization and electron accepting nature of the  $^{t\text{Bu,Tol}}\text{DHP}$  ligand.

*In Chapter V*, I discuss my most recent work, building onto the hydrogenation catalysis previously observed, to study olefin isomerization of  $^{t\text{Bu,Tol}}\text{DHP}$ Co complex with boranes. We are able to demonstrate post-synthetic modification of the  $^{t\text{Bu,Tol}}\text{DHP}$  ligand with a family of boranes, allowing for tunable olefin-isomerization, including some trans-to-cis isomerization of pre-existing double bonds.

*In Chapter VI*, I discuss another unusual species—of a [<sup>t</sup>Bu,<sup>Tol</sup>DHP]CoOK complex, with an unusual deprotonated oxyl moiety. The  $pK_a$  of the OH bond of the [<sup>t</sup>Bu,<sup>Tol</sup>DHP]CoOH complex is assessed, and the reactivity of the potassium complex investigated.

This thesis also contains *multiple appendices* which contain supporting data for the previous chapters, as well as some cherished, but unpublished explorations.

Please note, all chapters have an independent compound numbering system. Characterization spectra are provided in the corresponding appendix for each chapter.

## **Preface: Metals, Ligands, and Something Close to First Principles**

*Who IS the electron, Miffy?*

In the interests of the non-chemists, and specifically, the physicist reading my thesis, I want to start from a few basic principles. Matter is made up of atoms—which have a positively charged nucleus and an electron cloud that surrounds them.<sup>1</sup> The approximate size of the atom is largely determined by both the number of electrons and how tightly the nucleus attracts them to itself, and the more protons and neutrons inside that nucleus will affect reactivity as well as size.<sup>2</sup> For most elements, only the outermost electrons are used in reactivity and bonding (the so-called valence electrons), and this is key, because chemistry, fundamentally, is about the bonds between atoms. Their formation, existence, the changes in electron density along them, their breaking, and what you can accomplish with the resultant molecules is what every chemist—from natural product synthesizer to hardcore spectroscopist—is all about.

Generally, bonding lies along a spectrum—from ionic to covalent, with ionic bonds being a give-and-take and covalent bonds being equally shared.<sup>2</sup> However, though general instruction in chemistry deals primarily with the s- and p- blocks on the periodic table, the very nature of bonding is made richer and more complex when you get to the d-block—the transition metals.<sup>3</sup> Why? Transition metals can transition—they have multiple preferred electron counts and they have the d-orbitals to put them in. They can also make true covalent bonds—with each other and with other elements—an ability which can be compromised when you move to the f-block. As chemists, we have spent hundreds of years putting different ligands, or other molecular moieties, on these metal centers to tune where the electron cloud for that metal center is located and how many d-electrons are in it. They do this by hybridizing their own orbitals with that of the metal to form a new hybridized orbital with its own energy. Through considerations the relative energy of each of the

starting orbitals (metal and ligand), we can approximate those energies and rationalize trends we observe in bond-strength and reactivity.

In many ways, a unligated metal is like an untuned violin—you can make sounds by drawing the bow across the strings, but to make music you need to have each string loosened or tightened to get the sound you want—knowing that the sound you want may be different depending whether you're playing Vivaldi or Tchaikovsky.<sup>4</sup> Even a metal center in a surface does not stand alone, but with its fellows and with any inevitable surface oxides that appear.

For many synthetic chemists, this is the end of the story. However, it does not have to be. Like the gentlemen in *Pianomania*<sup>5</sup> show—there are more things you can do to a violin than just tune and play.<sup>4</sup> Why can't a violin be a grand piano leg? Why can't we make a ligand an equal player in reactivity to a metal center? The answer is, we can, and nature already has. The most metal-ligand cooperative systems and multifunctional ligands known are enzymes—metal-containing and metal-free—capable of sustaining life with an elegant and robust mechanisms for moving protons and electrons, sourcing them from readily available inert sources, making and breaking essential bonds, and doing so at blindingly fast rates. They use motifs such as redox-active frameworks, proton-storing motifs, hydrogen-bonding structural components, and charged groups to engender the kinds of reactions that make life possible and that synthetic systems struggle to emulate without the use of second- or third-row transition metals (precious metals).

Despite this, synthetic recognition of ligands as partners, and not merely parts, in reactivity has lagged behind. Nevertheless, some of the most ubiquitous ligands, additives, and surfaces are non-innocent and engage in redox-behavior and sometimes even proton storage—bipyridines and derivatives,<sup>6</sup> TEMPO and other nitrosyl radicals,<sup>7-12</sup> and even ceria surfaces (CeO<sub>2</sub>).<sup>13</sup>

Though ligands have been tuned for their steric properties or donor properties, most synthetic systems are still frequently designed to put all the onus for proton and electron storage on metal centers—which dramatically limits both reactivity as well as competent catalytic metals. First row metals have a strong preference for one electron transformations and radical steps, making them challenging to use in multi-electron and proton steps, compared to second- and third- row metals which prefer two-electron cycles. First row metals are significantly more abundant as a whole, and natural and heterogenous systems often show them to be capable of the same essential transformations as the lower rows—but they need help! By incorporating proximal other metals (to create multi-metallic compounds) or redox-active organic moieties, the one-electron propensity for first row metals can be overcome, and two-electron (and more) chemistry can occur. With a sufficiently complex ligand (as observed in enzymes), there is the practical advantage of allowing nearly unlimited stable and accessible H-atom storage—as you are no longer limited to the number of ligands or electrons one metal can store while still having enough room around the metal center to be catalytically active. We have sought to add to this literature through the intentional design and study of redox-active, proton-storing ligands—particularly looking through the lens of H-atom and dihydrogen transfer.<sup>14</sup>

## References

1. Gray, H. B. *Chemical Bonds: An Introduction to Atomic and Molecular Structure*; University Science Books: Sausalito, CA. **1994**; *1*, 2-37.
2. Gray, H. B. *Chemical Bonds: An Introduction to Atomic and Molecular Structure*; University Science Books: Sausalito, CA. **1994**; *1*, 40-70.
3. Gray, H. B. *Chemical Bonds: An Introduction to Atomic and Molecular Structure*; University Science Books: Sausalito, CA. **1994**; *1*, 150-187.
4. (2009) Pianomania. WILDArtFILM, OVALmedia Berlin&Cologne, OVALinternational GbR, Germany and Austria.
5. Thank you to Annika Bowers
6. Tarrango, M.; Ye, S.; Neese, F. Electronic structure analysis of electrochemical CO<sub>2</sub> reduction by iron-porphyrins reveals basic requirements for design of catalysts bearing non-innocent ligands. *Chem. Sci.* **2022**, *13*, 10029-10047.

7. a) Mader, E. A.; Mayer, J. M. *Inorg. Chem.* **2010**, 49, 8, 3685–3687.; b) Lomont, J. P.; Nguyen, S. C.; Harris, C. B. *J. Am. Chem. Soc.* **2013**, 135, 30, 11266–11273.; c) Tao, X.; Kehr, G.; Wang, X.; Daniliuc, C. G.; Grimme, S.; Erker, G. *Chem. A Eur. Jour.* **2016**, 22, 28, 9504–9507.; d) Walroth, R. C.; Miles, K. C.; Lukens, J. T.; MacMillan, S. N.; Stahl, S. S.; Lancaster, K. M. *J. Am. Chem. Soc.* **2017**, 139, 38, 13507–13517.; e) Ryan, M. C.; Whitmire, L. D.; McCann, S.D.; Stahl, S. S. *Inorg. Chem.* **2019**, 58, 15, 10194–10200.
8. a) Lauber, M. B.; Stahl, S. S. *ACS Catal.* **2013**, 3, 11, 2612–2616.; b) Ryland, B. L.; Stahl, S. S. *Angewandte. Chem. Int. Ed.* **2014**, 53, 34, 8824–8838.; c) Steves, J. E.; Stahl, S. S. *J. Org. Chem.* **2015**, 80, 21, 11184–11188.; d) Badalyan, A.; Stahl, S. S. *Nature.* **2016**, 535–406–410.; e) Nutting, J. E.; Mao, K.; Stahl, S. S. *J. Am. Chem. Soc.* **2021**, 143, 28, 10565–10570.
9. a) Steves, J. E.; Stahl, S. S. *J. Am. Chem. Soc.* **2013**, 135, 42, 15742–15745.; b) Rahmi, A.; Azarpira, A.; Kim, H.; Ralph, J.; Stahl, S. S. *J. Am. Chem. Soc.* **2013**, 135, 17, 6415–6418.; c) Rafiee, M.; Miles, K. C.; Stahl, S. S. *J. Am. Chem. Soc.* **2015**, 137, 46, 14751–14757.; d) Zultanshki, S. L.; Zhao, J.; Stahl, S. S. *J. Am. Chem. Soc.* **2016**, 138, 20, 6416–6419.; e) Rafiee, M.; Konz, Z. M.; Graaf, M. D.; Koolman, H. F.; Stahl, S. S. *ACS Catal.* **2018**, 8, 7, 6738–6744., f) Rafiee, M.; Alherech, M.; Karlen, S. D.; Stahl, S. S. *J. Am. Chem. Soc.* **2019**, 141, 38, 15266–15276.; g) Piszal, P. E.; Vasilopoulos, A.; Stahl, S. S. *Angewandte. Chem. Int. Ed.* **2019**, 58, 35, 12211–12215.
10. a) Kim, J.; Stahl, S. S. *ACS Catal.* **2013**, 3, 7, 1652–1656.; b) Xie, X.; Stahl, S. S. *J. Am. Chem. Soc.* **2015**, 137, 11, 3767–3770.; c) Miles, K. C.; Abrams, M. L.; Landis, C. R.; Stahl, S. S. *Org. Lett.* **2016**, 18, 15, 3590–3593.; d) Wang, F.; Rafiee, M.; Stahl, S. S. *Angewandte. Chem. Int. Ed.* **2018**, 57, 22, 6686–6690.
11. a) Michel, C.; Belanzoni, P.; Gamez, P.; Reedijk, J.; Baerends, E. J. *Inorg. Chem.* **2009**, 48, 24, 11909–11920.; b) Cheng, L.; Wang, J.; Wang, M.; Wu, Z.; *Inorg. Chem.* **2010**, 49, 20, 9392–9399.; c) Belanzoni, P.; Michel, C.; Baerends, E. J. *Inorg. Chem.* **2011**, 50, 23, 11896–11904.; d) Hoover, J. M.; Ryland, B. L.; Stahl, S. S. *ACS Catal.* **2013**, 3, 11, 2599–2605.; e) Ryland, B. L.; McCann, S. D.; Brunold, T. C.; Stahl, S. S. *J. Am. Chem. Soc.* **2014**, 136,34, 12166–12173.
12. a) Gerken, J. B.; Stahl, S. S. *ACS Cent. Sci.* **2015**, 1, 5, 234–243.; b) Gerken, J. B.; Pang, Y. Q.; Lauber, M. B.; Stahl, S. S. *J. Org. Chem.* **2018**, 83, 14, 7323–7330.; c) Nutting, G. E.; Rafiee, M.; Stahl, S. S. *Chem. Rev.* **2018**, 118, 9, 4834–4885.; d) Wang, F.; Stahl, S. S. *Acc. Chem. Res.* **2020**, 53, 3, 561–574.
13. Paladugu, S.; Metz, P. C.; Luo, S.; Li, M.; Liu, J.; Meyer, H.; Wu, Y.; Wu, Z.; Page, K. In Situ Neutron Scattering Studies on the Oxidation and Reduction of CeO<sub>2</sub> and Pt–CeO<sub>2</sub> Nanorods. *J. Phys. Chem.* **2023**, 127, 7, 3689.
14. a) Anferov, S. W.; Filatov, A. S.; Anderson, J. S. *ACS Catal.* **2022**, 12, 16, 9933.; b) Anferov, S. W.; Anderson, J. S. *J. Coord. Chem.* **2022**, 75, 11–14, 1853–1864.; c) Anferov, S. W.; Boyn, J-N.; Mazziotti, D. A.; Anderson, J. S. *J. Am. Chem. Soc.* **2024**, 146, 9, 5855–5863.; d) Anferov, S. W.; McNamara, L. E.; Anderson, J. S. *In Preparation.*; e) Anferov, S. W.; Krupinski, A.; Anderson, J. S. *Submitted.*
-

## Chapter I: Introduction to Metal-Ligand Cooperativity

*p-block alone weak, p-block together strong*

This chapter has been adapted from the following: Anferov, S. W.;\* Czaikowski, M. E.\*;

Anderson, J. S. *Trends in Chemistry*, **2021**, 3, 12, 993. and Anferov, S. W.;\* Czaikowski, M.

E.\*; Anderson, J. S. *Chem Catalysis*, **2024**, 4, 100922, 1.

Selectively and efficiently directing the flow of protons and electrons, in many cases multiple equivalents of both, underpins many challenging chemical transformations. Transition metal centers feature prominently as catalytic centers precisely due to the ease with which they mediate such reactivity. Despite the broad application of transition metals, it is becoming increasingly apparent that relying on the reactivity of the metal center alone is not sufficient for some of the most challenging transformations. Cooperativity between metal centers and ancillary supporting ligands can enable greater rates and enhanced selectivity.

The advantages of metal-ligand cooperativity are best illustrated by the secondary coordination sphere of metalloenzymes where hydrogen-bonding interactions, proton-shuttling pathways, and electron transfer cofactors facilitate precisely-tuned reactivity (**Figure 1A**). Synthetic chemists have mimicked these strategies to great effect, with many examples of supporting ligands that have hydrogen bonding motifs or can store protons or electrons. Natural systems, however, are not limited to a single one of these features, but rather utilize all of these strategies synergistically (**Figure 1A**).

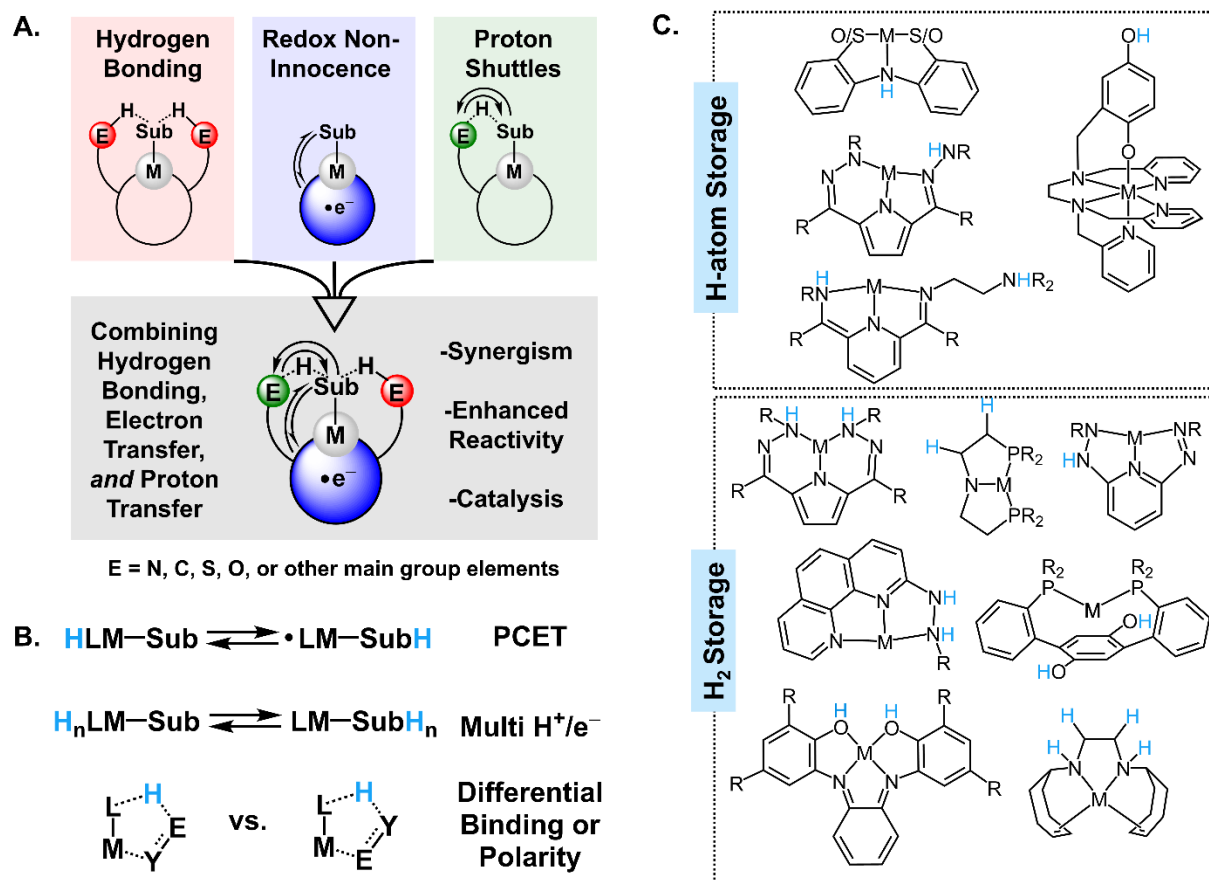


**Figure 1.** Overview of strategies to store both  $\text{H}^+$  and  $\text{e}^-$  on ligand scaffolds. **A.** Advantages of combining different strategies. **B.** Selected reactions and applications. **C.** Ligand scaffolds capable of H-atom or  $\text{H}_2$  storage.

While the success of incorporating hydrogen bonding motifs, proton shuttles, or electron reservoirs into ligands has been thoroughly demonstrated over the past few decades, there are many compelling advantages of combining all of these features. Reversible storage of protons *and* electrons can assist in the mediation of proton-coupled-electron-transfer (PCET) instead of solely proton-transfer (PT) or electron-transfer (ET) (Figure 1B). Furthermore, storing H-atom equivalents on a ligand scaffold in addition to on the metal center should enable more challenging multi-proton/multi-electron reactivity. Utilizing various storage groups can also dictate differential

selectivity due to orthogonal polarities in E–H and M–H bonds (**Figure 1B**). The combination of these effects promises enhanced reactivity and selectivity. However, significant limitations to realizing these benefits lie in the design of these necessarily complex ligands. Ideal scaffolds must include both electron and proton storage sites while maintaining more traditional ligand characteristics, such as ease of synthesis, preserving open coordination sites, modulating the energetics of catalytic intermediates, and maintaining stability under reaction conditions.

While this is a daunting set of design criteria, there has been exciting progress in this area with several examples of ligands that store full H-atom and H<sub>2</sub> equivalents (**Figure 1C**). Select examples in this area will be highlighted, with a focus on trends in recent reports as well as promising future directions. Emphasis is placed on systems that apply these proton and electron equivalents towards synthetic or catalytic transformations. Excluded are systems with limited experimental evidence for involvement of the ligand.

Most of the ligands that engage in PCET rely upon conjugated systems that have previously been shown to exhibit redox-active behavior. The main design principle to enable PCET reactivity is the inclusion of a Lewis basic moiety where a proton can be stored (**Figure 1C**). Such sites also have the advantage of providing hydrogen bonding motifs.

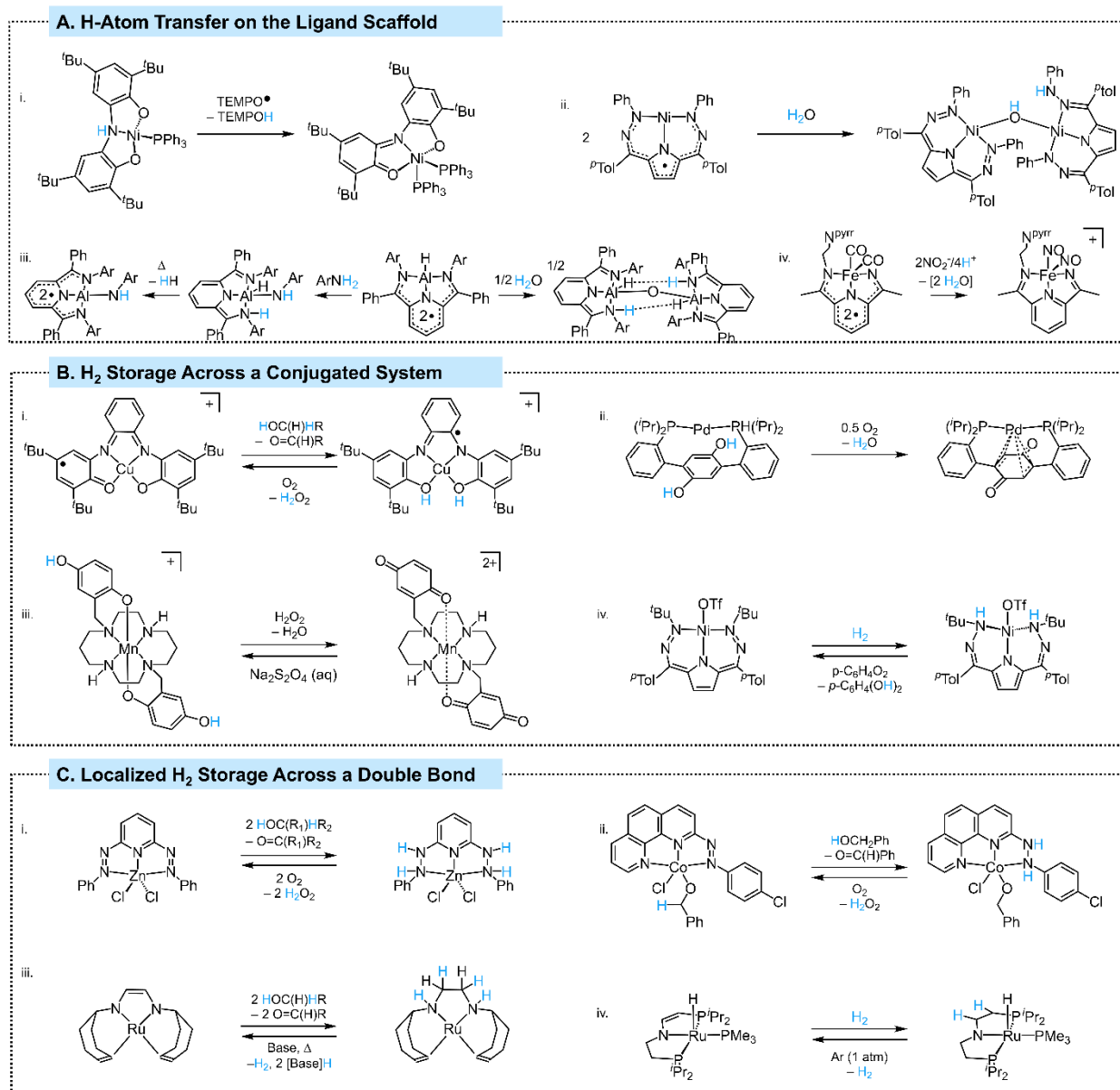


**Figure 2.** Selected examples where ancillary ligands can store **A)** H-atoms [1-4], **B)** H<sub>2</sub> across an extended conjugated system [5-8], and **C)** H<sub>2</sub> across a double bond [9-12].

One successful application of this strategy comes from the Heyduk group, where O/S-N-O/S pincer ligands perform PT, PTET, and PTETET reactivity depending on the substrate utilized (**Figure 2Ai**).<sup>1</sup> A separate example of a pincer ligand has been reported by our laboratory where this approach enables the ligand-promoted homolytic activation of water to form a bridging

hydroxide which can subsequently perform O-atom transfer reactivity (**Figure 2Aii**).<sup>2</sup> Prototypical redox-active pyridinediimine scaffolds also feature prominently in this area. The Berben group has used aluminum complexes for stoichiometric ligand-promoted activation of water and amines which was later expanded to include catalytic oxidative couplings of benzylic amines (**Figure 2Aiii**).<sup>3</sup> Gilbertson and coworkers also invoke PTETET with an iron pyridinediimine complex featuring an appended base that serves as a proton shuttle in enhancing rates of catalytic nitrite reduction (**Figure 2Aiv**).<sup>4</sup>

The storage and transfer of a full equivalent or more of H<sub>2</sub> on the ligand scaffold enables more diverse reactivity. Furthermore, this strategy also mimics systems in enzyme active sites. While successful implementations of this strategy are still limited, two general approaches have emerged: storing H<sub>2</sub> across an extended conjugated framework (**Figure 2B**) or across a localized double bond (**Figure 2C**). Both of these tactics have different benefits. Extended  $\pi$ -systems have the advantage of accessible redox chemistry, as well as more flexible arrangement of the H-substituents. Conversely, localized double bonds can be more easily appended onto ligand scaffolds, and multiple localized double bonds make storing multiple equivalents of H<sub>2</sub> more facile.

An early example of ligand-based proton and electron storage comes from a galactose oxidase model complex with a salen-like diaminobenzene ligand (**Figure 2Bi**).<sup>5</sup> The Agapie group also used a bis-phosphine ligand with a strategically positioned hydroquinone moiety to transfer H<sub>2</sub> in the reduction of dioxygen to water (**Figure 2Bii**).<sup>6</sup> Ligand-based H<sub>2</sub> transfer is enforced by the coordination of the quinoid moiety to the metal center which inhibits oxygen binding. Goldsmith and coworkers have also incorporated hydroquinone-based motifs into ligands for novel applications in H<sub>2</sub>O<sub>2</sub> dismutation or sensing in MRI contrast agents (**Figure 2Biii**).<sup>7</sup> Direct H<sub>2</sub>

scission and storage across the above-mentioned dihydrazonopyrrole ligand backbone allows for the Ni-catalyzed hydrogenation of benzoquinone (**Figure 2Biv**).<sup>8</sup> Density functional theory (DFT) calculations and kinetic measurements suggest metal assisted H<sub>2</sub> splitting where an intermediate consisting of a metal hydride and a protonated ligand undergoes hydride transfer to form the hydrogenated product.

Goswami and coworkers utilized a related hydrazine-based pincer ligand, but in this case H<sub>2</sub> storage occurs at localized N=N bonds. In this example, two successive alcohol dehydrogenations lead to storage of 4(H<sup>+</sup>, e<sup>-</sup>) on the ligand with a redox-inactive Zn metal center (**Figure 2Ci**).<sup>9</sup> These hydrogenated complexes can subsequently reduce dioxygen to hydrogen peroxide to enable aerobic catalysis. Related N=N motifs have also been employed in the catalytic generation of quinazolin-4(3H)-ones from amides and alcohols (**Figure 2Cii**).<sup>10</sup> DFT calculations on this Co(II)-aryldiazo system from the Paul group support that ligand-based redox circumvents more energetically taxing metal-centered multi-electron redox steps.

The Grützmacher group has reported an example where H<sub>2</sub> incorporation occurs across a C=C double bond. This system incorporates H<sub>2</sub> + 2(H<sup>+</sup>) on the diazadiene ligand moiety (**Figure 2Ciii**).<sup>11</sup> The ligand functions cooperatively with a Ru metal-center to activate C-H bonds in alcohols and transfer an H-atom equivalent to the unsaturated C=C groups on the ligand backbone. Mechanistic investigations indicate that this process occurs in a successive manner, and the catalytic cycle is closed when the fully reduced metal-ligand complex releases H<sub>2</sub> under basic conditions. Reversible hydrogenation of a C=C bond has also been observed in a PNP-type ligand scaffold reported by Schneider and coworkers. Here, the authors noted that H<sub>2</sub> storage and release can also serve to tune metal-centered reactivity (**Figure 2Civ**).<sup>12</sup> The hydrogenated ligand backbone exhibits stronger  $\pi$ -donation and alters primary coordination sphere interactions.

In addition to the thermal examples listed thus far, the application of electrochemical methods can further extend the applicability of redox-active, proton-storing ligands. In contrast to thermal catalytic platforms, electrochemical systems exhibit additional tunability as separate  $H^+$  and  $e^-$  sources can be used rather than stoichiometric reducing agents (i.e.  $H_2$ ). This allows modulation of both the thermodynamics and the kinetics of a given reaction. For the examples discussed below, many perform electrolysis at constant potential. The ability to choose a specific potential for these reactions provides a precise control over driving force to a degree that is not feasible with chemical reductants which are limited to the inherent properties of the reductant. Alternatively, some examples also employ constant current electrolysis, favored by many for synthetic applications due to operational simplicity. As a final note, most of the examples utilizing this strategy employ comparatively abundant and inexpensive first row transition metals as opposed to expensive precious metal catalysts.<sup>13</sup>

There are several approaches to metal-ligand cooperativity in these processes, which are highlighted in Figure 3. Pendant or backbone amine groups can serve as proton/H-atom shuttles likely because they can be weakly basic and have relatively weak bond dissociation energies (BDEs) when coupled with a redox-active moiety. Furthermore, extensive p-conjugation using bipyridine and terpyridine ligands, among other scaffolds, stabilizes ligand-based radicals for metal-ligand cooperative redox transformations of a substrate.

As many electro-reductive transformations with added proton sources must compete with hydrogen evolution reactivity (HER), achieving good Faradaic efficiencies (FE) for targeted organic transformations requires minimization of this parasitic reaction. Several strategies using ligand design, choice of metal, acid  $pK_a$ , solvent, electrode material, and applied potential can be effective.<sup>14,15</sup>

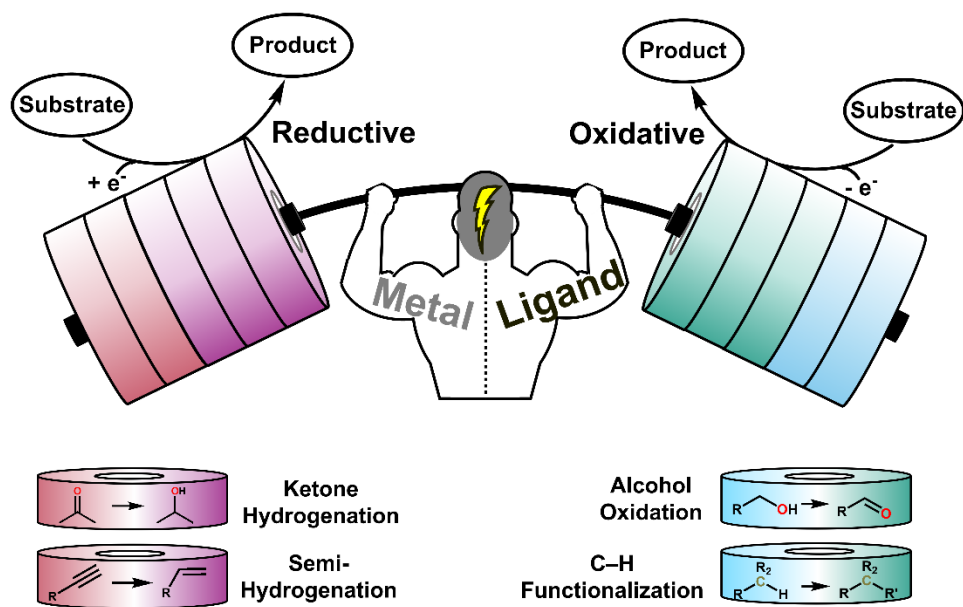


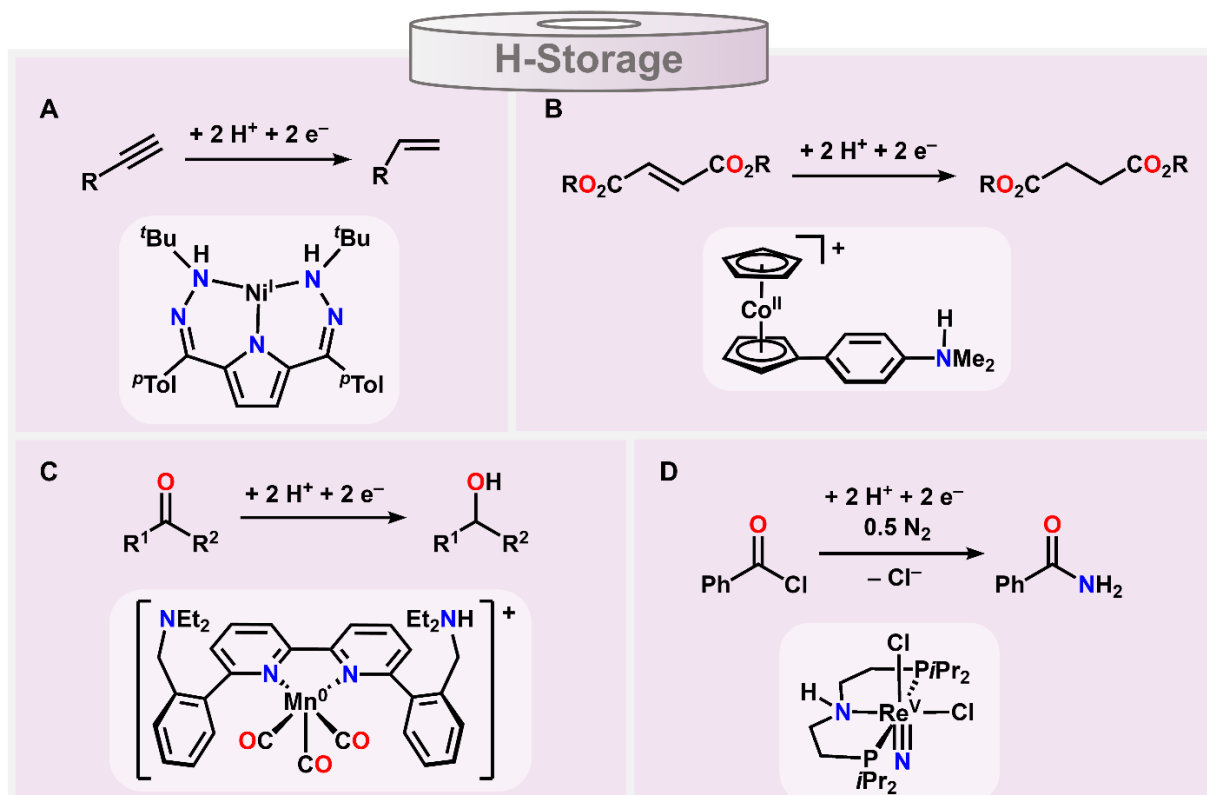
**Figure 3.** Overview showing the strength of metal-ligand cooperativity in leveraging electrochemistry for electrosynthesis in both reductive and oxidative reactivity. Some commonly catalyzed reactions are shown as examples.

These strategies are highlighted below and manage to effectively dampen HER and direct reducing H-atom equivalents towards a desired substrate.

### REDUCTIVE ELECTROSYNTHESIS WITH METAL-LIGAND COOPERATIVITY

Transformations such as ketone reduction to alcohols and alkene/alkyne hydrogenation have been demonstrated to proceed electrochemically using catalysts that can store an H-atom ( $H^+ + e^-$ ).<sup>16,17,18</sup> Installing pendant amine arms in the secondary coordination sphere of an *o*-substituted bipyridine ligand facilitates proton transfer from the ligand to a Mn center upon one-electron reduction to yield a Mn–H complex (proposed intermediate shown in **Scheme 1C**). Here, it is likely that the well-precedented redox non-innocence of the bipyridine scaffold plays an important role. Electrochemical evidence for this ligand-assisted proton transfer comes in the form of an irreversible pre-wave before the catalytic reductive feature in the cyclic voltammogram (CV). This

**Scheme 1.** Reductive electrocatalytic transformations enabled by catalysts with ligand-based H-storage. Isolable (D) and transient (A, B, C) intermediate structures from the proposed catalytic cycles are depicted to highlight the properties of each ligand.



feature is proposed to correspond to the formation of a Mn-H intermediate from a reduced, arm-protonated Mn complex. Supporting this proposal, the peak current for the pre-wave increases when titrating additional acid. The Mn-H species cannot form in the presence of H<sub>2</sub> alone, which highlights the unique thermodynamic advantage of having separate H<sup>+</sup> + e<sup>-</sup> sources in an electrochemical set-up. The authors were able to favor ketone hydrogenation over H<sub>2</sub> evolution by using a weaker acid (TFE) and achieved an FE of 80% for *iso*-propanol formation from acetone.

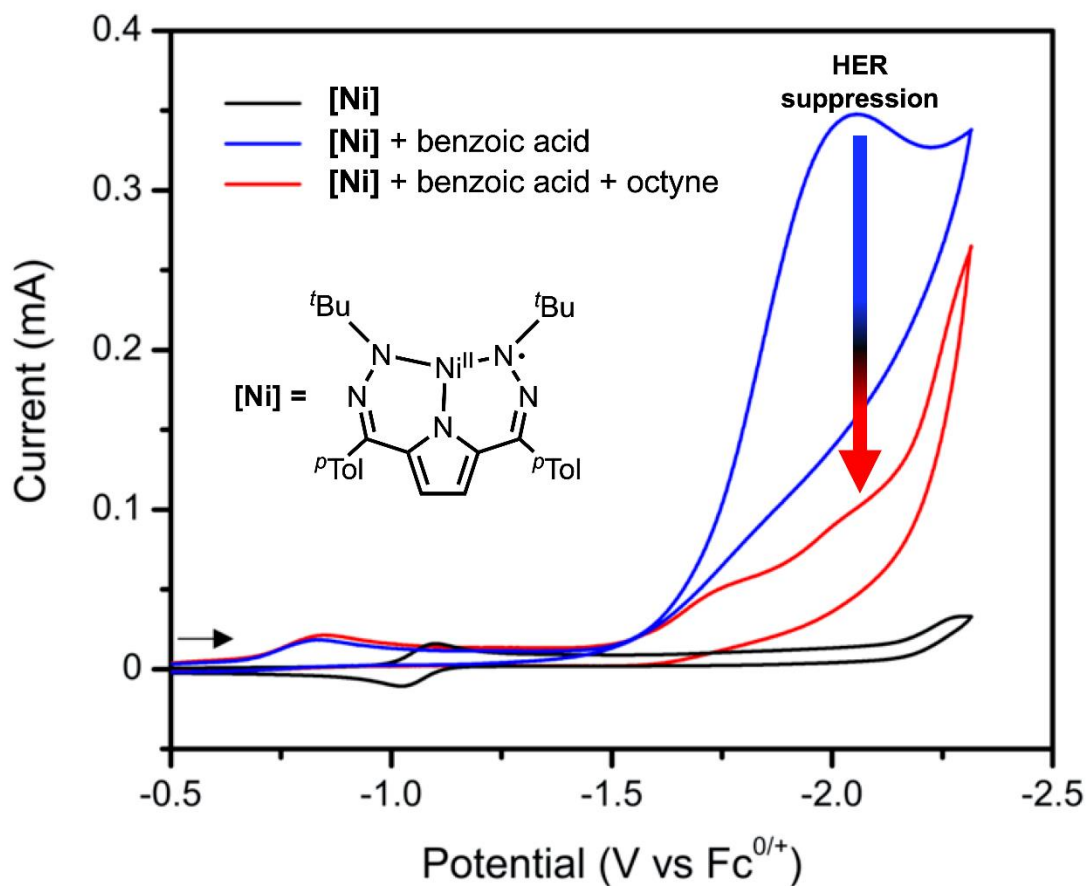
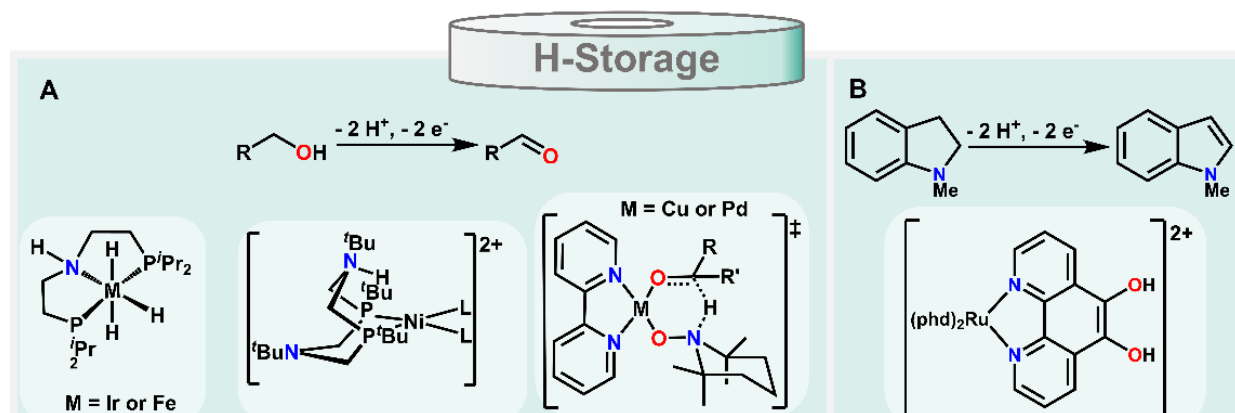


**Figure 4.** CV of (<sup>tBu,Tol</sup>DHP)Ni ([Ni], 1 mM) with added benzoic acid (10 mM), and with 1-octyne (10 mM) showing suppression of HER current upon the addition of substrate. 0.1 M TBAPF<sub>6</sub> in MeCN, 100 mV s<sup>-1</sup>. (adapted with permission)

Ligand design can also be employed to minimize undesired HER. In the case of a cobaltocenium-dimethylaniline complex, the phenyl ring spacer decouples the redox and proton transfer sites on the mediator, inhibiting HER while still enabling reactivity with a substrate (putative intermediate shown in **Scheme 1B**). No substrate binding is observed experimentally or computationally to the Co center. However, DFT calculations predict that ligand templating with the electron-withdrawing groups on the olefin substrate is critical for selectivity. The ester substituents are predicted to p-stack with the cyclopentadienyl ligand to stabilize the anionic intermediate and

**Scheme 2.** Organometallic Complexes with H-atom Storing Ligands Utilized in Metal-Cooperative Oxidative Electrocatalysis. Isolable (A, B) intermediate structures, as well as one transition state (A), from the proposed catalytic cycles are depicted to highlight the properties of each ligand.



prevent dimerization. The ease of H-atom transfer from the mediator to a substrate is also enabled by the weak bond dissociation free energy (BDFE) of 39 kcal/mol for the N–H bond.

Recently, our group has investigated the electrocatalytic semi-hydrogenation reactivity of a three-coordinate Ni complex with a ligand that stores 2 H-atom ( $\text{H}^+ + \text{e}^-$ ) equivalents (putative intermediate shown in **Scheme 1A**). A transient highly active Ni(I) species is generated at reducing potentials which can engage in reactivity. While this complex can react with  $\text{H}_2$  in its oxidized form, the resulting Ni(II) complex is less reducing than the electro-generated species and reacts sluggishly with H-atom acceptor substrates.<sup>19</sup> Analysis of CV studies shows that the catalytic HER wave is suppressed and altered in waveform by the addition of an alkyne substrate, indicating a change in reactivity (**Figure 4**). As might be expected from the CV experiments, the FE for alkene formation is close to 50% for several substrates. Importantly, these results demonstrate that even catalysts competent for HER can be used for other reductive processes if substrate binding and reduction are kinetically competitive.

In addition to multiple thermal examples of metal-ligand cooperativity using unsaturated PNP pincer ligands, this ligand scaffold also enables electrocatalysis. A rhenium PNP complex was shown to both activate  $N_2$  and facilitate a reductive N transfer (isolated intermediate shown in **Scheme 1D**).<sup>20</sup> A benzoyl chloride substrate was converted to benzamide, and equal yields of benzonitrile and benzoic acid. Combining an applied potential along with 2,6-dichlorophenol enables ligand reduction to turn over the catalytic cycle. This example highlights how the adoption of electrochemistry in a multi-step cycle or synthesis can provide a selective and efficient means to achieve a reductive transformation.

## **OXIDATIVE ELECTROSYNTHESIS WITH METAL-LIGAND COOPERATIVITY**

H-storing metal-cooperative ligands figure prominently in both alcohol oxidation reactivity as well as dehydrogenative systems. These motifs are often invoked or demonstrated to store, transfer, or release H-atom equivalents. Notably, most of the examples utilizing H- storing ligands are also amenable to use with first-row metals.

One important sub-category of oxidative electrocatalysis is alcohol oxidation. Particularly prominent work has been done with aminoxyl radicals, such as (2,2,6,6-tetramethylpiperidin-1-yl)oxyl (TEMPO), under both metal-free and metal containing conditions (**Scheme 2A**).<sup>21,22,23,24</sup> This alcohol oxidation catalysis goes through the transition state shown as the final part of **Scheme 2A**, and the established mechanism for this reaction (**Figure 5B**) utilizes the H-atom accepting nature of TEMPO to work cooperatively with a  $Cu^{2+}$  to  $Cu^{1+}$  redox cycle to engender two-electron chemistry similar to that more typical for second and third row metals. There has also been important systematic work to standardize and compare various alcohol oxidation electrocatalysts, creating a cohesive arc across systems with a variety of metals and ligands (**Scheme 2A, 2C, Figure 5**).<sup>21-25</sup>

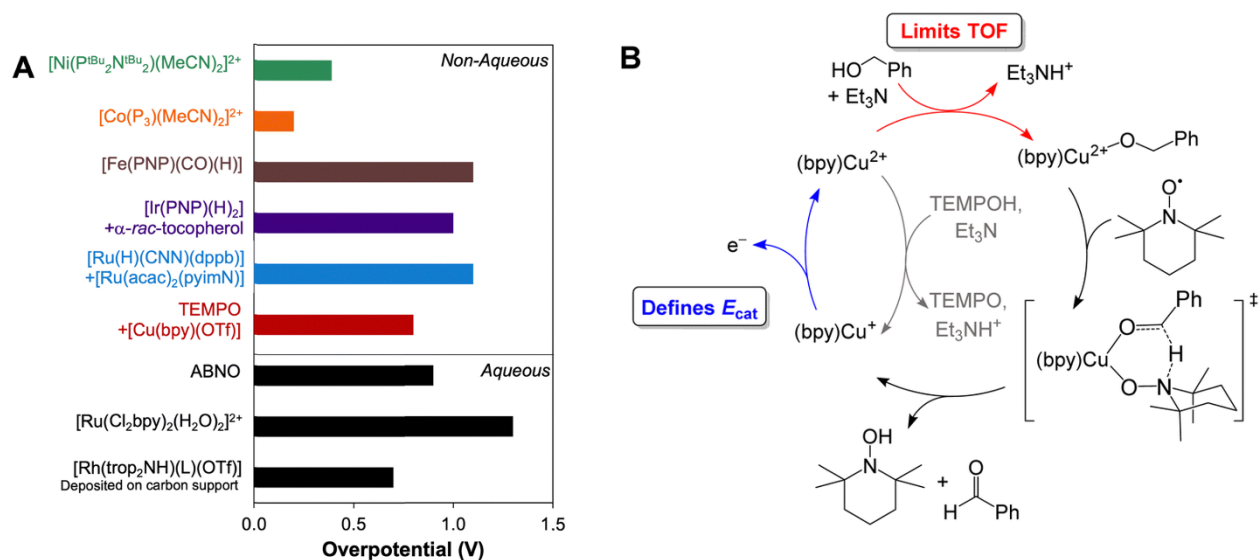


**Figure 5.** (A) Comparison between alcohol oxidation overpotentials. (B) Mechanism for Cu/bpy/TEMPO alcohol oxidation catalysis. Reproduced from ref. 22 with permission from the Royal Society of Chemistry.

As one interesting observation, we note that HER catalysts have been shown to be particularly promising for oxidative organic electrochemical applications. This is true even for some catalysts with comparatively poor activity, demonstrating how electrochemistry can repurpose systems for alternative productive reactivity in direct organic transformations. The first two complexes shown in **Scheme 2A**— $[\text{M}(\text{PNP})(\text{H})_2]$  ( $\text{M} = \text{Fe}$  or  $\text{Ir}$ ) and  $[\text{Ni}(\text{P}^{\text{iBu}}_2\text{N}^{\text{iBu}}_2)(\text{MeCN})_2][\text{BF}_4]_2$ —are hydrogen evolution catalysts that are also active for alcohol oxidation chemistry.<sup>21</sup> The activity of these complexes has been compared with other systems, including catalysts both with and without metal-ligand cooperativity, particularly in comparison to the above-mentioned TEMPO system. The utility of a ligand which can cooperatively store protons and electrons is evident from comparing catalyst overpotentials (**Figure 5A**).<sup>22</sup> The Ni complex with a proton-transferring ligand is a particularly good example of how first-row metals can have their reactivity expanded with multifunctional ligands.

A proton-transferring Rh system mounted on a carbon-support is also capable of directly oxidizing ethanol to acetate bypassing intermediate oxidation products.<sup>26</sup> Another example of oxidative electrocatalysis includes dehydrogenation using a H-atom storing Ru complex (**Scheme 2B**). Here, a 1,10-phenanthroline-5,6-dione (phd) ligand accepts H<sub>2</sub> while oxidizing N-substituted indoline substrates. An electrocyclic hydroxide transfer is invoked in this mechanism, and this catalyst exhibits broad substrate scope including indolines, other amines, and even some non-heterocyclic structures.<sup>24, 27</sup>

## CONCLUSIONS

Metal-ligand cooperativity is a powerful strategy in thermal catalysis. This approach provides avenues to facilitate the transfer of protons and electrons to a given substrate, and also enables the stabilization of more oxidized or reduced species. These benefits can be particularly important for first row metals where redox-active ligands can facilitate 2-electron pathways usually reserved for the less abundant second- and third-row metals.

While the benefits of metal-ligand cooperativity are well-established in thermal catalysis, the application of this strategy is much less explored in the context of electrosynthesis, particularly for mid-scale chemical synthesis or modifications beyond renewable fuel generation. Still, there are several examples which illustrate the utility of metal-ligand cooperativity in electrosynthesis. Specific themes include using redox-active or proton/H-atom storing ligands to change product selectivity or tune FE's against parasitic reactions such as HER. In general, development of electrocatalytic methods with high selectivity can be a complementary addition to thermal, photochemical, or other types of catalysis. Generally, while leveraging ligand-based storage of protons and electrons is still a nascent area, the above examples demonstrate that this strategy enables the transfer of multiple proton and electron equivalents in stoichiometric and catalytic

systems. The future of this field lies in moving beyond proof-of-concept by tuning and controlling these intricate systems to take advantage of their unique flexibility with challenging substrate targets.

## References

1. Charette, B. J. et al., Exploring Ligand-Centered Hydride and H-Atom Transfer. *Inorg. Chem.* **2021**, *60* (7), 5367-5375.
2. Chang, M.-C. et al. Reversible homolytic activation of water via metal–ligand cooperativity in a T-shaped Ni(II) complex. *Chem. Sci.* **2019**, *10* (5), 1360-1367.
3. Myers, T. W. et al. Aluminum –Ligand Cooperative N–H Bond Activation and an Example of Dehydrogenative Coupling. *J. Am. Chem. Soc.* **2013**, *135* (27), 9988-9990.
4. Cheung, P. M. et al., Hemilabile Proton Relays and Redox Activity Lead to {FeNO}<sub>xx</sub> and Significant Rate Enhancements in NO<sub>2</sub>- Reduction. *J. Am. Chem. Soc.* **2018**, *140*, 49, 17040-17050.
5. Chaudhuri, P. et al. Aerobic Oxidation of Primary Alcohols (Including Methanol) by Copper(II)– and Zinc(II)–Phenoxy Radical Catalysts. *J. Am. Chem. Soc.* **1999**, *121* (41), 9599-9610.
6. Horak, K. T. et al. Dioxygen Reduction by a Pd(0)–Hydroquinone Diphosphine Complex. *J. Am. Chem. Soc.* **2016**, *138* (10), 3443-3452.
7. Karbalaei, S. et al. A Macrocyclic Ligand Framework That Improves Both the Stability and T1-Weighted MRI Response of Quinol-Containing H<sub>2</sub>O<sub>2</sub> Sensors. *Inorg. Chem.* **2021**, *60* (12), 8368-8379.
8. McNeece, A. J. et al. Catalytic hydrogenation enabled by ligand-based storage of hydrogen. *Chem. Comm.* **2021**, *57* (32), 3869-3872.
9. Pramanick, R. et al. An Azoaromatic Ligand as Four Electron Four Proton Reservoir: Catalytic Dehydrogenation of Alcohols by Its Zinc(II) Complex. *Inorg. Chem.* **2018**, *57* (12), 6816-6824.
10. Sinha, S. et al. Cobalt complexes of redox noninnocent azo-aromatic pincers. Isolation, characterization, and application as catalysts for the synthesis of quinazolin-4(3H)-ones. *Dalton Trans.* **2020**, *49* (25), 8448-8459.
11. Rodríguez-Lugo, R. E. et al. A homogeneous transition metal complex for clean hydrogen production from methanol–water mixtures. *Nature Chem.* **2013**, *5* (4), 342-347.
12. Käß, M. et al. Ruthenium Complexes with Cooperative PNP Ligands: Bifunctional Catalysts for the Dehydrogenation of Ammonia–Borane. *Angew. Chem., Int. Ed.* **2019**, *48* (5), 905-907.
13. a) Suryanarayanan, V.; Noel, M., A comparative evaluation on the voltammetric behavior of boron-doped diamond (BDD) and glassy carbon (GC) electrodes in different electrolyte media. *Journal of Electroanalytical Chemistry* **2010**, *642* (1), 69-74.; b) Fokin, I.; Kuessner, K.-T.; Siewert, I., Electroreduction of Carbonyl Compounds Catalyzed by a Manganese Complex. *ACS Catal.* **2022**, *12* (14), 8632-8640.; c) Derosa, J.; Garrido-Barros, P.; Peters, J. C., Electrocatalytic Reduction of C–C  $\pi$ -Bonds via a Cobaltocene-Derived Concerted Proton–Electron Transfer Mediator: Fumarate Hydrogenation as a Model Study. *J. Am. Chem. Soc.* **2021**, *143* (25), 9303-9307.; d) Czaikowski, M. E.; Anferov, S. W.; Tascher, A. P.; Anderson, J. S., Electrocatalytic Semihydrogenation of Terminal Alkynes Using Ligand-Based Transfer of Protons and Electrons. *J. Am. Chem. Soc.* **2024**, *146* (1), 476-486.; e) McNeece, A. J.; Jesse, K. A.; Filatov, A.

- S.; Schneider, J. E.; Anderson, J. S., Catalytic hydrogenation enabled by ligand-based storage of hydrogen. *Chem. Commun.* **2021**, *57*, 3869-3872.; f) Badalyan, A.; Stahl, S. S., Cooperative electrocatalytic alcohol oxidation with electron-proton-transfer mediators. *Nature* **2016**, *535* (7612), 406-410.; g) Speelman, A. L.; Gerken, J. B.; Heins, S. P.; Wiedner, E. S.; Stahl, S. S.; Appel, A. M. Determining overpotentials for the oxidation of alcohols by molecular electrocatalysts in non-aqueous solvents. *Energy & Environmental Science*, 2022, *10*.; h) Bruns, D. L.; Stahl, S. S. Thermodynamic–Kinetic Comparison of Palladium(II)-Mediated Alcohol and Hydroquinone Oxidation. *Organometallics* 2022, *41*, 22, 3161–3166.; i) Stamoulis, A. G.; Bruns, D. L.; Stahl, S. S. Optimizing the Synthetic Potential of O<sub>2</sub>: Implications of Overpotential in Homogeneous Aerobic Oxidation Catalysis. *J. Am. Chem. Soc.* **2023**, *145*, 17515.; j) Ozawa, H.; Hino, T.; Ohtsu, H.; Wada, T.; Tanaka, K., A new type of electrochemical oxidation of alcohols mediated with a ruthenium–dioxolene–amine complex in neutral water. *Inorganica Chim. Acta* **2011**, *366* (1), 298-302.; k) Bevilacqua, M.; Bianchini, C.; Marchionni, A.; Filippi, J.; Layacchi, A.; Miller, H.; Oberhauser, W.; Vizza, F.; Granozzi, G.; Artiglia, L.; Annen, S. P.; Krumeich, F.; Grützmacher, H. Improvement in the efficiency of an Organometallic Fuel Cell by tuning the molecular architecture of the anode electrocatalyst and the nature of the carbon support. *Energy Environ. Sci.*, **2012**, *5*, 8608-8620.; l) Li, B.; Wendlandt, A. E.; Stahl, S. S. Replacement of Stoichiometric DDQ with a Low Potential o-Quinone Catalyst Enabling Aerobic Dehydrogenation of Tertiary Indolines in Pharmaceutical Intermediates. *Org. Lett.* **2019**, *21*, 4, 1176-1181.
14. Rountree, E. S.; McCarthy, B. D.; Eisenhart, T. T.; Dempsey, J. L., Evaluation of Homogeneous Electrocatalysts by Cyclic Voltammetry. *Inorganic Chemistry* **2014**, *53* (19), 9983-10002.
15. Suryanarayanan, V.; Noel, M., A comparative evaluation on the voltammetric behavior of boron-doped diamond (BDD) and glassy carbon (GC) electrodes in different electrolyte media. *Journal of Electroanalytical Chemistry* **2010**, *642* (1), 69-74.
16. Fokin, I.; Kuessner, K.-T.; Siewert, I., Electroreduction of Carbonyl Compounds Catalyzed by a Manganese Complex. *ACS Catal.* **2022**, *12* (14), 8632-8640.
17. Derosa, J.; Garrido-Barros, P.; Peters, J. C., Electrocatalytic Reduction of C–C  $\pi$ -Bonds via a Cobaltocene-Derived Concerted Proton–Electron Transfer Mediator: Fumarate Hydrogenation as a Model Study. *J. Am. Chem. Soc.* **2021**, *143* (25), 9303-9307.
18. Czaikowski, M. E.; Anferov, S. W.; Tascher, A. P.; Anderson, J. S., Electrocatalytic Semihydrogenation of Terminal Alkynes Using Ligand-Based Transfer of Protons and Electrons. *J. Am. Chem. Soc.* **2024**, *146* (1), 476-486.
19. McNeece, A. J.; Jesse, K. A.; Filatov, A. S.; Schneider, J. E.; Anderson, J. S., Catalytic hydrogenation enabled by ligand-based storage of hydrogen. *Chem. Commun.* **2021**, *57*, 3869-3872.
20. Schendzielorz, F.; Finger, M.; Abbenseth, J.; Würtele, C.; Krewald, V.; Schneider, S., Metal-Ligand Cooperative Synthesis of Benzonitrile by Electrochemical Reduction and Photolytic Splitting of Dinitrogen. *Angew. Chem. Int. Ed.* **2019**, *58* (3), 830-834.
21. Badalyan, A.; Stahl, S. S., Cooperative electrocatalytic alcohol oxidation with electron-proton-transfer mediators. *Nature* **2016**, *535* (7612), 406-410.;
22. Speelman, A. L.; Gerken, J. B.; Heins, S. P.; Wiedner, E. S.; Stahl, S. S.; Appel, A. M. Determining overpotentials for the oxidation of alcohols by molecular electrocatalysts in non-aqueous solvents. *Energy & Environmental Science*, 2022, *10*
23. Bruns, D. L.; Stahl, S. S. Thermodynamic–Kinetic Comparison of Palladium(II)-Mediated Alcohol and Hydroquinone Oxidation. *Organometallics* 2022, *41*, 22, 3161–3166.

24. Stamoulis, A. G.; Bruns, D. L.; Stahl, S. S. Optimizing the Synthetic Potential of O<sub>2</sub>: Implications of Overpotential in Homogeneous Aerobic Oxidation Catalysis. *J. Am. Chem. Soc.* **2023**, *145*, 17515.
25. Ozawa, H.; Hino, T.; Ohtsu, H.; Wada, T.; Tanaka, K., A new type of electrochemical oxidation of alcohols mediated with a ruthenium–dioxolene–amine complex in neutral water. *Inorganica Chim. Acta* **2011**, *366* (1), 298-302.;
26. Bevilacqua, M.; Bianchini, C.; Marchionni, A.; Filippi, J.; Layacchi, A.; Miller, H.; Oberhauser, W.; Vizza, F.; Granozzi, G.; Artiglia, L.; Annen, S. P.; Krumeich, F.; Grützmacher, H. Improvement in the efficiency of an OrganoMetallic Fuel Cell by tuning the molecular architecture of the anode electrocatalyst and the nature of the carbon support. *Energy Environ. Sci.*, **2012**, *5*, 8608-8620
27. Li, B.; Wendlandt, A. E.; Stahl, S. S. Replacement of Stoichiometric DDQ with a Low Potential o-Quinone Catalyst Enabling Aerobic Dehydrogenation of Tertiary Indolines in Pharmaceutical Intermediates. *Org. Lett.* **2019**, *21*, 4, 1176-1181.
-



# Chapter II: Cobalt-Catalyzed Hydrogenation Reactions Enabled by Ligand-Based Storage of Dihydrogen

*Starting at the Very Beginning: With Hydrogen*

This chapter has been adapted from the following: Anferov, S. W.; Filatov, A. S.; Anderson, J. S. *ACS Catal.* **2022**, *12*, 16, 9933.

## Introduction

As discussed in the previous chapter, The efficient shuttling of protons and electrons is key for many chemical transformations. Metal centers are often employed to facilitate this reactivity, but multi-proton/electron transformations remain challenging, particularly with abundant first-row transition metals with predominant one-electron reactivity.<sup>1</sup> Natural

systems have evolved to optimize the use of first-row metals by leveraging a secondary coordination sphere tailored to the needs of a given reaction.<sup>2</sup> Given that the number of protons and electrons stored in the secondary coordination sphere is, in principle, only limited by ligand

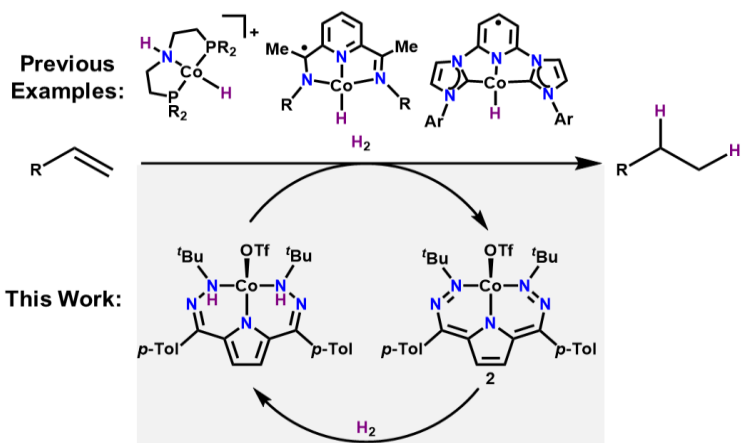
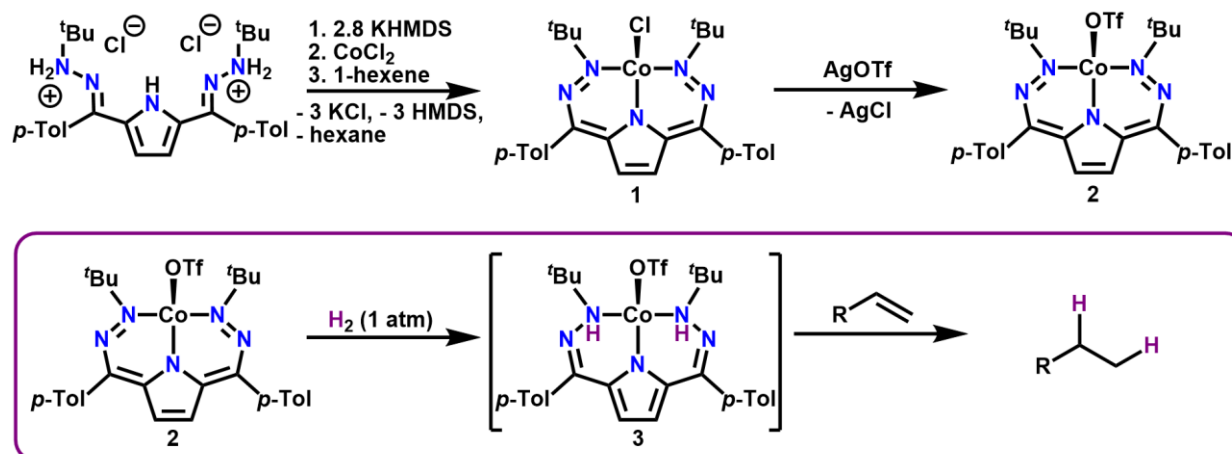


**Figure 1.** Existing Co-based hydrogenation catalysts or active species<sup>12ce,15a; 14abde</sup> and the current system highlighting ligand-based H<sub>2</sub> storage.

**Scheme 2.** Synthesis of <sup>t</sup>Bu,<sup>Tol</sup>DHP complexes of Co and hydrogenation reactivity.



design, this strategy also opens the door for challenging reactions requiring the transfer of many proton and electron equivalents.

Common secondary sphere motifs utilized in synthetic systems include hydrogen bonding ligands,<sup>3</sup> proton-shuttling functionalities,<sup>4</sup> and redox-active sites that enable electron storage and transfer.<sup>5</sup> Significant effort over the past few decades has illustrated the value of these strategies in facilitating or altering reactivity patterns, but examples where both protons and electrons can be stored on ancillary ligands are comparatively less common. There are several well-defined systems that store H-atom equivalents,<sup>6</sup> and examples of the storage of a full equivalent of dihydrogen in a ligand backbone are even more rare.<sup>7,8</sup> Despite their scarcity, such ligand scaffolds are promising candidates to efficiently facilitate challenging multi-proton/electron transfers in catalysis.

Our laboratory has been interested in first-row transition metal complexes ligated by dihydrazonopyrrole (DHP) ligands. These complexes can reversibly transfer dihydrogen stored on the ligand framework, which enables the catalytic hydrogenation of benzoquinone in a Ni-based system.<sup>9,10</sup> Related Fe complexes are also able to transfer H-atoms to O<sub>2</sub> to generate hydroperoxo intermediates and ultimately H<sub>2</sub>O<sub>2</sub> using ligand-derived H-atom equivalents.<sup>11</sup> We rationalized that striking a balance between redox and spin-state flexibility, as present with Fe complexes, and

more classic organometallic metals, such as Ni, might be advantageous for new catalytic transformations.<sup>10,11</sup>

In this context, Co features prominently among first-row transition metals in hydrogenation catalysis. Unlike Rh and Ir, Co does not necessarily proceed through classical two-electron transformations and, as with other first-row transition metals, exhibits a propensity for single-electron steps and varied spin states.<sup>12-14</sup> These alternative trends can also be leveraged to obtain altered reactivity. For instance, recent reports have illustrated how Co complexes with ligands that can store protons or electrons can efficiently mediate catalytic hydrogenations, with some

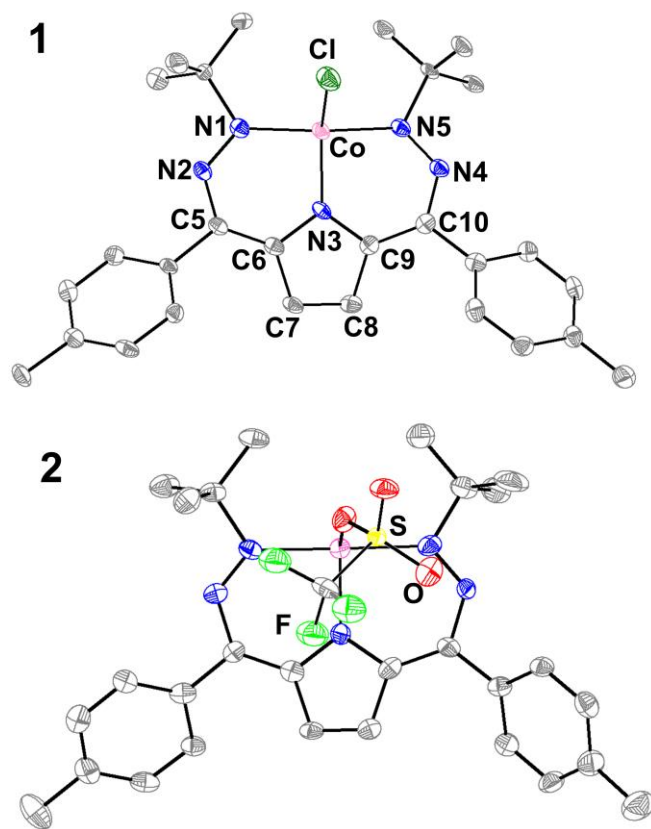


**Figure 2.** SXRDR Structures (from left to right) of **1** and **2**. All displacement ellipsoids shown at 50% and hydrogens omitted for clarity.

examples exhibiting alternative mechanistic pathways in the presence of light (**Figure 1**).<sup>12,14</sup>

Given this precedent for Co in hydrogenation chemistry and the opportunities that it presents as a first-row metal, we were interested in examining the interplay between Co centers and DHP ligands in H-transfer chemistry. Specifically, we sought to investigate whether Co DHP complexes were viable hydrogenation catalysts and, if so, whether the DHP ligand would enable alternative mechanisms to more canonical organometallic pathways.<sup>12-14</sup>

Here, we present a series of *t*Bu,TolDHP Co related Ni complexes

catalysts that mediate olefin hydrogenation via a ligand-assisted hydrogenation pathway. Catalysis occurs efficiently under mild conditions, comparable with the best Co hydrogenation catalysts currently known.<sup>14e</sup>

<sup>15</sup> Spectroscopic, computational, and mechanistic investigations demonstrate that catalysis proceeds via a radical H-atom transfer mechanism supported by the *t*Bu,TolDHP ligand. These results

illustrate how cooperativity

between Co centers and ligands which can store H-atom or H<sub>2</sub> equivalents enables efficient catalysis with novel mechanistic paradigms.

## Results and Discussion

**Table 1.** Selected bond lengths (Å) and angles (°) of **1**, **2**, and

	<b>1</b>	<b>2</b> *	[DHP <sup>2-</sup> ]NiL <sup>9a</sup>	[DHP <sup>-</sup> ]NiL <sup>+9a</sup>
M-N1/M-N5	1.891(5)	1.994(8)	1.866(2)	1.864(2)
	1.883(4)	2.000(8)	1.863(2)	1.860(2)
M-N3	1.861(4)	1.916(8)	1.872(2)	1.869(2)
N1-N2/ N4-N5	1.303(6)	1.27 (1)	1.342(2)	1.302(2)
	1.288(6)	1.25(1)	1.337(3)	1.314(2)
M-X(Cl/O/P)	2.198(2)	2.168(7)	2.2319(7)	2.2630(7)
M-X(N/O)	--	2.126(7)	--	--
N2-C5/ N4-C10	1.343(7)	1.37(1)	1.319(3)	1.348(2)
	1.338(7)	1.39(1)	1.322(2)	1.342(3)
C5-C6/ C9-C10	1.383(8)	1.38 (1)	1.417(3)	1.388(3)
	1.388(8)	1.38(1)	1.425(3)	1.393(3)
C6-C7/ C8-C9	1.434(8)	1.43(1)	1.413(3)	1.444(3)
	1.433(8)	1.45(1)	1.421(3)	1.452(3)
C7-C8	1.351(8)	1.31(1)	1.371 (3)	1.343 (3)
N1-M-N5	164.5(2)	178.1(3)	163.59(8)	161.85(7)
N3-M-X	129.1(2)	113.2(3)	145.30(6)	142.64(5)
		105.1(3)		

\*Crystallizes as polymeric chain, monomer shown. L = PMe<sub>3</sub> as described in the text.

## Synthesis and Characterization of **1**

Deprotonation of  $t^{\text{Bu,Tol}}\text{DHP}\cdot 2\text{HCl}^{9\text{c}}$  with 2.8 equiv of KHMDS followed by the rapid addition of a  $\text{CoCl}_2$  suspension in THF and a single equivalent of 1-hexene (acting as a  $\text{H}_2$  acceptor) provides  $[t^{\text{Bu,Tol}}\text{DHP}]\text{CoCl}$  (**1**) as a magenta-purple solid in 75%

yield (**Scheme 1**). We note this reaction still provides **1** as the major product in the absence of 1-hexene as a  $\text{H}_2$  acceptor, albeit in lower yields. Dark purple crystals suitable for single-crystal X-ray diffraction (SXRD) reveal a four-coordinate Co complex.

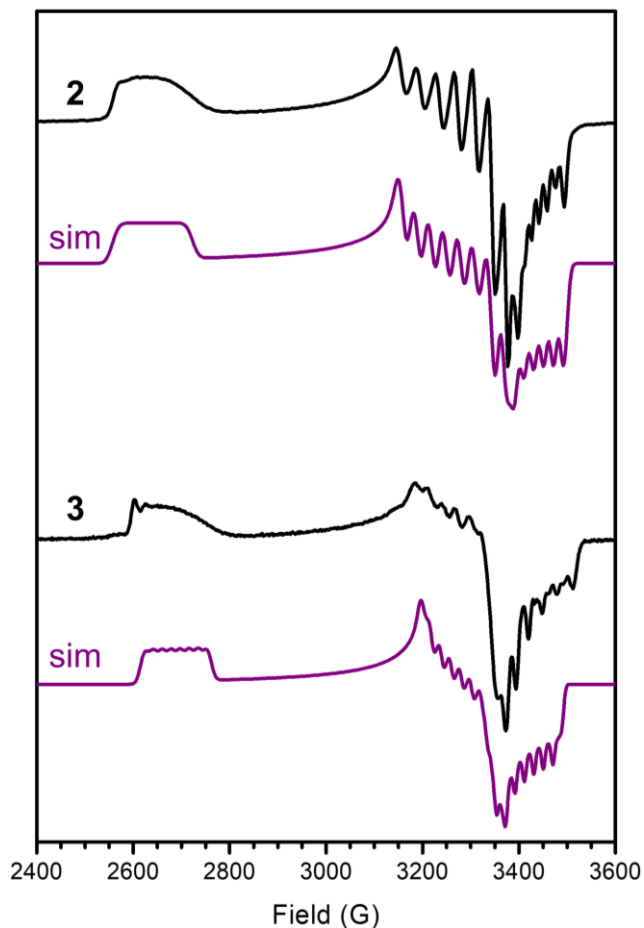


**Figure 3.** Perpendicular mode X-band EPR spectrum from top to bottom of 15 mM solutions of **2** and **3** at 15.9 K in toluene and 20 K in toluene respectively. Simulation shown in black lines for each. Simulation parameters for: **2**:  $g = 2.01, 2.11, 2.61$ ; Co-A = +56.5, +89.0, +75.6 MHz; N-A = +12.1, +5.9, +11.2 MHz. **3**:  $g = 2.02, 2.10, 2.56$ ; Co-A = +54.8, +61.0, +66.8 MHz, N-A = +23.1, +24.5, -14.1 MHz. Experimental conditions: microwave frequency 9.6304 GHz, microwave power 0.2 mW. The full and simulated spectra are shown in the SI (Appendix I: **Figure S21-S27, Table S1**).

The geometry of **1** can be quantified with  $\tau_4$  and  $\tau_4'$  values of 0.473 and 0.363, respectively, suggesting a see-saw complex with some tetrahedral character (**Figure 2** and **Table 1**).<sup>16</sup> Complex **1** is paramagnetic with an  $S = 1/2$  solution spin state as determined by Evans' method. This suggests either a low-spin Co(II) center with a DHP<sup>-</sup> ligand or a Co(III) center with a DHP<sup>2-</sup> ligand radical. We note that there are several examples of low-spin Co(II) complexes in similar geometries, including a number of imino-pyridine ligated Co(II) complexes as well as Co porphyrin and corrin species.<sup>17,18, 21</sup>

The structure of **1** provides the opportunity to examine limiting electronic structures. We have found that the electronic structure of the DHP ligand results in changes to specific bonds in the scaffold in a diagnostic manner, namely, the N1-N2/N4-N5, C5-C6/C9-C10, and C7-C8 distances.<sup>9,10</sup> Comparison of these distances between **1** and the previously reported four-coordinate Ni complexes [<sup>Ph,Tol</sup>DHP]NiPMe<sub>3</sub><sup>n+</sup> ( $n = 0$  and  $1$ ) suggests that the DHP ligand in **1** is best considered as a closed-shell monoanionic DHP<sup>-</sup> unit, thereby implying a Co(II) oxidation state.<sup>9a</sup> However, this interpretation is convoluted by the differing metal centers and ligand sets in this comparison.

Complex **1** displays four distinct redox waves in its cyclic voltammogram (CV, Appendix I: **Figure S19**). This electrochemical data shows that the <sup>tBu,Tol</sup>DHP scaffold supports unusually rich redox flexibility in this system. Despite this, complex **1** does not exhibit discernible reactivity with H<sub>2</sub>. We hypothesized that the exchange of chloride for a less-coordinating anion could promote reactivity with H<sub>2</sub> and potentially catalysis.

### Synthesis and Characterization of **2**

Complex **1** reacts with AgOTf in a mixture of benzene/acetonitrile to produce [<sup>tBu,Tol</sup>DHP]CoOTf (**2**) as a maroon solid (**Scheme 1**). Similar to **1**, complex **2** is also paramagnetic

with an  $S = 1/2$  spin state as determined by Evans' method. SXRD analysis on the very dark crystals of **2** reveals a Co center that is five-coordinate due to the formation of a polymeric chain from bridging OTf<sup>-</sup> ligands in the solid state. The  $\tau_5$  value for this complex is 0.605, putting it closer to trigonal bipyramidal than square pyramidal (at 1 and 0, respectively).<sup>19</sup> Examination of the monomeric repeat unit of **2** reveals that the bond lengths within the DHP ligand undergo changes from those in **1**, which suggests a more distinctively oxidized DHP<sup>-</sup> ligand, and hence also a Co(II) oxidation state assignment (**Figure 1** and **Table 1**). The CV of **2** is qualitatively similar to that of **1**, albeit less reversible overall, likely due to enhanced lability of the OTf<sup>-</sup> counteranion (Appendix I: **Figure S20**).

We then acquired electron paramagnetic resonance (EPR) spectroscopy to better understand the relative electronic structures of complexes **1** and **2**. The EPR of **1** is rhombic, with  $g$ -values of 2.02, 2.10, and 2.58 (Appendix I: **Figures S21 and S22**). EPR spectra of organic radicals are typically more isotropic and with all  $g$ -values near  $g = 2.0$ , suggesting that a Co(II) electronic structure may be appropriate.<sup>20</sup> Indeed, literature examples where a five- or six-coordinate Co(III) center is bound to a ligand radical as well as previous examples with DHP radical ligands, namely, [<sup>*t*Bu,Tol</sup>DHP<sup>2•</sup>]<sup>-</sup>Ni and [<sup>Ph,Tol</sup>DHP<sup>2•</sup>]<sup>-</sup>Ni, all have smaller  $g$ -anisotropy than that of **1**, further supporting a [DHP<sup>-</sup>]Co(II) resonance structure.<sup>9a,9c,21</sup> While the greater  $g$ -anisotropy of **1** is different from low spin, square-planar cobalt complexes,<sup>22</sup> it is distinctly similar to related tetrahedral or see-saw complexes.<sup>23</sup> The best simulation we have obtained uses hyperfine coupling (MHz) to both <sup>59</sup>Co ( $A_{xx} = 57.6$ ,  $A_{yy} = 62.4$ ,  $A_{zz} = 58.8$ ) and <sup>14</sup>N ( $A_{xx} = 35.4$ ,  $A_{yy} = 44.7$ ,  $A_{zz} = 10.7$ ), although we note that the complicated pattern means that alternative spin systems, for instance, those with coupling to more than one <sup>14</sup>N nucleus, may also provide satisfactory fits. While the  $g$ -anisotropy and <sup>59</sup>Co hyperfine constants support a Co(II) oxidation

state, the large  $^{14}\text{N}$  hyperfine suggests that there is still significant spin on the DHP ligand. Density Functional Theory (DFT) calculations with the B3P functional support this notion. While the majority of the spin density is localized on Co, a significant fraction (30%) is present on the DHP ligand (Appendix I: **Figure S35**).

The EPR spectrum of **2** is similarly rhombic to that of **1** with  $g$ -values of 2.01, 2.11, and 2.61, and our best simulation similarly features coupling (MHz) to both  $^{59}\text{Co}$  ( $A_{xx} = 56.5$ ,  $A_{yy} = 89.0$ ,  $A_{zz} = 75.6$ ) and  $^{14}\text{N}$  ( $A_{xx} = 12.1$ ,  $A_{yy} = 5.9$ ,  $A_{zz} = 11.2$ ) (**Figure 3**). As with **1**, this data suggests that the best description of **2** is as a low-spin Co(II) center with an oxidized monoanionic  $^{\text{tBu,Tol}}\text{DHP}$  ligand. Consistent with the structural data above, the relative  $g$ -anisotropies and hyperfine constants between **1** and **2** both support that **2** is closer to a “pure” Co(II) resonance structure, although we note that DFT calculations still support some radical character on the DHP ligand (20%, Appendix I: **Figure S37**).

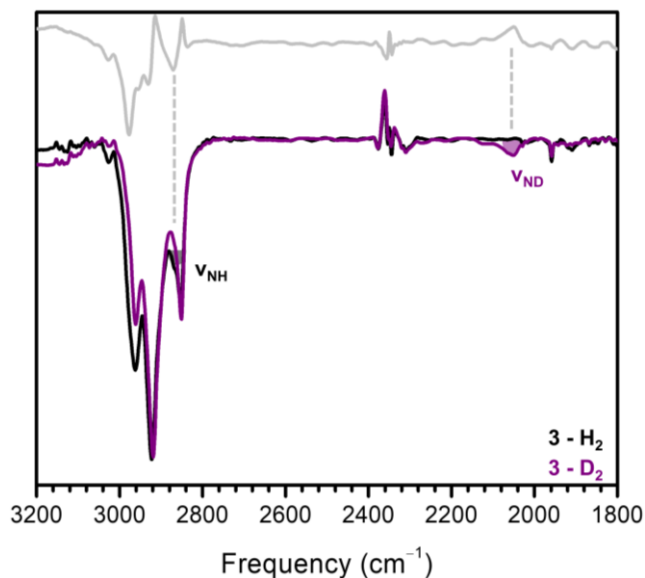


**Figure 4.** Thin Film IR spectrum of **3** and **3-D<sub>2</sub>** with difference spectrum inset.

As a final probe of electronic structure, we obtained Co K-edge X-ray absorption spectroscopy (XAS) data on both **1** and **2**. The pre-edge feature for **1** is only slightly shifted to higher energy from **2** by 0.4 eV (from 7709.3 to 7709.7 eV), which is at the experimental resolution, and the K-edges for these two complexes are also quite similar (Appendix I: **Figures S28 and S29**).<sup>24</sup> This data again supports similar electronic structures

between **1** and **2** and are consistent with other Co(II) complexes.<sup>14b, 25</sup> Thus, while the electronic structures of these complexes, particularly **1**, are highly covalent with reasonably invoked DHP non-innocence, the best limiting resonance contributor is [DHP<sup>-</sup>]Co(II).

### Generation and Characterization of **3**

While **1** shows no reactivity with H<sub>2</sub>, addition of H<sub>2</sub> to cold solutions of **2** results in a new magenta product (**3**) (**Scheme 1**). Complex **3** forms very slowly, taking over 48 h for complete conversion at -25 °C, and is unstable at and above 0 °C. The use of D<sub>2</sub> results in significantly slower conversion but still allows for the formation of enough **3-D<sub>2</sub>** for IR characterization (**Figure 4**). Though **3** is unstable to higher temperatures, it is stable to vacuum once formed.

The <sup>1</sup>H NMR spectrum of **3** is paramagnetic and broad (Appendix I: **Figure S2**). This is consistent with 2 e<sup>-</sup> reactivity with H<sub>2</sub>, and we have tentatively assigned **3** as the hydrogenated product, [<sup>t</sup>Bu,<sup>Tol</sup>DHP-H<sub>2</sub>]CoOTf, analogously to the reactivity observed with a related Ni system.<sup>10</sup> The EPR signal of **3** at 20 K further supports this assignment, with an observed major *S* = 1/2 signal along with a small amount (<10%) of unconverted **2** (**Figure 3**, bottom). Fitting of the major species reveals parameters that are quite similar to **1** and **2**, with *g*-values of 2.02, 2.10, and 2.56 and hyperfine coupling (MHz) to both <sup>59</sup>Co (*A<sub>xx</sub>* = 54.8, *A<sub>yy</sub>* = 61.0, *A<sub>zz</sub>* = 66.8) and <sup>14</sup>N (*A<sub>xx</sub>* = 23.1.645, *A<sub>yy</sub>* = 24.5, *A<sub>zz</sub>* = -14.1). Importantly, the EPR spectrum of **3** is less consistent with a Co-H assignment; inclusion of any significant hyperfine coupling to <sup>1</sup>H notably worsens the fit. The Co K-edge XAS data for **3** has the same 0.4 eV shift to lower energy versus **1**, which again supports a very similar Co oxidation state across these three compounds (Appendix I: **Figures S30 and S31**).

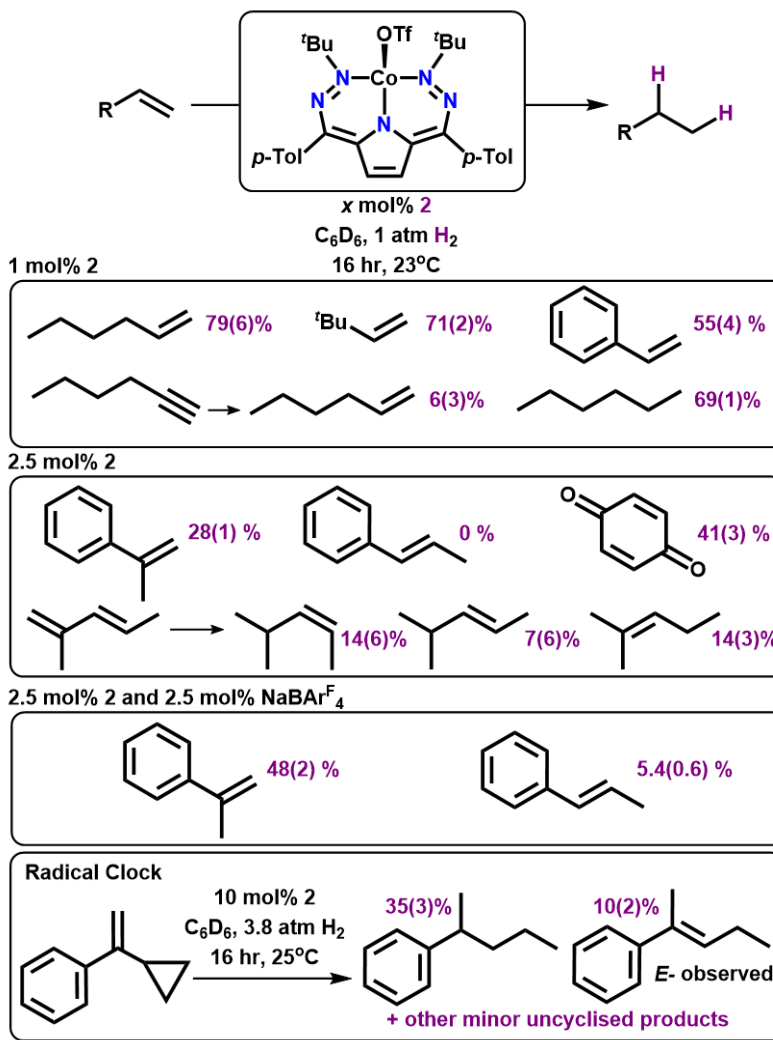
We then turned to verifying the presence and investigating the localization of the added protons from hydrogenation. Hydrogenated and deuterated samples were prepared at -25 °C in

minimal toluene over 48 or 72 h under  $\sim 3$  atm of  $H_2$  or  $D_2$ , respectively. These samples were kept cold throughout drying and sample preparation. Both mineral oil and thin-film IR samples reproducibly show a clear N–D stretch in the deuterated samples around  $2065\text{ cm}^{-1}$  (**Figure 4**, Appendix I: **Table S63 and eq S1**). The corresponding isotopically shifted feature is not immediately apparent in the spectrum of proteo-**3** due to convolution with C–H stretches, but a subtraction spectrum does indicate the presence of a feature underneath these other stretches at  $\sim 2870\text{ cm}^{-1}$  that is consistent with a N–H functionality and which closely corresponds to the DFT-predicted N–H stretch of  $2922\text{ cm}^{-1}$  (Appendix I: **Table S63**). This result confirms that the reactivity with  $H_2$  involves the formation of N–H's on the  $^{tBu,Tol}DHP$  ligand. As a final verification of the assigned structure of **3**, time-dependent DFT (TD-DFT) calculations were performed to compare the predicted and experimental UV–visible (UV–vis) spectra of **3**. The theoretical UV–vis spectrum of **3** using the PBE0 functional on the previously optimized geometry matches well with the experimental spectrum, further supporting our assignment (Appendix I: **Figure S87**).

## Hydrogenation Catalysis

Given the reactivity observed with dihydrogen to form **3**, we wanted to test if **2** could be used as a hydrogenation catalyst. Given its use in the synthesis of **1**, we initially chose 1-hexene as a test substrate under mild conditions (1 atm of H<sub>2</sub>, 23 °C). We observed 79(6)% conversion to hexane with 1% catalyst loading of **2** under these conditions, and thus we proceeded to investigate the scope of this reaction with other olefins (**Table 2**).

**Table 2.** Hydrogenation Substrate Scope with **2**



Terminal mono-substituted

olefins are all efficiently hydrogenated, even with comparatively large substrates; 3,3-dimethylbutene is hydrogenated in 71(2)% yield. Alkynes can also be reduced; hydrogenation of 1-hexyne with **2** provides hexane with 69(1)% yield and only 6(3)% of the singly hydrogenated product 1-hexene. A more moderate yield of 55(4)% is obtained with styrene.

Significantly attenuated yields are observed with more sterically encumbering substrates, such as  $\alpha$ -methyl styrene, which is hydrogenated in only 28(1)% yield, even with a higher 2.5%

catalyst loading. This suggests that steric limitations play a major role in catalysis by **2**, which is perhaps unsurprising given the large *t*-Bu substituents on the DHP ligand. Reactivity is shut down completely with  $\beta$ -methyl styrene even at 2.5% catalyst loadings. Based on mechanistic DFT calculations (see below), we decided to investigate whether OTf<sup>-</sup>-abstracting reagents might enable higher conversions with these sterically encumbering substrates. In situ addition of NaBAr<sub>4</sub><sup>F</sup> (BAr<sub>4</sub><sup>F</sup> = tetrakis[3,5-bis(trifluoromethyl)phenyl]borate) as an OTf<sup>-</sup> abstractor to the catalytic mixture approximately doubles the yield of cumene from  $\alpha$ -methyl styrene to 48(2)% and furthermore enables detectable hydrogenation yields (~5%) for  $\beta$ -methyl styrene. Conversely, the addition of LiOTf to catalytic reactions with  $\alpha$ -methyl styrene lowers the yield to 5.8%. These results suggest that the dissociation of triflate is likely important during catalysis and is consistent with DFT calculations that support lower energy pathways for the cationic fragment [(<sup>*t*</sup>Bu,<sup>*tol*</sup>DHP)Co]<sup>+</sup> (**Scheme 2**).

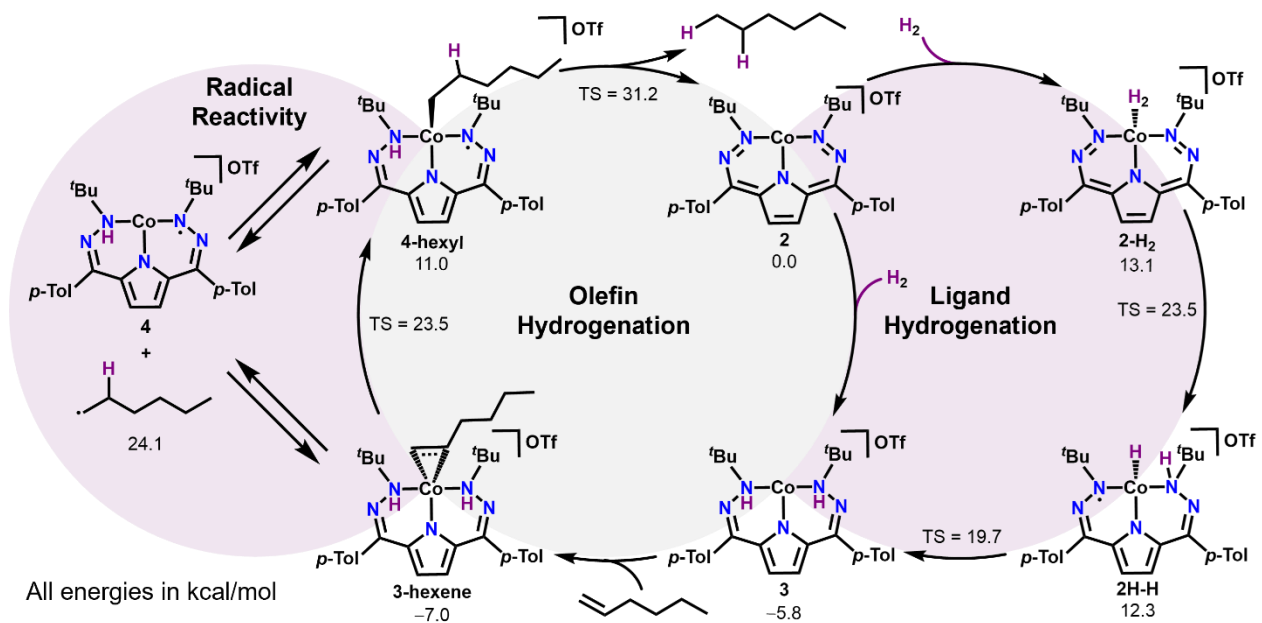
We also investigated the regioselectivity of hydrogenation with the substrate trans-2-methyl-1,3-pentene. Here, selectivity for the hydrogenation of the terminal, disubstituted olefin, is observed with ~35% yield, consistent with the reactivity trends from mono-olefinic substrates. Interestingly, the hydrogenated products show *cis/trans* isomerization as well as migration of the internal double bond to the more thermodynamically favorable tri-substituted position. Given the limited hydrogenation reactivity with internal mono-olefins, we hypothesized that the isomerization of this substrate might be due to a radical pathway for hydrogenation and undertook mechanistic experiments to explore this possibility.

The hydrogenation of  $\alpha$ -cyclopropyl styrene as a radical clock test substrate with 10% cat. loading of **2** showed exclusive cyclopropyl ring-opened products, as would be expected for a radical reaction.<sup>26</sup> For this substrate, the major product is doubly hydrogenated *sec*-pentylbenzene

in 35(3)% yield. We also observe the tri-substituted olefin product 2-phenylpent-2-ene in 10(2)% yield. This product is the expected intermediate olefin formed after ring-opening. Regardless of the exact product distribution, the absence of any hydrogenated products with an intact cyclopropyl ring strongly suggests a radical mechanism and also suggests related radical reactions to form the observed olefin migration products from trans-2-methyl-1,3-pentene.

The agency of radical reactivity in the hydrogenation catalysis of **2** is noteworthy, as Co-based hydrogenation catalysts frequently go through classical organometallic mechanisms featuring Co–H intermediates without radical reactivity.<sup>14g</sup> Indeed, there has been recent interest in discovering Co catalysts with alternative mechanisms, in some cases switched with light.<sup>14g</sup> The absence of any observable Co–H species upon hydrogenation of **2** and the observed radical reactivity in hydrogenation catalysis suggested to us the possibility of an unusual DHP ligand-promoted radical hydrogenation mechanism. While such a mechanism is supported by our experimental data, we also wanted to use DFT calculations to obtain a clearer picture of accessible pathways.

**Scheme 2.** Mechanism for the synthesis of **3** as well as for the hydrogenations of olefins (1-hexene used as model substrate)



### Computational Analysis

All of the experimental data on **3** is consistent with the assignment of a hydrogenated ligand with a Co(II) center generated from the reaction of **2** with H<sub>2</sub>. This proposed assignment of **3** and other catalytically relevant intermediates was therefore investigated using DFT calculations (**Scheme 2**, Appendix I: **Figures S56–S57, S64–S65, and S85–S86**). Geometry optimizations and frequency calculations for postulated intermediates and transition states along two key cycles, addition of H<sub>2</sub> to the DHP scaffold (**Scheme 2** right) as well as 1-hexene hydrogenation (**Scheme 2** middle), were calculated using the O3LYP functional and basis sets of def2-SVP on H, def2-TZVPP on Co, and def2-TZVP on N and C atoms (**Scheme 2**). Both doublet and quartet spin states were considered, and the results suggest that both spin states are relevant for catalysis.

The mechanism to form **3** was investigated both with OTf<sup>-</sup> bound to Co and also with an outer sphere (unbound) OTf<sup>-</sup>. The transition state energies found for the outer sphere

OTf<sup>-</sup> pathway are generally lower in energy, sometimes significantly than for reactivity with OTf<sup>-</sup> bound to Co. This observation is consistent with the enhanced yields we observe with added NaBAR<sub>4</sub><sup>F</sup> as a OTf<sup>-</sup> abstractor. The initial hydrogenation of **2** is overall favorable with a free energy of -5.8 kcal/mol. The pathway to form this species goes first 13.1 kcal/mol uphill from **2** through an  $S = 1/2$  Co-H<sub>2</sub> adduct (**2-H<sub>2</sub>**). A high-energy transition state between **2-H<sub>2</sub>** and an  $S = 1/2$  Co hydride (**2H-H**) with a singly hydrogenated DHP ligand is 23.5 kcal/mol uphill from **2**. Intermediate **2H-H** can then proceed through a low-energy (7.4 kcal/mol versus **2H-H**) transition state to generate **3**.

The DFT-predicted pathway for olefin hydrogenation proceeds through roughly thermoneutral binding of 1-hexene to **3** (-1.2 kcal/mol) to form an  $S = 3/2$  high-spin 1-hexene adduct (**3-hexene**). We then considered two branching pathways from this olefin adduct. Firstly, **3-hexene** could go through an ene-reaction-like transformation to generate a Co-alkyl product, **4-hexyl**. This reaction is unfavorable by 18.0 kcal/mol with a transition state 25.5 kcal/mol uphill in energy from **3-hexene**. We note that the depicted primary product is significantly lower in energy than the formal 2,1 insertion product, likely driven by the sterics of the *t*-Bu groups and thus possibly explaining the preference of the system for terminal olefins. Subsequent loss of alkane and regeneration of **2** proceeds through a high-energy transition state of 31.2 kcal/mol versus **2**. While this pathway is potentially feasible, the facile room-temperature activity of **2** and the observed radical reactivity also prompted us to evaluate separate radical intermediates.

Intermediate **3-hexene** may also transfer an H-atom to the bound 1-hexene to generate a hexyl radical and a singly hydrogenated Co complex **4**. This reaction to generate a terminal hexyl radical is 31.1 kcal/mol uphill in energy from **3-hexene** and is comparable in energy to the highest lying transition state for DHP hydrogenation (30.5 kcal/mol higher than **3-hexene**). The

comparatively low energy of these free radical intermediates suggests a very weak Co–C bond in **4-hexyl**, and indeed, the loss of a primary hexyl radical from this intermediate is only 13.1 kcal/mol uphill in energy, and the formation of secondary radicals is even more accessible (Appendix I: **Figures S85 and S86**). As expected, subsequent H-atom abstraction from **4** by a hexyl radical is extremely favorable.

Without additional experimental details, which are difficult to obtain on this paramagnetic system, it is difficult to determine whether the hexene hydrogenation steps proceed exclusively through Co-bound species, such as **4-hexyl**, or if direct H-atom transfer to generate outer sphere carbon radicals dominates. We suspect that the mechanism features both alkyl radical and metal-alkyl species, which may explain the steric preferences for hydrogenation as well as the radical-derived products observed in mechanistic experiments. Furthermore, we note two additional mechanistic paradigms which deserve discussion. First, while we have limited our discussion to the above cationic pathway with an outer sphere  $\text{OTf}^-$ , some of the putative intermediates with bound alkyl and  $\text{OTf}^-$  groups are slightly lower in energy, particularly for the later C–H bond forming steps, suggesting that additional ligation by counterions or solvent may facilitate cycles with bound alkyl substituents (Appendix I: **Figures S56 and S57**). Second, an additional pathway where intermediate **2H-H** directly binds and inserts olefin may be possible, although we think that the rate of olefin binding to **2H-H**, which would be a bimolecular process, is not likely to be competitive with the low barrier intramolecular reaction to proceed to **3**.

Nevertheless, the computed reaction pathways support the agency of the DHP ligand in hydrogenation and the absence of classic organometallic steps such as insertions from hydride intermediates. The calculations also suggest that improvements on yield or scope might be

obtained by reducing the sterics on our catalyst and utilizing a more weakly coordinating anion than OTf<sup>-</sup>.

## Conclusions

In this study, we have synthesized a series of Co(II) complexes with the redox-active <sup>*t*Bu,Tol</sup>DHP ligand scaffold. The CoOTf complex (**2**) forms a thermally unstable hydrogenated species (**3**) when exposed to dihydrogen, which can be characterized spectroscopically and computationally to confirm its assignment as a Co(II) complex with a hydrogenated DHP ligand. Complex **2** is also a competent catalyst for the hydrogenation of olefins at room temperature with 1 atmosphere of H<sub>2</sub>. Catalyst **2** selectively hydrogenates terminal alkenes, and it can also drive rearrangements of olefins into more thermodynamically favored products, likely through radical pathways. The agency of radical intermediates has been confirmed by the ring-opening of the radical clock  $\alpha$ -cyclopropyl styrene in hydrogenation reactions. Our results demonstrate that the combination of ligand-based multi-proton and electron storage enables hydrogenation catalysis under mild conditions and, furthermore, that this ligand-centric paradigm enables alternative mechanistic pathways to more classic organometallic catalysts.

## Experimental Section

### General Methods

All chemicals were purchased from commercial suppliers and used without further purification. All manipulations were carried out under an atmosphere of N<sub>2</sub> using standard Schlenk and glovebox techniques. Glassware was dried at 180 °C for a minimum of 2 h and cooled under vacuum prior to use. Solvents were dried on a solvent purification system from Pure Process Technology and stored over 4 Å molecular sieves under N<sub>2</sub>. Tetrahydrofuran (THF) was stirred over NaK alloy and run through an additional alumina column prior to use to ensure dryness.

Solvents were tested for H<sub>2</sub>O and O<sub>2</sub> using a standard solution of sodium-benzophenone ketyl radical anion. CD<sub>3</sub>CN, C<sub>6</sub>D<sub>6</sub>, and d<sub>8</sub>-toluene were dried over 4 Å molecular sieves under N<sub>2</sub>.  $\alpha$ -cyclopropyl styrene was prepared following a previously reported procedure.<sup>27</sup>

<sup>1</sup>H and <sup>19</sup>F NMR spectra were recorded on Bruker DRX 400 or 500 spectrometers. Chemical shifts are reported in ppm units referenced to residual solvent resonances for <sup>1</sup>H spectra. UV–visible Spectra were recorded on a Bruker Evolution 300 spectrometer and analyzed using VisionPro software. A standard 1 cm quartz cuvette with an airtight screw cap with a puncturable Teflon seal was used for all measurements. A Unisoku CoolSpek cryostat was used for low-temperature measurements. <sup>1</sup>H and <sup>19</sup>F NMR spectra were recorded on either Bruker DRX 400 or AVANCE-500 spectrometers. IR spectra were obtained on a Bruker Tensor II spectrometer with the OPUS software suite. All IR samples were collected between KBr plates. EPR spectra were recorded on an Elexsys E500 Spectrometer with an Oxford ESR 900 X-band cryostat and a Bruker ColdEdge Stinger. EPR data was analyzed using the EasySpin MATLAB suite.<sup>28</sup> Single-crystal X-ray diffraction data was collected in-house using Bruker D8 Venture diffractometer equipped with Mo microfocus X-ray tube ( $\lambda = 0.71073$  Å).

X-ray near-edge absorption spectra (XANES) were employed to probe the local environment of Co. All sample preparation was performed under an inert atmosphere. Frozen solution samples were prepared by making a concentrated solution of the starting material in toluene (acetonitrile was added for solubility where indicated). This solution was then syringed into a precooled Teflon cuvette lined with Kapton tape in liquid nitrogen and then stored in liquid nitrogen until collection. Data was acquired at the Advanced Photon Source at Argonne National Labs with a bending magnet source with ring energy at 7.00 GeV. Co K-edge data was acquired at the MRCAT 10-BM beamline. The incident, transmitted, and reference X-ray intensities were

monitored using gas ionization chambers. A metallic Co foil standard was used as a reference for energy calibration and was measured simultaneously with experimental samples. X-ray absorption spectra were collected at room temperature. Data collected was processed using the Demeter software suite, and Fityk was used for more precise pre-edge fitting.

### **Co(<sup>t</sup>Bu,<sup>Tol</sup>DHP)Cl (1)**

In a 20 mL vial in the glovebox, 1–2 mL of THF was added until the [<sup>t</sup>Bu,<sup>Tol</sup>DHP-H<sub>4</sub>][Cl]<sub>2</sub> ligand salt<sup>9c</sup> (0.172 g, 1 equiv 0.333 mmol) dissolved completely as a yellow solution. A concentrated solution of KHMDS (0.186 g, 2.8 equiv, 0.932 mmol) in 1–2 mL THF was added dropwise with stirring. The solution turned from yellow to a bright red color, then darkened to a brownish green upon complete addition. After these color changes and additions were completed, CoCl<sub>2</sub> (0.043 g, 1 equiv, 0.331 mmol), suspended in 1–2 mL of THF was added to the reaction mixture, which resulted in a color change to a brown-purple color. 1-hexene (41 μL, 1 equiv, 0.33 mmol) was added, with a resulting color change to a luminous magenta-purple. Shortly after the addition of 1-hexene, the reaction mixture was dried under vacuum to provide a purple solid. This solid was extracted with copious amounts of petroleum ether (50–60 mL). After drying this solution, **1** was obtained as a magenta-purple solid. Yield: 0.134 g, 75%. Single crystals for XRD were grown via cooling a petroleum ether solution at –35 °C. <sup>1</sup>H NMR (400 MHz, C<sub>6</sub>D<sub>6</sub>, RT): δ = no signals. Magnetic susceptibility: Evans' method (C<sub>6</sub>D<sub>6</sub>, RT, μ<sub>B</sub>): μ<sub>eff</sub> = 1.74. UV–vis, nm in benzene, (ε, M<sup>-1</sup> cm<sup>-1</sup>): 553 (3900). Anal. Calcd C, 62.86; H, 6.41; N, 13.09; found: C, 62.58; H, 5.97; N, 11.46. HRMS (EI) *m/z*: [M]<sup>+</sup> calcd for **1**: C<sub>28</sub>H<sub>34</sub>N<sub>5</sub>ClCo 534.1835; found, 534.184.

### **Co(<sup>t</sup>Bu,<sup>Tol</sup>DHP)OTf (2)**

In a 20 mL vial in the glovebox, 2 mL of benzene was added to Co(<sup>Tol</sup>,<sup>t</sup>Bu)DHP)Cl (**1**) (0.060 g, 1 equiv, 0.11 mmol). A solution of silver triflate (0.028 g, 1 equiv, 0.11 mmol) in a mixture of

1:1 benzene/acetonitrile (2 mL) was added to the bright purple solution of **1**. The reaction was stirred for 1 h, over which time its color changed from emerald green immediately after addition to an olive color with concomitant formation of gray solids on the sides of the vial. This reaction mixture was dried under vacuum, after which the product was extracted with 10–20 mL of diethyl ether. Yield: 0.065 g, 89%. Single crystals suitable for XRD of **2** were grown out of a concentrated petroleum ether solution at  $-35\text{ }^{\circ}\text{C}$ .  $^1\text{H NMR}$  (400 MHz,  $\text{C}_6\text{D}_6$ , RT):  $\delta = 24.20$  (bs), 10.17 (s), 9.07 (bs), 7.36 (s), 6.96(s), 6.87(bs), 4.06 (s). Magnetic susceptibility: Evans' method for **2** ( $\text{C}_6\text{D}_6$ , RT,  $\mu_{\text{B}}$ ):  $\mu_{\text{eff}} = 1.71$ , UV–vis, nm in toluene, ( $\epsilon$ ,  $\text{M}^{-1}\text{cm}^{-1}$ ): 516 (3700). Anal. Calcd C, 53.70; H, 5.28; N, 10.80; found, 54.32, 5.55, 10.31. HRMS (EI)  $m/z$ :  $[\text{M}]^+$  calcd for **2**:  $\text{C}_{29}\text{H}_{34}\text{N}_5\text{O}_3\text{F}_3\text{S Co}$  648.1666; found, 648.1665.

### Reactivity with $\text{H}_2$

A 100 mL Schlenk flask with 8 mg of **2** with 50–100  $\mu\text{L}$  of toluene was prepared in the glovebox. This solution was frozen in liquid nitrogen, and the headspace was evacuated under vacuum. The flask was then backfilled with 1 atm of  $\text{H}_2$ , which is equivalent to  $\sim 3.8$  atm of  $\text{H}_2$  at room temperature. The flask was then relocated into a freezer at  $-25\text{ }^{\circ}\text{C}$ , where it was allowed to react for 30–36 h without stirring. Upon completion of the reaction with  $\text{H}_2$ , the reddish-purple color of **2** converts to a pinker purple, indicating the formation of **3**. Complex **3** is stable to vacuum and is relatively stable as a solid to air but decomposes rapidly if exposed to air in the solution state. This complex is relatively stable below  $0\text{ }^{\circ}\text{C}$ , but slow decomposition occurs at this temperature and above. To characterize this product, the reaction vessel was pumped back into the nitrogen-filled glovebox and placed into a  $-35\text{ }^{\circ}\text{C}$  freezer. The cold solution was then dried rapidly under vacuum and then analyzed by various techniques, as described below. IR (Nujol mull between KBr plates,  $\text{cm}^{-1}$ ): 3180 (N–H, w), 3170 (N–H, w), 1641 (s).

## Preparation of IR samples of **3**

### Nujol Mull

Complex **3** (8 mg), prepared in the method described above, was mixed in a cold mortar and pestle with minimal nujol to form a mustard-like suspension. This mixture was dolloped on a cooled KBr plate, and a second plate was placed on top. The sample was then transferred in an air-free temporary container to the spectrometer, and a spectrum was collected.

### Thin Film on KBr Plate

Complex **3** (8 mg), prepared in the method described above, was dissolved in cold, dry diethyl ether to form a concentrated solution. This was dropped on a cooled KBr plate, and a second plate was placed on top. The sample was then transferred in an air-free temporary container to the spectrometer, and a spectrum was collected.

## References

1. (a) Crabtree, R. H. *Organometallic Chemistry of the Transition Metals*, 6th ed.; 2014; pp 55– 56.; (b) Wen, J.; Wang, F.; Zhang, X. Asymmetric hydrogenation catalyzed by first-row transition metal complexes. *Chem. Soc. Rev.* **2021**, *50*, 3211– 3237.
2. (a) Ito, N.; Phillips, S. E. V.; Stevens, C.; Ogel, Z. B.; McPherson, M. J.; Keen, J. N.; Yadav, K. D. S.; Knowles, P. F. Novel thioether bond revealed by a 1.7 Å crystal structure of galactose oxidase. *Nature* **1991**, *350*, 87– 90.; (b) Ito, N.; Phillips, S. E. V.; Stevens, C.; Ogel, Z. B.; McPherson, M. J.; Keen, J. N.; Yadav, K. D. S.; Knowles, P. F. Three-dimensional structure of galactose oxidase: an enzyme with a built-in secondary cofactor. *Faraday Discuss.* **1992**, *93*, 75.; (c) Branchaud, B. P.; Montagne-Smith, M. P.; Kosman, D. J.; McLaren, F. R. Mechanism-based inactivation of galactose oxidase: evidence for a radical mechanism. *J. Am. Chem. Soc.* **1993**, *115*, 798.; (d) Whittaker, M. M.; Whittaker, J. M. Ligand interactions with galactose oxidase: mechanistic insights. *Biophys. J.* **1993**, *64*, 762.; (e) Ito, N.; Phillips, S. E. V.; Yadav, K. D. S.; Knowles, P. F. Crystal structure of a free radical enzyme, galactose oxidase. *J. Mol. Biol.* **1994**, *238*, 794.; (f) Knowles, P. F.; Ito, N. *Perspectives in Bio-inorganic Chemistry*, Jai Press Ltd., 1994; Vol. 2, pp 207– 244.; (g) Wachter, R. M.; Branchaud, B. P. Molecular modeling studies on oxidation of hexopyranoses by galactose oxidase. An active site topology apparently designed to catalyze radical reactions, either concerted or stepwise. *J. Am. Chem. Soc.* **1996**, *118*, 2782.; (h) Wachter, R. M.; Montagne-Smith, M. P.; Branchaud, B. P.  $\beta$ -Haloethanol substrates as probes for radical mechanisms for galactose oxidase. *J. Am. Chem. Soc.* **1997**, *119*, 7743.; (i) Whittaker, M. M.; Ballou, D. P.; Whittaker, J. W. Kinetic isotope effects as probes of the mechanism of galactose oxidase. *Biochemistry* **1998**, *37*, 8426.; (j) Whittaker, J.

W.; Whittaker, M. M. Radical copper oxidases, one electron at a time. *Pure Appl. Chem.* **1998**, *70*, 903.; (k) Chaudhuri, P.; Hess, M.; Müller, J.; Hildenbrand, K.; Bill, E.; Weyhermüller, T.; Wieghardt, K. Aerobic oxidation of primary alcohols (including methanol) by Copper (II)– and Zinc (II)– phenoxyl radical catalysts. *J. Am. Chem. Soc.* **1999**, *121*, 9599– 9610.; (l) Cook, S. A.; Hill, E. A.; Borovik, A. S. Lessons from nature: a bio-inspired approach to molecular design. *Biochemistry* **2015**, *54*, 4167– 4180.; (m) Baumgardner, D. F.; Parks, W. E.; Gilbertson, J. D. Harnessing the active site triad: merging hemilability, proton responsivity, and ligand-based redox-activity. *Dalton Trans.* **2020**, *49*, 960– 965.

3. Cook, S. A.; Borovik, A. S. Molecular designs for controlling the local environments around metal ions. *Acc. Chem. Res.* **2015**, *48*, 2407– 2414.

4. (a) Rakowski Dubois, M.; Dubois, D. L. Development of Molecular Electrocatalysts for CO<sub>2</sub> Reduction and H<sub>2</sub> Production/Oxidation. *Acc. Chem. Res.* **2009**, *42*, 1974– 1982.; (b) Zell, T.; Milstein, D. Hydrogenation and dehydrogenation iron pincer catalysts capable of metal–ligand cooperation by aromatization/dearomatization. *Acc. Chem. Res.* **2015**, *48*, 1979– 1994.; (c) Pegis, M. L.; Wise, C. F.; Martin, D. J.; Mayer, J. M. Oxygen reduction by homogeneous molecular catalysts and electrocatalysts. *Chem. Rev.* **2018**, *118*, 2340– 2391.

5. (a) Luca, O. R.; Crabtree, R. H. Redox-active ligands in catalysis. *Chem. Soc. Rev.* **2013**, *42*, 1440– 1459.; (b) Arevalo, R.; Chirik, P. J. Enabling two-electron pathways with iron and cobalt: from ligand design to catalytic applications. *J. Am. Chem. Soc.* **2019**, *141*, 9106– 9123.; (c) Ott, J. C.; Bürgy, D.; Guan, H.; Gade, L. H. 3d Metal Complexes in T-shaped Geometry as a Gateway to Metalloradical Reactivity. *Acc. Chem. Res.* **2022**, *55*, 857– 868

6. (a) Käß, M.; Friedrich, A.; Drees, M.; Schneider, S. Ruthenium Complexes with Cooperative PNP Ligands: Bifunctional Catalysts for the Dehydrogenation of Ammonia–Borane. *Angew. Chem., Int. Ed.* **2009**, *48*, 905– 907.; (b) Khaskin, E.; Iron, M. A.; Shimon, L. J. W.; Zhang, J.; Milstein, D. N– H activation of amines and ammonia by Ru via metal– ligand cooperation. *J. Am. Chem. Soc.* **2010**, *132*, 8542.; (c) Feller, M.; Diskin-Posner, Y.; Shimon, L. J. W.; Ben-Ari, E.; Milstein, D. N–H Activation by Rh (I) via Metal–Ligand Cooperation. *Organometallics* **2012**, *31*, 4083.; (d) He, L. P.; Chen, T.; Gong, D.; Lai, Z.; Huang, K. W. Enhanced reactivities toward amines by introducing an imine arm to the pincer ligand: direct coupling of two amines to form an imine without oxidant. *Organometallics* **2012**, *31*, 5208.; (e) Rodríguez-Lugo, R. E.; Trincado, M.; Vogt, M.; Tewes, F.; Santiso-Quinones, G.; Grützmacher, H. A homogeneous transition metal complex for clean hydrogen production from methanol–water mixtures. *Nat. Chem.* **2013**, *5*, 342– 347.; (f) Myers, T. W.; Berben, L. A. Aluminum–ligand cooperative N–H bond activation and an example of dehydrogenative coupling. *J. Am. Chem. Soc.* **2013**, *135*, 9988– 9990.; (g) Xu, R.; Chakraborty, S.; Bellows, S. M.; Yuan, H.; Cundari, T. R.; Jones, W. D. Iron-Catalyzed Homogeneous Hydrogenation of Alkenes under Mild Conditions by a Stepwise, Bifunctional Mechanism. *ACS Catal.* **2016**, *6*, 2127– 2135.; (h) Sherbow, T. J.; Fettinger, J. C.; Berben, L. A. Control of Ligand pKa Values Tunes the Electrocatalytic Dihydrogen Evolution Mechanism in a Redox-Active Aluminum(III) Complex. *Inorg. Chem.* **2017**, *56*, 8651– 8660.; (i) Rajabimoghadam, K.; Darwish, Y.; Bashir, Y.; Pirman, D.; Eichelberger, S.; Sieler, M. A.; Swart, M.; Garcia-Bosch, I. Catalytic aerobic oxidation of alcohols by copper complexes bearing redox-active ligands with tunable H-bonding groups. *J. Am. Chem. Soc.* **2018**, *140*, 16625– 16634.; (j) Sinha, S.; Das, S.; Mondal, R.; Mandal, S.; Paul, N. D. Cobalt complexes of redox noninnocent azo-aromatic

pincers. Isolation, characterization, and application as catalysts for the synthesis of quinazolin-4 (3 H)-ones. *Dalton Trans.* **2020**, *49*, 8448– 8459.

7. (a) Thompson, E. J.; Berben, L. A. Electrocatalytic Hydrogen Production by an Aluminum (III) Complex: Ligand-Based Proton and Electron Transfer. *Angew. Chem., Int. Ed.* **2015**, *54*, 11642– 11646.; (b) Margulieux, G. W.; Bezdek, M. J.; Turner, Z. R.; Chirik, P. J. Ammonia Activation, H<sub>2</sub> Evolution and Nitride Formation from a Molybdenum Complex with a Chemically and Redox Noninnocent Ligand. *J. Am. Chem. Soc.* **2017**, *139*, 6110– 6113.; (c) Dauth, A.; Gellrich, U.; Diskin-Posner, Y.; Ben-David, Y.; Milstein, D. The ferraquinone–ferrahydroquinone couple: combining quinonic and metal-based reactivity. *J. Am. Chem. Soc.* **2017**, *139*, 2799– 2807.; (d) Rosenkoetter, K. E.; Wojnar, M. K.; Charette, B. J.; Ziller, J. W.; Heyduk, A. F. Hydrogen-atom noninnocence of a tridentate [SNS] pincer ligand. *Inorg. Chem.* **2018**, *57*, 9728– 9737.; (e) Ward, M. B.; Scheitler, A.; Yu, M.; Senft, L.; Zillmann, A. S.; Gorden, J. D.; Schwartz, D. D.; Ivanović-Burmazović, D. D.; Goldsmith, C. R. Superoxide dismutase activity enabled by a redox-active ligand rather than metal. *Nat. Chem.* **2018**, *10*, 1207– 1212.; (f) Alig, L.; Fritz, M.; Schneider, S. First-Row Transition Metal (De)Hydrogenation Catalysis Based On Functional Pincer Ligands. *Chem. Rev.* **2019**, *119*, 2681– 275.; (g) Drummond, M. J.; Ford, C. L.; Gray, D. L.; Popescu, C. V.; Fout, A. R. Radical Rebound Hydroxylation Versus H-Atom Transfer in Non-Heme Iron(III)-Hydroxo Complexes: Reactivity and Structural Differentiation. *J. Am. Chem. Soc.* **2019**, *141*, 6639– 6650.
8. (a) Purse, B. W.; Tran, L.-H.; Piera, J.; Åkermark, B.; Bäckvall, J.-E. Bäckvall, Synthesis of New Hybrid Hydroquinone/Cobalt Schiff Base Catalysts: Efficient Electron-Transfer Mediators in Aerobic Oxidation. *Chem. – Eur. J.* **2008**, *14*, 7500– 7503.; (b) Myers, T. W.; Berben, L. A. Aluminium–ligand cooperation promotes selective dehydrogenation of formic acid to H<sub>2</sub> and CO<sub>2</sub>. *Chem. Sci.* **2014**, *5*, 2771– 2777.; (c) Henthorn, J. T.; Lin, S.; Agapie, T. Combination of Redox-Active Ligand and Lewis Acid for Dioxygen Reduction with  $\pi$ -Bound Molybdenum–Quinonoid Complexes. *J. Am. Chem. Soc.* **2015**, *137*, 1458– 1464.; (d) Lagaditis, P. O.; Schluschaß, B.; Demeshko, S.; Würtele, C.; Schneider, S. Square-Planar Cobalt (III) Pincer Complex. *Inorg. Chem.* **2016**, *55*, 4529– 4536.; (e) Schneck, F.; Finger, M.; Tromp, M.; Schneider, S. Chemical Non-Innocence of an Aliphatic PNP Pincer Ligand. *Chem. – Eur. J.* **2017**, *23*, 33– 37.; (f) Lindley, B. M.; Bruch, Q. J.; White, P. S.; Hasanayn, F.; Miller, A. J. M. Ammonia Synthesis from a Pincer Ruthenium Nitride via Metal–Ligand Cooperative Proton-Coupled Electron Transfer. *J. Am. Chem. Soc.* **2017**, *139*, 5305– 5308.; (g) Pramanick, R.; Bhattacharjee, R.; Sengupta, D.; Datta, A.; Goswami, S. An azoaromatic ligand as four electron four proton reservoir: catalytic dehydrogenation of alcohols by its zinc (II) complex. *Inorg. Chem.* **2018**, *57*, 6816– 6824.; (h) Jain, R.; Mamun, A. A.; Buchanan, R. M.; Kozlowski, P. M.; Grapperhaus, C. A. Ligand-assisted metal-centered electrocatalytic hydrogen evolution upon reduction of a bis (thiosemicarbazonato) Ni (II) complex. *Inorg. Chem.* **2018**, *57*, 13486– 13493.; (i) Sherbow, T. J.; Thompson, E. J.; Arnold, A.; Sayler, R. I.; Britt, R. D.; Berben, L. A. Electrochemical Reduction of N<sub>2</sub> to NH<sub>3</sub> at Low Potential by a Molecular Aluminum Complex. *Chem. – Eur. J.* **2019**, *25*, 454– 458.
9. (a) Chang, M.-C.; McNeece, A. J.; Hill, E. A.; Filatov, A. S.; Anderson, J. S. Ligand-Based Storage of Protons and Electrons in Dihydranonopyrrole Complexes of Nickel. *Chem. – Eur. J.* **2018**, *24*, 8001– 8008.; (b) Chang, M.-C.; Jesse, K. A.; Filatov, A. S.; Anderson, J. S. Reversible homolytic activation of water via metal–ligand cooperativity in a T-shaped Ni (ii) complex. *Chem. Sci.* **2019**, *10*, 1360– 1367.; (c) McNeece, A. J.; Jesse, K. A.; Xie, J.; Filatov, A.

S.; Anderson, J. S. Generation and Oxidative Reactivity of a Ni (II) Superoxo Complex via Ligand-Based Redox Non-Innocence. *J. Am. Chem. Soc.* **2020**, *142*, 10824– 10832.

10. McNeece, A. J.; Jesse, K. A.; Filatov, A. S.; Schneider, J. E.; Anderson, J. S. Catalytic hydrogenation enabled by ligand-based storage of hydrogen. *Chem. Commun.* **2021**, *57*, 3869– 3872.

11. Jesse, K. A.; Anferov, S. W.; Collins, K. A.; Valdez-Moriera, J. A.; Czaikowski, M. E.; Filatov, A. S.; Anderson, J. S. Direct Aerobic Generation of a Ferric Hydroperoxo Intermediate Via a Preorganized Secondary Coordination Sphere. *J. Am. Chem. Soc.* **2021**, *143*, 18121– 18130.

12. (a) Fryzuk, M. D.; Leznoff, D. B.; Thompson, R. C.; Rettig, S. J. One-electron transformations of paramagnetic cobalt complexes. Synthesis and structure of cobalt (II) amidodiphosphine halide and alkyl complexes and their reaction with alkyl halides. *J. Am. Chem. Soc.* **1998**, *120*, 10126– 10135.; (b) Lyaskovskyy, V.; de Bruin, B. Redox non-innocent ligands: versatile new tools to control catalytic reactions. *ACS Catal.* **2012**, *2*, 270– 279.; (c) Zhang, G.; Hanson, S. K. Cobalt-catalyzed transfer hydrogenation of C=O and C=N bonds. *Chem. Commun.* **2013**, *49*, 10151– 10153.; (d) Zhang, G.; Vasudevan, K. V.; Scott, B. L.; Hanson, S. K. Understanding the mechanisms of cobalt-catalyzed hydrogenation and dehydrogenation reactions. *J. Am. Chem. Soc.* **2013**, *135*, 8668– 8681.; (e) Jing, Y.; Chen, X.; Yang, X. Computational mechanistic study of the hydrogenation and dehydrogenation reactions catalyzed by cobalt pincer complexes. *Organometallics*, **2015**, *34*, 5716– 5722.; (f) Fu, S.; Chen, N.-Y.; Liu, X.; Shao, Z.; Luo, S.-P.; Liu, Q. Ligand-Controlled Cobalt-Catalyzed Transfer Hydrogenation of Alkynes: Stereodivergent Synthesis of Z- and E-Alkenes. *J. Am. Chem. Soc.* **2016**, *138*, 8588– 8594.; (g) Qi, X.; Liu, X.; Qu, L.-B.; Liu, Q.; Lan, Y. Mechanistic insight into cobalt-catalyzed stereodivergent semihydrogenation of alkynes: The story of selectivity control. *J. Catal.* **2018**, *362*, 25– 34.; (h) Liu, X.; Zhang, W.; Wang, Y.; Zhang, Z.-X.; Jiao, L.; Liu, Q. Cobalt-catalyzed regioselective olefin isomerization under kinetic control. *J. Am. Chem. Soc.* **2018**, *140*, 6873– 6882 .; (i) Merz, L. S.; Blasius, C. K.; Wadepohl, H.; Gade, L. H. Square planar cobalt (II) hydride versus T-shaped cobalt (I): structural characterization and dihydrogen activation with PNP–cobalt pincer complexes. *Inorg. Chem.* **2019**, *58*, 6102– 6113.; (j) Ai, W.; Zhong, R.; Liu, X.; Liu, Q. Hydride transfer reactions catalyzed by cobalt complexes. *Chem. Rev.* **2019**, *119*, 2876– 2953.; (k) Sang, S.; Unruh, T.; Demeshko, S.; Domenianni, L. I.; van Leest, N. P.; Marquetand, P.; Schneck, F.; Würtele, C.; de Zwart, F. J.; de Bruin, B.; González, L.; Vöhringer, P.; Schneider, S. Photo-Initiated Cobalt-Catalyzed Radical Olefin Hydrogenation. *Chem. – Eur. J.* **2021**, *27*, 16978– 16989.

13. (a) Kooistra, T. M.; Knijnenburg, Q.; Smits, J. M. M.; Horton, A. D.; Budzelaar, P. H. M.; Gal, A. W. Olefin Polymerization with [bis(imino)pyridyl]Co<sup>II</sup>Cl<sub>2</sub>]: Generation of the Active Species Involves CoI. *Angew. Chem., Int. Ed.* **2001**, *40*, 4719– 4722.; (b) Knijnenburg, Q.; Hetterscheid, D.; Kooistra, T. M.; Budzelaar, P. H. M. The Electronic Structure of (Diiminopyridine)cobalt(I) Complexes. *Eur. J. Inorg. Chem.* **2004**, *2004*, 1204– 1211.; (c) Knijnenburg, Q.; Horton, A. D.; Heijden, H. V. d.; Kooistra, T. M.; Hetterscheid, D. G. H.; Smits, J. M. M.; Bruien, B. D.; Budzelaar, P. H. M.; Gal, A. W. Olefin hydrogenation using diimine pyridine complexes of Co and Rh. *J. Mol. Catal. A: Chem.* **2005**, *232*, 151– 159.; (d) Hopmann, K. H. Cobalt–bis (imino) pyridine-catalyzed asymmetric hydrogenation: electronic structure, mechanism, and stereoselectivity. *Organometallics* **2013**, *32*, 6388– 6399.; (e) Guo, J.; Cheng, B.; Shen, X.; Lu, Z. Cobalt-catalyzed asymmetric sequential hydroboration/hydrogenation of internal alkynes. *J. Am. Chem. Soc.* **2017**, *139*, 15316– 15319.

14. (a) Monfette, S.; Turner, Z. R.; Semproni, S. P.; Chirik, P. J. Enantiopure C1-Symmetric Bis(imino)pyridine Cobalt Complexes for Asymmetric Alkene Hydrogenation. *J. Am. Chem. Soc.* **2012**, *134*, 4561– 4564.; (b) Yu, R. P.; Darmon, J. M.; Milsmann, C.; Daut, G. W.; Stieber, S. C. E.; DeBeer, S.; Chirik, P. J. Catalytic hydrogenation activity and electronic structure determination of bis (arylimidazol-2-ylidene) pyridine cobalt alkyl and hydride complexes. *J. Am. Chem. Soc.* **2013**, *135*, 13168.; (c) Semproni, S. P.; Milsmann, C.; Chirik, P. J. *J. Am. Chem. Soc.* **2014**, *136*, 9211– 9224.; (d) Chirik, P. J. Iron-and cobalt-catalyzed alkene hydrogenation: catalysis with both redox-active and strong field ligands. *Acc. Chem. Res.* **2015**, *48*, 1687– 1695.; (e) Friedfeld, M. R.; Shevlin, M.; Margulieux, G. W.; Campeau, L.-C.; Chirik, P. J. Cobalt-catalyzed enantioselective hydrogenation of minimally functionalized alkenes: isotopic labeling provides insight into the origin of stereoselectivity and alkene insertion preferences. *J. Am. Chem. Soc.* **2016**, *138*, 3314– 3324.; (f) Viereck, P.; Krautwald, S.; Pabst, T. P.; Chirik, P. J. A boron activating effect enables cobalt-catalyzed asymmetric hydrogenation of sterically hindered alkenes. *J. Am. Chem. Soc.* **2020**, *142*, 3923– 3930.; (g) Mendelsohn, L. N.; MacNeil, C. S.; Tian, L.; Park, Y.; Scholes, G. D.; Chirik, P. J. Visible-Light-Enhanced Cobalt-Catalyzed Hydrogenation: Switchable Catalysis Enabled by Divergence between Thermal and Photochemical Pathways. *ACS Catal.* **2021**, *11*, 1351– 1360.
15. (a) Zhang, G.; Scott, B. L.; Hanson, S. K. Mild and Homogeneous Cobalt-Catalyzed Hydrogenation of C=C, C=O, and C=N Bonds. *Angew. Chem., Int. Ed.* **2012**, *51*, 12102– 12106.; (b) Lin, T. P.; Peters, J. C. Boryl–metal bonds facilitate cobalt/nickel-catalyzed olefin hydrogenation. *J. Am. Chem. Soc.* **2014**, *136*, 13672– 13683.
16. (a) Yang, L.; Powell, D. R.; Houser, R. P. Structural variation in copper(I) complexes with pyridylmethylamide ligands: structural analysis with a new four-coordinate geometry index,  $\tau_4$ . *Dalton Trans.* **2007**, 955.; (b) Okuniewski, A.; Rosiak, D.; Chojnacki, J.; Becker, B. Coordination polymers and molecular structures among complexes of mercury (II) halides with selected 1-benzoylthioureas. *Polyhedron.* **2015**, *90*, 47– 57.
17. Bowman, A. C.; Milsmann, C.; Bill, E.; Lobkovsky, E.; Weyhermüller, T.; Wieghardt, K.; Chirik, P. J. Reduced N-Alkyl Substituted Bis(imino)pyridine Cobalt Complexes: Molecular and Electronic Structures for Compounds Varying by Three Oxidation States. *Inorg. Chem.* **2010**, *49*, 6110– 6123.
18. Jensen, K. P.; Ryde, U. Comparison of the chemical properties of iron and cobalt porphyrins and corrins. *ChemBioChem* **2003**, *4*, 413– 424.
19. Addison, A. W.; Rao, N. T.; Reedijk, J.; van Rijn, J.; Verschoor, G. C. Synthesis, structure, and spectroscopic properties of copper(II) compounds containing nitrogen–sulphur donor ligands; the crystal and molecular structure of aqua[1,7-bis(N-methylbenzimidazol-2'-yl)-2,6-dithiaheptane]copper(II) perchlorate. *J. Chem. Soc., Dalton Trans.* **1984**, 7, 1349– 1356.
20. (a) Scott, J.; Gambarotta, S.; Korobkov, I.; Knijnenburg, Q.; de Bruin, B.; Budzelaar, P. H. M. Formation of a Paramagnetic Al Complex and Extrusion of Fe during the Reaction of (Diiminepyridine)Fe with  $AlR_3$  (R = Me, Et). *J. Am. Chem. Soc.* **2005**, *127*, 17204.; (b) Bowman, A. C.; Milsmann, C.; Atienza, C. C. H.; Lobkovsky, E.; Wieghardt, K.; Chirik, P. J. Synthesis and molecular and electronic structures of reduced bis (imino) pyridine cobalt dinitrogen complexes: ligand versus metal reduction. *J. Am. Chem. Soc.* **2010**, *132*, 1676.; (c) Milsmann, C.; Turner, Z. R.; Semproni, S. P.; Chirik, P. J. Azo N= N Bond Cleavage with a Redox-Active Vanadium Compound Involving Metal–Ligand Cooperativity. *Angew. Chem., Int. Ed.* **2012**, *51*, 5386.; (d) Yu, R. P.; Darmon, J. M.; Milsmann, C.; Margulieux, G. W.; Stieber, S. C. E.; DeBeer, S.; Chirik, P. J. Catalytic hydrogenation activity and electronic structure determination of bis

(arylimidazol-2-ylidene) pyridine cobalt alkyl and hydride complexes. *J. Am. Chem. Soc.* **2013**, *135*, 13168–13184.

21. (a) Poddel'sky, A. I.; Cherkasov, V. K.; Abakumov, G. A. Transition metal complexes with bulky 4, 6-di-tert-butyl-N-aryl (alkyl)-o-iminobenzoquinonato ligands: Structure, EPR and magnetism. *Coord. Chem. Rev.* **2009**, *253*, 291–324.; (b) Goswami, M.; Lyaskovskyy, V.; Domingos, S. R.; Buma, W. J.; Woutersen, S.; Troeppner, O.; Ivanović-Burmazović, I.; Lu, H.; Cui, S.; Zhang, X. P.; Reijerse, E. J.; DeBeer, S.; van Schooneveld, M. M.; Pfaff, F. F.; Ray, K.; de Bruin, Bas. Characterization of porphyrin-Co (III)-'nitrene radical' species relevant in catalytic nitrene transfer reactions. *J. Am. Chem. Soc.* **2015**, *137*, 5468–5479.; (c) Kuijpers, P. F.; van der Vlugt, J. I.; Schneider, S.; de Bruin, B. Nitrene radical intermediates in catalytic synthesis. *Chem. — Eur. J.* **2017**, *23*, 13819–13829.; (d) Jiang, H.; Lang, K.; Lu, H.; Wojtas, L.; Zhang, X. P. Asymmetric radical bicyclization of allyl azidoformates via cobalt (II)-based metalloradical catalysis. *J. Am. Chem. Soc.* **2017**, *139*, 9164–9167.; (e) Reckziegel, A.; Kour, M.; Battistella, B.; Mebs, S.; Beuthert, K.; Berger, R.; Werncke, C. G. High-Spin Imido Cobalt Complexes with Imidyl Radical Character. *Angew. Chem., Int. Ed.* **2021**, *60*, 15376.

22. (a) Hay-Motherwell, R. S.; Wilkinson, G.; Hussain, B.; Hursthouse, M. B. Alkyl complexes of cobalt (II). X-ray crystal structures of  $(\text{Me}_2\text{NCH}_2\text{CH}_2\text{NMe}_2)_2\text{CoR}_2$ ,  $\text{R} = \text{CH}_2\text{SiMe}_3$ ,  $\text{CH}_2\text{CMe}_3$ ,  $[(\text{Me}_2\text{NCH}_2\text{CH}_2\text{NMe}_2)_2\text{Li}]_2[\text{Co}(\text{CH}_2\text{SiMe}_3)_4]$  and  $[(\text{Me}_2\text{NCH}_2\text{CH}_2\text{NMe}_2)_2\text{Li}][\text{CoCl}\{\text{CH}(\text{SiMe}_3)_2\}_2]$ . *Polyhedron* **1990**, *9*, 931.; (b) Scott, J.; Gambarotta, S.; Korobkov, I.; Knijnenburg, Q.; de Bruin, B.; Budzelaar, P. H. M. Formation of a Paramagnetic Al Complex and Extrusion of Fe during the Reaction of (Diiminepyridine)Fe with  $\text{AlR}_3$  ( $\text{R} = \text{Me}, \text{Et}$ ). *J. Am. Chem. Soc.* **2005**, *127*, 17204. (c) Bowman, A. C.; Milsman, C.; Atienza, C. C. H.; Lobkovsky, E.; Wieghardt, K.; Chirik, P. J. Synthesis and molecular and electronic structures of reduced bis(imino) pyridine cobalt dinitrogen complexes: ligand versus metal reduction. *J. Am. Chem. Soc.* **2010**, *132*, 1676.; (d) Mo, Z.; Li, Y.; Lee, H. K.; Deng, L. Square-Planar Cobalt Complexes with Monodentate N-Heterocyclic Carbene Ligation: Synthesis, Structure, and Catalytic Application. *Organometallics* **2011**, *30*, 4687.; (e) Bowman, A. C.; Milsman, C.; Bill, E.; Turner, Z. R.; Lobkovsky, E.; DeBeer, S.; Wieghardt, K.; Chirik, P. J. Synthesis and Electronic Structure Determination of N-Alkyl-Substituted Bis(imino)pyridine Iron Imides Exhibiting Spin Crossover Behavior. *J. Am. Chem. Soc.* **2011**, *133*, 17353.

23. (a) Jenkins, D. M.; Di Bilio, A. J.; Allen, M. J.; Betley, T. A.; Peters, J. C. Elucidation of a low spin cobalt (II) system in a distorted tetrahedral geometry. *J. Am. Chem. Soc.* **2002**, *124*, 15336–15350.; (b) Harris, C. F.; Bayless, M. B.; van Leest, N. P.; Bruch, Q. J.; Livesay, B. N.; Bacsá, J.; Hardcastle, K. I.; Shores, M. P.; de Bruin, B.; Soper, J. D. Redox-Active Bis(phenolate) N-Heterocyclic Carbene [OCO] Pincer Ligands Support Cobalt Electron Transfer Series Spanning Four Oxidation States. *Inorg. Chem.* **2017**, *56*, 12421–12435.; (c) Liu, Y.; Du, J.; Deng, L. Synthesis, Structure, and Reactivity of Low-Spin Cobalt(II) Imido Complexes  $[(\text{Me}_3\text{P})_3\text{Co}(\text{NAr})]$ . *Inorg. Chem.* **2017**, *56*, 8278–8286.; (d) Spillecke, L.; Tripathi, S.; Koo, C.; Bahr, A.; Swain, A.; Haldar, R.; Ansari, M.; Jasinski, J.; Rajaraman, G.; Shanmugam, M.; Klingeler, R. Role of Coordination Geometry on the Magnetic Relaxation Dynamics of Isomeric Five-Coordinate Low-Spin Co (II) Complexes. *Inorg. Chem.* **2022**, *61*, 317–327.

24. Sarangi, R.; Cho, J.; Nam, W.; Solomon, E. I. XAS and DFT Investigation of Mononuclear Cobalt(III) Peroxo Complexes: Electronic Control of the Geometric Structure in  $\text{CoO}_2$  versus  $\text{NiO}_2$  Systems. *Inorg. Chem.* **2011**, *50*, 614–620.

25. Tomson, N. C.; Crimmin, M. R.; Petrenko, T.; Rosebrugh, L. E.; Sproules, S.; Boyd, W. C.; Bergman, R. G.; DeBeer, S.; Toste, F. D.; Wieghardt, K. A step beyond the Feltham–Enemark

notation: spectroscopic and correlated ab Initio computational support for an antiferromagnetically coupled M (II)–(NO)– description of Tp\* M (NO)(M= Co, Ni). *J. Am. Chem. Soc.* **2011**, *133*, 18785.

26. Masnovi, J.; Samsel, E. G.; Bullock, R. M. Cyclopropylbenzyl Radical Clocks. *J. Chem. Soc., Chem. Commun.* **1989**, 1044– 1045.

27. Martin, J.; Knüpfer, C.; Eyselien, J.; Färber, C.; Grams, S.; Langer, J.; Thum, K.; Wiesinger, M.; Harder, S. Highly Active Superbulky Alkaline Earth Metal Amide Catalysts for Hydrogenation of Challenging Alkenes and Aromatic Rings. *Angew. Chem., Int. Ed.* **2020**, *59*, 9102– 9112.

28. Stoll, S.; Schweiger, A. EasySpin, a comprehensive software package for spectral simulation and analysis in EPR. *J. Magn. Reson.* **2006**, *178*, 42– 55.

---

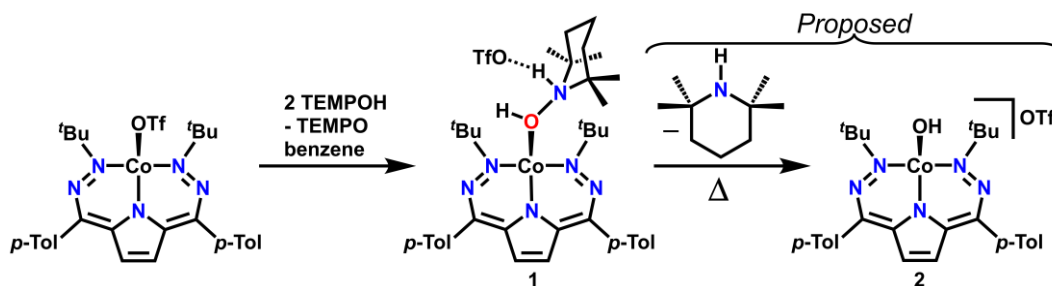


intermediates have been proposed, examples of structurally characterized transition metal adducts of TEMPO remain rare.<sup>8,9</sup> Furthermore, the structurally characterized adducts that have been reported only span a limited range of TEMPO oxidation/protonation states (**Scheme 1**)—generally either one of the dehydrogenated TEMPO species (i.e. TEMPO/TEMPO<sup>-</sup>)<sup>8</sup> or singly hydrogenated analogs, with the proton bound to the nitrogen and the oxygen to the metal center.<sup>9</sup>

Our laboratory has been exploring the use of dihydrazonopyrrole (DHP) ligands which can reversibly store multiple H-atom equivalents.<sup>10</sup> Previously, we have characterized and isolated a Co triflate complex on the redox-active <sup>t</sup>Bu,Tol<sup>DHP</sup> ligand scaffold and demonstrated how ligand-based storage of H-atoms can facilitate hydrogenation catalysis.<sup>11</sup>

While investigating H-atom storage on dihydrazonopyrrole ligands, we tested the use of TEMPOH as an H-atom donor which led us to isolate an adduct of an unusual oxidation state of TEMPO, 1-hydroxy-2,2,6,6-tetramethylpiperidin-1-ium (TEMPOH<sub>2</sub><sup>+</sup>). The resulting complex [(<sup>t</sup>Bu,Tol<sup>DHP</sup>)Co(TEMPOH<sub>2</sub><sup>+</sup>)] [OTf] (**1**) contains a full equivalent of H<sub>2</sub> relative to an oxoammonium cation, making it the first structurally characterized example of this oxidation state of TEMPO bound to a metal center. This complex has been characterized by single-crystal X-ray diffraction, IR spectroscopy, as well as reactivity studies which suggest its instability to N–O homolysis. Computational studies with density functional theory (DFT) reveal that this unusual complex is

**Scheme 2.** Synthesis of **1** and proposed decomposition



formed via a coupled proton-electron transfer from an additional TEMPOH molecule. The isolation of this compound suggests that similar redox isomers of aminoxyl compounds are possible catalytic intermediates.

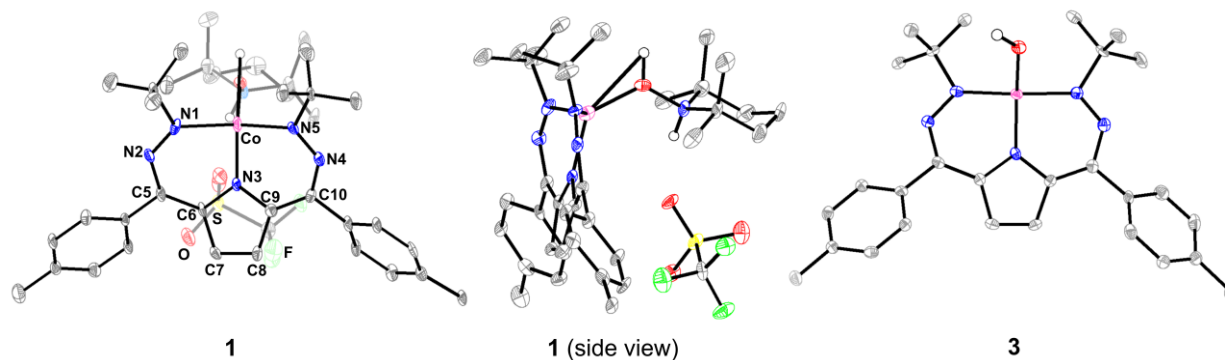
## Results and discussion

### Synthesis and characterization of **1**

Two equivalents of TEMPOH were dissolved in a minimal amount of benzene and then added to a benzene solution of the previously reported compound (<sup>*t*</sup>Bu,<sup>*o*</sup>TolDHP)CoOTf (**Scheme 2**).<sup>11</sup> This mixture was allowed to stir for 18 hours, after which it was concentrated under vacuum and extracted with petroleum ether. Magenta crystals of **1** suitable for single crystal X-ray diffraction (SXRD) were then grown from a concentrated petroleum ether solution at  $-35\text{ }^{\circ}\text{C}$ . The structure of **1** reveals a TEMPOH<sub>2</sub><sup>+</sup> molecule bound to a four-coordinate Co center (**Figure 1**).

The N–H and O–H protons of the TEMPOH<sub>2</sub><sup>+</sup> ligand can be located in the difference map and were freely refined. A clear hydrogen-bonding interaction of moderate strength between the N–H proton and the OTf<sup>−</sup> counterion is apparent (O–H = 1.96(8) Å, N–H = 0.95(8) Å, N–O =

**Figure 1.** SXRD Structures (from left to right) of **1**, **1** rotated to see the hydrogen-bonding interaction, and **3**. All displacement ellipsoids shown at 50% and hydrogens omitted for clarity, with the exception of O–H/N–H protons which are shown with a ball-and-stick model.



2.877(9) Å, N-H-O  $\angle$  = 161.2°).<sup>12</sup> The geometry of **1** at Co can be quantified with  $\tau_4$  and  $\tau_4'$  values of 0.56 and 0.65 respectively (with the  $\alpha$  and  $\beta$  angles being the N-Co-N and the N-Co-(OH) angles respectively).<sup>13</sup>

The structural parameters observed for the bound TEMPOH<sub>2</sub><sup>+</sup> ligand are all consistent with the presence of two protons on this moiety. The N-O bond of 1.434(8) Å is most similar to that of the free 1-hydroxy-2,2,6,6-tetramethylpiperidin-1-ium chloride ([TEMPOH<sub>2</sub><sup>+</sup>][Cl])<sup>14</sup> and is also in the range of single N-O bonds. The 1.56(1) and 1.55(1) Å N-C bond lengths are also similar to [TEMPOH<sub>2</sub><sup>+</sup>][Cl]. The oxidation state of the <sup>t</sup>Bu,<sup>Tol</sup>DHP ligand itself is most similar to that of the (<sup>t</sup>Bu,<sup>Tol</sup>DHP)CoOTf starting material, suggesting that the DHP ligand is best described as monoanionic and thus implying a Co(I) center in **1**.

We then utilized IR spectroscopy to further corroborate the presence of the protons on the TEMPOH<sub>2</sub><sup>+</sup> ligand of **1**. The obtained spectrum clearly shows O-H/N-H stretches in the 3000-3150 cm<sup>-1</sup> region, with broad features at ~3100 cm<sup>-1</sup> and ~3050 cm<sup>-1</sup> respectively. This is in agreement with the DFT calculated frequencies where the basis-set and functional adjusted values are 3180 cm<sup>-1</sup> for the O-H and 3067 cm<sup>-1</sup> for the N-H (**Figure 2**, Appendix II: **Table S7**). More generally, the computed IR spectrum also proves to be a good match for the experimental spectrum (Appendix II: **Figure S32**).

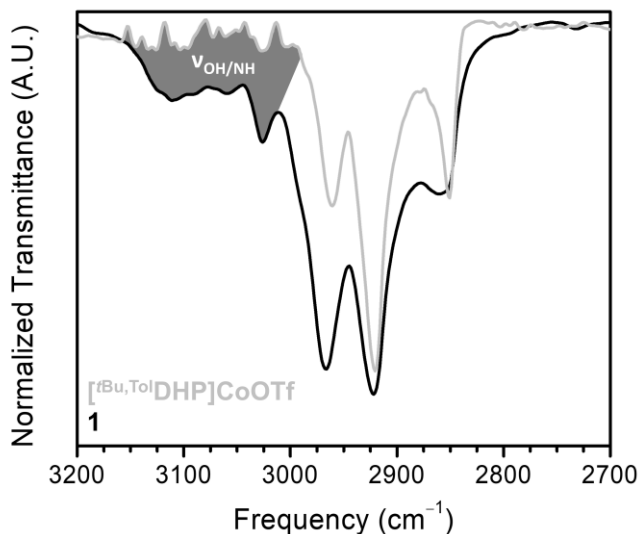
The N-hydroxypiperidinium ligand in **1**, which is a formally hydrogenated product of an oxoammonium cation, is the first example of this oxidation and protonation state of TEMPO bound to a metal center and is unusual more generally. Some examples of metal-bound TEMPO species with an N-H bond have been characterized, but none of these examples possess an additional H-atom equivalent stored on the TEMPO-derived moiety.

With the empirical formula and protonation state of **1** confirmed, we then turned to examining its electronic structure. Evans method of this complex reveals an  $S = 1$  spin state. DFT calculations on this triplet state suggest that the majority of the spin density resides on Co with some minor opposite spin density on the DHP ligand (Appendix II: **Figure S14**). Such a picture is most consistent with a high spin Co(I) center, although it is difficult to exclude some contribution from a Co(II)/DHP<sup>2-•</sup> resonance structure.

Given the propensity of TEMPOH/TEMPO to participate in H-atom transfer, we speculated that the formation of **1** might arise from transfer of additional H-atom equivalents to a TEMPOH adduct of Co. However, attempts to isolate such a Co-TEMPOH adduct have been unsuccessful and only lead to sub-stoichiometric conversion to **1** or, under dilute conditions, decomposition to other species. Given our inability to synthetically access a TEMPOH adduct, we instead turned to other experimental and **Figure 2**. Thin Film IR spectrum of **1** (black) and computational analyses to elucidate the (<sup>t</sup>Bu,<sup>Tol</sup>DHP)CoOTf (gray) with shaded area indicating formation and reactivity of **1**. O–H/N–H stretches.

### Mechanism of Formation of **1**

We hypothesized that the mechanism to form **1** proceeds from an initial binding of TEMPOH to (<sup>t</sup>Bu,<sup>Tol</sup>DHP)CoOTf. DFT calculations with a dissociated triflate anion suggest that this step is nearly thermoneutral by 0.06 kcal/mol. These calculations also



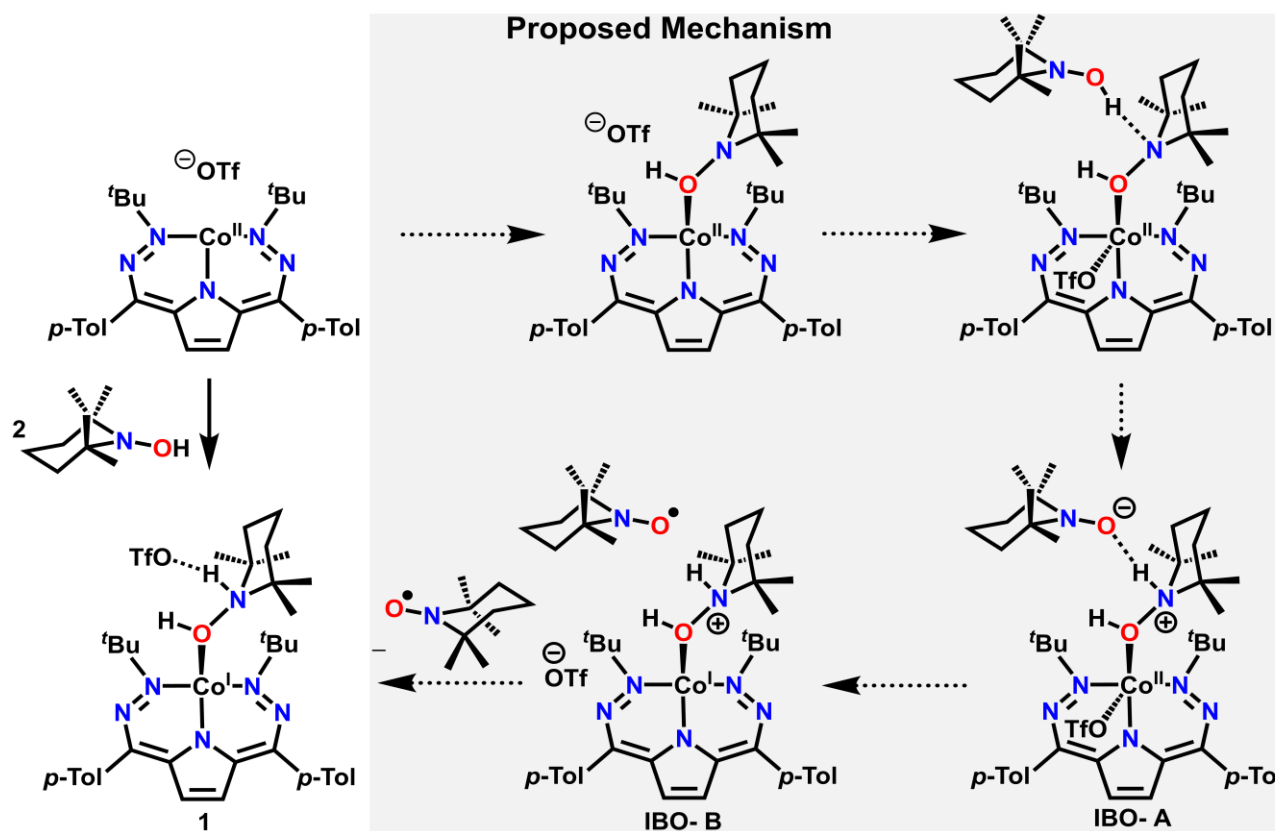
suggest this adduct is a low-spin Co(II)  $S = \frac{1}{2}$  species (**Scheme 3**). This adduct is then proposed

to react with a second equivalent of TEMPOH to form **1** in an overall downhill step (−7.4 kcal/mol). This overall reaction involves the formal transfer of an H-atom to the TEMPOH adduct of (<sup>t</sup>Bu,<sup>Tol</sup>DHP)CoOTf, but the exact flow of electrons is less clear. We therefore undertook a more detailed computational analysis of this step.

To obtain further detail on the flow of protons and electrons along this elementary step, we employed an intrinsic bond orbital (IBO) analysis as reported by Knizia and co-workers.<sup>15</sup> This computational technique enables analysis of the movement and localization of orbitals along a reaction coordinate. This allows us to visualize and quantify how the orbitals associated with electron transfer (**Figure 3**, blue orbital) and proton transfer (**Figure 3**, red orbital) change during net H-atom transfer.

To further assess the mechanism of H-atom transfer, we plotted the normalized orbital movement as a function of the N–H distance along the reaction coordinate (Appendix II: **Figure S31**). This analysis supports that there is a proton transfer from the unbound TEMPOH to the bound TEMPOH along with an electron transfer from the unbound TEMPOH to Co. This mechanistic picture is consistent with multi-site PCET reactivity, where a proton is transferred to the N of the bound TEMPOH, and an electron is transferred to the Co center. This is noteworthy, as TEMPOH is unlikely to accept an additional electron, but the presence of the Co center enables net PCET with Co as the electron acceptor. Unfortunately, the IBO analysis doesn't provide a very clear picture on whether this process is concerted or stepwise, but the overall movement of a proton and an electron is clear.

This mechanistic picture contrasts with some proposed paths for C–H activation performed by Lewis-acid activated TEMPO complexes of Fe and Al which primarily abstract C–Hs via a nitrogen-based radical on the TEMPO motif.<sup>16</sup> Our DFT analysis does not support this TEMPO-



**Scheme 3.** Proposed mechanism of the formation of **1**

radical pathway, showing little spin density on the nitrogen, and instead supports a metal-ligand-cooperative pathway for CPET, more similar to the proposed mechanism for Ni TEMPO complexes where a basic TEMPO nitrogen abstracts a proton.<sup>17</sup>

### Reactivity of **1**

Initially we note that, while it can be isolated for characterization, **1** decays slowly over time at room temperature. We assessed some possible routes of decomposition via DFT (such as disassociation of the entire fragment, hydrogenation of the metal or ligand, or release of TEMPO or TEMPOH, see Appendix II). We observed that the lowest energy byproducts were [ $(^t\text{Bu,Tol})\text{DHP}]\text{CoOH}][\text{OTf}]$  (**2**) and 2,2,6,6-tetramethylpiperidine (TMP). This is consistent with the precedent for O-atom transfer with TEMPO and related derivatives, arising from N–O homolysis to provide net hydroxide or oxo transfer.<sup>18</sup> Experimentally, we have some limited NMR evidence

that shows that the thermal decomposition product appears to be paramagnetic, consistent with calculations for **2** (Appendix II: **Figure S3**).

We have also been interested in generating this proposed Co product **2** independently. Towards this end, we initially synthesized the neutral hydroxide complex (<sup>*t*</sup>Bu,<sup>*Tol*</sup>DHP)CoOH (**3**) via salt metathesis from the Co–Cl precursor. The resulting maroon colored complex was readily extracted into petroleum ether, and crystals suitable for SXRD analysis could be obtained from concentrated petroleum ether solutions at –35 °C. The geometry of this complex can be quantified with  $\tau_4$  and  $\tau_4'$  values of 0.35 and 0.30 respectively (with the  $\alpha$  and  $\beta$  angles being the N–Co–N and the N–Co–O respectively). Unfortunately, we have been unable to oxidize **3** to the proposed cationic complex **2** (Appendix II: **Scheme S1**). Nevertheless, the difficulty in isolating **2** from this independent synthetic route circumstantially supports the difficulties in isolating such a complex from decompositions of **1**.

## Conclusions

In this study, we have synthesized a Co complex of an interesting oxidation and protonation state of TEMPO, a commonly utilized aminoxyl radical. This complex can be characterized and verified via IR spectroscopy and SXRD analysis. DFT studies were used to assess the formation of this complex and suggest it occurs through a multi-site proton coupled electron transfer. This species was also found to be thermally unstable, and we propose that its decomposition occurs through N–O cleavage of the bound TEMPOH<sub>2</sub><sup>+</sup> fragment to form an oxidized hydroxide complex and neutral 2,2,6,6-tetramethylpiperidine. These results demonstrate the utility of redox-active ligands in stabilizing novel complexes and support the inclusion of other oxidation states of TEMPO in mechanistic proposals.

## Experimental Section

## General Methods

All chemicals were purchased from commercial suppliers and used without further purification. All manipulations were carried out under an atmosphere of N<sub>2</sub> using standard Schlenk and glovebox techniques. Glassware was dried at 180 °C for a minimum of two hours and cooled under vacuum prior to use. Solvents were dried on a solvent purification system from Pure Process Technologies and stored over 4 Å molecular sieves under N<sub>2</sub>. Tetrahydrofuran (THF) was stirred over NaK alloy and run through an additional alumina column prior to use to ensure dryness. Solvents were tested for H<sub>2</sub>O and O<sub>2</sub> using a standard solution of sodium-benzophenone ketyl radical anion. CD<sub>3</sub>CN, C<sub>6</sub>D<sub>6</sub>, and d<sub>8</sub>-toluene were dried over 4 Å molecular sieves under N<sub>2</sub>.

<sup>1</sup>H and <sup>19</sup>F NMR spectra were recorded on Bruker DRX 400 or 500 spectrometers. Chemical shifts are reported in ppm units referenced to residual solvent resonances for <sup>1</sup>H spectra. UV-Visible Spectra were recorded on a Bruker Evolution 300 spectrometer and analyzed using VisionPro software. A standard 1 cm quartz cuvette with an airtight screw cap with a puncturable Teflon seal was used for all measurements. A Unisoku CoolSpek cryostat was used for high-temperature measurements. <sup>1</sup>H and <sup>19</sup>F NMR spectra were recorded on either Bruker DRX-400 or AVANCE-500 spectrometers. IR spectra were obtained on a Bruker Tensor II spectrometer with the OPUS software suite. All IR samples were collected between KBr plates. Single crystal X-ray diffraction data were collected in-house using Bruker D8 Venture diffractometer equipped with Mo microfocus X-ray tube ( $\lambda = 0.71073 \text{ \AA}$ ). Electrochemical measurements were carried out using a BAS Epsilon potentiostat and using BAS Epsilon software version 1.40.67 NT. Magnetic moments were determined using the Evans method.<sup>19</sup> (<sup>*t*</sup>Bu,<sup>*Tol*</sup>DHP)CoOTf and (<sup>*t*</sup>Bu,<sup>*Tol*</sup>DHP)CoCl were prepared as was reported according to their literature procedures.<sup>11</sup>

**Co(<sup>*t*</sup>Bu,<sup>*Tol*</sup>DHP)(TEMPOH<sub>2</sub><sup>+</sup>)(OTf) (1)**

In a 20 mL vial in the glovebox, 1-2 mL of benzene was added until (<sup>t</sup>Bu,<sup>Tol</sup>DHP)CoOTf (11.8 mg, 1 eq. 0.018 mmol) dissolved completely as a reddish-purple solution. A concentrated solution of TEMPOH (5.7 mg, 2 equiv., 0.036 mmol) in 1-2 mL benzene was added with stirring. The solution turned from reddish-purple to a brighter pinker purple over the next 18 hours. After these color changes were complete, the solution was dried *in vacuo*, and minimal petroleum ether was added to the solids. This petroleum ether fraction could be filtered and dried *in vacuo* to obtain 61.3% (9.0 mg) crude **1**, which could be recrystallized out of concentrated petroleum ether. The remaining solids undissolved in petroleum ether could be taken up in benzene, filtered and dried *in vacuo* to obtain 31.3% (4.6 mg) significantly purer **1**, which could be used without further purification. Single crystals for XRD were grown via cooling a petroleum ether solution of this product at -35°C. The NMR was slightly concentration dependent, and the reported NMR is at 2.36 μM. <sup>1</sup>H NMR (400 MHz, C<sub>6</sub>D<sub>6</sub>, RT): δ = 30.11 (br s), 10.13 (br s), 9.87 (br s), 6.59 (br s), 3.94 (br s), 2.2 (br s), 1.77 (br s), 1.36 (br s). Magnetic Susceptibility: Evans' Method (C<sub>6</sub>D<sub>6</sub>, RT, μ<sub>B</sub>): μ<sub>eff</sub> = 2.79; IR (Nujol mull between KBr plates, cm<sup>-1</sup>): 3027.28, 3058.6 (N-H), 3111.2 cm<sup>-1</sup> (O-H), 3186.20. UV-vis, nm in toluene or benzene, (ε, M<sup>-1</sup>cm<sup>-1</sup>): 397 (7967), 544 (7085), 714 (1955). HRMS (EI) m/z: [M]<sup>+</sup> calculated for **1**: C<sub>38</sub>H<sub>54</sub>N<sub>6</sub>O<sub>4</sub>F<sub>3</sub>SCo 806.3211 found 806.3165; The thermal instability of this compound has precluded satisfactory combustion analysis—as demonstrated by UV-Vis and NMR.

### Co(<sup>t</sup>Bu,<sup>Tol</sup>DHP)OH(**3**)

In a 20 mL vial in the glovebox, 2 mL of tetrahydrofuran (THF) was added to Co(<sup>t</sup>Bu,<sup>Tol</sup>DHP)Cl (20 mg, 1 eq., 0.04 mmol). A suspension of sodium hydroxide (7 mg, 5 eq., 0.180 mmol) in THF was added to the bright purple solution of Co(<sup>t</sup>Bu,<sup>Tol</sup>DHP)Cl. After stirring for 18 hours, this bright purple solution was dried *in vacuo*, and the product could be extracted into

petroleum ether. Yield: 15 mg, 80%. Single crystals of **2** suitable for SXRD were grown out of a concentrated petroleum ether solution at  $-35^{\circ}\text{C}$ .  $^1\text{H}$  NMR (400 MHz,  $\text{C}_6\text{D}_6$ , RT):  $\delta = 9.42$  (bs), 7.88 (bs), 7.04 (bs), 2.24 (bs), 2.11 (bs), 1.96 (bs). Magnetic Susceptibility: Evans' Method for **2** ( $\text{C}_6\text{D}_6$ , RT, 500 MHz,  $\mu_{\text{B}}$ ):  $\mu_{\text{eff}} = 1.80$ , IR (thin film between KBr plates,  $\text{cm}^{-1}$ ): 3025.04 (O–H, s), 3058.48, 3090.71. UV-vis, nm in toluene, ( $\epsilon$ ,  $\text{M}^{-1}\text{cm}^{-1}$ ): 555 (3904). HRMS (EI)  $m/z$ :  $[\text{M}]^+$  calculated for **2**:  $\text{C}_{29}\text{H}_{34}\text{N}_5\text{O}_3\text{F}_3\text{SCo}$  516.2174 found 516.2171.

### Preparation of IR samples of $\text{Co}(\text{}^t\text{Bu,TolDHP})\text{OTf}$ , **1** and **3**

#### Thin film on KBr plate

The complex to be analyzed (8 mg), prepared in the method described above, was dissolved in dry diethyl ether or dichloromethane under inert ( $\text{N}_2$ ) glovebox atmosphere to form a concentrated solution. This was drop cast on a KBr plate. The solvent was allowed to evaporate, and a second plate was placed on top. The sample was then transferred in an air-free temporary container to the spectrometer, and a spectrum collected.

### References

1. a) Mader, E. A.; Mayer, J. M. *Inorg. Chem.* **2010**, 49, 8, 3685–3687.; b) Lomont, J. P.; Nguyen, S. C.; Harris, C. B. *J. Am. Chem. Soc.* **2013**, 135, 30, 11266–11273.; c) Tao, X.; Kehr, G.; Wang, X.; Daniliuc, C. G.; Grimme, S.; Erker, G. *Chem. A Eur. Jour.* **2016**, 22, 28, 9504–9507.; d) Walroth, R. C.; Miles, K. C.; Lukens, J. T.; MacMillan, S. N.; Stahl, S. S.; Lancaster, K. M. *J. Am. Chem. Soc.* **2017**, 139, 38, 13507–13517.; e) Ryan, M. C.; Whitmire, L. D.; McCann, S.D.; Stahl, S. S. *Inorg. Chem.* **2019**, 58, 15, 10194–10200.
2. a) Lauber, M. B.; Stahl, S. S. *ACS Catal.* **2013**, 3, 11, 2612–2616.; b) Ryland, B. L.; Stahl, S. S. *Angewandte. Chem. Int. Ed.* **2014**, 53, 34, 8824–8838.; c) Steves, J. E.; Stahl, S. S. *J. Org. Chem.* **2015**, 80, 21, 11184–11188.; d) Badalyan, A.; Stahl, S. S. *Nature.* **2016**, 535–406–410.; e) Nutting, J. E.; Mao, K.; Stahl, S. S. *J. Am. Chem. Soc.* **2021**, 143, 28, 10565–10570.
3. a) Steves, J. E.; Stahl, S. S. *J. Am. Chem. Soc.* **2013**, 135, 42, 15742–15745.; b) Rahmi, A.; Azarpira, A.; Kim, H.; Ralph, J.; Stahl, S. S. *J. Am. Chem. Soc.* **2013**, 135, 17, 6415–6418.; c) Rafiee, M.; Miles, K. C.; Stahl, S. S. *J. Am. Chem. Soc.* **2015**, 137, 46, 14751–14757.; d) Zultanshki, S. L.; Zhao, J.; Stahl, S. S. *J. Am. Chem. Soc.* **2016**, 138, 20, 6416–6419.; e) Rafiee, M.; Konz, Z. M.; Graaf, M. D.; Koolman, H. F.; Stahl, S. S. *ACS Catal.* **2018**, 8, 7, 6738–6744.; f) Rafiee, M.; Alherech, M.; Karlen, S. D.; Stahl, S. S. *J. Am. Chem. Soc.* **2019**, 141, 38, 15266–

- 15276.; g) Piszal, P. E.; Vasilopoulos, A.; Stahl, S. S. *Angewandte. Chem. Int. Ed.* **2019**, 58, 35, 12211-12215.
4. a) Kim, J.; Stahl, S. S. *ACS Catal.* **2013**, 3, 7, 1652–1656.; b) Xie, X.; Stahl, S. S. *J. Am. Chem. Soc.* **2015**, 137, 11, 3767–3770.; c) Miles, K. C.; Abrams, M. L.; Landis, C. R.; Stahl, S. S. *Org. Lett.* **2016**, 18, 15, 3590–3593.; d) Wang, F.; Rafiee, M.; Stahl, S. S. *Angewandte. Chem. Int. Ed.* **2018**, 57, 22, 6686-6690.
5. a) Michel, C.; Belanzoni, P.; Gamez, P.; Reedijk, J.; Baerends, E. J. *Inorg. Chem.* **2009**, 48, 24, 11909-11920.; b) Cheng, L.; Wang, J.; Wang, M.; Wu, Z.; *Inorg. Chem.* **2010**, 49, 20, 9392-9399.; c) Belanzoni, P.; Michel, C.; Baerends, E. J. *Inorg. Chem.* **2011**, 50, 23, 11896-11904.; d) Hoover, J. M.; Ryland, B. L.; Stahl, S. S. *ACS Catal.* **2013**, 3, 11, 2599-2605.; e) Ryland, B. L.; McCann, S. D.; Brunold, T. C.; Stahl, S. S. *J. Am. Chem. Soc.* **2014**, 136,34, 12166-12173.
6. a) Gerken, J. B.; Stahl, S. S. *ACS Cent. Sci.* **2015**, 1, 5, 234–243.; b) Gerken, J. B.; Pang, Y. Q.; Lauber, M. B.; Stahl, S. S. *J. Org. Chem.* **2018**, 83, 14, 7323–7330.; c) Nutting, G. E.; Rafiee, M.; Stahl, S. S. *Chem. Rev.* **2018**, 118, 9, 4834–4885.; d) Wang, F.; Stahl, S. S. *Acc. Chem. Res.* **2020**, 53, 3, 561–574.
7. Dijkstra, A.; Arends, I. W. C. E.; Sheldon, R. A. *Org. Biomol. Chem.*, **2003**, 1, 3232-3237.
8. a) Dickman, M. H.; Doedens, R. J.; *Inorg. Chem.* **1981**, 20, 8, 2677-2681.; b) Dickman, M. H.; Doedens, R. J. *Inorg. Chem.* **1982**, 21, 3, 682-684.; c) Jaitner, P.; Huber, W.; Gieren, A.; Betz, H. *J. Organometallic Chem.*, **1986**, 311, 379-385.; d) Porter, L. C.; Dickman, M. H.; Doedens, R. J. *Inorg. Chem.* **1986**, 25, 5, 678-684.; e) Caneschi, A.; Grand, A.; Laugier, J.; Rey, P.; Subra, R. *J. Am. Chem. Soc.* **1988**, 110, 7, 2307-2309.; f) Laugier, J.; Latour, J. M.; Caneschi, A.; Rey, P. *Inorg. Chem.* **1991**, 30, 23, 4474-4477.
9. a) Ahlers, C.; Dickman, M. H. *Inorg. Chem.* **1998**, 37, 24, 6337-6340.; b) Hetterscheid, D. G. H.; Kaiser, J.; Reijerse, E.; Peters, T. P. J.; Thewissen, S.; Blok, A. N. J.; Smits, J. M. M.; de Gelder, R. de Bruin, B. *J. Am. Chem. Soc.* **2005**, 127, 6, 1895-1905.
10. a) M.-C. Chang, K. A. Jesse, A. S. Filatov and J. S. Anderson, *Chem. Sci.*, 2019, **10**, 1360–1367.; b) McNeece, A. J.; Jesse, K. A.; Filatov, A. S.; Schneider, J. E.; Anderson, J. S. *Chem. Comm.* **2021**, 57, 32, 3869-3872.; c) Jesse, K. A.; Anferov, S. W.; Collins, K. A.; Valdez-Moriera, J. A.; Czaikowski, M. E.; Filatov, A. S.; Anderson, J. S. *J. Am. Chem. Soc.* **2021**, 143, 18121-18130.; d) Czaikowski, M. E.; McNeece, A. J.; Boyn, J-N.; Jesse, K. A.; Anferov, S. W.; Filatov, A. S.; Mazziotti, D. A.; Anderson, J. S. *J. Am. Chem. Soc.* **2022**, 144, 34, 15569-15580.
11. Anferov, S. W.; Filatov, A. S.; Anderson, J. S. *ACS Catal.* **2022**, 12, 16, 9933-9943.
12. T. Steiner *Angew. Chem., Int. Ed.*, 2002, **41**, 48 —76.
13. a) Yang, L.; Powell, D. R.; Houser, R. P. *Dalton Trans.* **2007**, 955.; b) Okuniewski, A.; Rosiak, D.; Chojnacki, J.; Becker, B. *Polyhedron.* **2015**, 90, 47–57.
14. Stefan, S.; Belaj, F.; Madl, T.; Pietschnig, R. *Eur. Jour. Inorg. Chem.* **2010**, 2, 289-297.
15. a) Knizia, G. Intrinsic Atomic Orbitals: An Unbiased Bridge between Quantum Theory and Chemical Concepts.. *J. Chem. Theory Comput.* **2013**, 9 (11), 4834– 4843.; b) Knizia, G.; Klein, J. E. M. N. Electron Flow in Reaction Mechanisms-Revealed from First Principles. *Angew. Chem., Int. Ed.* **2015**, 54 (18), 5518– 5522.; c) Klein, J. E. M. N.; Knizia, G. CPCET versus HAT: A Direct Theoretical Method for Distinguishing X-H Bond-Activation Mechanisms.. *Angew. Chem., Int. Ed.* **2018**, 57 (37), 11913– 11917.
16. Scepaniak, J. J.; Wright, A. M.; Lewis, R. A.; Wu, G.; Hayton, T. W. *J. Am. Chem. Soc.* **2012**, 134, 47, 19350-1353.
17. Isrow, D.; Captain, B. *Inorg. Chem.* **2011**, 50, 13, 5864-5866.

18. a) Huang, K.; Waymouth, R. M. *J. Am. Chem. Soc.* **2002**, 124, 28, 8200-8201.; b) Smith, J. M.; Mayberry, D. E.; Margarit, C. G.; Sutter, J.; Wang, H.; Meyer, K.; Bontchev, R. P. *J. Am. Chem. Soc.* **2012**, 134, 15, 6516-6519.
19. Jenkins, D. M.; Peters, J. C. *J. Am. Chem. Soc.* **2005**, 127 (19), 7148– 7165.
-

## Chapter IV: Selective Cobalt Mediated Formation of Hydrogen

### Peroxide from Water Under Mild Conditions Via Ligand Redox

#### Non-Innocence

##### *Just Add Water*

This chapter has been adapted from the following: Anferov, S. W.; Boyn, J-N.; Mazziotti, D. A.; Anderson, J. S. *J. Am. Chem. Soc.* **2024**, *146*, 9, 5855–5863.

#### Introduction

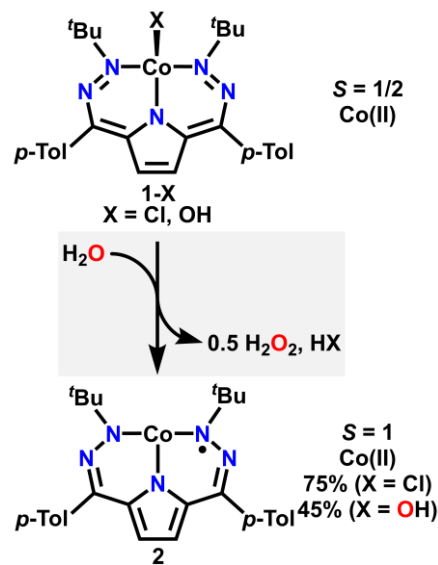
H<sub>2</sub>O<sub>2</sub> is an important oxidant which is used on a megaton scale in processes ranging from consumer products to bulk industrial bleaching.<sup>1</sup> The dominant production route for H<sub>2</sub>O<sub>2</sub> is the anthraquinone process which uses hydrogen and oxygen gas in a stepwise fashion to generate H<sub>2</sub>O<sub>2</sub>, a process that also typically incorporates a precious metal catalyst in order to hydrogenate the quinone. While employed industrially on a large scale, there are several drawbacks to the anthraquinone process including the flammable nature of H<sub>2</sub>/O<sub>2</sub>,<sup>2</sup> the corresponding requirement for stepwise reactions, as well as the use of currently petroleum derived H<sub>2</sub>. These shortcomings have spurred a great deal of investigation into alternative synthetic routes for H<sub>2</sub>O<sub>2</sub> production, with some exciting developments in recent years.<sup>3,4,5</sup> Still, many of the best catalysts use precious metals, forcing conditions, or require separation between O<sub>2</sub> and H<sub>2</sub> cycling. The use of abundant metal catalysts would be advantageous due to cost and scarcity, but examples using first-row transition metals are limited.<sup>5</sup>

Therefore, interest remains high in discovering alternative H<sub>2</sub>O<sub>2</sub> production pathways that are: low-cost, non-flammable, highly selective, and simple to operate. Electrocatalysis could fulfill these criteria and has been extensively utilized to take O<sub>2</sub> to H<sub>2</sub>O,<sup>6</sup> O<sub>2</sub> to H<sub>2</sub>O<sub>2</sub>,<sup>7</sup> or H<sub>2</sub>O to O<sub>2</sub>.<sup>8,9,10,11</sup>

However, electrocatalysts typically have low selectivity for H<sub>2</sub>O oxidation to H<sub>2</sub>O<sub>2</sub> as O<sub>2</sub> formation is more exergonic and therefore occurs at milder potentials. In fact, H<sub>2</sub>O<sub>2</sub> production is typically viewed as a deleterious side reaction in O<sub>2</sub> evolution electrocatalysis. Precious metals or harsh conditions are still often required in the few reported examples for electrocatalytic H<sub>2</sub>O<sub>2</sub> formation from H<sub>2</sub>O and mechanistic insights are still limited.<sup>12,13,14</sup> This is consistent with the fact that H<sub>2</sub>O<sub>2</sub> is less favorable to synthesize than O<sub>2</sub>, with a thermodynamic potential of 1.76 V compared to 1.23 V vs. RHE respectively.<sup>7b,14b</sup>

We have been interested in using metal-ligand cooperative H-atom shuttling to facilitate oxidative and reductive catalysis, particularly within a family of dihydrazonopyrrole (DHP) ligands.<sup>15</sup> We previously observed an unusual homolytic O—H activation of H<sub>2</sub>O with the

dihydrazonopyrrole complex (<sup>Ph,Tol</sup>DHP)Ni which resulted in net dihydrogen abstraction and O-atom transfer reactivity.<sup>15b</sup> We postulated that this net H-atom abstraction from H<sub>2</sub>O could be leveraged for a related oxidative catalytic process. There are many examples of Co-based H<sub>2</sub>O oxidation catalysts,<sup>11</sup> and although most systems generate O<sub>2</sub> from H<sub>2</sub>O, there are a few reported systems that generate H<sub>2</sub>O<sub>2</sub>.<sup>14</sup> We also recently reported a DHP Co complex, and we therefore investigated this system for H<sub>2</sub>O oxidation reactivity and catalysis.



**Scheme 1.** (<sup>tBu, Tol</sup>DHP)CoX<sup>15f, h</sup> reactivity with H<sub>2</sub>O.

Here we report an unusual reaction between water and the previously reported complex  $(^{t\text{Bu,Tol}}\text{DHP})\text{CoCl}$  (**1**) to generate the reduced, formally 3-coordinate Co complex  $(^{t\text{Bu,Tol}}\text{DHP})\text{Co}$  (**2**) (**Scheme 1**). Product analysis reveals the formation of  $\text{H}_2\text{O}_2$  as the byproduct of this reaction, and mechanistic analysis supports a metal-ligand cooperative pathway. This system is competent for electrocatalytic  $\text{H}_2\text{O}$  oxidation to  $\text{H}_2\text{O}_2$  at low overpotentials with perfect selectivity against  $\text{O}_2$  formation. These results show how careful design of the secondary coordination sphere can enable selectivity even for thermodynamically less favorable products in catalysis and provide a proof-of-concept for direct  $\text{H}_2\text{O}$  to  $\text{H}_2\text{O}_2$  electrocatalysis.

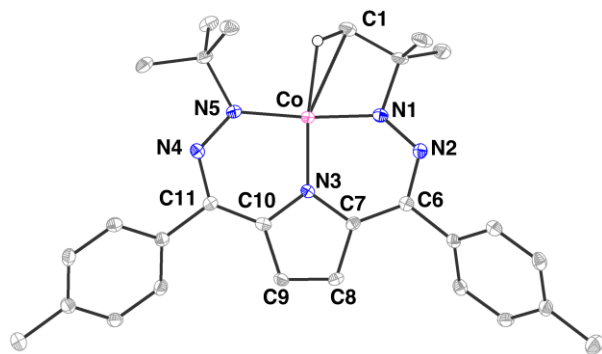


**Figure 1.** Single-crystal structure of  $(^{t\text{Bu,Tol}}\text{DHP})\text{Co}$  (**2**). Selected bond lengths (Å): Co–N1/N5: 1.796(2), 1.847(2); Co–N3: 1.821(2); N1–N2/N4–N5: 1.323(2), 1.318(2); Co–(C1–H): 1.770(2); N2–C5/N4–C10: 1.343(3), 1.336(3); C5–C6/C9–C10: 1.403(3), 1.402(3); C6–C7/C8–C9: 1.436(3), 1.433(3); C7–C8: 1.353(3). Selected bond angles (°): N1–Co–N5: 172.33(8); N3–Co–(C1–H): 162.15(8).

## Results and Discussion

### *Synthesis and Characterization of 2*

Given the previously observed reactivity with DHP systems of Ni, we began by investigating the reactivity of **1** with  $\text{H}_2\text{O}$ . Addition of one equivalent of  $\text{H}_2\text{O}$  to a deep purple solution of  $(^{t\text{Bu,Tol}}\text{DHP})\text{CoCl}$  (**1**)<sup>15f</sup> in diethyl ether led to a subtle color change and the isolation of a new compound,  $(^{t\text{Bu,Tol}}\text{DHP})\text{Co}$  (**2**) as a purple solid (**Scheme 1**). This reduced species can also be obtained using more traditional chemical reductants, such as decamethylcobaltacene, as well as from **1-OTf**. This complex is paramagnetic with an  $S = 1$  spin state as determined by

Evans' method. This spin state suggests either a low-spin  $S = 1/2$  Co(II) center ferromagnetically coupled with a  $\text{DHP}^{2-\bullet}$  ligand radical, a high spin  $S = 3/2$  Co(II) center antiferromagnetically coupled with a  $\text{DHP}^{2-\bullet}$  ligand radical, or an intermediate spin  $S = 1$  Co(I) center with a diamagnetic  $\text{DHP}^{1-}$  ligand.

SXRD analysis on dark purple needles of **2** reveals a formally three-coordinate Co center that has a fourth coordinating moiety in the form of an agostic interaction between the Co center and a *tert*-butyl C–H (**Figure 1**). Using the N1–Co–N5 and N3–Co–(C1–H bond) angles, the  $\tau_4$  value for this complex is 0.179 and the  $\tau_4'$  value is 0.147, putting it closer to square planar than tetrahedral (at 0 and 1 respectively).<sup>16</sup>

The Co–(C1–H) interaction is best described as agostic, not anagostic, as the distance between Co and the H of the interacting C–H bond, which can be resolved in the difference map, is 1.89(2) Å, within the ~ 1.8–2.3 Å range for an agostic bond vs. anagostic bonds which are typically longer.<sup>17</sup> The Co–H–C1 angle is 110.1(2)°, also well within the acceptable range for an agostic interaction. While <sup>1</sup>H NMR is frequently also used as a diagnostic for agostic interactions, the paramagnetic state of **2** prevents its use here.

Comparison of the bond lengths in **2** with the previously reported structures of **1**, (<sup>*t*</sup>Bu, TolDHP)CoOH (**1-OH**), and related DHP complexes of Ni provides more insight on the formal electronic structure of this newly synthesized compound. We have found that redox changes on the DHP ligand result in diagnostic changes to specific bonds, namely N1–N2/N4–N5, C5–C6/C9–C10, and C7–C8. Comparison of these distances between **2** and **1**, **1-OH**, and the Ni complexes (<sup>Ph, Tol</sup>DHP)NiPMe<sub>3</sub><sup>*n*+</sup> (*n* = 0 and 1)<sup>15a</sup> suggests that the DHP ligand in **2** is best considered as a dianionic  $\text{DHP}^{2-\bullet}$  unit, implying a high-spin Co(II) center. DFT calculations on **2** support this electronic structure assignment. A calculated spin density plot of a PBE0/def2-TZVP optimized

structure of **2** most distinctly resembles a high spin Co(II) with an anti-ferromagnetically coupled ligand radical (Appendix III: **Figure S54**). However, these are highly covalent systems and concrete assignments of oxidation states are difficult. This electronic structure description is also consistent with previously isolated examples of antiferromagnetically coupled compounds with this ligand framework.<sup>15a,c,e,g</sup>

#### *Stoichiometric Hydrogen Peroxide Production from Water*

The yield of **2** from the reaction of **1** with H<sub>2</sub>O is high (75%), which raises the question of the oxidized product to balance the formal reduction from [(DHP<sup>2-</sup>)Co(II)]<sup>+</sup> to [(DHP<sup>-</sup>)Co(II)]. We additionally investigated whether other X-type ligands bound to Co would also serve as suitable synthons for the formation of **2**, and we indeed observe that addition of H<sub>2</sub>O to the Co–OH complex (**1-OH**) also forms **2**, albeit in lower yield (45(5)%). The DHP ligand is formally reduced by one electron in both of these reactions, presumably by H<sub>2</sub>O. This suggests that water oxidation byproducts might be likely candidates to balance this reaction, and the literature precedent for Co-catalyzed O<sub>2</sub> evolution from H<sub>2</sub>O led us to test for this product as a likely candidate. Surprisingly, no O<sub>2</sub> has been detected from these reactions via GC under any conditions, which required the consideration of alternative products, one of which could be H<sub>2</sub>O<sub>2</sub>.

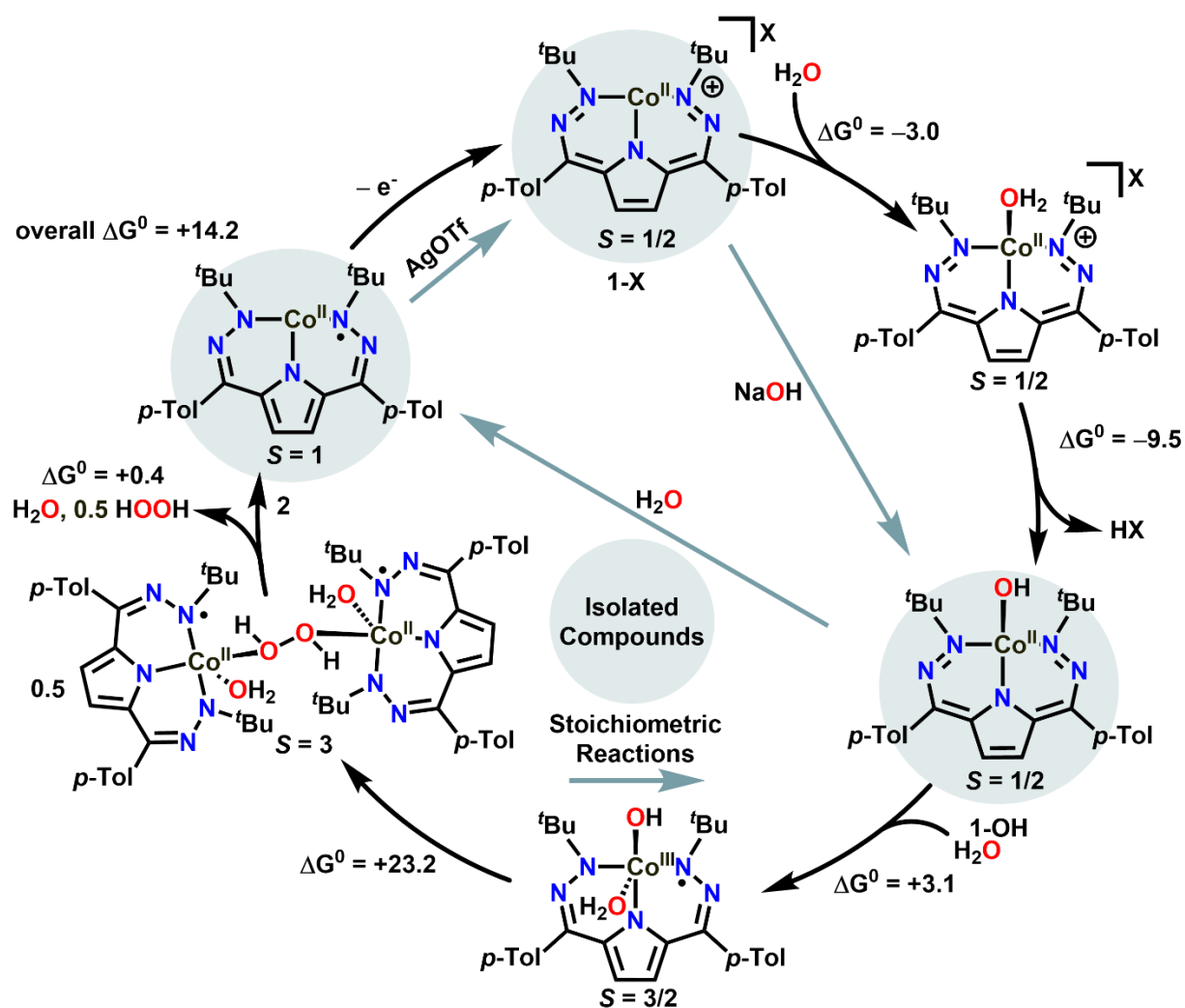
We therefore employed a H<sub>2</sub>O<sub>2</sub>-specific organic probe, 1,3-diphenylisobenzofuran.<sup>18</sup> This organic probe has been shown to only produce 9-hydroxyanthracen-10(9H)-one in the presence of H<sub>2</sub>O<sub>2</sub> (and not other oxidants) while 1,2-dibenzoylbenzene can be formed from H<sub>2</sub>O<sub>2</sub> and many other oxidants. The presence of 9-hydroxyanthracen-10(9H)-one after reacting **1** or **1-OH** with H<sub>2</sub>O in the presence of 1,3-diphenylisobenzofuran would therefore strongly indicate H<sub>2</sub>O<sub>2</sub> production. Indeed, GCMS analysis of the reaction of **1** and H<sub>2</sub>O in the presence of 1,3-diphenylisobenzofuran reveals a 10.2% yield of the H<sub>2</sub>O<sub>2</sub>-diagnostic product, 9-

hydroxyanthracen-10(9H)-one, and a 4.4% yield of 1,2-dibenzoylbenzene as another oxidation product (Appendix III: **Figure S69-S71**). While the presence of 9-hydroxyanthracen-10(9H)-one is conclusively indicative of H<sub>2</sub>O<sub>2</sub> formation, 1,2-dibenzoylbenzene is an intermediate oxidation product formed from 1,3-diphenylisobenzylfuran. Given that this probe usually incompletely captures formed H<sub>2</sub>O<sub>2</sub>,<sup>18</sup> this sets a lower bound of a 20.4% yield for H<sub>2</sub>O<sub>2</sub> production (since two equivalents are necessary to form the diagnostic product) and a lower bound of 24.8% yield for total oxidized product production from **1**.

In addition to 1,3-diphenylisobenzofuran, we can also use alternative oxidant probes such as triphenylphosphine or iodide to quantify the amount of oxidized products. Reacting **1** with 1 equiv. of H<sub>2</sub>O in the presence of 1 equiv. of PPh<sub>3</sub> gave 33% yield of the oxidized phosphine (Appendix III: **Figure S72-S73**). H<sub>2</sub>O<sub>2</sub> can be quantified from the reaction from **1** to **2** via an iodide assay, with a yield of 44(4)% of I<sub>3</sub><sup>-</sup>, supporting the expected 0.5 equivalents of H<sub>2</sub>O<sub>2</sub> being formed. These observations strongly support H<sub>2</sub>O<sub>2</sub> as a product of these reactions and they also suggest that a balanced reaction of **1** + H<sub>2</sub>O → **2** + HCl + 0.5 H<sub>2</sub>O<sub>2</sub> is plausible.

### *Mechanistic Interrogation*

We then wanted to understand a possible mechanism of this unusual transformation. Complex **1-OH** had been previously characterized, and we postulated that it might be a reasonable intermediate formed via H<sub>2</sub>O binding and deprotonation. However, the crucial step to form H<sub>2</sub>O<sub>2</sub> remained less clear, so we used density functional theory (DFT) calculations to evaluate possible mechanisms. After investigating several possible pathways via single-point energy calculations with O3LYP (**Scheme 2**, Appendix III: **Figure S50-S52**), the most energetically accessible mechanism is calculated to go first through acid elimination, then through a dimeric intermediate that releases H<sub>2</sub>O<sub>2</sub>. Utilizing PBE0 and with entropy contributions, we calculate that the first half



**Scheme 2.** Proposed mechanism for the molecular and catalytic generation of H<sub>2</sub>O<sub>2</sub> from the reaction between Co(<sup>t</sup>Bu,<sup>Tol</sup>DHP) complexes and H<sub>2</sub>O. All energies shown in kcal/mol.

of the mechanism to form **1-OH** from **1<sup>+</sup>** is exergonic, with an initial favorable binding of water of -3.0 kcal/mol, followed by acid elimination that is favorable by -9.5 kcal/mol to form **3**. Subsequent H<sub>2</sub>O binding is accessible and only slightly disfavored (endergonic by 3.1 kcal/mol).

Complex **1-OH** is an isolable low-spin  $S = 1/2$  species. However, DFT calculations predict that binding of a fifth ligand leads to a  $S = 3/2$  intermediate. While the low-spin (LS) state of **1-OH** is 17.9 kcal/mol below the high-spin (HS) state, with the addition of water, the HS state of **1-OH-H<sub>2</sub>O** becomes significantly lower (by 17.9 kcal/mol). Spin density plots reveal that more spin

is delocalized onto the DHP and OH ligands in the HS analogs, as expected (Appendix III: **Figure S58-S59**). Tautomerism calculations using different broken-symmetry fragment-guess wavefunctions in DFT echo this result—with addition of the H<sub>2</sub>O ligand significantly increasing Mulliken charge on Co, flipping the preference for Co<sup>III</sup> over Co<sup>II</sup> and increasing delocalization of the unpaired spin density (Appendix III: **Figure S67-S68**). This fifth ligand coordination is key to the predicted formation of the dimer, as calculations of subsequent steps that do not include a fifth ligand are not predicted to yield stable structures. Experimentally, we note that addition of an additional ligand is not limited to H<sub>2</sub>O, as addition of acetonitrile to **1-OH** also promotes the formation of **2** and H<sub>2</sub>O<sub>2</sub> (Appendix III: **Figure S4**). These analyses underscore the importance of the spin- and oxidation-state change induced by ligand coordination in helping to drive H<sub>2</sub>O<sub>2</sub> formation and echo previous observations of valence tautomerism in heme systems.<sup>19</sup>

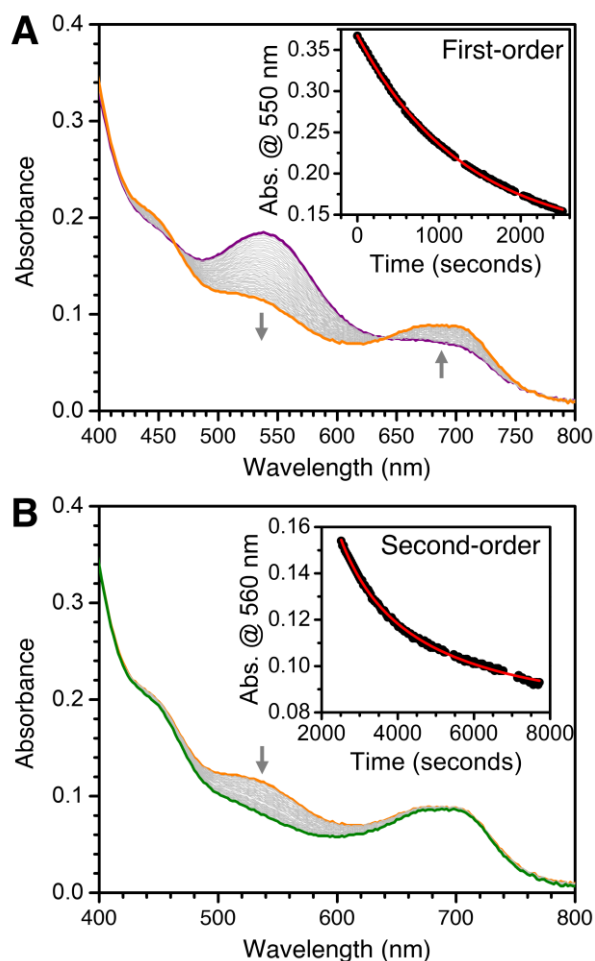


**Figure 2.** UV-vis of 0.094 mM **1-OH** reacting with acetonitrile under pseudo-first order conditions in diethyl ether at 2 °C. A) Traces taken during the first 2500 seconds of the reaction, with an inset showing a first-order fit to the absorbance at 560 nm. B) Traces taken from 2500 to 7700 seconds, with an inset showing a second-order fit to the absorbance at 560 nm. Details on fitting and parameters are provided in the SI.

The predicted rate determining step is the formation of the H<sub>2</sub>O<sub>2</sub> bridged dimer which is uphill by 23.2 kcal/mol from **1-OH-H<sub>2</sub>O**. As mentioned, we observe increased electron density on the -OH ligand in the putative 5-coordinate intermediate **1-OH-H<sub>2</sub>O** and it is possible that this increased radical character facilitates the subsequent dimerization step. Release of H<sub>2</sub>O<sub>2</sub> and H<sub>2</sub>O and production of **2** is nearly thermoneutral at only 0.4 kcal/mol endergonic.

Within this mechanism, **1**, **2**, and **1-OH** are all synthetically accessible which provides several avenues to perform mechanistic experiments (**Scheme 2**). The DFT predicted rate determining step suggests that a 2<sup>nd</sup> order process might be expected from kinetic analyses. We therefore used UV-vis to monitor the addition of either H<sub>2</sub>O or an exogenous ligand (acetonitrile) to **1-OH** under pseudo-first order conditions. This analysis reveals

consecutive isosbestic transformations (**Figure 2A, B**). The first transformation is rapid and first-order. We interpret this conversion as a ligand binding event (**Scheme 2**). A slower, second-order transformation is then observed (**Figure 2B**).

We then used an Eyring analysis to test whether the observed rates were qualitatively consistent with the barriers predicted from DFT. We note that slightly different values between experiment and DFT are expected due to the use of acetonitrile instead of H<sub>2</sub>O as our added ligand in our kinetic measurements for experimental ease. We find that  $\Delta H^\ddagger = 11.4(3)$  kcal/mol and  $\Delta S^\ddagger = -28(1)$  cal/(mol•K) for the second order process. These values provide a 22 °C  $\Delta G^\ddagger = 19.8(3)$  kcal/mol, in good agreement with the DFT predicted barrier for this process. Furthermore, the negative entropy of activation also supports a dimerization.

The DFT calculations above suggest a dimerization pathway, and we therefore assign this second-order process to that step. These measurements were done in triplicate to ensure fidelity, and both first order and second order fits are done via an Espenson treatment (Appendix III: **Figure S12-S18**).<sup>20</sup> The complicated feature observed around 700 nm is also consistent with the major feature in the DFT-predicted spectrum of such a dimeric species (Appendix III: **Figure S48-S49**). The transformation is not isosbestic at longer timepoints, likely due to degradation that occurs as H<sub>2</sub>O<sub>2</sub> is released from the dimer. We note that H<sub>2</sub>O<sub>2</sub> reacts with the starting complex and the intermediates that we can isolate, consistent with this hypothesis.

The DFT calculations predict an endergonic conversion of **1-X** to **2** even though we observe this reaction to be spontaneous with added H<sub>2</sub>O or MeCN (Appendix III: **Figure S4**). While the accuracy of the energetics from DFT is likely limited due to the complicated electronic structure of this putative dimeric intermediate, we also propose that oxidative complex or solvent degradation from formed H<sub>2</sub>O<sub>2</sub> or acid helps drive this reaction. Notably, inclusion of a mild base

(2,6-lutidine) or a H<sub>2</sub>O<sub>2</sub> trap (NaI) makes the overall reaction exergonic (Appendix III: **Figure S66, Table S9**). This computational prediction is also supported experimentally. Reaction of **1-Cl** with H<sub>2</sub>O in a biphasic reaction in the presence of both 2,6-lutidine and NaI allows for the characterization of the stoichiometry of this reaction. <sup>1</sup>H NMR quantification with an internal standard reveals a 78% yield of <sup>t</sup>Bu,TolDHPCo(MeCN) (**2-MeCN**) and an 89% yield of [2,6-lutidinium][Cl]. Concomitant quantification of NaI<sub>3</sub> shows an 80% yield of the expected half-equivalent formed (Appendix III: **Figure S3**). The observations of high yields of both the protonated base as well as oxidation of the added H<sub>2</sub>O<sub>2</sub> trap supports both the proposed stoichiometry as well as the role of sacrificial base/reductant in this process.

It is less clear what the sacrificial base/reductant is in reactions without added reagents, i.e. the direct reaction between **1-X** or **1-OH** with H<sub>2</sub>O or MeCN. We hypothesize that some amount of the starting DHP Co complex serves in this role, consistent with the sub-stoichiometric yields of **2** that are observed. Indeed, oxidized ligand products are observed in the GCMS following the crude reaction from **1-OH** to **2** that are not observed in the GCMS of either isolated complex (Appendix III: **Figure S74-S75**). We note literature precedent that acetonitrile and H<sub>2</sub>O<sub>2</sub> mixtures can form peroxyacetimidic acid in equilibrium, which is then capable of oxidizing tertiary amines.<sup>21</sup> Finally, the IR spectrum of crude freshly formed **2** shows a number of low-intensity N–H stretches, consistent with protonated DHP fragments serving a sacrificial role in this reaction (Appendix III: **Figure S20-S21**).

All of these observations suggest that an overall endergonic process to generate H<sub>2</sub>O<sub>2</sub> predicted from DFT calculations is likely driven by H<sub>2</sub>O<sub>2</sub> consumption from various oxidative decomposition pathways. While this mechanistic proposal is tentative due to the complexity of the system, all computational and experimental data obtained thus far support this general pathway.

Despite convolutions from mechanistic complexity and decomposition pathways, the generation of **2**, which can be stoichiometrically oxidized back to **1-OTf**, suggests that a catalytic cycle should be possible.

### *Catalytic Hydrogen Peroxide Production from Water*

We initially wanted to examine the feasibility of catalysis using chemical oxidants.

Addition of H<sub>2</sub>O and AgOTf in acetonitrile to 5 mol% of **2** results in the growth of a new <sup>1</sup>H NMR peak at 8.6 ppm (Appendix III: **Figure S6**), where H<sub>2</sub>O<sub>2</sub> appears in MeCN, providing direct evidence for the presence of H<sub>2</sub>O<sub>2</sub>.<sup>22</sup>

Integration of this <sup>1</sup>H NMR spectrum reveals that ~50% of the H<sub>2</sub>O peak is consumed and that ~5.5 equivalents of H<sub>2</sub>O<sub>2</sub> per Co center are formed. Unassigned organic peaks are also observed, which suggests some degree of ligand decomposition, consistent with our previous results suggesting ligand-oxidation is occurring and potentially helping drive H<sub>2</sub>O<sub>2</sub> formation. These results support catalytic water oxidation to

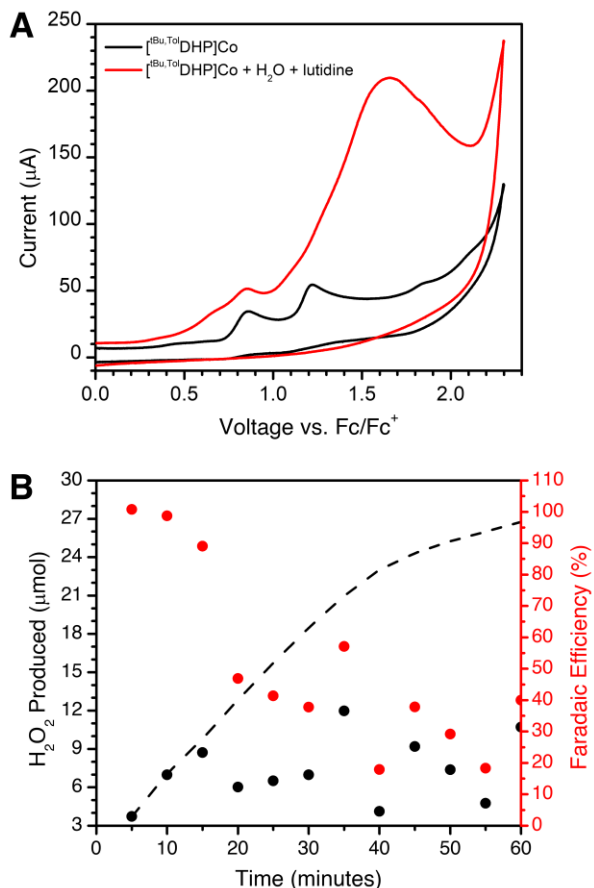


**Figure 3.** A) Current enhancement observed in the presence of **1**, H<sub>2</sub>O, and 2,6-lutidine (1 mM **1**, 320 mM H<sub>2</sub>O, and 160 mM 2,6-lutidine in acetonitrile with 0.1 M NBu<sub>4</sub>PF<sub>6</sub>). B) Theoretical yield (black) and experimental yield (red) determined via NaI assay in micromoles of H<sub>2</sub>O<sub>2</sub> plotted against time (seconds).

H<sub>2</sub>O<sub>2</sub> mediated by **2**. However, we also wanted to corroborate this observation via an orthogonal technique, namely with electrochemistry.

Complex **2** displays four distinct redox waves in its cyclic voltammogram (CV) in THF (Appendix III: **Figure S24**). This is similar to the CV of **1** in THF with some small shifts likely derived from differences in counter-anions.<sup>15f,h</sup> This electrochemical data exhibits the unusually rich redox-flexibility characteristic of the <sup>t</sup>Bu,<sup>Tol</sup>DHP scaffold. Acetonitrile, which is the most tractable solvent for electrochemical studies, significantly complicates the voltammogram by adding new features and making some previous features irreversible, putatively due to solvent coordination (Appendix III: **Figure S23**). With the addition of H<sub>2</sub>O and a mild base, in the form of 2,6-lutidine, catalytic current enhancement can be observed in the CV (**Figure 3A**). The oxidative feature at 0.85 V before the onset of catalysis can likely be assigned to the first oxidation of the acetonitrile or water adduct of **2**. The shape of the catalytic wave is complex even at varying scan rates, making detailed interpretation, for instance with foot-of-the wave analysis, difficult (Appendix III: **Figure S30**).<sup>23</sup> **1**, **1-OTf**, and **2** all display similar electrocatalytic features under similar conditions (Appendix III: **Figure S27-S29**). In acetonitrile, the thermodynamic potential for H<sub>2</sub>O oxidation to H<sub>2</sub>O<sub>2</sub> in the presence of 2,6-lutidine is 0.944 V vs. Fc/Fc<sup>+</sup> and while a precise value for overpotential is difficult to ascertain due to the complicated CV waveform our observed catalytic onset is clearly just above this thermodynamic value (Appendix III: **Equation S4**).

We performed H<sub>2</sub>O<sub>2</sub> quantification to determine the Faradaic efficiency for this product (**Figure 3**). Unlike our chemical reactions above, we can quantify with NaI assays for these electrochemical reactions.<sup>24</sup> When monitored over time we observe an average 41% Faradaic efficiency for H<sub>2</sub>O<sub>2</sub> production over 60 minutes, with notably higher values (>90%) at early timepoints. Furthermore, we see the net amount of detected H<sub>2</sub>O<sub>2</sub> plateau after ~30 minutes

(**Figure 3B**). We attribute both of these observations to the side-reaction of  $\text{H}_2\text{O}_2$  with the catalyst or the electrolyte solution over time. Over 60 minutes 13 C of current is passed, which corresponds to  $10 e^-$  per Co and a TON of 5 assuming 100% Faradaic efficiency for  $\text{H}_2\text{O}_2$  or 2.2 if the average Faradaic efficiency is used. These TON are highly reproducible, an average TON of 6(2) was obtained over 8 individual runs.

Evidence for the instability of **1** in the presence of excess  $\text{H}_2\text{O}_2$  can be confirmed by CVs taken in the presence of **1**, 2,6-lutidine and varied amounts of  $\text{H}_2\text{O}_2 \cdot 2\text{OPPh}_3$ . Though robust with 1 equivalent of  $\text{H}_2\text{O}_2 \cdot 2\text{OPPh}_3$ , the voltammogram of this solution begins to change with 10 or more equivalents of this  $\text{H}_2\text{O}_2$  surrogate and shows significant changes after 20 equivalents consistent with the decomposition of **1** after sufficient  $\text{H}_2\text{O}_2$  production (Appendix III: **Figure S36**).

Importantly, no  $\text{O}_2$  has been detected via GC from any experimental set-up, supporting that  $\text{H}_2\text{O}_2$  is the sole product of electrocatalysis (Appendix III: **Figure S76**). The observed decrease in current and Faradaic efficiency argues against some decomposed product mediating catalysis such as an oxide. However, we also obtained further experimental evidence against the agency of any solid-state catalysts. Removal of the electrode after bulk electrolysis and subsequent analysis by CV shows no catalytic current (Appendix III: **Figure S26**). Furthermore, SEM/EDS analysis on the electrode after bulk electrolysis also shows no evidence for the formation of  $\text{CoO}_x$  materials (Appendix III: **Figure S77-S78**).<sup>25</sup> Additionally, a control using solely  $\text{CoCl}_2$  generates only  $\text{O}_2$  as a product of electrocatalysis under analogous conditions (Appendix III: **Figure S34**). We note that some  $\text{CoO}_x$  materials are competent for the more unusual production of  $\text{H}_2\text{O}_2$ , but this is more typically observed under acidic conditions.<sup>26</sup> All of these combined observations support a molecular catalyst for the observed  $\text{H}_2\text{O}_2$  formation.

## *Conclusion*

Here we present a molecular system that selectively produces H<sub>2</sub>O<sub>2</sub> stoichiometrically and catalytically. Calculations, isolable intermediates, and kinetic analyses suggest that H<sub>2</sub>O<sub>2</sub> formation proceeds through dimerization to form a H<sub>2</sub>O<sub>2</sub>-bridged dimeric intermediate. This overall pathway is facilitated by the redox-activity of the dihydrazonopyrrole ligand scaffold on this system.

It is noteworthy that H<sub>2</sub>O<sub>2</sub> is the only observed product in these reactions, with no generation of O<sub>2</sub> despite the thermodynamic preference for this product. High selectivity for H<sub>2</sub>O<sub>2</sub> over O<sub>2</sub> is unusual in homogenous electrocatalysts. Related catalytic systems that electrochemically generate H<sub>2</sub>O<sub>2</sub> from H<sub>2</sub>O show Faradaic efficiencies that range broadly between 15-85%, with significant current fractions going to O<sub>2</sub> production or even other side-reactions.<sup>12,13,14</sup> High Faradaic efficiency for H<sub>2</sub>O<sub>2</sub> in the absence of concurrent O<sub>2</sub> production is quite rare. Co corrole systems are among the best H<sub>2</sub>O to H<sub>2</sub>O<sub>2</sub> electrocatalysts, but even these examples have imperfect selectivity with ~20% or more of the Faradaic efficiency going to O<sub>2</sub>.<sup>14</sup>

A further unique feature of the present system is its proposed mechanism. Other homogenous electrocatalysts, including the aforementioned corrole systems, either do not make mechanistic proposals or invoke the activity of free hydroxyl radicals, or OH<sup>-</sup> attack on a reactive oxo-/hydroxo- species.<sup>12,13,14</sup> The mechanistic experiments provided here by both DFT and UV-vis monitoring suggest a comparatively unique bimetallic pathway. The observed stoichiometric reactivity is also unusual; molecular complexes that directly generate H<sub>2</sub>O<sub>2</sub> from H<sub>2</sub>O without added oxidant are rare. While the low stability of the current system limits its catalytic utility, these results do demonstrate how molecular design principles can enable selectivity for

thermodynamically more difficult products, further underscoring how metal-ligand cooperativity can enable new reactivity and catalysis.

## Experimental Section

### General Methods

All chemicals were purchased from commercial suppliers and used without further purification. All manipulations were carried out under an atmosphere of N<sub>2</sub> using standard Schlenk and glovebox techniques. Glassware was dried at 180 °C for a minimum of two hours and cooled under vacuum prior to use. Solvents were dried on a solvent purification system from Pure Process Technologies and stored over 4 Å molecular sieves under N<sub>2</sub>. Tetrahydrofuran (THF) was stirred over NaK alloy and run through an additional alumina column prior to use to ensure dryness. Solvents were tested for H<sub>2</sub>O and O<sub>2</sub> using a standard solution of sodium-benzophenone ketyl radical anion. CD<sub>3</sub>CN, C<sub>6</sub>D<sub>6</sub>, and d<sub>8</sub>-toluene were dried over 4 Å molecular sieves under N<sub>2</sub>.

<sup>1</sup>H and <sup>19</sup>F NMR spectra were recorded on Bruker DRX 400 or 500 spectrometers. Chemical shifts are reported in ppm units referenced to residual solvent resonances for <sup>1</sup>H and <sup>31</sup>H{<sup>1</sup>H} spectra. UV-visible Spectra were recorded on a Bruker Evolution 300 spectrometer and analyzed using VisionPro software. A standard 1 cm quartz cuvette with an airtight screw cap with a puncturable Teflon seal was used for all measurements. A Unisoku CoolSpek cryostat was used for low-temperature measurements. <sup>1</sup>H and <sup>19</sup>F NMR spectra were recorded on either Bruker DRX-400 or AVANCE-500 spectrometers. IR spectra were recorded on either a Bruker Tensor II spectrometer with the OPUS software suite as DCM thin films between KBr plates or a Bruker α II spectrometer in a nitrogen, dry glovebox with the OPUS software suite as diethyl ether thin films on a Platinum Diamond ATR module. Single crystal X-ray diffraction data were collected in-house using Bruker D8 Venture diffractometer equipped with Mo microfocus X-ray tube ( $\lambda =$

0.71073 Å). Combustion analysis was performed by Midwest Microlab. Electrochemical measurements were carried out using a BAS Epsilon potentiostat and using BAS Epsilon software version 1.40.67 NT. Magnetic moments were determined using the Evans method.<sup>27</sup>

### *Electrochemical experiments*

Experiments were performed inside the glovebox with a MeCN/0.1 M NBu<sub>4</sub>NPF<sub>6</sub> electrolyte solution at room temperature. Cyclic voltammetry measurements were made with a [Co] = 1 mM using a glassy carbon working electrode, platinum wire counter electrode, and silver wire pseudoreference electrode and were referenced to internal Fc/Fc<sup>+</sup> by adding ferrocene at the end of the measurements. A one-compartment glass cell was filled with 4 mL of electrolyte solution. The working electrode was polished over a microcloth pad (Buehler) using alumina slurry (0.05 mm EMS), followed by rinsing with deionized water and isopropyl alcohol. Reference and counter electrodes were rinsed with acetone. CVs were recorded at a scan rate of 200 mV/s scanning oxidatively.

Electrolyses were performed in a sealed H-type glass cell with anode and cathode chambers separated by a glass frit. A graphite rod electrode, Pt-mesh electrode, and a silver wire pseudoreference electrode were used as working, counter, and reference electrodes, respectively. To each chamber of the H-cell was added 10 mL of electrolyte solution and stir bars. Typically, 5.4 mg of (DHP)CoCl (final concentration 1 mM), 160 equiv. of 2,6-lutidine, and 320 equiv. of H<sub>2</sub>O were added to the cathodic chamber. 320 equiv. of H<sub>2</sub>O was also added to the anodic chamber. Post-electrolysis, the sealed atmosphere was sampled with a gas-tight syringe and analyzed by GC for O<sub>2</sub>.

**(<sup>t</sup>Bu, Tol<sup>1</sup>DHP)Co (2)**

In a 20 mL vial in the glovebox, 1-2 mL of diethyl ether was added until (<sup>t</sup>Bu, TolDHP)CoCl (**1**, 15.0 mg, 0.028 mmol)<sup>15f</sup> dissolved completely to generate a purple solution. A concentrated solution of 10  $\mu$ L of H<sub>2</sub>O or D<sub>2</sub>O in 1 mL of diethyl ether was prepared. From this stock solution a 3  $\mu$ L aliquot was taken (1 equiv., 0.028 mmol) and added to the solution of **1**. The solution remained purple and was allowed to react for 1 hour. After this time the solution was dried *in vacuo* and the remaining solids were extracted with petroleum ether. This petroleum ether fraction could be filtered and dried *in vacuo* to obtain crude **2** in 75% yield (0.0105 g, 0.0210 mmol). This crude solid can be recrystallized out of concentrated petroleum ether. We note that additional crops of material can be obtained by benzene extraction of any remaining solids. Single crystals for XRD were grown via cooling a diethyl ether solution of this product at  $-35^{\circ}\text{C}$ . We note that similar procedures with alternative bound anions (i.e. OTf<sup>-</sup> or OH<sup>-</sup> also provide **2**, albeit in slightly lower yield (45(5)%, 0.0063g, 0.126 mmol, for X = OH). <sup>1</sup>H NMR (400 MHz, C<sub>7</sub>D<sub>8</sub>, RT):  $\delta$  = 7.47 (br s), 2.72 (br s). Magnetic Susceptibility: Evans' Method (C<sub>6</sub>D<sub>6</sub>, RT,  $\mu_{\text{B}}$ ):  $\mu_{\text{eff}}$  = 2.90; UV-vis, nm in diethyl ether, ( $\epsilon$ , M<sup>-1</sup>cm<sup>-1</sup>): 4342.64. HRMS (EI) m/z: [M]<sup>+</sup> calculated for **1**: C<sub>28</sub>H<sub>34</sub>N<sub>5</sub>Co 499.2121 found: 499.2164.

### Reoxidation of (<sup>t</sup>Bu, TolDHP)Co (**2**) to (<sup>t</sup>Bu, TolDHP)CoOTf (**1-OTf**)

In a 20 mL vial in the glovebox, 2 mL of acetonitrile was added to (<sup>t</sup>Bu, TolDHP)Co (0.002 g, 1 eq., 0.0039 mmol). A solution of silver triflate (0.001g, 1 eq., 0.0039 mmol) in acetonitrile was added dropwise, resulting in a color-change from brown/purple to dark green. This was stirred for 30-60 minutes, and subsequently dried *in vacuo* to a dark maroon solid which could then be collected into benzene. Yield: 0.0024 g, 92%. The NMR was found to match the previously reported NMR for **5**.<sup>15f</sup> This reaction could also be followed by NMR and seemed to have quantitative yields with no overoxidation occurring.

### **Biphasic reaction of (<sup>t</sup>Bu, Tol)<sup>DHP</sup>CoCl (**1**) to (<sup>t</sup>Bu, Tol)<sup>DHP</sup>Co(MeCN) (**2-MeCN**)**

In a 20 mL vial in the glovebox, 2 mL of diethyl ether was added to (<sup>t</sup>Bu, Tol)<sup>DHP</sup>CoCl (**1**) (0.0011 g, 1 eq., 0.0020 mmol). A solution of sodium iodide (0.003 g, 10 eq., 0.0200 mmol) in H<sub>2</sub>O was added, and the resulting solution stirred for 30 minutes. The diethyl ether solution was pipetted off and subsequently dried *in vacuo* to a dark purple solid. This solid was dissolved in CD<sub>3</sub>CN, and the yield of NaI<sub>3</sub> in the H<sub>2</sub>O fraction was quantified by UV-Vis. Yield **2-MeCN**: 0.0008 g, 78%, Yield NaI<sub>3</sub>: 40% (relative to **1**), Yield 2,6-lutidinium chloride: 89%. The NMR was found to match that previously reported for NMR for **2-MeCN**.

### **Preparation of UV-Vis samples for H<sub>2</sub>O<sub>2</sub> quantification via I<sub>3</sub><sup>-</sup>**

#### **Post-Bulk Electrolysis**

The remaining acetonitrile solution from the bulk electrolysis was placed into a vial with excess NaI and stirred over 4-5 hours before drying *in vacuo*. The solids were washed with toluene to remove organic products, and then extracted into acetonitrile or water. An aliquot was measured by syringe and transferred into a cuvette for UV-vis analysis. For larger runs, a volumetric flask was used to measure volume, and a known amount was transferred into the cuvette by syringe. The extinction coefficient of I<sub>3</sub><sup>-</sup> does not vary significantly between acetonitrile and water, but nevertheless, we made sure water was always present in excess in order to maintain consistency.<sup>28</sup>

#### **Molecular Reactions**

The procedure above for the synthesis of **2** was altered in the following fashion in order to obtain yields with NaI (5-10 equiv.). **1** (2 mg, 0.0037 mmol) was dissolved in 50 μL of dichloromethane and a NaI (5 equiv.) solution in 2.5 mL of H<sub>2</sub>O was added to this solution. The biphasic mixture was stirred for 30 minutes, then the I<sub>3</sub><sup>-</sup> content of the H<sub>2</sub>O layer was quantified by UV-Vis.

## References

1. (a) Jones, C. W.; Clark, J. H. In *Applications of Hydrogen Peroxide and Derivatives*, Jones, C. W., Ed.; Royal Society of Chemistry: Cambridge, U.K., **1999**; 1– 35.; (b) Eul, W.; Moeller, A.; Steiner, N. Hydrogen peroxide. In *Kirk-Othmer Encyclopedia of Chemical Technology*; Wiley, **2001**.; (c) Campos-Martin, J. M.; Blanco-Brieva, G.; Fierro, J. L. G. Hydrogen Peroxide Synthesis: An Outlook beyond the Anthraquinone Process. *Angew. Chem., Int. Ed.* **2006**, *45*, 6962.; (d) Chen, Q. Development of an Anthraquinone Process for the Production of Hydrogen Peroxide in a Trickle Bed Reactor-From Bench Scale to Industrial Scale. *Chem. Eng. Process.* **2008**, *47*, 787–792.; (e) Lewis, R. J.; Hutchings, G. J. Recent Advances in the Direct Synthesis of H<sub>2</sub>O<sub>2</sub>. *ChemCatChem* **2019**, *11*, 298.
2. Schröder, V.; Emonts, B.; Janßen, H.; Schulze, H.-P. Explosion Limits of Hydrogen/Oxygen Mixtures at Initial Pressures up to 200 bar. *Chem. Eng. Technol.* **2004**, *27*, 847.
3. (a) Choudhary, V. R.; Gaikwad, A. G.; Sansare, S. D. Nonhazardous Direct Oxidation of Hydrogen to Hydrogen Peroxide Using a Novel Membrane Catalyst. *Angew. Chem., Int. Ed.* **2001**, *40*, 1776.; (b) Edwards, J. K.; Solsona, B.; Ntainjua, E. N.; Carley, A. F.; Herzing, A. A.; Kiely, C. J.; Hutchings, G. J. Switching Off Hydrogen Peroxide Hydrogenation in the Direct Synthesis Process. *Science* **2009**, *323*, 1037.; (c) Edwards, J. K.; Freakley, S. J.; Carley, A. F.; Kiely, C. J.; Hutchings, G. J. Strategies for Designing Supported Gold–Palladium Bimetallic Catalysts for the Direct Synthesis of Hydrogen Peroxide. *Acc. Chem. Res.* **2014**, *47*, 845.; (d) Freakley, S. J.; He, Q.; Harrhy, J. H.; Lu, L.; Crole, D. A.; Morgan, D. J.; Ntainjua, E. N.; Edwards, J. K.; Carley, A. F.; Borisevich, A. Y.; Kiely, C. J.; Hutchings, G. J. Palladium-tin catalysts for the direct synthesis of H<sub>2</sub>O<sub>2</sub> with high selectivity. *Science* **2016**, *351*, 965.; (e) Wilson, N. M.; Flaherty, D. W. Mechanism for the direct synthesis of H<sub>2</sub>O<sub>2</sub> on Pd clusters: heterolytic reaction pathways at the liquid–solid interface. *J. Am. Chem. Soc.* **2016**, *138*, 574.; (f) Shi, X.; Siahrostami, S.; Li, G.-L.; Zhang, Y.; Shakthranont, P.; Studt, F.; Jaramillo, T. F.; Zheng, X.; Norskov, J. K. Understanding activity trends in electrochemical water oxidation to form hydrogen peroxide. *Nature Comm.* **2017**, *8*, 701.; (g) Liu, J.; Zou, Y.; Jin, B.; Zhang, K.; Park, J. H. Hydrogen Peroxide Production from Solar Water Oxidation. *ACS Energy Lett.* **2019**, *4*, 12, 3018.
4. (a) Gamage, S. N.; James, B. R. Catalytic Formation of an Amide Hydroperoxide and Hydrogen Peroxide using Rhodium Complexes and Dioxygen/Dihydrogen Mixtures. *J. Chem. Soc., Chem. Commun.* **1989**, 1624.; (b) Shibata, S.; Suenobu, T.; Fukuzumi, S. Direct Synthesis of Hydrogen Peroxide from Hydrogen and Oxygen by Using a Water-Soluble Iridium Complex and Flavin Mononucleotide. *Angew. Chem., Int. Ed.* **2013**, *52*, 12327.; (c) Ogo, S.; Yatabe, T.; Tome, T.; Takenaka, R.; Shiota, Y.; Kato, K. Safe, One-Pot, Homogeneous Direct Synthesis of H<sub>2</sub>O<sub>2</sub>. *J. Am. Chem. Soc.* **2023**, *145*, 8, 4384.
5. (a) Yamanaka, I.; Onizawa, T.; Takenaka, S.; Otsuka, K. Direct and Continuous Production of Hydrogen Peroxide with 93% Selectivity Using a Fuel-Cell System. *Angew. Chem., Int. Ed.* **2003**, *42*, 3653.; (b) Xia, C.; Xia, Y.; Zhu, P.; Fan, L.; Wang, H. Direct electrosynthesis of pure aqueous H<sub>2</sub>O<sub>2</sub> solutions up to 20% by weight using a solid electrolyte. *Science*. **2019**, *366*, 226.; (c) Ledendecker, M.; Pizzutilo, E.; Malta, G.; Fortunato, G. V.; Mayrhofer, K. J. J.; Hutchings, G. J.; Freakley, S. J. Isolated Pd Sites as Selective Catalysts for Electrochemical and Direct Hydrogen Peroxide Synthesis. *ACS Catalysis* **2020**, *10* (10), 5928.

6. Tse, E. C. M.; Barile, C. J.; Kirchschrager, N. A.; Li, Y.; Gewaris, J. P.; Zimmerman, S. C.; Hosseini, A.; Gewirth, A. A. Proton transfer dynamics control the mechanism of O<sub>2</sub> reduction by a non-precious metal electrocatalyst. *Nat. Mat.* **2016**, *15*, 754.
7. (a) Wang, Y-H.; Mondal, B.; Stahl, S. S. Molecular Cobalt Catalysts for O<sub>2</sub> Reduction to H<sub>2</sub>O<sub>2</sub>: Benchmarking Catalyst Performance via Rate-Overpotential Correlations. *ACS Catal.* **2020**, *10*, 20, 12031.; (b) Rana, A.; Lee, Y-M.; Li, X.; Cao, R.; Fukuzumi, S.; Nam, W. Highly Efficient Catalytic Two-Electron Two-Proton Reduction of Dioxygen to Hydrogen Peroxide with a Cobalt Corrole Complex. *ACS Catal.* **2021**, *11*, 5, 3073.
8. (a) Chen, Z.; Concepcion, J. J.; Hull, J. F.; Hoertz, P. G.; Meyer, T. J. Catalytic water oxidation on derivatized nanoITO. *Dalton Trans.*, **2010**, *39*, 6950.; (b) Chen, Z.; Concepcion, J. J.; Hu, X.; Yang, W.; Hoertz, P. G., A.; Meyer, T. J. Concerted O atom-proton transfer in the O-O bond forming step in water oxidation. *PNAS*, **2010**, *107*, 7225.
9. (a) Chen, Z.; Concepcion, J. J.; Luo, H.; Hull, J. F.; Paul, A.; Meyer, T. J. Nonaqueous Catalytic Water Oxidation. *J. Am. Chem. Soc.* **2010**, *132*, 17670. (b) Hidalgo-Acosta, J. C.; Mendez, M. A.; Scanlon, M. D.; Vrabel, H.; Amstutz, V.; Adamiak, W.; Opallo, M.; Girault, H. H. Catalysis of water oxidation in acetonitrile by iridium oxide nanoparticles. *Chem. Sci.* **2015**, *6*, 1761.
10. (a) Mirzakulova, E.; Khatmullin, R.; Walpita, J.; Corrigan, T.; Vargas-Barbosa, N. M.; Vyas, S.; Oottikkal, S.; Manzer, S. F.; Hadad, C. M.; Glusac, K. D. Electrode-assisted water oxidation by a flavin derivative. *Nature Chemistry*, **2012**, *3*, 794-801.; (b) Fisher, K. J.; Materna, K. L.; Mercado, B. Q.; Crabtree, R. H.; Brudvig, G. W. Electrocatalytic Water Oxidation by a Copper(II) Complex of an Oxidation-Resistant Ligand. *ACS Catal.* **2017**, *7*, 3384.; (c) Hsu, W-C.; Wang, Y-H. Homogenous Water Oxidation Catalyzed by First Row Transition Metal Complexes: Unveiling the Relationship between Turnover Frequency and Reaction Overpotential. *ChemSusChem.* **2022**, *15*, e202102378. (h<sub>2</sub>o to O<sub>2</sub> nonprecious)
11. (a) Brunshwig, B. S.; Chou, M. H.; Creutz, C.; Ghosh, P.; Sutin, N. Mechanisms of Water Oxidation to Oxygen: Cobalt(IV) as an Intermediate in the Aquocobalt(II)-Catalyzed Reaction. *J. Am. Chem. Soc.* **1983**, *105*, 4833.; (b) Dogutan, D. K.; McGuire, R.; Nocera, D. G. Electrocatalytic Water Oxidation by Cobalt (III) Hangman β-Octafluoro Corroles. *J. Am. Chem. Soc.* **2011**, *133*, 9178.; (c) McCool, N. S.; Robinson, D. M.; Sheats, J. E.; Dismukes, G. C. A Co<sub>4</sub>O<sub>4</sub> “Cubane” Water Oxidation Catalyst Inspired by Photosynthesis. *J. Am. Chem. Soc.* **2011**, *133*, 11446.; (d) Wang, D.; Groves, J.T. Efficient water oxidation catalyzed by homogeneous cationic cobalt porphyrins with critical roles for the buffer base *PNAS*, **2013**, *110*, 15579.; (e) Ishizuka, T.; Watanabe, A.; Kotani, H.; Hong, D.; Staonaka, K.; Wada, T.; Shiota, Y.; Yoshizawa, K.; Ohara, K.; Yamaguchi, K.; Kato, S.; Fukuzumi, S.; Kojima, T. Homogenous Photocatalytic Water Oxidation with a Dinuclear CoIII-Pyridylmethylamine Complex. *Inorg. Chem.* **2016**, *55*, 1154.; (f) Khosrowabadi Kotyk, J. F.; Hanna, C. M.; Combs, R. L.; Ziller, J. W.; Yang, J. Y. Intramolecular hydrogen-bonding in a cobalt aqua complex and electrochemical water oxidation activity. *Chem. Sci.*, **2018**, *9*, 2750.; (g) Du, H-Y; Chen, S-C; Su, X-J; Jiao, L.; Zhang, M-T. Redox-Active Ligand Assisted Multielectron Catalysis: A Case of Co<sup>III</sup> Complex as Water Oxidation Catalyst *J. Am. Chem. Soc.* **2018**, *140*, 4, 1557.; (h) Biswas, S.; Bose, S.; Debgupta, D.; Das, P.; Biswas, A. N. Redox-active ligand assisted electrocatalytic water oxidation by a mononuclear cobalt complex. *Dalton Trans.* **2020**, *49*, 7155.; (i) Bera, M.; Kaur, S.; Keshari, K.; Moonshiram, D.; Parja, S. Characterization of Reaction Intermediates Involved in the Water Oxidation Reaction of a Molecular Cobalt Complex *Inorg. Chem.* **2022**, *61*, 51, 21035.
12. Shi, X.; Back, S.; Gill, T. M.; Siahrostami, S.; Zheng, X. Electrochemical Synthesis of H<sub>2</sub>O<sub>2</sub> by Two-Electron Water Oxidation Reaction Review. *Chem.* **2021**, *7*, 38. (review of chem h<sub>2</sub>o<sub>2</sub>)

13. (a) Kuttassery, F.; Sagawa, S.; Mathew, S.; Sagawa, S. Remello, S. N.; Thomas, A.; Yamamoto, D.; Onuki, S.; Nabetani, Y.; Tachibana, H.; Inoue, H. One Electron-Initiated Two-Electron Oxidation of Water by Aluminum Porphyrins with Earth's Most Abundant Metal. *ChemSusChem*. **2017**, *10*, 1909.; (b) Han, Z.; Horak, K. T.; Lee, H. B.; Agapie, T. Tetranuclear Manganese Models of the OEC Displaying Hydrogen Bonding Interactions: Application to Electrocatalytic Water Oxidation to Hydrogen Peroxide. *J. Am. Chem. Soc.* **2017**, *139*, 9108.; (c) Deutscher, J.; Corona, T.; Warm, K.; Engelmann, X.; Sobottka, S.; Braun-Cula, B.; Sarkar, B.; Ray, K. Water Oxidation Reaction Mediated by an Octanuclear Iron-Oxo Cluster. *Eur. J. Inorg. Chem.* **2018**, 4925.; (d) Kuttassery, F.; Sagawa, S.; Mathew, S.; Nabetani, Y.; Iwase, A.; Kudo, A.; Tachibana, H.; Inoue, H. Water Splitting on Aluminum Porphyrins To Form Hydrogen and Hydrogen Peroxide by One Photon of Visible Light. *ACS Appl. Energy Mater.* **2019**, *2*, 8045.; (e) Ohsaki, Y.; Thomas, A.; Kuttassery, F.; Mathew, S.; Remello, S. N.; Shimada, T.; Ishida, T.; Takagi, S.; Tachibana, H.; Inoue, H. Two-electron oxidation of water to form hydrogen peroxide initiated by one-electron oxidation of Tin (IV)-porphyrins. *Journal of Photochemistry & Photobiology A: Chemistry* **2020**, *401*, 112732.23.; (f) Mavrikis, S.; Goltz, M.; Perry, S. C.; Bogdan, F.; Leung, P. K.; Rosiwal, S.; Wang, L.; Ponce de Leon, C. Effective Hydrogen Peroxide Production from Electrochemical Water Oxidation. *ACS Energy Lett.* **2021**, *6*, 2369.; (g) Mavrikis, S.; Perry, S. C.; Leung, P. K.; Wang, L.; Ponce de Leon, C. Recent Advances in Electrochemical Water Oxidation to Produce Hydrogen Peroxide: A Mechanistic Perspective. *ACS Sustainable Chem. Eng.* **2021**, *9*, 76.
14. (a) Hong, Y. H.; Han, J. W.; Jung, J.; Nakagawa, T.; Lee, Y-M; Nam, W.; Fukuzumi, S. Photocatalytic Oxygenation Reactions with a Cobalt Porphyrin Complex Using Water as an Oxygen Source and Dioxygen as an Oxidant *J. Am. Chem. Soc.* **2019**, *141*, 23, 9155.; (b) Mondal, B.; Chattopadhyay, S.; Dey, S.; Mahammed, A.; Mitra, K.; Rana, A.; Gross, Z.; Dey, A. Elucidation of Factors That Govern the  $2e^-/2H^+$  vs.  $4e^-/4H^+$  Selectivity of Water Oxidation by a Cobalt Corrole. *J. Am. Chem. Soc.* **2020**, *142*, 50, 21040.; (c) Vaillard, V. A.; Nieres, P. D.; Vaillard, S. E.; Doctorovich, F.; Sarkar, B.; Neuman, N. I. Cobalt, Iron, and Manganese Metalloporroles in Catalytic Oxidation of Water. An Overview of the Synthesis, Selected Redox and Electronic Properties, and Catalytic Activities. *Eur. J. Inorg. Chem.* **2022**, e202100767.
15. (a) Chang, M-C.; McNeece, A. J.; Hill, E. A.; Filatov, A. S.; Anderson, J. S. Ligand-Based Storage of Protons and Electrons in Dihydrozopyrrole Complexes of Nickel. *Chem. Eur. J.*, **2018**, *24*, 8001.; (b) Chang, M-C; Jesse, K. A.; Filatov, A. S.; Anderson, J. S. Reversible Homolytic Activation of Water via Metal-Ligand Cooperativity in a T-shaped Ni(II) Complex. *Chem. Sci.* **2019**, *10*, 1360.; (c) McNeece, A. J.; Jesse, K. A.; Xie, J.; Filatov, A. S.; Anderson, J. S. Generation and Oxidative Reactivity of a Ni(II) Superoxo Complex via Ligand-Based Redox Non-Innocence. *J. Am. Chem. Soc.* **2020**, *142*, 10824.; (d) McNeece, A. J.; Jesse, K. A.; Filatov, A. S.; Schneider, J. E.; Anderson, J. S. Catalytic hydrogenation enabled by ligand-based storage of hydrogen. *Chem. Comm.* **2021**, *57*, 3869.; (e) Jesse, K. A.; Anferov, S. W.; Collins, K. A.; Valdez-Moriera, J. A.; Czaikowski, M. E.; Filatov, A. S.; Anderson, J. S. Direct Aerobic Generation of a Ferric Hydroperoxo Intermediate Via a Preorganized Secondary Coordination Sphere. *J. Am. Chem. Soc.* **2021**, *143*, 18121.; (f) Anferov, S. W.; Filatov, A. S.; Anderson, J. S. Cobalt-Catalyzed Hydrogenation Reactions Enabled by Ligand-Based Storage of Dihydrogen. *ACS Catal.* **2022**, *12*, 16, 9933.; (g) Czaikowski, M. E.; McNeece, A. J.; Boyn, J-N.; Jesse, K. A.; Anferov, S. W.; Filatov, A. S.; Mazziotti, D. A.; Anderson, J. S. Generation and Aerobic Oxidative Catalysis of a Cu(II) Superoxo Complex Supported by a Redox-Active Ligand *J. Am. Chem. Soc.*

- 2022**, *144*, 34, 15569.; (h) Anferov, S. W.; Anderson, J. S. A cobalt adduct of an N-hydroxypiperidinium cation. *J. Coord. Chem.* **2022**, *75*, 11-14, 1853.
- 16.(a) Yang, L.; Powell, D. R.; Houser, R. P. Structural variation in copper(I) complexes with pyridylmethylamide ligands: structural analysis with a new four-coordinate geometry index,  $\tau_4$ . *Dalton Trans.* **2007**, *9*, 955.; (b) Okuniewski, A.; Rosiak, D.; Chojnacki, J.; Becker, B. Coordination polymers and molecular structures among complexes of mercury(II) halides with selected 1-benzoylthioureas. *Polyhedron.* **2015**, *90*, 47.
17. Brookhart, M.; Green, M. L. H.; Parkin, G. Agostic interactions in transition metal compounds. *PNAS*, **2007**, *104* (17), 6908.
18. Źamojć, K.; Zdrowowicz, M.; Rudnicki-Velasquez, P. B.; Krzymiński, K.; Zaborowski, B.; Niedziałkowski, P.; Jacewicz, D.; Chmurzyński, L. The development of 1,3-diphenylisobenzofuran as a highly selective probe for the detection and quantitative determination of hydrogen peroxide. *Free Radical Res.* **2017**, *51*, 38.
19. Das, P. K.; Samanta, S.; McQuarters, A. B.; Lehnert, N.; Dey, A. Valence tautomerism in synthetic models of cytochrome P450. *PNAS*, **2016**, *113* (24), 6611-6616.
20. Espenson, J. H. *Chemical Kinetics and Reaction Mechanisms*; McGraw-Hill Custom Publishing, New York Etc., **1981**.
21. Laus, G. Kinetics of acetonitrile-assisted oxidation of tertiary amines by hydrogen peroxide. *J. Chem. Soc., Perkin Trans. 2*, **2001**, 864.
22. Wickramasinghe, L. A.; Sharp, P. R. Dihydrogen Trioxide (HOOH) Photoelimination from a Platinum(IV) Hydroperoxo-Hydroxo Complex *J. Am. Chem. Soc.* **2014**, *136*, 40, 13979.
23. Rountree, E. S.; McCarthy, B.D.; Eisenhart, T. T.; Dempsey, J. L. Evaluation of Homogeneous Electrocatalysts by Cyclic Voltammetry. *Inorg. Chem.* **2014**, *53*, 9983–10002
24. Wang, M.; Qiu, S; Yang, H.; Huang, Y.; Dai, L.; Zhang, B.; Zqu, J. Spectrophotometric determination of hydrogen peroxide in water with peroxidase-catalyzed oxidation of potassium iodide and its applications to hydroxylamine-involved Fenton and Fenton-like systems. *Chemosphere*, **2021**, *270*, 129448.
25. Wang, J-W.; Sahoo, P.; Lu, T-B. Reinvestigation of Water Oxidation Catalyzed by a Dinuclear Cobalt Polypyridine Complex: Identification of  $\text{CoO}_x$  as a Real Heterogenous Catalyst. *ACS Catal.* **2016**, *6*, 5062.
26. Gerken, J. B.; McAlpin, J. G.; Chen, J. Y. C.; Rigsby, M. L.; Casey, W. H.; Britt, R. D.; Stahl, S. S. Electrochemical Water Oxidation with Cobalt-Based Electrocatalysts from pH 0–14: The Thermodynamic Basis for Catalyst Structure, Stability, and Activity. *J. Am. Chem. Soc.* **2011**, *133*, 36, 14431.
27. Jenkins, D. M.; Peters, J. C. Spin-State Tuning at Pseudotetrahedral  $d^7$  Ions: Examining the Structural and Magnetic Phenomena of Four-Coordinate  $[\text{BP}_3]\text{Co}^{\text{II}}\text{-X}$  Systems *J. Am. Chem. Soc.* **2005**, *127* (19), 7148– 7165.
28. Jessup, W.; Dean, R. T.; Gebicki, J. M. Iodometric determination of hydroperoxides in lipids and proteins. *Methods in Enzymology*, **1994**, *233*, 289.
-

## Chapter V: Tunable Olefin Isomerization via In-Situ Modification of a H-atom Storing Ligand

*Walking by yourself, Do the Redox-Neutral Shuffle*

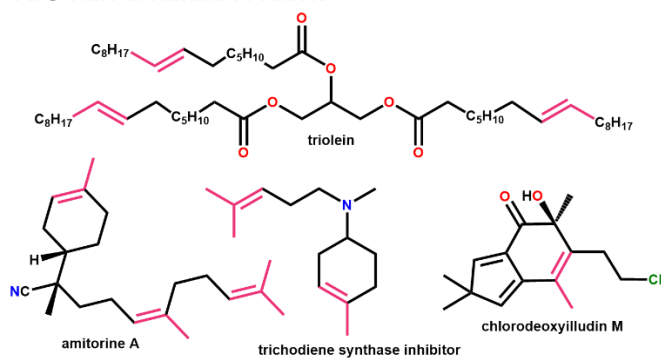
This chapter has been adapted from the following: Anferov, S. W.; McNamara, L. E.; Anderson, J. S. *In Preparation*.

### Introduction

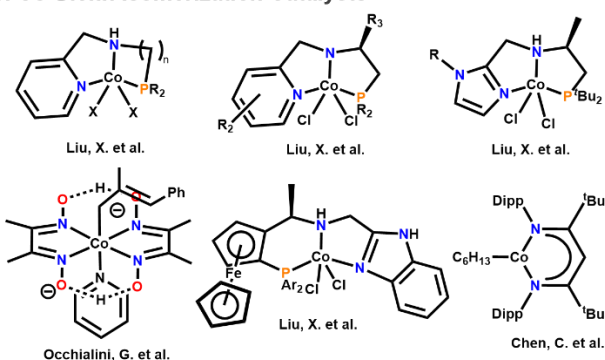
Alkenes provide a broadly useful synthetic handle for further functionalization. Terminal alkenes are frequently initial products, for instance via Wittig chemistry, but internal alkenes provide a broader scope. While internal alkenes have many synthetic routes, alkene metathesis being one example, selective double bond isomerization from existing alkene functionalities is an efficient and atom-economical approach.<sup>1</sup> This sort of selective migration also enables the facile interconversion of chemical feedstocks. There has therefore been a surge of interest in alkene isomerization catalysis as an ideal method to localize existing double bonds into desired positions or conformations.

The quasi-degenerate energies of alkene migration make selectivity a challenge. Most systems operate under thermodynamic control and preferentially localize alkenes to the most exergonic site, typically the most highly substituted position. For instance, there have been a number of catalysts which mediate the isomerization of 1- to 2-alkenes.<sup>2,3</sup> This can be particularly useful for the synthesis of natural products with cyclic alkenes; 1-methyl-cyclohex-1-ene motifs are challenging to synthesize by other routes (**Figure 1**).<sup>4</sup> However, good selectivity in these systems is only realized with cyclic or specifically functionalized substrates with some thermodynamic preference.<sup>6</sup> Isomerizations with multiple products that are close in energy, for

### A. Olefins in Natural Products



### B. Co Olefin Isomerization Catalysts



### C. This Work:

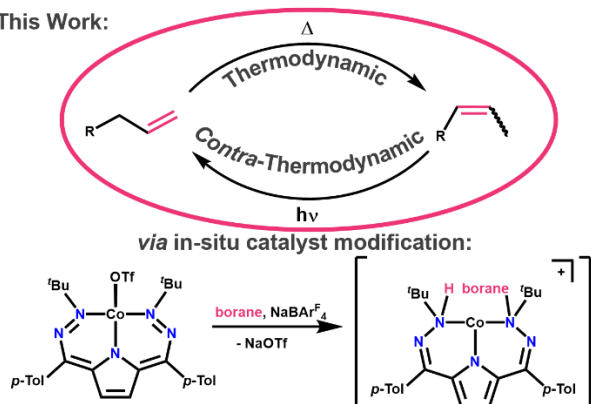


**Figure 1:** Alkene isomerization overview. A: Natural products accessible via 1- to 2- alkene isomerization. B: Co-based olefin isomerization catalysts in the literature. C: This work—reversible and selective olefin isomerization by an in-situ generated catalyst.

instance selective single position migration from the 1- to 2-position in a linear chain without further migration along the chain, remain particularly difficult.<sup>1,5,6,7</sup> Migrations along the unsaturated long chains of fatty acids and related glycerin esters provide one biological example of where both alkene position and E/Z stereochemistry are pivotal for function and even health (**Figure 1**).<sup>5,8</sup>

Beyond discriminating between thermodynamically equivalent products, selecting for endergonic transformations is an even greater challenge. As one example, most catalysts produce a thermodynamic ratio of E/Z isomers even though Z products have several advantages, for instance in the fatty acid products mentioned above.<sup>8</sup> This and related contra-thermodynamic selectivity remain a broad and fundamental challenge. A brute force approach is multi-step oxidation/reduction, but these

strategies are intensive and challenging to broadly apply.<sup>9</sup>

Photochemical activation is an alternative approach that has produced notable results in this area. Accessible excited states can provide kinetic access to endergonic products.<sup>10</sup> This approach has been applied for contra-thermodynamic E:Z bond conversions, although these examples are typically limited to styrenyl or otherwise conjugated double bonds, with few, if any, examples of simple, non-functionalized alkene E:Z bond isomerization.<sup>11</sup>

Aside from Z selective processes, there are select examples of contra-thermodynamic 2-to-1 or deconjugative migrations.<sup>12,13</sup> Despite these exciting advances, there is a dearth of selective isomerizations with selectivity among many energetically degenerate sites. Many of the catalysts used in these transformations are complex—requiring heavy-metal photo-sensitizers and co-catalysts, as well as high energy light.<sup>12</sup> Furthermore, specific catalysts mediate either thermodynamic or contra-thermodynamic isomerization. There are currently no examples that exhibit switchable isomerization catalysis where selectivity is dictated by experimental conditions<sup>14</sup>

We previously reported hydrogenation chemistry with (*t*Bu,TolDHP)Ni and (*t*Bu,TolDHP)Co catalysts (*t*Bu,TolDHP = 2,5-bis((2-(*tert*-butyl)hydrazineylidene)(*p*-tolyl)methyl)-1*H*-pyrrole).<sup>15-16</sup> We had noted that (*t*Bu,TolDHP)Co catalysts exhibited some isomerization reactivity with more complex substrates.<sup>15</sup> Namely, the diene E-2-methyl-1,3-pentene exhibited hydrogenation along with isomerization to both E-2-methyl-pent-2-ene and Z-2-methyl-pent-3-ene. This observation led us to investigate whether we could mediate selective alkene isomerizations with this system.

Herein we report thermal alkene transposition by (*t*Bu,TolDHP)CoOTf (**1**) with excellent selectivity for single bond migrations even in long-chain alkanes. Furthermore, this system also mediates photoactivated contra-thermodynamic reactivity; irradiation with low energy light results

in E to Z isomerization and the migration of internal to terminal alkenes. This catalyst also exhibits switchable control over alkene position depending on reaction conditions. Mechanistic studies reveal that this reactivity is enabled by in-situ, asymmetric catalyst ligand borylation. While related in-situ ligand functionalizations have been noted with other organometallic catalysts,<sup>17</sup> this is the first time this sort of ligand functionalization can be modulated to tune catalysis.

## Results and Discussion

### Thermodynamic Alkene Transpositions

**Table 1:** Thermal olefin isomerization with **1** at different catalyst loadings.

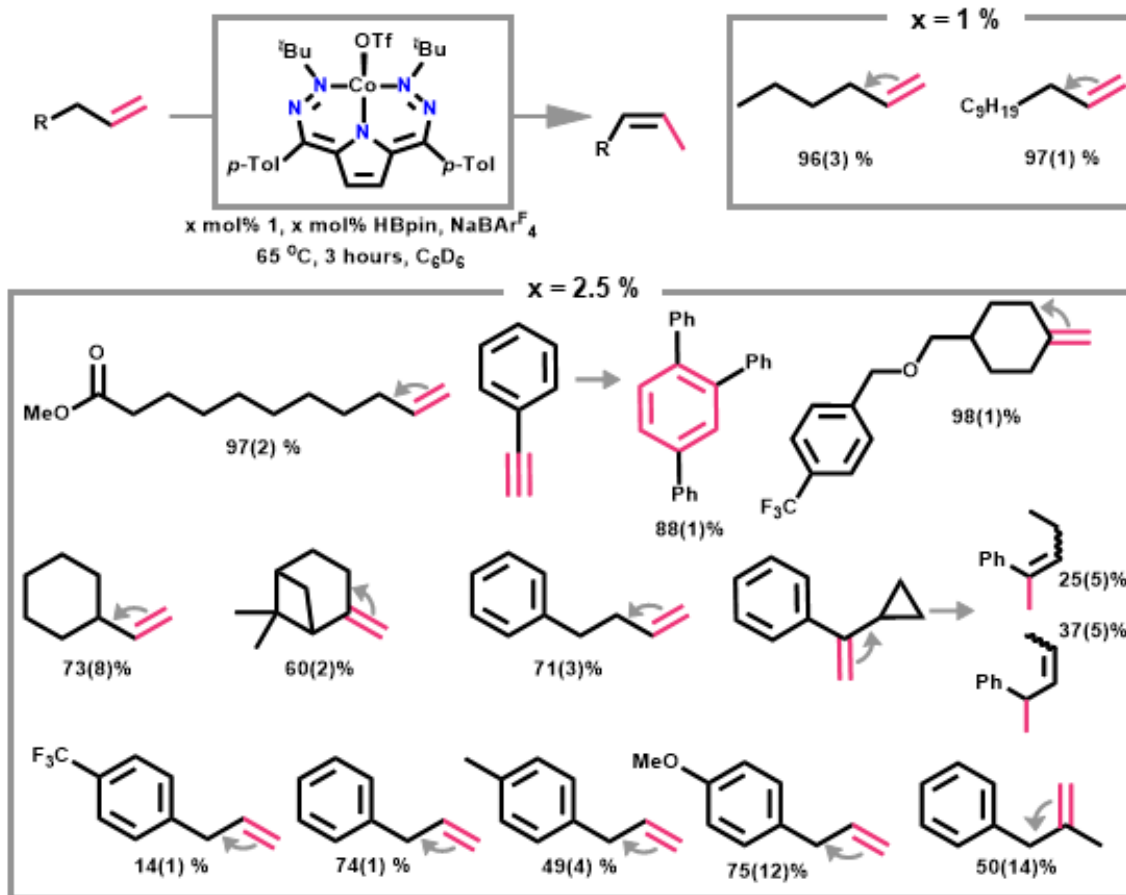
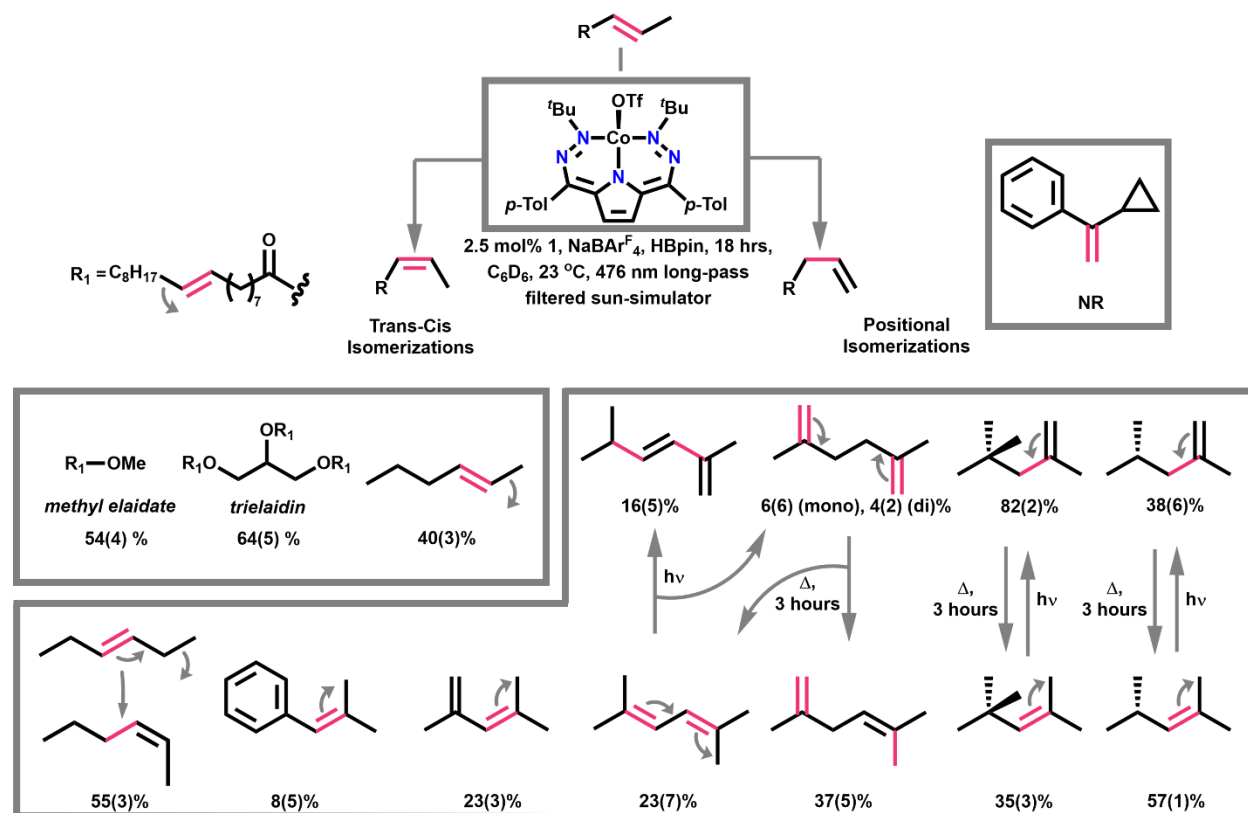


**Table 2.** Contra-thermodynamic and switchable catalysis, with standard conditions as 2.5 mol% **1**, 2.5 mol% borane, 2.5 mol% NaBAR<sup>F</sup><sub>4</sub> with 476 long-pass filtered sun-simulator lamp for 18 hours in C<sub>6</sub>D<sub>6</sub>



Initially, we tested a variety of H-atom donating reagents as cocatalysts for selective isomerization. Initial trials with H<sub>2</sub>, silanes, or other hydride sources resulted in either hydrogenation or no reaction respectively. However, addition of stoichiometric HBPin to **1** results in color changes that suggest the formation of a new species (**2**, Appendix IV: **Figure S12**). We therefore examined the isomerization of 1-hexene with 5 mol% **1** and HBPin. This mixture results in complete conversion to 2-hexene over two weeks at room temperature. Significantly accelerated rates are observed with the addition of stoichiometric NaBAR<sup>F</sup><sub>4</sub> as a triflate abstractor and mild heat (65 °C). These conditions provide 2-hexene in 96(3)% yield with 1 mol% loadings of **1** and HBPin in 3 hours. Interestingly, we observe no evidence of further isomerization to 3-hexene in these

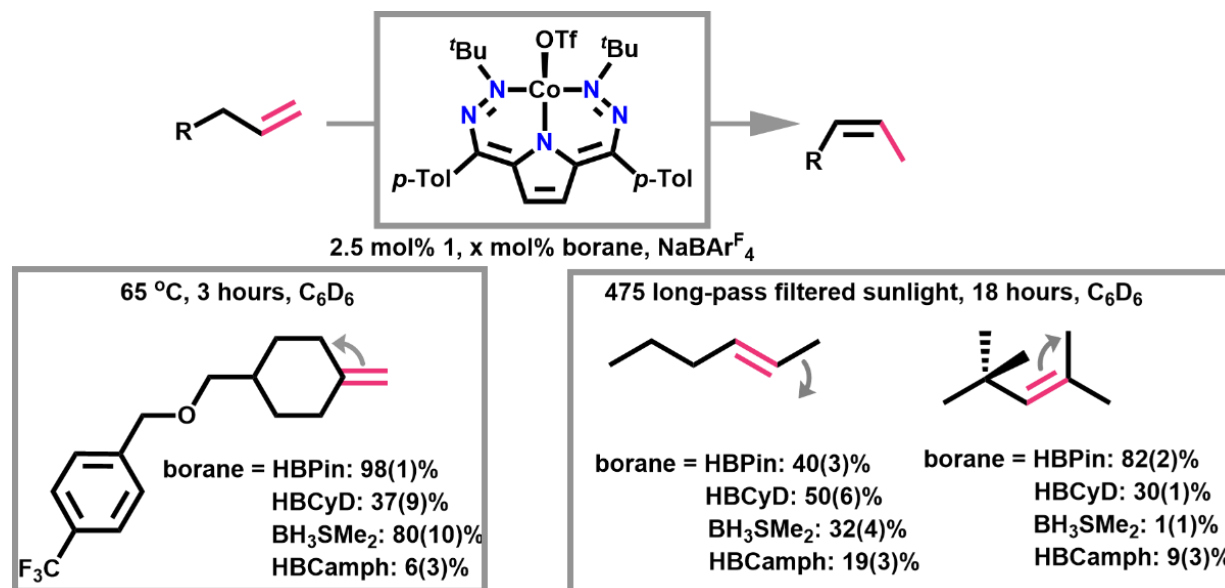
reactions. This excellent activity and selectivity prompted us to investigate the scope of this reaction with other alkenes (**Table 1**).

Complex **1** is excellent at 1 to 2 isomerizations of linear alkenes with >95% yields. We observe an expected preference for E selectivity, with 3.8(5) E:Z with 2.0(2) E:Z ratios respectively. Consistent with the previously observed hydrogenation chemistry of **1**, the steric bulk of the alkene has a profound impact on reactivity and moving to larger substrates requires an increase in catalyst loading to 2.5 mol%. This higher catalysts loading enables 97(2)% 1 to 2 transposition of methyl 1-undecenoate. This reaction also results in an increased preference for the Z-isomer (0.8(1) E: 1 Z) which is discussed more below. Selectivity for single position isomerization is general beyond long alkane chains. One example is 4-phenyl but-1-ene which isomerizes in 71(3)% yield to 4-phenyl but-2-ene instead of the more thermodynamically favored 4-phenyl but-3-ene. Vinyl cyclohexane similarly provides 73(8)% of the singly isomerized internal alkene product. Tri-substituted alkenes are viable substrates albeit with slightly lower yields: 60(2)% for alpha-pinene and 50(14)% for 2-methyl-3-phenyl-prop-2-ene from beta-pinene and 2-methyl-3-phenyl-prop-1-ene respectively. Similarly, a para-trifluoromethylbenzylated analog of cyclohexane-4-methylene methanol is converted in 98(1)% yield to the singly isomerized product.

A Hammett series using allyl benzenes reveals divergent reactivity. More electron-rich rings show greater conversion than electron-poor rings but trends in these data are difficult to interpret due to significant degrees of polymerization with several of these substrates. Alpha-cyclopropyl-styrene was used to test for the presence of radical intermediates and provides a ~62% yield of ring-opened products. This suggests a likely role for radical intermediates, consistent with previous observations from the hydrogenation reactivity of **1**.<sup>15</sup> Altogether, **1** exhibits high activity

**Table 3.** Variations on added borane.

CyD: cis-1,2-cyclohexane diol, Camph: ( $\pm$ )-exo,exo-2,3-Camphanediol



for alkene isomerizations which is comparable with some of the best catalysts known. The selectivity for single position isomerizations exhibited by **1** is even more noteworthy.

#### *Contra-Thermodynamic Alkene Isomerizations*

The above thermal alkene isomerization reactions for 1-undecenoate methyl ester and 1-dodecene exhibited generally larger amounts of thermodynamically unfavorable Z isomers. Contra-thermodynamic reactivity is unlikely without some additional energy input, and most of the examples discussed above leverage photochemical conditions. The standard catalytic conditions for thermal catalysis were performed in the presence of ambient light, and we hypothesized that a competing photochemical process might be the cause of the higher Z:E ratios. We therefore performed photocatalytic trials with 476 nm long-pass filtered simulated sunlight with 2.5 mol% loading of **1**, HBPIn, and NaBARF<sub>4</sub>. These conditions enable both E to Z isomerization as well as 3- to 2-alkene and 2- to 1-endergonic alkene isomerizations (**Table 2**).

While a solar simulator was used for consistency between catalytic trials, we also observe that running trials in ambient sunlight leads to comparable yields. Under these conditions trans-2-hexene can be converted to cis-2-hexene in 40(3)% yield, and a fatty acid surrogate, methyl elaidate, is converted to methyl oleate in 54(4)% yield. This ratio is distinctively higher than the thermodynamically predicted Boltzman population ratio of ~0.1 (Appendix IV: **Table S2**). Trans-3-hexene converts to primarily 2-hexene with a 72(5)% yield of Z-2-hexene under optimized conditions. 2,4,4-trimethyl-pent-2-ene and 2,4-dimethyl-pent-2-ene undergo 2 to 1 alkene migration to the terminal position with 82(2)% yield and 38(6)% yield respectively. While these endergonic isomerizations are more accessible for alkyl substrates, styrenyl- allyl transpositions are more challenging. This contrasts some of the previously observed contra-thermodynamic reactivity.<sup>12</sup>

Inspired by the unusually weak preference for conjugation observed in isomerizing 1,5-cyclooctadiene (with 33(2)% yield of 1,4-cyclooctadiene, relative to only 28(2)% of the conjugated 1,3-cyclooctadiene) (See SI), we were also interested in investigating contra-thermodynamic de-conjugation reactivity with 2,4-dimethyl-1,3-pentadiene and 2,5-dimethyl-2,4-hexadiene, While we observe sterics likely playing a impactful role in limiting reactivity with 2,4-dimethyl-1,3-pentadiene, with only 23(3)% yield of deconjugated products, we observe 30(10)% yield of contra-thermodynamically isomerized products from 2,5-dimethyl-2,4-hexadiene, with 2,5-dimethylhexa-1,3-diene as the major product.

The fact that we observe differing thermodynamic and contra-thermodynamic reactivity with the same catalysts opens the possibility of switchable selectivity. Indeed, 2,4,4-trimethyl-pent-1-ene and 2,4-dimethyl-pent-1-ene can also be converted into 2,4,4-trimethyl-pent-2-ene and 2,4-dimethyl-pent-2-ene in 35(3)% yield and 57(1)% yield respectively under standard thermal

conditions. Similarly, we can reverse reactivity for 2,5-dimethyl-1,5-hexadiene to 60(10)% thermodynamically isomerized products. This means that the relative ratio of 1- and 2-alkenes in this substrate can be tuned in the same catalytic mixture by using heat or light.

### Catalyst Characterization

We hypothesized that borane addition to **1** to generate the putative intermediate **2** either resulted in a borylated product or in net H-atom transfer. We therefore modeled both mono-hydrogenated catalysts as well as hydroborated complexes using DFT calculations. We observe that both types of products are energetically feasible, with a DHP ligand hydroborated product being slightly favored (Appendix IV: **Figure S61-65, Figure 2**). The spin-state of in-situ formed **2** was first assayed with  $^1\text{H}$  NMR spectroscopy which reveals a paramagnetic product. X-band

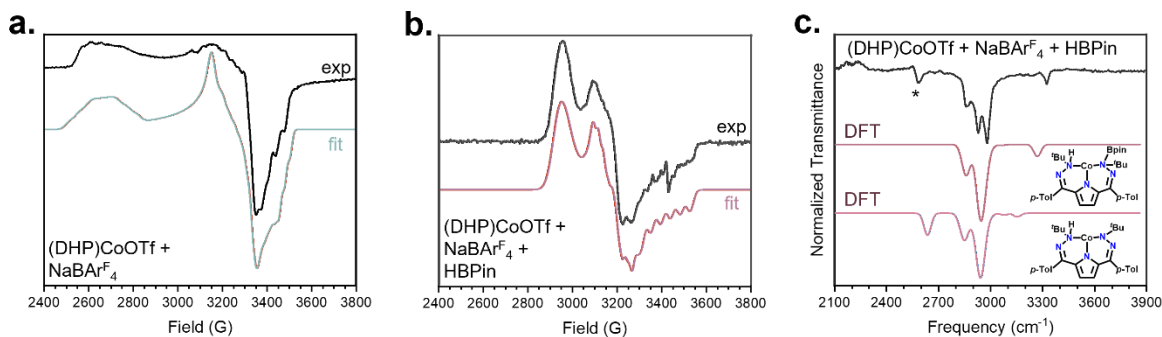


**Figure 2:** a) In-situ EPR of **1** + NaBArF<sub>4</sub> with fit in red. Experimental conditions: 15 K, MW freq. 9.639, MW power. 2.0 mW. Simulation parameters:  $g_{1,2,3} = 2.02, 2.12, 2.58$ ;  $^{59}\text{Co}$   $A_{1,2,3} = +56.2, +73.6, +108.5$  MHz;  $^{14}\text{N}$   $A_{1,2,3} = +73.5, +12.7, +172.4$  MHz. b) In-situ EPR of **1** + NaBArF<sub>4</sub> + HBPin. Experimental conditions: 127 K, MW freq. 9.639, MW power. 2.0 mW. Simulation parameters:  $g_{1,2,3} = 2.04, 2.16, 2.33$ ;  $^{59}\text{Co}$   $A_{1,2,3} = +73.9, +72.9, +234.5$  MHz,  $^{14}\text{N}$   $A_{1,2,3} = +20.3, +16.1, -10.4$  MHz. c) IR spectra of **1** + NaBArF<sub>4</sub> + HBPin (black) with simulations of a ligand borylated complex (red) and a hydrogenated complex (blue). Signals for HBPin shown with \*

EPR spectroscopy of **2** demonstrates the formation of an  $S = 1/2$  species (**Figure 2**, Appendix IV: **Figure S23-25**). As any product of H-atom transfer would be necessarily integer spin, these data support that HBpin addition to the complex is more likely. Two feasible assignments include a metal boryl complex with a singly hydrogenated <sup>*t*Bu,Tol</sup>DHP ligand or a product where H–B addition has occurred across the ligand backbone. We note that a metal boryl species is less likely based on a large barrier to form such a species suggested by DFT calculations (Appendix IV: **Figure S61, S64**).

The most concrete evidence for hydroboration of the DHP ligand backbone comes from vibrational spectroscopy. In-situ mixtures of **2** exhibit a clear N–H stretch in their IR spectra. DFT analysis suggests this is most consistent with the stretch for the hydroborated ligand. Comparison of the IR spectrum of **2** to the calculated IR for the non-borylated complex and the metal boryl complex further confirms the assignment of **2** as a product where the DHP ligand has been hydroborated (**Figure 2**, Appendix IV: **Figure S19-20, Table S8**). X-ray absorption spectroscopy also supports a Co(II) center (Figure S26-30, Table S2), and masses consistent with a hydroborylated ligand are visible in post-catalytic GCMS runs (**Appendix IV: Figure S103**). This evidence strongly supports the assignment of **2** as an in-situ hydroborated complex.

This assignment suggests that yields/selectivities can be tuned via different borane co-catalysts. While HBPin provides generally good yields, HBCyD (CyD = cis-1,2-cyclohexane diol) increases E/Z ratios. Other boranes were generally lower yielding with some exceptions. HBCat (Cat = catechol) leads to extremely diminished yields (3% isomerization of 1-hexene to 2-hexene with 1 E: 2 Z product ratio). BH<sub>3</sub>SMe<sub>2</sub> works, better than the CyD analog in some instances, but also gives generally lower yields than HBPin. This borane is also susceptible to hydrogenation reactivity if present in excess, adding another wrinkle to its reactivity. We also tried a second, more

sterically hindered chiral borane (HBCamph), from ( $\pm$ )-exo,exo-2,3-Camphanediol, which both led to differential reactivity and selectivity as well. Though the arm dissociation proposed in the DFT cycle suggests other ligand modifications might be required for high enantioselectivity, we do see a subtle increase in ee (2.6%) between the HBPIn yields and the HBCyD yields. With HBCamph, we observe consistently lower yields, but as yet have not had the opportunity to assess ee in these products.

### DFT Computed Catalytic Cycle

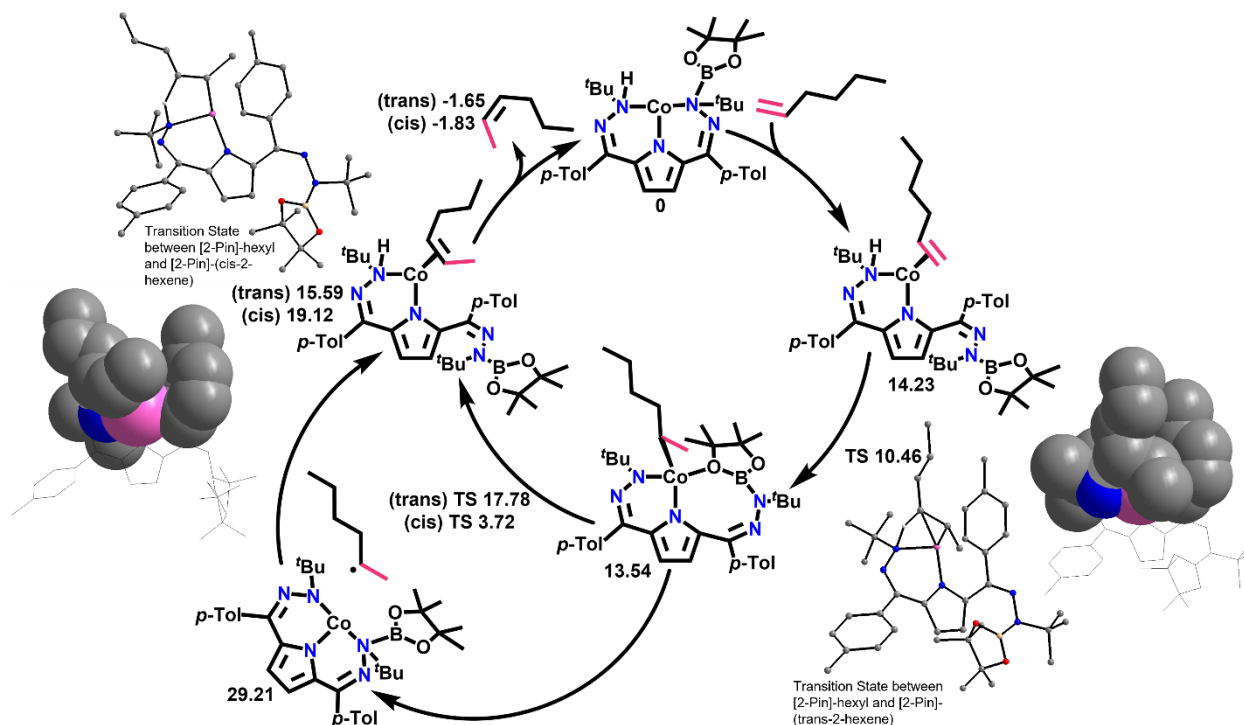


**Figure 3.** DFT computed energies and pathway for isomerization. Energies shown in kcal/mol, and all energies shown are free energies.

We can propose a feasible catalytic cycle based on the combined experimental and DFT results. Calculations with 1-hexene suggest an initial endergonic initial alkene coordination to the hydroborated complex (14.23 kcal/mol), followed by a low transition state barrier of 10.46

kcal/mol to form an alkyl complex via formal H-atom transfer. This endergonic binding is likely due to steric pressure inducing dissociation of one of the <sup>t</sup>Bu,TolDHP arms and provides a plausible explanation for the observed selectivity in the system. As observed previously for the hydrogenation catalysis, there is an accessible Co–C bond cleavage from the Co-alkyl intermediate to form an outer-sphere alkyl radical species (only 15.67 kcal/mol uphill). This energy is comparable to the transition state energy for E-2-hexene formation (17.78 kcal/mol). Interestingly, the transition state for Z-2-hexene is substantially lower (3.72 kcal/mol). This large transition state energy difference provides a plausible explanation for the Z-selective isomerizations we observe. Alkene release is an overall exergonic process as expected.

The barriers to the initial alkyl formation also help justify some of the contra-thermodynamic 3-2 and 2-1 isomerization observed, since the barrier to release the terminal alkene is less than the barrier for E-alkenes, but higher than that for Z-alkenes. We note that while both **1** and **2**, are emissive, the emission spectrum of **2** when excited at 450 nm leads to a broad peak centered at 550 which under our photochemical conditions should be fully accessible (Appendix IV: **Figure S18**). While there are a number of roles light could be playing in this reactivity, it is possible that a photochemically excited state, potentially with a dissociated ligand arm, enables direct access to a Co-alkyl. From this alkyl species, either low-energy Z-selective H-atom abstraction or terminal H-atom abstraction are both more accessible than collapse back to E-2-hexene. Another alternative is an increased favorability for an inner-sphere, non-radical mechanism for the light-gated reactivity. This has been observed previously in other light accelerated Co-catalyzed reactivity.<sup>18</sup> We do note that alpha-cyclopropyl styrene, which ring-opens under thermal conditions, exhibits negligible ring-opening under photochemical conditions. This leads us to believe that both of these hypotheses could be relevant to catalysis, but

illuminating precise information on the nature of the many excited state complexes possible will be a challenge. Regardless of the exact photophysical details, this general pathway provides a plausible explanation for the observed switch in selectivity with light.

## Conclusions

Here we present a highly modular and efficient catalyst for both thermodynamic and contra-thermodynamic alkene isomerization. Characterization supports an in-situ catalyst modification with borane which can be leveraged for different yields and selectivity. Beyond this reactivity, reaction conditions can be tuned to favor either thermodynamic 1-to-2-alkene transposition under thermal conditions or contra-thermodynamic 2-to-1-alkene transposition and/or enhanced Z:E ratios under photochemical conditions. This reactivity is broad across many substrates, and with some notably difficult transformations. One particular application of this system is the selective trans-to-cis isomerization of long-chain alkenes without additional isomerization. This <sup>t</sup>Bu,TolDHP ligated system therefore represents an unusual example of a modular and switchable catalyst which enables a wide range of alkene isomerization reactivity within a single catalyst architecture. A key feature of this reactivity is the non-innocence of the ligand, both via in-situ modification as well as in the ability to shuttle H-atoms to and from alkene substrates.

## Methods

All chemicals were purchased from commercial suppliers and used without further purification when not otherwise stated. All manipulations were carried out under an atmosphere of N<sub>2</sub> using standard Schlenk and glovebox techniques. Glassware was dried at 180 °C for a minimum of two hours and cooled under vacuum prior to use. Solvents were dried on a solvent purification system from Pure Process Technologies and stored over 4 Å molecular sieves under N<sub>2</sub>. Tetrahydrofuran (THF), diethyl ether (Et<sub>2</sub>O) and benzene were stirred over NaK alloy separately and run through

an additional alumina column prior to use to ensure dryness. Solvents were tested for H<sub>2</sub>O and O<sub>2</sub> using a standard solution of sodium-benzophenone ketyl radical anion. CD<sub>3</sub>CN, C<sub>6</sub>D<sub>6</sub>, and *d*<sub>8</sub>-toluene were dried over 4 Å molecular sieves under N<sub>2</sub>.

<sup>1</sup>H and <sup>19</sup>F NMR spectra were recorded on Bruker DRX 400 spectrometers when not otherwise stated. Chemical shifts are reported in ppm units referenced to residual solvent resonances for <sup>1</sup>H and <sup>13</sup>C{<sup>1</sup>H} spectra. UV-visible Spectra were recorded on a Bruker Evolution 300 spectrometer and analyzed using VisionPro software. A standard 1 cm quartz cuvette with an airtight screw cap with a puncturable Teflon seal was used for all measurements. A Unisoku CoolSpek cryostat was used for low-temperature measurements. IR spectra were recorded on a Bruker α II spectrometer in a nitrogen, dry glovebox with the OPUS software suite as diethyl ether thin films on a Platinum Diamond ATR module. Combustion analysis was performed by Midwest Microlab. α-cyclopropyl styrene was prepared following a previously reported procedure<sup>19</sup> as was cyclohexyldiol and (±)-exo,exo-2,3-Camphanediol borane.<sup>20</sup> **1** was prepared as described in previous work.<sup>15,16</sup>

X-ray near-edge absorption spectra (XANES) were employed to probe the local environment of Co. Frozen solution samples were prepared by making a concentrated solution of the starting material in benzene. This solution was then syringed into a pre-cooled Teflon window lined with Kapton tape in liquid nitrogen, then stored in liquid nitrogen until collection. Data were acquired at SSRL with a bending magnet source with ring energy at 7.00 GeV. Co K-edge data were acquired at the SSRL 7-3 and 9-3- beam line. The incident, transmitted and reference X-ray intensities were monitored using gas ionization chambers. A metallic Co foil standard was used as a reference for energy calibration and was measured simultaneously with experimental samples. X-ray absorption spectra were collected at 8 K. Data collected was processed using the Demeter software suite, and Fityk was used for more precise pre-edge fitting.

### *Reactivity with Boranes*

A J-Young or standard NMR tube was charged with 0.5 mg (0.0008 mmol, 1 equiv.) of **1**, 0.7- 2.0 mg NaBAR<sup>F</sup><sub>4</sub> (0.0008-0.0023 mmol, 1-3 equiv. excess due to limited solubility in benzene) , and 1 equiv. of the borane of choice: pinacolborane (HBPin), cis-cyclohexane diol borane (HBCyD), borane dimethyl sulfide adduct (BH<sub>3</sub>SMe<sub>2</sub>), (±)-exo,exo-2,3-Camphanediol borane (HBCamph), or catecholborane (HBCat) with 0.6 mL of C<sub>6</sub>D<sub>6</sub>. Et<sub>2</sub>O, toluene and to a limited extent, dichloromethane (CH<sub>2</sub>Cl<sub>2</sub>) or acetonitrile (MeCN), are also feasible solvents for this reaction. The solution was observed to change color from the reddish-purple of **1** to the true red of **2**. These compounds are unstable at room temperature, but indefinitely stable at temperatures below 0°C. The cold solution can be dried and analyzed by various techniques as described below.

### *Preparation of IR samples of 2-BPin*

#### *Thin film on ATR IR*

In a 20 mL vial in the glovebox, 1-2 mL of diethyl ether was added until **1** and 1 equiv. NaBAR<sup>F</sup><sub>4</sub> dissolved completely to generate a purple solution. A drop of HBpin was added, and the resulting red solution dropped on an ATR crystal in a nitrogen filled drybox, allowed to evaporate, and a spectrum collected. The control spectra of **1**, **1** + NaBAR<sup>F</sup><sub>4</sub>, NaBAR<sup>F</sup><sub>4</sub> only, and HBpin only were also collected.

### **References**

1. Mayer, M.;Welther, A.; Jacobi von Wangelin, A. Iron-Catalyzed Isomerizations of Olefins. *ChemCatChem*, **3**, 1567 (2011). (b) Mamone, P.; Grünberg, M. F.; Fromm, A.;Khan, B. A.; Goßen, L. J. [Pd(μ-Br)(PtBu<sub>3</sub>)<sub>2</sub>] as a highly active isomerization catalyst: synthesis of enol esters from allylic esters. *Org. Lett.* **14**, 3716 (2012). (c) Zhuo, L.-G.; Yao, Z.-K.; Yu, Z.-X. Synthesis of Z-Alkenes from Rh(I)-Catalyzed Olefin Isomerization of β,γ-Unsaturated Ketones. *Org.Lett.* **15**, 4634 (2013). (d) Trost, B. M.; Cregg, J. J.; Quach, N. Isomerization of N-Allyl Amides To Form Geometrically Defined Di-, Tri-, and Tetrasubstituted Enamides. *J. Am. Chem. Soc.* **139**, 5133 (2017). (e) Kocen, A. L.; Brookhart, M.; Daugulis, O. Palladium-catalysed alkene chain-running isomerization. *Chem. Commun.* **53**, 10010 (2017).

2. (a) Jennerjahn, R.; Jackstell, R.; Piras, I.; Franke, R.; Jiao, H.; Bauer, M.; Beller, M. Benign catalysis with iron: unique selectivity in catalytic isomerization reactions of alkenes. *ChemSusChem* **5**, 734 (2012). (b) Larsen, C. R.; Erdogan, G.; Grotjahn, D. B. General Catalyst Control of the Monoisomerization of 1-Alkenes to trans-2-Alkenes. *J. Am. Chem. Soc.* **136**, 1226 (2014). (c) Chen, C.; Dugan, T. R.; Brennessel, W. W.; Weix, D. J.; Holland, P. L. Z-Selective Alkene Isomerization by High-Spin Cobalt(II) Complexes. *J. Am. Chem. Soc.* **136**, 945 (2014). (d) Schmidt, A.; Nödling, A. R.; Hilt, G. An Alternative Mechanism for the Cobalt-Catalyzed Isomerization of Terminal Alkenes to (Z)-2-Alkenes. *Angew. Chem., Int. Ed.* **54**, 801 (2015). (e) Wang, Y.; Qin, C.; Jia, X.; Leng, X.; Huang, Z. An Agostic Iridium Pincer Complex as a Highly Efficient and Selective Catalyst for Monoisomerization of 1-Alkenes to trans-2-Alkenes. *Angew. Chem., Int. Ed.* **56**, 1614 (2017).
3. (a) Lim, H. J.; Smith, C. R.; RajanBabu, T. V. Facile Pd (II)- and Ni (II)-catalyzed isomerization of terminal alkenes into 2-alkenes. *J. Org. Chem.* **74**, 4565 (2009).; (b) Kobayashi, T.; Yorimitsu, H.; Oshima, K. Cobalt-Catalyzed Isomerization of 1-Alkenes to  $\epsilon$ -2-Alkenes with Dimethylphenylsilylmethylmagnesium Chloride and Its Application to the Stereoselective Synthesis of (E)-Alkenylsilanes. *Chem. - Asian J.* **4**, 1078 (2009).; (c) Gauthier, D.; Lindhardt, A. T.; Olsen, E. P. K.; Overgaard, J.; Skrydstrup, T. In situ generated bulky palladium hydride complexes as catalysts for the efficient isomerization of alkenes. Selective transformation of terminal alkenes to 2-alkenes. *J. Am. Chem. Soc.* **132**, 7998 (2010).; (d) Larsen, C. R.; Grotjahn, D. B. Stereoselective alkene isomerization over one position, *J. Am. Chem. Soc.* **134**, 10357 (2012).; (e) Liu, X.; Zhang, W.; Wang, Y.; Zhang, Z.-X.; Jiao, L.; Liu, Q. Cobalt-Catalyzed Regioselective Alkene Isomerization Under Kinetic Control. *J. Am. Chem. Soc.* **140**, 22, 6873–6882 (2018). ; (f) Liu, X.; Rong, X.; Liu, S.; Lan, Y.; Liu, Q. Cobalt-Catalyzed Desymmetric Isomerization of Exocyclic Alkenes. *J. Am. Chem. Soc.* **143**, 49, 20633–20639 (2021).
4. (a) Cane, D. E.; Yang, G.; Coates, R. M.; Pyun, H. J.; Hohn, T.M. Trichodiene Synthase. Synergistic Inhibition by Inorganic Pyrophosphate and Aza Analogs of the Bisabolyl Cation. *J. Org. Chem.* **57**, 3454–3462 (1992). (b) O'Neill, P. M.; Stocks, P. A.; Pugh, M. D.; Araujo, N. C.; Korshin, E. E.; Bickley, J. F.; Ward, S. A.; Bray, P. G.; Pasini, E.; Davies, J.; Verissimo, E.; Bachi, M. D. Design and Synthesis of Endoperoxide Antimalarial Prodrug Models. *Angew. Chem., Int. Ed.* **43**, 4193–4197 (2004). (c) Park, P. K.; O'Malley, S. J.; Schmidt, D. R.; Leighton, J. L. Total Synthesis of Dolabelide D. *J. Am. Chem. Soc.* **128**, 2796–2797 (2006). (d) Ota, K.; Hamamoto, Y.; Eda, W.; Tamura, K.; Sawada, A.; Hoshino, A.; Mitome, H.; Kamaike, K.; Miyaoka, H. Amitorines A and B, Nitrogenous Diterpene Metabolites of *Theonella swinhoei*: Isolation, Structure Elucidation, and Asymmetric Synthesis. *J. Nat. Prod.* **79**, 996–1004 (2016). (e) Ota, K.; Yamazaki, I.; Saigoku, T.; Fukui, M.; Miyata, T.; Kamaike, K.; Shirahata, T.; Mizuno, F.; Asada, Y.; Hirotsu, M.; Ino, C.; Yoshikawa, T.; Kobayashi, Y.; Miyaoka, H. Phellilane L, Sesquiterpene Metabolite of *Phellinus linteus*: Isolation, Structure Elucidation, and Asymmetric Total Synthesis. *J. Org. Chem.* **82**, 12377–12385 (2017). (f) You, C.; Li, X.; Gong, Q.; Wen, J.; Zhang, X. Nickel-Catalyzed Desymmetric Hydrogenation of Cyclohexadienones: An Efficient Approach to All-Carbon Quaternary Stereocenters. *J. Am. Chem. Soc.* **141**, 14560–14564 (2019).
5. (a) Donohoe, T. J.; O'Riordan, T. J. C.; Rosa, C. P. Ruthenium-catalyzed isomerization of terminal alkenes to internal alkenes. *Angew. Chem., Int. Ed.* **48**, 1014 (2009). (b) Hilt, G. Double Bond Isomerisation and Migration--New Playgrounds for Transition Metal-Catalysis. *ChemCatChem* **6**, 2484 (2014). (c) Holland, P. L. Distinctive reaction pathways at base metals in high-spin organometallic catalysts. *Acc. Chem. Res.* **48**, 1696 (2015).

6. (a) Seayad, A.; Ahmed, M.; Klein, H.; Jackstell, R.; Gross, T.; Beller, M. Internal to linear amines *Science* **297**, 1676 (2002). (b) Arisawa, M.; Terada, Y.; Nakagawa, M.; Nishida, A. Selective Isomerization of a Terminal Catalyzed by a Ruthenium Complex: The Synthesis of Indoles through Ring-Closing Metathesis. *Angew. Chem., Int. Ed.* **41**, 4732 (2002). (c) Grotjahn, D. B.; Larsen, C. R.; Gustafson, J. L.; Nair, R.; Sharma, A. Extensive isomerization of alkenes using a bifunctional catalyst: an alkene zipper. *J. Am. Chem. Soc.*, **129**, 9592 (2007). (d) Pünner, F.; Schmidt, A.; Hilt, G. Up the Hill: Selective Double-Bond Isomerization of Terminal 1,3-Dienes towards Z-1,3-Dienes or 2Z,4E-Dienes. *Angew. Chem., Int. Ed.* **51**, 1270 (2012). (e) Werner, E. W.; Mei, T.-S.; Burckle, A. J.; Sigman, M. S. Enantioselective Heck arylations of acyclic alkenyl alcohols using a redox-relay strategy. *Science* **338**, 1455 (2012). (f) Kochi, T.; Hamasaki, T.; Aoyama, Y.; Kawasaki, J.; Kakiuchi, F. Chain-Walking Strategy for Organic Synthesis: Catalytic Cycloisomerization of 1,n-Dienes. *J. Am. Chem. Soc.* **134**, 16544 (2012). (g) Obligacion, J. V.; Chirik, P. J. Bis (imino) pyridine cobalt-catalyzed alkene isomerization–hydroboration: a strategy for remote hydrofunctionalization with terminal selectivity. *J. Am. Chem. Soc.* **135**, 19107 (2013). (h) Li, H.; Mazet, C. Steric parameters in the Ir-catalyzed regio- and diastereoselective isomerization of primary allylic alcohols. *Org. Lett.* **15**, 6170 (2013). (i) Larionov, E.; Lin, L.; Guénee, L.; Mazet, C. Scope and mechanism in palladium-catalyzed isomerizations of highly substituted allylic, homoallylic, and alkenyl alcohols. *J. Am. Chem. Soc.* **136**, 16882 (2014). (j) Masarwa, A.; Didier, D.; Zabrodski, T.; Schinkel, M.; Ackermann, L.; Marek, I. Merging allylic carbon–hydrogen and selective carbon–carbon bond activation. *Nature* **505**, 199 (2014). (k) Vasseur, A.; Bruffaerts, J.; Marek, I. Remote functionalization through alkene isomerization. *Nat. Chem.* **8**, 209 (2016). (l) Martínez, J. I.; Smith, J. J.; Hepburn, H. B.; Lam, H. W. Chain Walking of Allylrhodium Species Towards Esters During Rhodium-Catalyzed Nucleophilic Allylations of Imines. *Angew. Chem., Int. Ed.* **55**, 1108 (2016). (m) Lin, L.; Romano, C.; Mazet, C. Palladium-catalyzed long-range deconjugative isomerization of highly substituted  $\alpha$ ,  $\beta$ -unsaturated carbonyl compounds, *J. Am. Chem. Soc.* **138**, 10344 (2016). (n) Liniger, M.; Liu, Y.; Stoltz, B. M. Sequential ruthenium catalysis for olefin isomerization and oxidation: Application to the synthesis of unusual amino acids. *J. Am. Chem. Soc.* **139**, 13944 (2017).
7. (a) Chianese, A. R.; Shaner, S. E.; Tandler, J. A.; Pudalov, D. M.; Shopov, D. Y.; Kim, D.; Rogers, S. L.; Mo, A. Iridium complexes of bulky CCC-pincer N-heterocyclic carbene ligands: steric control of coordination number and catalytic alkene isomerization. *Organometallics* **31**, 7359 (2012). (b) Castro-Rodrigo, R.; Chakraborty, S.; Munjanja, L.; Brennessel, W. W.; Jones, W. D. Synthesis, characterization, and reactivities of molybdenum and tungsten PONOP pincer complexes. *Organometallics* **35**, 3124 (2016).; (c) Perdriau, S.; Chang, M.-C.; Otten, E.; Heeres, H. J.; de Vries, J. G. Alkene isomerisation catalysed by a ruthenium PNN pincer complex. *Chem. Eur. J.* **20**, 15434–15442 (2014).; (d) Liu, X.; Zhang, W.; Wang, Y.; Zhang, Z.-X.; Jiao, L.; Liu, Q. Cobalt-catalyzed regioselective olefin isomerization under kinetic control. *J. Am. Chem. Soc.* **140**, 6873–6882 (2018).
8. Wang, Z.; Yang, T.; Brenna, J. T.; Wang, D. H. Fatty acid isomerism: analysis and selected biological functions. *Food Funct.* **15**, 1071 (2024).
9. (a) Vasseur, A.; Bruffaerts, J.; Marek, I. Remote functionalization through alkene isomerization. *Nat. Chem.* **8**, 209–219 (2016).; (b) Sommer, H.; Juliá-Hernández, F.; Martín, R.; Marek, I. Walking Metals for Remote Functionalization. *ACS Cent. Sci.* **4**, 153–165 (2018).; (c) Hanna, S.; Butcher, T. W.; Hartwig, J. F. Contra-thermodynamic Olefin Isomerization by Chain-Walking Hydrofunctionalization and Formal Retro-hydrofunctionalization. *Org.*

*Lett.* **21**, 7129– 7133 (2019).; (d) Hanna, S.; Wills, T.; Butcher, T. W.; Hartwig, J. F. Palladium-Catalyzed Oxidative Dehydrosilylation for Contra-Thermodynamic Olefin Isomerization. *ACS Catal.* **10**, 8736– 8741 (2020). (e) Fiorito, D.; Scaringi, S.; Mazet, C. Transition Metal-Catalyzed Alkene Isomerization as an Enabling Technology in Tandem, Sequential and Domino Processes. *Chem. Soc. Rev.* **50**, 1391– 1406 (2021).; (f) Wang, Q.; Jung, H.; Kim, D.; Chang, S.. Iridium-Catalyzed Migratory Terminal C(sp<sup>3</sup>)–H Amidation of Heteroatom-Substituted Internal Alkenes via Olefin Chain Walking. *J. Am. Chem. Soc.* **145** (45), 24940-24951 (2023).; (g) Li, C.; Zhang, K.; Zhao, W. Catalytic Contra-Thermodynamic Isomerization–Asymmetric Hydroboration of Alkenyl Alcohols and Amines. *ACS Catalysis* **14** (7) , 5458-5468 (2024).

10. (a) Hölzl-Hobmeier, A.; Bauer, A.; Silva, A. V.; Huber, S. M.; Bannwarth, C.; Bach, T. Catalytic deracemization of chiral allenes by sensitized excitation with visible light. *Nature* **564**, 240– 243 (2018).; (b) Shin, N. Y.; Ryss, J. M.; Zhang, X.; Miller, S. J.; Knowles, R. R. Light-driven deracemization enabled by excited-state electron transfer. *Science* **366**, 364– 369 (2019).; (c) Wang, Y.; Carder, H. M.; Wendlandt, A. E. Synthesis of rare sugar isomers through site-selective epimerization. *Nature* **578**, 403– 408 (2020).

11. (a) Dugave, C.; Demange, L. Cis-Trans Isomerization of Organic Molecules and Biomolecules: Implications and Applications. *Chem. Rev.* **103**, 2475– 2532 (2003).; (b) Metternich, J. B.; Gilmour, R. Photocatalytic E→Z Isomerization of Alkenes. *Synlett* **27**, 2541– 2552 (2016). (c) Neveselý, T.; Wienhold, M.; Molloy, J. J.; Gilmour, R. Advances in the E→Z Isomerization of Alkenes Using Small Molecule Photocatalysts. *Chem. Rev.* **122**, 2, 2650–2694 (2021).

12. (a) Zhao, K.; Knowles, R. R. Contra-Thermodynamic Positional Isomerization of Olefins . *J. Am. Chem. Soc.* **144**, 1, 137-144 (2022).; (b) Occhialini, G.; Palani, V.; Wendlandt, A. E. Catalytic, *contra*-Thermodynamic Positional Alkene Isomerization. *J. Am. Chem. Soc.* **144**, 1, 145-152 (2022).; (c) Palani, V.; Wendlandt, A. E. Strain-Inducing Positional Alkene Isomerization. *J. Am. Chem. Soc.* **145** (36) , 20053-20061 (2023).

13. (a) Arnold, D. R.; Mines, S. A. Radical ions in Photochemistry. 18. The Photosensitized (Electron Transfer) Tautomerization of Alkenes; the 1,1-diphenyl alkene system. *Can. J. Chem.* **65**, 2312– 2314 (1987).; (b) Arnold, D. R.; Mines, S. A. Radical ions in Photochemistry. 21. The Photosensitized (Electron Transfer) Tautomerization of Alkenes; the phenyl alkene system. *Can. J. Chem.* **67**, 689– 698 (1989).; (c) Mangion, D.; Kendall, J.; Arnold, D. R. Photosensitized (Electron-Transfer) Deconjugation of 1-Arylcyclohexenes. *Org. Lett.* **3**, 45– 48 (2001).

14. Sun, X.; Chen, J.; Ritter, T. Catalytic Dehydrogenative Decarboxyolefination of Carboxylic Acids. *Nat. Chem.* **10**, 1229–1233 (2018).

15. Anferov, S. W.; Filatov, A. S.; Anderson, J. S. Cobalt-Catalyzed Hydrogenation Reactions Enabled by Ligand-Based Storage of Dihydrogen. *ACS Catal.* **12**, 16, 9933-9943 (2022).

16. (a) McNeece, A. J.; Jesse, K. A.; Filatov, A. S.; Schneider, J. E.; Anderson, J. S. Catalytic Hydrogenation Enabled by Ligand-Based Storage of Hydrogen. *Chem. Commun.* **57**, 3869-3872 (2021).; (b) Jesse, K. A.; Anferov, S. W.; Collins, K. A.; Valdez-Moriera, J. A.; Czaikowski, M. E.; Filatov, A. S.; Anderson, J. S. Direct Aerobic Generation of a Ferric Hydroperoxo Intermediate via a Preorganized Secondary Coordination Sphere. *J. Am. Chem. Soc.* **143**, 18121-18130 (2021).; (c) Anferov, S. W.; Anderson, J. S. A Cobalt Adduct of an N-hydroxy-piperidinium Cation. *J. Coord. Chem.* **75**, 11-14, 1853-1864 (2022).; (d) Czaikowski, M. E.;

Anferov, S. W.; Tascher, A. P.; Anderson, J. S. Electrocatalytic Semi-Hydrogenation of Terminal Alkynes using Ligand-Based Transfer of Protons and Electrons. *J. Am. Chem. Soc.* **146**, 1, 476–486 (2024). (e) Anferov, S. W.; Boyn, J-N.; Mazziotti, D. A.; Anderson, J. S. Selective Cobalt Mediated Formation of Hydrogen Peroxide from Water Under Mild Conditions Via Ligand Redox Non-Innocence. *J. Am. Chem. Soc.* **146**, 9, 5855–5863 (2024).

17. (a) Mellino, S.; Stevenson, L. C.; Clot, E.; Mountford, P. Reactions of Titanium Imides and Hydrazides with Boranes. *Organometallics* **36**, 17, 3329 (2017). (b) Polezhaev, A. V.; Liss, C. J.; Telser, J.; Chen, C-H.; Caulton, K. G. A PNNH Pincer Ligand Allows Access to Monovalent Iron. *Chem. A Eur. Jour.* **24**, 6, 1330 (2018).; (c) Hatzis, G. P.; Thomas, C. M. Metal-ligand cooperativity across two sites of a square planar iron(II) complex ligated by a tetradentate PNNP ligand. *Chem. Comm.* **56**, 8611 (2020). (d) Elsby, M. R.; Son, M.; Oh, C.; Martin, J.; Baik, M-H.; Baker, R. T. Mechanistic Study of Metal-Ligand Cooperativity in Mn(II)-Catalyzed Hydroborations: Hemilabile SNS Ligand Enables Metal Hydride-Free Reaction Pathway. *ACS Catal.* **11**, 15, 9043 (2021). (e) Gao, H.; Jia, J.; Tung, C-H.; Wang, W. Iron-Catalyzed Selective Hydroboration of CO<sub>2</sub> by Cooperative B-H Bond Activation. *Organometallics* **42**, 10, 944 (2023). (f) Afandiyeva, M.; Wu, X.; Brennessel, W. W.; Kadam, A. A.; Kennedy, C. R. Secondary-sphere preorganization enables nickel-catalyzed hydroboration. *Chem. Comm.* **59**, 13450 (2023).

18. Mendelsohn, L. N.; MacNeil, C. S.; Tian, L.; Park, Y.; Scholes, G. D.; Chirik, P. J. Visible-Light-Enhanced Cobalt-Catalyzed Hydrogenation: Switchable Catalysis Enabled by Divergence between Thermal and Photochemical Pathways. *ACS Catal.* **11**, 3, 1351-1360 (2021).

19. Martin, J.; Knüpfer, C.; Eyselien, J.; Färber, C.; Grams, S.; Langer, J.; Thum, K.; Wiesinger, M.; Harder, S. Highly Active Superbulky Alkaline Earth Metal Amide Catalysts for Hydrogenation of Challenging Alkenes and Aromatic Rings. *Angewandte Chem.* **23**, 9102-9112 (2020).

20. Marcuccio, S. M.; Rodopoulos, M.; Weigold, H. Boronic Compounds, 1998. <https://patents.google.com/patent/US6515160B2/en?q=US6515160B2+patent> (accessed 2024-05-29).

---

1.

## Chapter VI: Synthesis of a Potassium Capped Terminal Oxido

*It's an OK Complex!*

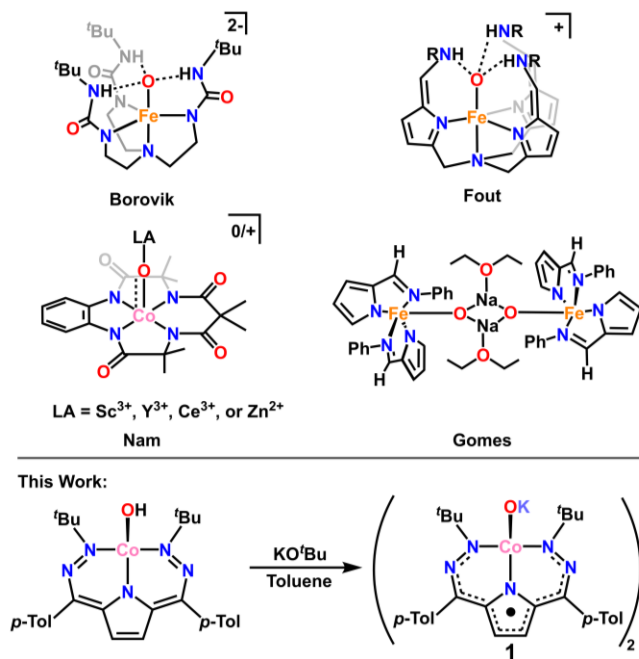
This chapter has been adapted from the following: Anferov, S. W.; Krupinski, A.; Anderson, J.

*S. Submitted.*

Transition metal-oxo compounds are widely studied for the role they play in both natural and synthetic systems.<sup>1</sup> They are central intermediates in a wide range of oxidative transformations including oxygen transfer and C-H activation.<sup>1-3</sup> In biological systems, key oxo complexes are present in the active sites of enzymatic structures such as cytochrome P450 and photosystem II.

These systems have inspired study on various synthetic complexes which can similarly facilitate or model oxidative reactivity.<sup>4</sup> Such complexes are commonly synthesized with mid-transition metals (i.e. Fe and Mn) both for their biological relevance but also for their synthetic accessibility and precedent.<sup>1</sup> However, oxo complexes of later transition metals (groups 9-11)

are more challenging to access due to the increasing number of antibonding electrons which disrupt M–O bonding. Therefore, stabilization of late



**Scheme 1.** Top: Examples of previously reported metal oxidos stabilized by hydrogen bonding or Lewis acid interactions. Bottom: Synthesis of 1 from [<sup>t</sup>Bu,Tol-DHP]CoOH.

transition metal oxo complexes frequently requires symmetry changes away from octahedral geometries to stabilize metal-oxygen bonding and avoid running up against the “oxo wall.”<sup>1, 5, 6</sup>

High d-electron counts in the absence of stabilizing geometry changes results in weakened M–O bonding and complexes that are best thought of as oxidos due to O-localized lone pairs and charge. This is a generally unfavorable scenario, and terminal oxido complexes are expected to be highly reactive. In the absence of significantly stabilizing  $\pi$ -bonding, other methods must be

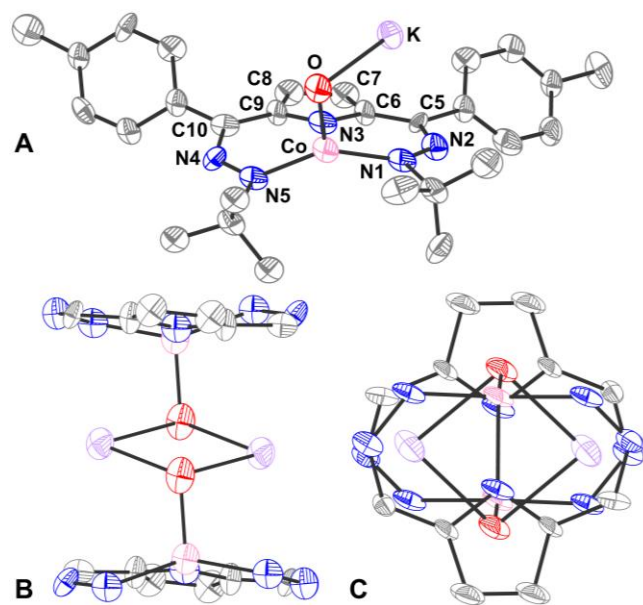


**Figure 1.** (A) SXR structure of 1. (A) One half of the dimeric unit with the full DHP ligand. (B) A side view focusing on the O<sub>2</sub>K<sub>2</sub> core with peripheral groups omitted. (C) A top view showing the stacked interactions with the K cations with peripheral groups omitted. Co (pink), N (blue), C (grey), O (red), K (violet). Ellipsoids at 50% and hydrogens omitted for clarity.

employed to isolate these complexes.

Indeed, there are several elegant examples in the literature where formally singly bonded terminal oxidos can be stabilized through secondary coordination sphere hydrogen bonding (H-bonding).<sup>7-12</sup>

Notably, Borovik and coworkers isolated a singly bonded Fe(III)-oxido complex, [Fe(III)H<sub>3</sub>buea(O)]<sup>2-</sup>, stabilized via a hydrogen bonding cavity around the oxygen atom.<sup>8,9</sup> Subsequently, Fout and coworkers isolated another singly bonded Fe(III)-oxido complex, [N(afa<sup>Cy</sup>)<sub>3</sub>Fe(III)(O)](OTf), stabilized via a separate H-bonding framework (Scheme 1).<sup>10-12</sup>

**Table 1.** Selected bond lengths (Å) and angles (°) of (**1**) and related complexes.

	<b>1</b>	[DHP <sup>2-</sup> ] Co <sup>III</sup> OH <sup>26</sup>	Fe <sup>III</sup> -O Borovik <sup>8</sup>	Fe <sup>III</sup> -O Fout <sup>11</sup>	Fe <sup>II</sup> -O-Na Gomes <sup>25</sup>
M-O	1.96(1))	1.825(2)	1.813(3)	1.8079(9)	1.973(5)
O-M'1(Li/Na/K)/	2.58(1)	—	—	—	2.263(6)
O-M'2(Li/Na/K)	2.64(1)	—	—	—	2.289(6)
	<b>1</b>	[DHP <sup>2-</sup> ] Co <sup>III</sup> OH <sup>26</sup>	[DHP <sup>2-</sup> ] Co <sup>II</sup> (MeCN) <sup>32</sup>	[DHP <sup>1-</sup> ] Co <sup>II</sup> OTf <sup>32</sup>	
N1-N2/ N4-N5	1.38(2) 1.32(2)	1.306(3) 1.302(3)	1.325(5) 1.320(5)	1.273(10) 1.249(10)	
C5-C6/ C9-C10	1.44(2) 1.42(2)	1.390(4) 1.383(4)	1.402(6) 1.399(6)	1.387(13) 1.392(13)	
C7-C8	1.39(2)	1.349 (4)	1.351(6)	1.315(13)	
N1-M-N5	149.1(5)	162.4(1)	160.51(12)	178.1(3)	
N3-M-X (O/N)	107.4(5)	143.5(1)	114.32(13)	113.152 105.240	

An alternative method of stabilizing metal-oxygen bonds, and one that is employed in photosynthesis,<sup>13</sup> is the use of Lewis acid stabilizers. There are several examples where Lewis-acidic (Sc<sup>3+</sup> and Ce<sup>3+</sup>) metals have been used to stabilize Co-oxo complexes (among other M-oxo complexes, **Scheme 1**).<sup>14-22</sup> Still, most of these examples are in high (>3) oxidation states and have some degree of metal-oxygen multiple bonding, unlike the previously mentioned H-bonding examples. Stabilization of metal-oxygen bonds by alkali metals and alkaline earth metals is an even rarer sub-category of Lewis acid stabilization. Jones and coworkers have reported the use of lithium<sup>23</sup> and Borovik and coworkers have reported the use of calcium<sup>24</sup> in stabilizing Co-hydroxide complexes. However, there is only one crystallographically characterized example of an alkali metal capped oxido complex from Gomes and coworkers who isolated and crystallographically characterized a sodium capped Fe(II)-oxido complex.<sup>25</sup>

In this work we report the first example of a Lewis acid stabilized Co-oxido, with potassium as the stabilizing Lewis acid. The complex [<sup>*t*</sup>Bu,TolDHP]CoOK (**1**) was synthesized from the previously reported hydroxide—[<sup>*t*</sup>Bu,TolDHP]CoOH—via direct deprotonation (<sup>*t*</sup>Bu,TolDHP: 2,5-

bis((2-(*tert*-butyl)hydrazineylidene)(*p*-tolyl)methyl)-1*H*-pyrrole).<sup>26,27</sup> Complex **1** has been characterized by single-crystal X-ray diffraction (SXRD), high resolution mass spectrometry, and electron paramagnetic resonance (EPR), UV-vis, infrared (IR), and nuclear magnetic resonance (<sup>1</sup>H NMR) spectroscopies. The combination of these techniques reveals that **1** has an unusually distorted geometry and a formally Co(III) electronic structure with a DHP ligand radical. Isolation of this compound also enables the experimental bracketing of the p*K*<sub>a</sub> of the Co-bound hydroxide motif which can be extrapolated to <17, and likely ~12.5 in water. These findings shed further light on the bonding and structure of late transition metal oxo/oxido complexes and provide a rare opportunity to obtain experimental acidity data for these species.

The oxido complex [<sup>*t*Bu,Tol</sup>DHP]CoOK (**1**) can be synthesized through the addition of 1-5 equivalents of KO<sup>*t*Bu</sup> (due to limited solubility) as a slurry to a dark purple solution of [<sup>*t*Bu,Tol</sup>DHP]CoOH in toluene (**Scheme 1**). The solution was stirred for 1 hour until a homogeneous dark purple solution was obtained. Drying and extraction provides **1** as a purple solid. The absence of an O–H stretch can be verified by the IR spectrum of this complex which confirms the deprotonation of the starting -OH moiety (Appendix V:**Figure S15**). Crystals of **1** can be grown out of a concentrated petroleum ether solution at –35 °C. SXRD analysis on dark purple needles shows a dimeric structure with a four-coordinate Co center and an O ligand in a roughly seesaw geometry (**Figure 1**). The O ligands in the dimer are bridged with two K<sup>+</sup> cations in a four-membered ring. Using the compound's N1–M–N5 and N3–M–O bond angles, the τ<sub>4</sub> and the τ<sub>4</sub>' values can be determined as 0.731 and 0.602 respectively. These values put complex **1** closest to a seesaw geometry (0.5), leaning towards tetrahedral.<sup>28,29</sup>

Comparison of the bond lengths of **1** with the parent hydroxide complex and previously reported metal oxidos reveals some unusual geometric trends (**Table 1**). In contrast to metal-oxo complexes

with multiple bonding that results in shorter M–O interactions, there is a significant elongation of the Co–O bond of **1** to 1.96(1) Å from the 1.825(2) Å length observed in the parent Co–OH. This M–O bond distance is also long when compared to Borovik’s and Fout’s Fe(III)–O complexes where the Fe–O distances are 1.813(3) Å and 1.8079(9) Å respectively. The bond is also longer than Nam’s Lewis acid stabilized compounds, [(TAML)Co(IV)(O)(M<sup>n+</sup>)], though this is unsurprising as those compounds are proposed to have partial double bond character.<sup>18</sup> Perhaps more surprisingly, the Co–O bond length in **1** also lies outside the general range of other Co–O single bonds from the literature (1.784(3) Å – 1.921(3) Å).<sup>7,18,19,30,31</sup> This observed bond elongation is likely attributed to stronger  $\pi$ -repulsion between O and the Co d-electrons. This  $\pi$ -repulsion is putatively higher due to the weaker acidity of the alkali metal bonded to the oxygen versus the proton in the corresponding hydroxide complex [<sup>t</sup>Bu,<sup>Tol</sup>DHP]CoOH. This hypothesis is supported by the similar bond length of Gomes’ previously reported Fe(II)–O complex, 1.973(5) Å, which is also presumably elongated by the sodium ion’s weak Lewis acidity. An interesting conclusion from the longer length of the Co–O bond in **1** is the comparatively weaker stabilization provided by alkali metal Lewis acids in contrast with the hydrogen bonding scaffolds employed by Borovik, Fout, and others.

The effect of the alkali metal can further be contextualized by comparison with Jones’ hydroxide complex which has a similar “diamond-like” core. All three complexes have an O–M’ (M’=Li/Na/K) bond about 2 Å long.<sup>23</sup> Among these bonds, the Li–O bonds are shortest, followed by the Na–O bonds and K–O bonds which is consistent with the increase in ionic radii of each alkali metal. Further comparisons among the complexes’ geometries cannot be made because of different coordination environments around the transition metal centers.

The structural parameters of **1** also provide insight into its electronic structure. It should be noted that while [<sup>t</sup>Bu,<sup>Tol</sup>DHP]CoOH is formally a Co(II) complex, it is more accurately considered with contributing Co(II)/Co(III) resonance structures with partial ligand radical character. In fact, [<sup>t</sup>Bu,<sup>Tol</sup>DHP]CoOH is closest to a Co(III) oxidation state, as indicated by diagnostic changes in bond lengths when compared to clear-cut examples of a Co(II)DHP<sup>1-</sup> complex ([<sup>t</sup>Bu,<sup>Tol</sup>DHP]CoOTf) and Co(II)DHP<sup>2-</sup> complex ([<sup>t</sup>Bu,<sup>Tol</sup>DHP]Co(MeCN)) as standards.<sup>32,33</sup> The metal-ligand redox-tautomerism observed in the structures of these complexes has been previously discussed.<sup>32</sup>

Comparison of the DHP ligand bond lengths in **1** with [<sup>t</sup>Bu,<sup>Tol</sup>DHP]CoOH reveals additional significant distortions. While the parent hydroxide compound geometry lies closer to square planar—with a  $\tau_4$  of 0.38 and  $\tau_4'$  of 0.33—exchanging the H<sup>+</sup> for K<sup>+</sup> skews the complex towards

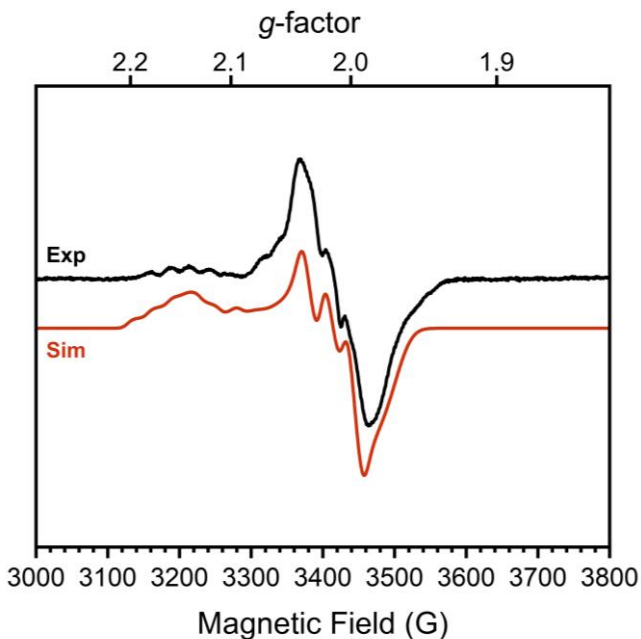


**Figure 2.** X-band EPR spectrum (black) and simulated spectrum (red) of a 15 mM solution of **1** (dimer) in toluene at 25 K. Conditions: MW frequency, 9.63 GHz; MW power, 2.0 mW. Simulation parameters:  $g_{x,y,z} = 2.143 \ 2.015 \ 1.983$ ;  $^{59}\text{Co } A_{x,y,z} = 37.85 \ 7.06 \ 22.66$  MHz;  $^{14}\text{N } A_{x,y,z} = 85.39, \ 87.94, \ 22.66$  MHz;  $\text{HStrain}_{x,y,z} = 41.7975, \ 32.2248, \ 100$ .

a tetrahedrally distorted seesaw. This effect plausibly arises from potassium ion interactions with the  $\pi$  system on the DHP metallacycle. Such bond elongation from K<sup>+</sup> has been previously observed, for instance, in work by Holland and coworkers.<sup>34</sup> Further evidence of perturbative alkali cation interactions with the DHP backbone are evident from altered bond lengths. Several diagnostic bonds (N1(4)–N2(5), C5(9)–C6(10), and C7–C8) can typically be analyzed to probe redox state, but all of these bonds are significantly elongated in **1**, putatively due to interaction with the K<sup>+</sup> cation. However, the C7–C8 bond at the back of the pyrrole ring is most removed from the K<sup>+</sup> cation and provides a useful metric to assay the electronic structure of the DHP ligand. Comparison of this distance in **1** and other DHP complexes reveals that the best oxidation state assignment for **1** is likely Co(III) with a ligand-

a tetrahedrally distorted seesaw. This effect plausibly arises from potassium ion interactions with the  $\pi$  system on the DHP metallacycle. Such bond elongation from K<sup>+</sup> has been previously observed, for instance, in work by Holland and coworkers.<sup>34</sup> Further evidence of perturbative alkali cation interactions with the DHP backbone are evident from altered bond lengths. Several diagnostic bonds (N1(4)–N2(5), C5(9)–C6(10), and C7–C8) can typically be analyzed to probe redox state, but all of these bonds are significantly elongated in **1**, putatively due to interaction with the K<sup>+</sup> cation. However, the C7–C8 bond

based radical. A cyclic voltammogram of **1** shows additional oxidative features but we have not yet been able to isolate any oxidized complexes (Appendix V: **Figure S16**).

To confirm this formal oxidation state assignment, the electronic structure of **1** was further investigated with EPR spectroscopy (**Figure 2**). The X-band EPR spectrum of **1** has a rhombic signal with features at  $g_{x,y,z} = 2.143, 2.015, 1.983$  which are comparable to the signals of the parent hydroxide complex (Appendix V: Figure S21). The isotropic  $g$ -value for this complex is less deviated from the free-electron value than the starting complex (2.047 vs. 2.146) suggesting a smaller proportion of spin density localized at the Co center and consequently more DHP ligand radical character. The hyperfine coupling values support this assessment, as we observe larger coupling to N ( $^{14}\text{N } A_{x,y,z} = 85.39, 87.94, 22.66$  MHz) than to Co ( $^{59}\text{Co } A_{x,y,z} = 37.85, 7.06, 22.66$  MHz). These values sharply contrast with those of [ $^{t\text{Bu,Tol}}\text{DHP}$ Co(II)OTf] where the Co hyperfine couplings were larger than those for N.<sup>27</sup> Further supporting the Co(III) oxidation state assignment, these experimental Co <38 MHz hyperfine couplings are similar to literature values for previously reported Co(III)-superoxide complexes (isotropic  $^{59}\text{Co}$  hyperfine couplings of <45 MHz).<sup>35</sup> Thus, the EPR data supports more ligand-centered radical character and a formal Co(III) oxidation state.

Evans method on complex **1** reveals an effective magnetic moment  $\mu_{\text{eff}} = 3.62 \mu_{\text{B}}$  per dimeric unit. This moment is consistent with either two  $S = 1/2$  [ $^{t\text{Bu,Tol}}\text{DHP}$ CoOK] fragments which are ferromagnetically coupled in the dimer or, possibly, two weakly coupled doublets. The  $S = 1/2$  signal observed in EPR suggests that a weakly coupled pair of doublets is the most reasonable assignment, but some dissociation in solution is difficult to rule out. However, we note that all attempts to generate the monomer (i.e. with crown ethers) result in side reactivity and decomposition. This leads us to tentatively propose a weakly coupled dimer with the support of the EPR data.

Finally, the isolation of both **1** and [<sup>t</sup>Bu,<sup>Tol</sup>DHP]CoOH provides the possibility of determining the p*K*<sub>a</sub> of the Co–OH unit. This p*K*<sub>a</sub> is relevant to processes such as water oxidation, which has previously been observed in this system.<sup>32</sup> We initially noted that neither 2,6-lutidine, used in previous studies with this system, nor NaOH, used in the formation of the Co–OH complex,<sup>32</sup> result in deprotonation, although the poor solubility of NaOH in organic solvents complicates this conclusion. We undertook <sup>1</sup>H NMR p*K*<sub>a</sub> bracketing experiments using five weakly acidic alcohols. Protonation can be conveniently assayed by the appearance of a broad feature around 9.5 ppm, representative of the OH proton on the Co complex, which matches a feature present in the NMR spectrum of [<sup>t</sup>Bu,<sup>Tol</sup>DHP]Co(III)OH (Appendix V: **Figure S2**, **Figures S8-S12**). These studies reveal that protonation of **1** occurs with hexafluoroisopropanol (HFIP), phenol and trifluoroethanol (TFE), but not with 2,4,6-tritertbutyl phenol (TTBP) or tert-butanol. From these results, the p*K*<sub>a</sub> of **1** can be conservatively bracketed between TFE (p*K*<sub>a</sub>: 12.4 in water) and tert-butanol (p*K*<sub>a</sub>: 16.84 in water). A tighter bracket can be reasonably made with TTBP. However, we note that the p*K*<sub>a</sub> of TTBP is not as well reported in water (p*K*<sub>a</sub>: ~12.19, Appendix V: **Table S6**). This bracketing tracks with single-point DFT calculations (Appendix V: **Table S5**) and provides a useful general data point in examining the acidity of Co oxides and related species.

In summary, we report the synthesis of an unusual potassium capped terminal Co-oxido, [<sup>t</sup>Bu,<sup>Tol</sup>-DHP]CoOK, **1**. Complex **1** was characterized via SXR to reveal a seesaw structure which is unlike similar crystallographically-characterized structures seen in the literature. Structural and spectroscopic analyses reveal that the electronic structure of **1** is best described as a weakly coupled dimer with Co(III) metal centers and DHP ligand-based radicals. <sup>1</sup>H NMR spectroscopy enables bracketing of the p*K*<sub>a</sub> of this complex between 12.4 and 16.84 in water. The isolation of this unique compound expands how late metal oxidos can accessed and stabilized. Further

reactivity and oxidation studies would be an interesting avenue of investigation to examine the potential applications of [<sup>t</sup>Bu,<sup>Tol</sup>DHP]CoOK in oxidative reactivity.

## References

- 1 V.A. Larson, B. Battistella, K. Ray, N. Lehnert and W. Nam, *Nat. Rev. Chem.*, 2020, **4**, 404-419.
- 2 J.E. Schneider, M.K. Goetz and J.S. Anderson, *Chem. Comm.*, 2023, **59**, 8584-8587.
- 3 M.K. Goetz, E.A. Hill, A.S. Filatov and J.S. Anderson, *J. Am. Chem. Soc.*, 2018, **140**, 13176-13189.
- 4 J.E. Schneider, M.K. Goetz and J.S. Anderson, *Chem. Science.*, 2021, **12**, 4173-4183.
- 5 H.B. Gray and J.R. Winkler, *Acc. Chem. Res.*, 2018, **51**, 1850-1857.
- 6 J.R. Winkler and H.B. Gray, *Struct. Bond.*, 2012, **142**, 17-28.
- 7 B.S. Hammes, V.G. Young and A.S. Borovik, *Angew. Chem. Int. Ed.*, 1999, **38**, 666-669.
- 8 C.E. MacBeth, A.P. Golombek, V.G. Young, C. Yang, K. Kuczera, M.P. Hendrich and A.S. Borovik, *Science*, 2000, **289**, 938-941.
- 9 D.C. Lacy, R. Gupta, K.L. Stone, J. Greaves, J.W. Ziller, M.P. Hendrich, and A.S. Borovik, *J. Am. Chem. Soc.*, 2010, **132**, 12188-12190.
- 10 Z. Gordon, T.J. Miller, C.A. Leahy, E.M. Matson, M. Burgess, M.J. Drummond, C.V. Popescu, C.M. Smith, R.L. Lord, J. Rodríguez-López, and A.R. Fout, *Inorg. Chem.*, 2019, **58**, 15801-15811.
- 11 E.M. Matson, Y.J. Park and A.R. Fout, *J. Am. Chem. Soc.*, 2014, **136**, 17398-17401.
- 12 C.L. Ford, Y.J. Park, E.M. Matson, Z. Gordon and A.R. Fout, *Science*, 2016, **354**, 741-743.
- 13 M. Risch, K. Klingan, F. Ringleb, P. Chernev, I. Zaharieva, A. Fischer and H. Dau, *Chem. Sus. Chem.*, 2-12, **5**, 542-549.
- 14 D.M. Beagan, C. Rivera and N.K. Szymczak, *J. Am. Chem. Soc.*, 2024, **146**, 12375-12385.
- 15 A. Draksharapu, W. Rasheed, J.E.M.N. Klein and L. Que, *Angew. Chem. Int. Ed.*, 2017, **56**, 9091-9095.
- 16 J. Prakash, G.T. Rohde, K.K. Meier, A.J. Jasnowski, K.M. Van Heuvelen, E. Münck and L. Que, *J. Am. Chem. Soc.*, 2015, **137**, 3478-3481.
- 17 D.G. Karmalkar, M. Sankaralingam, M.S. Seo, R. Ezhov, Y.M. Le, Y.N. Pushkar, W.S. Kim, S. Fukuzumi and W. Nam, *Angew. Chem. Int. Ed.*, 2019, **58**, 16124-16129.
- 18 S. Hong, F.F. Pfaff, E. Kwon, Y. Wang, M.S. Seo, E. Bill, K. Ray and W. Nam, *Angew. Chem. Int. Ed.*, 2014, **53**, 10403-10407.
- 19 D.D. Malik, A. Chandra, M.S. Seo, Y.M. Lee, E.R. Farquhar, S. Mebs, H. Dau, K. Ray and W. Nam, *Dalton Trans.*, 2021, **50**, 11889-11898.
- 20 Y. Liu and T.C. Lau, *J. Am. Chem. Soc.*, 2019, **141**, 3755-3766.
- 21 S.A. Cook and A.S. Borovik, *Acc. Chem. Res.*, 2015, **48**, 2407-2414.
- 22 F.F. Pfaff, S. Kundu, M. Risch, S. Pandian, F. Heims, I. Pryjomska-Ray, P. Haack, R. Metzinger, E. Bill, H. Dau, P. Comba and K. Ray, *Angew. Chem. Int. Ed.*, 2011, **50**, 1711-1715.
- 23 J.H. Rivers and R.A. Jones, *Dalton Trans.*, 2013, **42**, 12898-12907.
- 24 D.C. Lacy, Y.J. Park, J.W. Ziller, J. Yano and A.S. Borovik, *J. Am. Chem. Soc.*, 2012, **132**, 17526-17535.

- 25 C.S.B Gomes, M.T. Duarte and P.T. Gomes, *J. Organomet. Chem.*, 2014, **760**, 167-176.
- 26 S.W. Anferov and J.S. Anderson, *J. Coord. Chem.*, 2022, **75**, 1853-1864.
- 27 S.W. Anferov, A.S. Filatov and J.S. Anderson, *ACS Catal.*, 2022, **12**, 9933-9943.
- 28 L. Yang, D.R. Powell and R.P. Houser, *Dalton Trans.*, 2007, **9**, 955-964.
- 29 A. Okuniewski, D. Rosiak, J. Chojnacki and B. Becker, *Polyhedron.*, 2015, **90**, 47-57.
- 30 G.S. Mandel, R. Marsh, W.P. Schaefer and N.S. Mandel, *Acta Cryst.*, 1977, **33**, 3185-3188.
- 31 X. Dai, P. Kapoor and T.H. Warren, *J. Am. Chem. Soc.*, 2004, **126**, 4798-4799.
- 32 S.W. Anferov, J. Boyn, D.A. Mazziotti, J.S. Anderson, *J. Am. Chem. Soc.*, 2024, **146**, 5855-5863.
- 33 M.-C. Chang, A.J. McNeece, E.A. Hill, A.S. Filatov and J.S. Anderson, *Chem. -Eur. J.*, 2018, **24**, 8001-8008.
- 34 T.M. Figg, P.L. Holland and T.R. Cundari, *Inorg. Chem.*, 2012, **51**, 7546-7550.
- 35 R.D. Jones, D.A. Summerville and F. Basolo, *Chem. Rev.*, 1979, **79**, 139-179.

## Chapter VII: Conclusions and Future Outlook

*If I have seen further...*

The many exciting metal-cooperative systems, including biological ones, that have preceded this work have directly enabled us to move past proof-of-concept studies into active and varied catalytic systems. In this thesis, I hope to have demonstrated the power of metal-ligand cooperativity, and its ability to extend catalysis in new and varied ways. Not only have I demonstrated the capability of these ligands to stabilize unusual motifs, such as a rare oxidation state of  $\text{TEMPOH}_2^+$  and a potassium-capped cobalt-oxido, but I have done reductive, oxidative, and redox-neutral catalysis, utilizing heat, electrochemical potential, and light to drive reactivity different directions.

Specifically, I have been able to accomplish reductive hydrogenation of olefins to alkanes, with distinctive terminal selectivity and a mechanism that features ligand-based H-atom equivalents and key radical intermediates. On the oxidative side, I have been able to showcase the unusual selective formation of hydrogen peroxide from water, which can be rendered catalytic with oxidative potential (chemical or electrochemical). Lastly, I have investigated redox-neutral olefin isomerization, with the ability to use heat or light to switch between thermodynamically preferred or contra-thermodynamic products respectively. This work highlights how a proton- and electron-storing ligand can access and access broad and varied reactivity with a first-row metal and is not limited to any one class of reaction. Since part of designing better catalysts is designing broadly applicable catalysts, instead of requiring specific ligands for specific purposes, showcasing how multifunctional ligands can engender this type of ubiquity also hopefully motivates more chemists to choose to use them.

For future directions, this specific Co-complex has already demonstrated reactivity with CO and CO<sub>2</sub>, with the potential of building to environmentally inspired reduction catalysts, more reactivity that is well-precedented for cobalt. In addition, there is also potential in working to expand both the coupling chemistry observed electrochemically with water into other small molecules or the light reactivity highlighted in Chapter V. We can also hopefully apply the lessons learned from the catalysis with Co to other metals—such as Fe—or to related ligand scaffolds. Lastly, the ideas behind this thesis, while herein applied to first row metals, are no less true when utilized in precious metal catalysts or even in non-innocent surfaces, and I hope all chemists seeking catalysts can find value in the reactions we have studied and endeavored to understand.

# Appendices: Supplementary Informations and Unpublished Work

## Appendix I: Chapter II Supplementary Information

### NMR spectroscopy

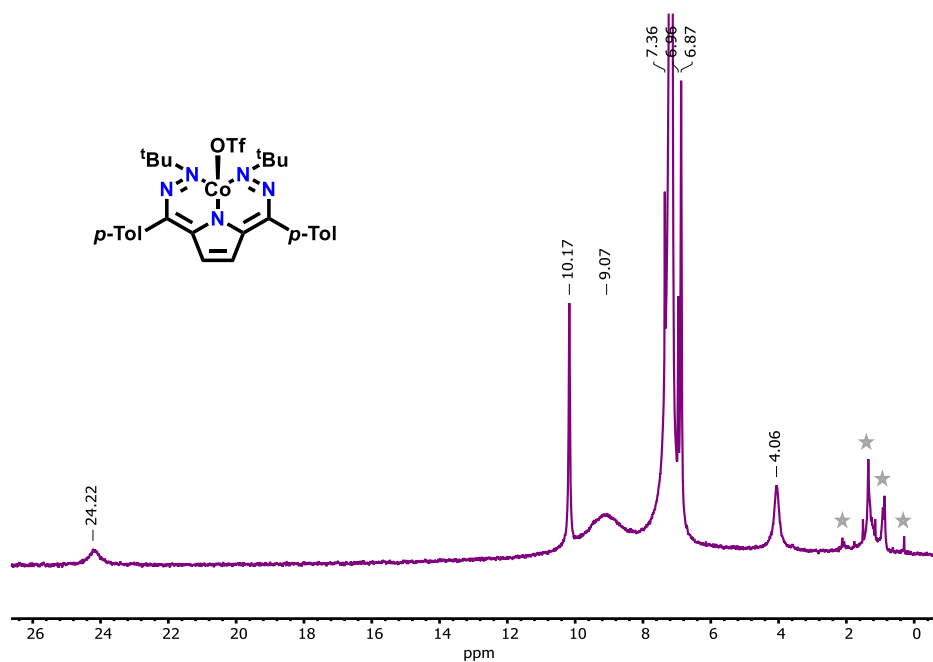


Figure S1.  $^1\text{H}$  NMR of **2** in  $\text{C}_6\text{D}_6$ . Residual solvent or grease marked with stars.

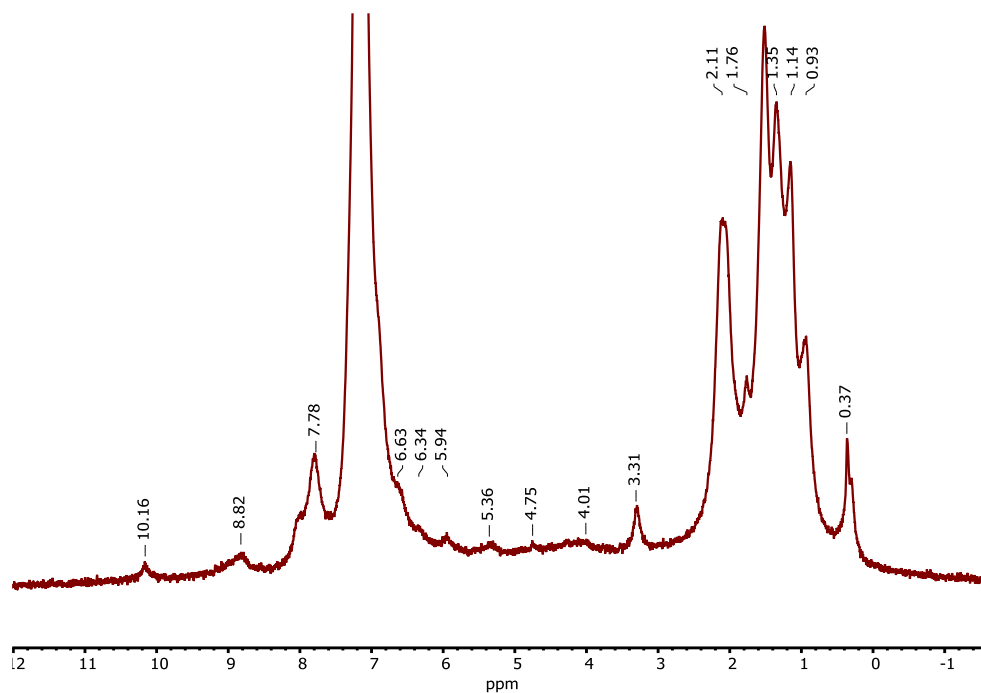


Figure S2.  $^1\text{H}$  NMR of **3** in  $\text{C}_6\text{D}_6$

### UV-vis spectroscopy

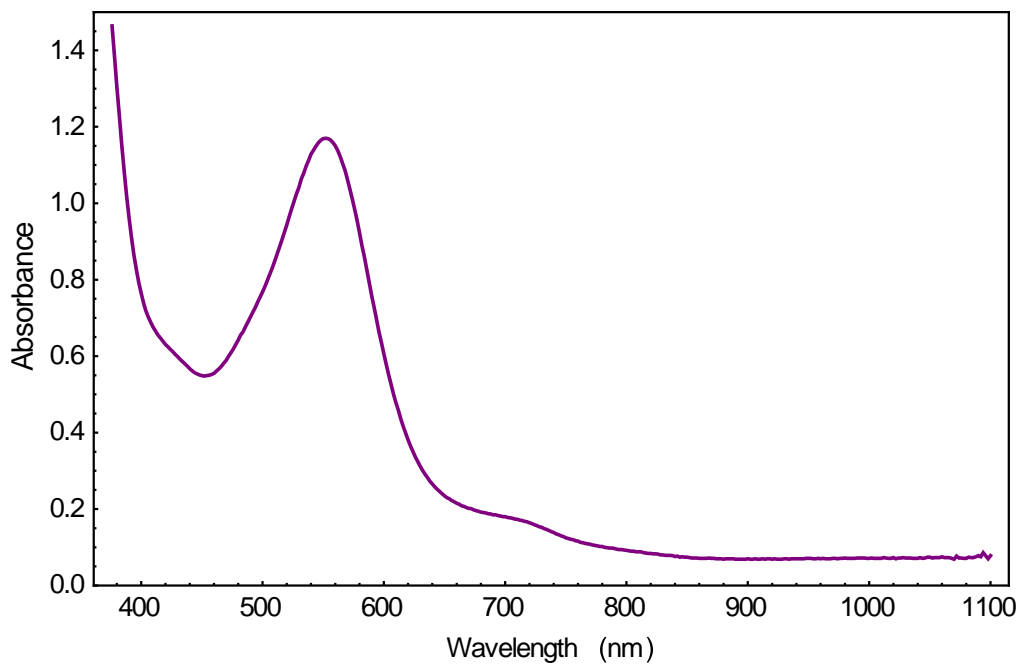


Figure S3. UV-vis of **1** from a 0.31 mM solution of **1** in toluene.

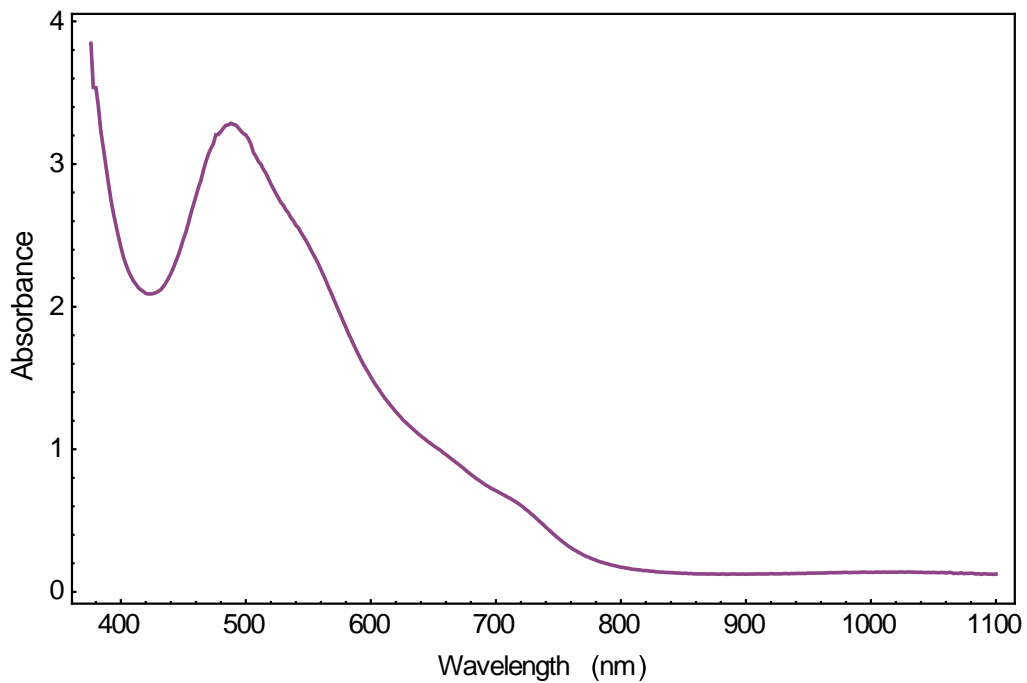


Figure S4. UV-vis of **2** from a 0.87 mM solution of **2** in benzene.

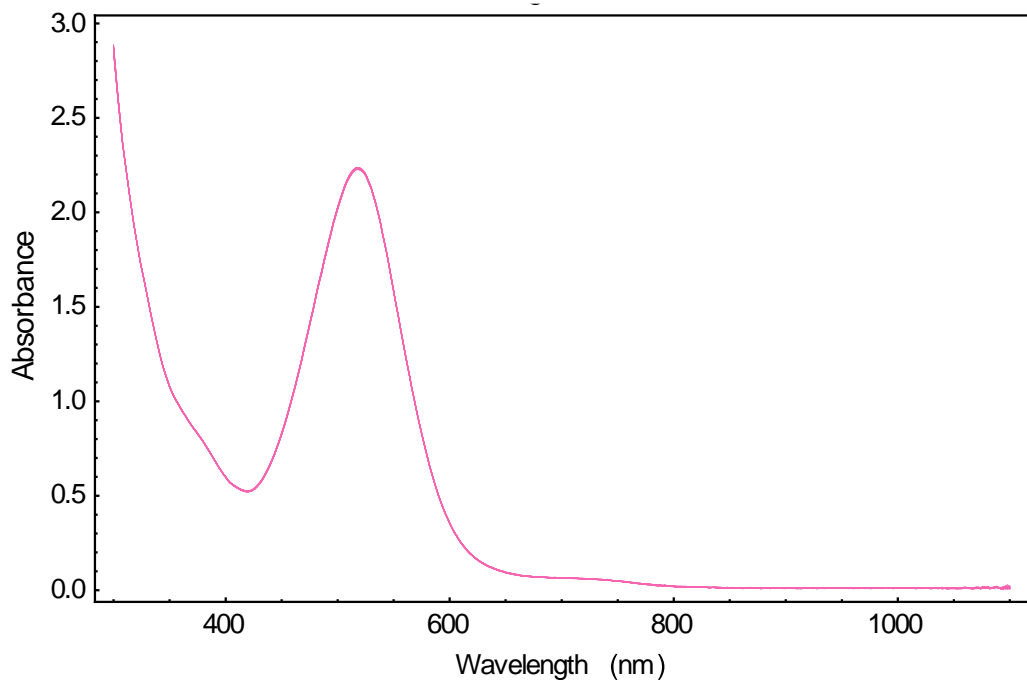


Figure S5. UV-vis of **3** from a solution in toluene at -35°C.

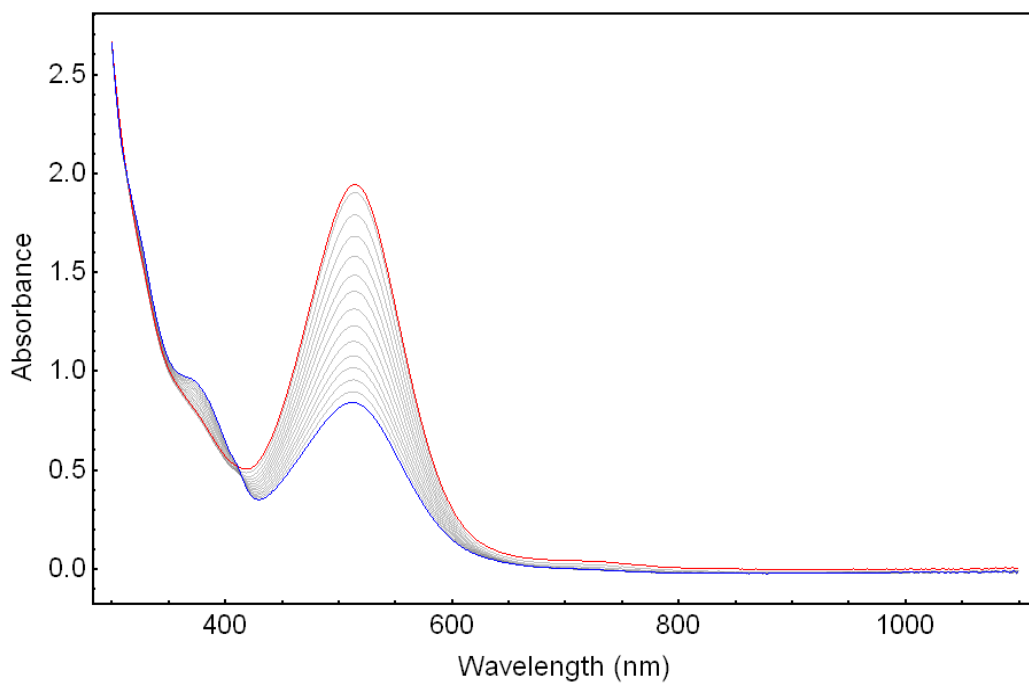


Figure S6. UV-vis of **3** in toluene at 0 °C over first 4.5 hours scans every 4.5 minutes

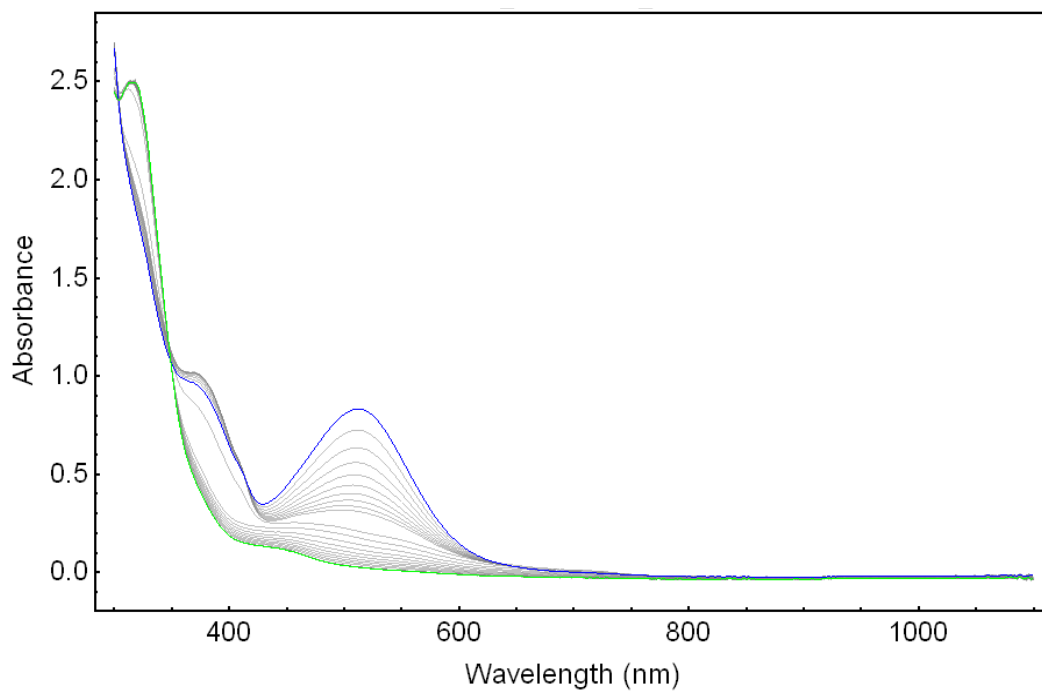


Figure S7. UV-vis of **3** in toluene at 0 °C for second 10.5 hours (starting at 4.5 hours), scans every 31.5 minutes

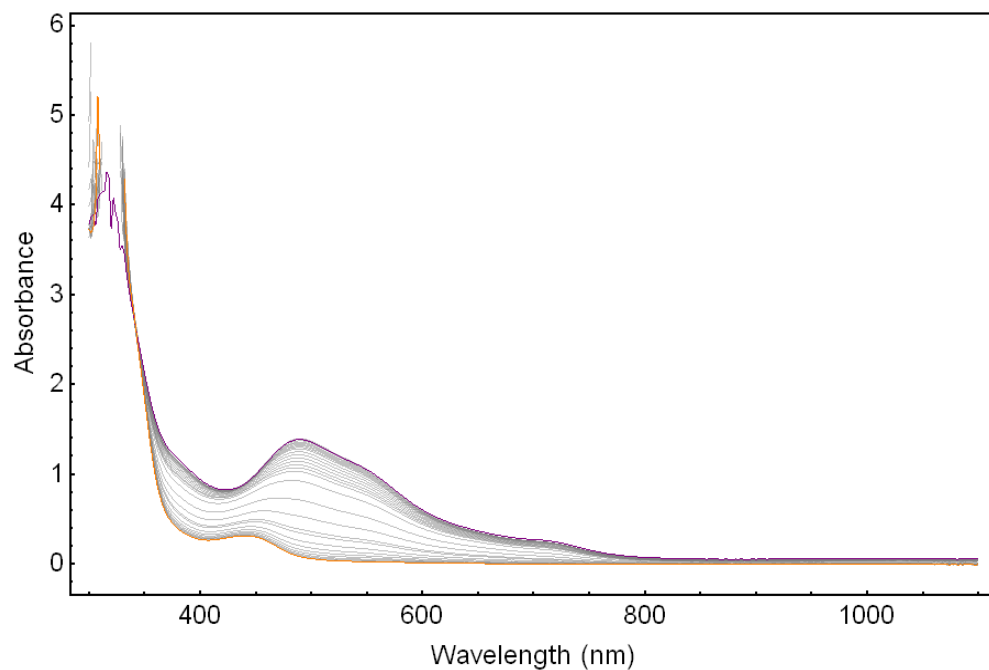


Figure S8. UV-vis of **2** + H<sub>2</sub> from a 0.24 mM solution of **2** in toluene (RT, scans every 13 minutes, 21 hours).

### Vibrational Spectroscopy

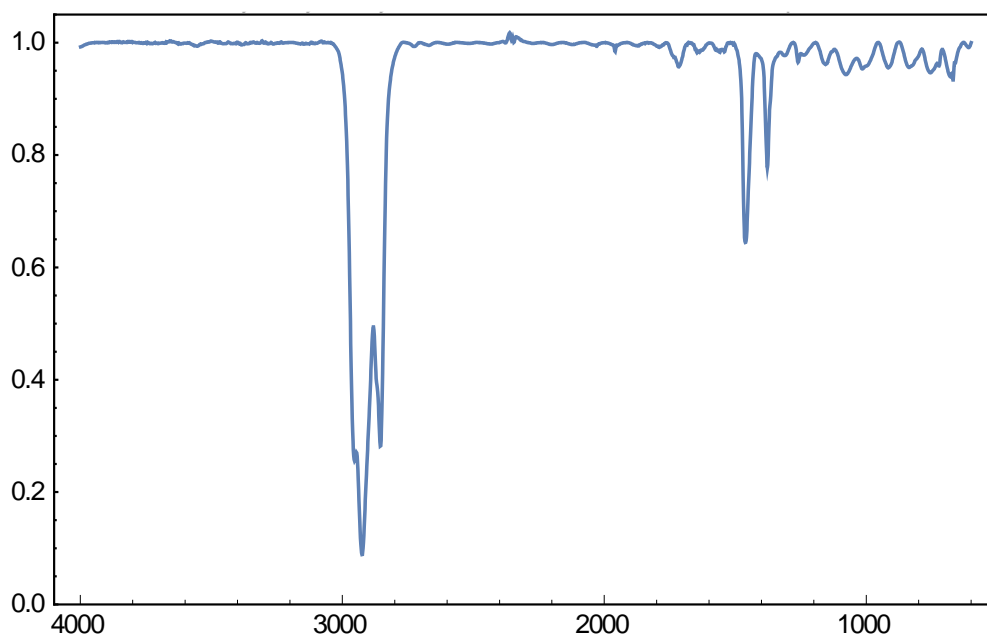


Figure S9. IR of nujol.

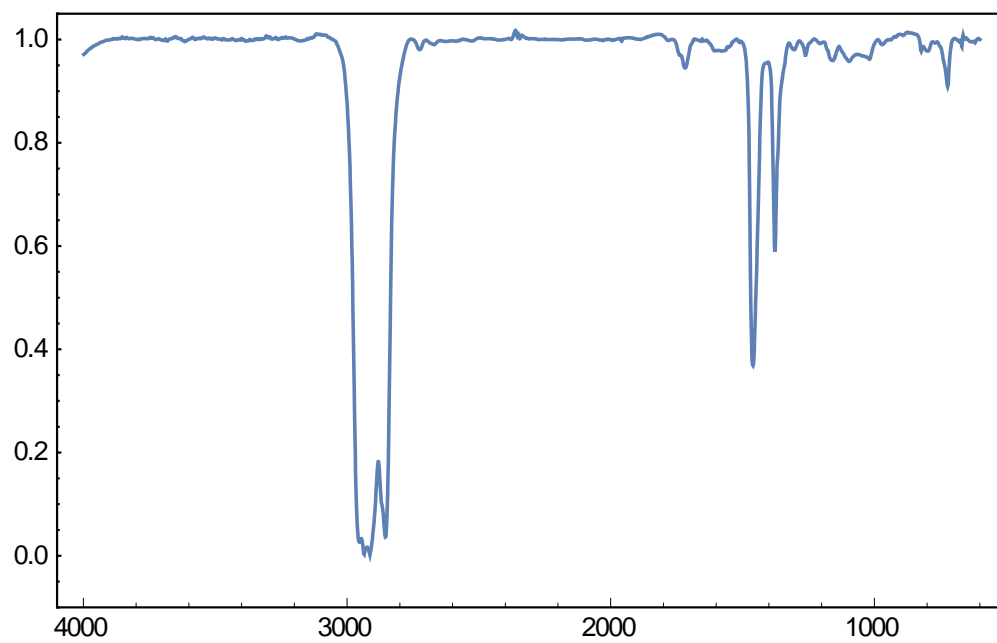


Figure S10. IR of **1** in nujol.

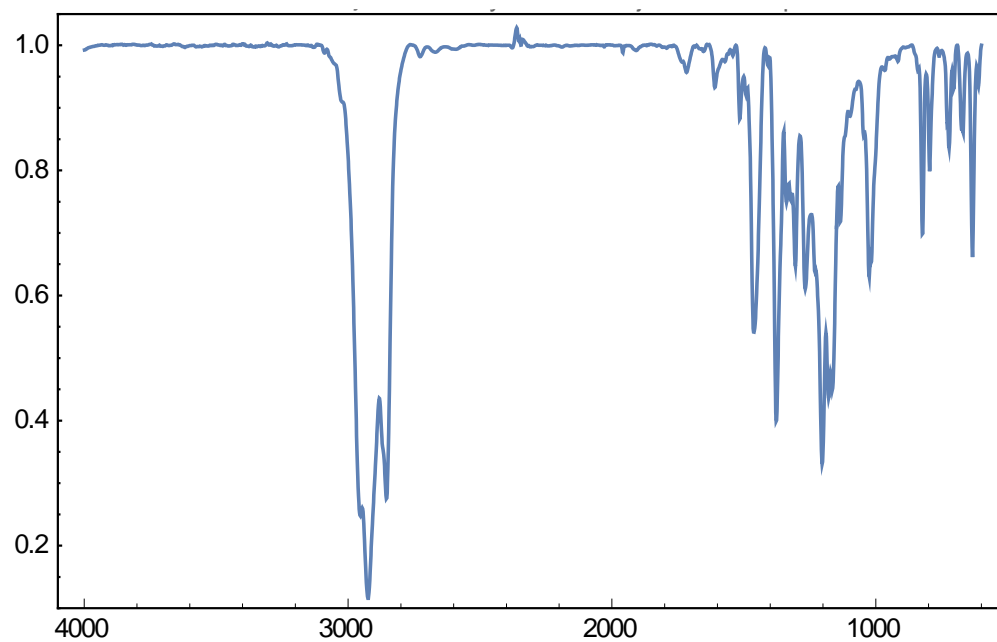


Figure S11. IR of **2** in nujol.

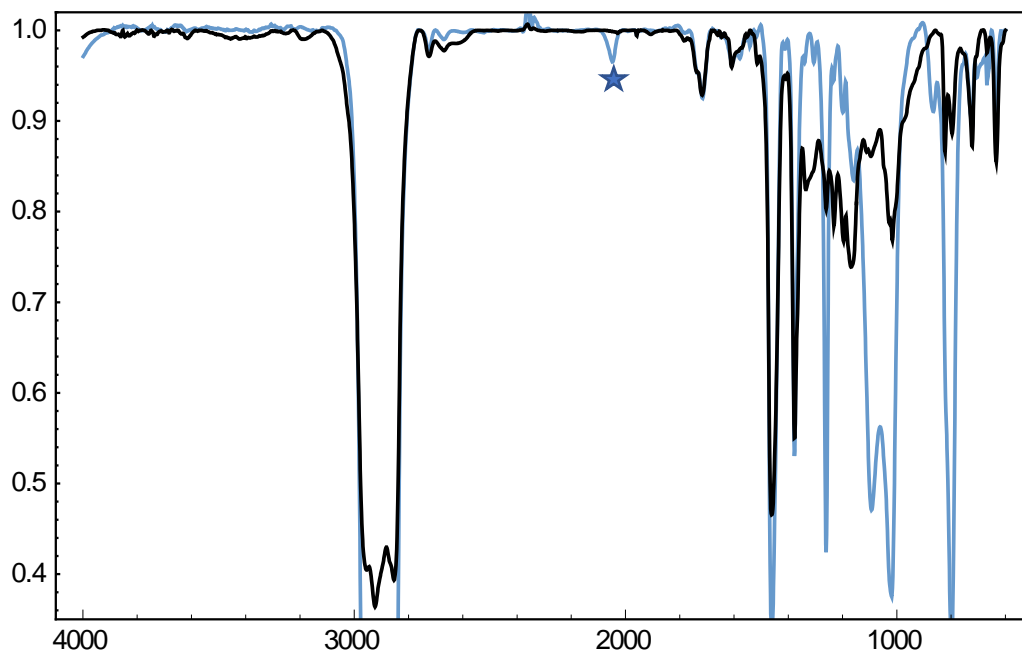


Figure S12. IR of **3** (black) and **3-D<sub>2</sub>** (blue) in nujol. Star indicates the N–D stretch.

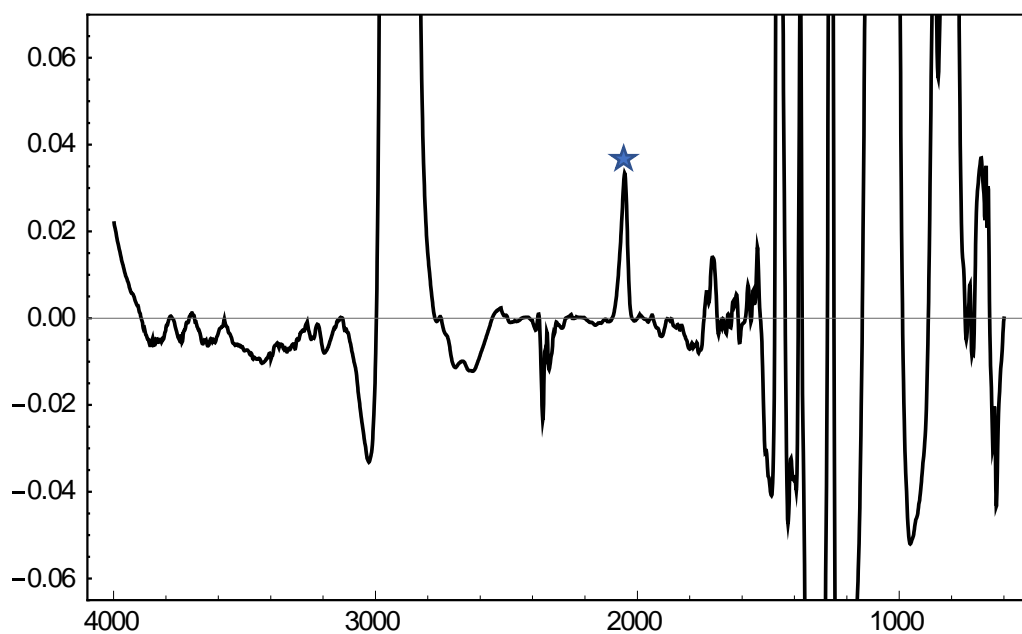


Figure S13. IR difference spectrum of **3** (black) and **3-D<sub>2</sub>** (blue) in nujol. Star indicates the N–D stretch.

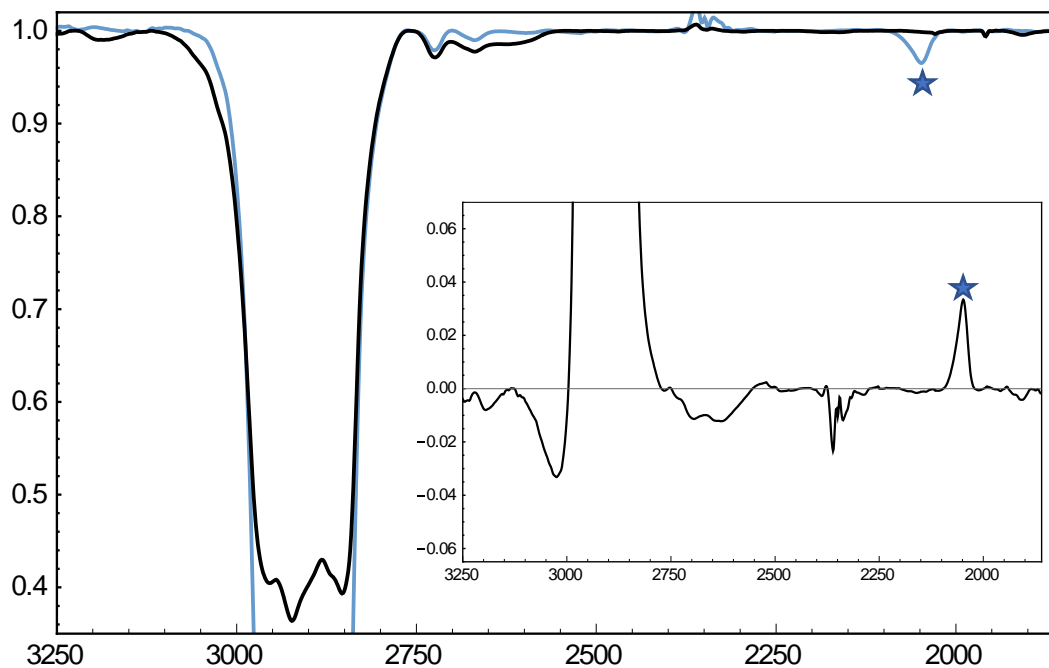


Figure S14. Zoomed IR with difference spectrum inset of **3** (black) and **3-D<sub>2</sub>** (blue) in nujol. Star indicates the N–D stretch.

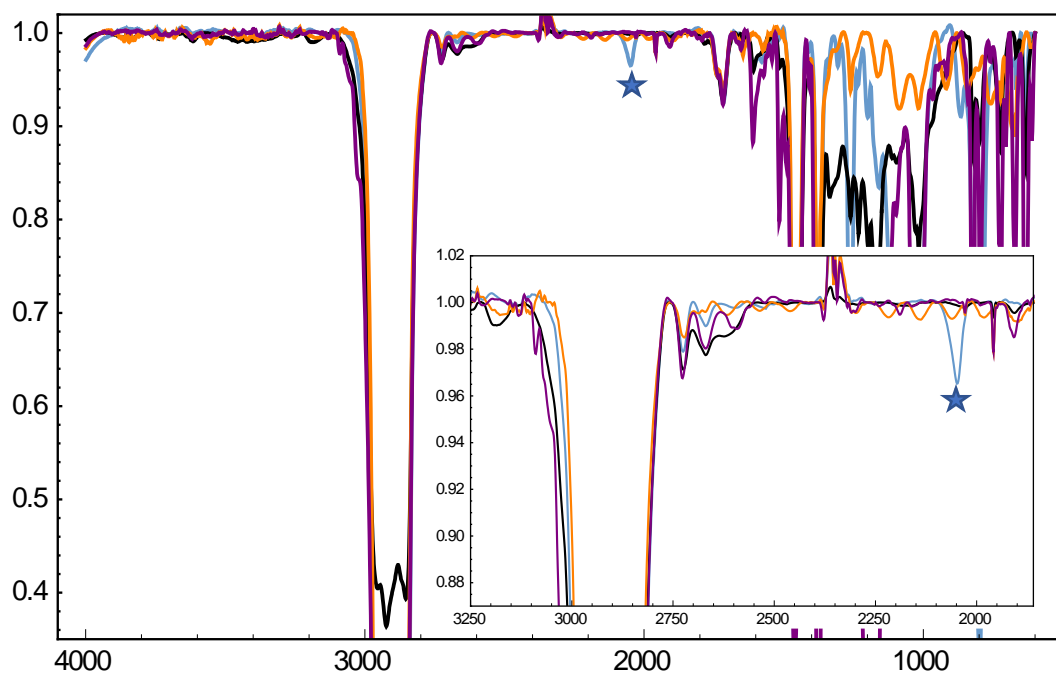


Figure S15. IR of nujol (orange) and **2** (purple), **3** (black) and **3-D<sub>2</sub>** (blue) in nujol. Star indicates the N–D stretch.

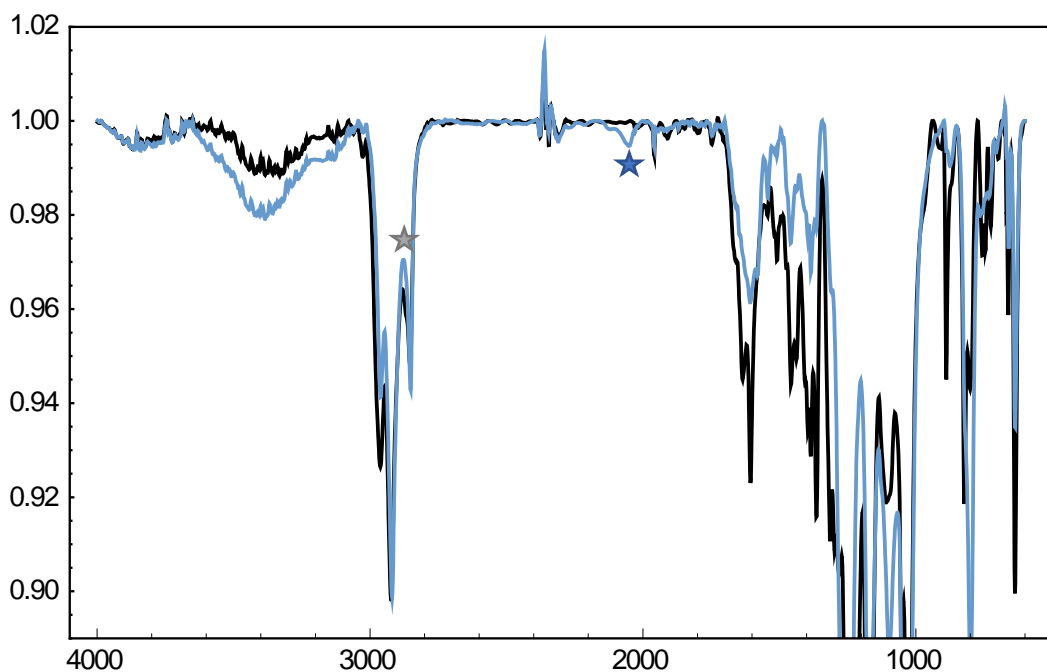


Figure S16. IR of **3** (black) and **3-D<sub>2</sub>** (blue) as a thin film on KBr. Blue star indicates the N–D stretch. Gray star indicates the proposed position of the N–H stretch.

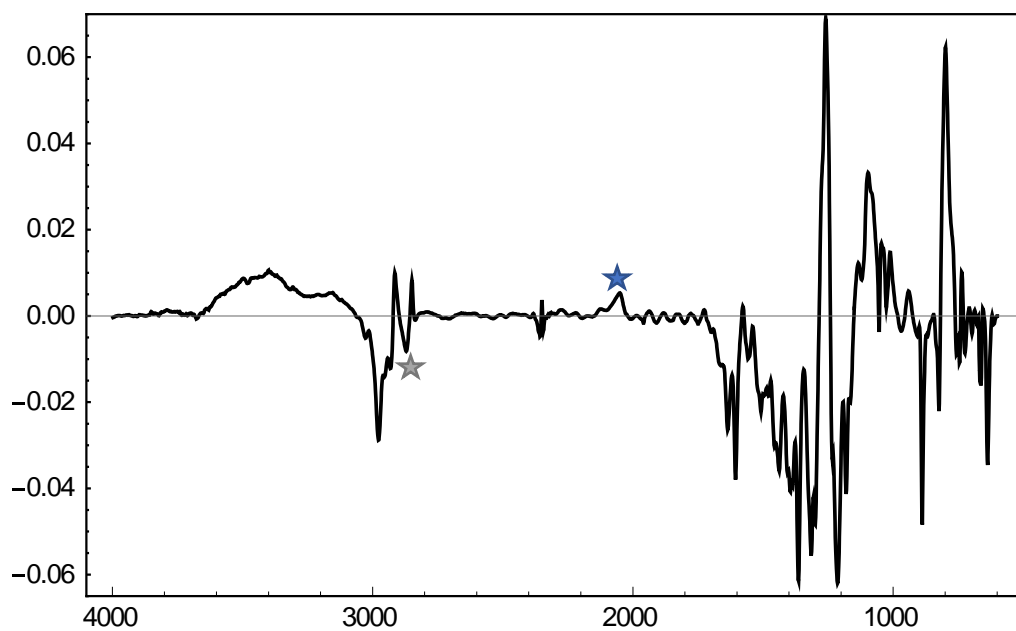


Figure S17. IR difference spectrum of **3** (black) and **3-D<sub>2</sub>** (blue) as a thin film on KBr. Blue star indicates the N–D stretch. Gray star indicates the proposed position of the N–H stretch.

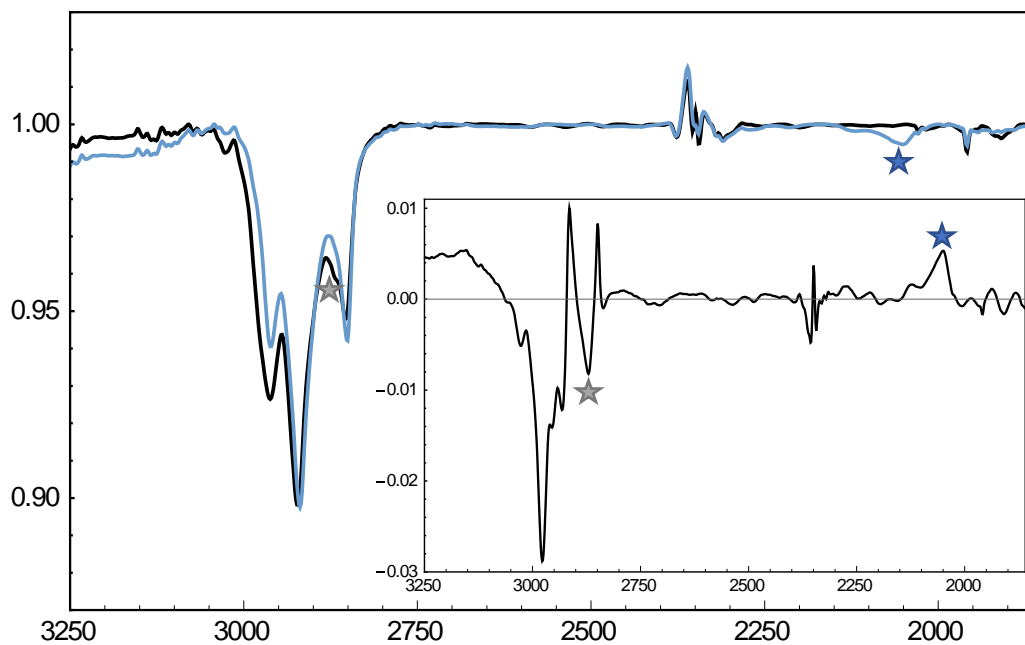


Figure S18. Zoomed IR with difference spectrum inset of **3** (black) and **3-D<sub>2</sub>** (blue) as a thin film on KBr. Blue star indicates the N–D stretch. Gray star indicates the proposed position of the N–H stretch.

### Cyclic Voltammetry

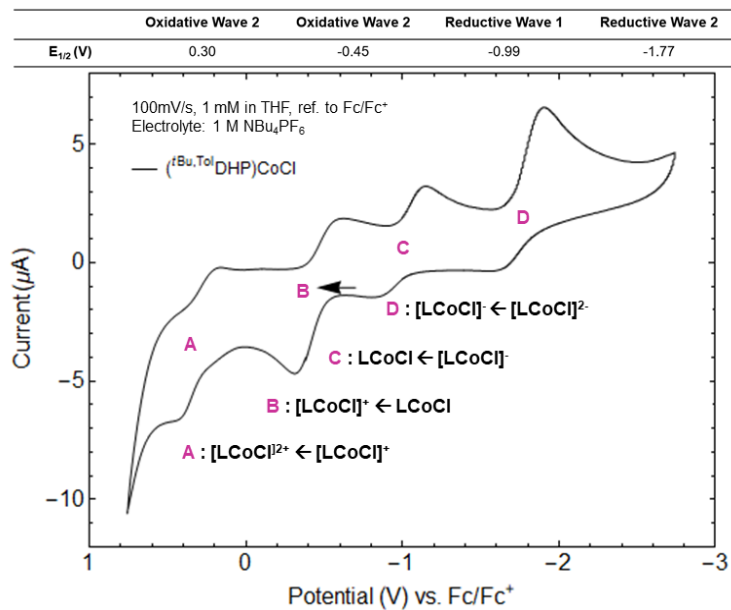


Figure S19. Cyclic Voltammogram of **1**.

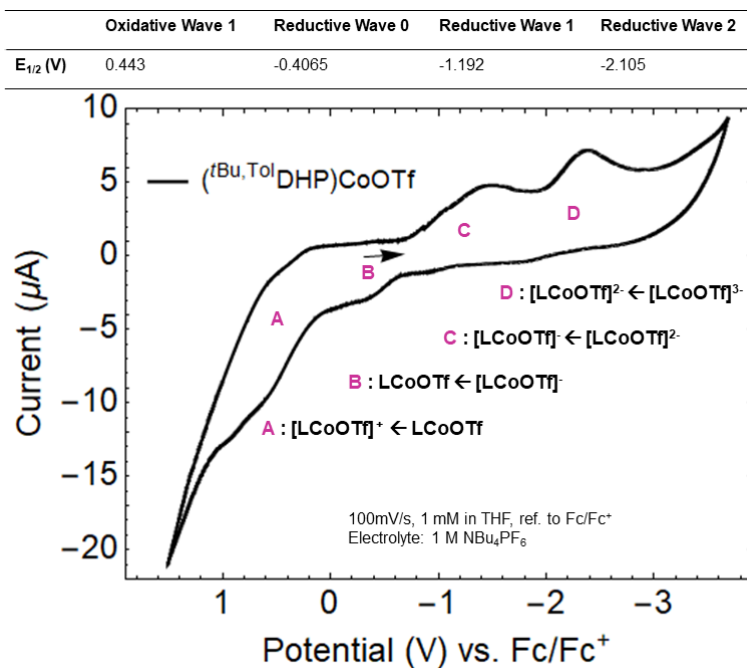


Figure S20. Cyclic Voltammogram of **2**.

### EPR Spectroscopy

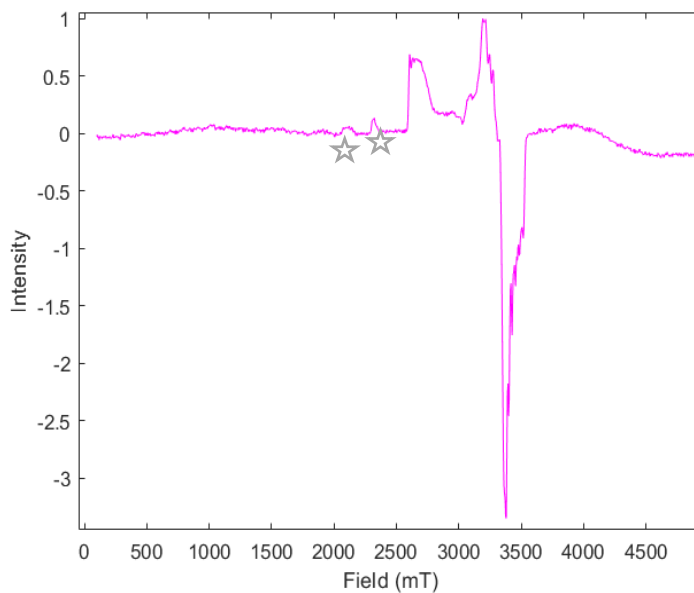


Figure S21. Full perpendicular-mode EPR spectrum of a 15 mM solution of **1** in toluene at 17 K. Some small unknown impurity peaks are marked. Conditions: MW frequency, 9.631 GHz; MW power, 2.0 mW.

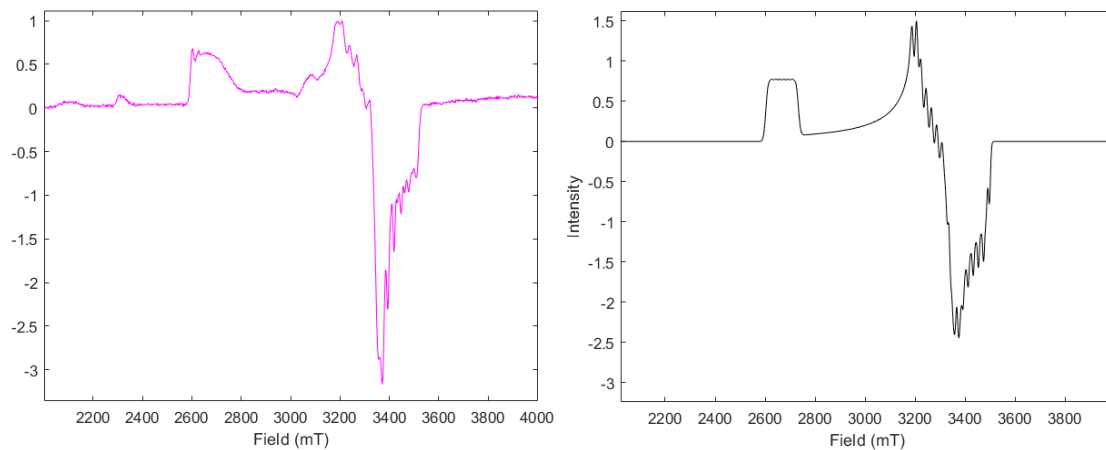


Figure S22. Small Window perpendicular-mode EPR spectrum (left) and simulated spectrum (right) of a 15 mM solution of **1** in toluene at 15 K. Conditions: MW frequency, 9.631 GHz; MW power, 2.0 mW.

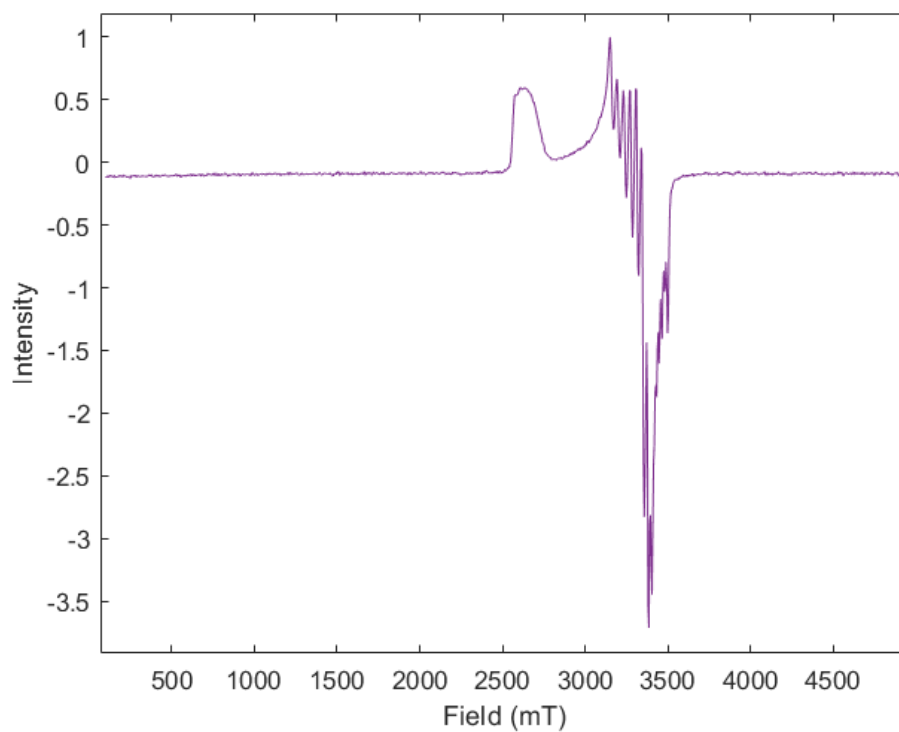


Figure S23. Full perpendicular-mode EPR spectrum of a 15 mM solution of **2** in toluene at 15 K. Conditions: MW frequency, 9.631 GHz; MW power, 2.0 mW.

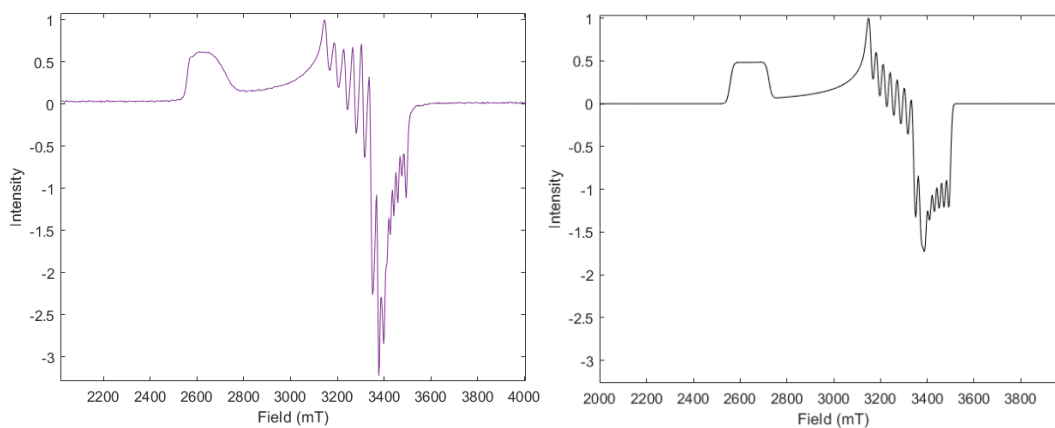


Figure S24. Small Window perpendicular-mode EPR spectrum (left) and simulated spectrum (right) of a 15 mM solution of **2** in toluene at 15 K. Conditions: MW frequency, 9.631 GHz; MW power, 2.0 mW.

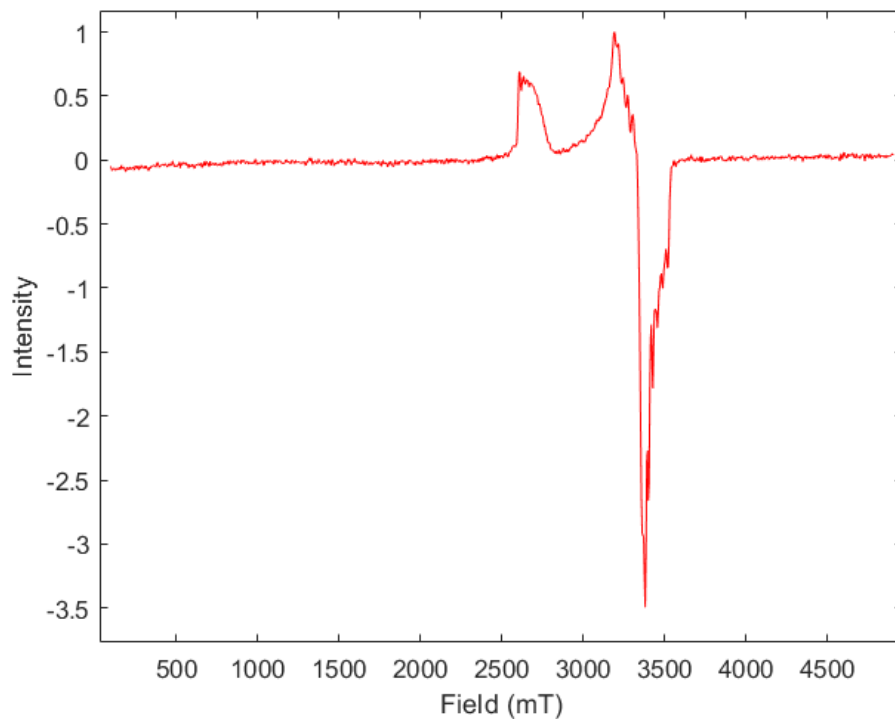


Figure S25. Full perpendicular-mode EPR spectrum of a 15 mM solution of **3** in toluene at 20 K. Conditions: MW frequency, 9.631 GHz; MW power, 2.0 mW.

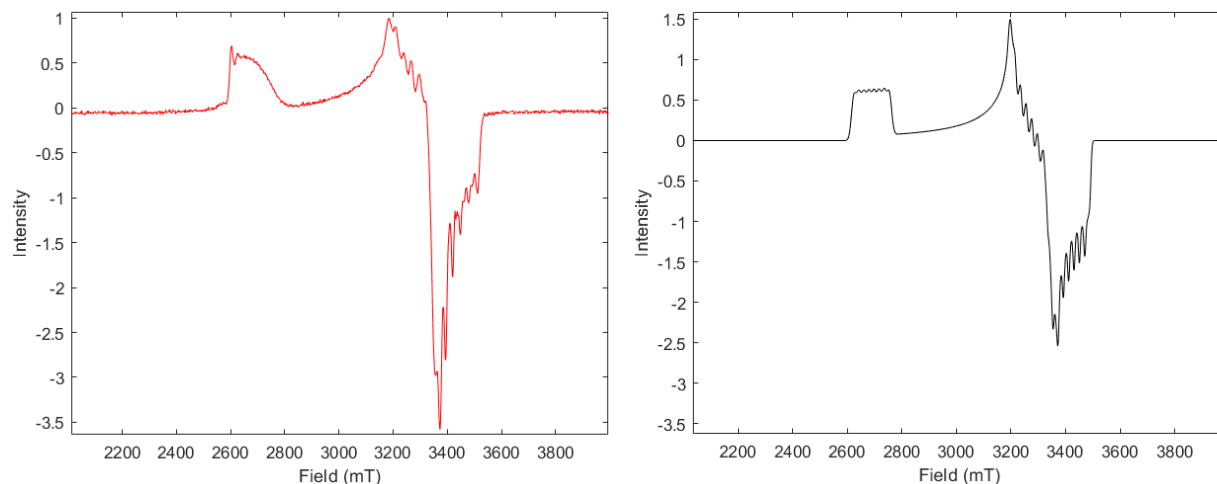


Figure S26. Small Window perpendicular-mode EPR spectrum (left) and simulated spectrum (right) of a 15 mM solution of **3** in toluene at 20 K. Conditions: MW frequency, 9.631 GHz; MW power, 2.0 mW.

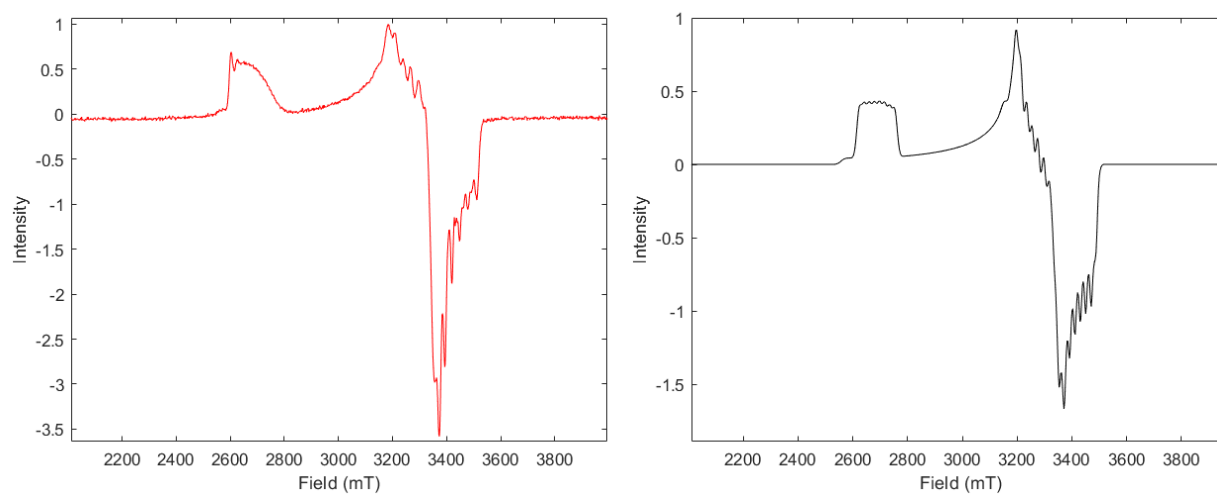


Figure S27. Small Window perpendicular-mode EPR spectrum and simulated spectrum overlay of a 15 mM solution of **3** in toluene at 20 K with 9.0% **2** impurity included. Conditions: MW frequency, 9.631 GHz; MW power, 2.0 mW.

Table S1. *g*-values for EPR

	<i>g</i> ( <i>x,y,z</i> )	<i>Co-A</i>	<i>N-A</i>	<i>H-strain</i>
<b>1</b>	(2.0162, 2.0965, 2.5792)	(57.6, 62.4, 58.8)	(35.4, 44.7, 10.7)	(29, 35, 71)
<b>2</b>	(2.0102, 2.1071, 2.6066)	(56.5, 89.0, 75.6)	(12.1, 5.9, 11.2)	(40, 60, 102)
<b>3</b>	(2.0162, 2.0965, 2.5592)	(54.8, 61.0, 66.8)	(23.1, 24.5, -14.1)	(28, 37, 66)

## Code to generate simulations of EPR Spectra.

**1:**

```
Exp2.mwFreq = 9.63;  
Exp2.nPoints = 2048;  
Exp2.Range = [150 450];  
Sys2.g = [2.0162 2.0965 2.5792];  
Sys2.Nucs = 'Co, N';  
Sys2.A = [57.6 62.4 58.8; 35.4 44.7 10.7];  
Sys2.HStrain = [29 35 71];  
Vary2.g = [0.01 0.01 0.01];  
Vary2.HStrain = [2 2 5];  
Vary2.A = [2 2 5; 2 2 5];  
plot(BCl,((ICl)/max(ICl)),BCl,1.5*pepper(Sys2,Exp2)/max(pepper(Sys2,Exp2)))
```

**2:**

```
Exp1.mwFreq=9.63;  
Exp1.Range = [150 450]  
Sys1.g = [2.0102 2.1070 2.6066]  
Exp1.nPoints = 1024  
Sys1.Nucs = 'Co, N';  
Sys1.A = [56.5 89.0 75.6; 12.1 5.9 11.2];  
Sys1.HStrain = [40 60 102];  
Vary1.g = [0.04 0.02 0.02];  
Vary1.HStrain = [10 10 10];  
Vary1.A = [20 20 20; 10 10 10];  
plot(Bo,(Io-Iblank)/max(Io-Iblank),Bo,pepper(Sys1,Exp1)/max(pepper(Sys1,Exp1)))
```

**3:**

```
Exp3.mwFreq=9.63;  
Exp3.nPoints = 2048;  
Exp3.Range = [150 450];  
Sys3.g = [2.0162 2.0965 2.5592];  
Sys3.Nucs = 'Co,N';  
Sys3.A = [54.8 61.0 66.8; 23.1 24.5 -14.1];  
Sys3.HStrain = [28 37 66];  
Vary3.g = [0.02 0.02 0.02];  
Vary3.HStrain = [5 5 10];  
Vary3.A = [8 8 15; 8 8 15];  
plot(BH2,(IH2)/max(IH2),BH2,pepper(Sys3,Exp3)/max(pepper(Sys3,Exp3)))
```

*or*

```
plot(BH2,((IH2)/max(IH2)),Bo,0.91*(pepper(Sys3,Exp3)/max(pepper(Sys3,Exp3)))+0.09*(pepper(Sys1,Exp1)/max(pepper(Sys1,Exp1))))
```

## X-ray Absorption Spectroscopy

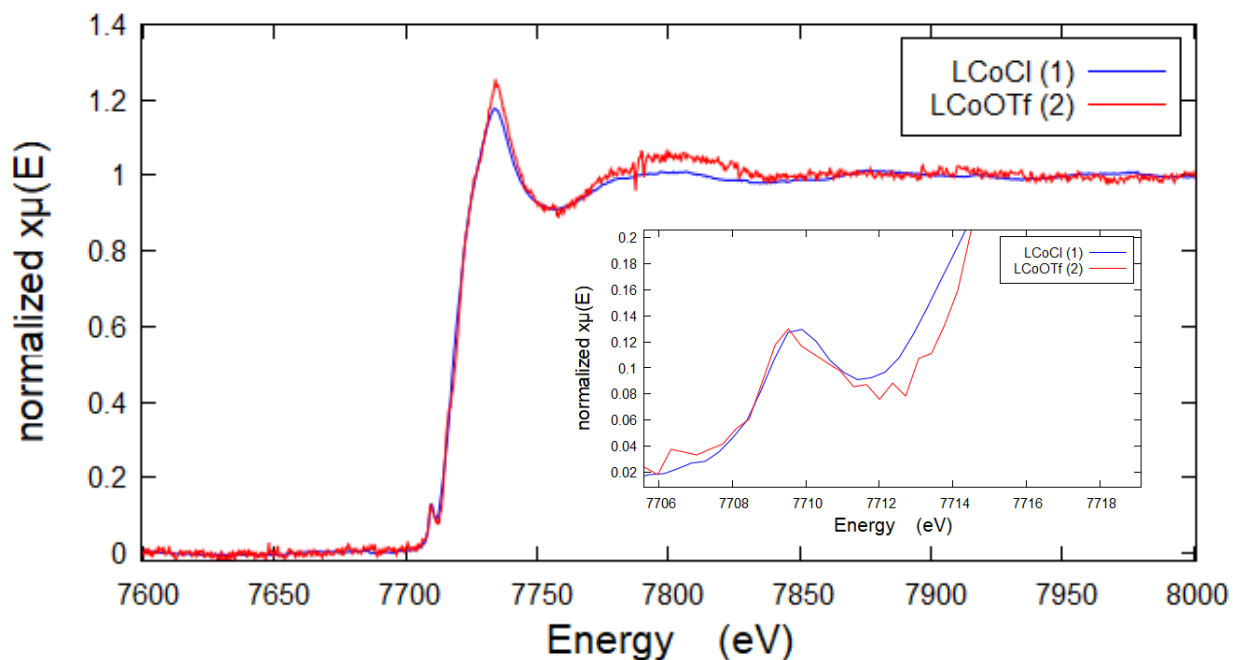


Figure S28. X-ray absorption spectra of **1** (red) and **2** (blue) with pre-edge features at 7709.7 and 7709.3 eV. These were all collected as frozen solutions at 183 K, with **1** and **2** in toluene. Inset: Pre-edge features.

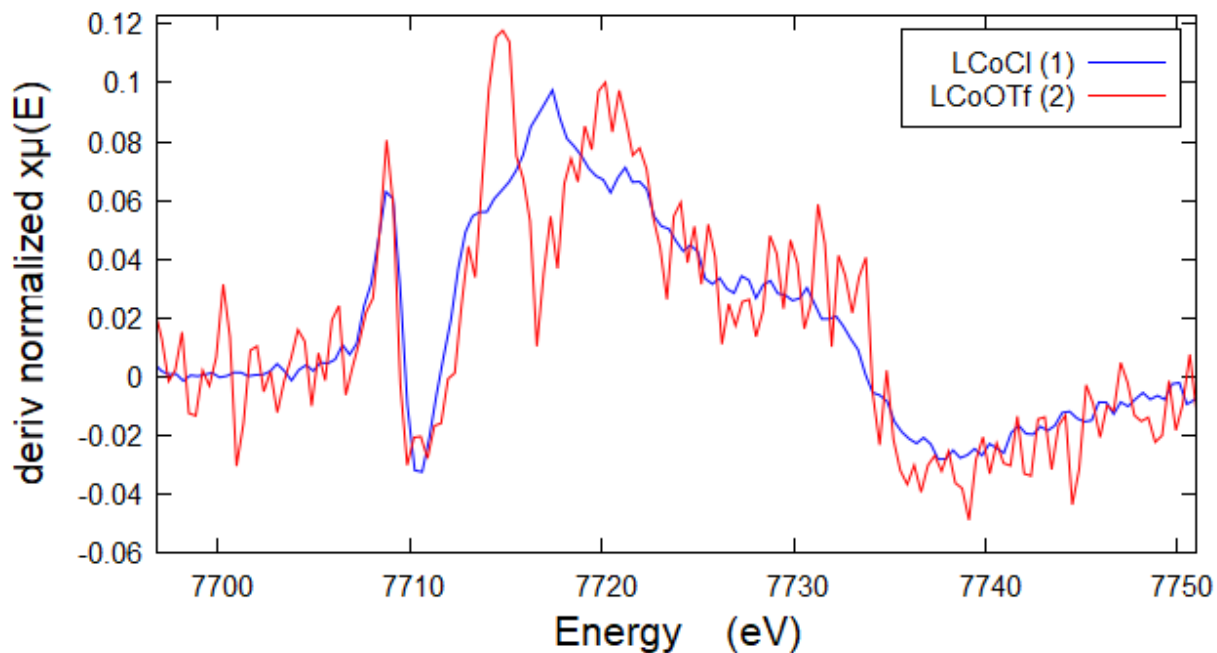


Figure S29. Derivative of X-ray absorption spectra of **1** (red) and **2** (blue).

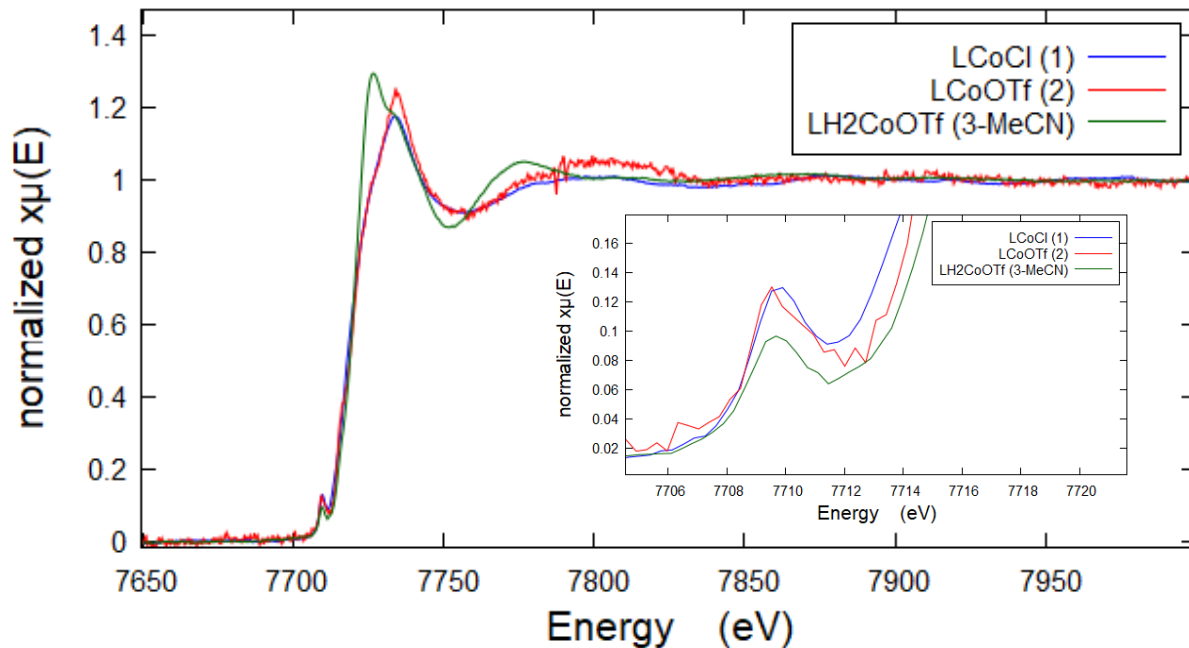


Figure S30. X-ray absorption spectra of **1** (blue), **2** (red) and **3-MeCN** (green) with pre-edge features at 7709.7, 7709.3, and 7709.3 eV respectively. These were all collected as frozen solutions at 183 K, with **1** and **2** in toluene and **3-MeCN** in a 1:4 MeCN:toluene mixture.

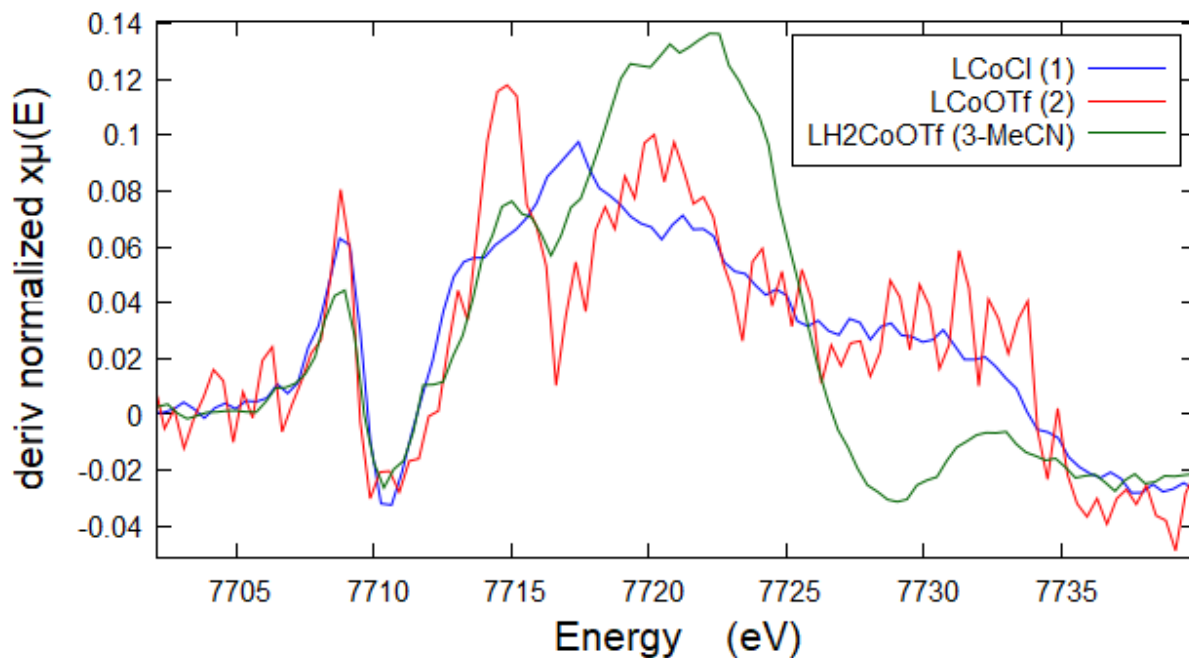


Figure S31. Derivative of X-ray absorption spectra of **1** (blue), **2** (red) and **3-MeCN** (green).

## Single Crystal X-ray Diffraction

### *X-Ray Structure Determination.*

The diffraction data were measured at 100 K on a Bruker D8 VENTURE with PHOTON 100 CMOS detector system equipped with a Mo-target micro-focus X-ray tube ( $\lambda = 0.71073 \text{ \AA}$ ). Data reduction and integration were performed with the APEX3 software package (Bruker AXS, version 2015.5-2, 2015). Data were scaled and corrected for absorption effects using the multi-scan procedure in SADABS (Bruker AXS, version 2014/5, 2015, part of Bruker APEX3 software package). The structure was solved by the dual method implemented in SHELXT<sup>1</sup> and refined by a full-matrix least-squares procedure using OLEX2<sup>2</sup> software package (XL refinement program version 2014/7<sup>3</sup>). Suitable crystals were mounted on a cryo-loop and transferred into the cold nitrogen stream of the Bruker D8 Venture diffractometer. C–H hydrogen atoms were constrained to idealized geometries and allowed to ride on their carrier atoms with an isotropic displacement parameter related to the equivalent displacement parameter of the carrier atoms. Finally, we note some B-level alerts for **2** related to the quality of the diffraction which was weak at higher angles. Despite this weak diffraction, the connectivity, assignment, and bond lengths for **2** are still suitable for discussion.

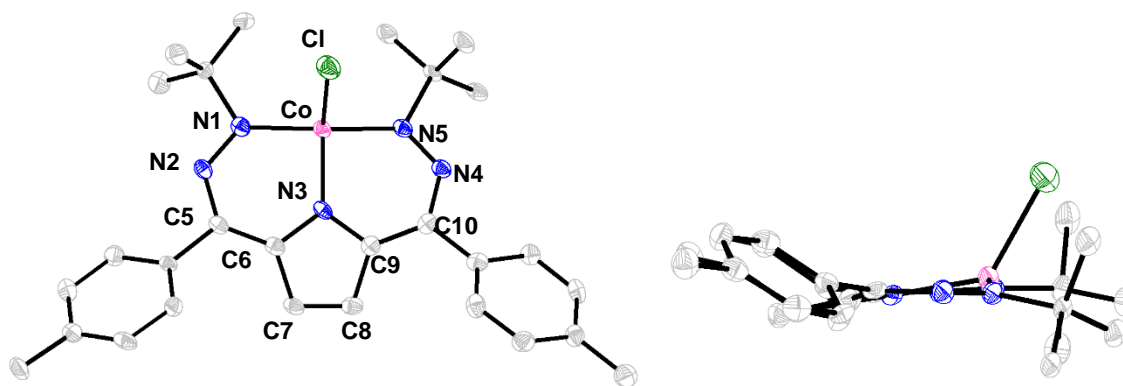


Figure S32. SXRd of **1**. Co (pink), N (blue), C (gray), Cl (green), H-atoms omitted. Selected bond lengths ( $\text{\AA}$ ): Co-N1/N5: 1.883(4), 1.891(5); Co-N3: 1.861(4); N1-N2/N4-N5: 1.303(6), 1.288(6); Co-Cl: 2.198(2); N2-C5/N4-C10: 1.343(7), 1.338(7); C5-C6/C9-C10: 1.388(8), 1.383(8); C6-C7/C8-C9: 1.434(8), 1.433(8); C7-C8: 1.351(8). Selected bond angles ( $^\circ$ ): N1-M-N5: 164.7(2); N3-M-Cl: 129.1(2).

Table S2. SXRd of **1**.

Empirical formula	$\text{C}_{28}\text{H}_{34}\text{ClCoN}_5$
Formula weight	534.98
Temperature/K	100(2)
Crystal system	monoclinic
Space group	$P2_1/n$
$a/\text{\AA}$	7.0908(10)
$b/\text{\AA}$	15.967(2)
$c/\text{\AA}$	23.272(3)
$\alpha/^\circ$	90

$\beta/^\circ$	93.817(4)
$\gamma/^\circ$	90
Volume/ $\text{\AA}^3$	2629.0(7)
Z	4
$\rho_{\text{calc}}/\text{g/cm}^3$	1.352
$\mu/\text{mm}^{-1}$	0.780
F(000)	1124.0
Crystal size/ $\text{mm}^3$	$0.15 \times 0.04 \times 0.025$
Radiation	MoK $\alpha$ ( $\lambda = 0.71073$ )
$2\theta$ range for data collection/ $^\circ$	4.338 to 50.804
Index ranges	$-8 \leq h \leq 8, -19 \leq k \leq 19, -28 \leq l \leq 28$
Reflections collected	34125
Independent reflections	4839 [ $R_{\text{int}} = 0.1513, R_{\text{sigma}} = 0.1075$ ]
Data/restraints/parameters	4839/0/324
Goodness-of-fit on $F^2$	1.141
Final R indexes [ $I \geq 2\sigma(I)$ ]	$R_1 = 0.0852, wR_2 = 0.1510$
Final R indexes [all data]	$R_1 = 0.1433, wR_2 = 0.1714$
Largest diff. peak/hole / $e \text{\AA}^{-3}$	0.83/-0.63

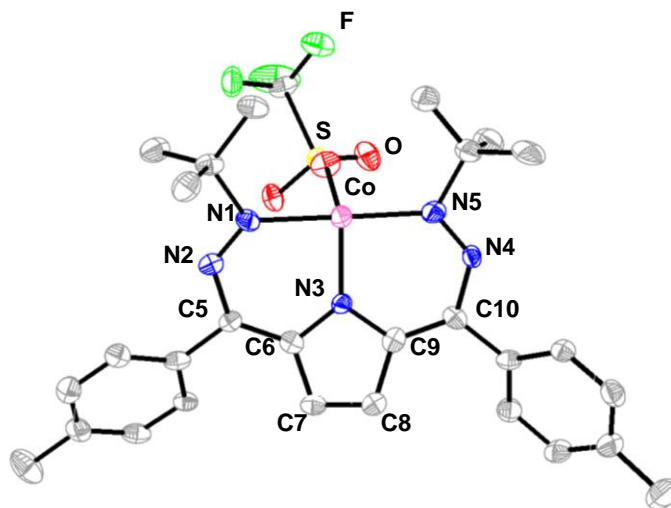


Figure S33. SXR of **2** (polymeric structure bridged by triflates). Co (pink), N (blue), C (gray), F (lime green), O (red), S (yellow), H-atoms omitted.

Selected bond lengths ( $\text{\AA}$ ): Co-N1/N5: 1.994(8), 2.000(8); Co-N3: 1.916(8); N1-N2/N4-N5: 1.274(10), 1.251(10); Co-O/Co-O: 2.168(7), 2.126(7); N2-C5/N4-C10: 1.371(11), 1.385(11); C5-C6/C9-C10: 1.383(13); C6-C7/C8-C9: 1.431(13), 1.452(13); C7-C8: 1.310(13). Selected bond angles ( $^\circ$ ): N1-M-N5: 178.1(3); N3-M-O: 113.2(3), 105.1(3).

Table S3. SXR of **2**.

Empirical formula	$\text{C}_{29}\text{H}_{34}\text{CoF}_3\text{N}_5\text{O}_3\text{S}$
Formula weight	648.60
Temperature/K	100.01

Crystal system	monoclinic
Space group	P2 <sub>1</sub> /c
a/Å	10.791(3)
b/Å	23.464(6)
c/Å	11.749(3)
α/°	90
β/°	97.322(8)
γ/°	90
Volume/Å <sup>3</sup>	2950.5(13)
Z	4
ρ <sub>calc</sub> /cm <sup>3</sup>	1.460
μ/mm <sup>-1</sup>	0.711
F(000)	1348.0
Crystal size/mm <sup>3</sup>	0.37 × 0.135 × 0.073
Radiation	MoKα (λ = 0.71073)
2θ range for data collection/°	4.926 to 51.438
Index ranges	-12 ≤ h ≤ 13, -28 ≤ k ≤ 28, -14 ≤ l ≤ 14
Reflections collected	33370
Independent reflections	5544 [R <sub>int</sub> = 0.2243, R <sub>sigma</sub> = 0.1243]
Data/restraints/parameters	5544/102/417
Goodness-of-fit on F <sup>2</sup>	1.058
Final R indexes [I ≥ 2σ (I)]	R <sub>1</sub> = 0.1276, wR <sub>2</sub> = 0.2773
Final R indexes [all data]	R <sub>1</sub> = 0.1696, wR <sub>2</sub> = 0.2994
Largest diff. peak/hole / e Å <sup>-3</sup>	1.21/-0.76

## Density Functional Theory (DFT)

### *Geometry Optimizations*

Geometry optimization calculations were performed with ORCA<sup>4</sup> software suite using density functional theory (DFT). Geometries were fully optimized starting from coordinates generated from finalized cifs of the compound crystal structures. The BP86 functional was used for geometry optimizations, spin density plot calculations, and frequency calculations on **1**, **2**, and **3** in ORCA 4. In ORCA 5, O3LYP was used to calculate transition state structures for the reactivity of **2** with H<sub>2</sub>, transition state structures for the reaction of **3** with 1-hexene, and the various isomers of 2-methyl-pent-1,3-ene and alpha-cyclopropyl styrene and their products. PBE0 in ORCA 4 was used for TDDFT calculations.

All these calculations were done with a basis set of def2-SVP on H. For the BP86 and PBE0 calculations, def2-TZVPP was used on Co, N, S, O and F, and def2-TZVP on C atoms. The resulting structures were confirmed to be minima on the potential energy surface by frequency calculations using ORCA. For the O3LYP calculations with triflate bound, def2-TZVPP was used on Co, N, S, O, most carbons and F, and def2-TZVP(-f) used on C atoms not part of the conjugated ligand. For O3LYP calculations without triflate bound, def2-TZVPP was used for Co, with def2-TZVP for all other N, C, O, S and F atoms.

Notation: LS: low spin, HS: high spin,

**2-H<sub>2</sub>**: [<sup>*t*</sup>Bu, Tol<sup>DHP</sup>Co-H<sub>2</sub>]OTf, **2-H<sub>2</sub><sup>+</sup>**: [<sup>*t*</sup>Bu, Tol<sup>DHP</sup>Co-H<sub>2</sub>]<sup>+</sup>,  
**2H-H**: [<sup>*t*</sup>Bu, Tol<sup>DHP-H</sup>Co-H]OTf, **2H-H<sup>+</sup>**: [<sup>*t*</sup>Bu, Tol<sup>DHP-H</sup>Co-H]<sup>+</sup>,  
**3**: [<sup>*t*</sup>Bu, Tol<sup>DHP-H<sub>2</sub></sup>Co]OTf, **3<sup>+</sup>**: [<sup>*t*</sup>Bu, Tol<sup>DHP-H<sub>2</sub></sup>Co]<sup>+</sup>,  
**4**: [<sup>*t*</sup>Bu, Tol<sup>DHP-H</sup>Co]OTf, **4<sup>+</sup>**: [<sup>*t*</sup>Bu, Tol<sup>DHP-H</sup>Co]<sup>+</sup>,  
**3-hexene**: [<sup>*t*</sup>Bu, Tol<sup>DHP-H<sub>2</sub></sup>Co(1-hexene)]OTf, **3-hexene<sup>+</sup>**: [<sup>*t*</sup>Bu, Tol<sup>DHP-H<sub>2</sub></sup>Co(1-hexene)]<sup>+</sup>,  
**4-hexyl-β**: [<sup>*t*</sup>Bu, Tol<sup>DHP-H</sup>Co(n-hexyl)]OTf, **4-hexyl-β<sup>+</sup>**: [<sup>*t*</sup>Bu, Tol<sup>DHP-H</sup>Co(n-hexyl)]<sup>+</sup>,  
**4-hexyl-α**: [<sup>*t*</sup>Bu, Tol<sup>DHP-H</sup>Co(2-hexyl)]OTf, **4-hexyl-α<sup>+</sup>**: [<sup>*t*</sup>Bu, Tol<sup>DHP-H</sup>Co(2-hexyl)]<sup>+</sup>,

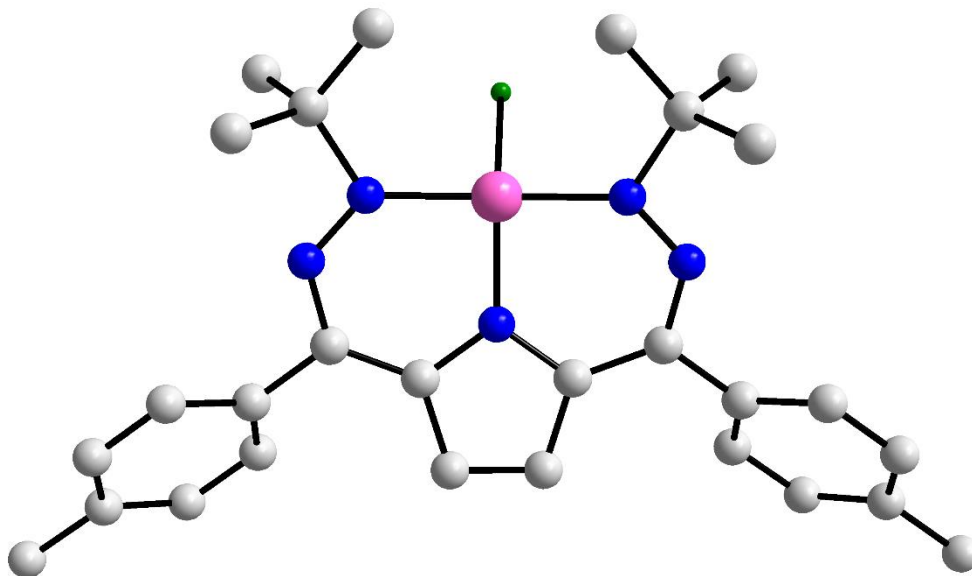


Figure 34. Calculated structure of **1**. All C–H hydrogen atoms have been removed for clarity.

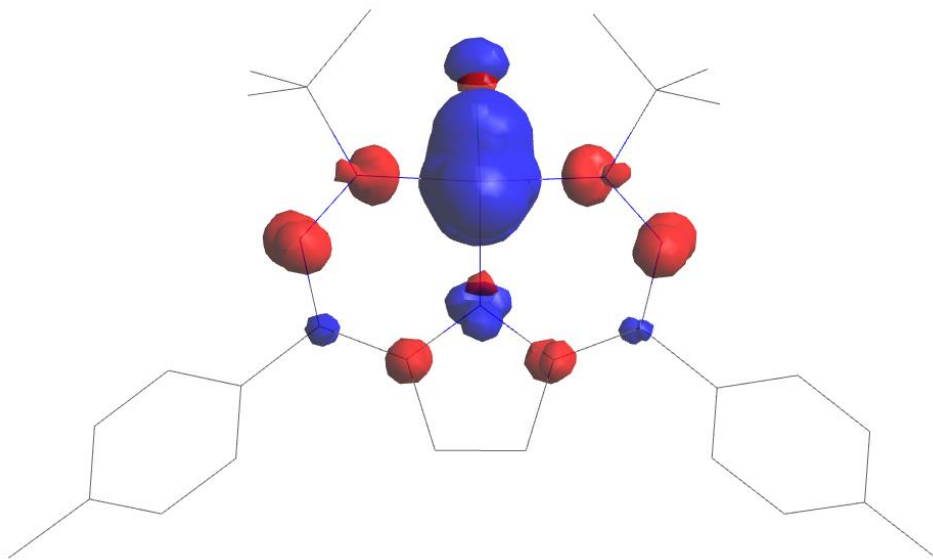


Figure S35. Spin density plot of **1** at an iso value of 0.003.

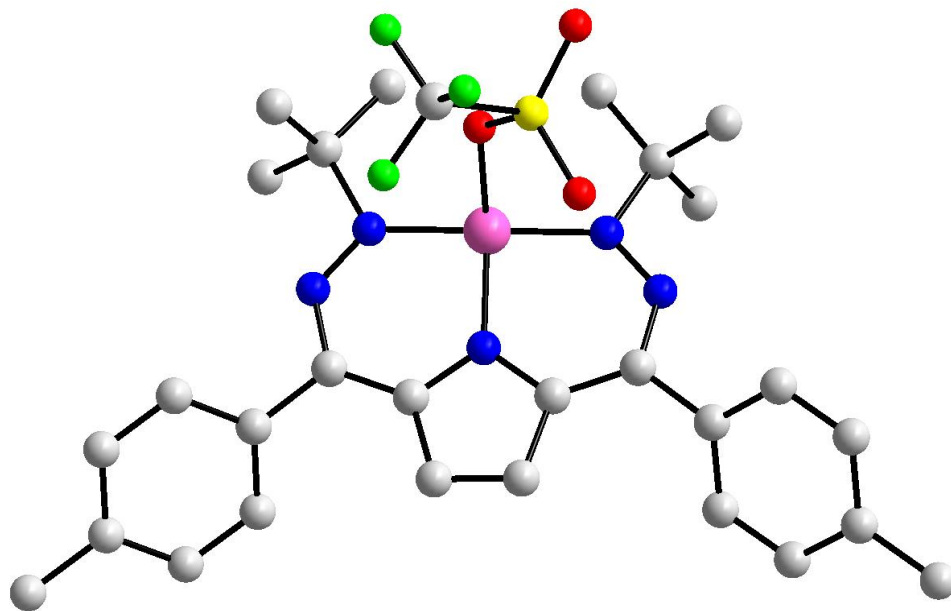


Figure S36. Calculated structure of **2**. All C–H hydrogen atoms have been removed for clarity.

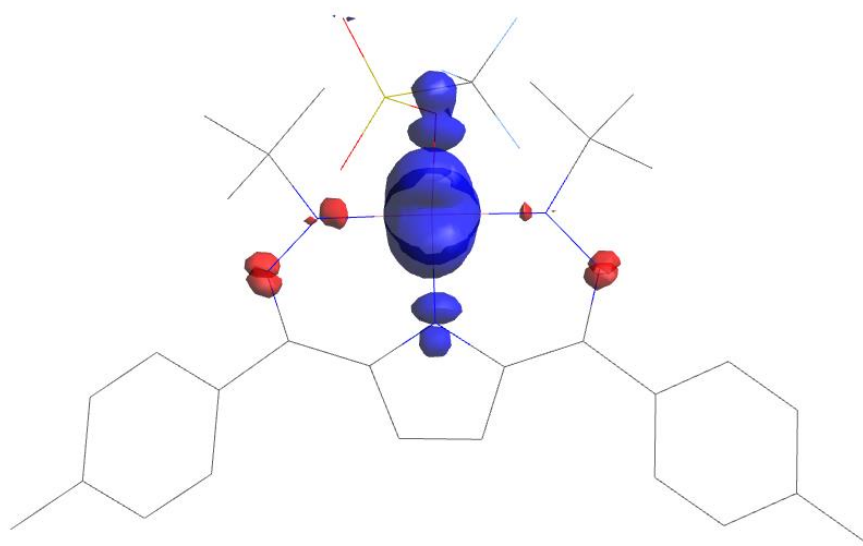


Figure S37. Spin density plot of **2** at an iso value of 0.005.

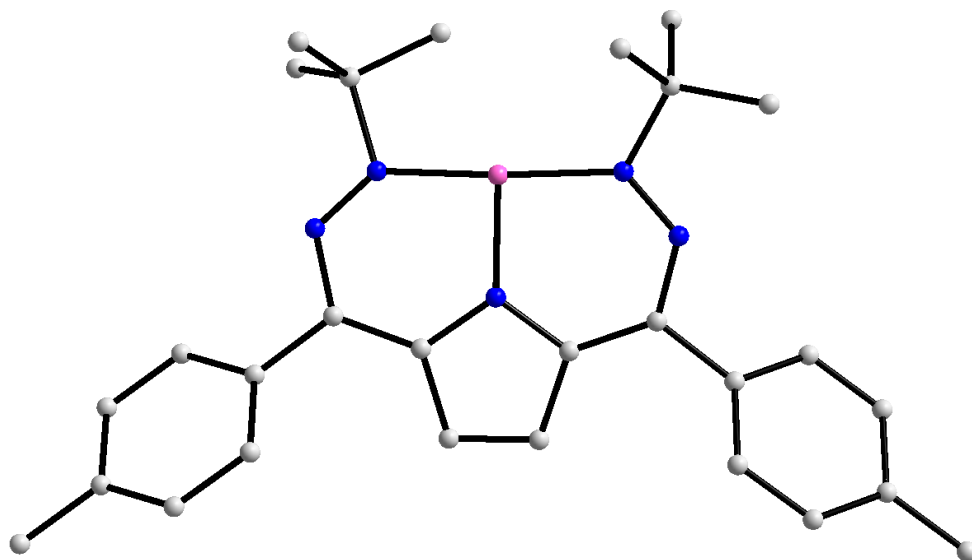


Figure S38. Calculated structure of  $[t\text{Bu, Tol}]\text{DHPCo}^+$  ( $2^+$ ). All C–H hydrogen atoms have been removed for clarity.

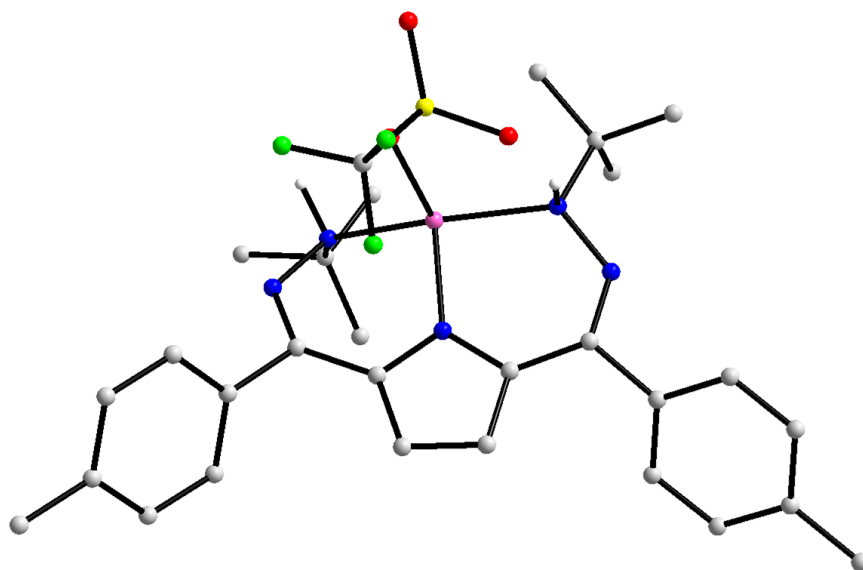


Figure S39. Calculated structure of **3-HS**. All C–H hydrogen atoms have been removed for clarity.

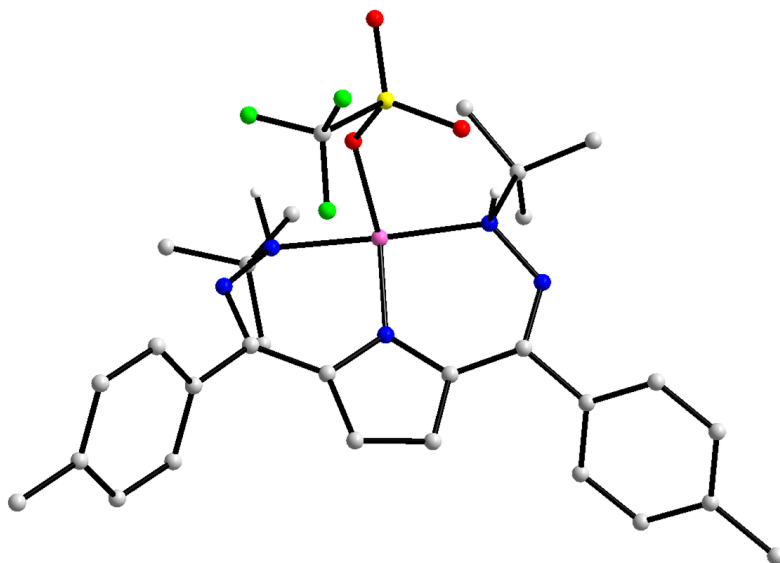


Figure S40. Calculated structure of **3-LS**. All C–H hydrogen atoms have been removed for clarity.

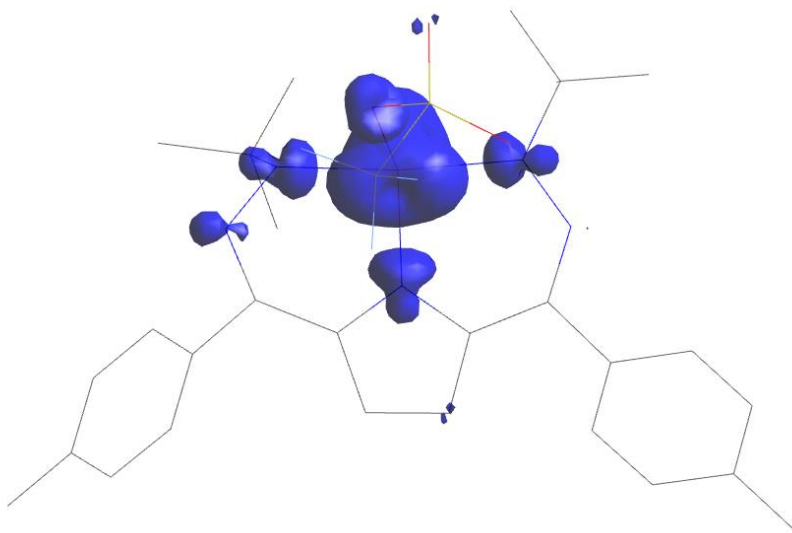


Figure S41. Spin density plot of **3-HS** at an iso value of 0.005.

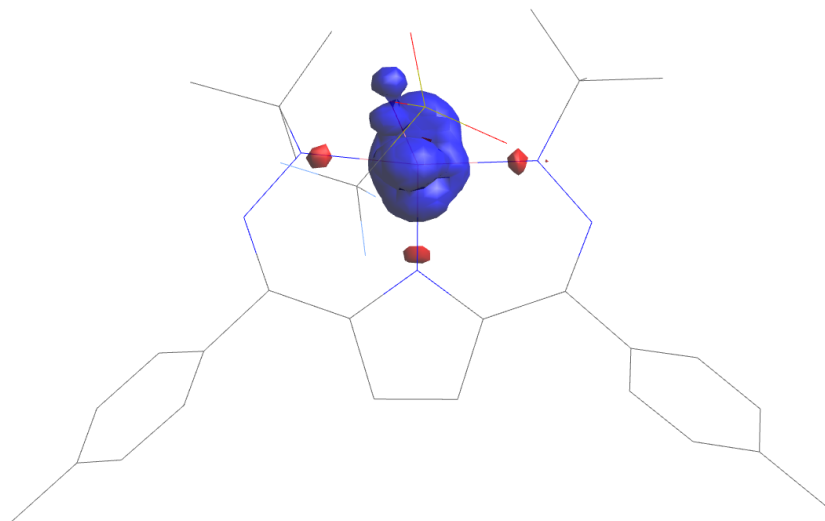


Figure S42. Spin density plot of **3-LS** at an iso value of 0.005.

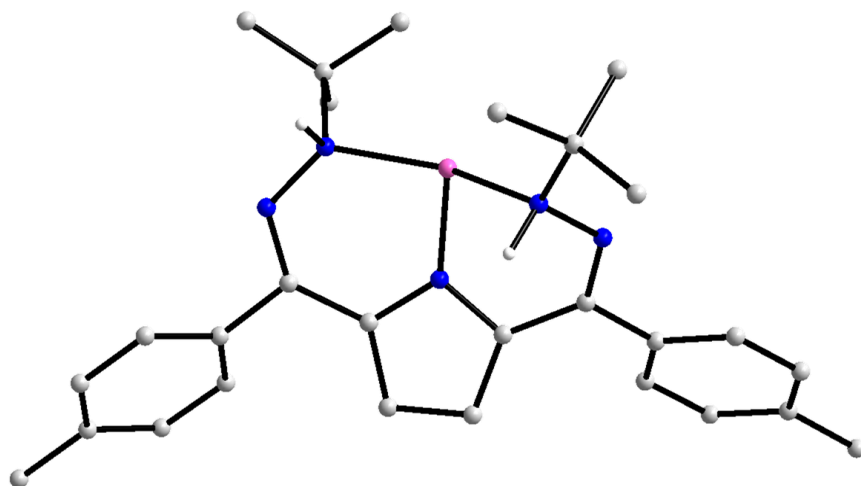


Figure S43. Calculated structure of  $[{}^{t\text{Bu, Tol}}\text{DHP-H}_2\text{Co}]^+\text{-HS}$  (**2-H<sub>2</sub><sup>+</sup>**). All C-H hydrogen atoms have been removed for clarity.

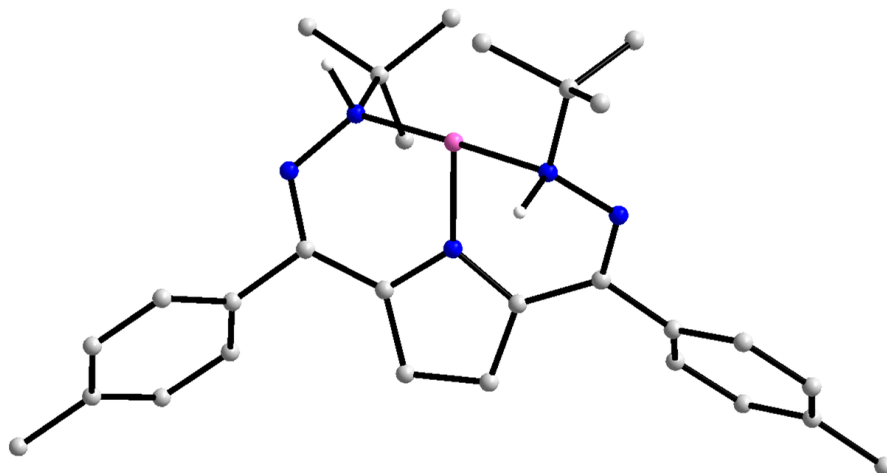


Figure S44. Calculated structure of  $[\text{tBu, TolDHP-H}_2\text{Co}]^+\text{-LS (2-H}_2^+)$ . All C–H hydrogen atoms have been removed for clarity.

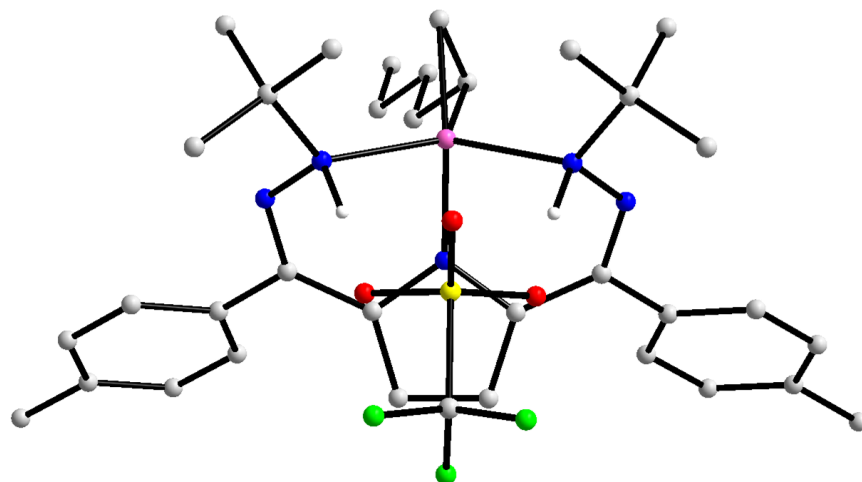


Figure S45. Calculated structure of a high spin **3-hexene**. All C–H hydrogen atoms have been removed for clarity

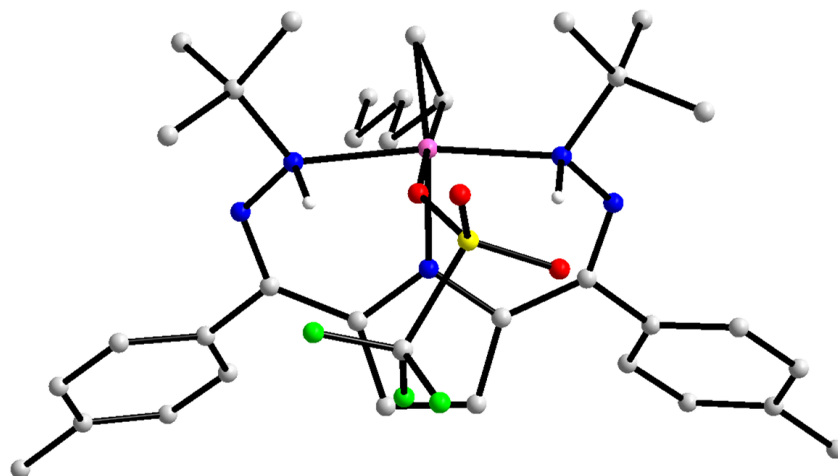


Figure S46. Calculated structure of a low spin **3-hexene**. All C–H hydrogen atoms have been removed for clarity

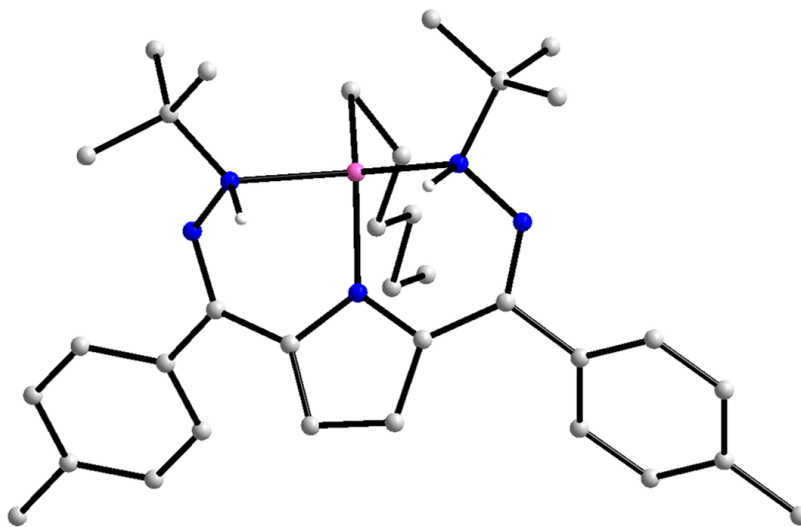


Figure S47. Calculated structure of a high spin **3-hexene<sup>+</sup>**. All C–H hydrogen atoms have been removed for clarity

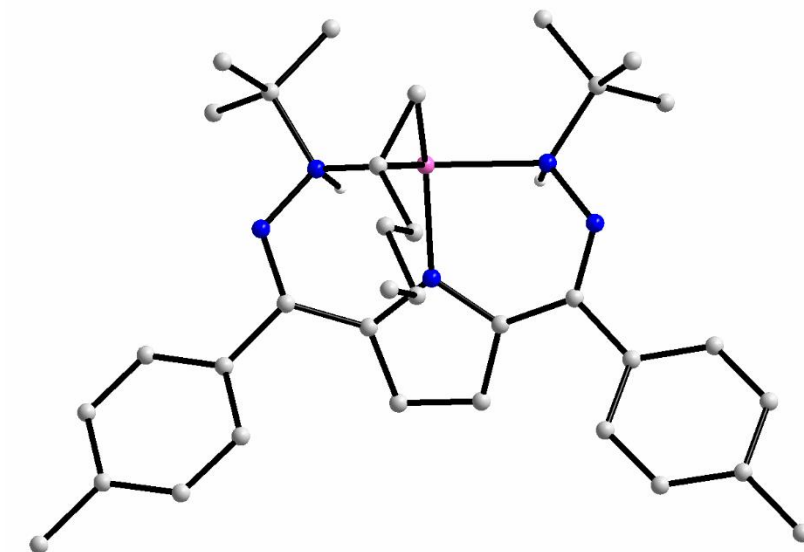


Figure S48. Calculated structure of a low spin **3-hexene<sup>+</sup>**. All C–H hydrogen atoms have been removed for clarity

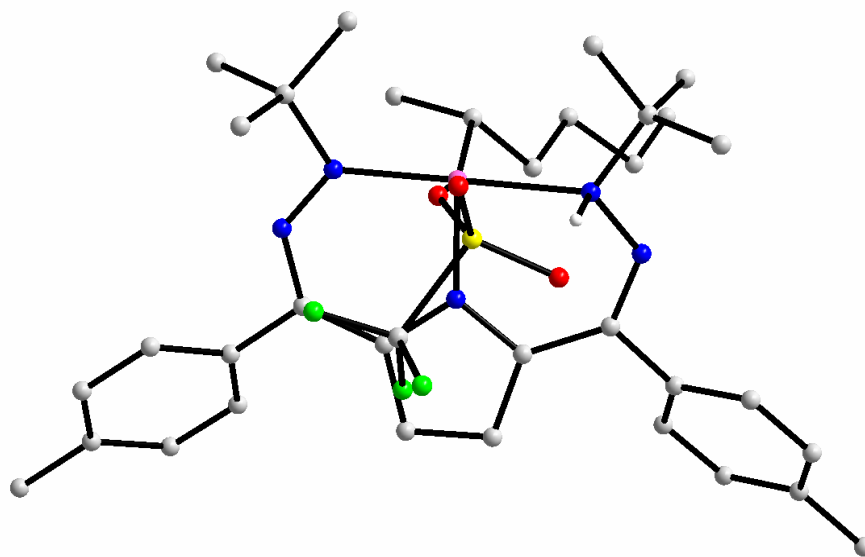


Figure S49. Calculated structure of a high spin **4-hexyl- $\alpha$** . Most C–H hydrogen atoms have been removed for clarity

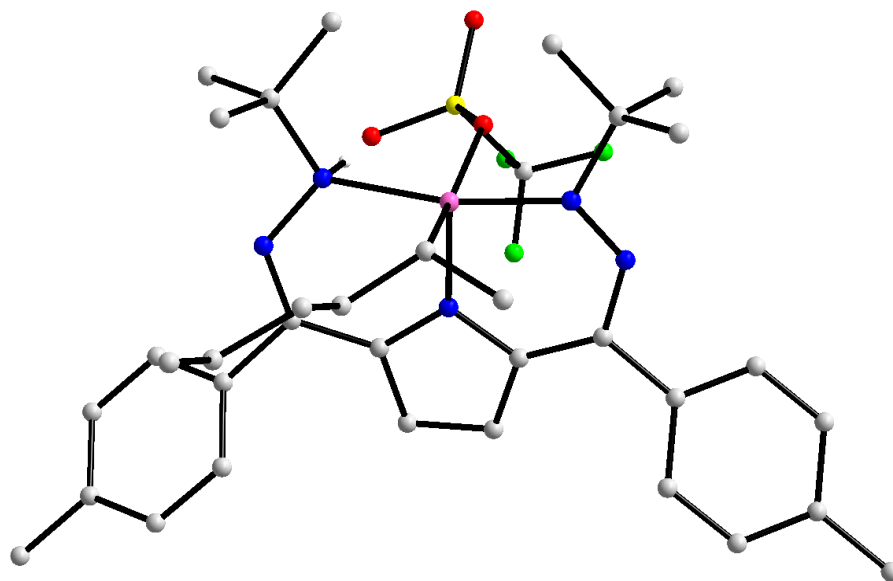


Figure S50. Calculated structure of a low spin **4-hexyl- $\alpha$** . Most C–H hydrogen atoms have been removed for clarity

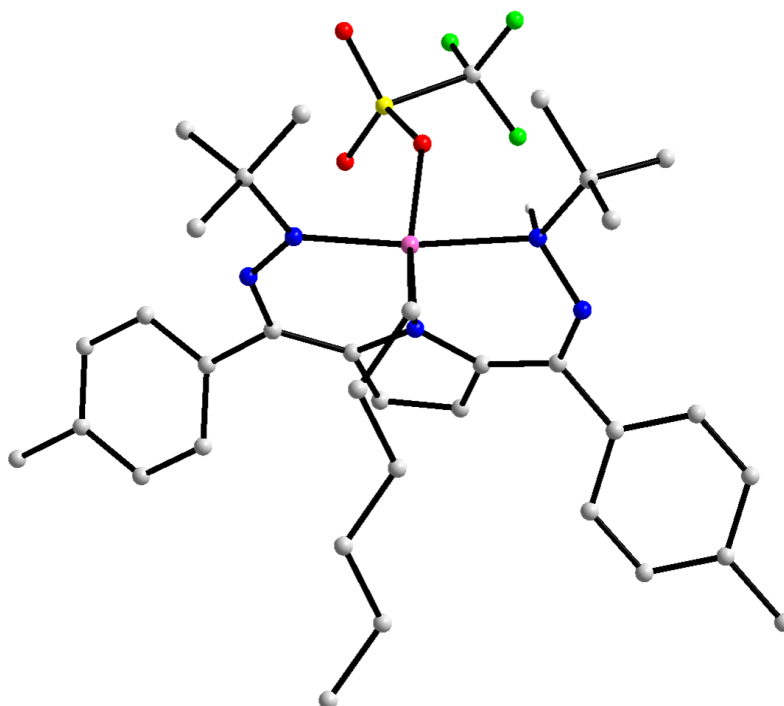


Figure S51. Calculated structure of a high spin **4-hexyl- $\beta$** . Most C–H hydrogen atoms have been removed for clarity

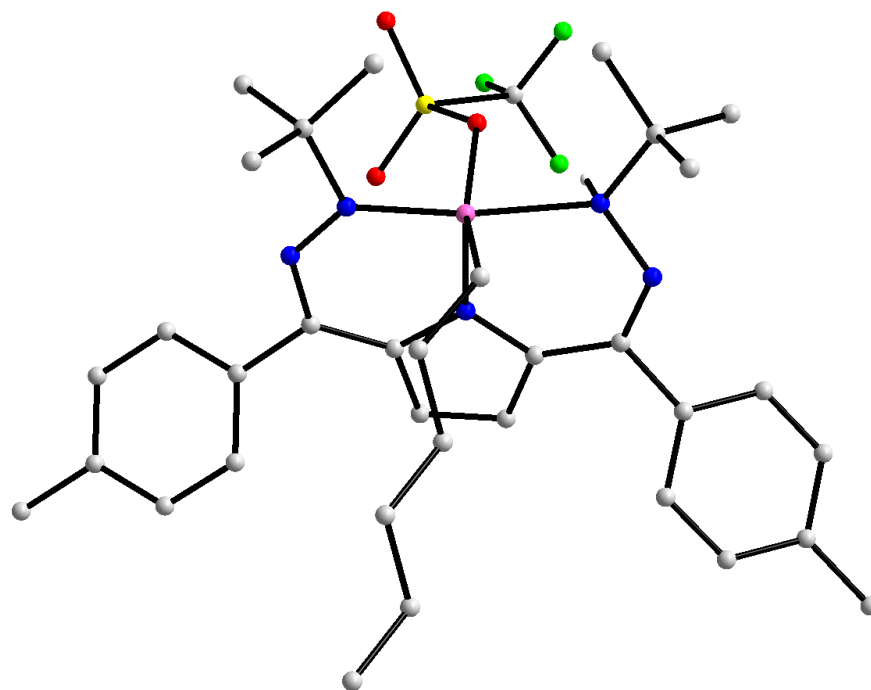


Figure S52. Calculated structure of a low spin **4-hexyl- $\beta$** . Most C–H hydrogen atoms have been removed for clarity

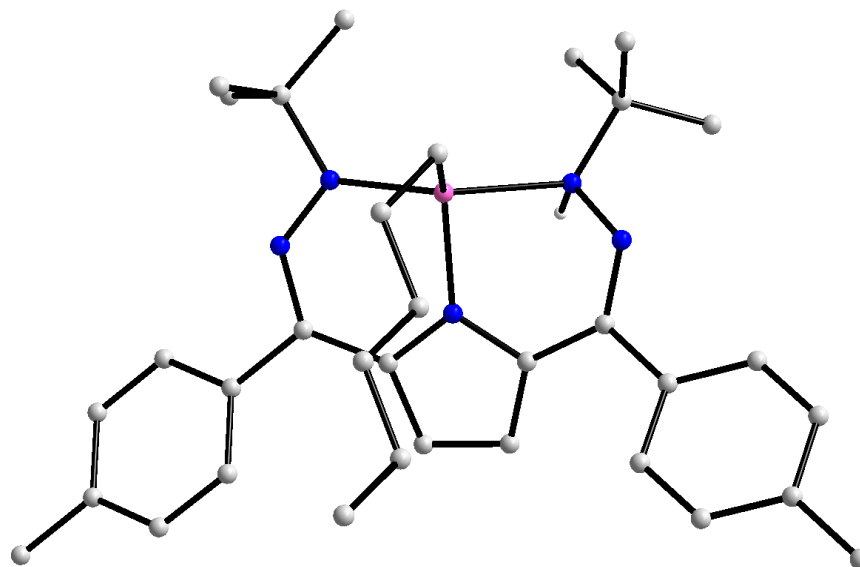


Figure S53. Calculated structure of a high spin **4-hexyl- $\beta^+$** . Most C–H hydrogen atoms have been removed for clarity

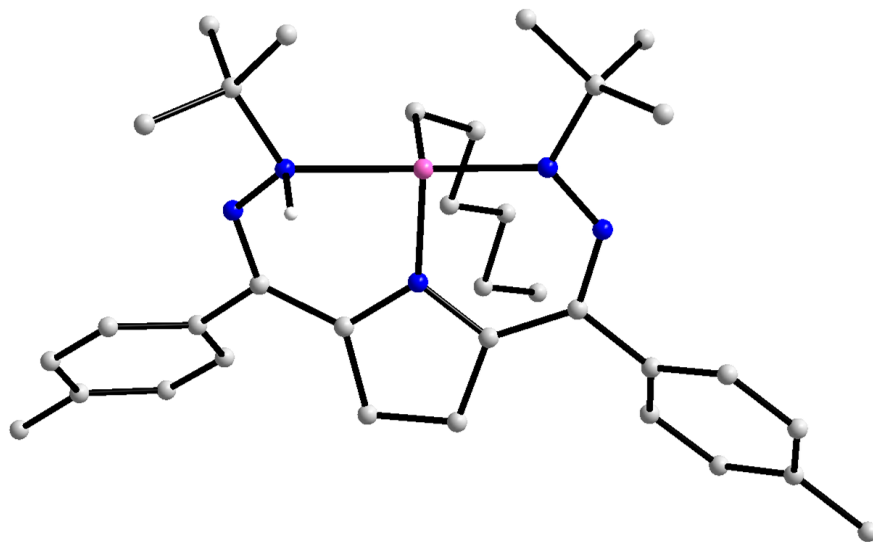


Figure S54. Calculated structure of a low spin **4-hexyl- $\beta^+$** . Most C–H hydrogen atoms have been removed for clarity

Table S4. Compared single point energies of intermediates along catalytic cycle for 1-hexene hydrogenation without accounting for entropic contributions.

	<b>2</b>	H <sub>2</sub>	1-hexene	<b>3</b>	<b>3-hexene</b>	<b>4-hexyl-<math>\alpha</math></b>	<b>4-hexyl-<math>\beta</math></b>	hexanes
HS- $S = 3/2$ (Eh)	-3702.05	N/A	N/A	-3703.25	-3938.56	-3938.48	-3938.52	N/A
LS- $S = 1/2$ (Eh)	-3702.06	N/A	N/A	-3703.24	-3938.54	-3938.53	-3938.54	N/A
$S = 0$ (Eh)	N/A	-1.15	-235.31	N/A	N/A	N/A	N/A	-236.52
$\Delta$ (HS-LS)	8.26	N/A	N/A	-0.25	-9.47	29.87	8.40	N/A
(kcal/mol)								

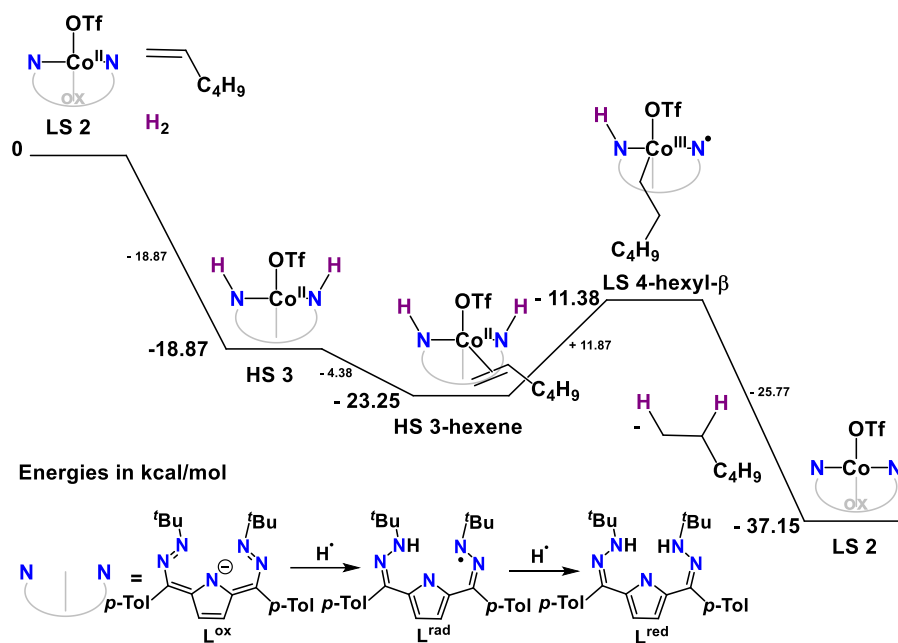


Figure S55. Simplified catalytic steps towards 1-hexene hydrogenation with the beta-carbon being the first to be hydrogenated (from single point energies, without accounting for entropic contributions).

Table S5. Compared Gibbs free energies of intermediates along catalytic cycle for 1-hexene hydrogenation with accounting for entropic contributions.

	2	H <sub>2</sub>	1-hexene	3	3-hexene	4-hexyl-β	TS 3-hexene -> 4-hexyl-β	TS 4-hexyl-β -> 2 + hexanes	hexanes
HS- <i>S</i> = 3/2 (Eh)	N/A	N/A	N/A	-3702.67	-3937.85	N/A	-3937.803	-3937.810	N/A
LS- <i>S</i> = 1/2 (Eh)	-3701.52	N/A	N/A	N/A	N/A	-3937.83			N/A
<i>S</i> = 0 (Eh)	N/A	-1.16	-235.18	N/A	N/A	N/A	N/A	N/A	-236.37

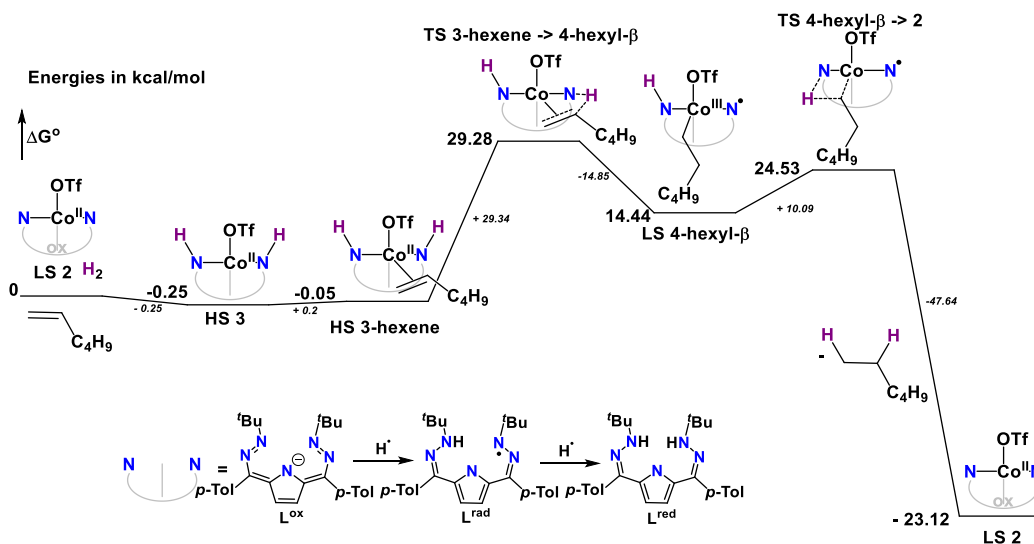


Figure S56. Simplified catalytic steps towards 1-hexene hydrogenation with the beta-carbon being the first to be hydrogenated (accounting for entropic contributions).

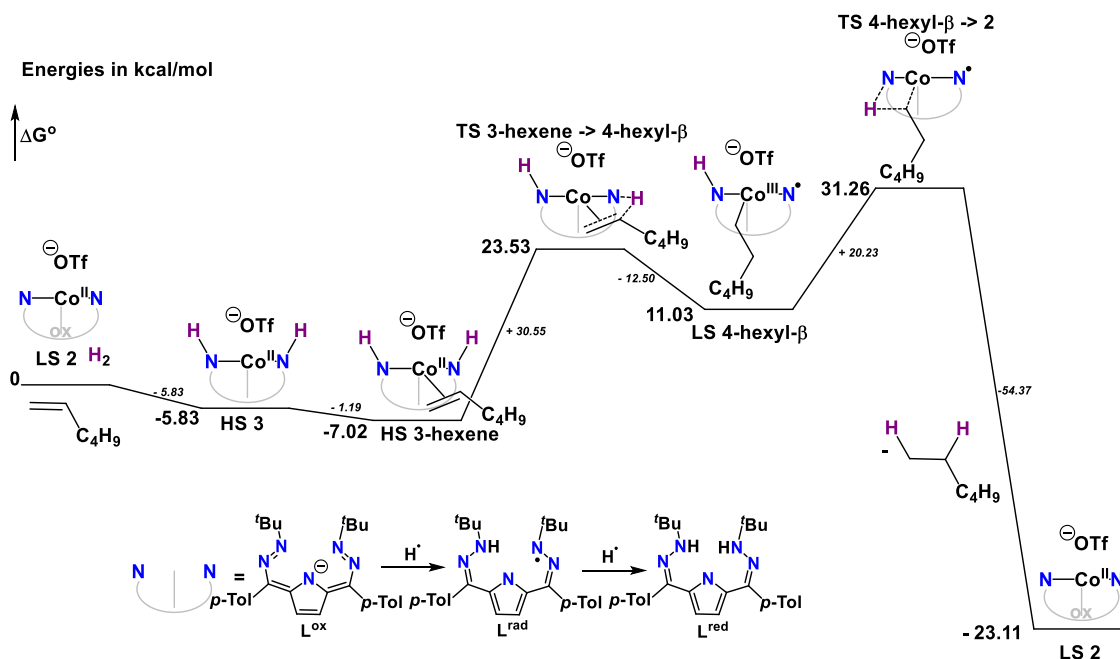


Figure S57. Simplified catalytic steps towards 1-hexene hydrogenation with the beta-carbon being the first to be hydrogenated without triflate (accounting for entropic contributions).

Table S6. Compared Gibbs free energies of intermediates along catalytic cycle for 1-hexene hydrogenation without triflate bound with accounting for entropic contributions.

	2	3	3-hexene	4-hexyl- $\beta$	TS 3-hexene $\rightarrow$ 4-hexyl- $\beta$	TS 4-hexyl- $\beta$ $\rightarrow$ 2 + hexanes
HS- $S = 3/2$ (Eh)	N/A	-2741.80	-2976.98	N/A	-2976.93	-2976.92
LS- $S = 1/2$ (Eh)	-2740.64	N/A	N/A	-2976.95		

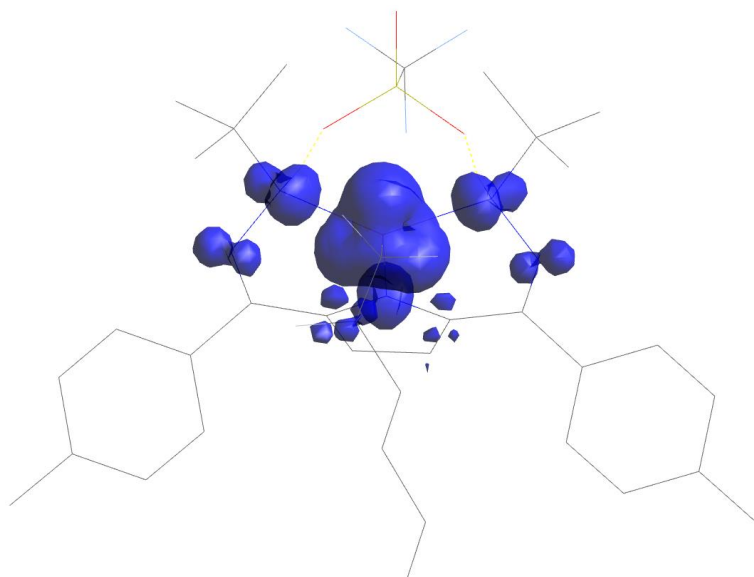


Figure S58. Spin density plot of **3-hexene** at an iso value of 0.005.

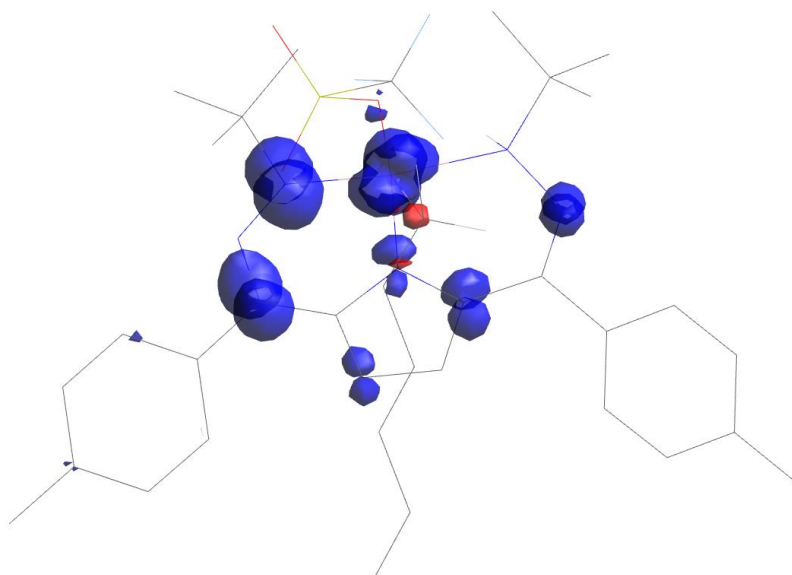


Figure S59. Spin density plot of **4-hexyl-β** at an iso value of 0.005.

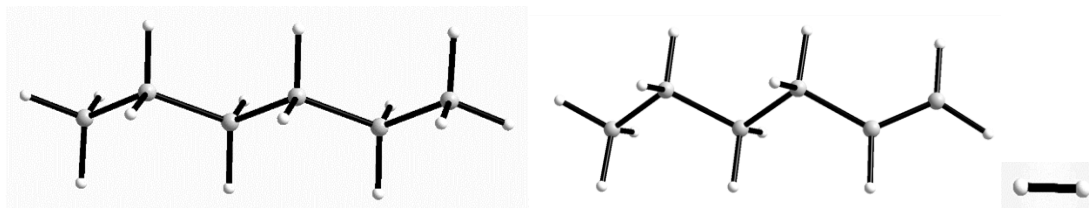


Figure S60. Calculated Structures of Hexanes, 1-hexene and H<sub>2</sub>.

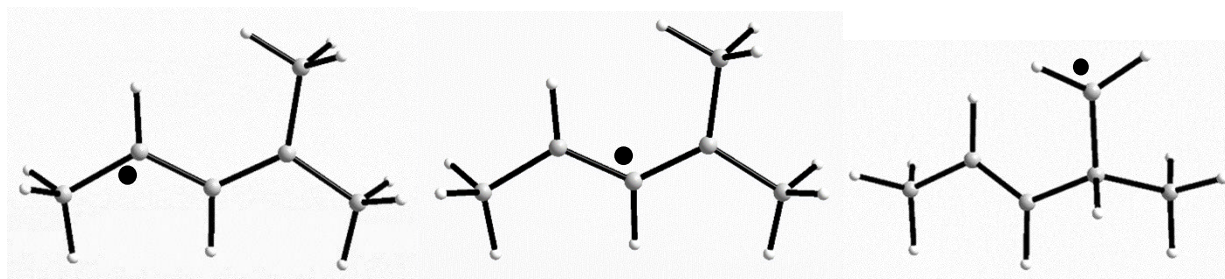


Figure S61. Energetically Compared 2-methyl-pent-1,3-ene Radical Isomer Structures. From left to right: tertiary radical structure, secondary radical structure and primary radical structure.

Table S7. Compared Gibbs free energies of 2-methyl-pent-1,3-ene radical isomers

	Tertiary Radical	Secondary Radical	Primary Radical
S = 1/2 (Eh)	-234.68343	-234.68344	-234.65
Energy Comparison	Second Highest	Lowest Energy	Highest Energy

Figure S62. Energetically compared 2-methyl-pent-1,3-ene non-radical isomer structures

Table S8. Compared Gibbs free energies of 2-methyl-pent-1,3-ene non-radical isomers

	Terminal Olefin	Internal-cis Olefin	Internal-trans Olefin	Isomerized Olefin
S = 0 (Eh)	-235.3097	-235.3080	-235.3095	-235.307
Energy Comparison	Lowest Energy	Second Highest	Second Lowest	Highest Energy

Table S9. Compared single point energies of intermediates towards ligand hydrogenation without accounting for entropic contributions.

	2	H <sub>2</sub>	3	2-H <sub>2</sub>	2H-H
HS- <i>S</i> = 3/2 (Eh)	-3702.05	N/A	-3703.25	-3703.19	-3703.20
LS- <i>S</i> = 1/2 (Eh)	-3702.06	N/A	-3703.24	-3703.21	-3703.21
<i>S</i> = 0 (Eh)	N/A	-1.15	N/A	N/A	N/A
Δ (HS-LS) (kcal/mol)	8.26	N/A	-0.25	+ 9.13	+ 10.12

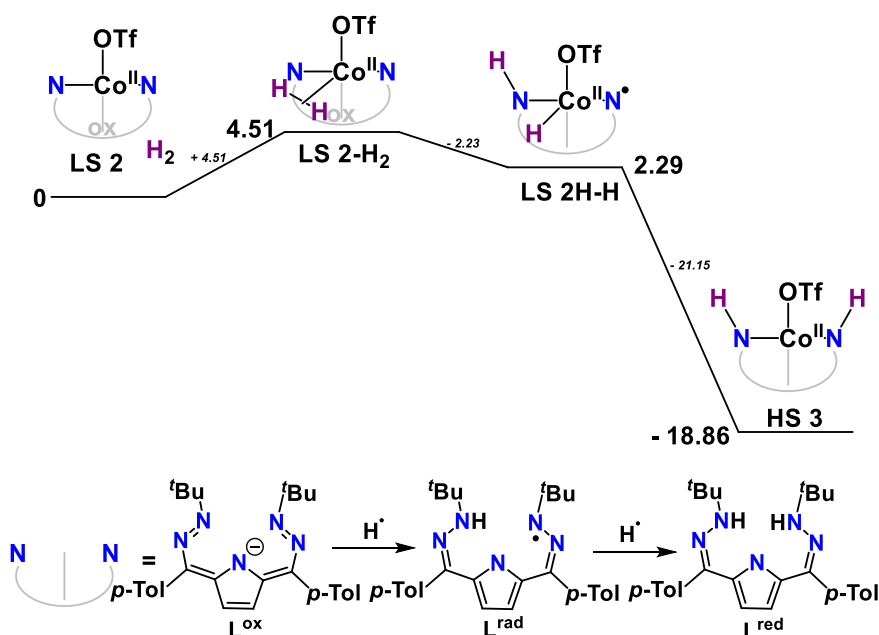


Figure S63. Simplified catalytic steps towards ligand hydrogenation (without accounting for entropic contributions).

Table S10. Compared Gibbs free energies of intermediates along catalytic cycle for ligand hydrogenation with accounting for entropic contributions.

	2	H <sub>2</sub>	3	2-H <sub>2</sub>	2H-H	TS H <sub>2</sub> → 2H-H	TS 2H-H → 3
HS- <i>S</i> = 3/2 (Eh)	-3701.52	N/A	-3702.68	N/A	N/A	-3702.639	-3702.642
LS- <i>S</i> = 1/2 (Eh)	N/A	N/A	N/A	-3702.659	-3702.656		
LS- <i>S</i> = 1/2 (Eh)	-2740.64	N/A	-2741.80	-2741.770	-2741.772	-2741.75	-2741.76
outer sphere OTf							

$S = 0$ (Eh)	N/A	-1.16	N/A	N/A	N/A	N/A	N/A
--------------	-----	-------	-----	-----	-----	-----	-----

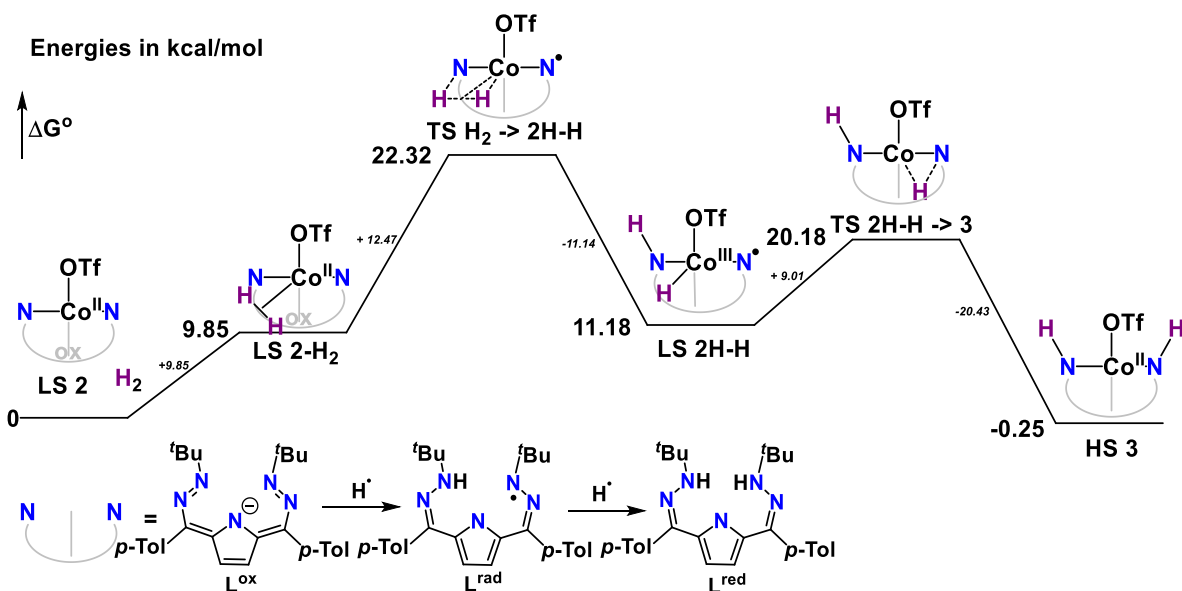


Figure S64. Simplified catalytic steps towards ligand-centered dihydrogen reactivity with triflate bound (accounting for entropic contributions).

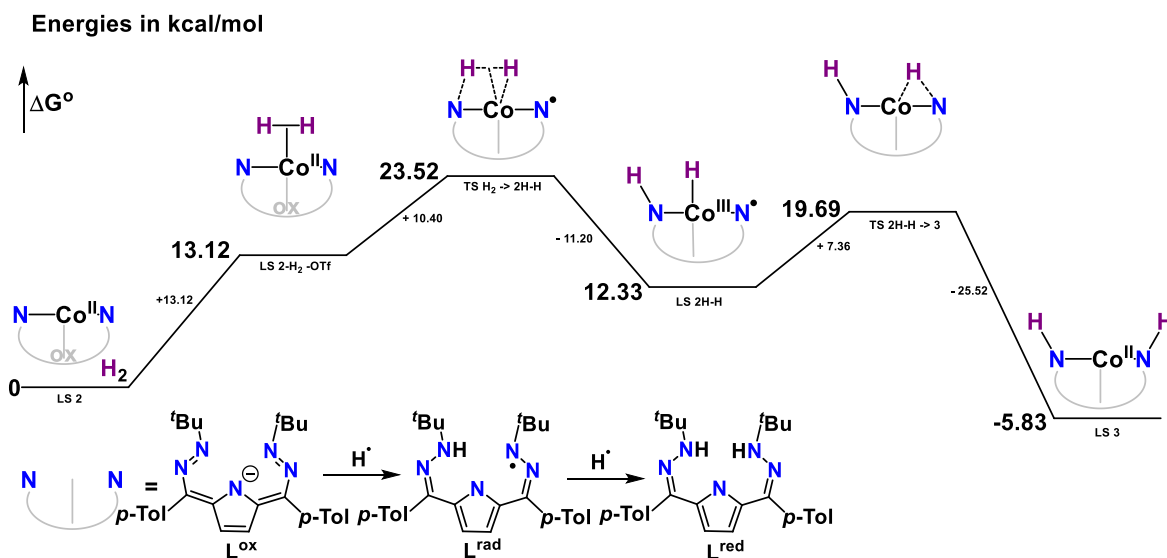


Figure S65. Simplified catalytic steps towards ligand-centered dihydrogen reactivity with the triflate anion outer-sphere (accounting for entropic contributions).

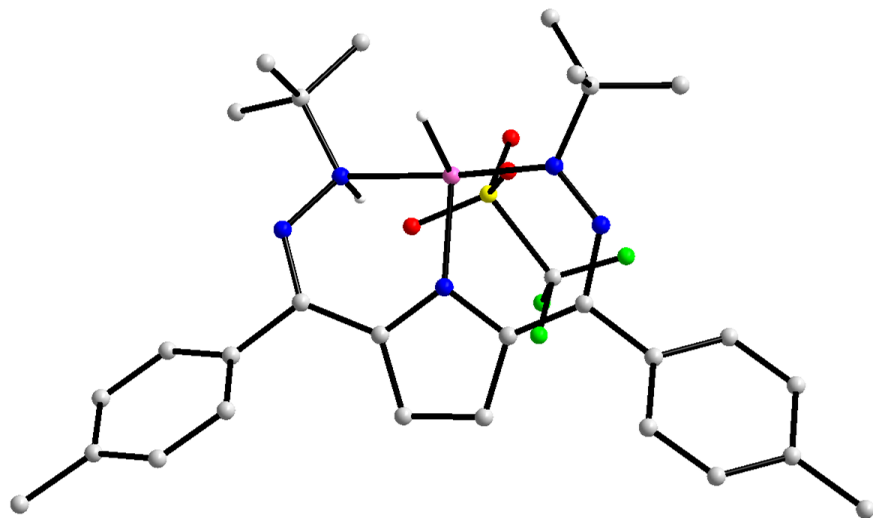


Figure S66. Calculated structure of high spin  $[(^t\text{Bu, Tol})\text{DHP-H})\text{CoH}]\text{OTf}$  (**2H-H**). All C-H hydrogen atoms have been removed for clarity.

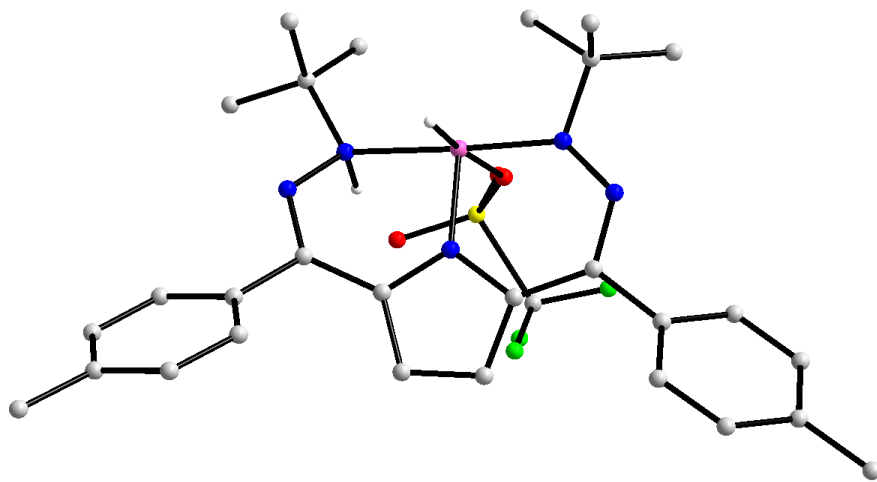


Figure S67. Calculated structure of low spin  $[(^t\text{Bu, Tol})\text{DHP-H})\text{CoH}]\text{OTf}$  (**2H-H**). All C-H hydrogen atoms have been removed for clarity.

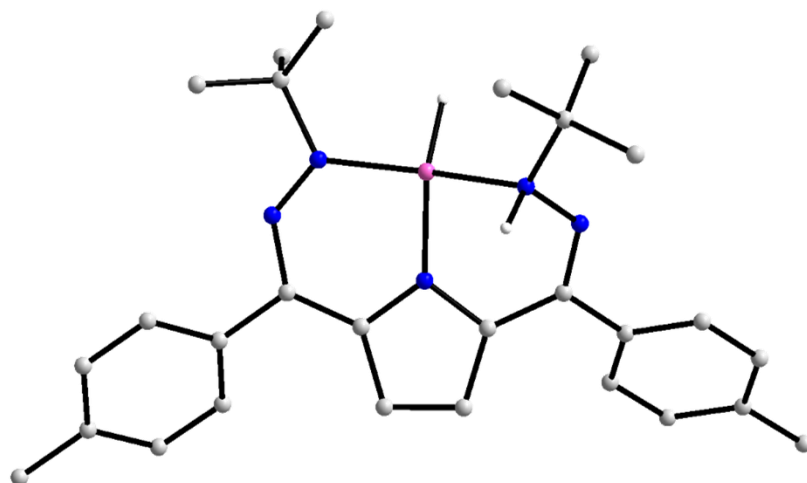


Figure S68. Calculated structure of high spin  $[(^t\text{Bu, TolDHP -H)CoH}]^+$  ( $2\mathbf{H-H}^+$ ). All C-H hydrogen atoms have been removed for clarity.

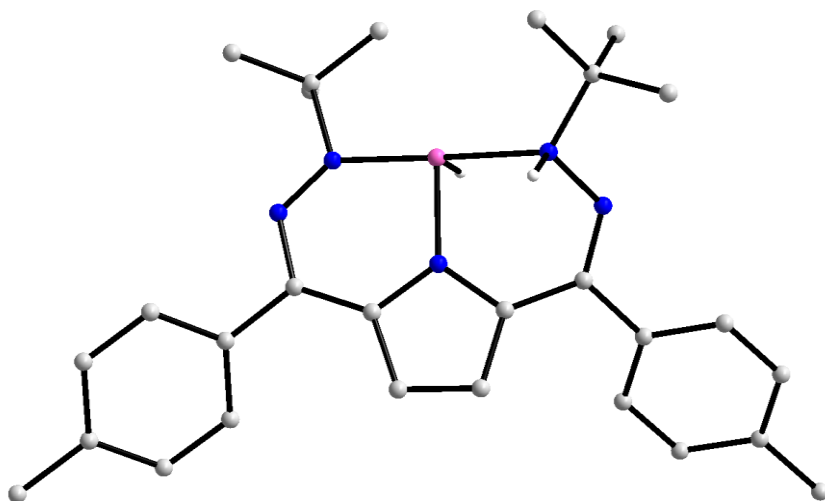


Figure S69. Calculated structure of low spin  $[(^t\text{Bu, TolDHP -H)CoH}]^+$  ( $2\mathbf{H-H}^+$ ). All C-H hydrogen atoms have been removed for clarity.

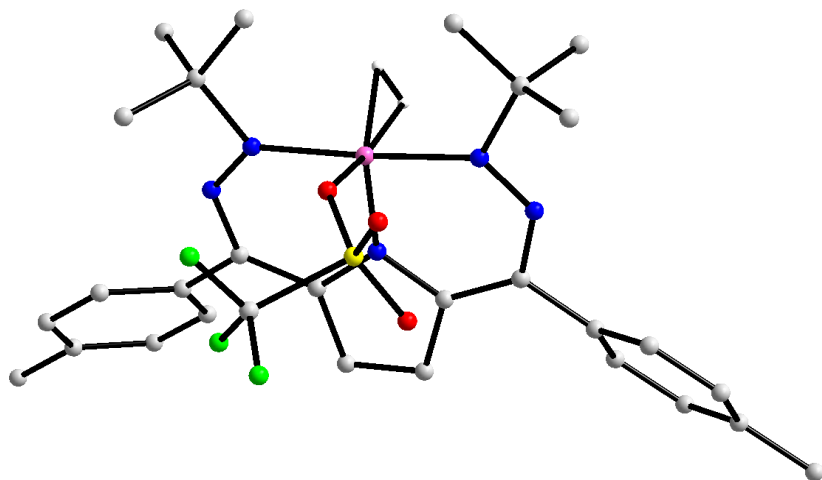


Figure 70. Calculated structure of low spin  $[(^{t\text{Bu}}, \text{Tol})\text{DHP})\text{CoH}_2]\text{OTf}$  (**2-H<sub>2</sub>**). All C–H hydrogen atoms have been removed for clarity.

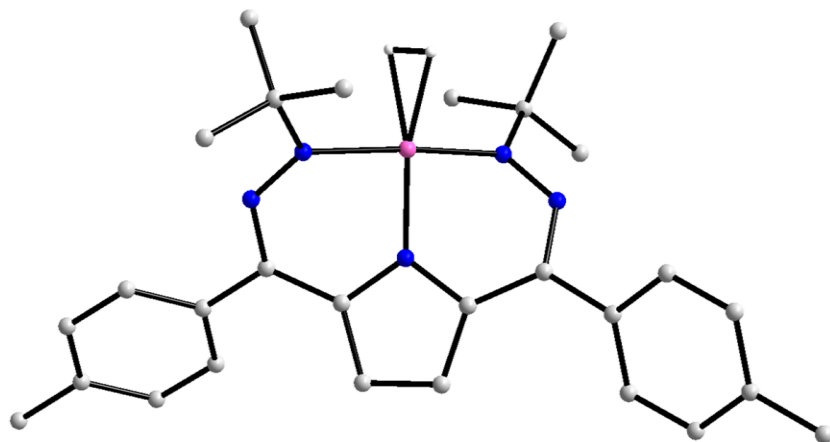


Figure S71. Calculated structure of high spin  $[(^{t\text{Bu}}, \text{Tol})\text{DHP})\text{CoH}_2]^+$  (**2-H<sub>2</sub><sup>+</sup>**). All C–H hydrogen atoms have been removed for clarity.

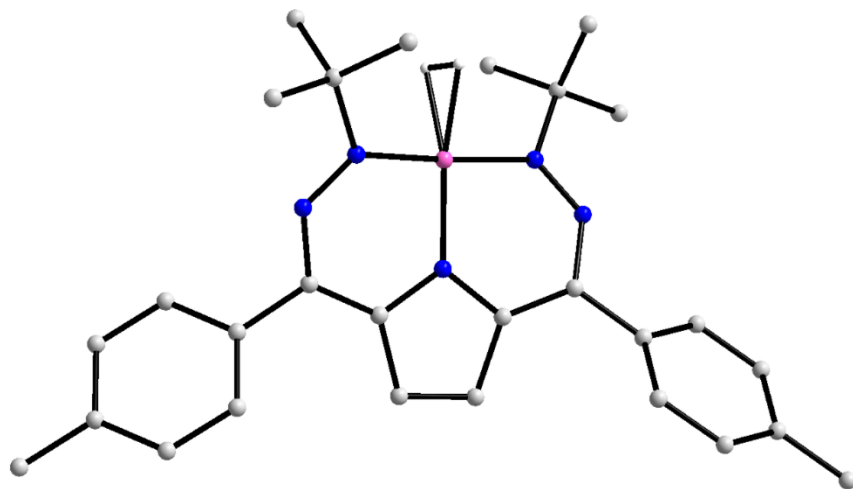


Figure S72. Calculated structure of low spin  $[(t\text{Bu, Tol})\text{DHP}]\text{CoH}_2^+$  (**2-H<sub>2</sub><sup>+</sup>**). All C–H hydrogen atoms have been removed for clarity.

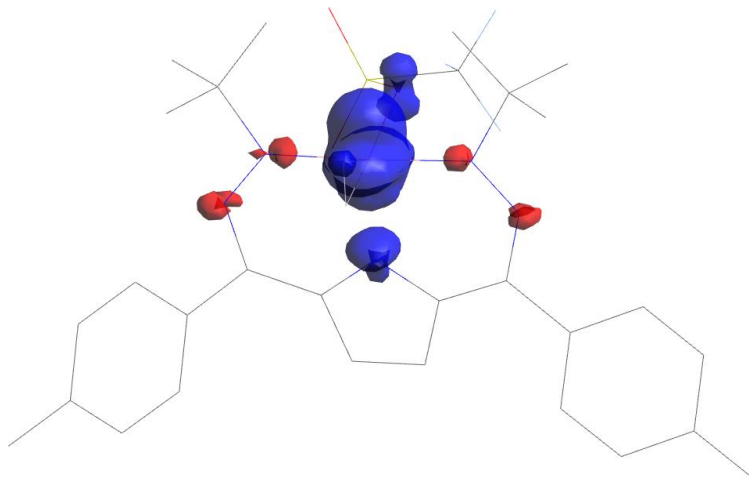


Figure S73. Spin density plot of **2-H<sub>2</sub>** at an iso value of 0.005.

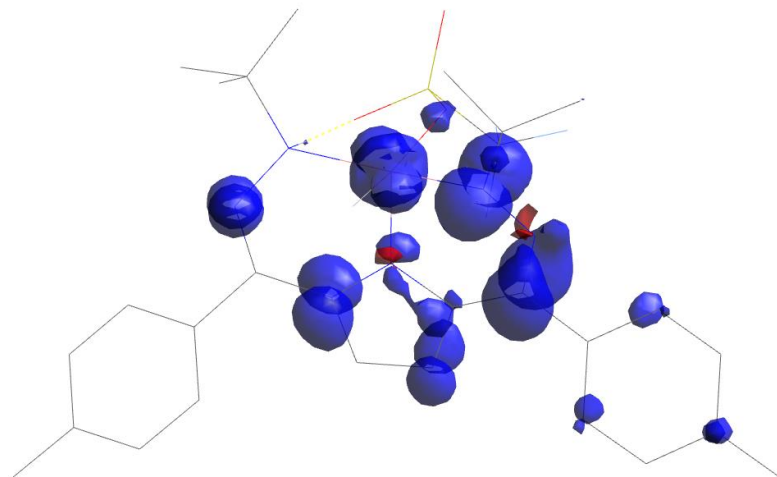


Figure S74. Spin density plot of **2H-H** at an iso value of 0.005.

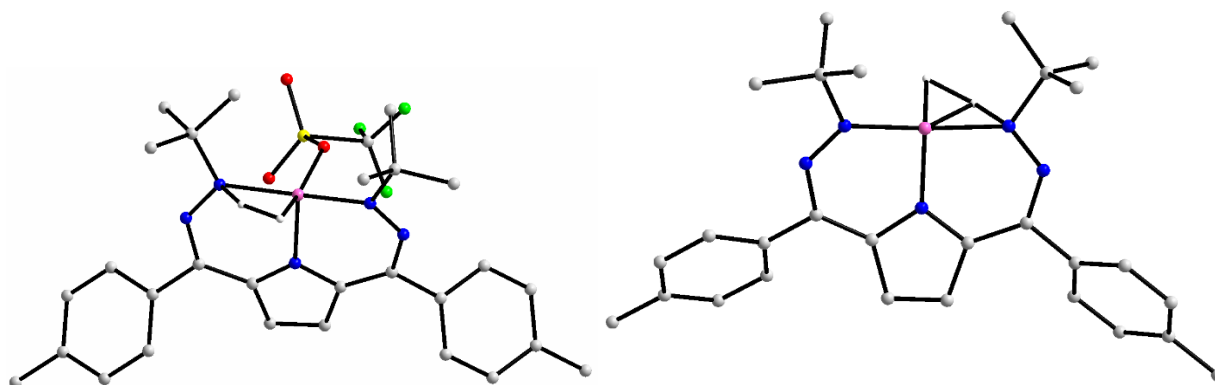


Figure S75. Transition state structure between low spin  $[(^{t\text{Bu}}, \text{Tol})\text{DHP})\text{CoH}_2]\text{OTf}$  (**2-H<sub>2</sub>**) and  $[(^{t\text{Bu}}, \text{Tol})\text{DHP} -\text{H})\text{CoH}]\text{OTf}$  (**2H-H**) and the triflate-free transition state. All C-H hydrogen atoms have been removed for clarity. Imaginary Frequency:  $-1136.61 \text{ cm}^{-1}$

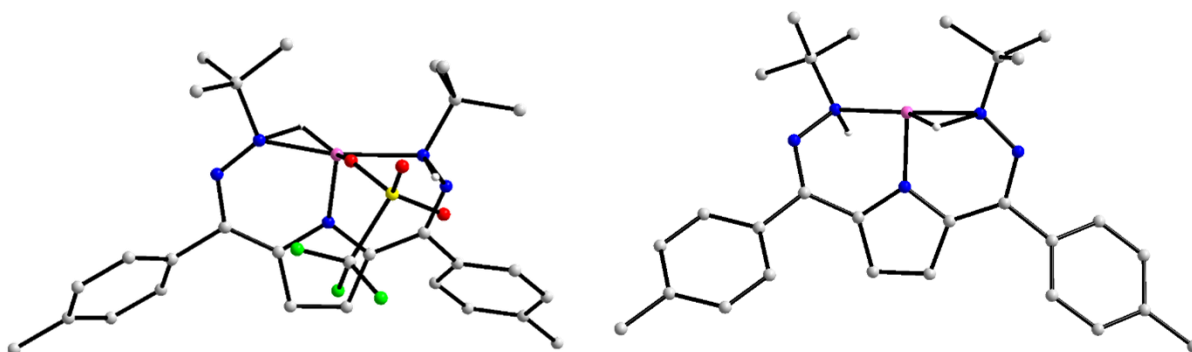


Figure S76. Transition state structure between low spin  $[(^{t}\text{Bu}, \text{TolDHP} -\text{H})\text{CoH}]\text{OTf}$  (**2H-H**) and **3** and triflate-free version. All C–H hydrogen atoms have been removed for clarity. Imaginary Frequency:  $-1214.45 \text{ cm}^{-1}$

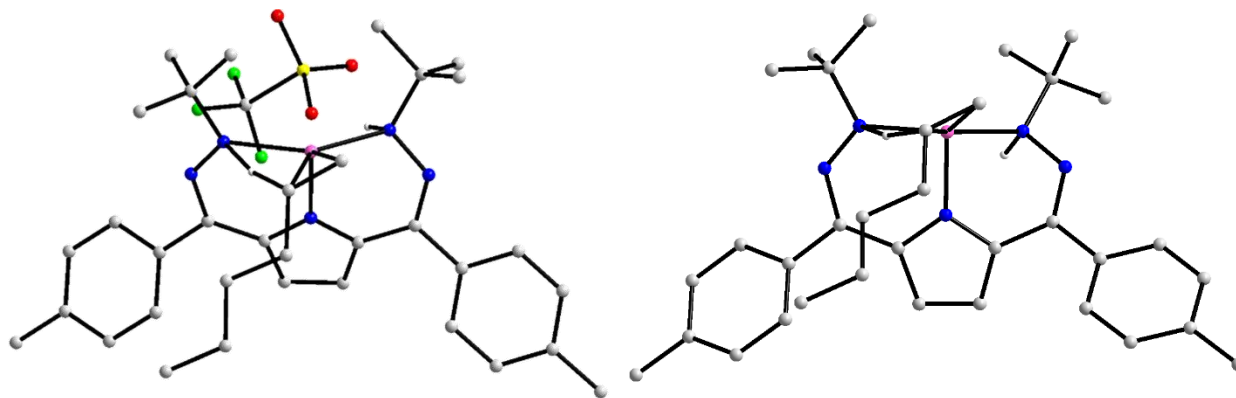


Figure S77. Transition state structure between high spin  $[(^{t}\text{Bu}, \text{TolDHP} -\text{H}_2)\text{Co}](1\text{-hexene})\text{OTf}$  (**3-hexene**) and low spin  $[(^{t}\text{Bu}, \text{TolDHP} -\text{H})\text{Co}](\text{hex})\text{OTf}$  (**4-hexyl-β**) (and triflate free version). All C–H hydrogen atoms have been removed for clarity. Imaginary Frequency:  $-1290.78 \text{ cm}^{-1}$

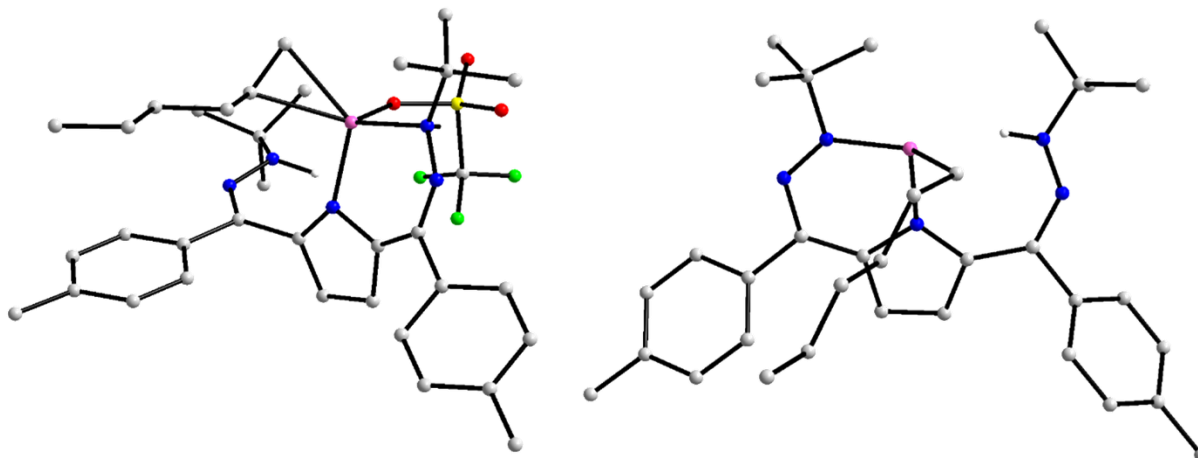


Figure S78. Transition state structure between low spin  $[(^{t}\text{Bu}, \text{TolDHP} -\text{H})\text{Co}](\text{hex})\text{OTf}$  (**4-hexyl-β**) and  $[(^{t}\text{Bu}, \text{TolDHP})\text{Co}]\text{OTf}/\text{hexanes}$  (**2**) and triflate-free version. All C–H hydrogen atoms have been removed for clarity. Imaginary Frequency:  $-131.33 \text{ cm}^{-1}$

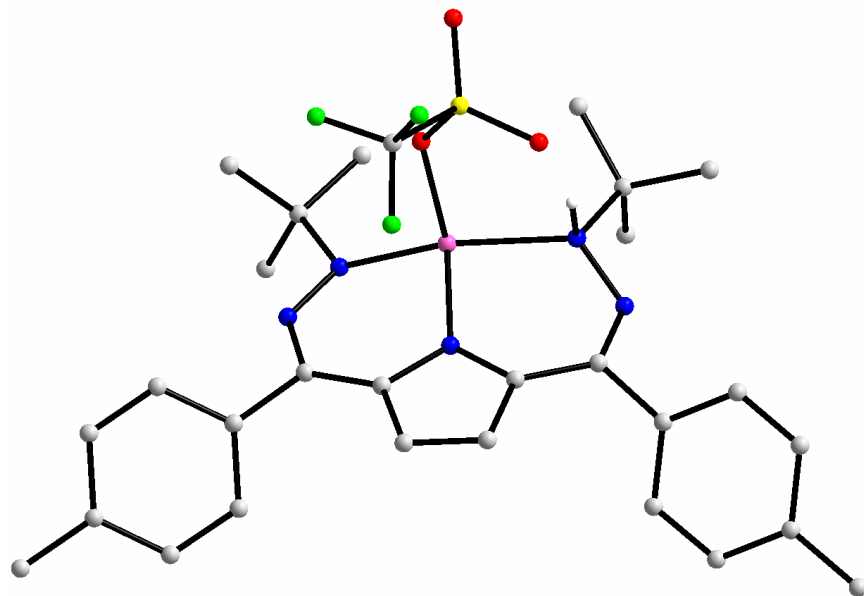


Figure S79. Calculated structure of high spin  $[(^{\text{tBu, Tol}}\text{DHP-H})\text{Co}]\text{OTf}$  (**4-HS**). All C-H hydrogen atoms have been removed for clarity.

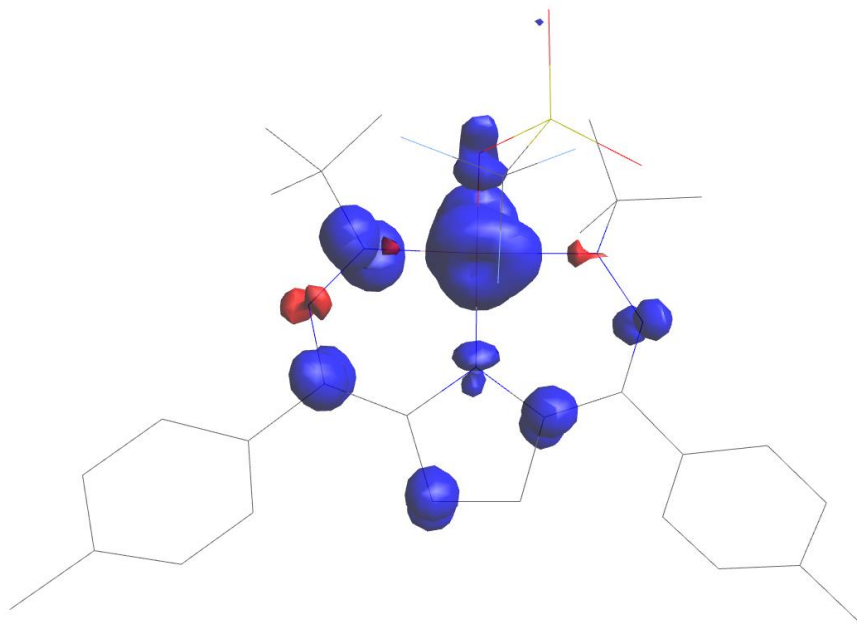


Figure S80. Spin density plot of **4-HS** at an iso value of 0.005.

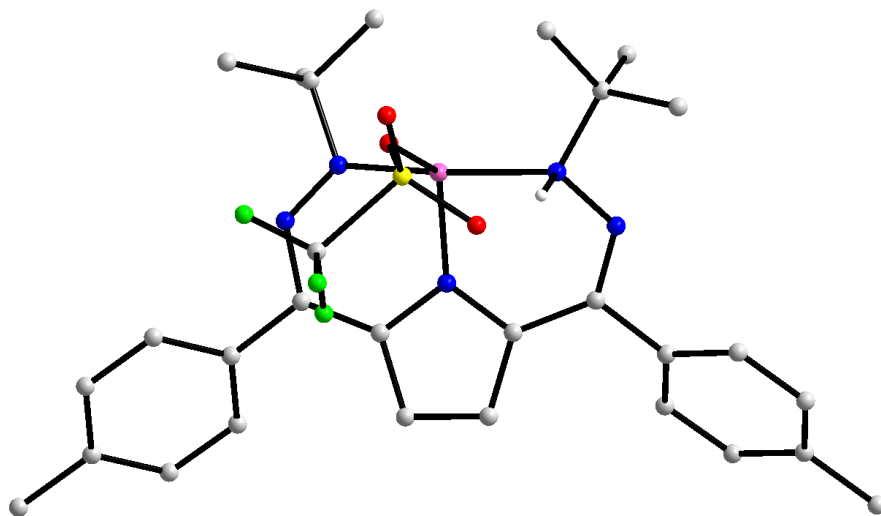


Figure S81. Calculated structure of low spin  $[(^{t\text{Bu, Tol}}\text{DHP-H})\text{Co}]\text{OTf}$  (**4-LS**). All C–H hydrogen atoms have been removed for clarity.

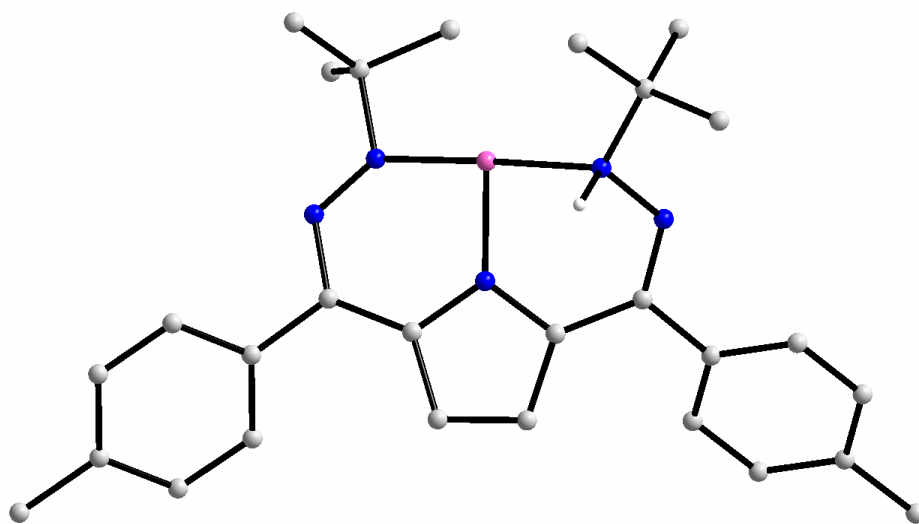


Figure S82. Calculated structure of high spin  $[(^{t\text{Bu, Tol}}\text{DHP-H})\text{Co}]$  (**4<sup>+</sup>-LS**). All C–H hydrogen atoms have been removed for clarity.

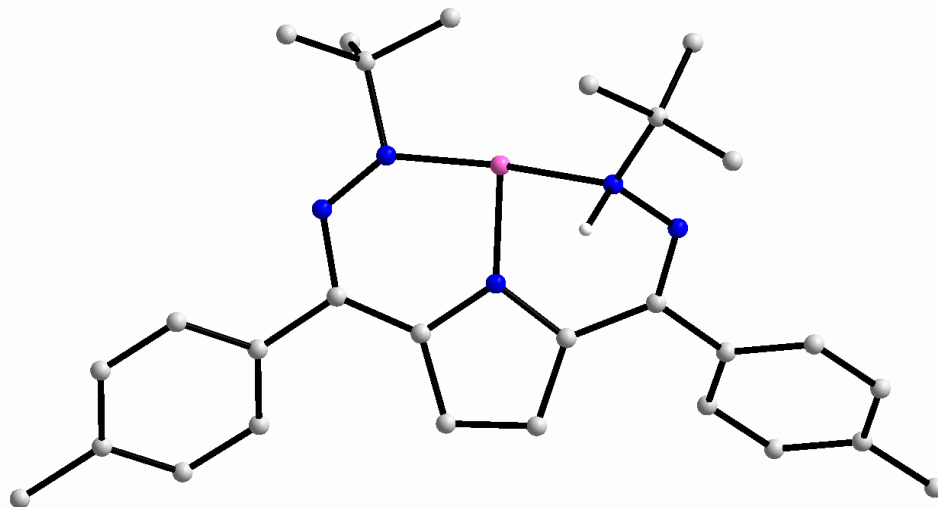


Figure S83. Calculated structure of low spin  $[(t\text{Bu, Tol})\text{DHP-H}]\text{Co}$  ( $4^+\text{-LS}$ ). All C–H hydrogen atoms have been removed for clarity.

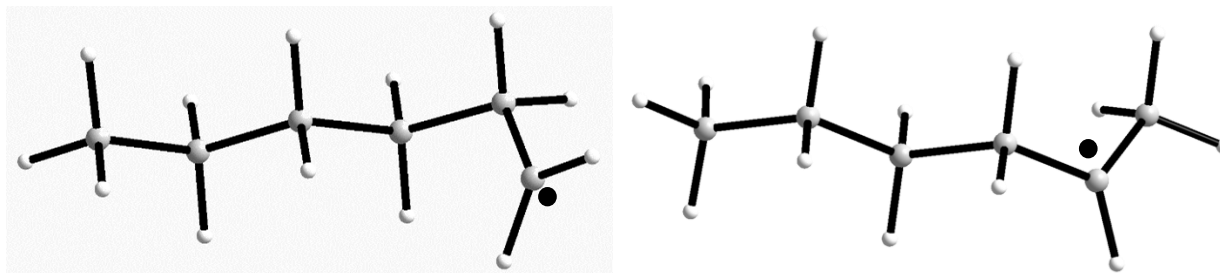


Figure S84. Calculated structures of 1-hexene primary and secondary radicals.

Table S11. Compared energies of radical-derived intermediates along catalytic cycle for 1-hexene hydrogenation without accounting for entropic contributions.

	Primary 1-hexene radical	Secondary 1-hexene radical	<b>4-HS</b>	<b>4<sup>+</sup>-HS</b>	<b>4-LS</b>	<b>4<sup>+</sup>-LS</b>
HS- $S = 1$ (Eh)	N/A	N/A	-3702.65	-2741.719	N/A	N/A
$S = 1/2$ (Eh)	-235.86	-235.86	N/A	N/A	N/A	N/A
LS- $S = 0$ (Eh)	N/A	N/A	N/A	N/A	-3702.62	-2741.716

Table S12. Compared Gibbs free energies of radical-derived intermediates along catalytic cycle for 1-hexene hydrogenation with accounting for entropic contributions.

	Primary 1-hexene radical	Secondary 1-hexene radical	4-HS	4 <sup>+</sup> -HS
HS- S = 1 (Eh)	N/A	N/A	-3702.11	-2741.21
S = 1/2 (Eh)	-235.72	-235.73	N/A	N/A

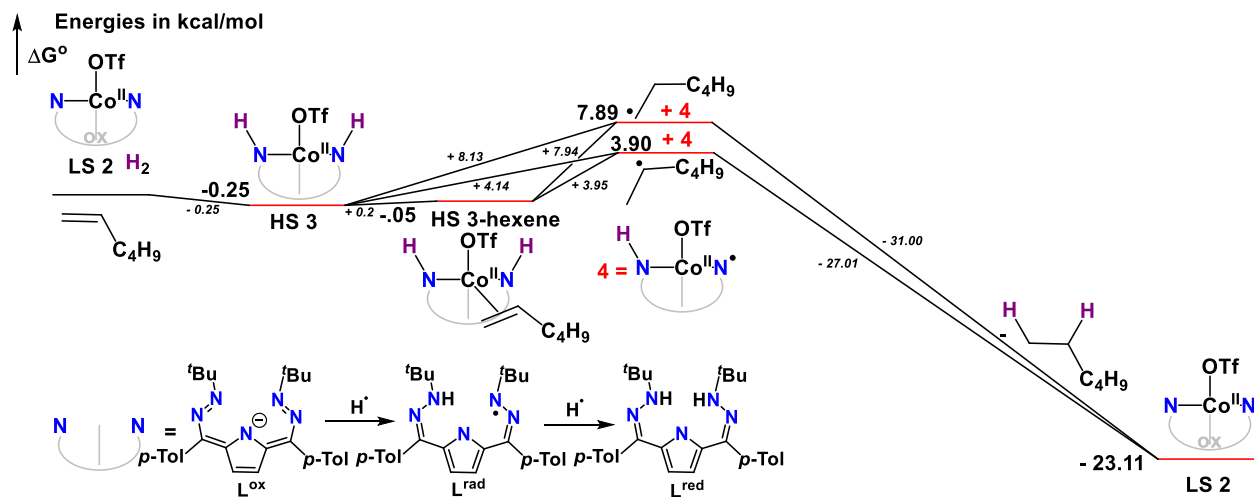


Figure S85. Simplified catalytic steps with radical pathways towards 1-hexene hydrogenation (with accounting for entropic contributions).

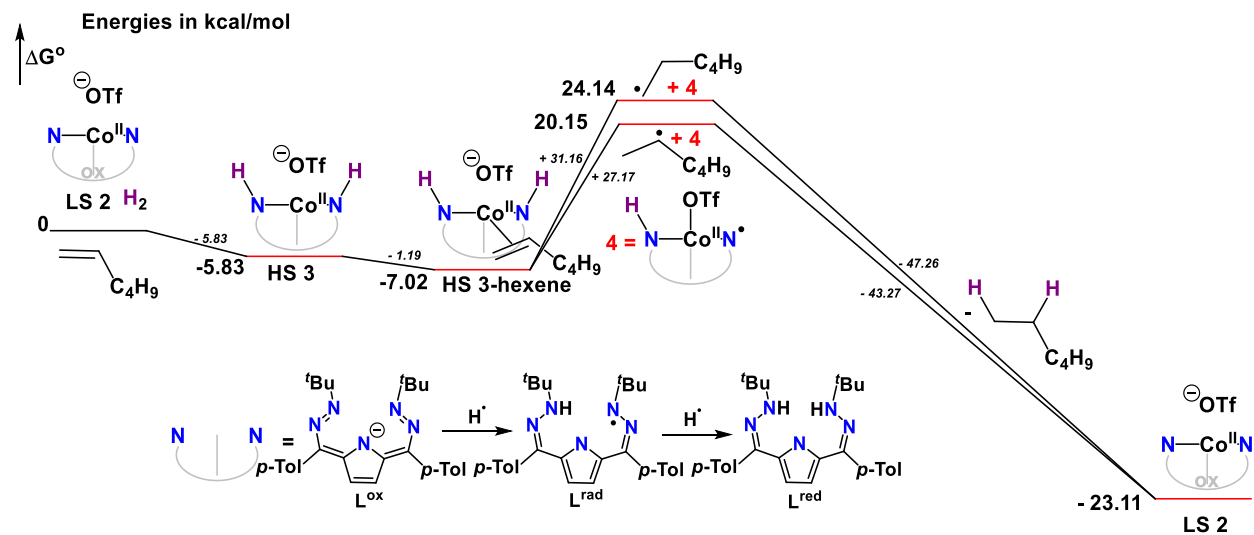


Figure S86. Simplified catalytic steps with radical pathways towards 1-hexene hydrogenation without triflate (accounting for entropic contributions).

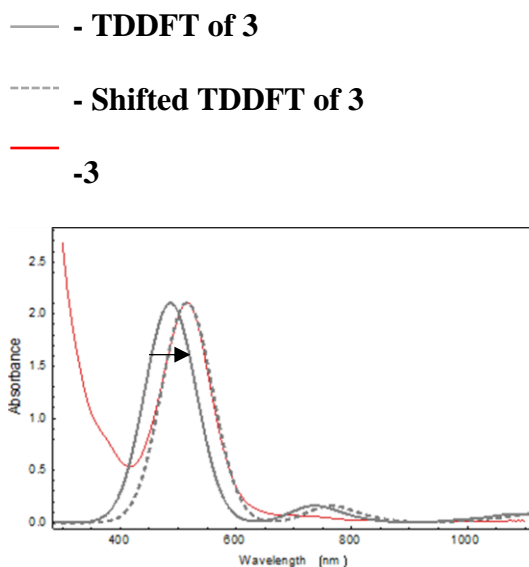


Figure S87. TDDFT of **3**. Note that TD-DFT typically underestimates the energies of transitions and a shift to match experimental data of 50-75 nm is common in the related Ni- and Fe-DHP complexes.

Table S13. Calculated vs. experimental values.

	N-H <sup>a</sup>	N-D <sup>a</sup>
experimental value	2811-2881 (avg. 2846)	~2050, range: 2031-2144 (avg. 2088)
theoretical value	3031	2115 (calc.)
Scaling Factor for B3P/TZVP <sup>5</sup>	0.964	
Scaled theoretical value	2922	2038
Theor./Exp.		
Ratio	0.99	-

<sup>a</sup> units of cm<sup>-1</sup>

The theoretical stretching frequencies were determined from the B3P DFT calculation for the structure of **3**. The ratio of the theoretical stretches compared to the observed is 0.99 for the more

resolvable N-D stretches, or in other words, shows that the data observed is a very good match for the theoretical values.

Equation S1. IR Verification Calculations (units on all IR frequencies are in  $\text{cm}^{-1}$ ).

$$\begin{aligned}
 \nu_e &= \frac{1}{2\pi} \sqrt{\frac{k}{\mu}} \\
 \mu_d &= \frac{14.01 * 2.014}{14.01 + 2.014} = 1.761, & \mu_h &= \frac{14.01 * 1.008}{14.01 + 1.008} = 0.9403 \\
 2050 &= \frac{1}{2\pi} \sqrt{\frac{k}{1.761}} \\
 k &= 2.921 \times 10^8 \\
 \nu_{eh} &= \frac{1}{2\pi} \sqrt{\frac{2.921 \times 10^8}{0.9403}} \\
 \nu_{eh} &= 2805 \rightarrow 0.7\% \text{ off from experimental average (2846)} \\
 2846 &= \frac{1}{2\pi} \sqrt{\frac{k}{0.9403}} \\
 k &= 3.007 \times 10^8 \\
 \nu_{eh} &= \frac{1}{2\pi} \sqrt{\frac{3.007 \times 10^8}{1.761}} \\
 \nu_{eh} &= 2080 \rightarrow 0.7\% \text{ off from experimental average (2050)}
 \end{aligned}$$

## Mass Spectrometry

<b>Data File</b>	010522-01052022_ldhcootf-a.d	<b>Sample Name</b>	01052022_ldhcootf
<b>Sample Type</b>	Sample	<b>Position</b>	P1-A-07
<b>Instrument Name</b>	G6224A TOF LCMS	<b>User Name</b>	Anderson-Sophie.Whitmeyer
<b>Acq Method</b>	FIA_P_M-Mixed_No-Water_50-3200_130V.m	<b>Acquired Time</b>	1/5/2022 11:09:57 AM
<b>IRM Calibration Status</b>	Success	<b>DA Method</b>	FIA_P_M-Mixed_No-Water_50-3200_130V.m
<b>Comment</b>			

### Compound Table

Label	Tgt Score	Mass Error (ppm)	Tgt Formula	Obs. RT	Ref. Mass	Obs. Mass
Cpd 1: C29 H35 D Co F3 N5 O3 S	8.25	19.45	C29 H35 D Co F3 N5 O3 S	0.118	651.1886	651.2012

Figure S88. HRMS of **3**. Due to the mixed  $\text{H}_2$  and  $\text{D}_2$  atmosphere, the mass is not exact, but it shows that there's a relatively clean formation of one hydrogenated species.

## General Catalytic Hydrogenation Procedures and Products

*Procedure for 1% loading:*

In a nitrogen-filled glovebox, a 250 mL Schlenk flask with a magnetic stir bar was charged with unsaturated substrate (0.077 mmol, 100 eq.), **2** (0.0005 g, 0.0008 mmol), mesitylene (0.002 mL, 0.014 mmol) (internal standard), and benzene- $d_6$  (0.1 mL). On a Schlenk line, the solution was freeze-pump-thaw-degassed, and warmed to room temperature with the contents under static vacuum. At room temperature, this vessel was backfilled with 1 atm  $H_2$  gas. The vessel was then sealed and left to stir for 18 hr. The dark red-purple **2** could be observed to pinken within the hour, turn greenish-red, and then begin to turn orange/yellow after 6 hours. After 18 hr, the vessel was shipped back into the nitrogen-filled glovebox and diluted to 0.7 mL total volume. This was then analyzed via  $^1H$  and  $^{19}F$  NMR, and checked by GC-MS as needed.

Procedure for 2.5% loading:

The general method described above was implemented with 0.031 mmol, 40 equiv. of unsaturated solvent used.

*Procedure for 2.5% loading with  $NaBAr^F_4$ :*

The general method described above was implemented with 0.031 mmol, 40 equiv. of unsaturated solvent used and with the addition of 0.0008 mmol, 1 equiv. of  $NaBAr^F_4$  pre-added to the reaction vessel with 0.07 mL of THF.

*Procedure for 10% loading:*

In a nitrogen-filled glovebox, a 250 mL Schlenk flask with a magnetic stir bar was charged with unsaturated substrate (0.0077 mmol, 10 eq.), **2** (0.0005 g, 0.0008 mmol), mesitylene (0.002 mL, 0.014 mmol) (internal standard), and benzene- $d_6$  (0.1 mL). On a Schlenk line, the solution was freeze-pump-thaw-degassed, and backfilled at 77 K with 3.8 atm  $H_2$  gas. The vessel was then sealed and left to stir for 18 hr. After 18 hr, the vessel was shipped back into the nitrogen-filled

glovebox and diluted to 0.7 mL total volume. This was then analyzed via  $^1\text{H}$  and  $^{19}\text{F}$  NMR as well as checked by GC-MS as needed.

*1-Hexene*: The title compound was purchased from TCI Chemicals and dried according to the general procedure for olefin preparations. The spectral data collected matched those previously reported.<sup>6</sup>  $^1\text{H}$  NMR (400 MHz,  $\text{C}_6\text{D}_6$ ):  $\delta$  0.83 (t, 3H,  $\text{CH}_3$ ), 1.25 (m, 4H,  $\text{CH}_2\text{CH}_2\text{CH}_3$ ), 1.96 (m, 2H,  $\text{CHCH}_2$ ), 4.98 (m, 2H,  $\text{CH}=\text{CH}_2$ ), 5.75 (m, 1H,  $\text{CH}=\text{CH}_2$ ).

*Hexane*: Hydrogenation of 1-hexene by the general procedure for 1% cat. loading yielded hexane as follows: (79.5, 72.0, 86.0) 79(6)% unisolated yields. The spectral data collected matched those previously reported.<sup>7</sup>  $^1\text{H}$  NMR (400 MHz,  $\text{C}_6\text{D}_6$ ):  $\delta$  = 1.19~1.32 (m, 8 H), 0.89 (t, 6 H).

*1-Hexyne*: The title compound was purchased from Sigma Aldrich and dried according to the general procedure for olefin preparations. The spectral data collected matched those previously reported.<sup>9</sup>  $^1\text{H}$  NMR (400 MHz,  $\text{C}_6\text{D}_6$ ):  $\delta$  0.71 (t, 3H,  $\text{CH}_3$ ), 1.19–1.33 (m, 4H,  $\text{CH}_2\text{CH}_2$ ), 1.77 (t, 1H,  $\equiv\text{CH}$ ), 1.93 (dt, 2H,  $\equiv\text{CHCH}_2$ ).

*Hexane and 1-Hexene*: Hydrogenation of 1-hexyne by the general procedure for 1% cat. loading yielded hexane and 1-hexene as follows: (68.3, 67.9, 69.8) 69(1)% and (5.1, 10.4, 1.9) 6(3)% respectively unisolated yields. The spectral data collected matched those previously reported (see above for NMR peaks).<sup>9,10</sup>

*Styrene*: The title compound was purchased from Acros Organics and dried according to the general procedure for olefin preparation. The spectral data collected matched those previously reported.<sup>9</sup>  $^1\text{H}$  NMR (400 MHz,  $\text{C}_6\text{D}_6$ ):  $\delta$  5.06 (dd, 1H, (*E*)- $\text{CHH}$ ), 5.59 (dd, 1H, (*Z*)- $\text{CHH}$ ), 6.57 (dd, 1H,  $\text{CH}$ ), 7.01–7.05 (m, 1H, *p*- $\text{C}_6\text{H}_5$ ), 7.08–7.12 (m, 2H, *m*- $\text{C}_6\text{H}_5$ ), 7.21–7.24 (m, 2H, *o*- $\text{C}_6\text{H}_5$ ).

*Ethyl benzene*: Hydrogenation of styrene by the general procedure for 1% cat. loading yielded ethyl benzene as follows: (52.6, 61.2, 55.5) 55(4)% unisolated yields. The spectral data collected matched those previously reported.<sup>8</sup> <sup>1</sup>H NMR (400 MHz, C<sub>6</sub>D<sub>6</sub>):  $\delta$  = 7.20-7.06 (m, 5H, ar), 2.45 (sept, 1H, CH), 1.49 (d, 6H, Me).

*3,3-Dimethylbutene*: The title compound was purchased from Sigma Aldrich and dried according to the general procedure for olefin preparations. The spectral data collected matched those previously reported.<sup>9,11</sup> <sup>1</sup>H NMR (400 MHz, C<sub>6</sub>D<sub>6</sub>):  $\delta$  = 5.84-5.79 (3 H), 0.96 (s, 9 H, <sup>t</sup>Bu).

*2,2-Dimethylbutane*: Hydrogenation of 3,3-dimethylbutene by the general procedure for 1% cat. loading yielded 2,2-dimethylbutane as follows: (74.2, 70.7, 70.0) 72(2)% unisolated yields. The spectral data collected matched those previously reported.<sup>10,11</sup> <sup>1</sup>H NMR (400 MHz, C<sub>6</sub>D<sub>6</sub>):  $\delta$  = 1.19 (q, J = 7.5 Hz, 2 H), 0.85 (s, 9 H), 0.81 (t, J = 7.5 Hz, 3 H).

*$\alpha$ -Methyl styrene*: The title compound was purchased from TCI Chemicals and dried according to the general procedure for olefin preparations. The spectral data collected matched those previously reported.<sup>1</sup> <sup>1</sup>H NMR (400 MHz, C<sub>6</sub>D<sub>6</sub>):  $\delta$  = 7.36-7.35 (m, 3H), 7.15-7.09 (d, 2 H), 5.35(s, 1H), 5.00 (s, 1H), 1.96 (s, 3H, Me). The hydrogenation of this complex under the NaBARF<sup>4</sup> containing conditions lead to hydrogenated products derived from radical coupling reactions, namely III and V as listed in this resource.<sup>9</sup> (III) <sup>1</sup>H NMR (400 MHz, C<sub>6</sub>D<sub>6</sub>):  $\delta$  = 7.00-7.30 (m, 10 H), 5.10 (d, 1 H), 4.74 (d, 1 H), 2.71 (s, 2 H), 1.15 (s, 6 H). (V) <sup>1</sup>H NMR (400 MHz, C<sub>6</sub>D<sub>6</sub>):  $\delta$  = 7.00-7.30 (m, 9 H), 2.33 (d, 1 H), 2.05 (d, 1 H), 1.58 (s, 3 H), 1.24 (s, 3 H), 1.00 (s, 3 H).

*Isopropyl benzene (cumene)*: Hydrogenation of  $\alpha$ -methyl styrene by the general procedure for 2.5% cat. loading yielded isopropyl benzene as follows: (27.2, 30.0, 26.7) 28(1)% unisolated yields. Utilizing the procedure for 2.5% catalyst loading with NaBARF<sup>4</sup> co-catalyst yield

isopropyl benzene as follows: (45.24, 49.90, 48.27) 48(2)% unisolated yields. The spectral data collected matched those previously reported.<sup>11</sup> <sup>1</sup>H NMR (400 MHz, C<sub>6</sub>D<sub>6</sub>):  $\delta$  = 7.19-7.06 (m 5 H), 2.74-2.50 (m, 1 H, CHMe<sub>2</sub>), 1.14-1.13 (d, 6 H, Me).

*$\beta$ -Methyl styrene*: The title compound was purchased from Sigma Aldrich and dried according to the general procedure for olefin preparations. The spectral data collected matched those previously reported.<sup>10</sup> <sup>1</sup>H NMR (400 MHz, C<sub>6</sub>D<sub>6</sub>):  $\delta$  = 7.25-7.00 (m, 5 H), 6.25 (d, 1 H), 6.0 (m, 1 H), 1.60 (d, 3 H).

*n-Propyl benzene*: Hydrogenation of  $\beta$ -methyl styrene by the general procedure for 2.5% cat. loading with NaBAr<sup>F</sup><sub>4</sub> co-catalyst yielded n-propyl benzene as follows: (5.60, 6.06, 4.66) 5.4(0.6)% unisolated yields. The spectral data collected matched those previously reported.<sup>10</sup> <sup>1</sup>H NMR (400 MHz, C<sub>6</sub>D<sub>6</sub>):  $\delta$  = 7.18 (d, 2 H), 7.03~7.11 (m, 3 H), 2.3 (t, 2 H), 1.52 (m, 2 H), 0.83 (t, 3 H).

*Benzoquinone*: The title compound was purchased from Sigma Aldrich and dried according to the general procedure for olefin preparations. The spectral data collected matched those previously reported.<sup>10</sup> <sup>1</sup>H NMR (400 MHz, C<sub>6</sub>D<sub>6</sub>):  $\delta$  = 5.92 (s, 4H)

*Hydroquinone*: Hydrogenation of benzoquinone by the general procedure for 2.5% cat. loading yielded hydroquinone as follows: (43.0, 43.4, 36.2) 41(3)% unisolated yields. The spectral data collected matched those previously reported.<sup>11</sup> <sup>1</sup>H NMR (400 MHz, C<sub>6</sub>D<sub>6</sub>):  $\delta$  = 7.85 (s, 2H), 6.36 (s, 4H).

*2-methyl-pent-1,3-ene*: The title compound was purchased from Sigma Aldrich and dried according to the general procedure for olefin preparations. The spectral data collected matched those previously reported.<sup>11</sup> <sup>1</sup>H NMR (400 MHz, C<sub>6</sub>D<sub>6</sub>):  $\delta$  = 4.792 (d, 1H), 4.785 (d, 1H), 6.102 (d, 1 H), 5.578 (q, 1H), 1.765 (s, 3H), 1.708 (d, 3 H).

*4-methyl-2-pentene (cis- and trans-) and 2-methyl-pent-2-ene*: Hydrogenation of 2-methyl-pent-1,3-ene by the general procedure for 2.5% cat. loading yielded products as follows: *trans-4-Methyl-2-pentene (trans-E)*: (19.3, 10.7, 9.3) 13(4)% *cis-4-Methyl-2-pentene (cis-E)*: (9.7, 6.5, 6.5) 8(1)% and *2-methyl-pent-2-ene*: (10.0, 15.6, 15.4) 14(3)% unisolated yields. The spectral data collected matched those previously reported.<sup>12</sup> *cis-4-Methyl-2-pentene (cis-E)*: <sup>1</sup>H NMR (400 MHz, C<sub>6</sub>D<sub>6</sub>):  $\delta$  = 5.36–5.20 (m, 2 H, =CHMe + =CH-*i*Pr), 2.55 (m, 1 H, -CHMe<sub>2</sub>), 1.51 (dd, 3 H, CH<sub>3</sub>-CH=), 0.91 [d, <sup>3</sup>J<sub>H,H</sub> = 6.4 Hz, 6 H, -C(CH<sub>3</sub>)<sub>2</sub>] ppm. *trans-4-Methyl-2-pentene (trans-E)*: <sup>1</sup>H NMR (400 MHz, C<sub>6</sub>D<sub>6</sub>):  $\delta$  = 5.72 (m, 1 H, =CH-*i*Pr), 5.34 (dq, 1 H, =CH-Me), 2.18 (m, 1 H, -CHMe<sub>2</sub>), 1.56 (dd, 3 H, CH<sub>3</sub>-CH=), 0.93 [d, 6 H, -C(CH<sub>3</sub>)<sub>2</sub>] ppm. *2-Methyl-2-pentene*: <sup>1</sup>H NMR (400 MHz, C<sub>6</sub>D<sub>6</sub>):  $\delta$  = 5.17-5.10 (m, 1H), 2.02-1.90 (m, 2H), 1.63 (d, 3H), 1.51 (d, 3H), 0.92 (t, 3H).

*$\alpha$ -cyclopropyl styrene*: The title compound was synthesized according to literature procedures<sup>13</sup> and dried according to the general procedure for olefin preparations. The spectral data collected matched those previously reported<sup>14</sup>: <sup>1</sup>H NMR (400 MHz, C<sub>6</sub>D<sub>6</sub>):  $\delta$  = 5.25 (1H), 4.87 (1H). <sup>1</sup>H NMR (400 MHz, CDCl<sub>3</sub>):  $\delta$  7.60 (d, 2H), 7.34 (t, 2H), 7.29 (d, 1H), 5.28 (s, 1H), 4.94 (s, 1H), 1.69-1.62 (m, 1H), 0.86-0.82 (m, 2H), 0.62-0.58 (m, 2H).

*Pentan-2-ylbenzene and (E)-pent-2-en-2-ylbenzene*: Hydrogenation of  $\alpha$ -cyclopropyl styrene by the general procedure for 10% cat. loading yielded products as follows: *pentan-2-ylbenzene* (31.0, 37.3, 35.4) 35(3)% and *(E)-pent-2-en-2-ylbenzene*: (11.0, 11.2, 7.5) 10(2)% unisolated yields. The spectral data collected matched those previously reported.<sup>15</sup> *Pentan-2-ylbenzene*: H NMR (400 MHz, CDCl<sub>3</sub>)  $\delta$  = 7.33 - 7.28 (m, 2 H), 7.23 - 7.15 (m, 3 H), 2.71 (sxt, 1 H), 1.65 - 1.49 (m, 3 H), 1.35 - 1.15 (m, 5 H), 0.88 (t, 3 H). *(E)-pent-2-en-2-ylbenzene*: H NMR (400

MHz, CDCl<sub>3</sub>) δ: 1.06 (t, 3H), 2.03 (s, 3H), 2.21 (dq, 2H), 5.77 (t, 1H), 7.21 (dd, 1H), 7.30 (dd, 8.0 Hz, 2H), 7.38 (d, 2H).

## Controls

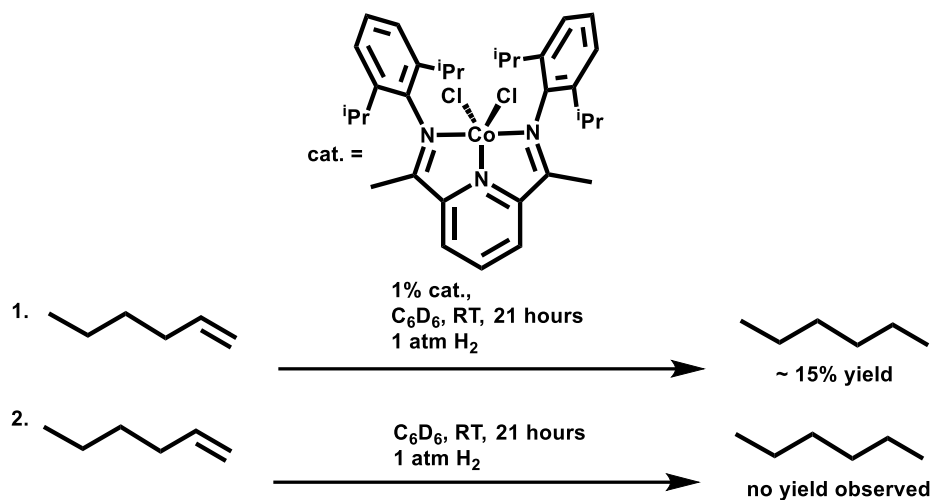


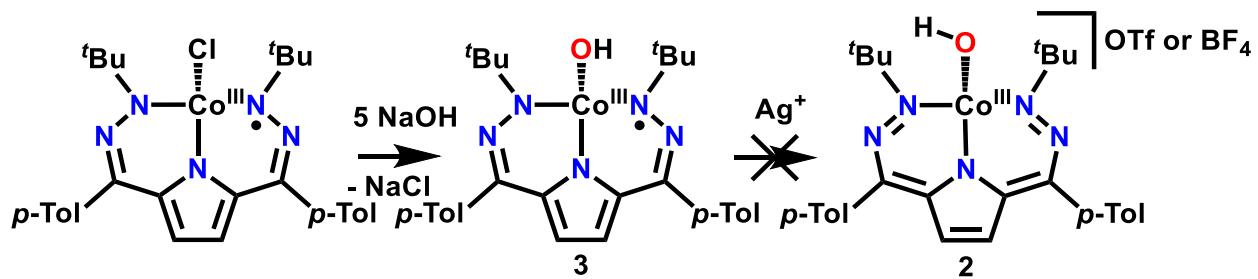
Figure S89. Controls (1.) with alternative cobalt catalyst<sup>16</sup> and (2.) with no cobalt-containing species. Some yield is observed from the alternative catalyst, but it is significantly less than that observed with 2, and no quantifiable yield was observed in the absence of cobalt catalyst.

## References

1. G. M. Sheldrick, Crystal structure refinement with SHELXL. *Acta Crystallogr.* **2015**, C71, 3-8.
2. O. V. Dolomanov, L. J. Bourhis, R. J. Gildea, A. K. Howard, H. Puschmann, OLEX2: a complete structure solution, refinement and analysis program, *J. Appl. Cryst.* **2009**, 42, 339.
3. G. M. Sheldrick. *Acta Crystallogr.* **2008**, A64, 112-122.
4. (a) Neese, F. The Orca Program System. *Wiley Interdiscip. Rev. Comput. Mol. Sci.* **2012**, 2, 73-78. (b) H - Kr: A. Schaefer, H. Horn and R. Ahlrichs, Fully optimized contracted Gaussian basis sets for atoms Li to Kr. *J. Chem. Phys.* **1992**, 97, 2571. (c) Rb - Xe: A. Schaefer, C. Huber and R. Ahlrichs, Fully optimized contracted Gaussian basis sets of triple zeta valence quality for atoms Rb to Xe. *J. Chem. Phys.* **1994** 100, 5829. (d) F. Weigend, R. Ahlrichs, Balanced basis sets of split valence, triple zeta valence and quadruple zeta valence quality for H to Rn: Design and assessment of accuracy. *Phys. Chem. Chem. Phys.* **2005**, 7, 3297.
5. NIST Computational Chemistry Comparison and Benchmark Database, NIST Standard Reference Database Number 101. Release 21, August 2020, Editor: Russell D. Johnson III
6. Schwieger, S.; Herzog, R.; Wagner, C.; Steinborn, D. Platina-β-diketones as catalysts for hydrosilylation and their reactivity towards hydrosilanes. *J. Organomet. Chem.* **2009**, 694, 3548-3558.

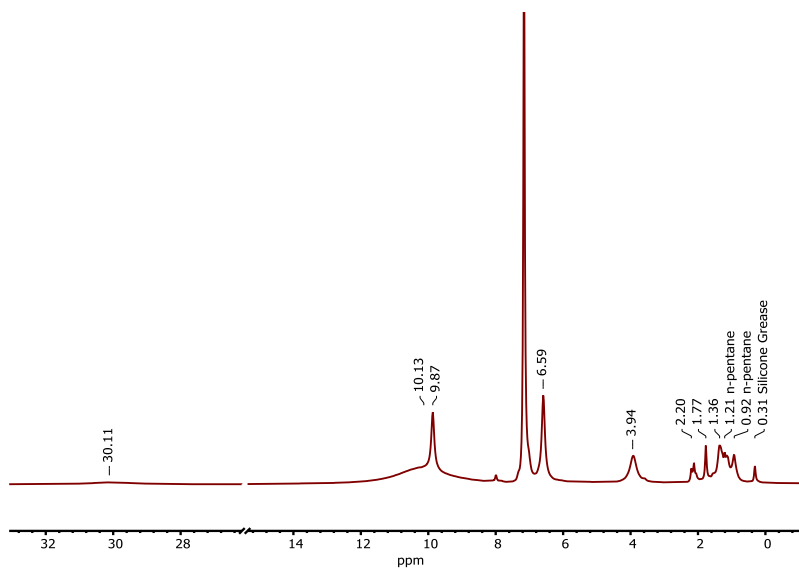
7. Wang, Y.; Chen, W.; Lu, Z.; Hua Li, Z.; Wang, H. Metal-Free HB(C<sub>6</sub>F<sub>5</sub>)<sub>2</sub>-Catalyzed Hydrogenation of Unfunctionalized Olefins and Mechanism Study of Borane-Mediated  $\sigma$ -Bond Metathesis. *Angew. Chem. Int. Ed.*, **2013**, *29*, 7496-7499.
  8. Spielmann, J.; Buch, F.; Harder, S. Early Main-Group Metal Catalysts for the Hydrogenation of Alkenes with H<sub>2</sub>. *Angew. Chem. Int. Ed.*, **2008**, *49*, 9434-9438.
  9. Henry, A. T.; Cosby, T. P. L.; Boyle, P.D.; Baines, K. M. Selective dimerization of  $\alpha$ -methylstyrene by tunable bis (catecholato) germane Lewis acid catalysts. *Dalton Trans.*, **2021**, *50*, 15906–15913.
  10. McNeece, A. J.; Jesse, K. A.; Filatov, A. S.; Schneider, J. E.; Anderson, J. S. Catalytic hydrogenation enabled by ligand-based storage of hydrogen. *ChemComm.* **2021**, *57*, 3869-3872.
  11. Harris, R. K.; Ng, S.; Connelly, A. Proton-coupled carbon-13 NMR spectra of butadienes. *Magn Reson Chem.* **1991**, *29*, 1152-1157.
  12. (a) Chahboun, G.; Petrisor, C. E.; Gómez-Bengoa, E.; Royo, E.; Cuenca, T. Insight into cis-to-trans Olefin Isomerisation Catalysed by Group 4 and 6 Cyclopentadienyl Compounds. *Eur. J. Inorg. Chem.* **2009**, *11*, 1514-1520.; (b) Pinkas, J.; Gyepes, R.; Císařová, I.; Kubišta, J.; Horáček, M.; Mach, K. Steric Effects in Reactions of Decamethyltitanocene Hydride with Internal Alkynes, Conjugated Diynes, and Conjugated Dienes. *Organometallics.* **2014**, *13*, 3399–3413.
  13. Kristensen, Steffan K.; Laursen, Simon L. R.; Taarning, Esben; Skrydstrup, Troels. Ex Situ Formation of Methanethiol: Application in the Gold (I)-Promoted Anti-Markovnikov Hydrothiolation of Olefins. *Angew. Chem. Int. Ed.*, **2018**, *57*, 42, 13887 – 13891.
  14. Masnovi, J.; Samsel, E. G.; Bullock, R. M. Cyclopropylbenzyl Radical Clocks. *J. Chem. Soc., ChemComm.* **1989**, 1044–1045.
  15. (a) Harada, S.; Matsuda, D.; Morikawa, T.; Nishida, A. Direct Synthesis of Enones by Visible-Light-Promoted Oxygenation of Trisubstituted Olefins Using Molecular Oxygen. *Synlett.* **2020**, *31*, 1372-1377.; (b) Bedford, R. B.; Brenner, P. B.; Carter, E.; Carvell, T. W.; Cogswell, P. M.; Gallagher, T.; Harvey, J. N.; Murphy, D. M.; Neeve, E. C.; Nunn, J.; Pye, D. R. Expedient Iron-Catalyzed Coupling of Alkyl, Benzyl and Allyl Halides with Arylboronic Esters. *Chem. A. Eur. Journal.* **2014**, *20*, 7935-7938.
  16. Britovsek, G. J. P.; Bruce, M.; Gibson, V. C.; Kimberley, B. S.; Maddox, P. J.; Mastroianni, S.; McTavish, S. J.; Redshaw, C.; Solan, G. A.; Stömberg, S.; White, A. J. P.; Williams, D. J. Iron and cobalt ethylene polymerization catalysts bearing 2, 6-bis (imino) pyridyl ligands: synthesis, structures, and polymerization studies. *J. Am. Chem. Soc.* **1999**, *121*, 38, 8728-8740
-

## Appendix II: Chapter III Supplementary Information



Scheme S1. Synthetic route to separately isolating proposed 2

### NMR spectroscopy



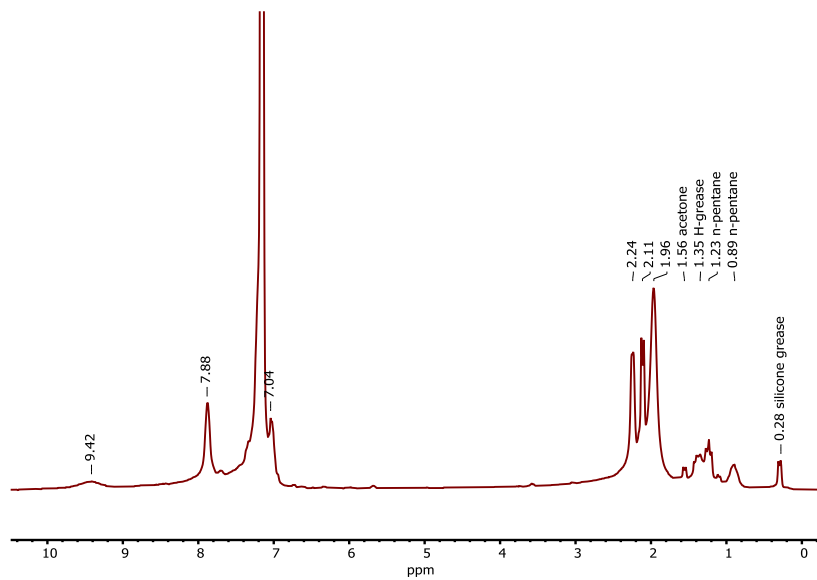


Figure S2.  $^1\text{H}$  NMR of  $(t\text{Bu,Tol})\text{DHP})\text{CoOH}$  (**3**) in  $\text{C}_6\text{D}_6$ .

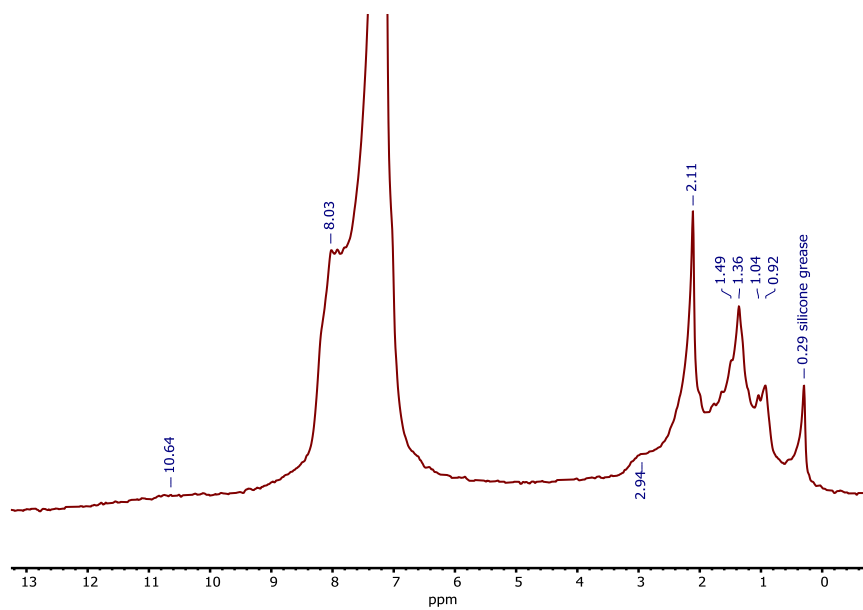


Figure S3.  $^1\text{H}$  NMR of  $(t\text{Bu,Tol})\text{DHP})\text{CoOH}(\text{OTf})$  (**2**) in  $\text{C}_6\text{D}_6$ .

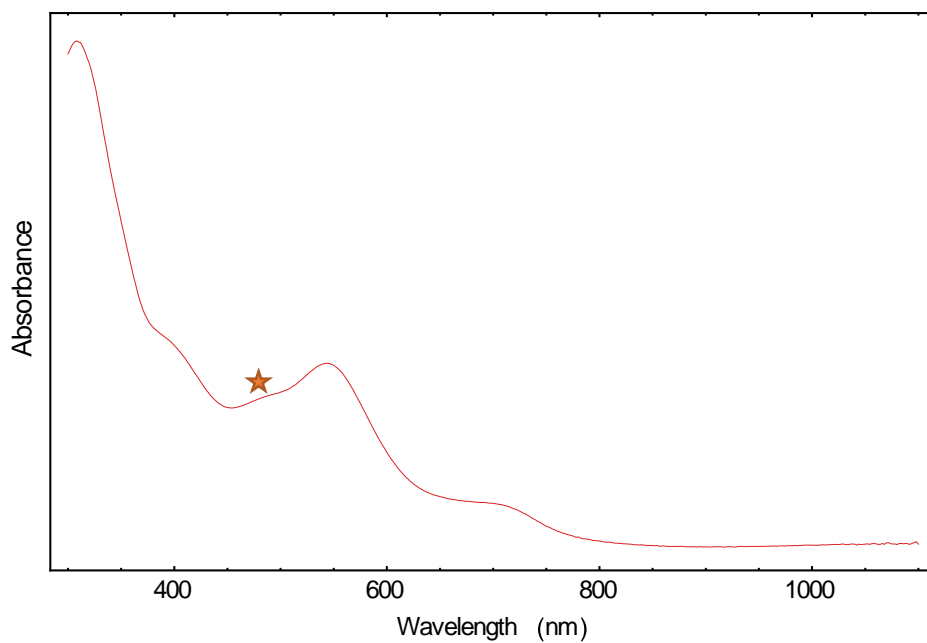


Figure S4. UV-vis of **1** from a 0.13 mM solution in toluene at room temperature. Orange marker indicates presence of putative thermal decomposition product (assigned as **2**)

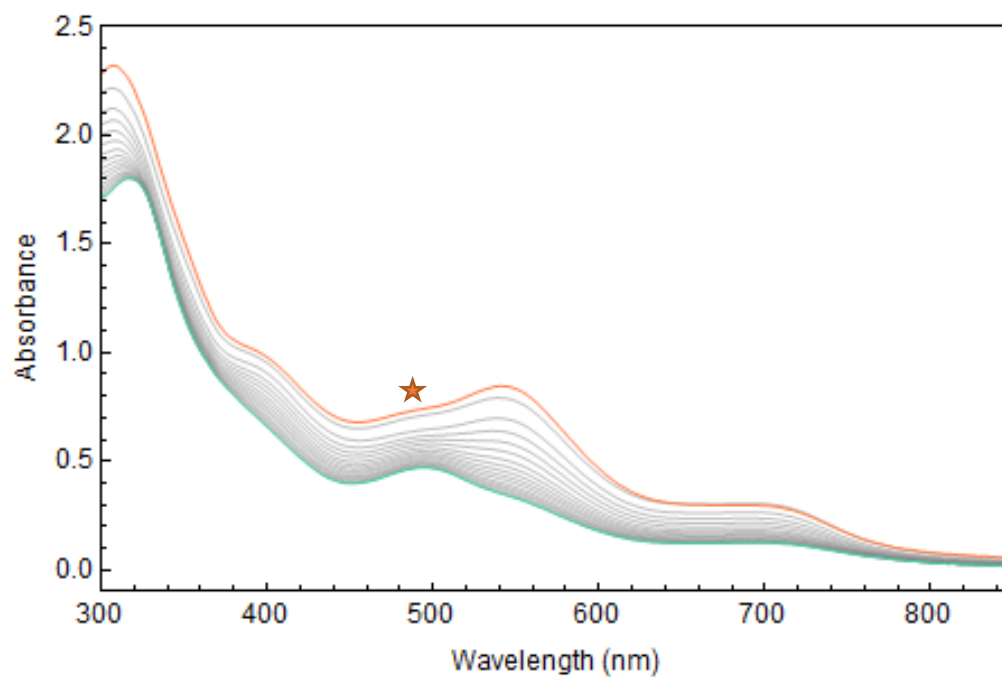


Figure S5. UV-vis of **1** from a 0.13 mM solution in toluene at room temperature heated for 60 °C for 3 hours (same decomposition occurs at RT at a slower rate). Orange marker indicates presence of putative thermal decomposition product (assigned as **2**)

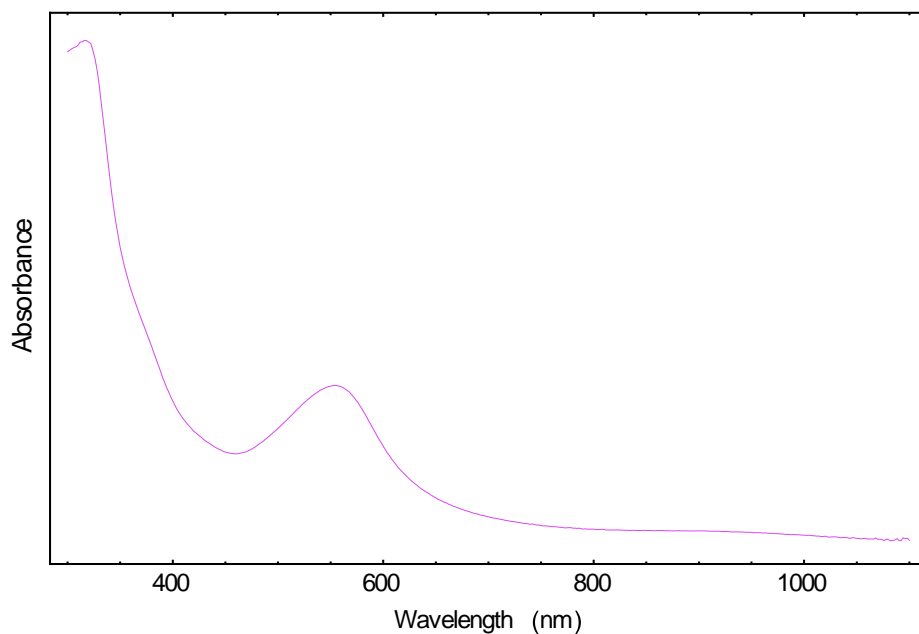


Figure S6. UV-vis of **3** from a 0.21 mM solution in toluene at room temperature

### Vibrational Spectroscopy

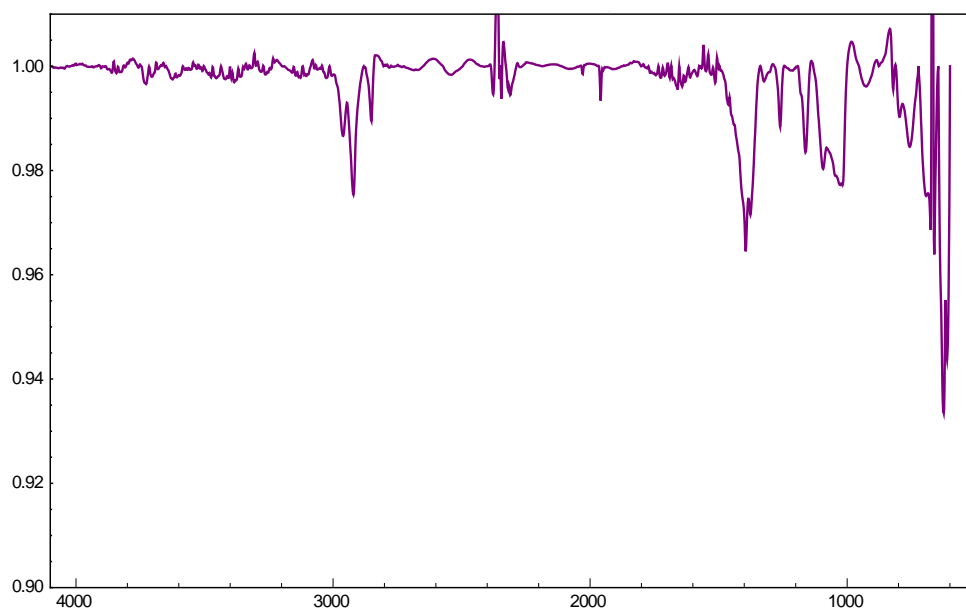


Figure S7. IR of (*t*Bu,Tol)<sup>DHP</sup>CoOTf as a thin film.

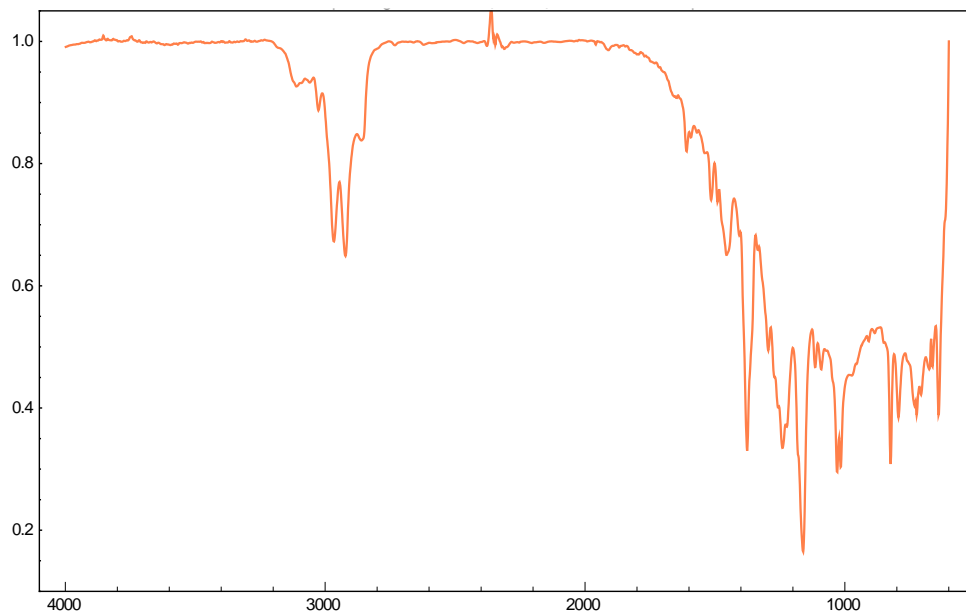


Figure S8. IR of **1** as a thin film.

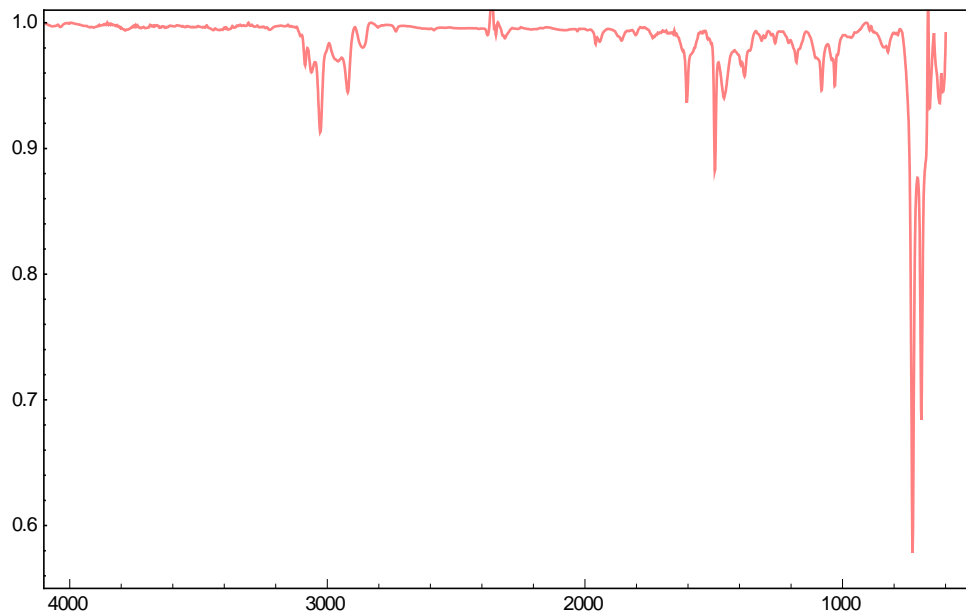


Figure S9. IR of (*t*Bu,Tol)<sup>DHP</sup>CoOH (**3**) as a thin film.

### Cyclic Voltammetry

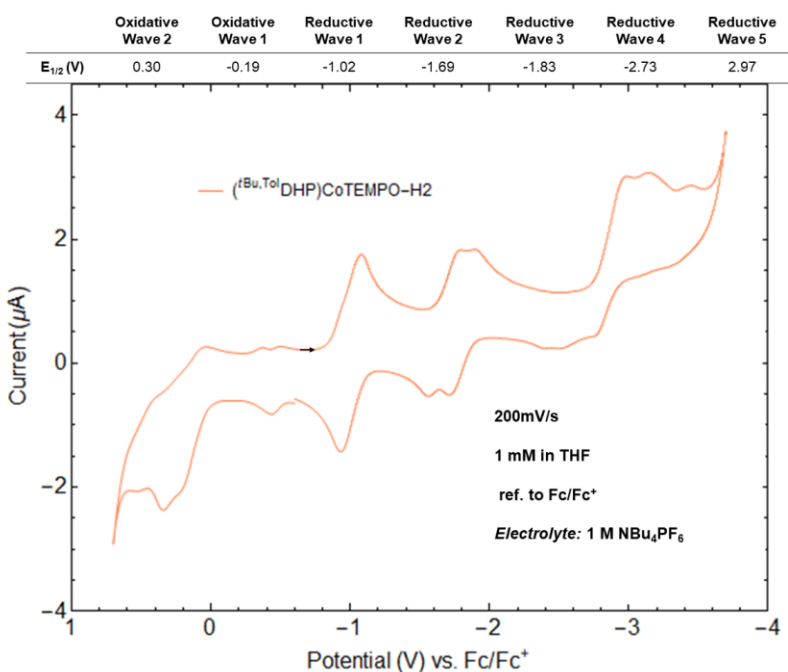


Figure S10. Cyclic voltammogram of **1**.

This complex is also highly redox active as shown by its complicated cyclic voltammogram, an unsurprising observation given the presence of potentially redox-active aminoxyl and DHP ligands. It is likely that some of these features are due to decomposition products, although we have not verified this hypothesis.

### Single Crystal X-ray Diffraction

#### *X-Ray Structure Determination.*

The diffraction data were measured at 100 K on a Bruker D8 VENTURE with PHOTON 100 CMOS detector system equipped with a Mo-target micro-focus X-ray tube ( $\lambda = 0.71073 \text{ \AA}$ ). Data reduction and integration were performed with the Bruker APEX3 software package (Bruker AXS, version 2015.5-2, 2015). Data were scaled and corrected for absorption effects using the multi-scan procedure as implemented in SADABS (Bruker AXS, version 2014/5, 2015, part of Bruker APEX3 software package). The structure was solved by the dual method implemented in

SHELXT<sup>1</sup> and refined by a full-matrix least-squares procedure using OLEX23<sup>2</sup> software package (XL refinement program version 2014/7<sup>3</sup>). Suitable crystals were mounted on a cryo-loop and transferred into the cold nitrogen stream of the Bruker D8 Venture diffractometer. C–H hydrogen atoms were generated by geometrical considerations, constrained to idealized geometries, and allowed to ride on their carrier atoms with an isotropic displacement parameter related to the equivalent displacement parameter of their carrier atoms. Finally, we note some B-level alerts for **1** and **3** related to the quality of the diffraction which was weak at higher angles. Despite this weak diffraction, the connectivity, assignment, and bond lengths for **1** and **3** are still suitable for discussion. B-level alerts for both structures concerning the O–H bonds were addressed by checking for the presence of suitable acceptors using commonly used (Jeffrey) H-bond criteria, and none were found. Similarly, the possibility of a dihydrogen bond was also assessed and chemically rule out for **1**.

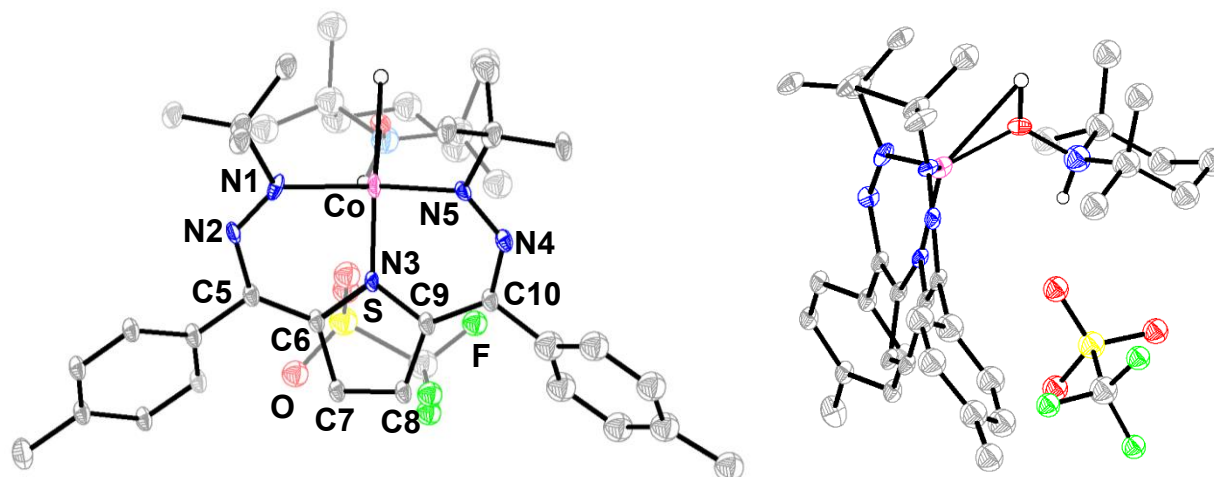


Figure S11. SXR of **1**. Co (pink), N (blue), C (gray), S (yellow), O (red), F (lime green), C–H H-atoms omitted.

Selected bond lengths (Å): Co–N1/N5: 2.031(6), 2.038(6); Co–N3: 1.915(6); N1–N2/N4–N5: 1.286(9), 1.266(9); Co–O/H: 1.906(7), 1.73(7); N2–C5/N4–C10: 1.36(1), 1.38(1); C5–C6/C9–C10:

1.39(1), 1.40(1); C6-C7/C8-C9: 1.45(1); C7-C8: 1.33(1). Selected bond angles (°): N1-M-N5: 135.8(3); N3-M-Cl: 128.8(2). This structure and further structural information can be found at CCDC # 2179903.

Table S1. SXRD of **1**.

Empirical formula	C <sub>41</sub> H <sub>57</sub> CoF <sub>3</sub> N <sub>6</sub> O <sub>4</sub> S
Formula weight	845.942
Temperature/K	100.0
Crystal system	monoclinic
Space group	P2 <sub>1</sub> /c
a/Å	14.934(3)
b/Å	12.542(2)
c/Å	21.913(4)
α/°	90
β/°	91.469(5)
γ/°	90
Volume/Å <sup>3</sup>	4102.8(13)
Z	4
ρ <sub>calc</sub> /cm <sup>3</sup>	1.370
μ/mm <sup>-1</sup>	0.531
F(000)	1790.8
Crystal size/mm <sup>3</sup>	0.264 × 0.1 × 0.031
Radiation	Mo Kα (λ = 0.71073)
2θ range for data collection/°	4.56 to 46.56
Index ranges	-16 ≤ h ≤ 16, -13 ≤ k ≤ 13, -24 ≤ l ≤ 24
Reflections collected	31927
Independent reflections	5881 [R <sub>int</sub> = 0.1605, R <sub>sigma</sub> = 0.1094]
Data/restraints/parameters	5881/0/456
Goodness-of-fit on F <sup>2</sup>	1.140
Final R indexes [I ≥ 2σ (I)]	R <sub>1</sub> = 0.0886, wR <sub>2</sub> = 0.1930
Final R indexes [all data]	R <sub>1</sub> = 0.1506, wR <sub>2</sub> = 0.2306
Largest diff. peak/hole / e Å <sup>-3</sup>	2.01/-1.13

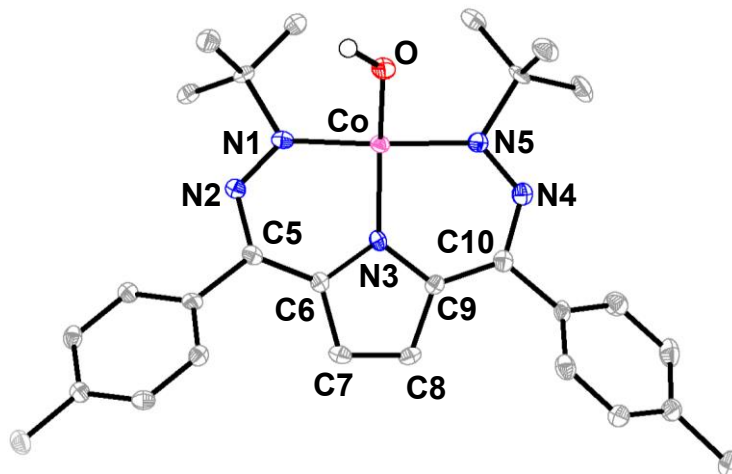


Figure S12. SXR of **2**. Co (pink), N (blue), C (gray), O (red), C–H H-atoms omitted.

Selected bond lengths (Å): Co–N1/N5: 1.889(3), 1.897(3); Co–N3: 1.861(3); N1–N2/N4–N5: 1.306(3), 1.302(3); Co–O: 1.825(2); N2–C5/N4–C10: 1.342(4), 1.350(4); C5–C6/C9–C10: 1.390(4), 1.383(4); C6–C7/C8–C9: 1.439(4), 1.438(4); C7–C8: 1.349(4). Selected bond angles (°): N1–M–N5: 162.4(1); N3–M–O: 143.5(1). This structure and further structural information can be found at CCDC # 2179904.

Table S2. SXR of **2**.

Identification code	0807_sw_73c
Empirical formula	C <sub>28</sub> H <sub>35</sub> CoN <sub>5</sub> O
Formula weight	516.54
Temperature/K	100(2)
Crystal system	orthorhombic
Space group	Pbca
a/Å	7.3580(4)
b/Å	15.7246(9)
c/Å	44.266(2)
$\alpha$ /°	90
$\beta$ /°	90
$\gamma$ /°	90
Volume/Å <sup>3</sup>	5121.6(5)
Z	8
$\rho_{\text{calc}}/\text{cm}^3$	1.340
$\mu/\text{mm}^{-1}$	0.700
F(000)	2184.0

Crystal size/mm <sup>3</sup>	0.32 × 0.18 × 0.16
Radiation	MoK $\alpha$ ( $\lambda$ = 0.71073)
2 $\theta$ range for data collection/ $^{\circ}$	5.182 to 46.616
Index ranges	-8 $\leq$ h $\leq$ 8, -17 $\leq$ k $\leq$ 17, -49 $\leq$ l $\leq$ 49
Reflections collected	69457
Independent reflections	3683 [R <sub>int</sub> = 0.1526, R <sub>sigma</sub> = 0.0457]
Data/restraints/parameters	3683/0/325
Goodness-of-fit on F <sup>2</sup>	1.086
Final R indexes [I $\geq$ 2 $\sigma$ (I)]	R <sub>1</sub> = 0.0422, wR <sub>2</sub> = 0.0679
Final R indexes [all data]	R <sub>1</sub> = 0.0729, wR <sub>2</sub> = 0.0753

## Density Functional Theory (DFT)

### *Geometry Optimizations*

Geometry optimization calculations were performed with ORCA<sup>4</sup> software suite using density functional theory (DFT). Geometries were fully optimized starting from coordinates generated from finalized cifs of the compound crystal structures. The BP86 functional was used for geometry optimizations, spin density plot calculations, and frequency calculations on **1**, **2**, and **3**. O3LYP was used to calculate the reaction coordinate with and without frequencies for the formation of **1**, the various decomposition pathways of **1**, and perform the IBO surface scan for the reactivity of **Int. 1** with TEMPOH.

For the BP86 calculations, def2-TZVPP was used on Co, N, S, O and F, and def2-TZVP on C atoms. The resulting structures were confirmed to be minima on the potential energy surface by frequency calculations using ORCA. For the O3LYP calculations with triflate bound, def2-TZVPP was used on Co, N, S, O, most carbons and F, and def2-TZVP(-f) used on C atoms not part of the conjugated ligand. For O3LYP calculations without triflate bound, def2-TZVPP was used for Co, with def2-TZVP for all other N, C, O, S and F atoms.

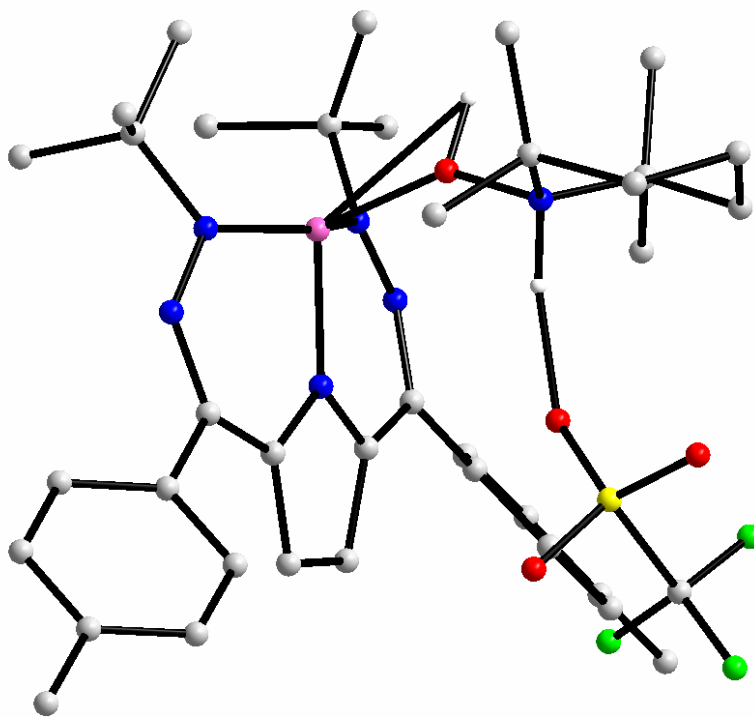


Figure S13. Calculated structure of **1**. All C–H hydrogen atoms have been removed for clarity.

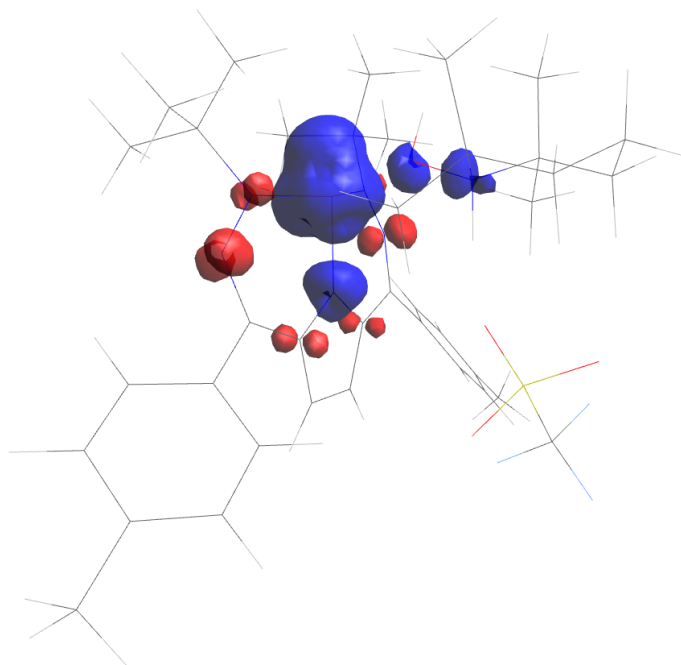


Figure S14. Spin density plot of **1** at an iso value of 0.005.

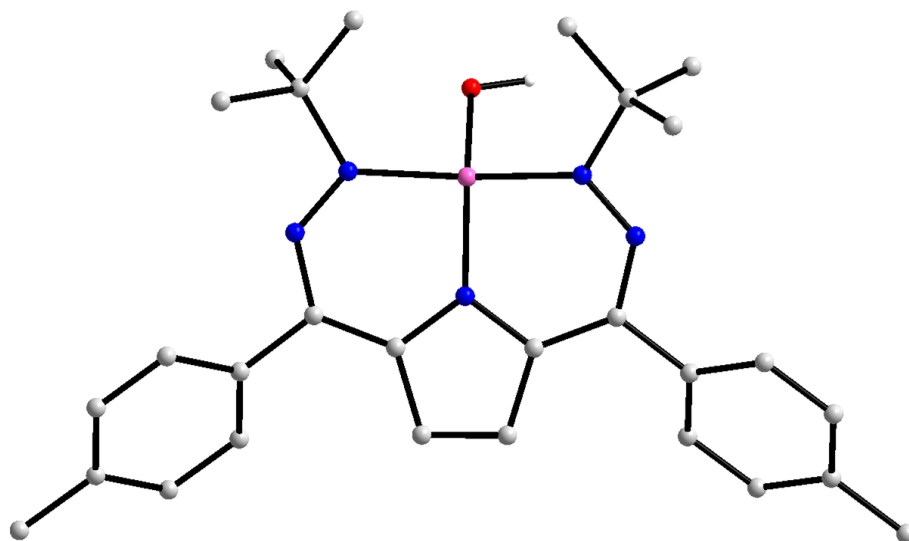


Figure S15. Calculated structure of **3**. All C–H hydrogen atoms have been removed for clarity.

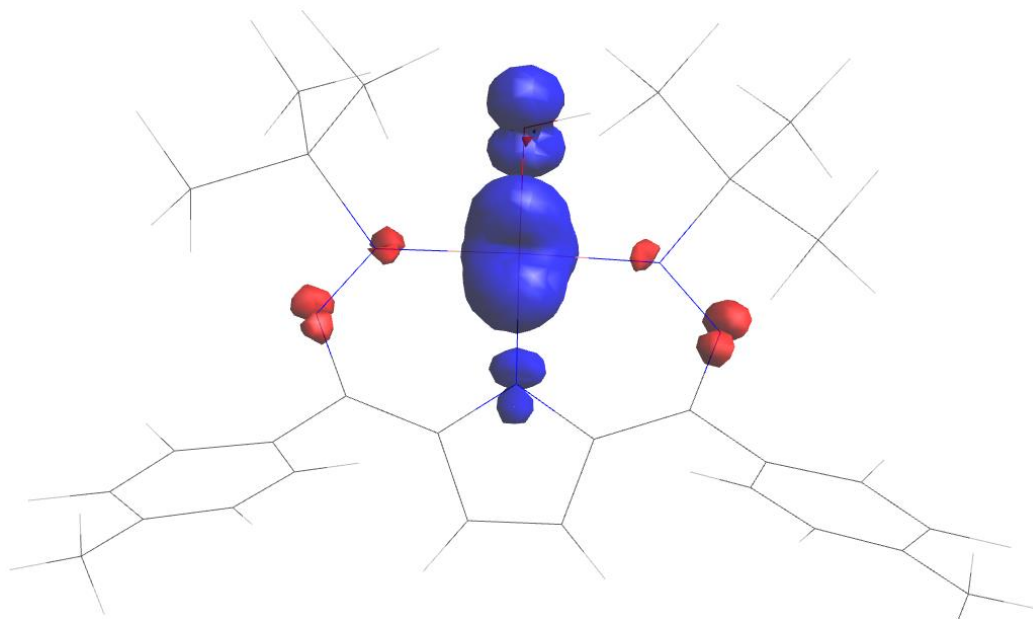


Figure S16. Spin density plot of **3** at an iso value of 0.005.

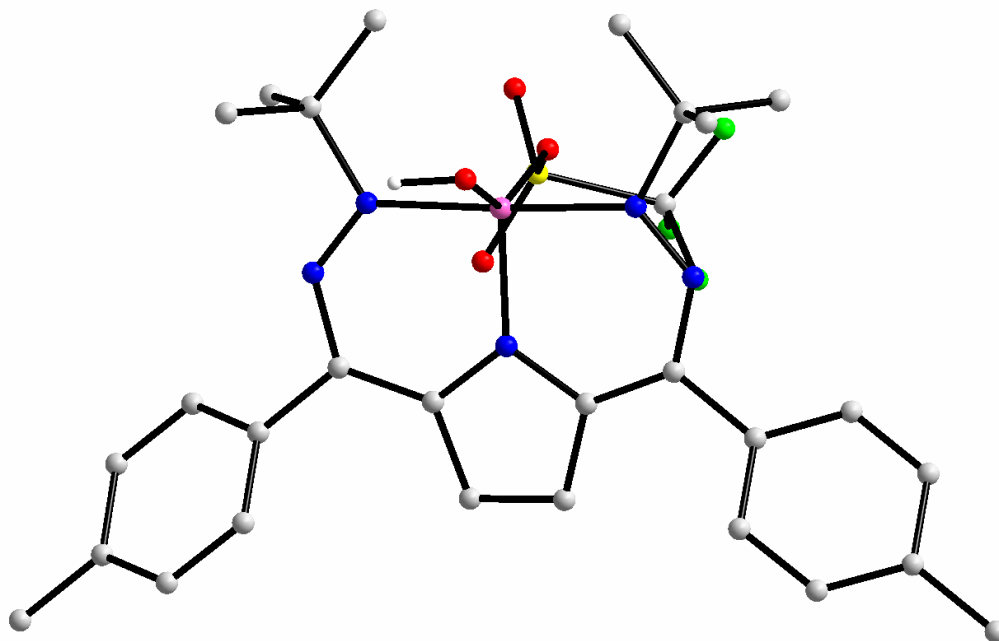


Figure S17. Calculated structure of **2**. All C–H hydrogen atoms have been removed for clarity.

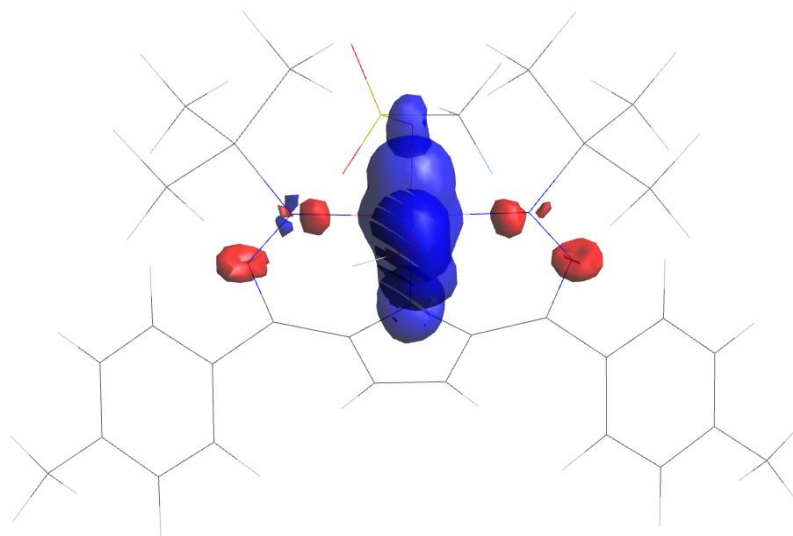


Figure S18. Spin density plot of **2** at an iso value of 0.005.

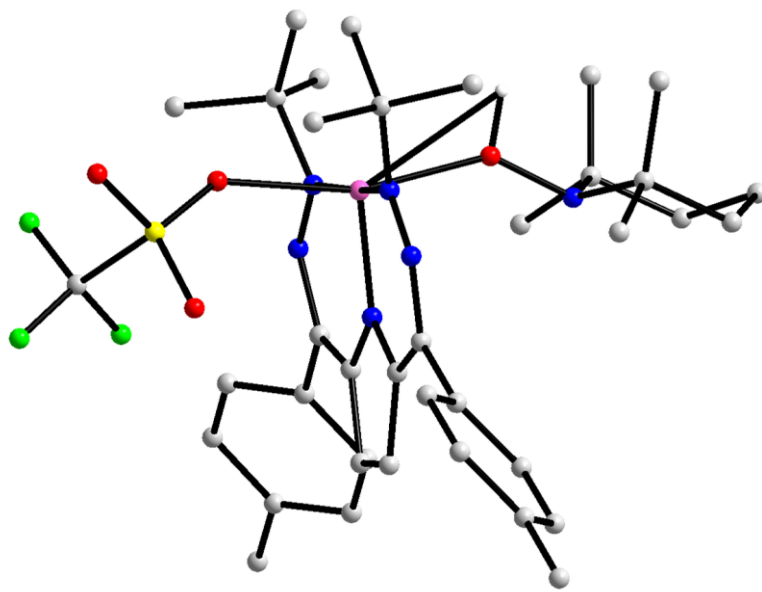


Figure S19. Calculated structure of [ $t\text{Bu,Tol}$ DHP]CoOTf(TEMPOH). All C–H hydrogen atoms have been removed for clarity.

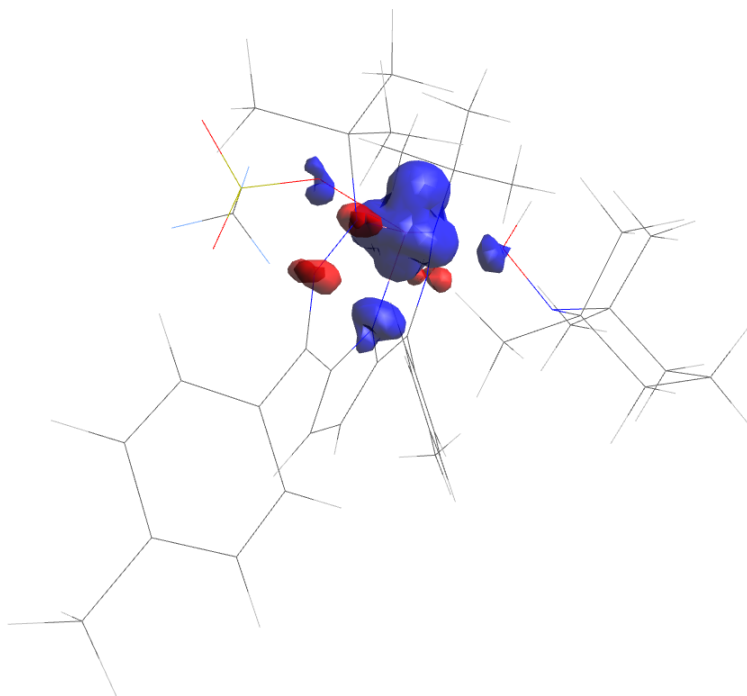


Figure S20. Spin density plot of [ $t\text{Bu,Tol}$ DHP]CoOTf(TEMPOH) at an iso value of 0.005.

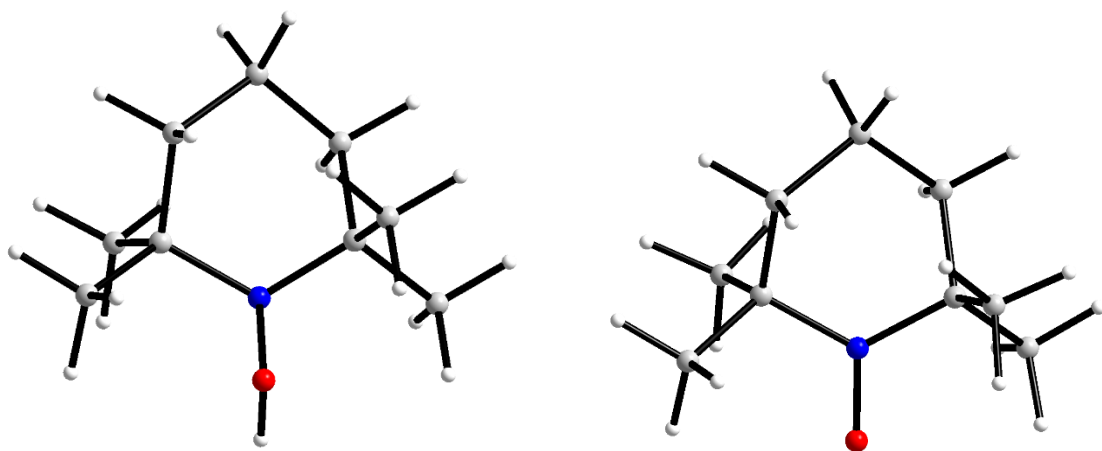


Figure S21. Calculated structure of TEMPOH and TEMPO radical.

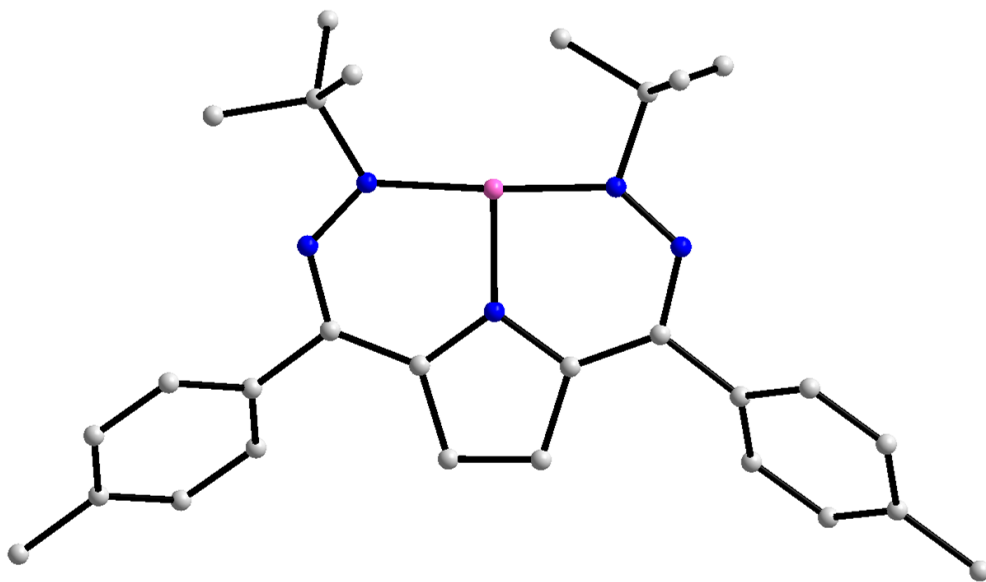


Figure S22. Calculated structure of  $[^{t\text{Bu,Tol}}\text{DHP}]\text{Co}$ . All C–H hydrogen atoms have been removed for clarity

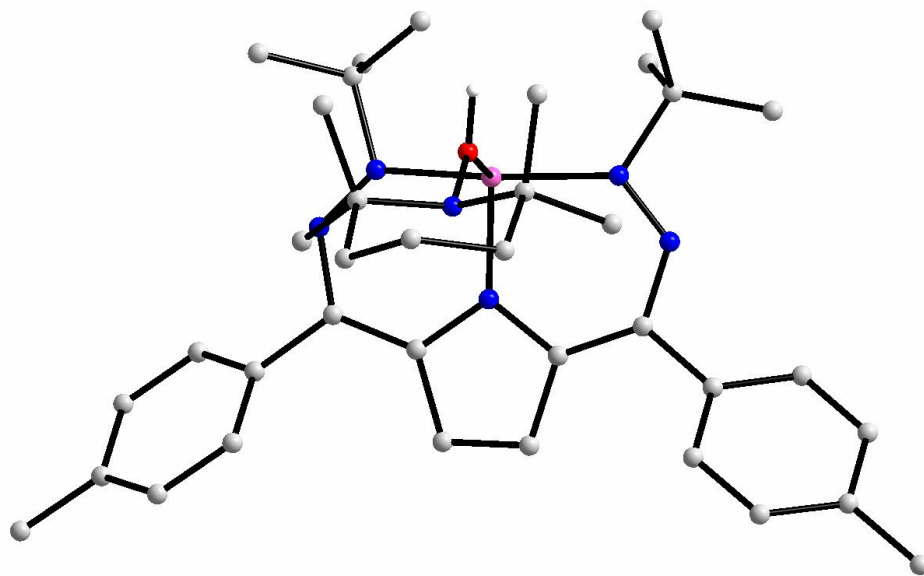


Figure S23. Calculated structure of  $[\text{tBu,TolDHP}]\text{Co}(\text{TEMPOH})^+$ . All C–H hydrogen atoms have been removed for clarity

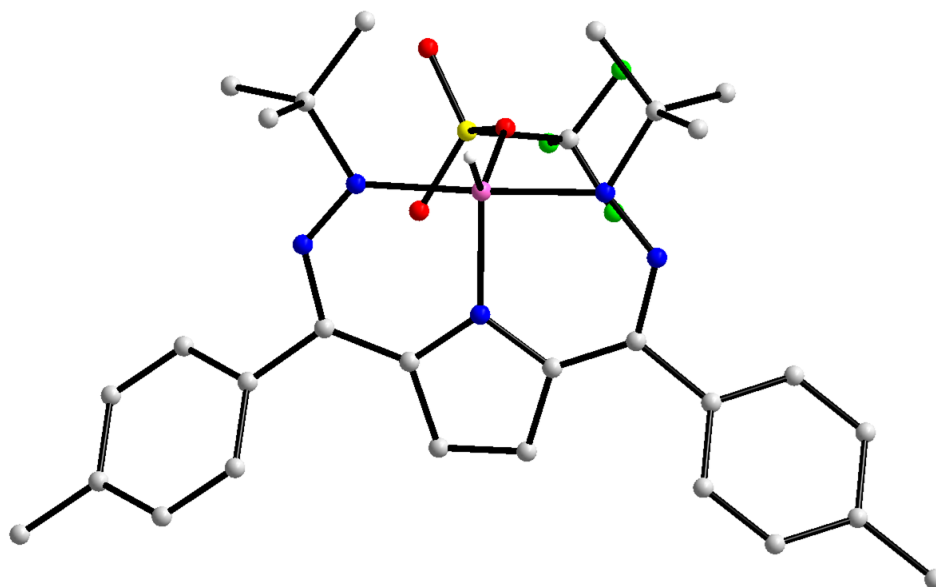


Figure S24. Calculated structure of  $[\text{tBu,TolDHP}]\text{Co-H}$ . All C–H hydrogen atoms have been removed for clarity

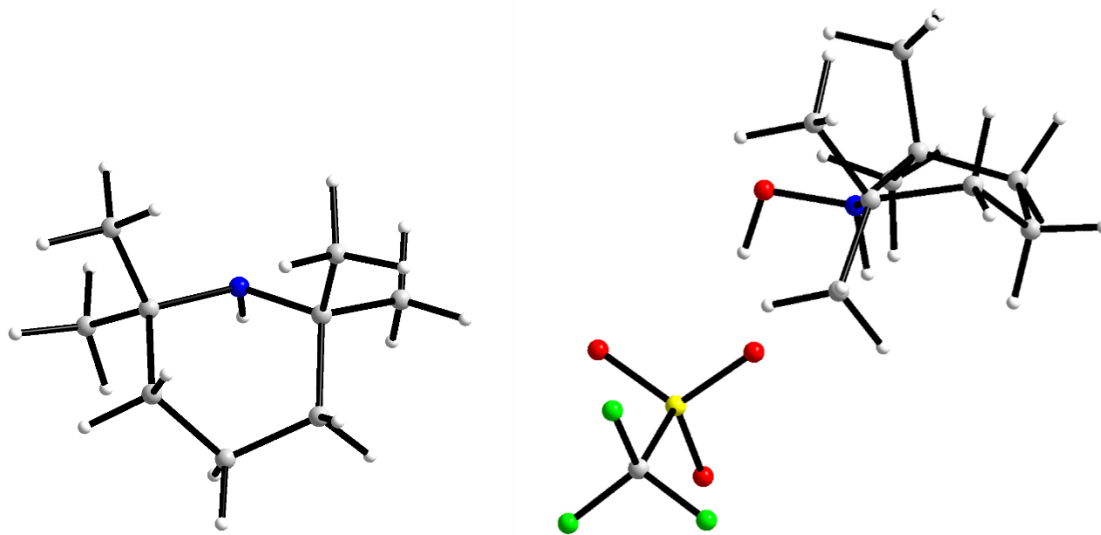


Figure S25. Calculated structure of 2,2,6,6-piperidine and [1-hydroxy-2,2,6,6-tetramethylpiperidin-1-ium][OTf]

Table S3. Compared electronic energies of intermediates to form **1** without accounting for entropic contributions.

	[ <sup><i>t</i></sup> Bu, Tol]DHP]CoOTf	TEMPOH	TEMPO	[ <sup><i>t</i></sup> Bu, Tol]DHP]CoOTf (TEMPOH)	<b>1</b>	<b>OTf</b>
HS- $S = 3/2$ (Eh)— charged	-2741.12	N/A	N/A	-3224.492	N/A	N/A
HS- $S = 1$ (Eh)— charged	N/A	N/A	N/A	N/A	N/A	N/A
LS- $S = 1/2$ (Eh)— charged	-2741.14	N/A	N/A	-3224.496	N/A	N/A
HS- $S = 3/2$ (Eh)	-3702.05	N/A	N/A	-4185.38	N/A	N/A
HS- $S = 1$ (Eh)	N/A	N/A	N/A	N/A	-4185.98	N/A
LS- $S = 1/2$ (Eh)	-3702.06	N/A	-482.75	-4185.39	N/A	N/A
$S = 0$ (Eh)	N/A	-483.33	N/A	N/A	N/A	-960.86
$\Delta$ (HS-LS) (kcal/mol)	12.55/8.26	N/A	N/A	2.51/5.74	N/A	N/A

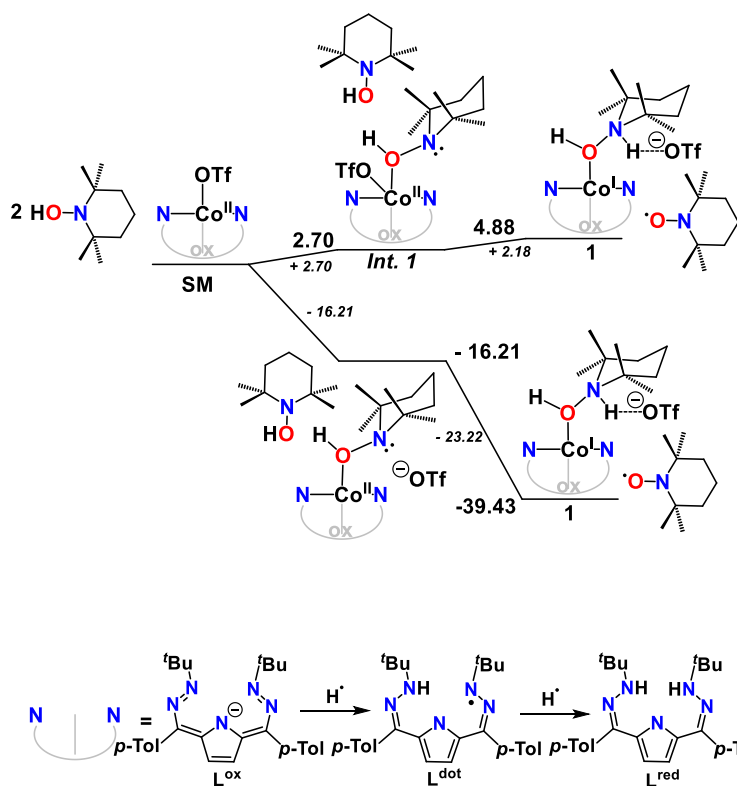


Figure S26. Simplified formation of **1** with electronic energies (without accounting for entropic contributions).

Table S4. Compared Gibbs free energies of intermediates to form **1** with accounting for entropic contributions.

	[ <sup>t</sup> Bu, Tol] <sup>DHP</sup> CoOTf	TEMPOH	TEMPO	[ <sup>t</sup> Bu, <sup>Tol</sup> DHP]CoOTf (TEMPOH)	<b>1</b>	<b>OTf</b>
LS- <i>S</i> = 1 (Eh)-- charged	N/A	N/A	N/A	N/A		N/A
LS- <i>S</i> = 1/2 (Eh)--charged	-2740.64	N/A	N/A	-3223.74	N/A	N/A
LS- <i>S</i> = 1 (Eh)	N/A	N/A	N/A	N/A	- 4185.19	N/A
LS- <i>S</i> = 1/2 (Eh)	-3702.06	N/A	-482.53	-4184.61	N/A	N/A
LS- <i>S</i> = 0 (Eh)	N/A	-483.10	N/A	N/A	N/A	- 960.86

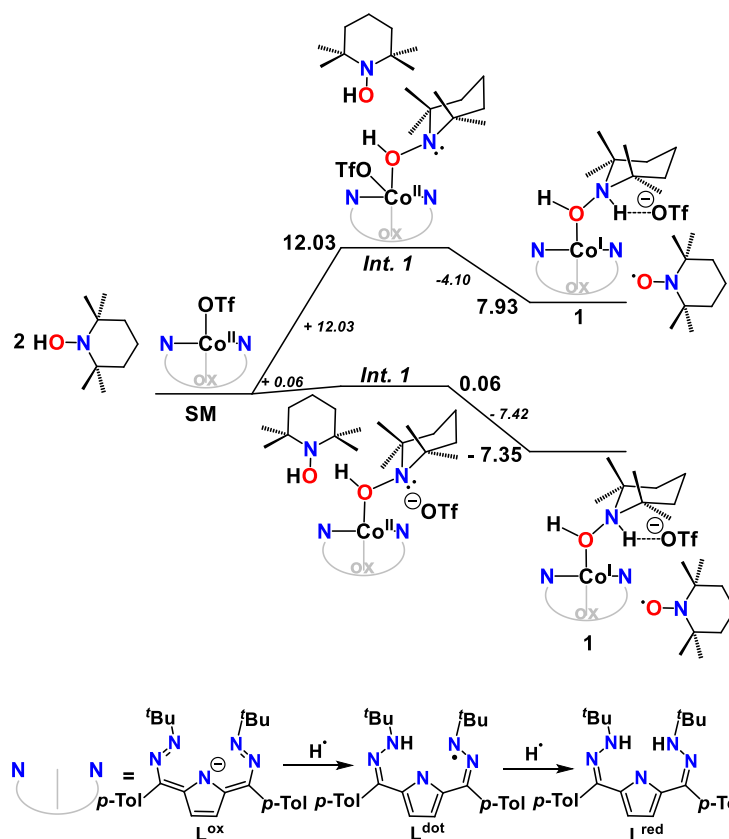


Figure S27. Simplified formation of **1** with Gibbs free energies (accounting for entropic contributions).

Table S5. Compared electronic energies of various potential intermediates along decomposition for **1** without accounting for entropic contributions.

	<b>2</b>	2,2,6,6-piperidine	[1-hydroxy-2,2,6,6-tetramethylpiperidin-1-ium][OTf]	[ <sup>t</sup> Bu, <sup>p</sup> Tol]DHP][OTf]Co-H	[ <sup>t</sup> Bu, <sup>p</sup> Tol]DHP-H]Co
$S = 3/2$ (Eh)	N/A	N/A	N/A	N/A	N/A
$S = 1$ (Eh)	-3777.77	N/A	N/A	-3702.61	-3702.65
$S = 1/2$ (Eh)	N/A	N/A	N/A	N/A	N/A
$S = 0$ (Eh)	-3777.77	-408.26	-1444.68	-3702.62	-3702.64

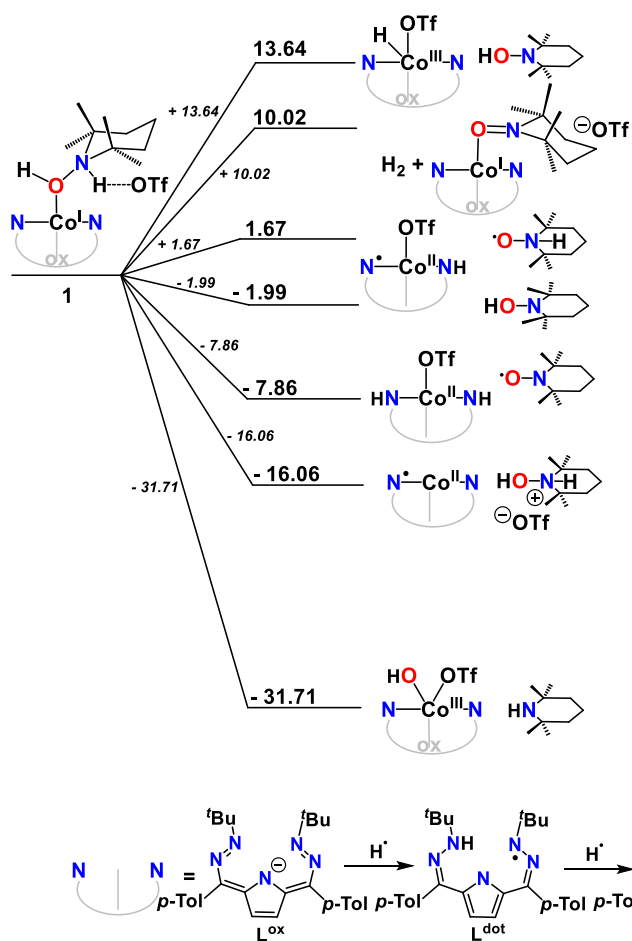


Figure S28. Simplified decomposition pathways for **1** with electronic energies (without accounting for entropic contributions).

Table S6. Compared Gibbs free energies of various potential intermediates along decomposition for **1** with accounting for entropic contributions.

$S = 1$ (Eh)	<b>2</b>	2,2,6,6-piperidine
$S = 0$ (Eh)	-3777.24	N/A
	N/A	-408.03

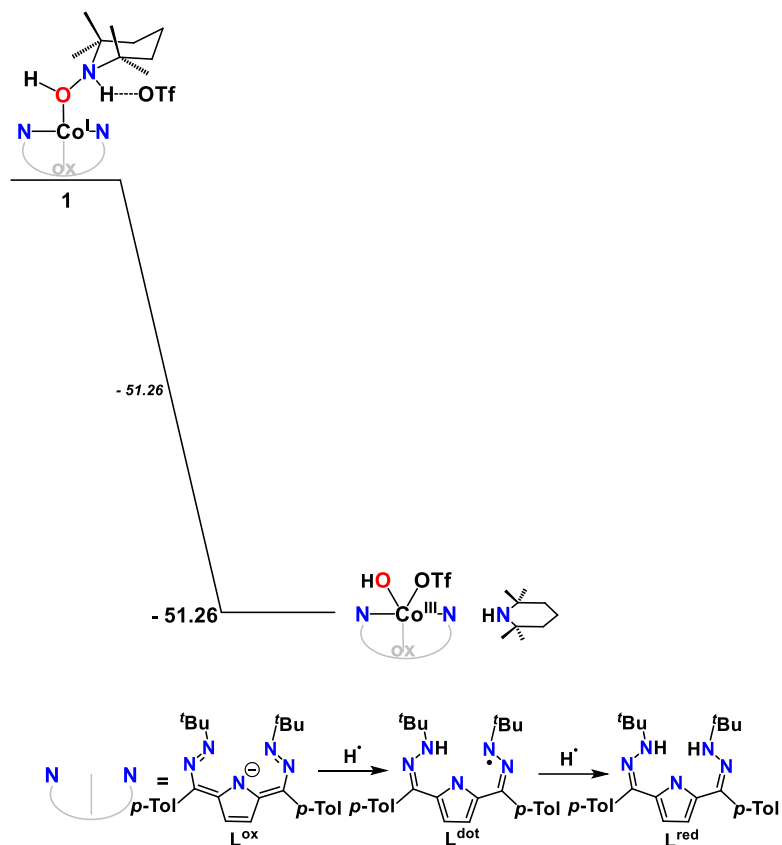
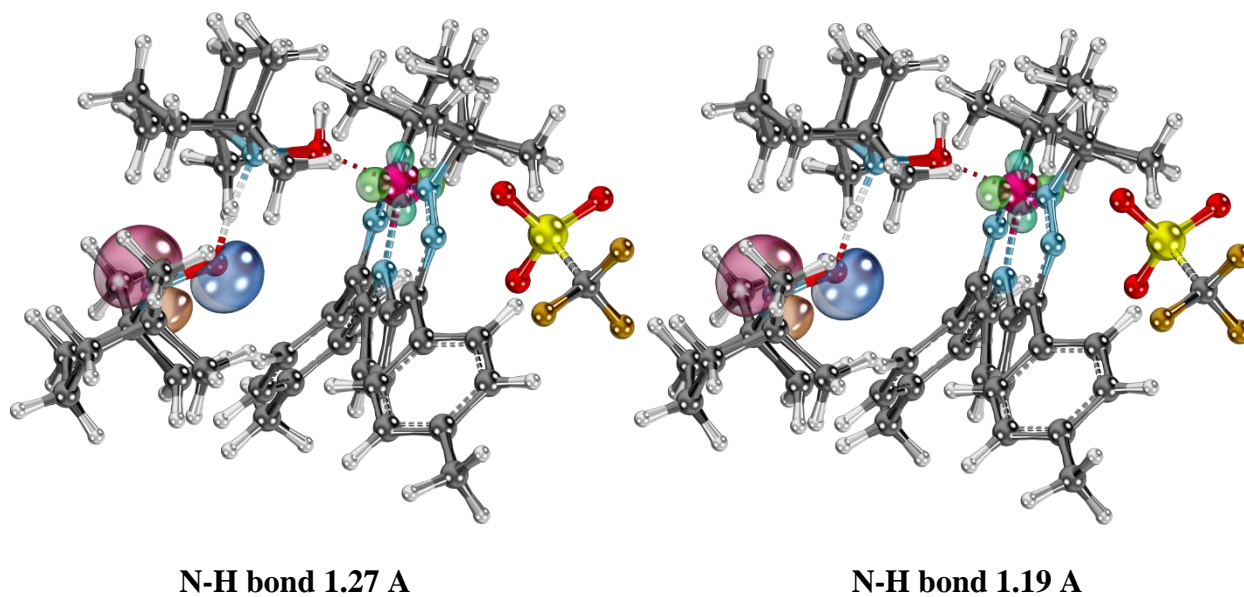


Figure S29. Simplified Gibbs free energy diagram of the decomposition pathways for **1** (accounting for entropic contributions).



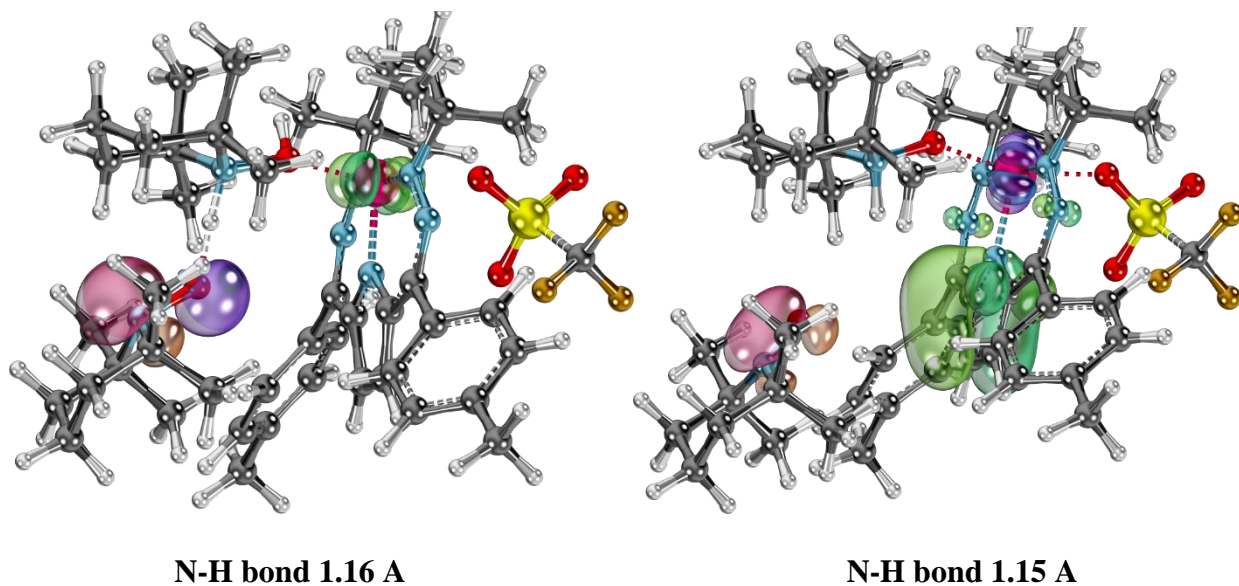


Figure S30. IBO surface scan showing the electron and proton transfer from a second equivalent of TEMPOH to  $[\text{t}^{\text{Bu}}, \text{Tol}]\text{DHPCoOTf}] \text{TEMPOH}$  to form **1**.

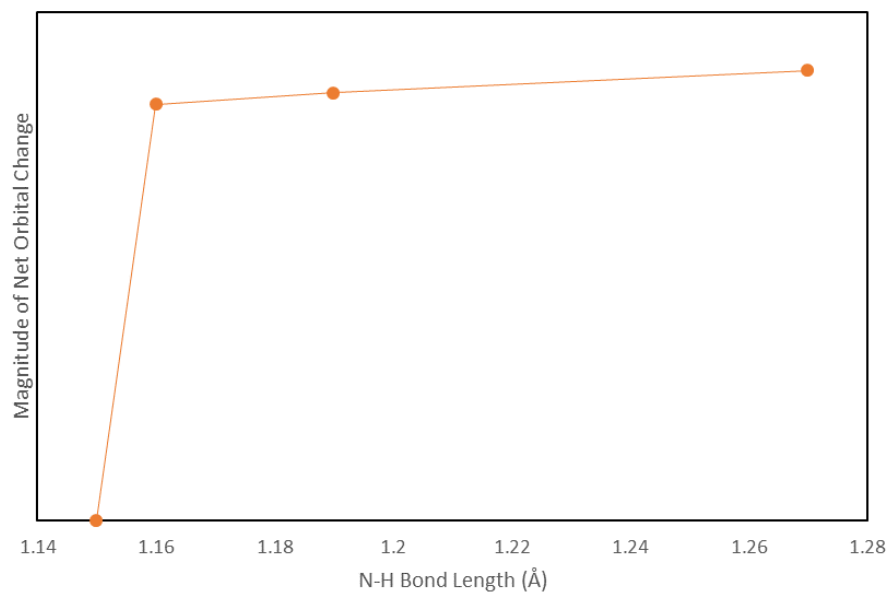


Figure S31. IBO surface scan showing the magnitude of orbital change over the steps shown in Figure S32 (showing the electron transfer from a second equivalent of TEMPOH-- going from  $[\text{t}^{\text{Bu}}, \text{Tol}]\text{DHPCoOTf}] \text{TEMPOH}$  to **1**).

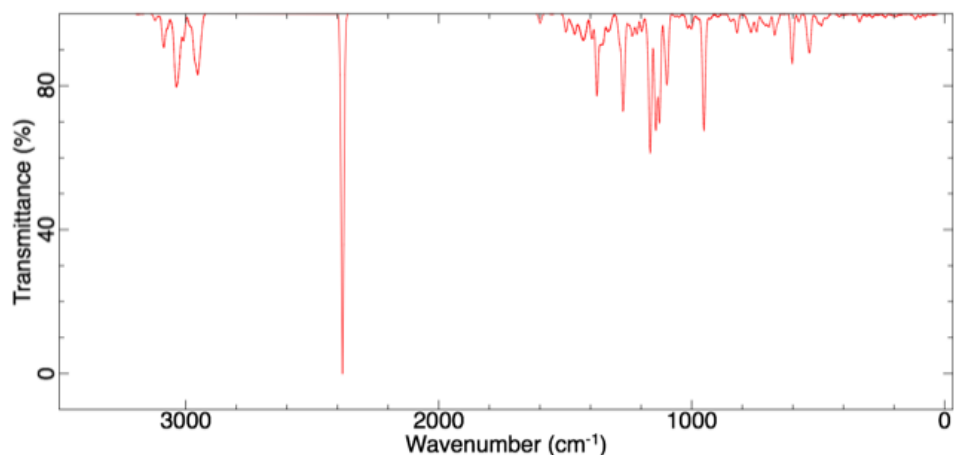


Figure S32. Calculated IR spectrum of **1**.

Table S7. Calculated vs. experimental values.

	(2) O-H <sup>a</sup>	(1) N-H <sup>a</sup>	(1) O-H <sup>a</sup>
experimental value		3058.6 (between 2945-3143)	3111.2, (between 2945-3143)
theoretical value		3066.8	3180.2 (calc.)
Scaling Factor for B3P/TZVP <sup>5</sup>		0.964	
		2956.4	3065.7
Theor./Exp.			
Ratio		0.97	0.99

<sup>a</sup> units of cm<sup>-1</sup>

The theoretical stretching frequencies were determined from the B3P DFT calculation for the structure of **1**. The ratio of the theoretical stretches compared to the observed is 0.99 for the O-H stretch and 0.97 for the N-H stretch, or in other words, shows that the data observed is a very good match for the theoretical values.

## References

1. G. M. Sheldrick, *Acta Cryst.* **2015**, *C71*, 3-8.

2. O. V. Dolomanov, L. J. Bourhis, R. J. Gildea, A. K. Howard, H. Puschmann, *J. Appl. Cryst.* **2009**, *42*, 339.
  3. G. M. Sheldrick. *Acta Cryst.* **2008**, *A64*, 112-122.
  4. (a) Neese, F. "The Orca Program System" *Wiley Interdisciplinary Reviews: Computational Molecular Science* **2012**, *2*, 73-78. (b) H - Kr: A. Schaefer, H. Horn and R. Ahlrichs, *J. Chem. Phys.* **1992**, *97*, 2571. (c) Rb - Xe: A. Schaefer, C. Huber and R. Ahlrichs, *J. Chem. Phys.* **1994**, *100*, 5829. (d) F. Weigend, R. Ahlrichs, *Phys. Chem. Chem. Phys.* **2005**, *7*, 3297.
  5. NIST Computational Chemistry Comparison and Benchmark Database, NIST Standard Reference Database Number 101. Release 21, August 2020, Editor: Russell D. Johnson III
-

## Appendix III: Chapter IV Supplementary Information

### NMR spectroscopy

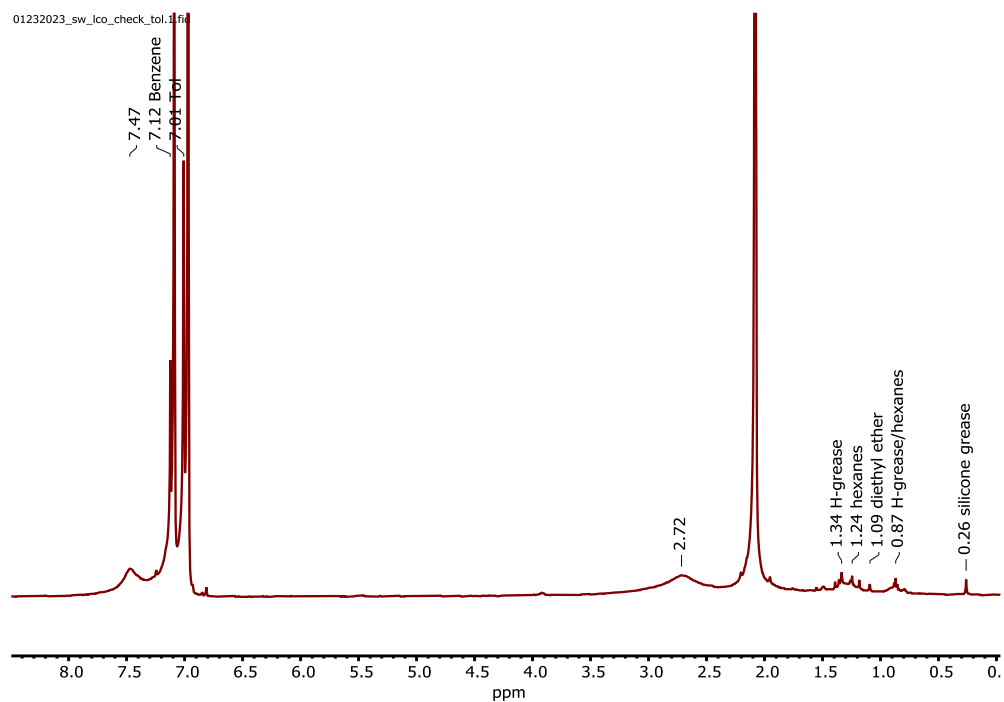


Figure S1.  $^1\text{H}$ NMR of  $(t\text{Bu},\text{Tol})\text{DHP})\text{Co}$  (**2**) in  $\text{C}_7\text{D}_8$ .

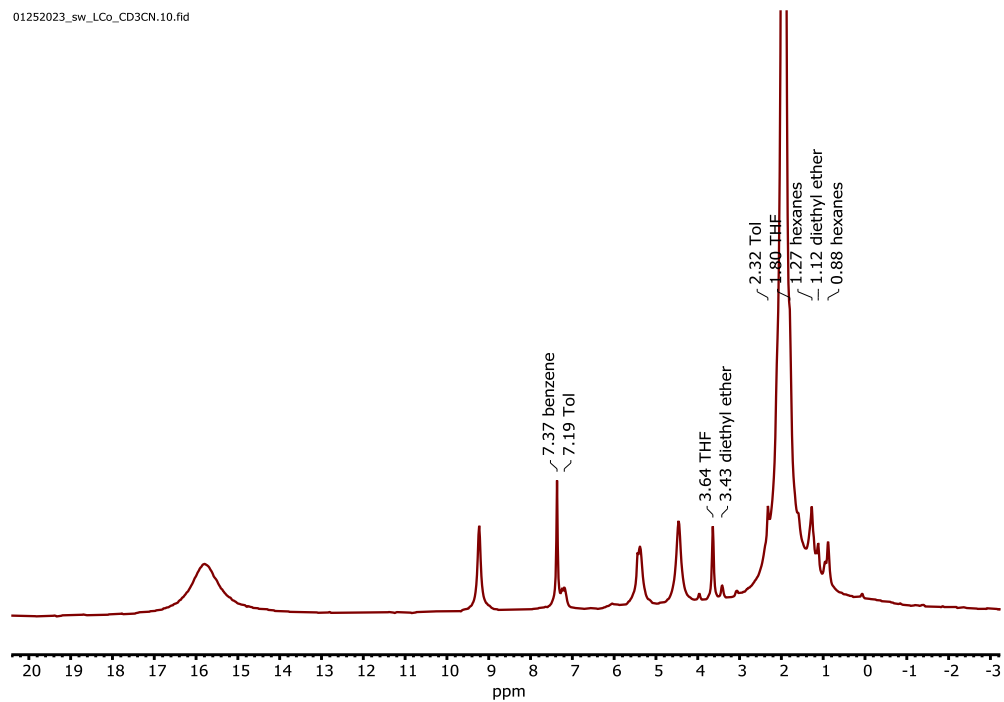


Figure S2.  $^1\text{H}$  NMR of ( $t^{\text{Bu,Tol}}$ DHP)Co (**2**) in  $\text{CD}_3\text{CN}$ .

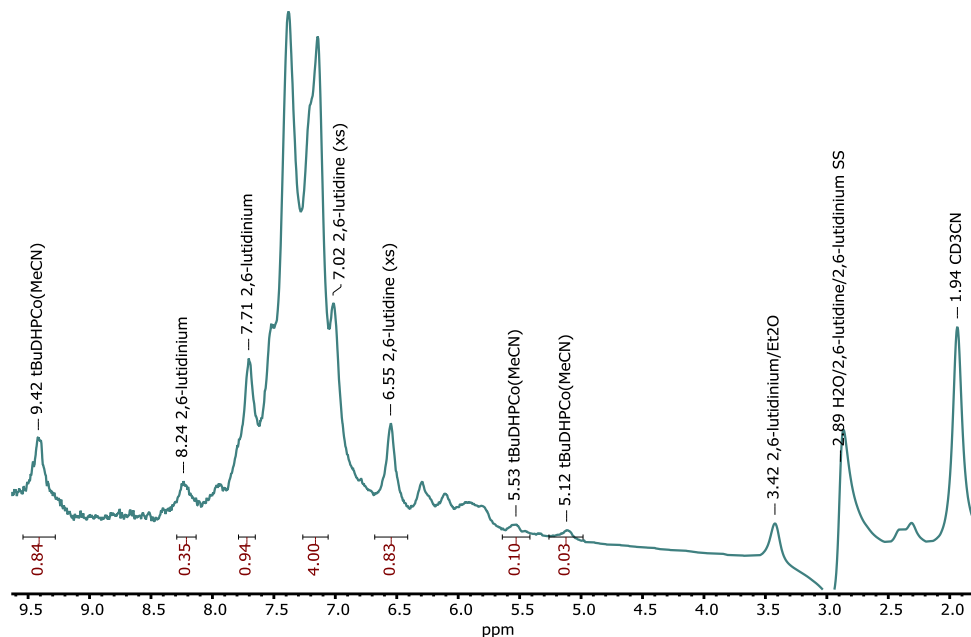


Figure S3.  $^1\text{H}$  NMR in  $\text{CD}_3\text{CN}$  of reaction between ( $t^{\text{Bu,Tol}}$ DHP)CoCl (**1**) in  $\text{Et}_2\text{O}$ ,  $\text{H}_2\text{O}$ , 2,6-lutidine, and NaI. Products observable are ( $t^{\text{Bu,Tol}}$ DHP)Co(MeCN) (**2-MeCN**), 2,6-lutidinium chloride, and residual 2,6-lutidine.

We could roughly quantify in the NMR 78% yield  $t^{\text{Bu,Tol}}$ DHPCo(MeCN) and 89% yield [2,6-lutidinium][Cl] relative to an internal standard of 1,2-difluorobenzene. A small amount of decomposition products (either due to lack of stability in MeCN or instability to acid or  $\text{H}_2\text{O}_2$ ) was also present, and concurrent quantification of  $\text{NaI}_3$  produced gave 40.0% yield (80% of the expected half-equivalent). This demonstrates a high yield of both the protonated base, as well as the product resulting from oxidation.

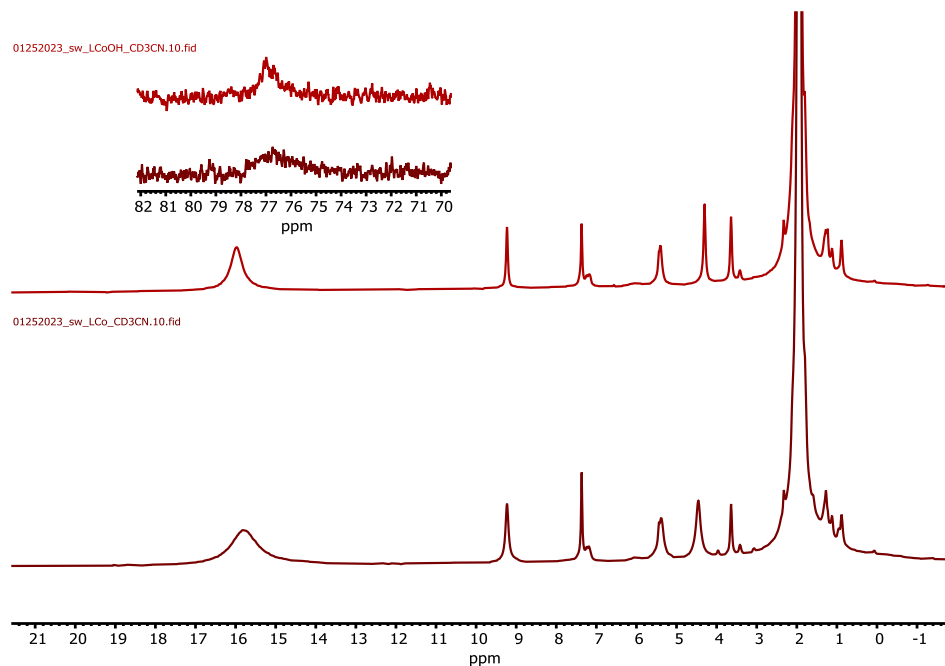


Figure S4. Comparison of  $^1\text{H}$  NMR of  $(t\text{Bu,TolDHP})\text{CoOH}$  (**1-OH**) in  $\text{CD}_3\text{CN}$  to  $^1\text{H}$  NMR of  $(t\text{Bu,TolDHP})\text{Co}$  (**2**) in  $\text{CD}_3\text{CN}$ .

Note that these spectra are identical, showing that **1-OH** converts to **2** with added MeCN.

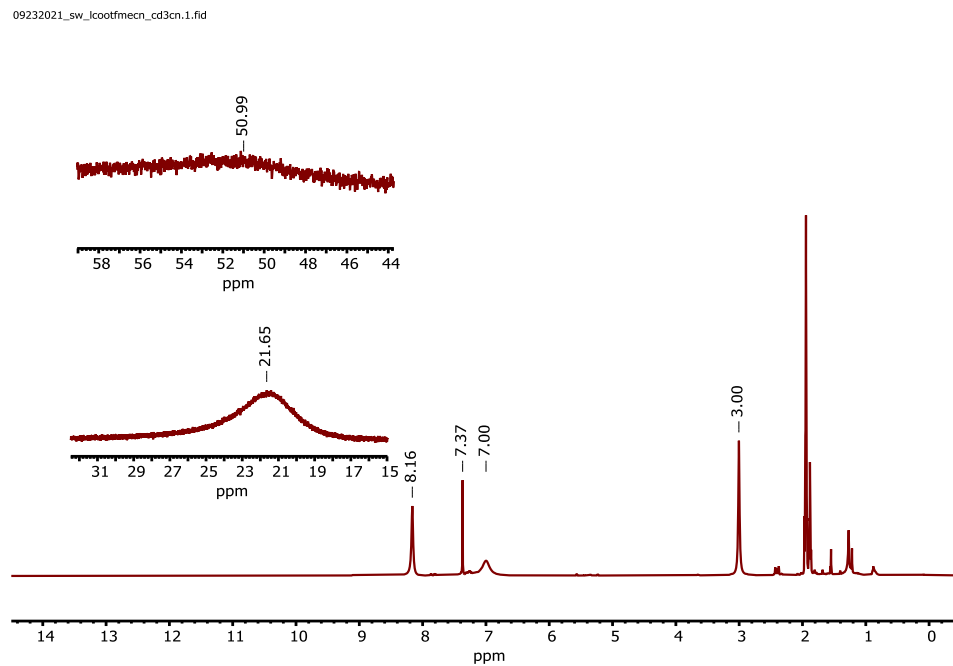


Figure S5.  $^1\text{H}$  NMR of  $(t\text{Bu,TolDHP})\text{CoOTf}$  (**1-OTf**) in  $\text{CD}_3\text{CN}$ .

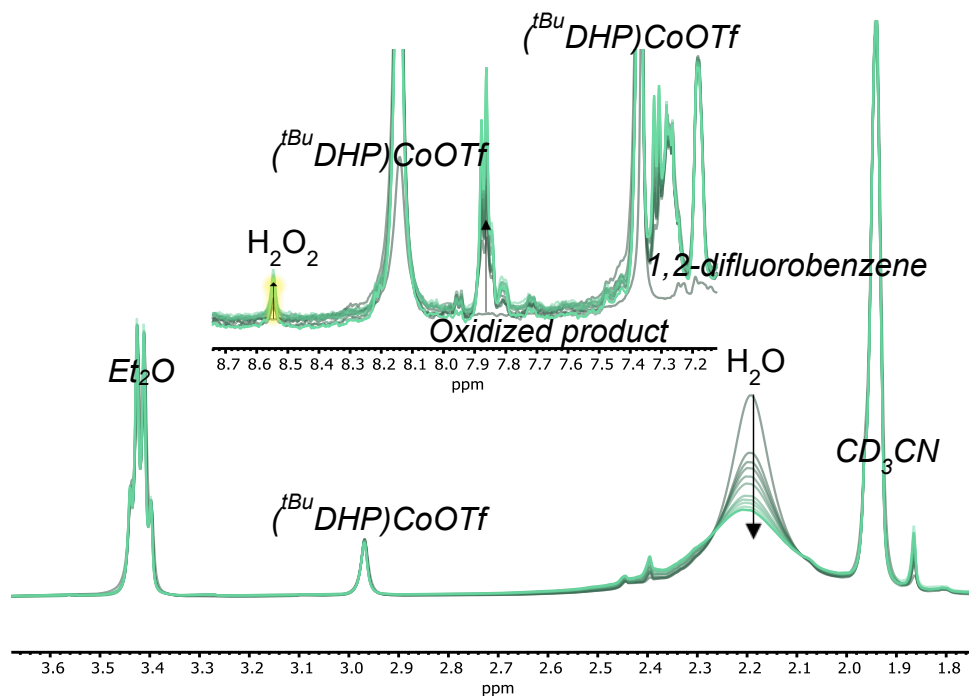


Figure S6.  $^1\text{H}$  NMRs of 20  $\text{H}_2\text{O}$  + 20  $\text{AgOTf}$  + **2** in  $\text{CD}_3\text{CN}$  over 1 hour.

Integrating over a series of timepoints, the  $\text{H}_2\text{O}$  peak at 2.25, a peak for **1-OTf** at 8.15, the two peaks for 1,2-difluorobenzene at 7.18 and 7.27, the  $\text{H}_2\text{O}_2$  peak at 8.6 and the solvent ( $\text{CD}_3\text{CN}$ ) residual peak at 1.94, it can be observed that after normalizing the solvent/difluorobenzene reference, the  $\text{H}_2\text{O}$  peak diminishes in area by 52% by the final timepoint, and up to 14% of that is reflected in the new  $\text{H}_2\text{O}_2$  peak. New peaks for an oxidized product from the ligand grow in at 7.85, 7.32, 2.39, and 1.86 ppm.

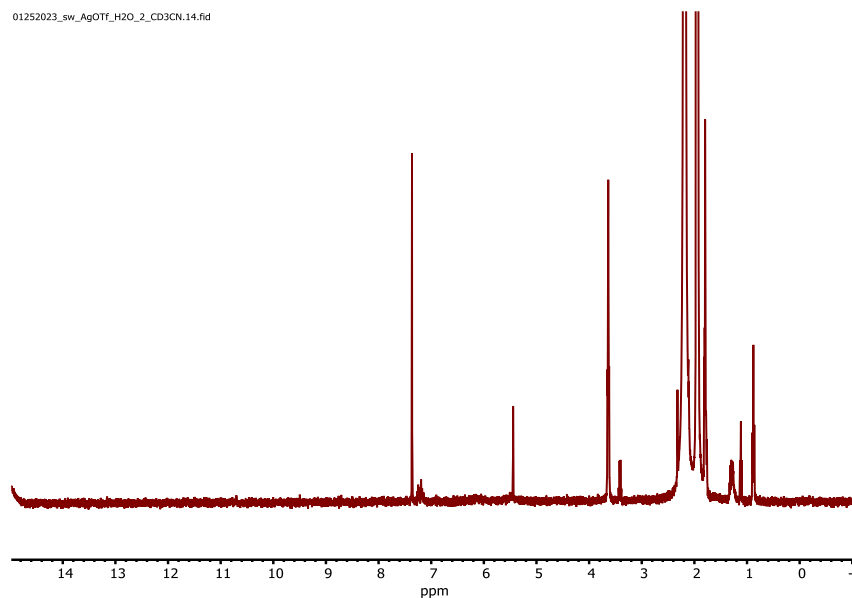


Figure S7. <sup>1</sup>H NMR of 20 H<sub>2</sub>O + 20 AgOTf in CD<sub>3</sub>CN.

### UV-vis spectroscopy

*All UV-Vis are done at scan speeds of 1200 nm/min unless otherwise specified*

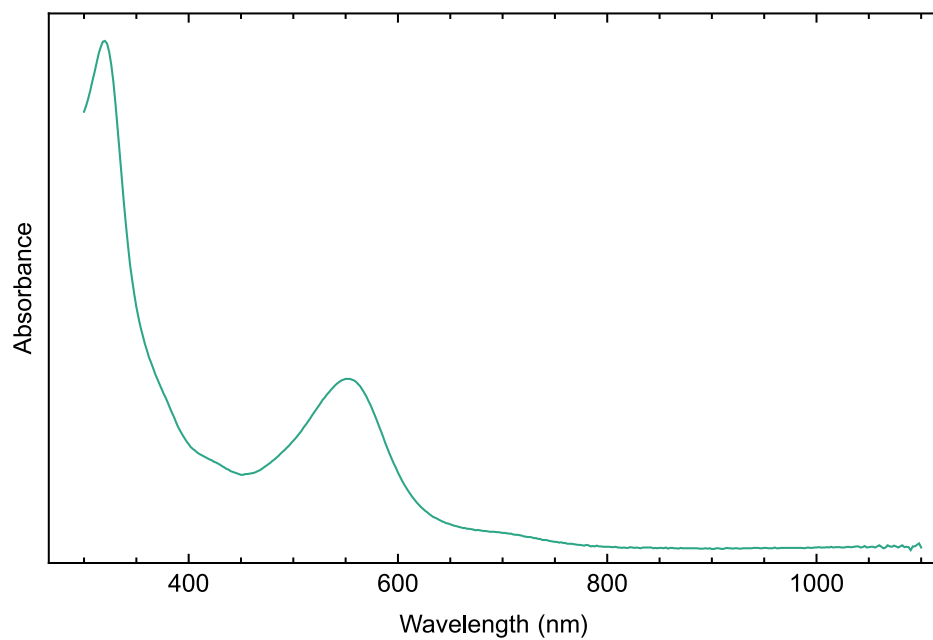


Figure S8. UV-vis of **2** from a 0.106 mM solution in diethyl ether at room temperature.

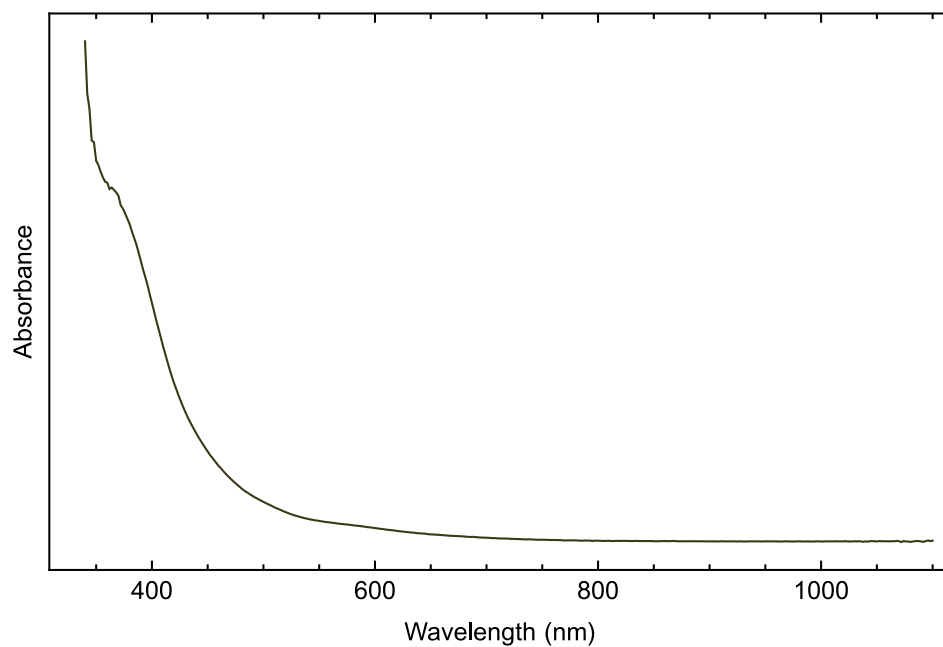


Figure S9. UV-vis of **2** from a 0.106 mM solution in diethyl ether at room temperature with 200 equiv. acetonitrile added/mixed in.

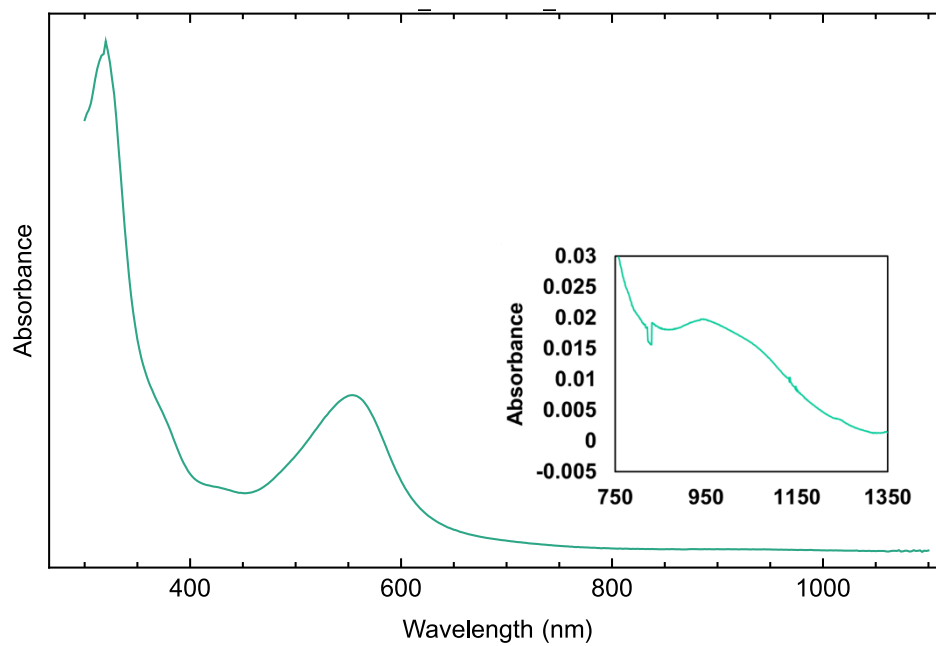


Figure S10. UV-vis of **1-OH** from a 0.153 mM solution in diethyl ether at room temperature.

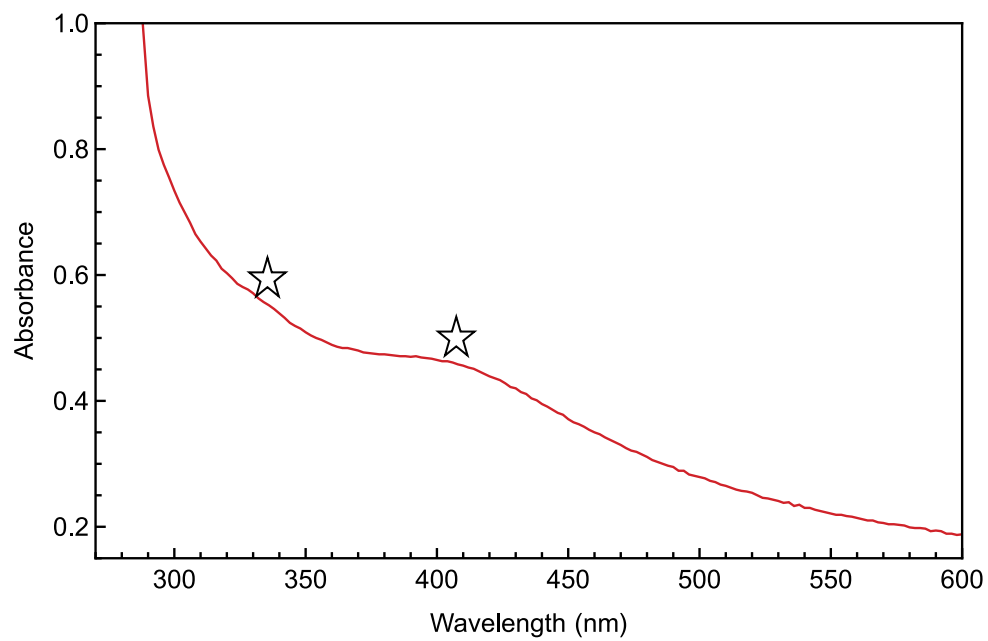


Figure S11. UV-vis of  $I_3^-$  generated from  $H_2O_2$  product and NaI from a solution in water at room temperature.

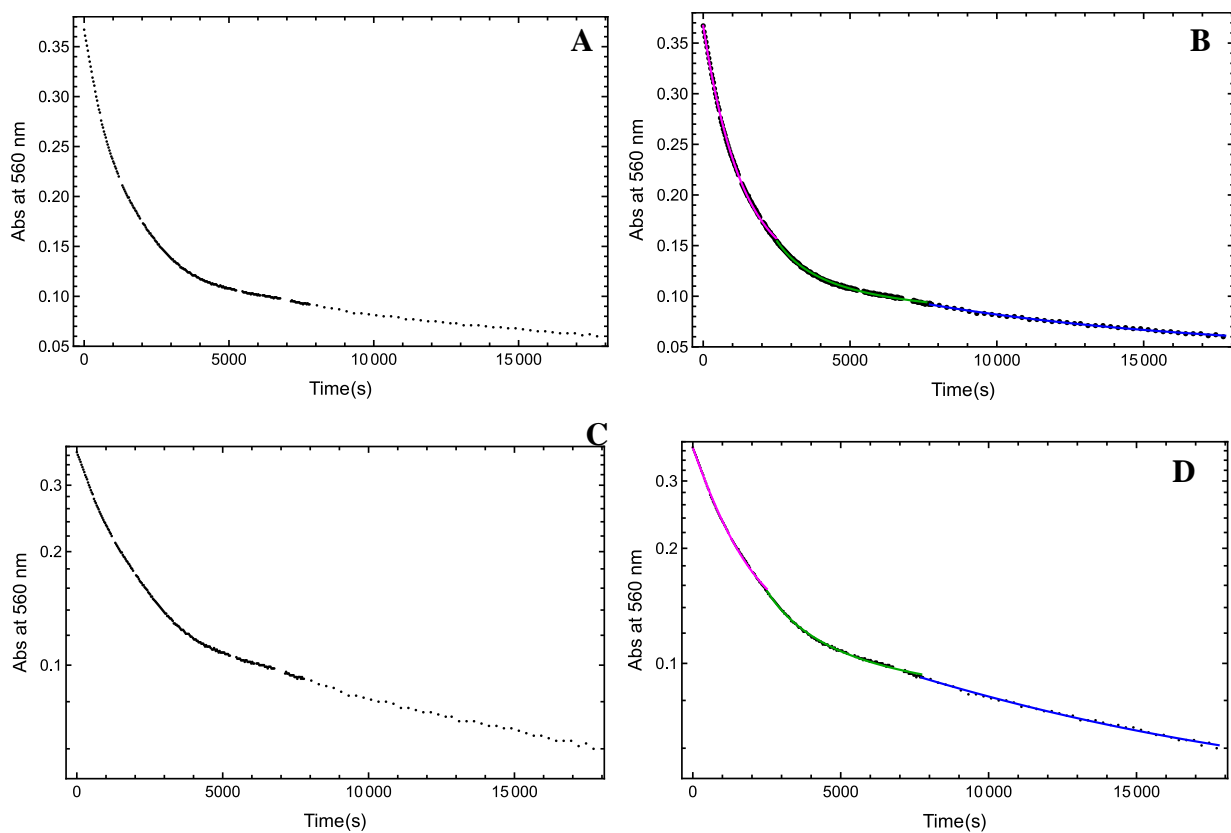


Figure S12. From left to right and top to bottom, A- Trace of the Reaction at 560 nm of **1-OH** (0.094 mM) with MeCN at 2 °C in diethyl ether, B- Fitted Trace of the Reaction at 560 nm of **1-OH** with MeCN at at 2 °C in diethyl ether, C- Log plot of 1 and D-Log plot of 2.

The varying colors correspond to the different fits for the formation of the different intermediates (pink, green, then blue). This reaction was done in triplicate, with this serving as a representative example.

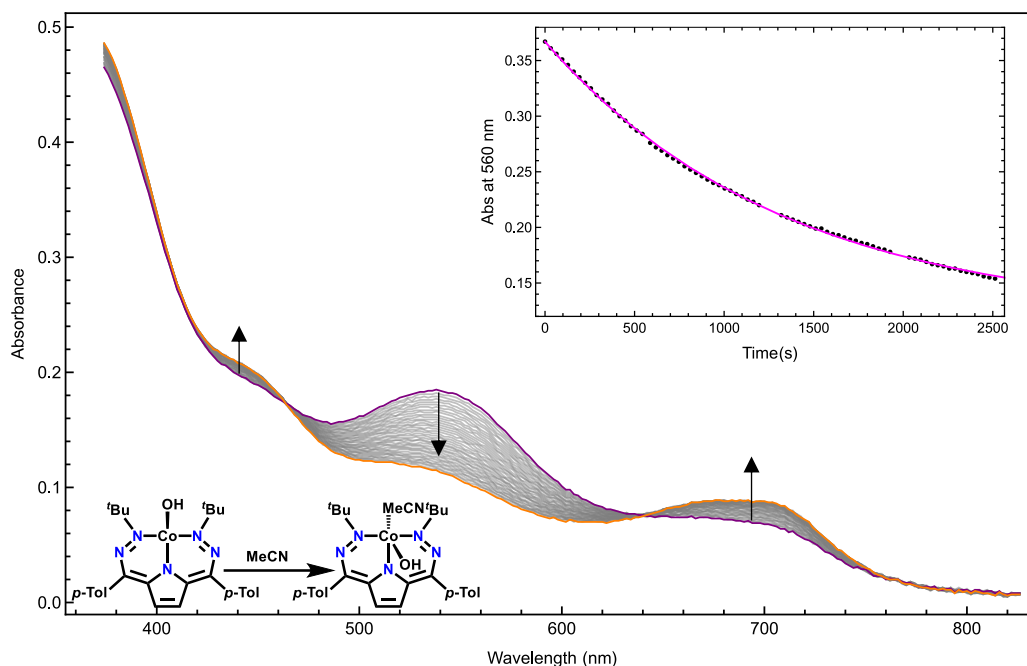


Figure S13. First intermediate formation in the reaction of **1-OH** (0.094 mM) with MeCN at 2 °C in diethyl ether with inset of the trace at 560 nm with the first-order fit of that data in magenta.

Equation 1. Derivation of fit shown above in Figure S13.<sup>1</sup>

$$[\text{Abs}] = (A_0 - A_{inf}) * e^{-k*t} + A_{inf}$$

$$[\text{Abs}] = ((0.367 - 0.119) * e^{-(0.000753)*t} + 0.119)$$

$$R^2 = 0.999971669949868$$

This fit derivation is from the Espenson treatment of first order fits<sup>4</sup> and takes into account both initial absorbance of reactant ( $A_0$ ) and the final absorbance for the reactant ( $A_{inf}$ ). In this fit,  $A_{inf}$ , and  $k$  parameters were used in the linear regression.

	"Estimate"	"Standard Error"
$k$	0.000753	0.0000057
$A_{inf}$	0.1189	0.00097

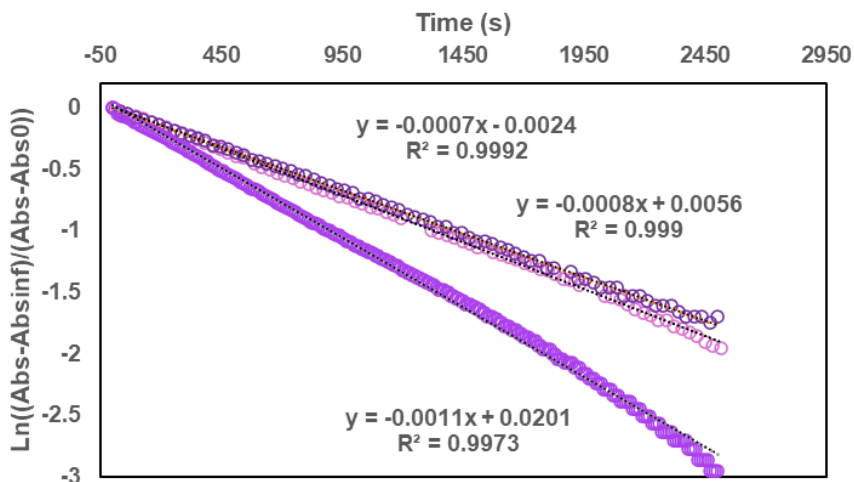


Figure S14. Linear fits for  $k$  in the first order fits of the data shown above (as well as a check for reproducibility in the reaction of **1-OH** at 0.094 mM, 0.043 mM, and 0.078 mM) with MeCN at 2 °C in diethyl ether.  $k_{\text{obs}} = 0.0009(2)$ .

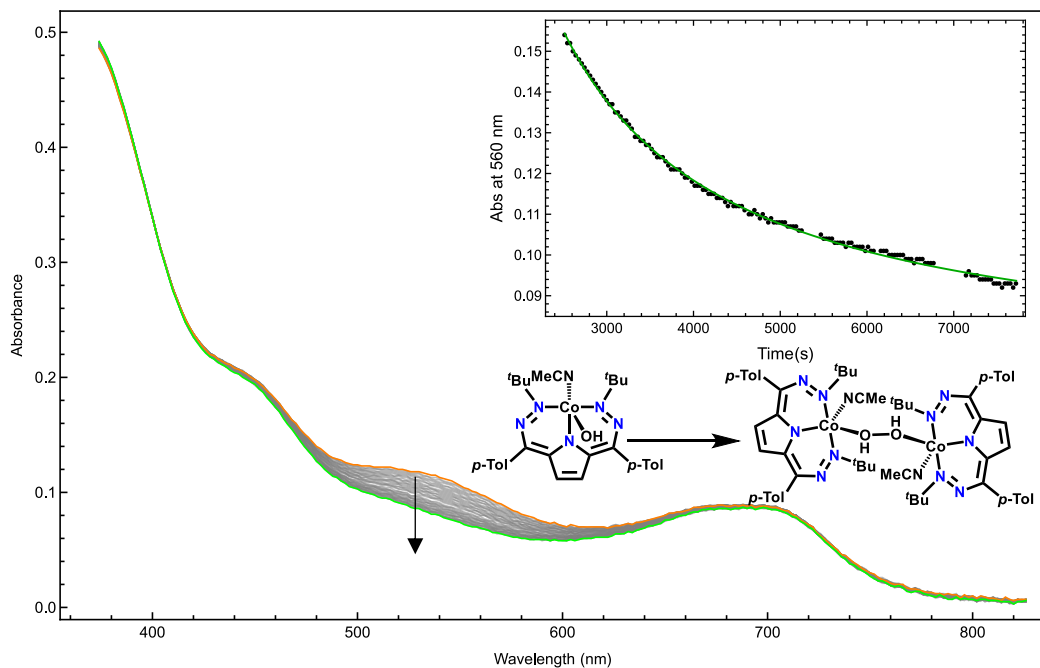


Figure S15. Second intermediate formation in the reaction of **1-OH** (0.094 mM) with MeCN at 2 °C in diethyl ether with inset of the trace at 560 nm with the second-order fit of that data in green.

Equation 2. Derivation of fit shown above in Figure S15.<sup>4</sup>

$$[\text{Abs}] = \left( \frac{A_0 + A_{inf} * (k * B_0)(t - t_0)}{1 + (k * B_0)(t - t_0)} \right)$$

$$[\text{Abs}] = \left( \frac{0.154 + 0.0709 * (0.000513)(t - 2513)}{1 + (0.000513)(t - 2513)} \right)$$

$$R^2 = 0.999916117467132$$

This fit derivation is from the Espenson treatment of second order fits<sup>4</sup> and takes into account both initial absorbance of reactant ( $A_0$ ) and product ( $B_0$ ), as well as the final absorbance for the reactant ( $A_{inf}$ ). In this fit,  $t_0$  was set to the initial time for the data-set, and other parameters were used in the linear regression. Due to the difficulty of determining  $B_0$  with fidelity, a  $k*B_0$  combined value is what is represented above.

""	"Estimate"	"Standard Error"
$k * B_0$	0.000513	0.0000098
$A_0$	0.1544	0.00026
$A_{inf}$	0.0709	0.0005

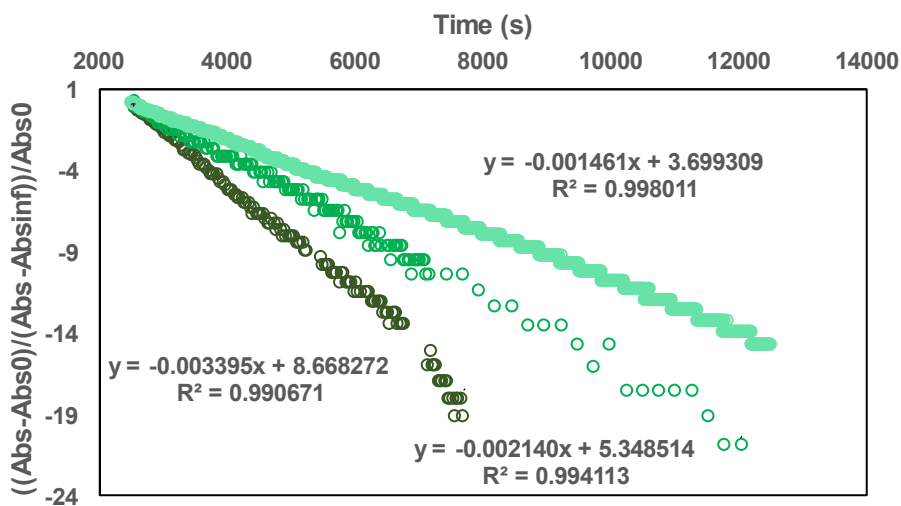


Figure S16. Linear fits in the second order fits of the data shown above (as well as check for reproducibility in the reaction of **1-OH** at 0.094 mM, 0.043 mM, and 0.078 mM) with MeCN at 2 °C in diethyl ether.  $k_{\text{obs}} = 0.0023(8)$ .

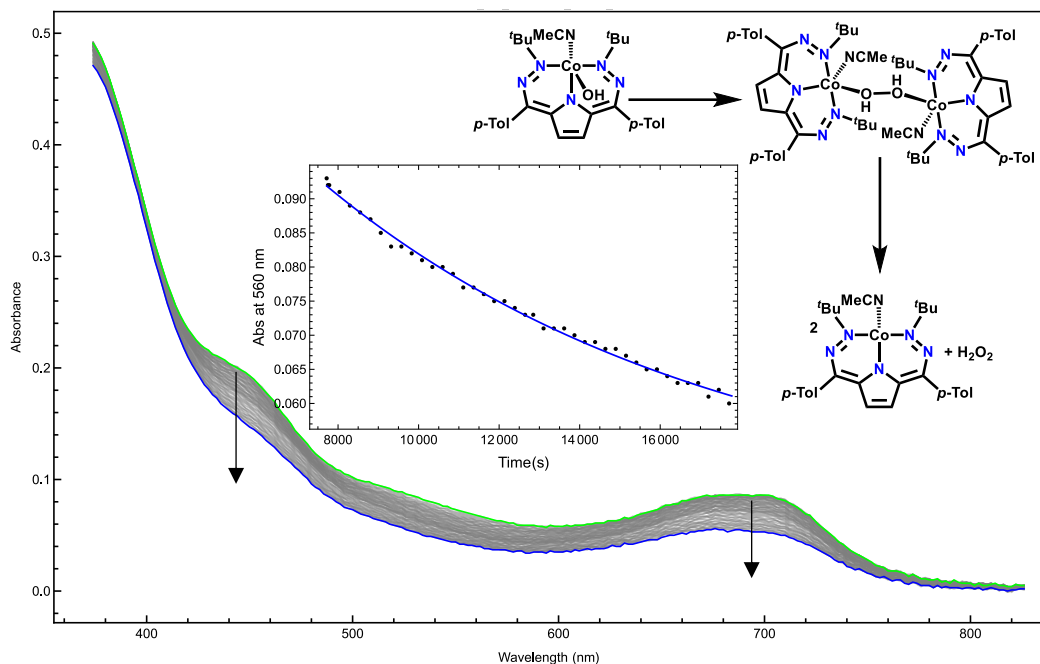


Figure S17. Third intermediate formation/bleaching begins in the reaction of **1-OH** (0.094 mM) with MeCN at 2 °C in diethyl ether with inset of the trace at 560 nm with the first-order fit of that data in blue.

This fit is based off-of limited data and is also less convincingly isosbestic.

Equation 3. Derivation of fit shown above in Figure S17.

$$[\text{Abs}] = (A_0 - A_{\text{inf}}) * e^{-k*t} + A_{\text{inf}}$$

$$[\text{Abs}] = ((0.149 - 0.0439) * e^{-(0.000102)*t} + 0.0439)$$

$$R^2 = 0.9999292480290332$$

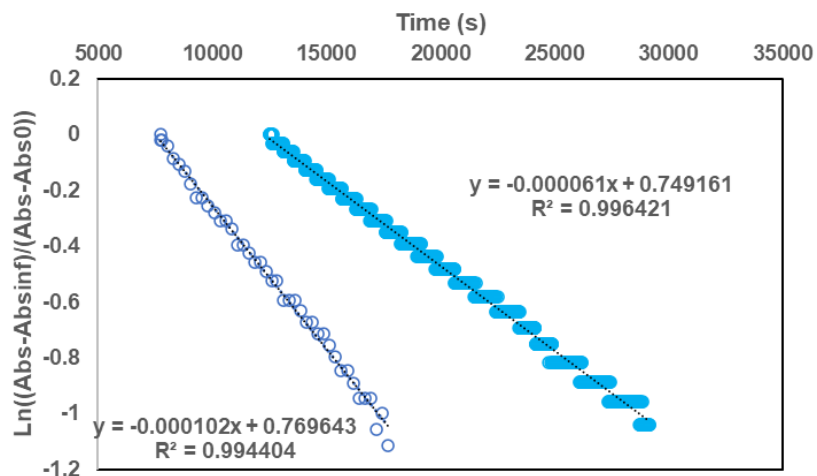


Figure S18. Linear fits in the second order fits of the data shown above (as well as check for reproducibility in the reaction of 1-OH at 0.094 mM, 0.043 mM, and 0.078 mM) with MeCN at 2 °C in diethyl ether.  $K_{\text{obs}} = 0.00008(2)$ .

### Vibrational Spectroscopy

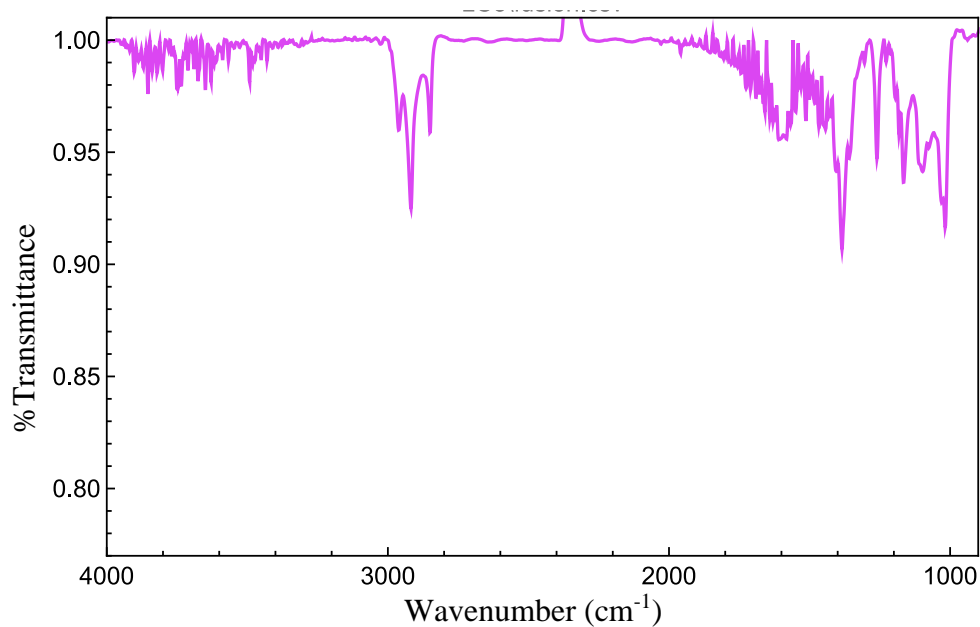


Figure S19. IR of **2** as a thin film. There is a peak for  $\text{CO}_2$  at  $2200 \text{ cm}^{-1}$  visible.

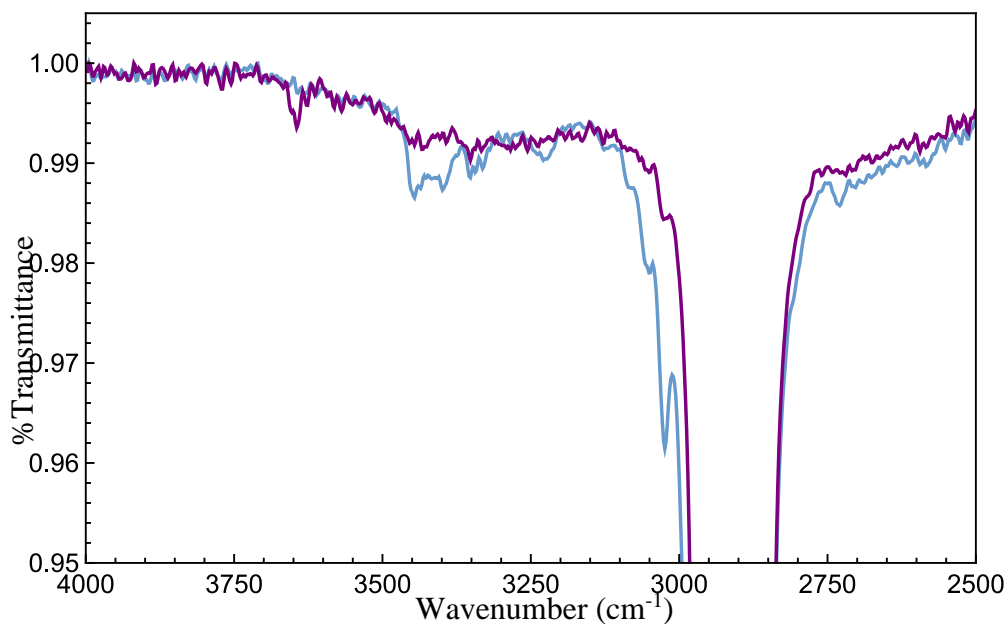


Figure S20. Zoomed in IR of crude **2** as a thin film (blue) and IR of **2** made in the presence of 2,6-lutidine as a thin film (purple). This data clearly shows additional peaks in the N-H region that are suppressed and replaced with a singular N-H peak in the presence of a base (2,6-lutidine, the base, becomes 2,6-lutidinium chloride)

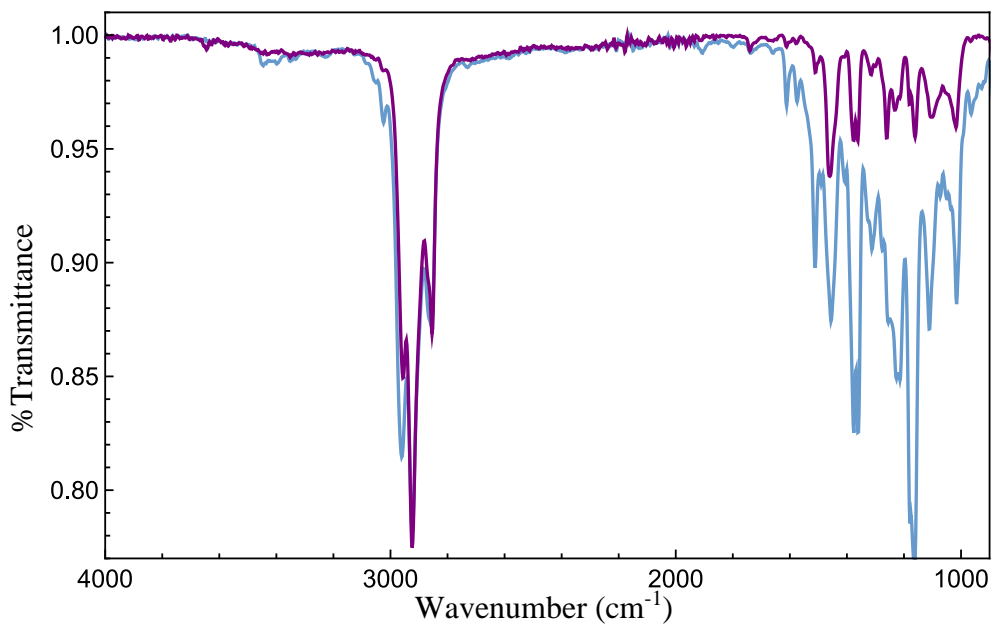


Figure S21. Full IR of crude **2** as a thin film (blue) and IR of **2** made in the presence of 2,6-lutidine as a thin film (purple).

### Cyclic Voltammetry

All cyclic voltammograms referenced to Fc/Fc<sup>+</sup> with exception of the CPEs and CCE which are referenced to Ag/AgCl.

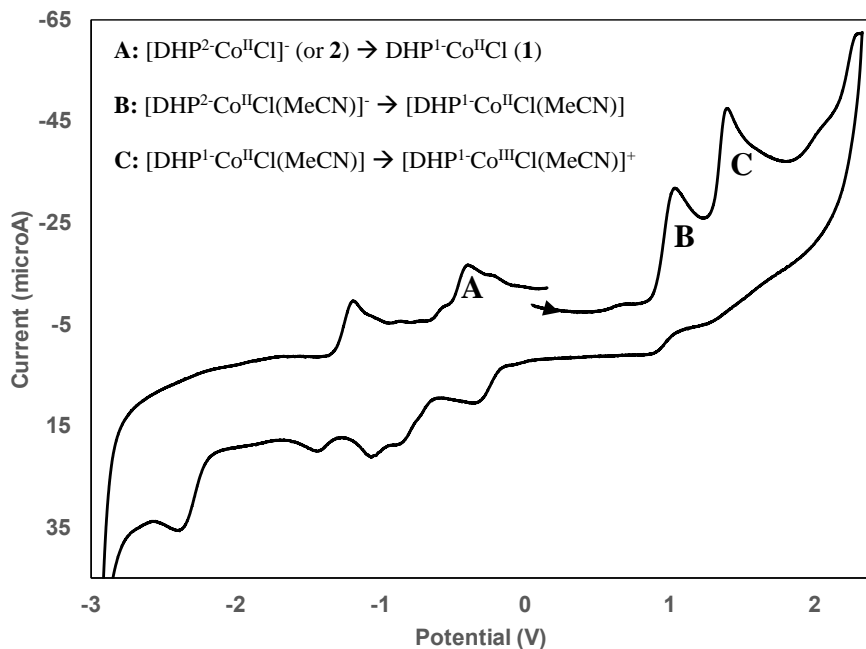


Figure S22. Cyclic Voltammogram of 1 mM of **1** in 0.1 M  $\text{NBU}_4\text{PF}_6$  acetonitrile (arrow placed at beginning of scan).

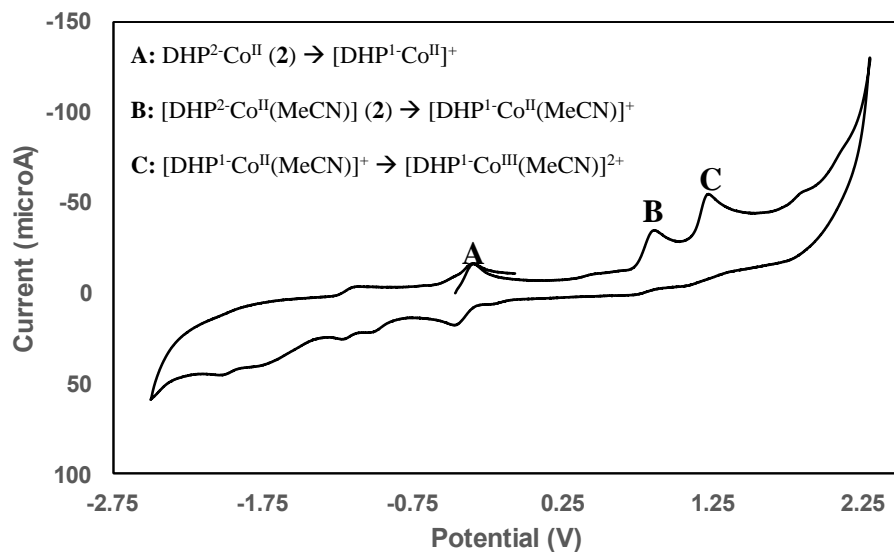


Figure S23. Cyclic Voltammogram of 1 mM of **2** in 0.1 M  $\text{NBu}_4\text{PF}_6$  acetonitrile.

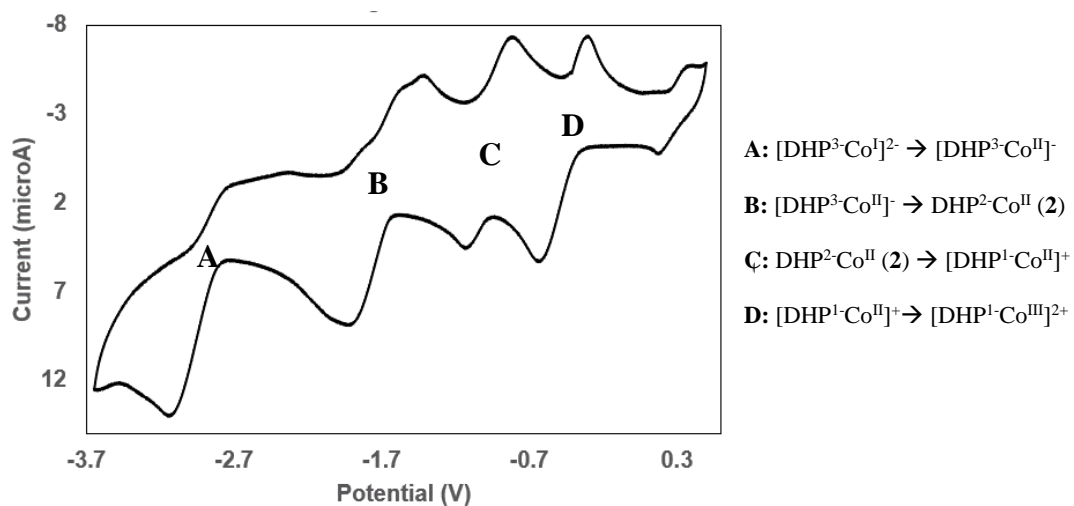


Figure S24. Cyclic Voltammogram of 1 mM of **2** in 0.1 M  $\text{NBu}_4\text{PF}_6$  tetrahydrofuran.

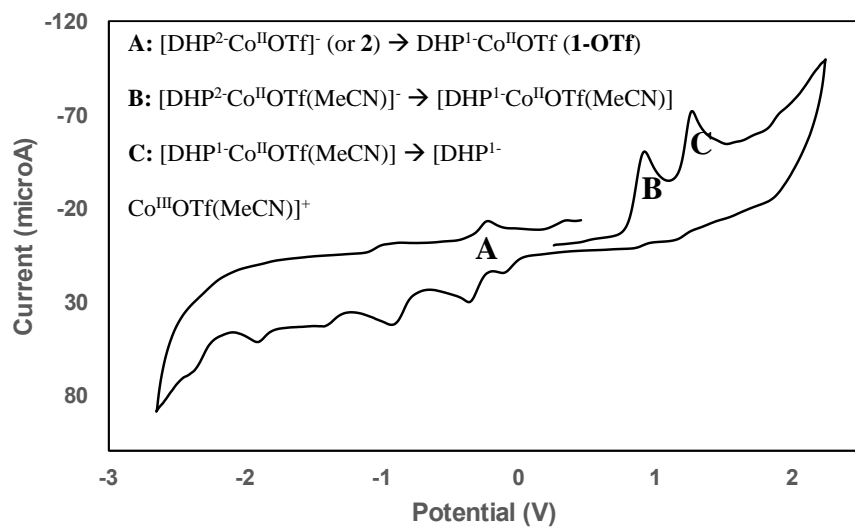


Figure S25. Cyclic Voltammogram of 1 mM of **1-OTf** in 0.1 M NBu<sub>4</sub>PF<sub>6</sub> acetonitrile.

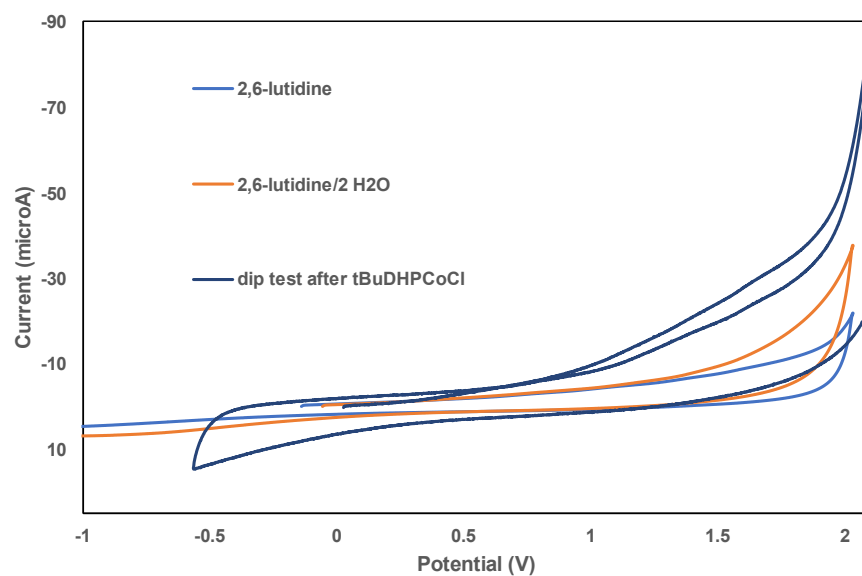


Figure S26. Cyclic Voltammogram of 0.16 M 2,6-lutidine, 0.32 M H<sub>2</sub>O and 0.16 M 2,6-lutidine, and a dip test of a used electrode in 0.32 M H<sub>2</sub>O and 0.16 M 2,6-lutidine in 0.1 M NBu<sub>4</sub>PF<sub>6</sub> acetonitrile.

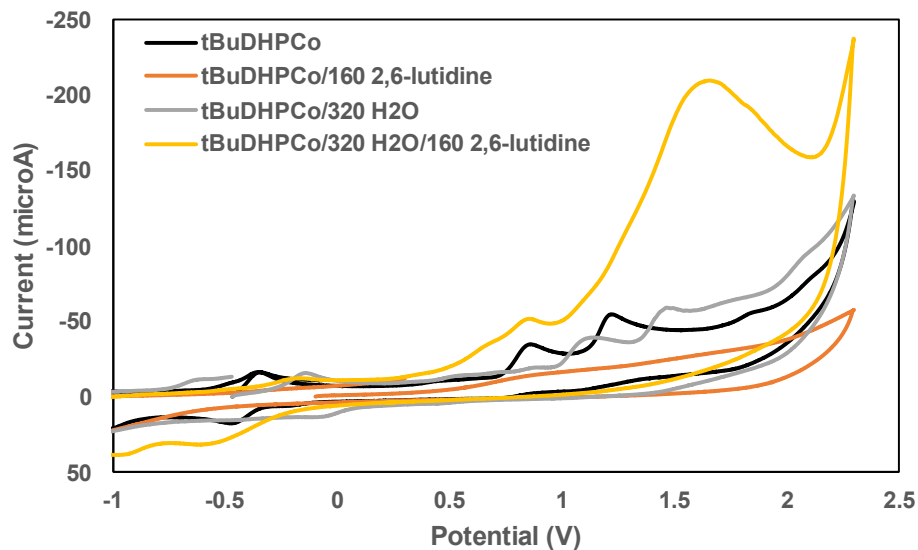


Figure S27. Cyclic Voltammograms of 1 mM **2**, H<sub>2</sub>O, and 2,6-lutidine in 0.1 M NBu<sub>4</sub>PF<sub>6</sub> in acetonitrile.

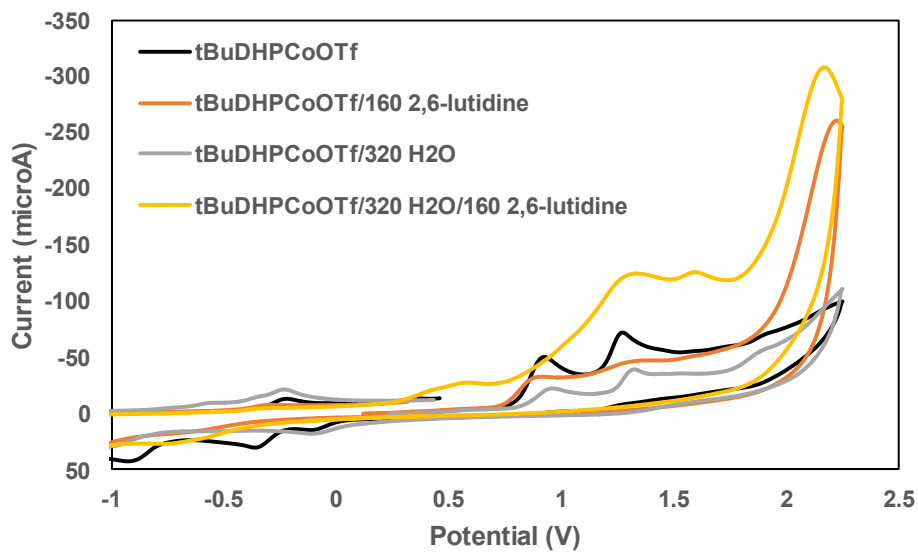


Figure S28. Cyclic Voltammograms of 1 mM **1-OTf**, H<sub>2</sub>O and 2,6-lutidine in 0.1 M NBu<sub>4</sub>PF<sub>6</sub> in acetonitrile.

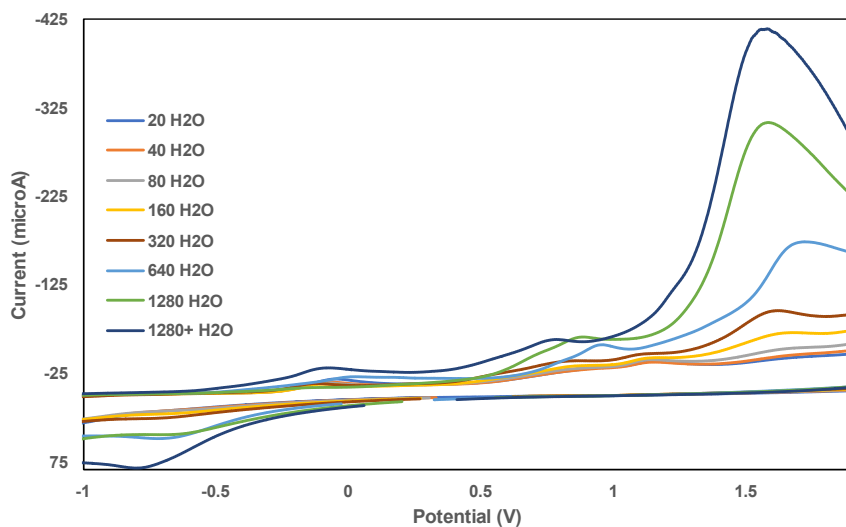


Figure S29. Cyclic Voltammograms of 1 mM **1**, 160 equiv. 2,6-lutidine, and variable amounts of H<sub>2</sub>O in 0.1 M NBu<sub>4</sub>PF<sub>6</sub> in acetonitrile.

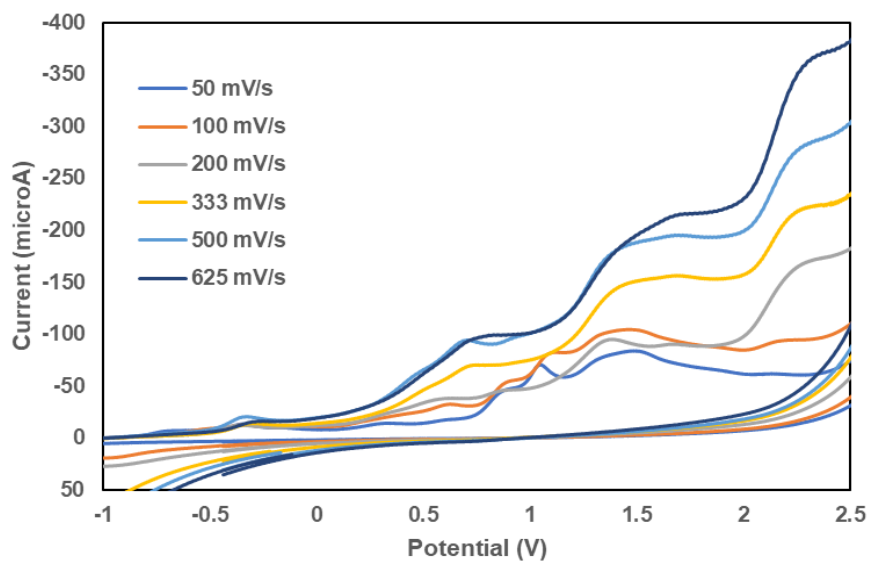


Figure S30. Cyclic Voltammograms of 1 mM **1**, 320 equiv. H<sub>2</sub>O and 160 equiv. 2,6-lutidine at varied scan rates in 0.1 M NBu<sub>4</sub>PF<sub>6</sub> acetonitrile.

Complicated peak shape makes it difficult to do foot-of-the-wave or other analyses.

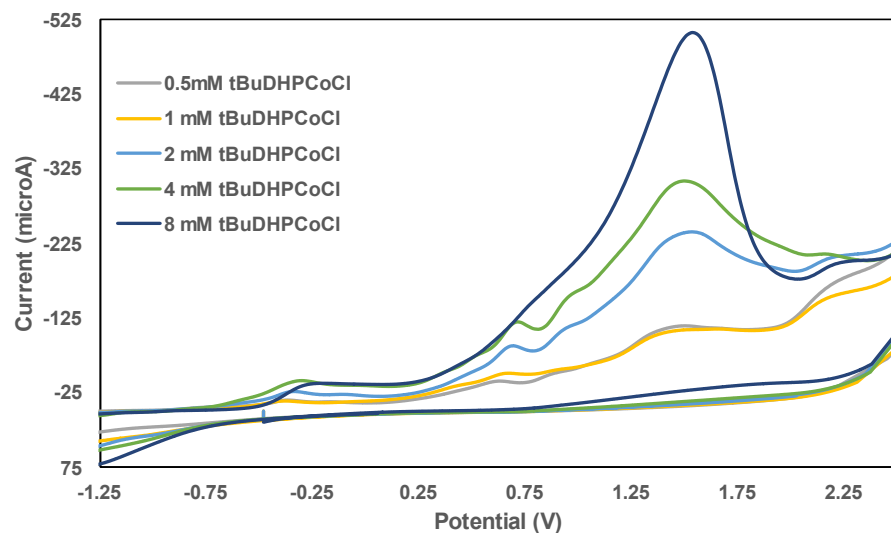


Figure S31. Cyclic Voltammograms of 0.32 M H<sub>2</sub>O and 0.16 M 2,6-lutidine in the presence of varied amounts of **1** in 0.1 M NBu<sub>4</sub>PF<sub>6</sub> acetonitrile.

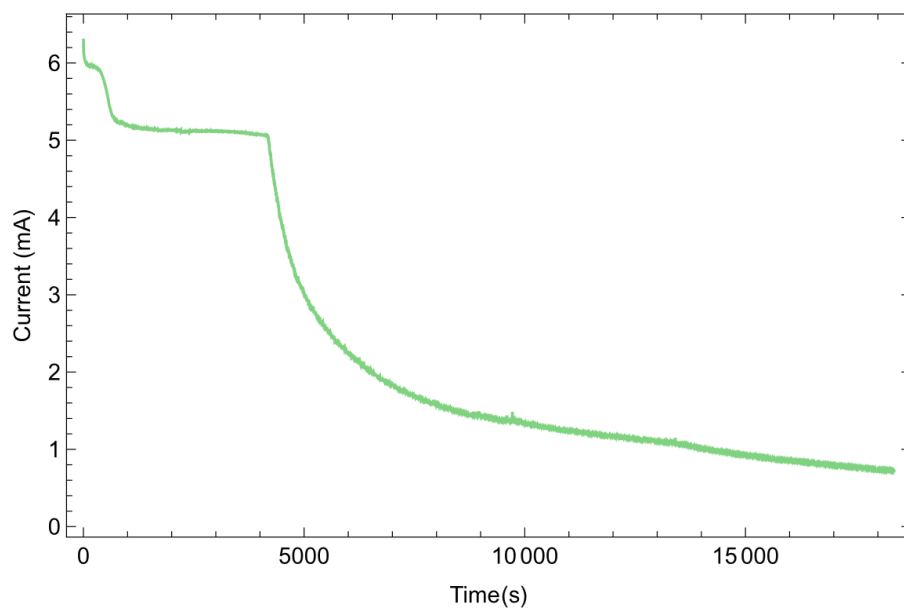


Figure S32. Bulk electrolysis at 1400 mV of 1 mM **1**, 320\*2 equiv. H<sub>2</sub>O (320 in each divided cell compartment) and 160 equiv. 2,6-lutidine in 0.1 M NBu<sub>4</sub>PF<sub>6</sub> acetonitrile.

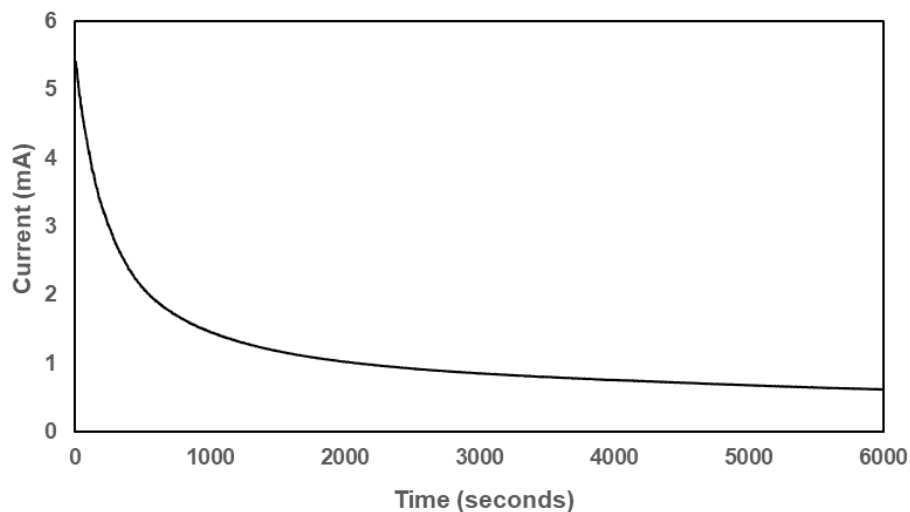


Figure S33. Bulk electrolysis at 1400 mV of 320\*2 equiv. H<sub>2</sub>O (320 in each divided cell compartment) and 160 equiv. 2,6-lutidine in 0.1 M NBu<sub>4</sub>PF<sub>6</sub> acetonitrile.

Trace O<sub>2</sub> could be detected from GC analysis, but NaI addition did not result in any visible NaI<sub>3</sub>.

Given the absence of O<sub>2</sub> in our GC traces for catalytic runs with **1**, we hypothesize that this background O<sub>2</sub> production is inhibited in the presence of our compound.

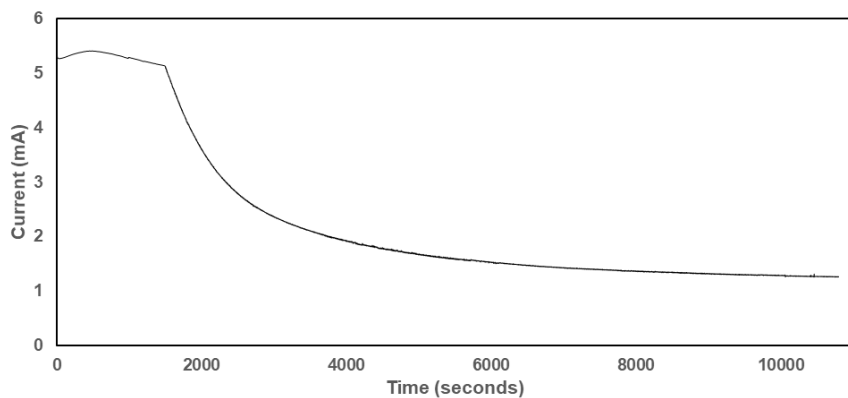


Figure S34. Bulk electrolysis at 1400 mV of 320\*2 equiv. H<sub>2</sub>O (320 in each divided cell compartment), CoCl<sub>2</sub> and 160 equiv. 2,6-lutidine in 0.1 M NBu<sub>4</sub>PF<sub>6</sub> acetonitrile.

O<sub>2</sub> could be detected from GC analysis, but NaI addition did not result in any visible NaI<sub>3</sub>.

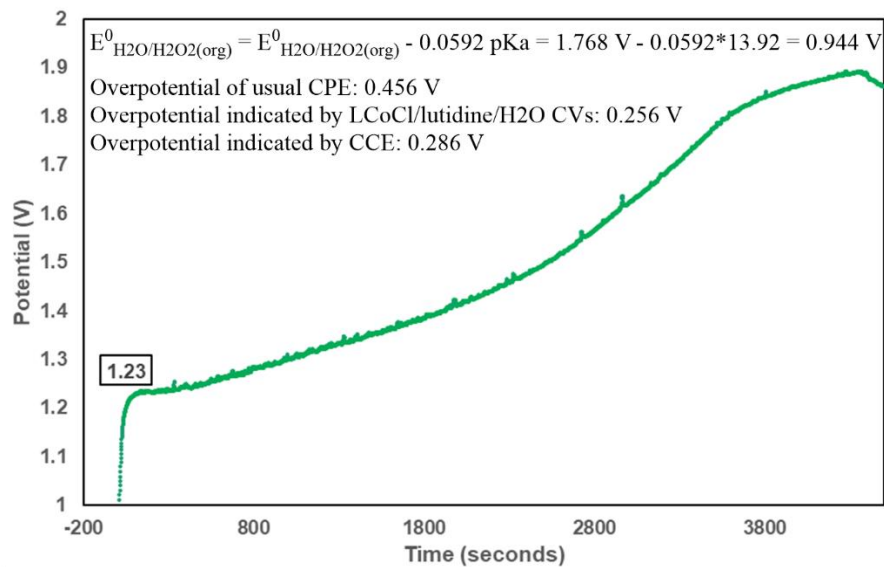


Figure S35. Bulk electrolysis at fixed 5.2 mA current in the presence of 1 mM **1**, 320\*2 equiv. H<sub>2</sub>O and 160 equiv. 2,6-lutidine in 0.1 M NBu<sub>4</sub>PF<sub>6</sub> acetonitrile.

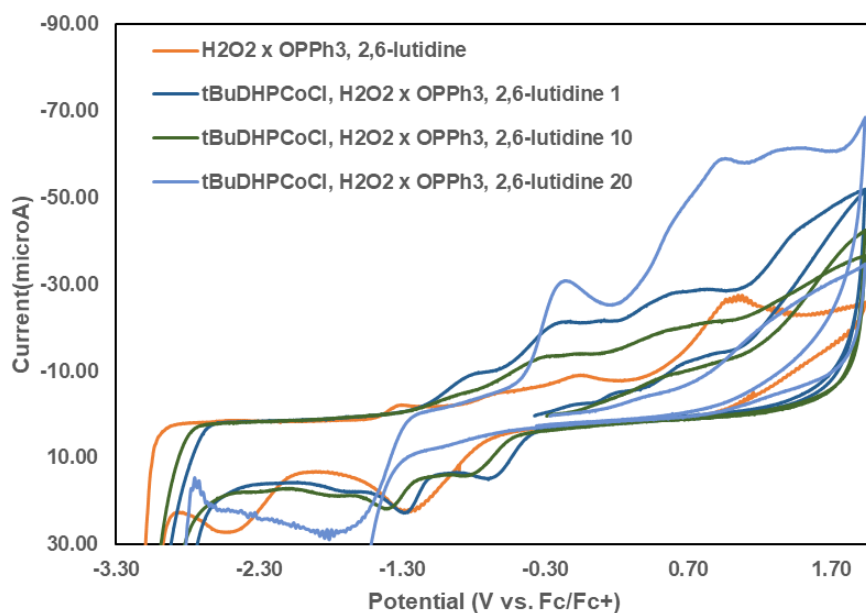


Figure S36. Cyclic Voltammograms of 1 mM **1** in the presence of H<sub>2</sub>O<sub>2</sub>•2-OPPh<sub>3</sub> and 160 equiv. 2,6-lutidine in 0.1 M NBu<sub>4</sub>PF<sub>6</sub> acetonitrile.

No significant changes are observed until excess peroxide (10-20 equiv.) are present, after which the spectrum changes significantly. This is consistent with decomposition with excess peroxide.

## Single Crystal X-ray Diffraction

### *X-Ray Structure Determination.*

The diffraction data were measured at 100 K on a Bruker D8 VENTURE with PHOTON 100 CMOS detector system equipped with a Mo-target micro-focus X-ray tube ( $\lambda = 0.71073 \text{ \AA}$ ). Data reduction and integration were performed with the Bruker APEX3 software package (Bruker AXS, version 2015.5-2, 2015). Data were scaled and corrected for absorption effects using the multi-scan procedure as implemented in SADABS (Bruker AXS, version 2014/5, 2015, part of Bruker APEX3 software package). The structure was solved by the dual method implemented in SHELXT<sup>2</sup> and refined by a full-matrix least-squares procedure using OLEX23<sup>3</sup> software package (XL refinement program version 2014/7<sup>4</sup>). Suitable crystals were mounted on a cryo-loop and transferred into the cold nitrogen stream of the Bruker D8 Venture diffractometer. C-H hydrogen atoms were generated by geometrical considerations, constrained to idealized geometries, and allowed to ride on their carrier atoms with an isotropic displacement parameter related to the equivalent displacement parameter of their carrier atoms.

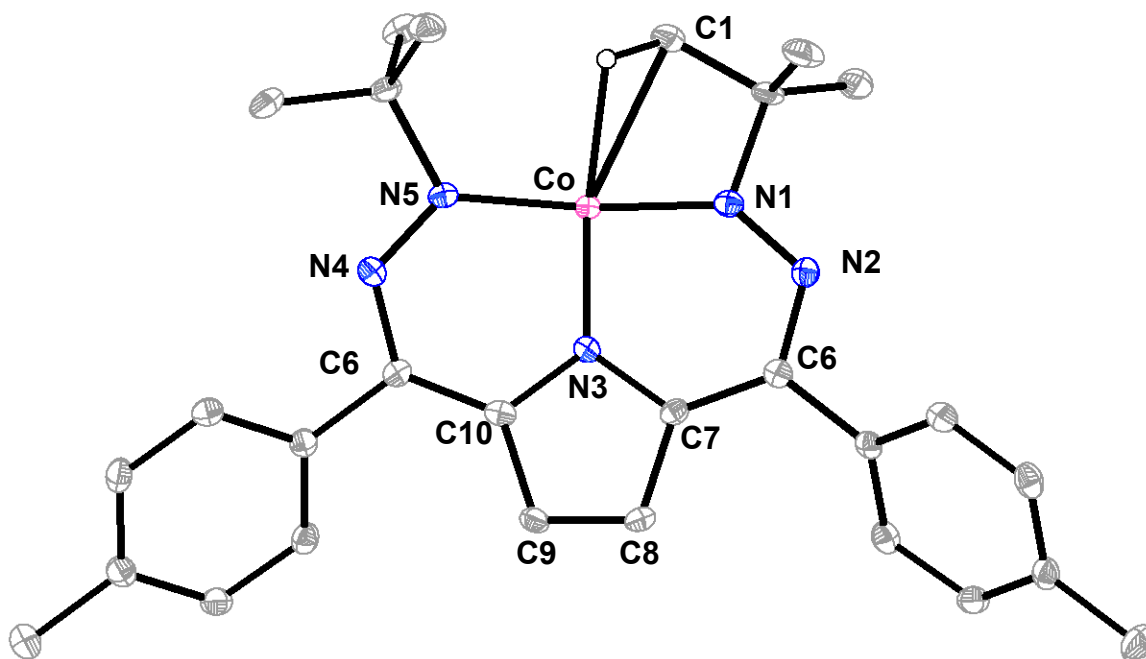


Figure S37. SXR of **2**. Co (pink), N (blue), C (gray), H(white). Most C-H H-atoms omitted. Selected bond lengths (Å): Co-N1/N5: 1.796(2), 1.847(2); Co-N3: 1.821(2); N1-N2/N4-N5: 1.323(2), 1.318(2); Co-C-H: 1.770(2); N2-C5/N4-C10: 1.343(3), 1.336(3); C5-C6/C9-C10: 1.403(3), 1.402(3); C6-C7/C8-C9: 1.436(3), 1.433(3); C7-C8: 1.353(3). Selected bond angles (°): N1-M-N5: 172.33(8); N3-M-(C-H): 162.15(8).

Table S1. SXR of **2**.

Empirical formula	C <sub>28</sub> H <sub>34</sub> CoN <sub>5</sub>
Formula weight	499.549
Temperature/K	100.06
Crystal system	monoclinic
Space group	P2 <sub>1</sub> /c
a/Å	13.8414(10)
b/Å	8.4418(6)
c/Å	21.6429(16)
α/°	90
β/°	103.258(2)
γ/°	90
Volume/Å <sup>3</sup>	2461.5(3)
Z	4
ρ <sub>calc</sub> /cm <sup>3</sup>	1.348

$\mu/\text{mm}^{-1}$	0.723
F(000)	1058.0
Crystal size/ $\text{mm}^3$	$0.06 \times 0.02 \times 0.02$
Radiation	Mo K $\alpha$ ( $\lambda = 0.71073$ )
2 $\theta$ range for data collection/ $^\circ$	5.2 to 54.3
Index ranges	$-15 \leq h \leq 17, -10 \leq k \leq 9, -26 \leq l \leq 27$
Reflections collected	39462
Independent reflections	5418 [ $R_{\text{int}} = 0.0758, R_{\text{sigma}} = 0.0593$ ]
Data/restraints/parameters	5418/0/326
Goodness-of-fit on $F^2$	1.051
Final R indexes [ $I \geq 2\sigma(I)$ ]	$R_1 = 0.0423, wR_2 = 0.0780$
Final R indexes [all data]	$R_1 = 0.0760, wR_2 = 0.0885$
Largest diff. peak/hole / $e \text{ \AA}^{-3}$	0.68/-0.66

## Density Functional Theory (DFT): Single Point Energies

### *Calculation Details*

Geometry optimization calculations and single point energy calculations were performed with ORCA<sup>5</sup> software suite using density functional theory (DFT). Geometries were fully optimized starting from coordinates generated from finalized cifs of the compound crystal structures when possible. The O3LYP functional was used for geometry optimizations, spin density plot calculations, and reaction coordinates on **2** and related compounds. For the O3LYP calculations, def2-TZVPP was used on Co, N, S, O, and F, and def2-TZVP on C and H atoms. These calculations were done as a first pass to screen possible mechanisms, but entropic contributions were not considered herein. Full free energy calculations are outlined below.

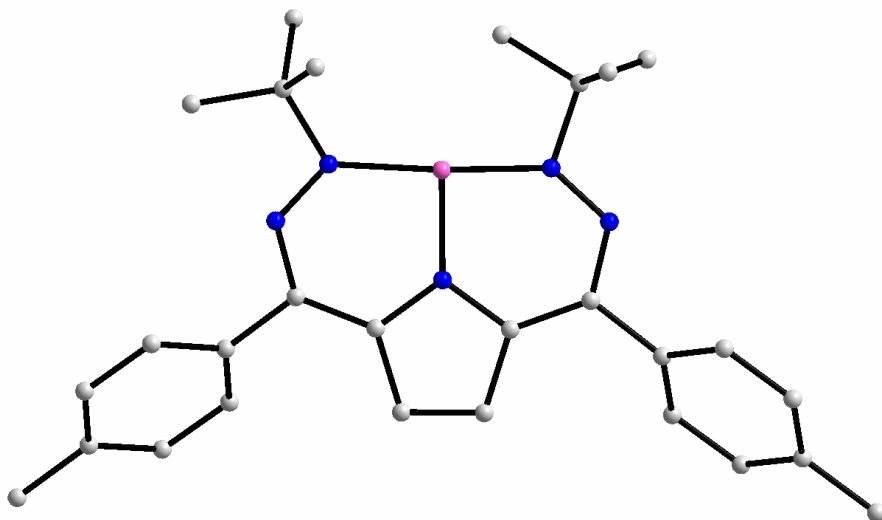


Figure S38. Calculated structure of **2**. All C–H hydrogen atoms have been removed for clarity.

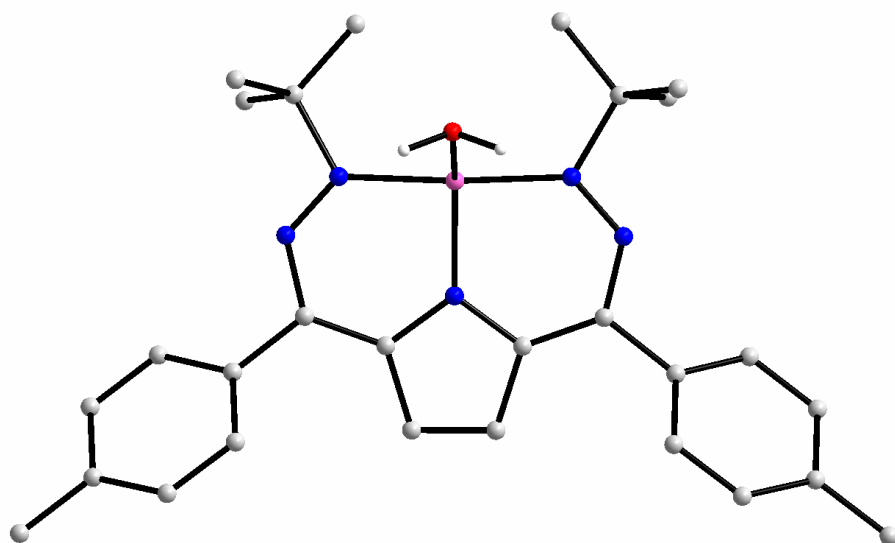


Figure S39. Calculated structure of **1-H<sub>2</sub>O<sup>+</sup>** (LS). All C–H hydrogen atoms have been removed for clarity.

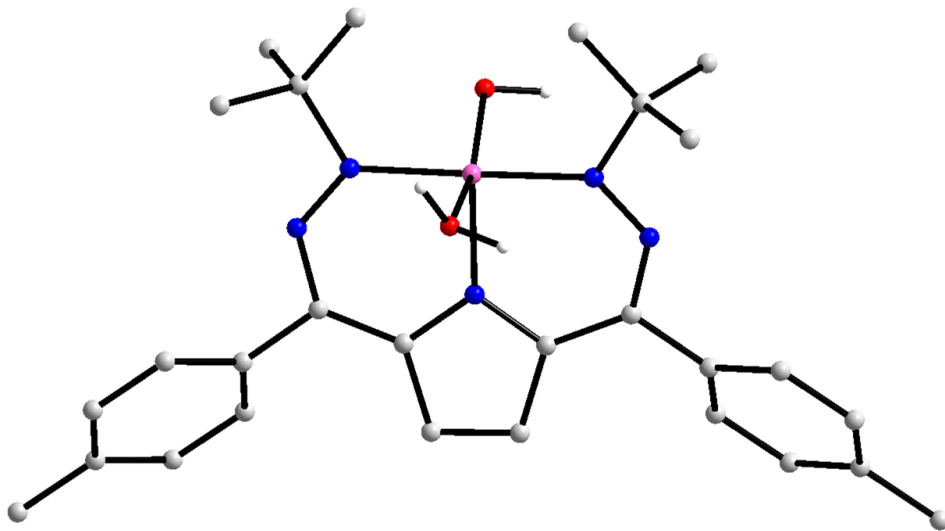


Figure S40. Calculated structure of **1-OH-H<sub>2</sub>O** (HS). All C-H hydrogen atoms have been removed for clarity.

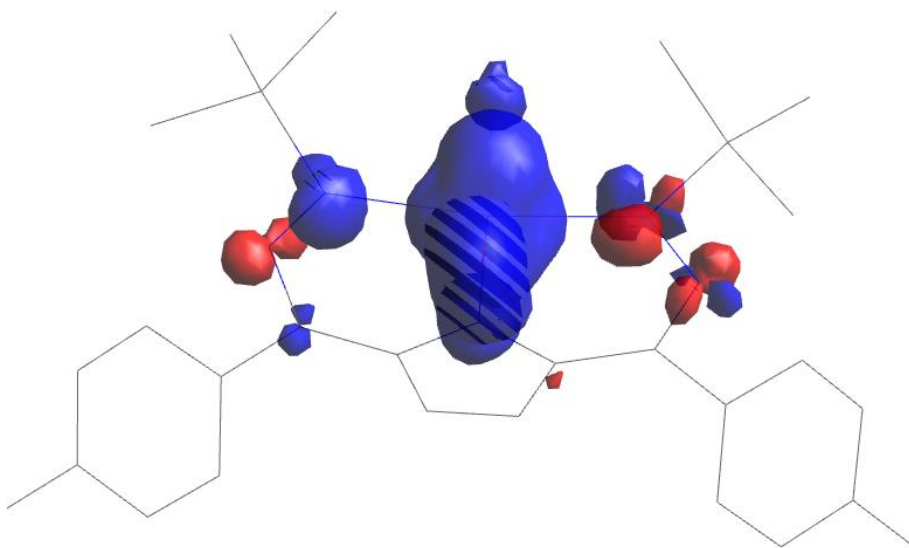


Figure S41. Spin density plot of **1-OH-H<sub>2</sub>O** (HS) at an iso value of 0.005.

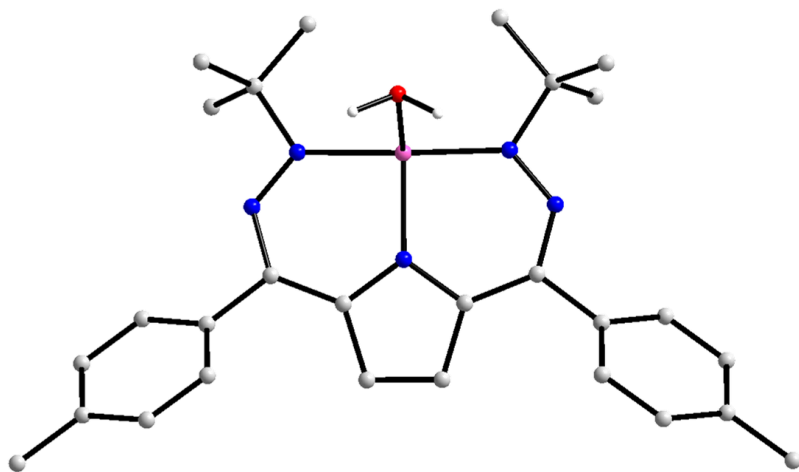


Figure S42. Calculated structure of **2-H<sub>2</sub>O** (LS). All C–H hydrogen atoms have been removed for clarity.

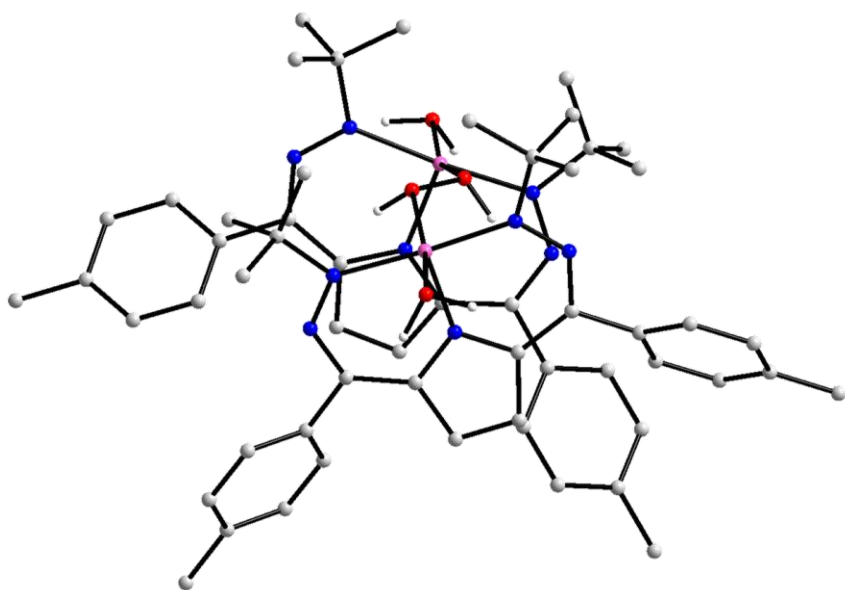


Figure S43. Calculated structure of **3-H<sub>2</sub>O** ( $S = 3$ , septet). All C–H hydrogen atoms have been removed for clarity.

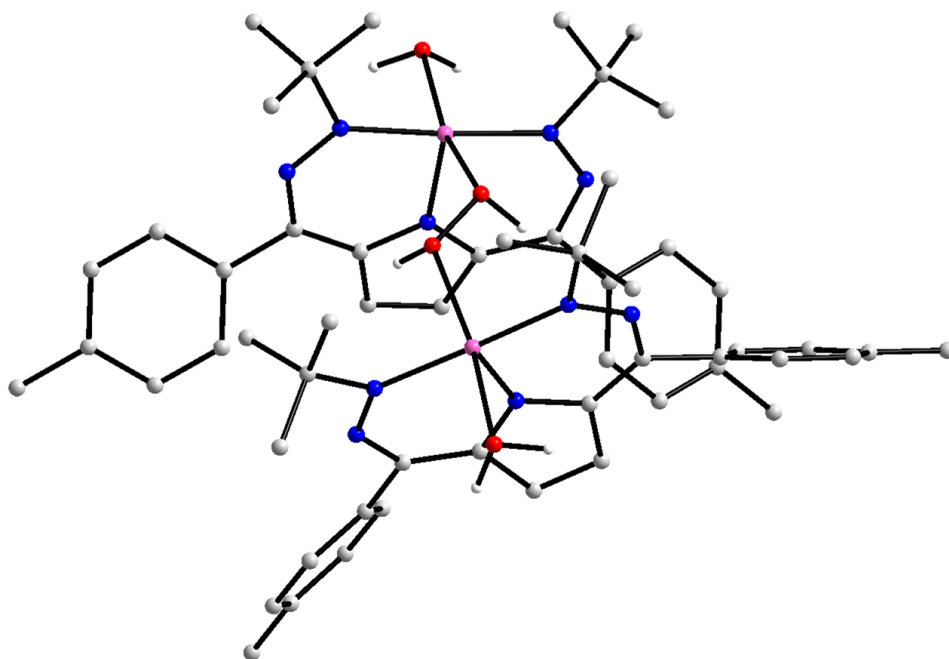


Figure S44. Calculated structure of **3-H<sub>2</sub>O** ( $S = 2$ , quintet). All C–H hydrogen atoms have been removed for clarity.

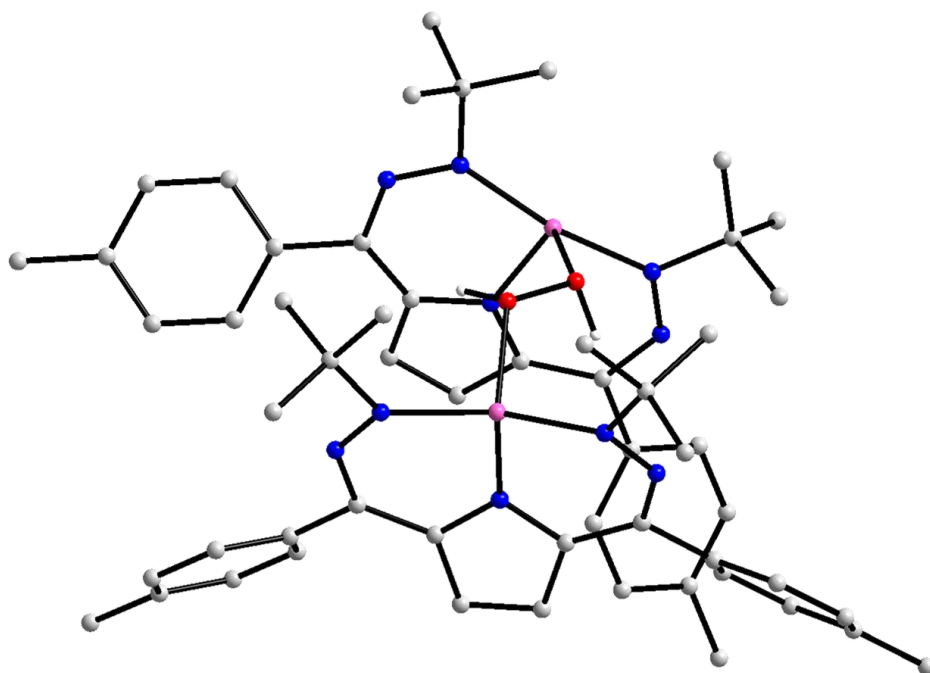


Figure S45. Calculated structure of **3** ( $S = 3$ , septet). All C–H hydrogen atoms have been removed for clarity.

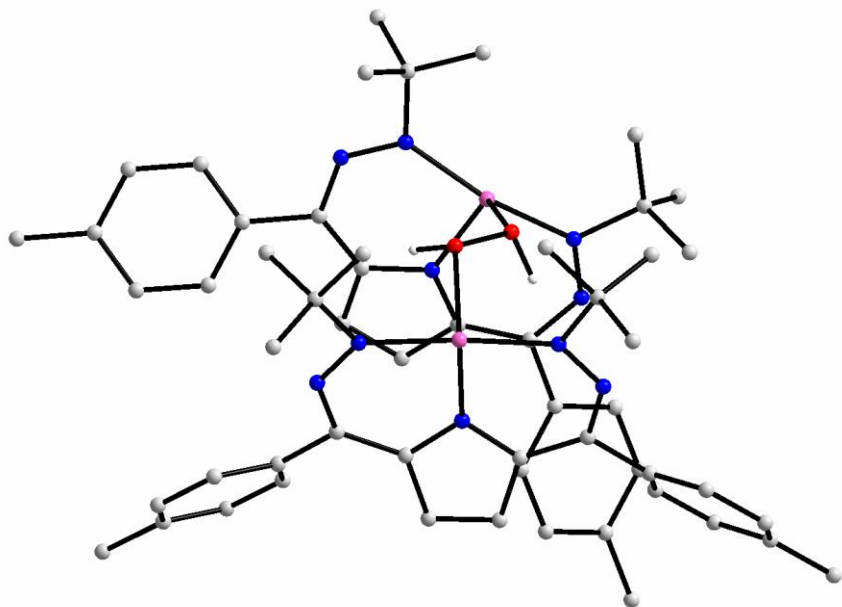


Figure S46. Calculated structure of **3** ( $S = 2$ , quintet). All C–H hydrogen atoms have been removed for clarity.

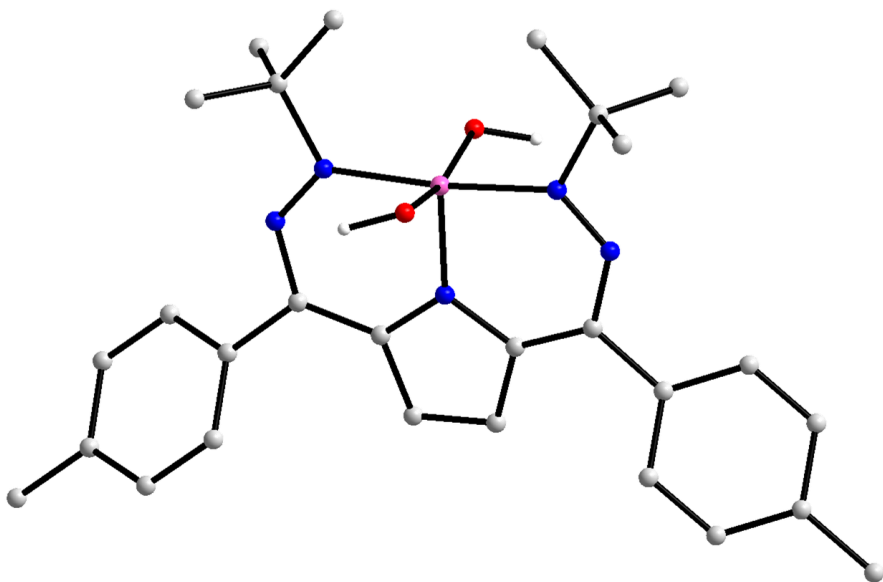


Figure S47. Calculated structure of **1-OH-OH** (HS). All C–H hydrogen atoms have been removed for clarity.

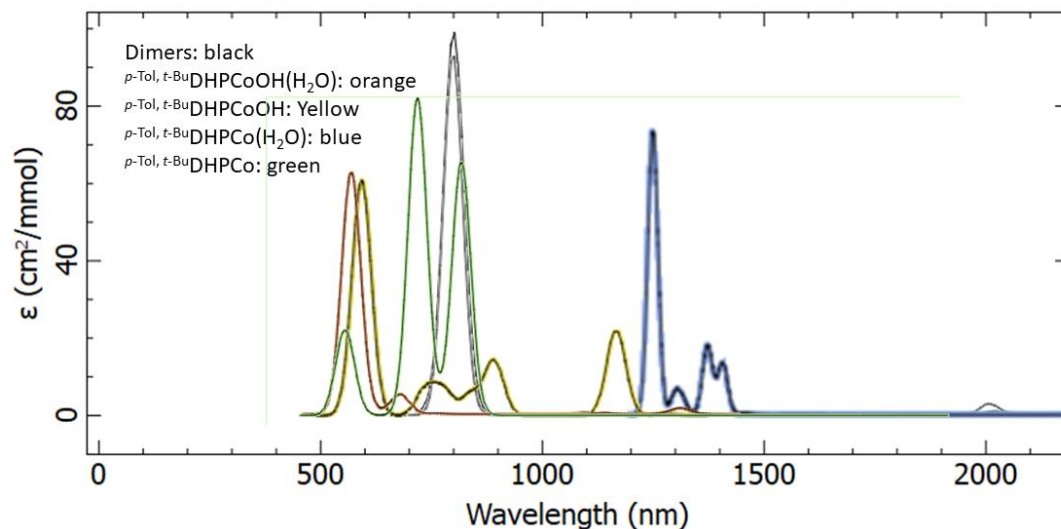
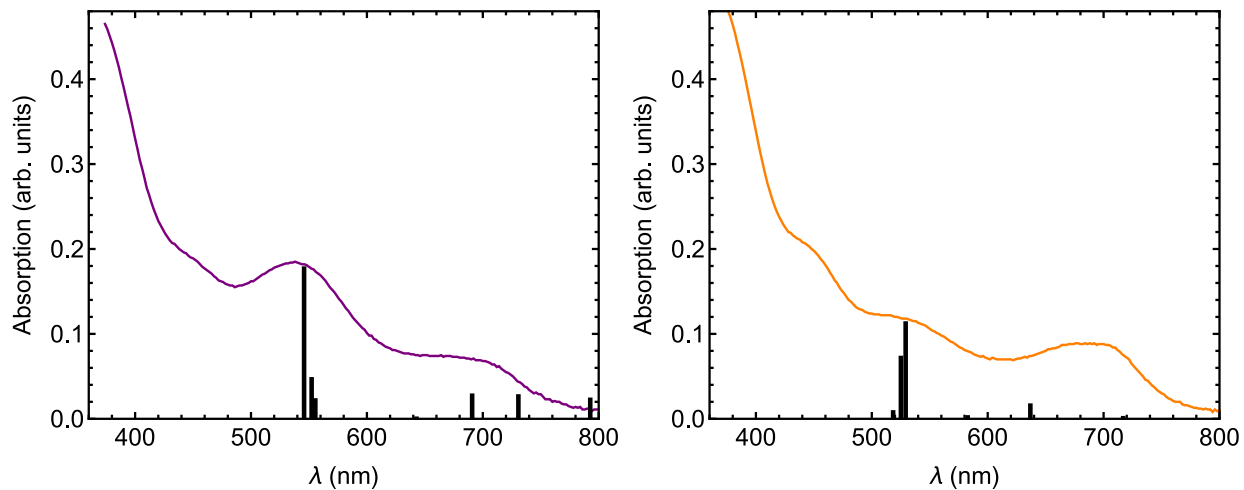


Figure S48. Calculated TD-DFT for relevant structures using PBE0 using def2-SV(P) basis sets for all atoms but Co. For Co def2-TZPP was used with an ECP assigned to the metal.



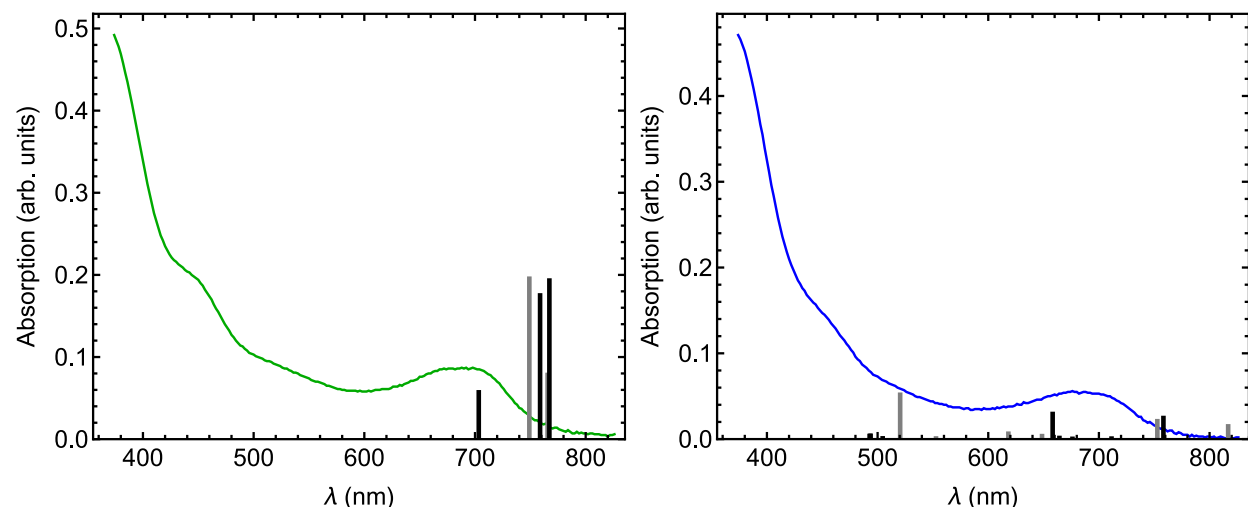


Figure S49. Calculated TD-DFT shown in Figure S48 plotted against the intermediates observed by UV-Vis.

Note that TD-DFT typically underestimates the energies of transitions and a shift to match experimental data of 50-75 nm is common in related Co-, Ni- and Fe-DHP complexes.

Starting from the top left, **1-OH** (purple) was used to calibrate DFT shifts. The data was adjusted by 55 nm to better match the known experimental data. The calibrated data was shown to correlate well for the assigned second UV-Vis intermediate--**1-OH-H<sub>2</sub>O** (top right, orange), the assigned third UV-Vis intermediate--either spin state of the water-bound dimer **3-H<sub>2</sub>O** [<sup>*t*Bu,*p*-Tol</sup>DHPCoHOOH<sup>*t*Bu,*p*-Tol</sup>DHP][H<sub>2</sub>O]<sub>2</sub> (bottom left, green, with *S* = 5 shown in gray, *S* = 7 shown in black), and the assigned final products in the UV-vis—either **2** or **2-H<sub>2</sub>O** (bottom right, blue, **2-H<sub>2</sub>O** shown in gray and **2** in black).

Table S2. Compared Energies of Isolable or Organic Intermediates to Form **2** From **1**, **1-OH** or **1-OTf** Without Accounting for Entropic Contributions.

All values given in Eh	<sup><i>t</i>Bu,</sup> TolDHPCoCl ( <b>1</b> )	<sup><i>t</i>Bu,</sup> TolDHPCo ( <b>2</b> )	<sup><i>t</i>Bu,</sup> TolDHPCoOH ( <b>1-OH</b> )	<sup><i>t</i>Bu,</sup> TolDHPCoOTf ( <b>1-OTf</b> )	H <sub>2</sub> O	H <sub>2</sub> O <sub>2</sub>	OH <sup>•</sup>	OH radical
HS- <i>S</i> =1	N/A	-2741.32	N/A	N/A	N/A	N/A	N/A	N/A
LS- <i>S</i> =1/2	-3201.21	N/A	-2817.05	-3702.06	N/A	N/A	N/A	-75.6258
<i>S</i> =0	N/A	N/A	N/A	N/A	-76.3155	-151.350	-75.7449	N/A

Table S3. Compared Energies of Organic Intermediates to Form **2** From **1**, **1-OH** or **1-OTf** Without Accounting for Entropic Contributions.

All values given in Eh	OTf	Cl	HOTf	2,6-lutidine	2,6-lutidinium <sup>+</sup>	[2,6-lutidinium][Cl]	[2,6-lutidinium][OTf]	HCl
S=0	-960.854	-459.936	-961.295	-326.273	-326.693	-786.740	-1287.62	-460.436

Table S4. Compared Energies of Cobalt Intermediates to Form **2** From **1**, **1-OH** or **1-OTf** Without Accounting for Entropic Contributions.

All values given in Eh	<i>t</i> Bu, TolDHPCoOH(H <sub>2</sub> O)	<i>t</i> Bu, TolDHPCo(OH) <sub>2</sub>	<i>t</i> Bu, TolDHPCo(H <sub>2</sub> O)	<i>t</i> Bu, TolDHPCo <sup>+</sup>	<i>t</i> Bu, TolDHPCo(H <sub>2</sub> O) <sup>+</sup>	<i>t</i> Bu, TolDHPCo(H <sub>2</sub> O)OTf	<i>t</i> Bu, TolDHPCo(H <sub>2</sub> O)Cl
HS-S=3/2	-2893.35	N/A	N/A	N/A	-2817.46	-3778.37	-3277.52
HS-S=1	N/A	-2892.76	-2817.64	N/A	N/A	N/A	N/A
LS-S=1/2	-2893.35	N/A	N/A	-2741.14	-2817.47	-3778.39	-3277.53
S=0	N/A	-2892.75	-2817.64	N/A	N/A	N/A	N/A
Δ(HS-LS)	-0.001	-0.01	0.001	Determined in previous work	0.01	0.02	0.01

Table S5. Compared Energies of Dimeric Intermediates to Form **2** From **1**, **1-OH** or **1-OTf** Without Accounting for Entropic Contributions.

All values given in Eh	<i>t</i> Bu, TolDHPCoHOOHCo <sup>t</sup> <i>t</i> Bu, TolDHP	<i>t</i> Bu, TolDHPCoHOOHCo <sup>t</sup> <i>t</i> Bu, TolDHP(H <sub>2</sub> O) <sub>2</sub>
HS-S=3	-5633.99	-5786.64
IS-S=2	-5634.00	-5786.65
Δ(HS-IS)	0.01	0.01



CPCM(Benzene), O3LYP  
 def2-TZVPP for Co, N, S, O, F,  
 def2-TZVP for C  
 def2-SV(P) for all other atoms

Energies given do not  
account for entropy contributions.

overall: +4.02 kcal/mol

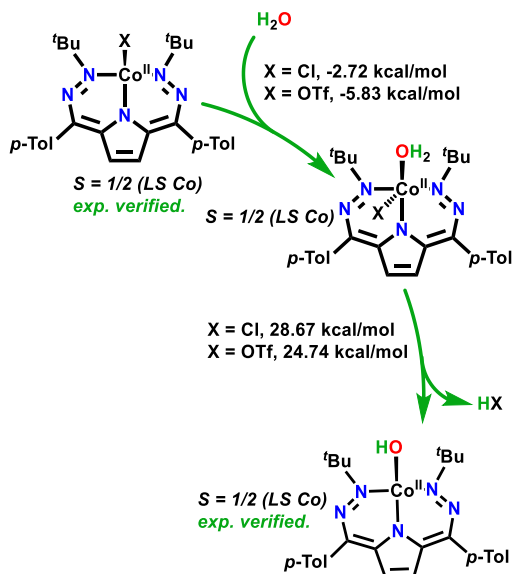


Figure S51. Formation of **2** from **1** or **1-OTf** with anion bound (without accounting for entropic contributions).

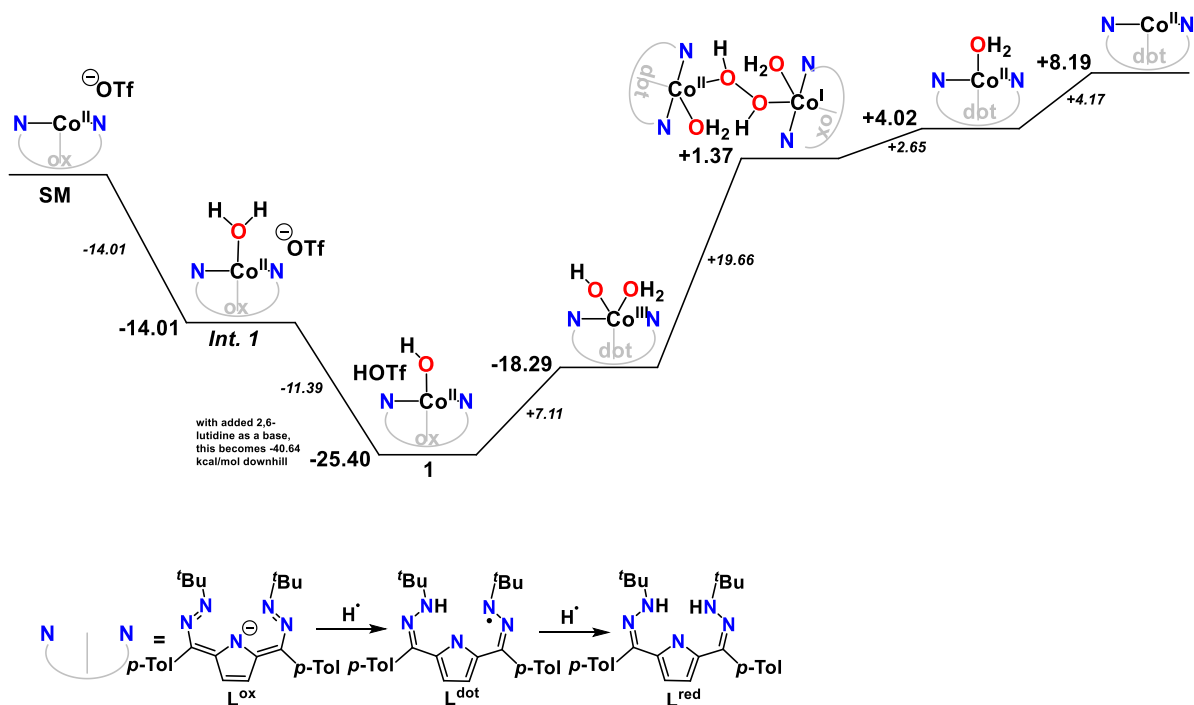


Figure S52. Reaction Coordinate: Formation of **2** from **1-OTf** (without accounting for entropic contributions).

## Density Functional Theory (DFT): Free Energies from Frequency Calculations

### *Calculation Details*

Geometries for free energy calculations were optimized using the PBE0 functional in combination with the def2-SVP basis set for H, C, N, and O, and the def2-TZVP basis set for Co, as implemented in Gaussian 16 Rev.A.03. Solvation effects were approximated via the polarizable continuum model and the D3 dispersion correction with Becke-Johnson Damping was applied. Final free energies were obtained through frequency calculations carried out at level of theory utilized for geometry optimization, followed by correction of the electronic energy via a single-point calculation utilizing the def2-TZVP basis set for all atoms.

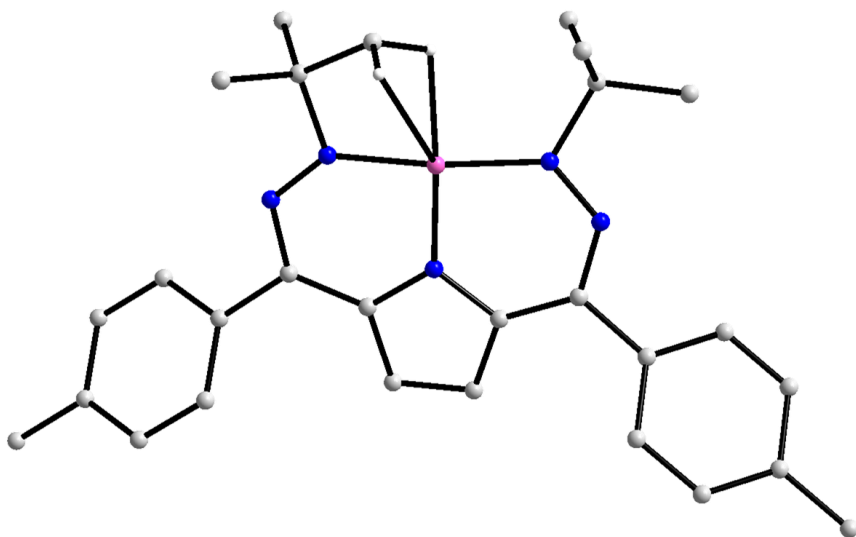


Figure S53. Calculated structure of **2**. All C–H hydrogen atoms have been removed for clarity.

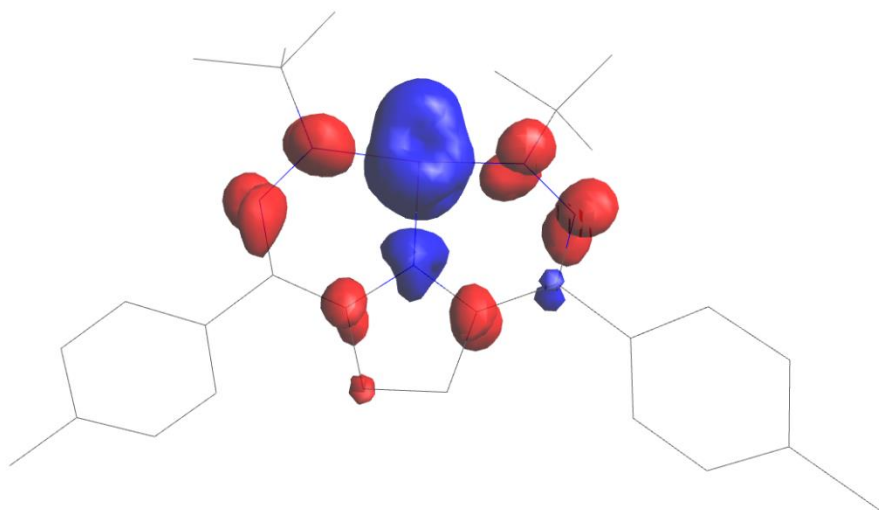


Figure S54. Spin density plot of **2** at an iso value of 0.005.

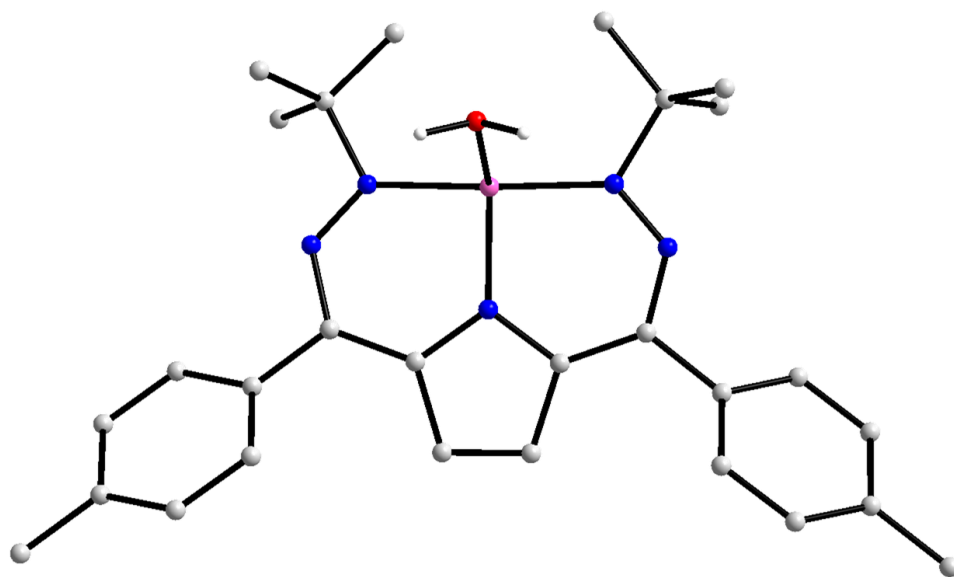


Figure S55. Calculated structure of **1-H<sub>2</sub>O<sup>+</sup>** (LS). All C-H hydrogen atoms have been removed for clarity.

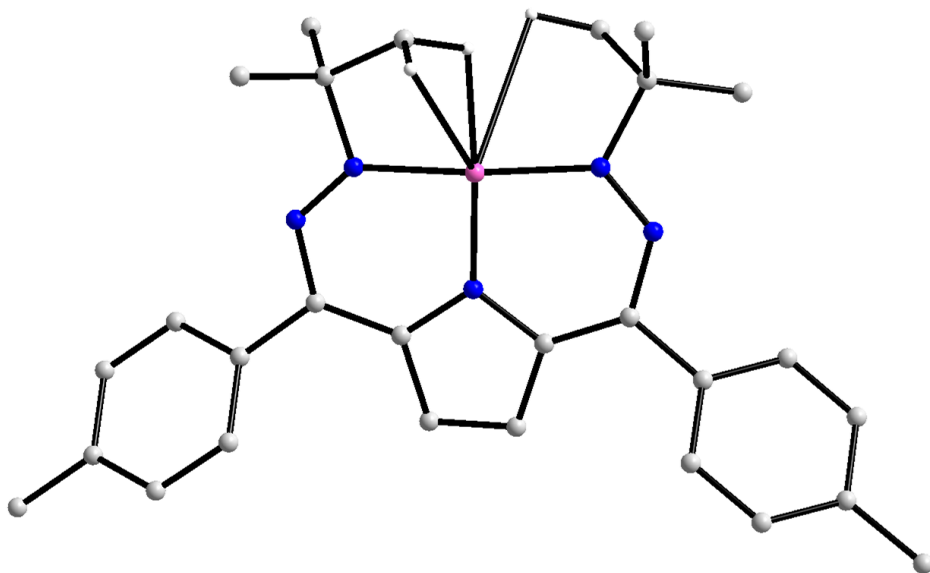


Figure S56. Calculated structure of  $1^+$  (LS). All C–H hydrogen atoms have been removed for clarity.

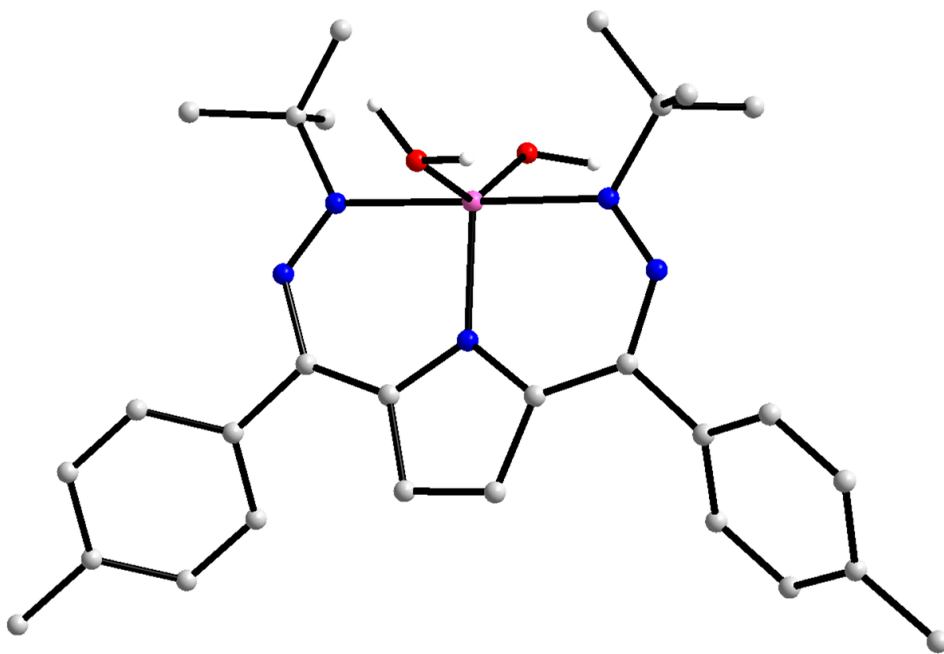


Figure S57. Calculated structure of  $1\text{-OH-H}_2\text{O}$  (HS). All C–H hydrogen atoms have been removed for clarity.

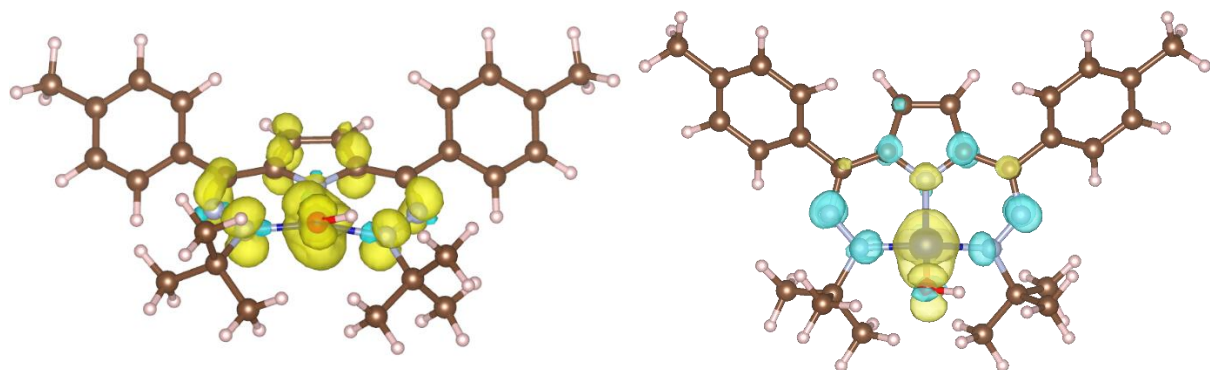


Figure S58. Spin density plot of **1-OH** (HS) (left) and **1-OH** (LS) (right).

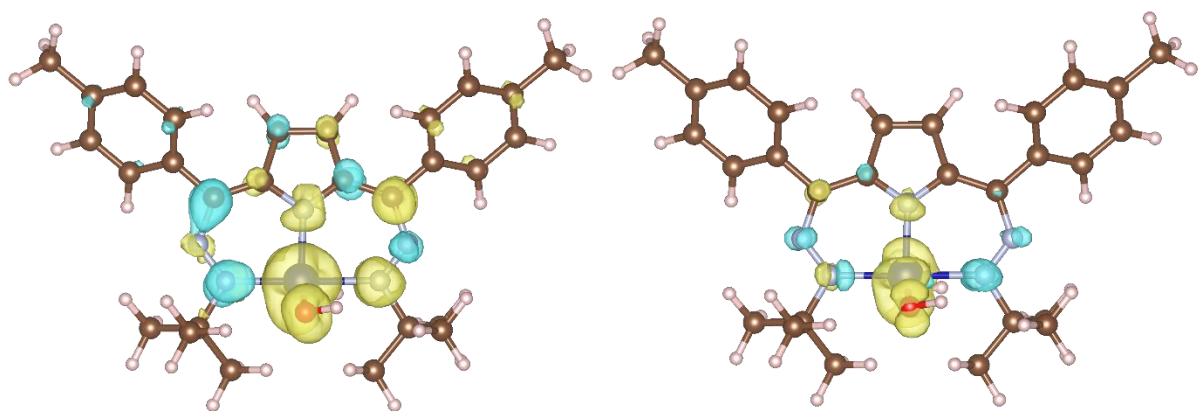


Figure S59. Spin density plot of **1-OH-H<sub>2</sub>O** (HS) (left) and **1-OH-H<sub>2</sub>O** (LS) (right).

Table S6. Compared Spin Densities and Energies of High and Low spin states of **1-OH** and **1-OH(H<sub>2</sub>O)**

Spin Densities

	<b>1-OH</b>		<b>1-OH-H<sub>2</sub>O</b>	
	LS	HS	LS	HS
sCo	1.219	1.971	1.028	2.707
cCo2	0.101	0.155	0.26	0.36
E	-2818.520737	-2818.492226	-2894.879049	-2894.90759
dE(HS-LS)		17.890596		-17.90858

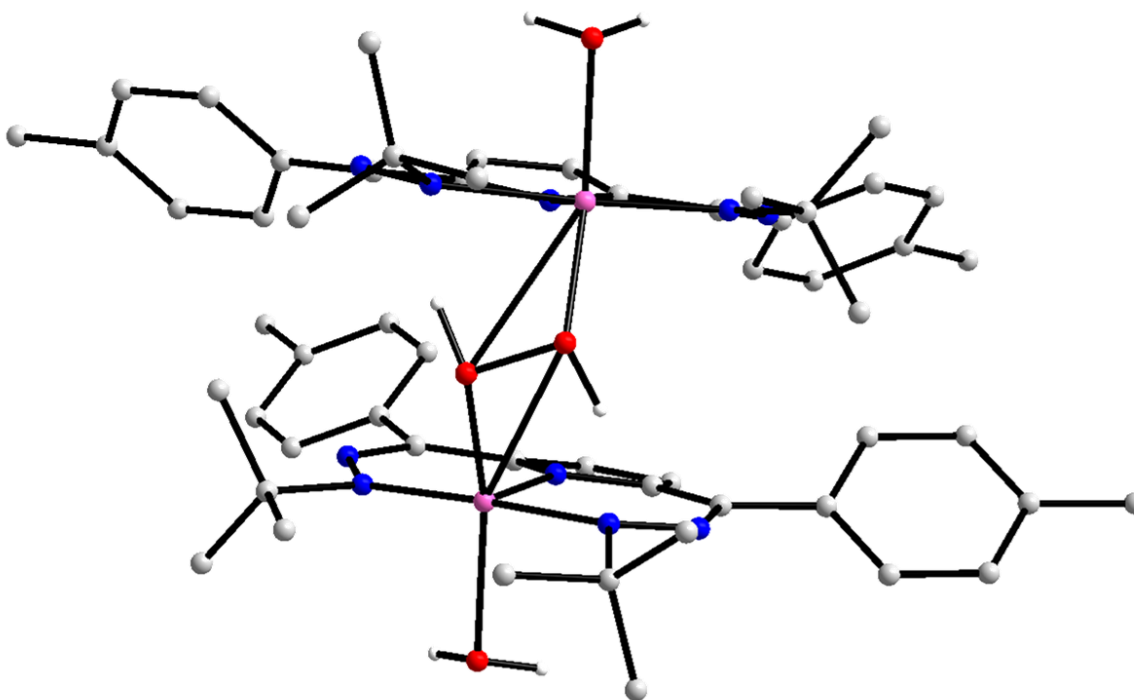


Figure S60. Calculated structure of **3-H<sub>2</sub>O** ( $S = 3$ , septet). All C–H hydrogen atoms have been removed for clarity.

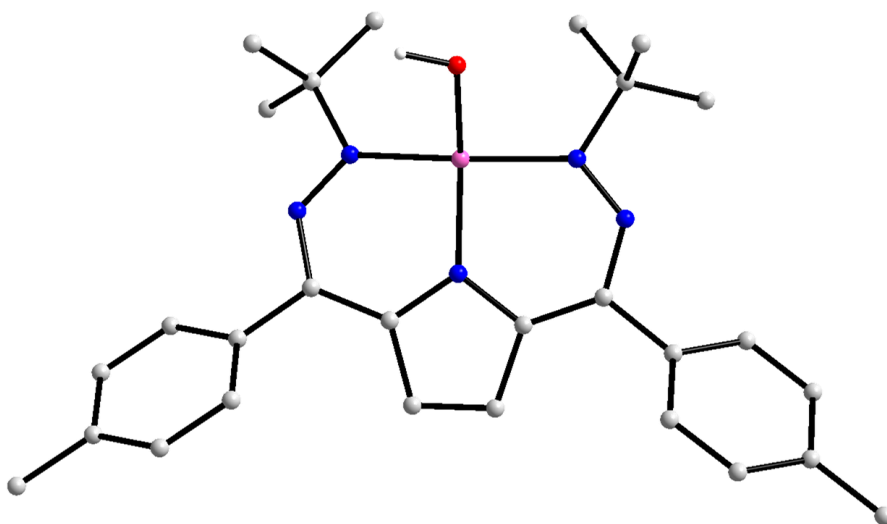


Figure S61. Calculated structure of **1-OH** ( $S = 1/2$ ). All C–H hydrogen atoms have been removed for clarity.

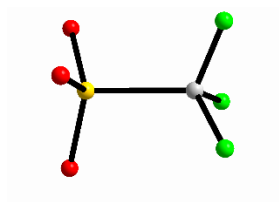


Figure S62. Calculated structure of triflate.

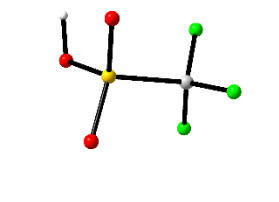


Figure S63. Calculated structure of triflic acid.



Figure S64. Calculated structure of H<sub>2</sub>O.



Figure S65. Calculated structure of H<sub>2</sub>O<sub>2</sub>.

Table S7. Compared Energies of Intermediates to form **2** from **1**<sup>+</sup> with entropic contributions.

	<sup>t</sup> Bu, Tol <sup>+</sup> DHPCo <sup>+</sup>	<sup>t</sup> Bu, Tol <sup>+</sup> DHPCo ( <b>2</b> )	<sup>t</sup> Bu, Tol <sup>+</sup> DHPCoOH ( <b>1-OH</b> )	<sup>t</sup> Bu, Tol <sup>+</sup> DHPCoOH(H <sub>2</sub> O) ( <b>1-OH-H<sub>2</sub>O</b> )	<sup>t</sup> Bu, Tol <sup>+</sup> DHPCo(H <sub>2</sub> O) <sup>+</sup>	( <sup>t</sup> Bu, Tol <sup>+</sup> DHPCo(HOOH) Co <sup>t</sup> Bu, Tol <sup>+</sup> DHP)(H <sub>2</sub> O) <sub>2</sub> ( <b>4</b> )
G (Eh)	-2742.04	-2742.22	-2818.00	-2894.38	-2818.43	-5788.68
S=	1/2	1	1/2	3/2	1/2	3

Table S8. Compared Energies of Intermediates to form **2** from **1**<sup>+</sup> with entropic contributions.

	2,6- lutidine	2,6-lutidinium triflate	NaI	NaI <sub>3</sub>	NaOTf	NaOH	OTf	HOTf	H <sub>2</sub> O	H <sub>2</sub> O <sub>2</sub>
G (Eh)	-326.6	-1288.2	-459.9	- 1055.4	- 1123.3	-238.0	- 961.22	-961.65	- 76.38	-151.45
S=	0	0	0	0	0	0	0	0	0	0

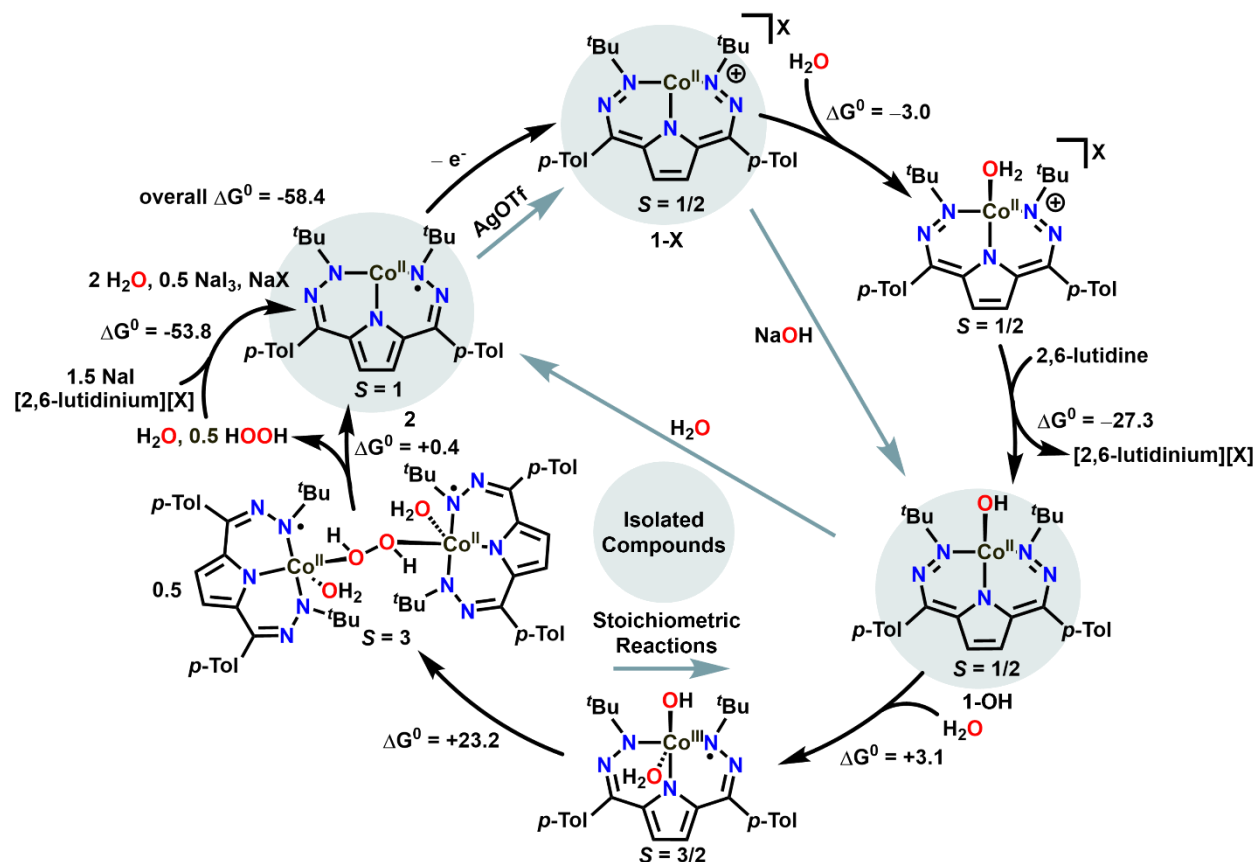


Figure S66. Formation of **2** from **1-OTf** (accounting for entropic contributions and including contributions from a base/oxidation substrate—2,6-lutidine and NaI).

Table S9. Compared Energies going to **2** from **1-OTf** with NaI, with lutidine, and with both.

$t\text{Bu,TolDHPCo}^+ + \text{OTf} + 2$	$t\text{Bu,TolDHPCo} + \text{H}_2\text{O} + 0.5$	$t\text{Bu,TolDHPCo}^+ + \text{OTf} + 2$	$t\text{Bu,TolDHPCo} + \text{H}_2\text{O} + 0.5$
$\text{H}_2\text{O} + 2,6\text{-lutidine} + 1.5$	$\text{NaI}_3 + [2,6\text{-lutidinium}][\text{OTf}]$	$\text{H}_2\text{O} + 2,6\text{-lutidine} + 1.5$	$t\text{Bu,TolDHPCo} + \text{H}_2\text{O} + 0.5$
<b>NaI</b>	<b>+ NaOH</b>	<b>NaI</b>	<b>NaI<sub>3</sub> + 2,6-lutidine + NaOTf</b>
-4872.49	-4872.52	-4872.49	-4872.58
	-21.30		-58.38
$t\text{Bu,TolDHPCo}^+ + \text{OTf} + 2$	$t\text{Bu,TolDHPCo} + \text{H}_2\text{O} + 0.5$	$t\text{Bu,TolDHPCo}^+ + \text{OTf} + 2$	$t\text{Bu,TolDHPCo} + 2 \text{H}_2\text{O} + 0.5$
$\text{H}_2\text{O} + 1.5 \text{NaI}$	$\text{NaI}_3 + \text{HOTf} + \text{NaOH}$	$\text{H}_2\text{O} + 1.5 \text{NaI}$	$\text{NaI}_3 + \text{NaOTf}$
-4545.94	-4545.94	-4545.94	-4546.03
	-3.41		-58.38

$t\text{Bu,Tol}^{\text{D}}\text{HPCo}^+ + \text{OTf} + 2$	$t\text{Bu,Tol}^{\text{D}}\text{HPCo} + \text{H}_2\text{O} + 0.5$
$\text{H}_2\text{O} + 2,6\text{-lutidine}$	$\text{H}_2\text{O}_2 + [2,6\text{-lutidinium}][\text{OTf}]$
-4182.57	-4182.57
	-3.69

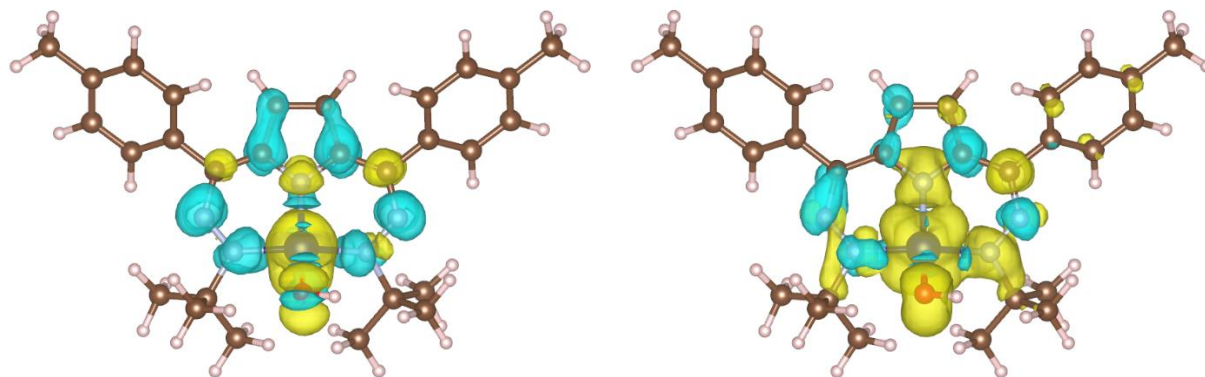


Figure S67. Unpaired Spin density plot of **1-OH** (Co<sup>II</sup>) (left) and **1-OH** (Co<sup>III</sup>) (right).

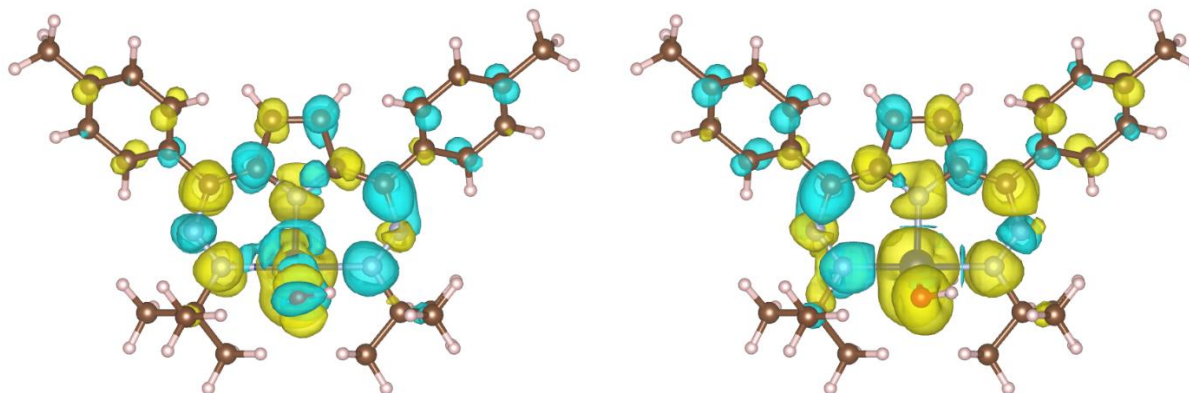


Figure S68. Spin density plot of **1-OH-H<sub>2</sub>O** (Co<sup>II</sup>) (left) and **1-OH-H<sub>2</sub>O** (Co<sup>III</sup>) (right).  
Table S10. Compared Mulliken Charges (cCo) and Tautomerism Energies of Co<sup>II</sup> vs. Co<sup>III</sup> in **1-OH** and **1-OH-(H<sub>2</sub>O)**

Tautomerism	LCo-OH		LCo-OH-H <sub>2</sub> O	
	Co II	Co III	Co II	Co III
sCo	1.226	2.747	1.039	2.702
cCo	0.087	0.196	0.285	0.351
E	-2818.42497	-2818.39232	-2894.78545	-2894.80469
dE(CoIII-CoII)	20.490385		-12.076865	

## Mass Spectrometry

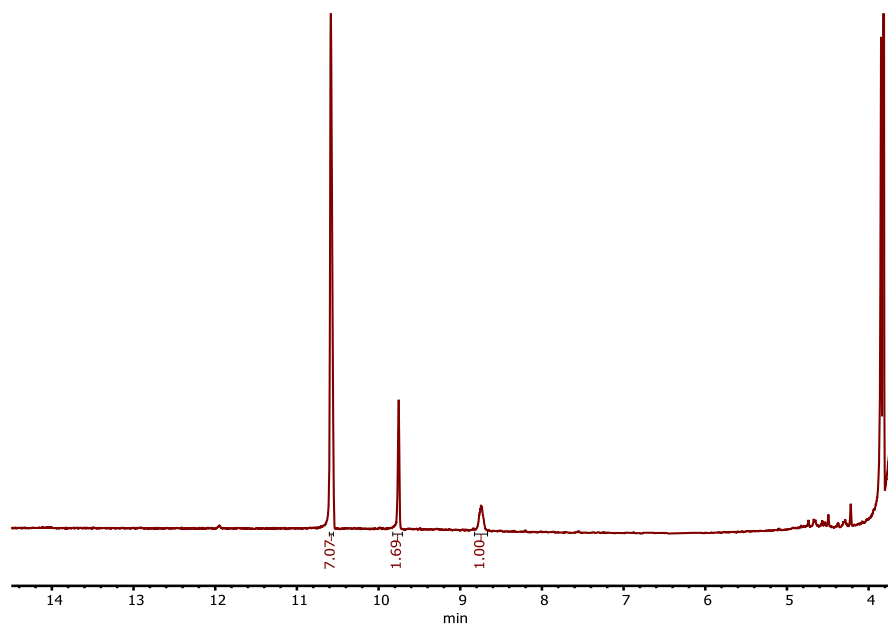


Figure S69. GCMS of reaction between 1, H<sub>2</sub>O and 1,3-diphenylisobenzofuran—the peak for the “H<sub>2</sub>O<sub>2</sub> product”—9-hydroxyanthracen-10(9H)-one— can be observed at 8.7 and roughly quantified from the starting material at 10.6 and other oxidation product peaks at 9.7-- 1,2-dibenzoylbenzene.

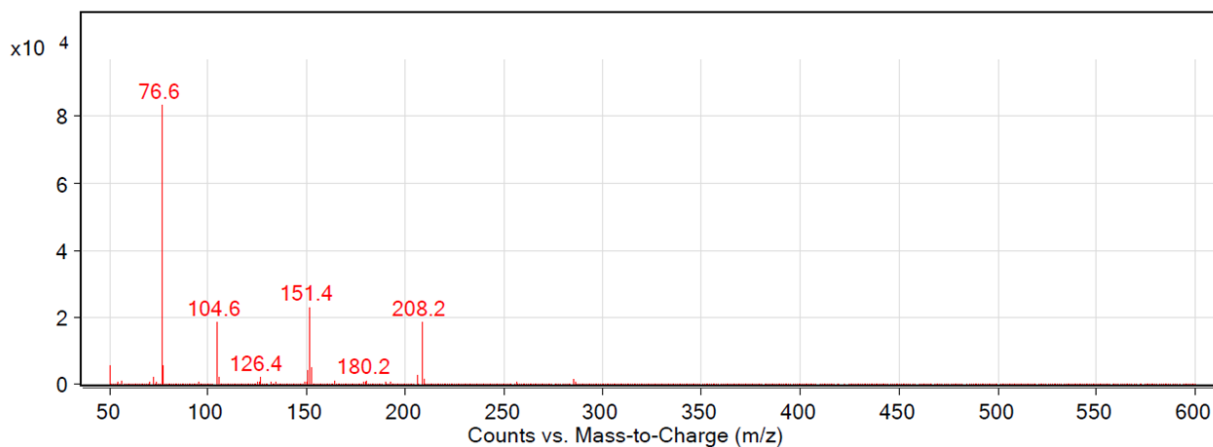


Figure S70. MS trace of 9-hydroxyanthracen-10(9H)-one —from 8.695-8.785 in the MS trace of the figure above.

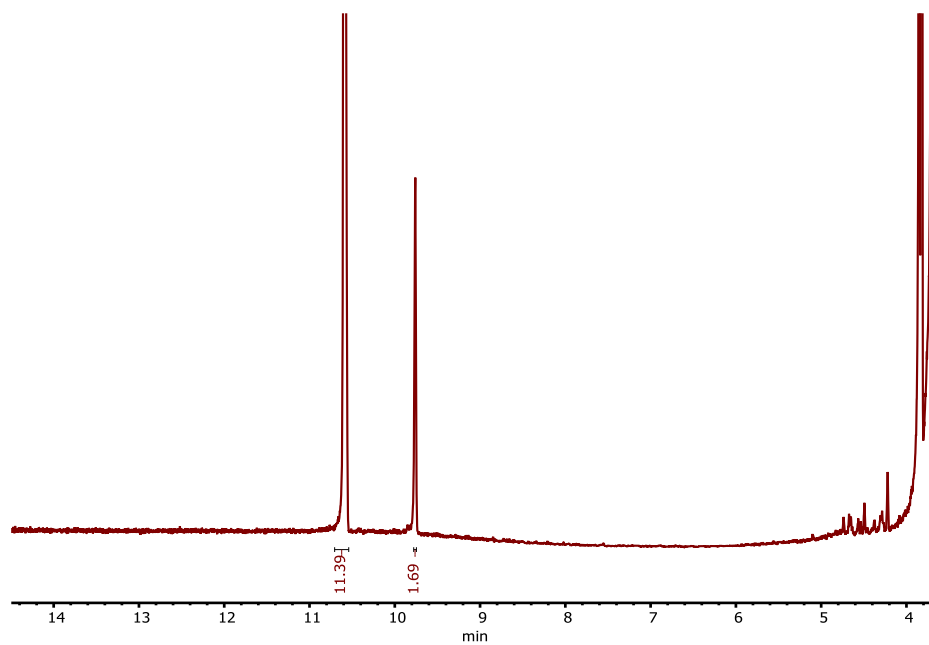


Figure S71. GCMS of 1,3-diphenylisobenzofuran as purchased—the peak for the “H<sub>2</sub>O<sub>2</sub> diagnostic product” is not present, however both the starting material at 10.6 and other oxidation product (in reduced quantity) at 9.7 peaks can be observed.

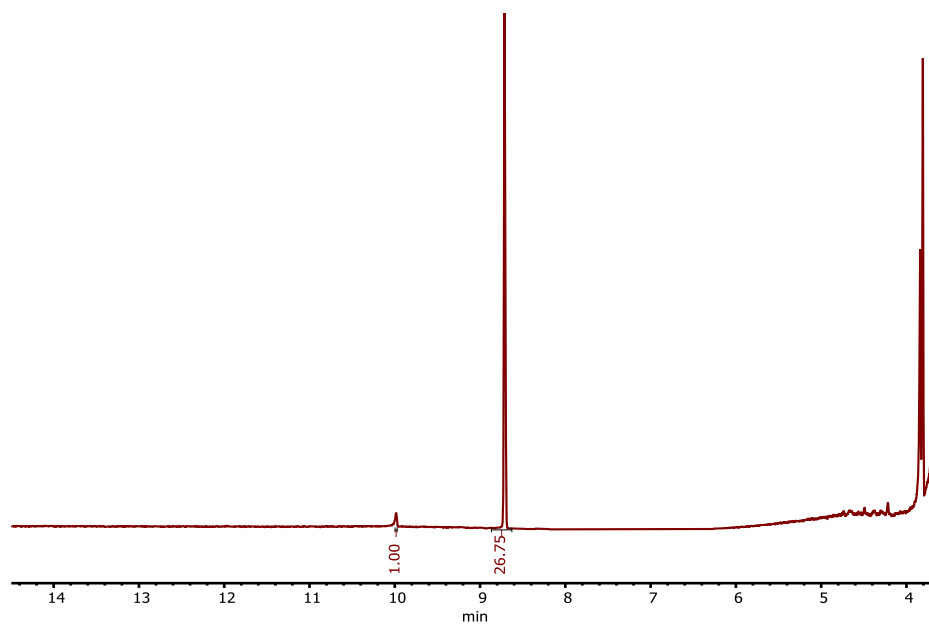


Figure S72. GCMS of reaction between 1, H<sub>2</sub>O and PPh<sub>3</sub>. 9.98 peak is triphenylphosphine oxide and 8.71 is starting material.

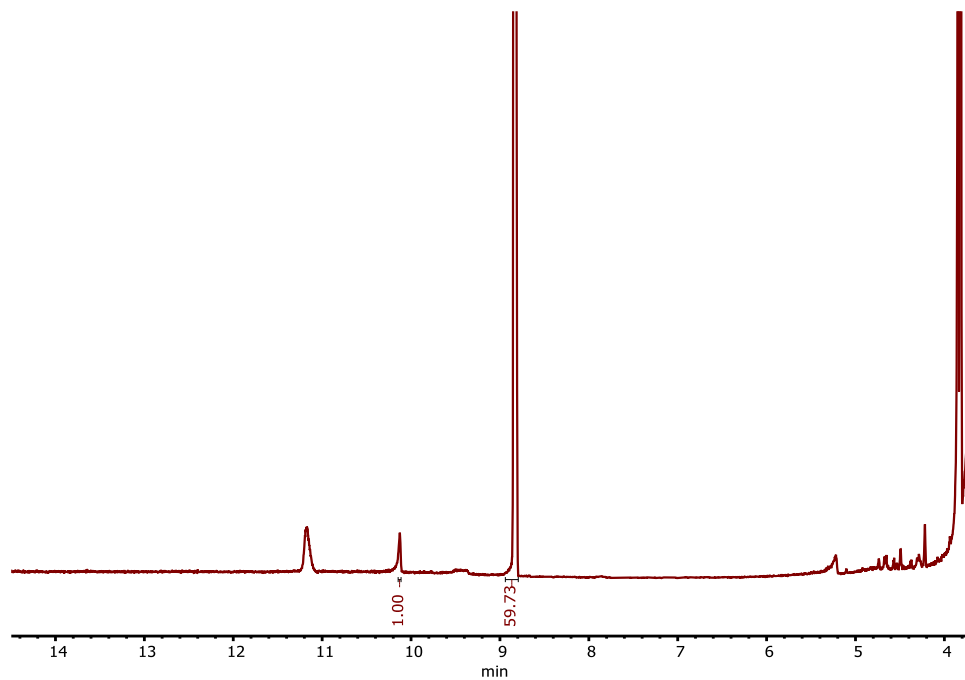


Figure S73. GCMS of  $\text{PPh}_3$  Starting Material. 9.98 peak is oxidized triphenylphosphine oxide, and 8.71 is starting material. A spurious peak from a previous user appears at 11.1.

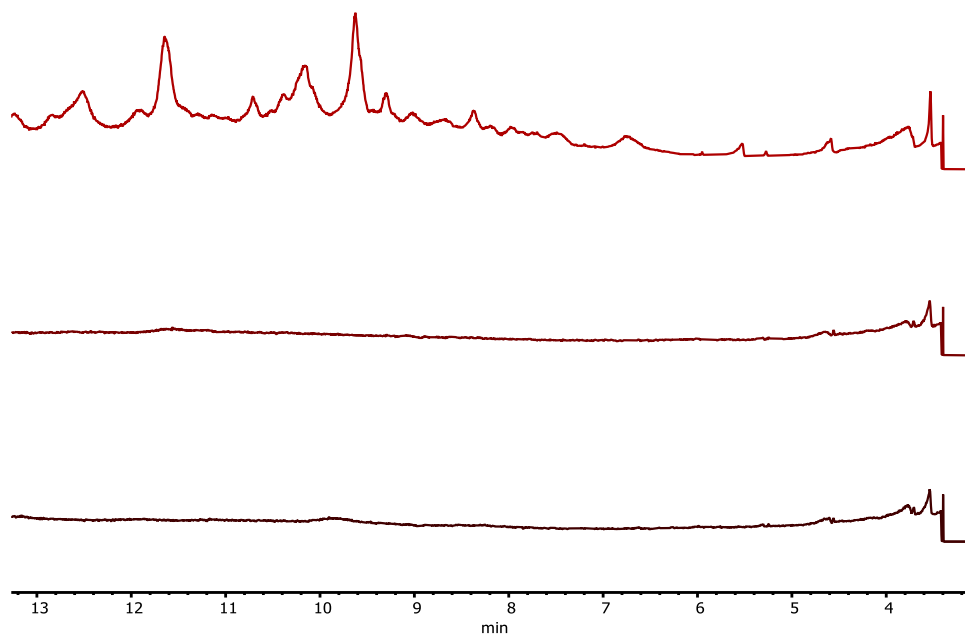


Figure S74. GCMS of Crude Reaction of **1-OH** and H<sub>2</sub>O in THF (top) and control GCMS' of **2** (middle) after purification in THF and **1-OH** (bottom) in THF. 9.63 peak matches [<sup>t</sup>Bu,TolDHP] + 2 O, the 10.17 peak matches [<sup>t</sup>Bu,TolDHP] + 3 O, and the 11.65 peak is best matched to [<sup>t</sup>Bu,TolDHP] + O. Neither control shows any oxidized ligand peaks.

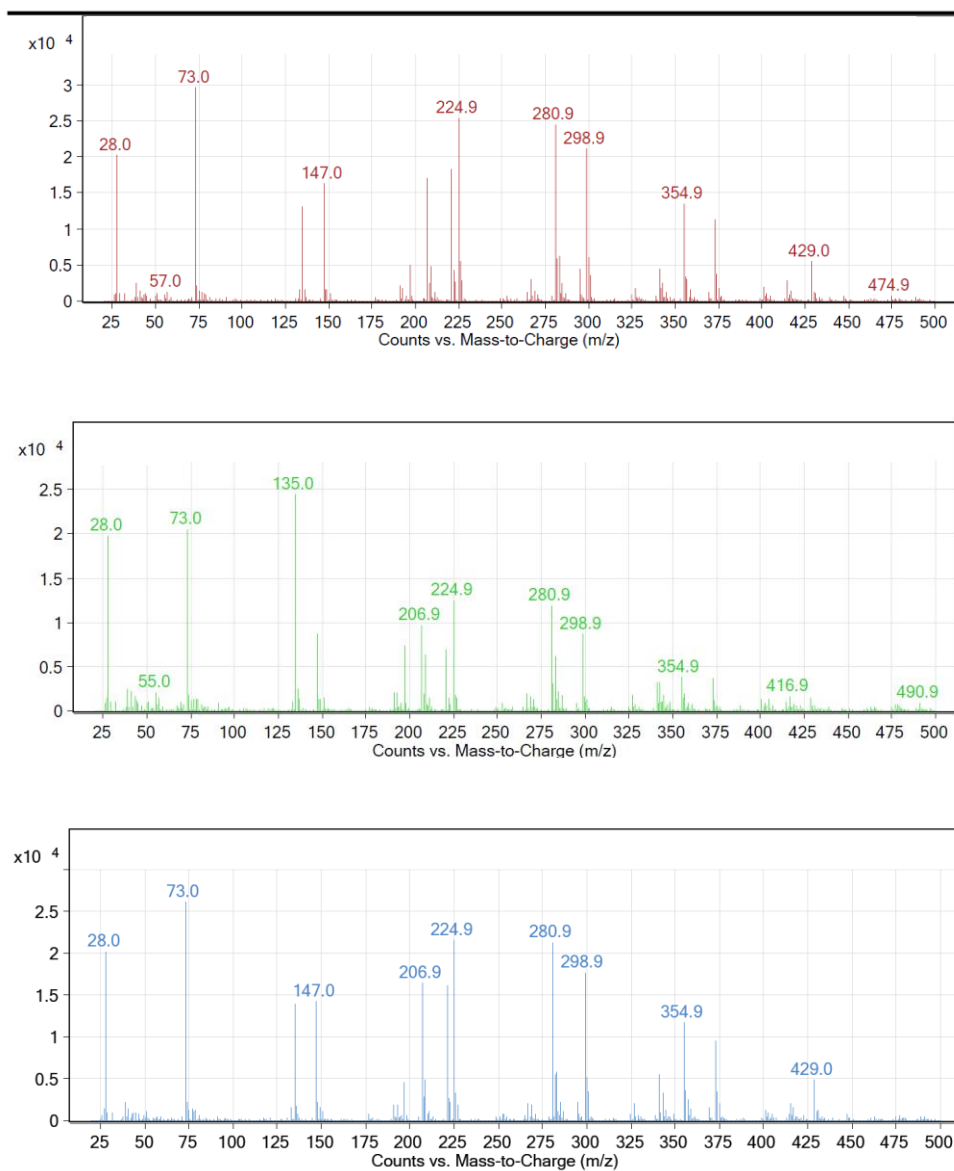


Figure S75. MS traces from top to bottom of [<sup>t</sup>Bu,TolDHP] + 2 O —from 9.554-9.679; [<sup>t</sup>Bu,TolDHP] + 3 O —from 10.123-10.237, and [<sup>t</sup>Bu,TolDHP] + O —from 11.569-11.968 in the figure above.

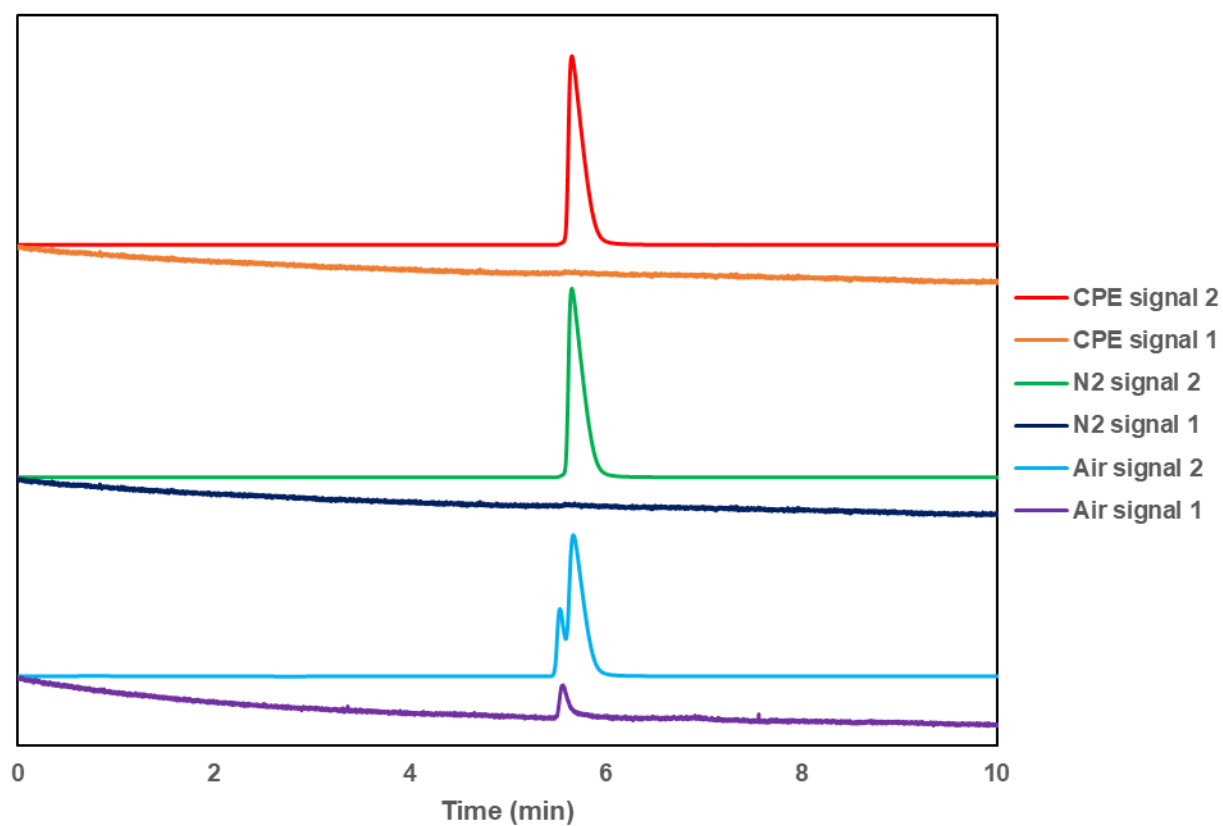


Figure S76. GC trace of electrocatalysis with **1**, H<sub>2</sub>O, and 2,6-lutidine (peak remaining is of nitrogen), a blank of the glovebox atmosphere, and a blank of air. Notably, the electrocatalysis with **1** shows no O<sub>2</sub>, and only the air blank shows a peak other than nitrogen.

## Controls for Cobalt Nanomaterials and Spurious Reactivity

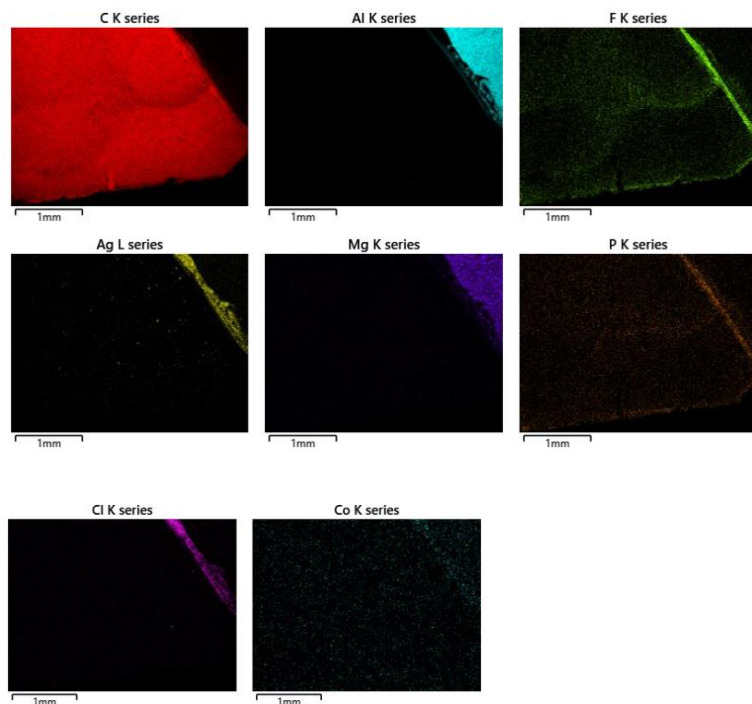
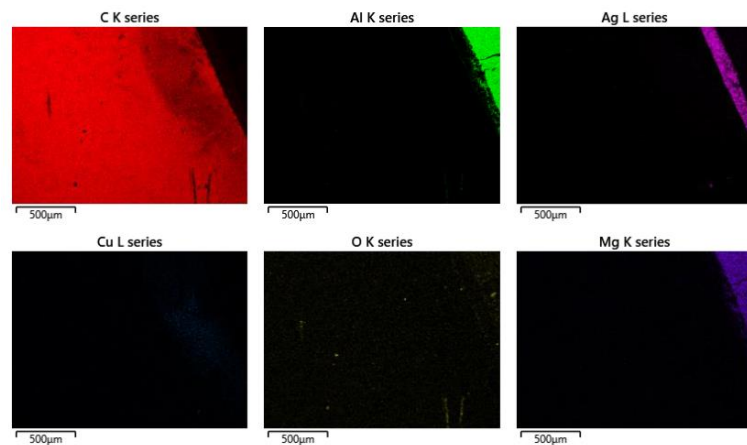


Figure S77. SEM/EDS images of an electrode dipped the solution for electrolysis—1 mM **1**, 160 equiv. 2,6-lutidine, 640 equiv. H<sub>2</sub>O, and 0.1 M NBu<sub>4</sub>PF<sub>6</sub> (with no current passed). There are no identifiable cobalt-containing materials after an acetonitrile rinse of the electrode. Visible are the glassy carbon plate, some residual NBu<sub>4</sub>PF<sub>6</sub>, and silver paste used as glue to affix the plate to an aluminum (with some Mg) holder.



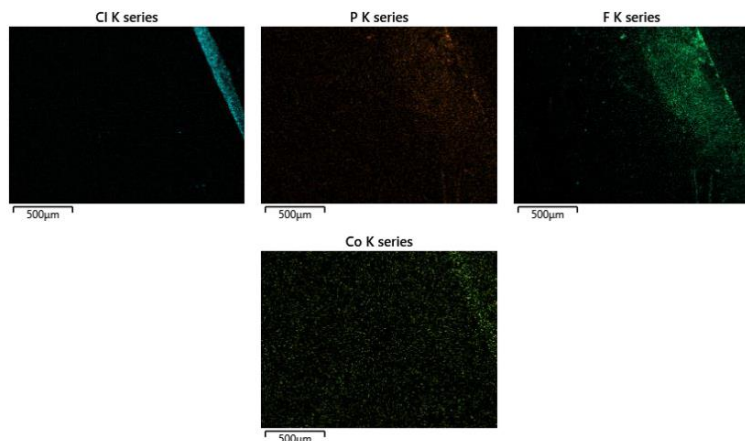
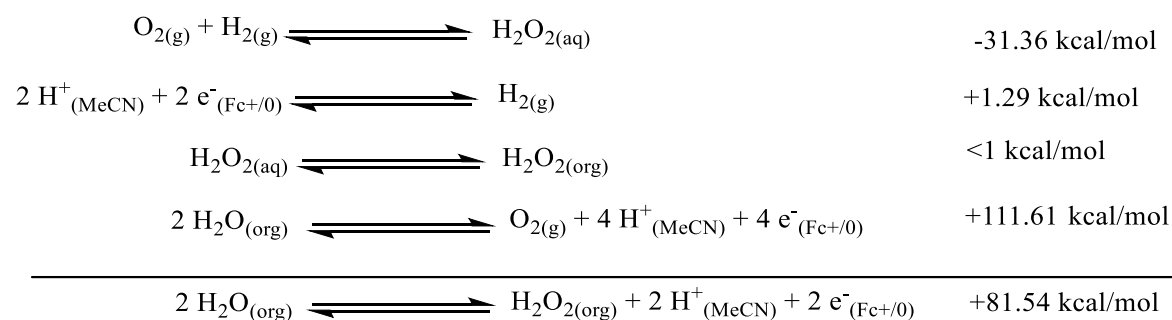


Figure S78. SEM/EDS images of a rinsed electrode post-electrolysis (2 hr at 1400 mV with 1 mM **1**, 160 equiv. 2,6-lutidine, 640 equiv. H<sub>2</sub>O, and 0.1 M NBu<sub>4</sub>PF<sub>6</sub>). There are no identifiable cobalt-containing materials after an acetonitrile rinse of the electrode post-electrolysis and no notable differences in the electrode that was dipped above vs. the sample which underwent electrolysis. Visible are the glassy carbon plate, some residual NBu<sub>4</sub>PF<sub>6</sub>, and silver paste used as glue to affix the plate to an aluminum (with some Mg) holder.

### Overpotential and Other Calculations



$$E_{\text{H}_2\text{O}/\text{H}_2\text{O}_2(\text{org})}^0 = \frac{\Delta G_{\text{H}_2\text{O}/\text{H}_2\text{O}_2(\text{org})}^0}{-nF} = \frac{+81.54}{-2 * 23.06} = 1.768 \text{ V vs. Fc/Fc}^{+/0}$$

$$\begin{aligned}
 E_{\text{H}_2\text{O}/\text{H}_2\text{O}_2(\text{org})}^0 &= E_{\text{H}_2\text{O}/\text{H}_2\text{O}_2(\text{org})}^0 - 0.0592 \text{ p}K_{\text{a}} \\
 &= 1.768 \text{ V} - 0.0592 * 13.92 = 0.944 \text{ V}
 \end{aligned}$$

Overpotential of CPE: 0.456 V

Overpotential indicated by LCoCl/lutidine/H<sub>2</sub>O CVs: 0.256 V

Equation S4. Derivation of Overpotential Calculation from free energies and literature values<sup>6</sup>

### Kinetic Measurements

To perform an Eyring analysis for the reaction of **1-OH** to **2** in the presence of excess acetonitrile, the intensity of the absorbance at 560 nm was monitored at a variety of temperatures. This point was chosen because it was on one of the few features (at 550 nm) that varied in each transformation (due to most of the intermediates having overlapping features). Thus, the rate of the formation of **2-MeCN** was determined by the decrease of the absorption at 560 nm that corresponded to the growth of the peak at 700 nm using a first order fit to the data. The second order rates were determined by the continued disappearance of the absorption at 560 nm with no change to the peak at 700 nm.

The rates calculated for the Eyring analysis of the reaction of **1-OH-MeCN** to **3-MeCN** give a line of best fit with an R<sup>2</sup> value of 0.95:

$$\ln \frac{k_y[B]}{T} = \frac{-\Delta H^\ddagger}{R} * \frac{1}{T} + \ln \frac{\kappa k_B}{h} + \frac{\Delta S^\ddagger}{R}$$

$$\ln \frac{k_y[B]}{T} = -5764.1 * \frac{1}{T} + 9.60$$

Equation S5. Eyring Equation Fit for second-order transformation of **1-OH-MeCN** to **3-MeCN**

Error in the y-intercept used to determine  $\Delta S^\ddagger$  was determined by propagation of error in the line of best fit (i.e. error in the y-intercept for the line of best fit). This resulted in  $\Delta S^\ddagger = -28 \pm 1$  cal/mol.

Error in the slope used to determine  $\Delta H^\ddagger$  was determined by propagation of error in the line of best fit (i.e. error in the slope calculated for the line of best fit). This resulted in  $\Delta H^\ddagger = 11.4 \pm 0.3$  kcal/mol.

This leads to a  $\Delta G^\ddagger$  of  $19.8 \pm 0.3$  kcal/mol, consistent with a less unfavorable dimerization in the presence of acetonitrile and a low transition state barrier, likely due to some amount of pre-organization in solution.

Table S11: Calculated data for Eyring analysis of **1-OH-MeCN** to **3-MeCN** at 560 nm

1/T (1/K)	Average $\ln(k_y[B_0]/T)$	Standard Deviation
0.00395	-13.100	0.318
0.0038	-12.484	0.639
0.003634	-11.040	0.753
0.00357	-11.298	1.320
0.003507	-10.504	0.613

Table S12. Rates of the reaction of **1-OH-MeCN** to **3-MeCN** at 560 nm.

Temperature (K)	Rate ( $M^{-1}s^{-1}$ )	Average rate ( $M^{-1}s^{-1}$ )	1/T (1/K)	Average $\ln(k[B]/T)$
253.15	$3.642 \times 10^{-4}$	$5.179 \times 10^{-4}$	0.003950	-13.100
	$5.011 \times 10^{-4}$			
	$6.884 \times 10^{-3}$			
263.15	$6.475 \times 10^{-4}$	$9.968 \times 10^{-4}$	0.003800	-12.484
	$5.513 \times 10^{-4}$			
	0.00179			
275.15	0.00513	$4.417 \times 10^{-3}$	0.003634	-11.040
	0.00653			
	0.00160			
280.15	0.00786	$3.473 \times 10^{-3}$	0.003570	-11.298
	$5.606 \times 10^{-4}$			
	0.00200			
285.15	0.00449	$7.820 \times 10^{-3}$	0.003507	-10.504
	0.0138			
	0.00516			

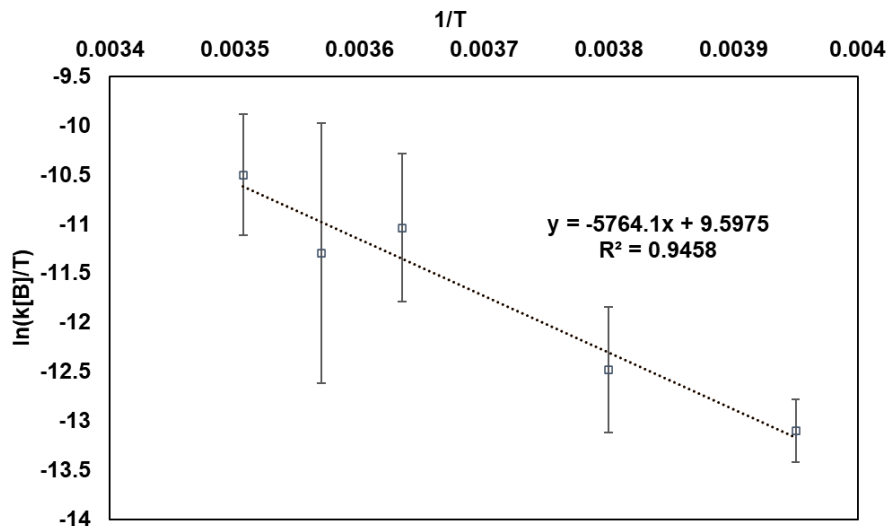


Figure S79. Eyring fit for second-order transformation from **1-OH-MeCN** to **3-MeCN**.

The rates calculated for the Eyring analysis of the reaction of **1-OH** to **1-OH-MeCN** are complicated at higher temperatures, as the initial first order segment is very short, and only the mixed second-order/first-order decay are easily fitted. However, using the three low temperature values, this can be approximated with a line of best fit with an  $R^2$  value of 0.87:

$$\ln \frac{k_x}{T} = \frac{-\Delta H^\ddagger}{R} * \frac{1}{T} + \ln \frac{\kappa k_B}{h} + \frac{\Delta S^\ddagger}{R}$$

$$\ln \frac{k_x}{T} = -5309.3 * \frac{1}{T} + 8.74$$

Equation S6. Eyring equation fit for second-order transformation of 1-OH-MeCN to 3-MeCN

Error in the y-intercept used to determine  $\Delta S^\ddagger$  was determined by propagation of error in the line of best fit (i.e. error in the y-intercept for the line of best fit). This resulted in  $\Delta S^\ddagger = -30 \pm 2$  cal/mol. Error in the slope used to determine  $\Delta H^\ddagger$  was determined by propagation of error in the line of best fit (i.e. error in the slope calculated for the line of best fit). This resulted in  $\Delta H^\ddagger = 10.5 \pm 0.4$  kcal/mol.

This leads to a  $\Delta G^\ddagger$  of  $19.4 \pm 0.4$  kcal/mol.

Table S13: Calculated data for Eyring analysis of **1-OH** to **1-OH-MeCN** at 560 nm

1/T (1/K)	Average ln(k <sub>v</sub> /T)	Standard Deviation
0.00395	-12.035	0.948
0.0038	-11.809	0.519
0.003634	-10.376	0.244
0.00357	-14.606	0.160
0.003507	-14.706	1.424

Table S14. Rates of the reaction of **1-OH** to **1-OH-MeCN** at 560 nm.

Temperature (K)	Rate (s <sup>-1</sup> )	Average rate (s <sup>-1</sup> )	1/T (1/K)	Average ln(k/T)
253.15	0.00208	0.00150	0.003950	-12.035
	0.000398			
	0.00205			
263.15	0.00305	0.00186	0.003800	-11.809
	0.00174			
	0.00108			
275.15	0.000753	0.00857	0.003634	-10.376
	0.000709			
	0.001111			
280.15	1.049*10 <sup>-4</sup>	1.271*10 <sup>-4</sup>	0.003570	-14.606
	1.363*10 <sup>-4</sup>			
	1.400*10 <sup>-4</sup>			
285.15	1.477*10 <sup>-5</sup>	1.171*10 <sup>-4</sup>	0.003507	-14.706
	2.431*10 <sup>-4</sup>			
	9.326*10 <sup>-5</sup>			

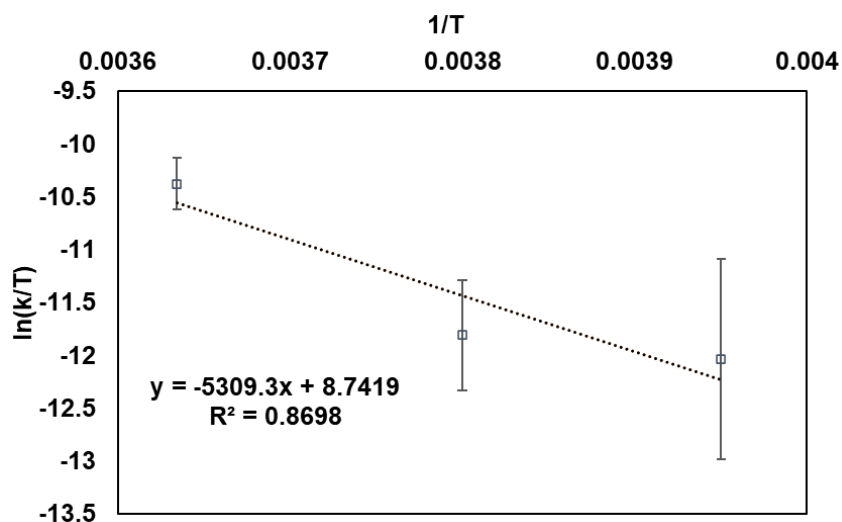


Figure S80. Eyring fit for first-order transformation from **1-OH** to **1-OH-MeCN**.

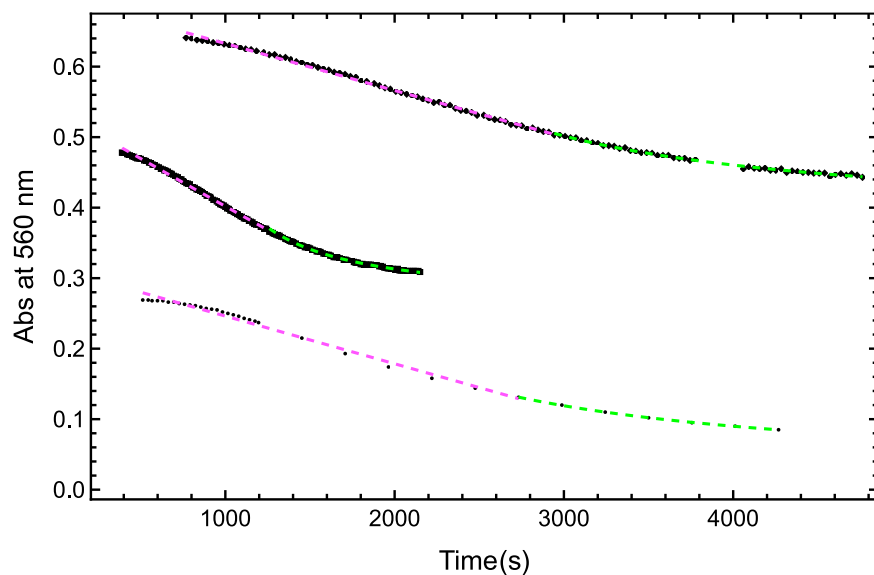


Figure S81. Absorbance at 560 nm, monitoring reaction at 12 °C. Pink lines are fits for the first-order process and green lines are fits for the second-order process. For temperatures above 2 °C, the fits are worse, and the second-order transformation is nearly concomitant with the following rapid first order transformation.

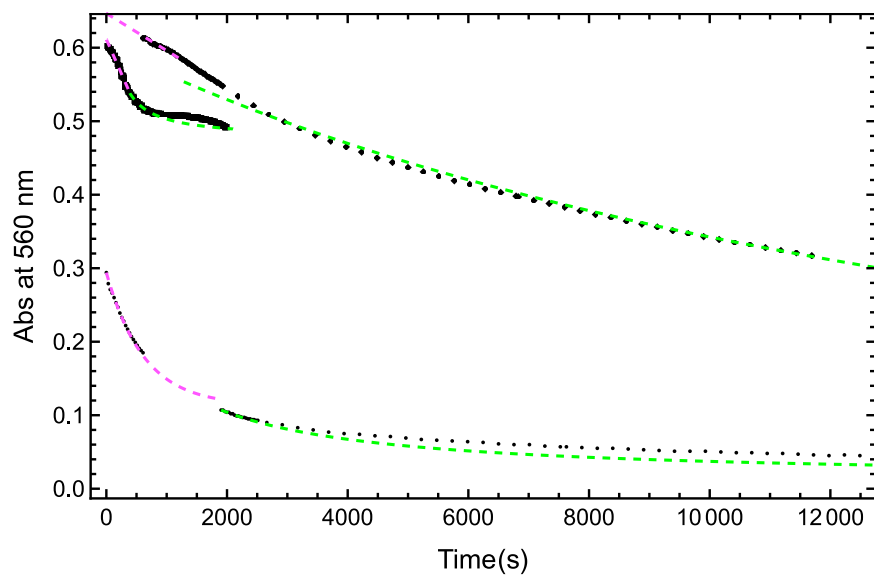


Figure S82. Absorbance at 560 nm, monitoring reaction at 7 °C. Pink lines are fits for the first-order process and green lines are fits for the second-order process. For temperatures above 2 °C,

the fits are worse, and the second-order transformation is nearly concomitant with the following rapid first order transformation.

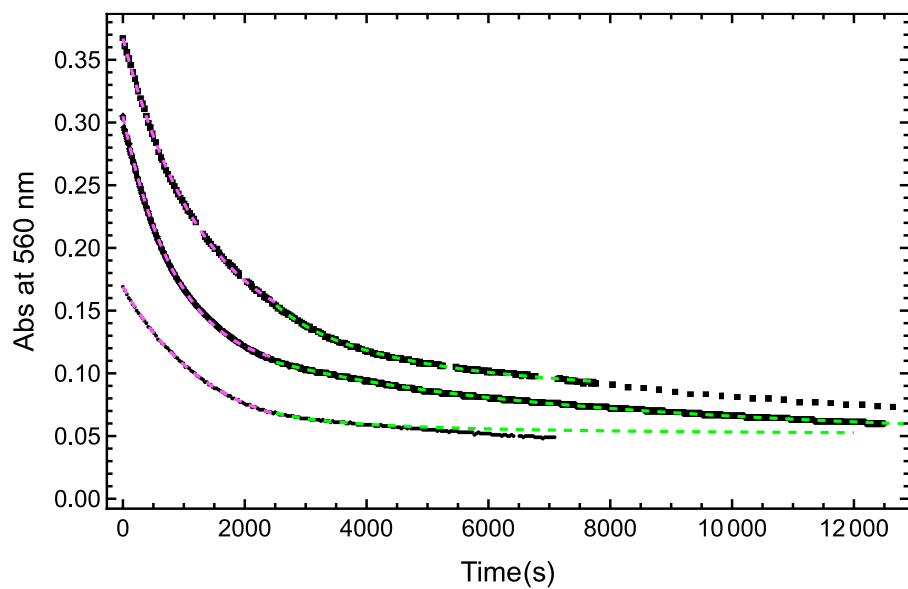


Figure S83. Absorbance at 560 nm, monitoring reaction at 2 °C. Pink lines are fits for the first-order process and green lines are fits for the second-order process.

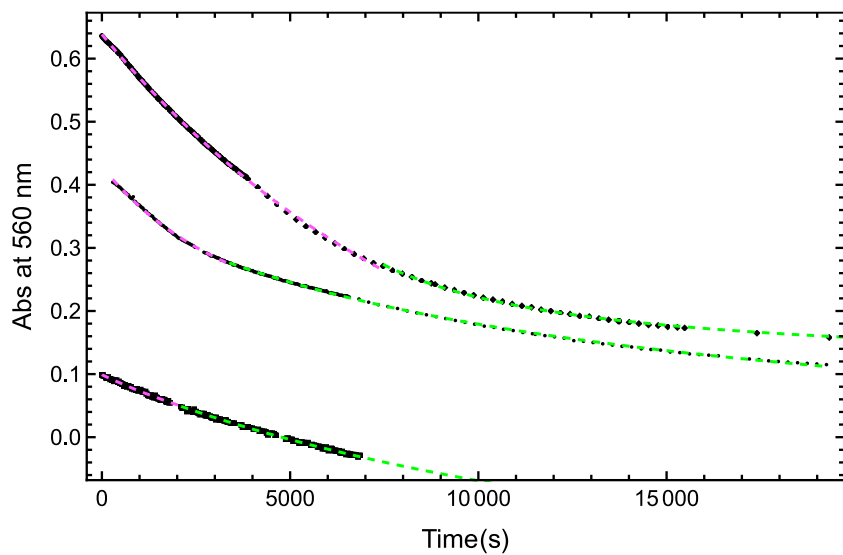


Figure S84. Absorbance at 560 nm, monitoring reaction at -10 °C. Pink lines are fits for the first-order process and green lines are fits for the second-order process.

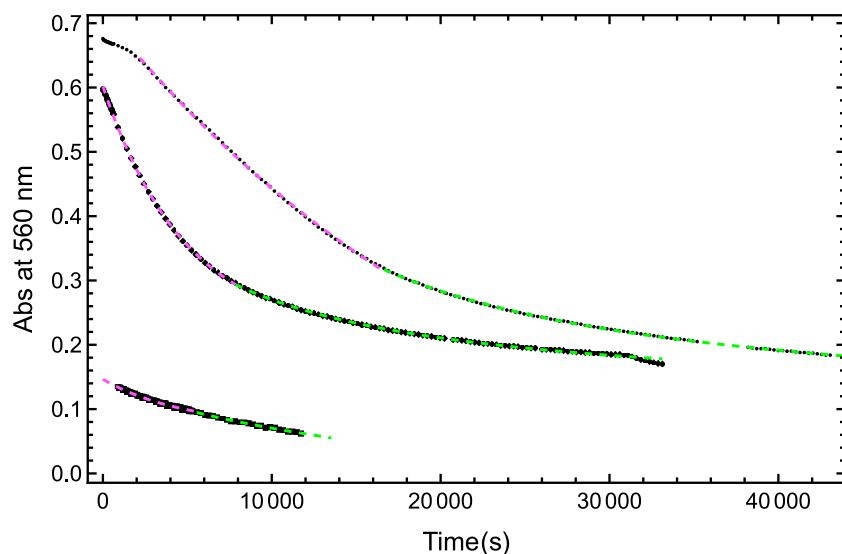


Figure S85. Absorbance at 560 nm, monitoring reaction at  $-20\text{ }^{\circ}\text{C}$ . Pink lines are fits for the first-order process and green lines are fits for the second-order process.

## References

1. (a) Espenson, J. H. *Chemical Kinetics and Reaction Mechanisms*; McGraw-Hill Custom Publishing, New York Etc., **1981**. (b) Goetz, M. K.; Anderson, J. S. *J. Am. Chem. Soc.* **2020**, *142*, 11, 5439–5441.
2. G. M. Sheldrick, *Acta Cryst.* **2015**, *C71*, 3-8.
3. O. V. Dolomanov, L. J. Bourhis, R. J. Gildea, A. K. Howard, H. Puschmann, *J. Appl. Cryst.* **2009**, *42*, 339.
4. G. M. Sheldrick. *Acta Cryst.* **2008**, *A64*, 112-122.
5. (a) Neese, F. "The Orca Program System" *Wiley Interdisciplinary Reviews: Computational Molecular Science* **2012**, *2*, 73-78. (b) H - Kr: A. Schaefer, H. Horn and R. Ahlrichs, *J. Chem. Phys.* **1992**, *97*, 2571. (c) Rb - Xe: A. Schaefer, C. Huber and R. Ahlrichs, *J. Chem. Phys.* **1994** *100*, 5829. (d) F. Weigend, R. Ahlrichs, *Phys. Chem. Chem. Phys.* **2005**, *7*, 3297.
6. Rana, A.; Lee, Y-M.; Li, X.; Cao, R.; Fukuzumi, S.; Nam, W. *ACS Catal.* **2021**, *11*, 5, 3073. Pegis, M. L.; Roberts, J. A. S.; Wasylenko, D. J.; Mader, E. A.; Appel, A. M.; Mayer, J. M. *Inorg. Chem.* **2015**, *54*, 24, 11883.

## Appendix IV: Chapter V Supplementary Information

### NMR spectroscopy Post-Catalysis

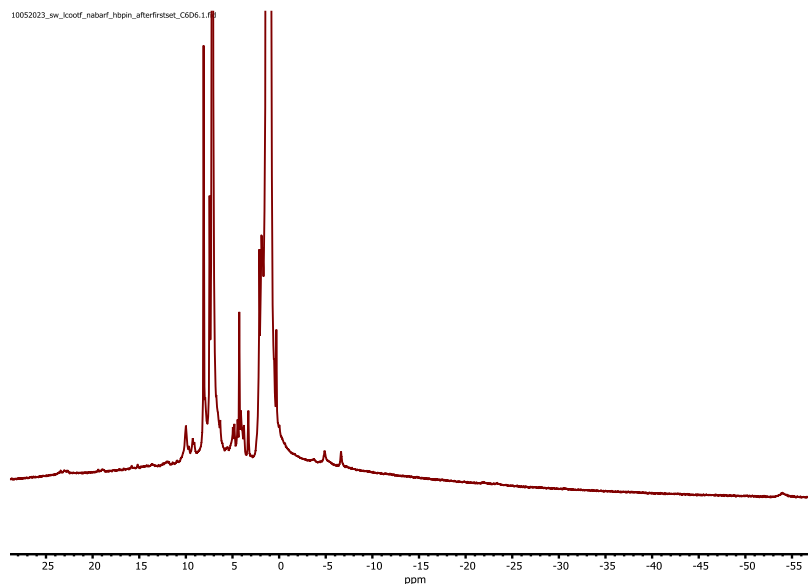


Figure S1.  $^1\text{H}$  NMR of  $[(t\text{Bu,Tol})\text{DHP-BPin})\text{Co}][\text{BARF}_4]$  (**2-BPin**) in  $\text{C}_6\text{D}_6$  on Bruker DRX 500 spectrometer .

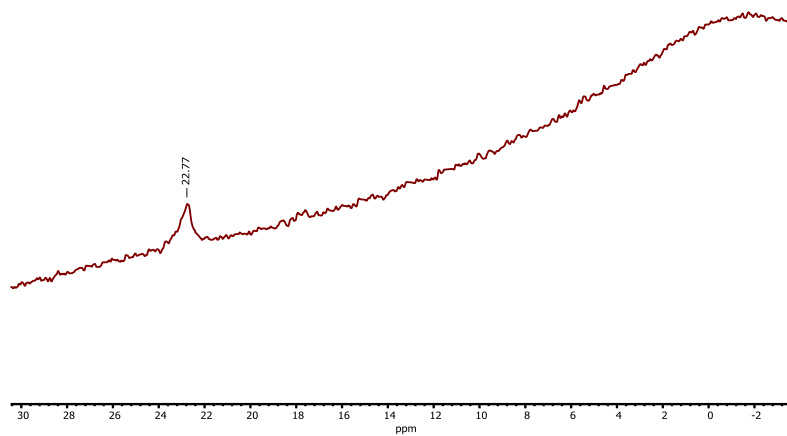


Figure S2.  $^{11}\text{B}$  NMR of  $[(t\text{Bu,Tol})\text{DHP-BPin})\text{Co}][\text{BARF}_4]$  (**2-BPin**) in  $\text{C}_6\text{D}_6$  on Bruker DRX 500 spectrometer .

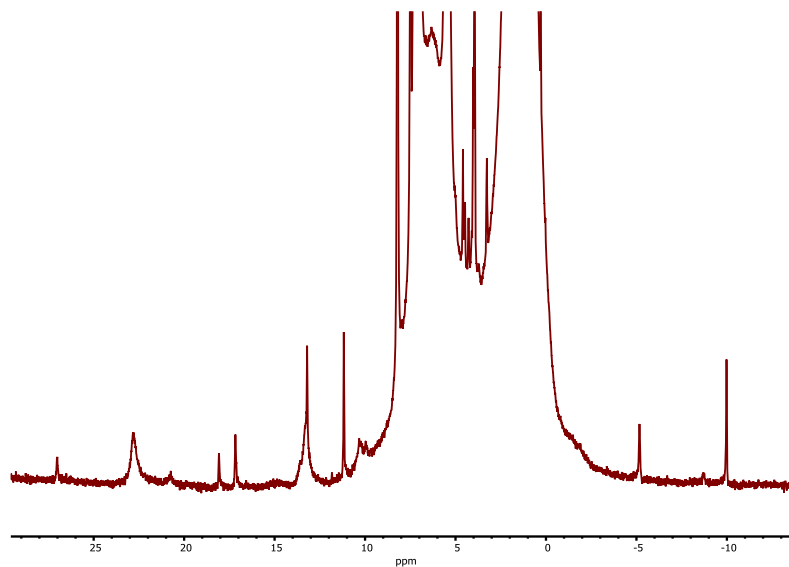


Figure S3. <sup>1</sup>H NMR of [(<sup>t</sup>Bu,<sup>Tol</sup>DHP-BCyD)Co][BAr<sup>F</sup><sub>4</sub>] (**2-BCyD**) in C<sub>6</sub>D<sub>6</sub>.

03262024\_0w\_kcoofthabar\_f\_dlohb3sm2\_cisHex\_C6D6.12.fid

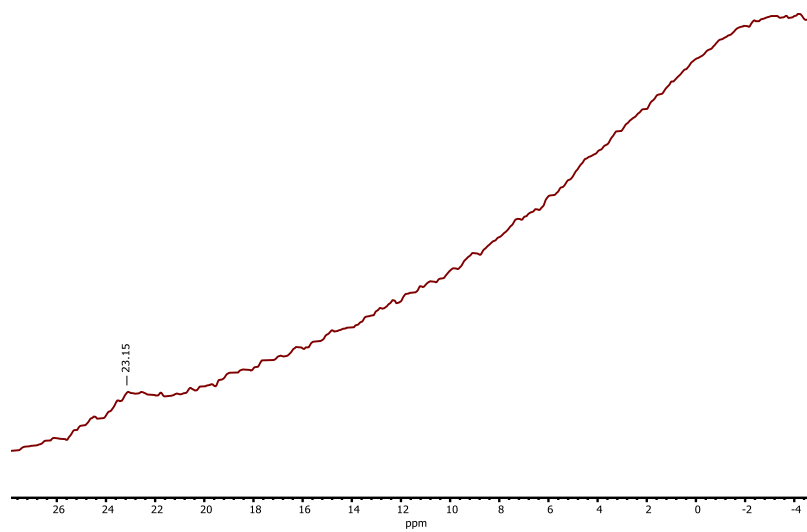


Figure S4. <sup>11</sup>B NMR of [(<sup>t</sup>Bu,<sup>Tol</sup>DHP-BCyD)Co][BAr<sup>F</sup><sub>4</sub>] (**2-BCyD**) in C<sub>6</sub>D<sub>6</sub>.

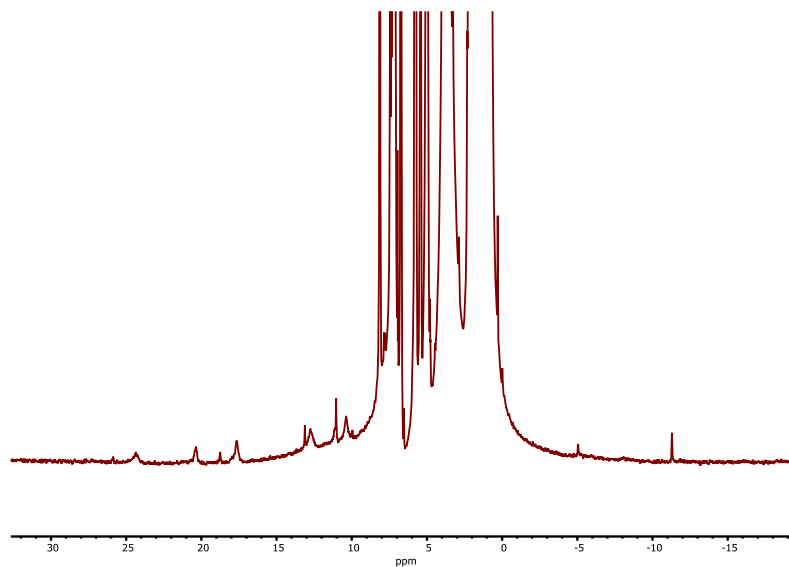


Figure S5. <sup>1</sup>H NMR of [(<sup>t</sup>Bu,<sup>Tol</sup>DHP-BH<sub>2</sub>)Co][BAr<sup>F</sup><sub>4</sub>] (**2-BH<sub>3</sub>**) in C<sub>6</sub>D<sub>6</sub>.

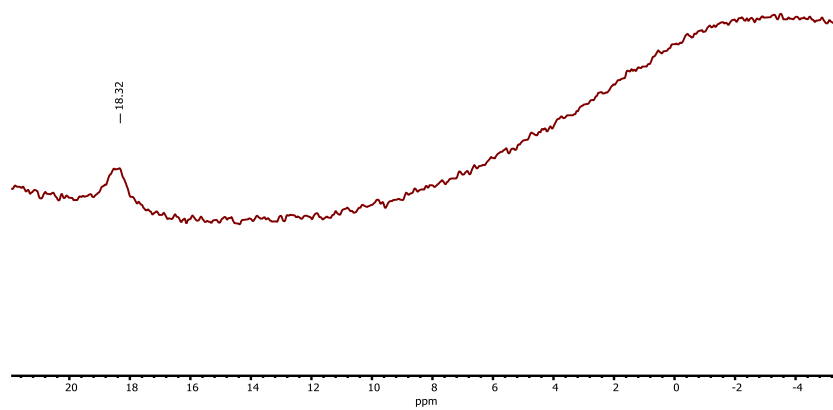


Figure S6. <sup>11</sup>B NMR of [(<sup>t</sup>Bu,<sup>Tol</sup>DHP-BH<sub>2</sub>)Co][BAr<sup>F</sup><sub>4</sub>] (**2-BH<sub>3</sub>**) in C<sub>6</sub>D<sub>6</sub>.

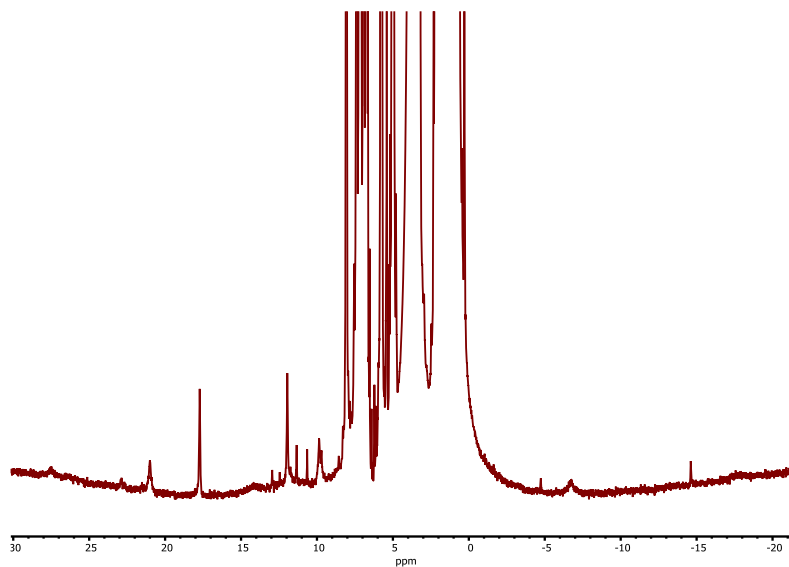


Figure S7. <sup>1</sup>H NMR of [(<sup>t</sup>Bu,<sup>Tol</sup>DHP-BCat)Co][BARF<sub>4</sub>] (**2-BCat**) in C<sub>6</sub>D<sub>6</sub>.

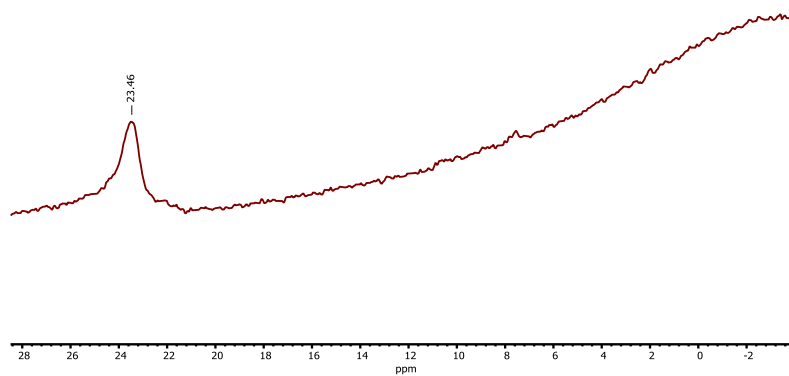


Figure S8. <sup>11</sup>B NMR of [(<sup>t</sup>Bu,<sup>Tol</sup>DHP-BCat)Co][BARF<sub>4</sub>] (**2-BCat**) in C<sub>6</sub>D<sub>6</sub>.

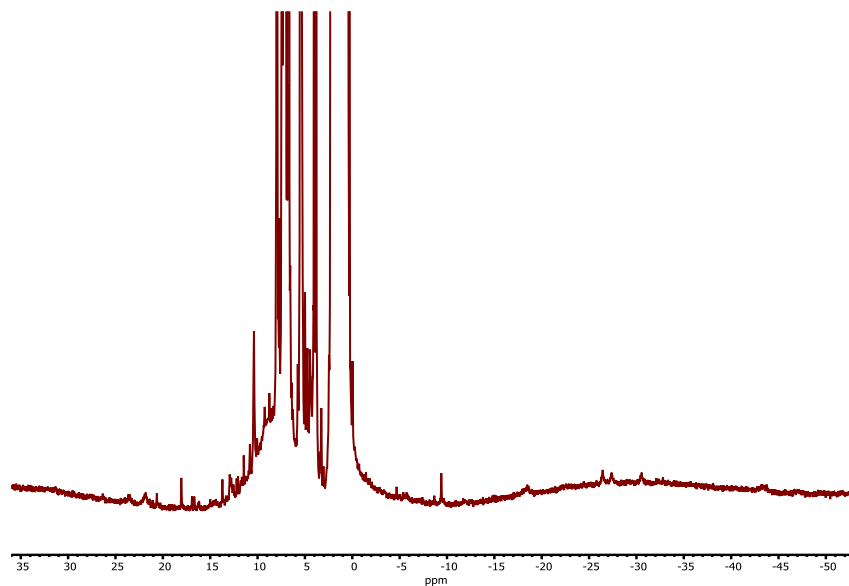


Figure S9.  $^1\text{H}$  NMR of  $[(^t\text{Bu,Tol})\text{DHP-BCamph})\text{Co}][\text{BAr}^{\text{F}}_4]$  (**2-BCamph**) in  $\text{C}_6\text{D}_6$ .

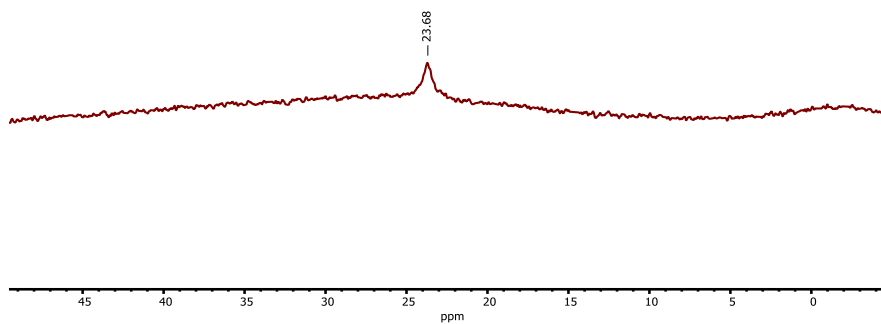


Figure S10.  $^{11}\text{B}$  NMR of  $[(^t\text{Bu,Tol})\text{DHP-BCamph})\text{Co}][\text{BAr}^{\text{F}}_4]$  (**2-BCamph**) in  $\text{C}_6\text{D}_6$ .

### UV-vis spectroscopy

*All UV-Vis are done at scan speeds of 1200 nm/min unless otherwise specified*

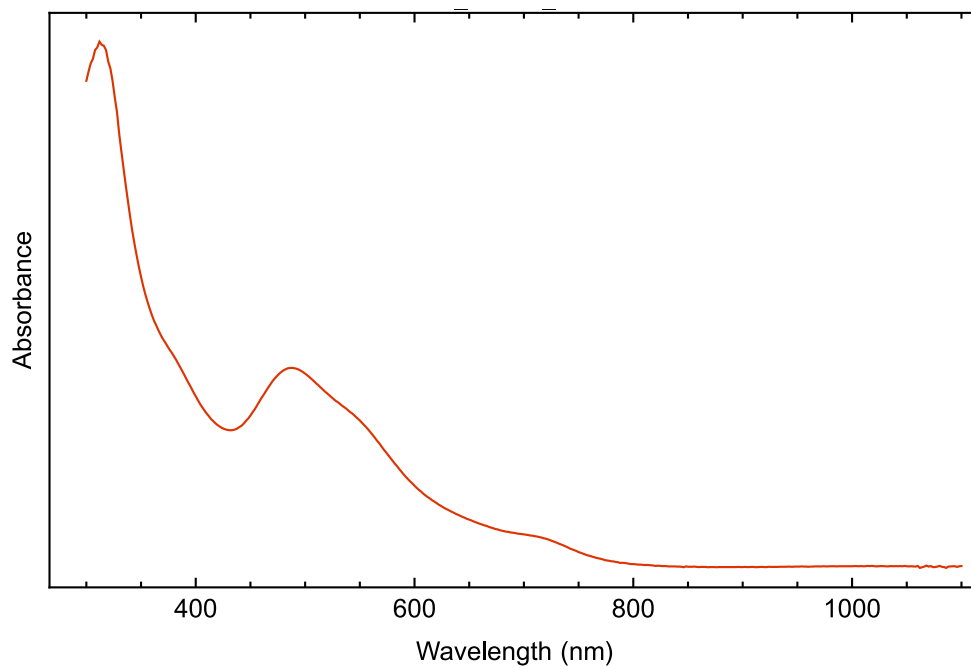


Figure S11. UV-vis of **1** + NaBAr<sup>F</sup><sub>4</sub> from a 0.110 mM solution in benzene at room temperature.

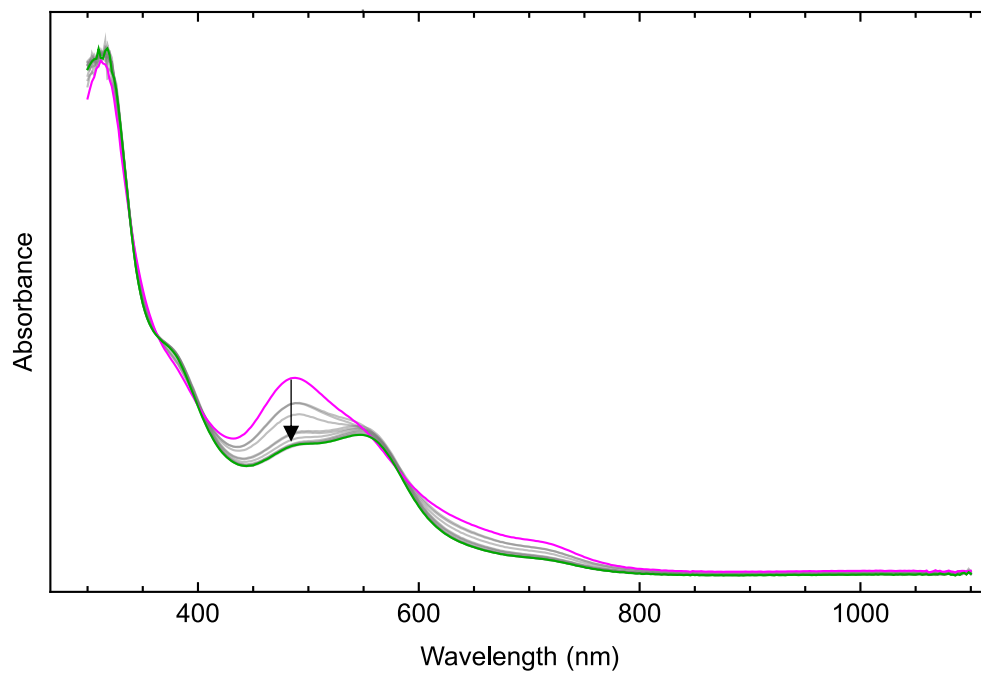


Figure S12. UV-vis of **1** + NaBAr<sup>F</sup><sub>4</sub> + HBpin from a 0.110 mM solution in benzene at room temperature. Scans taken every 53 seconds.

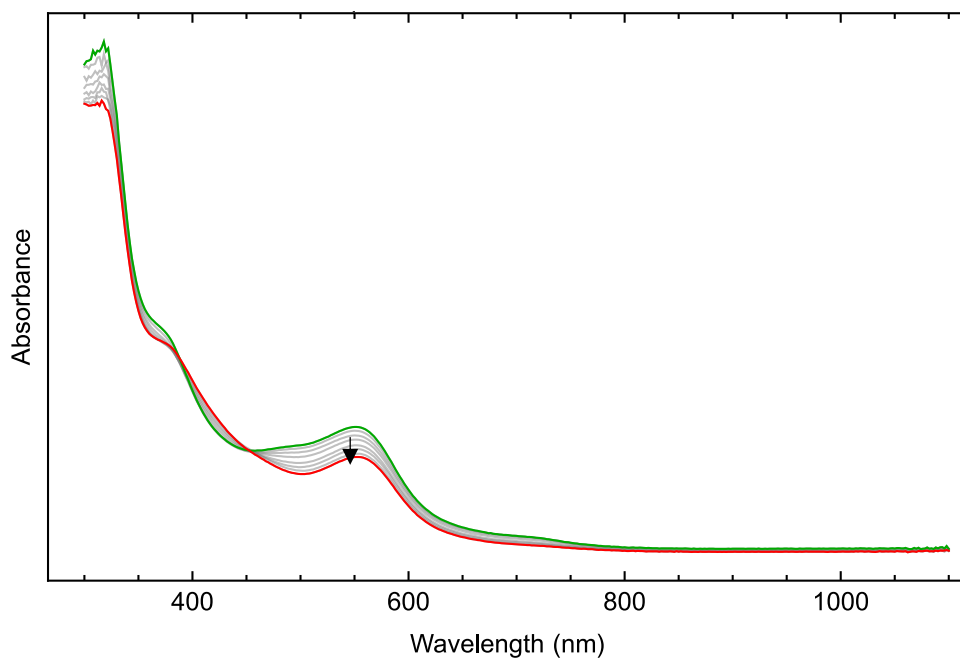


Figure S13. First UV-vis of **1** + NaBAR<sup>F</sup><sub>4</sub> + HBpin + 1-hexene from a 0.110 mM solution in benzene at room temperature. Scans taken every 53 seconds.

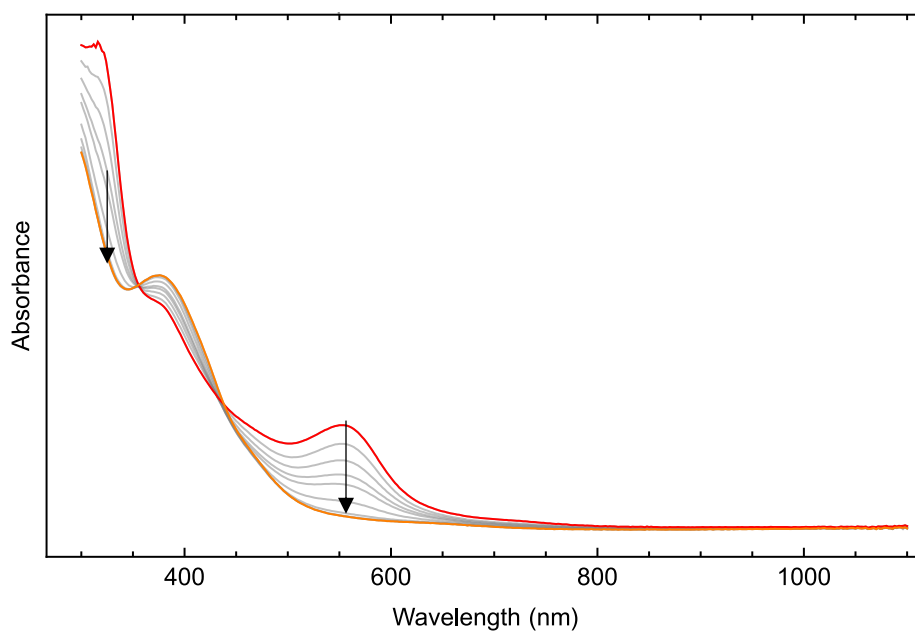


Figure S14. Second UV-vis of **1** + NaBAR<sup>F</sup><sub>4</sub> + HBpin + 1-hexene from a 0.110 mM solution in benzene at room temperature. Scans taken every 249 seconds.

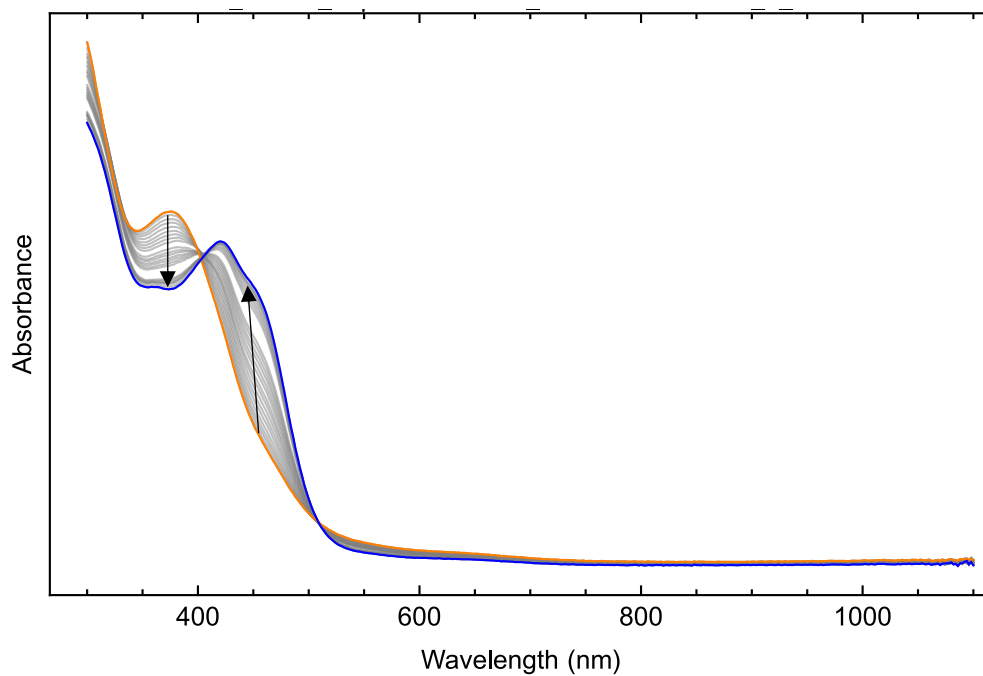


Figure S15. Third UV-vis of **1** + NaBAr<sup>F</sup><sub>4</sub> + HBpin + 1-hexene from a 0.110 mM solution in benzene at room temperature. Scans taken every 249 seconds.

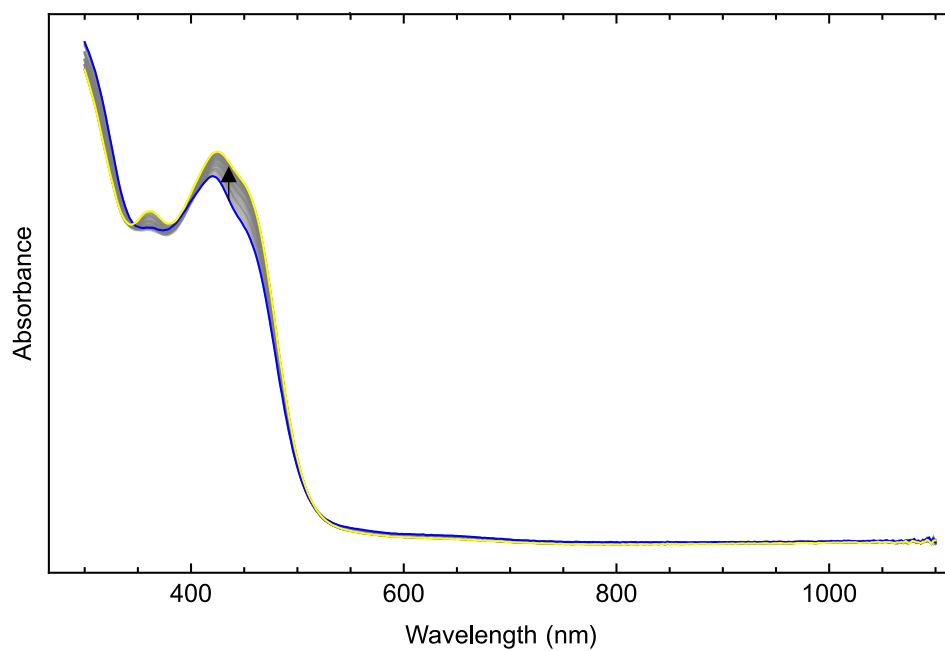


Figure S16. Fourth UV-vis of **1** + NaBAr<sub>F</sub><sup>24</sup> + HBpin + 1-hexene from a 0.110 mM solution in benzene at room temperature. Scans taken every 249 seconds.

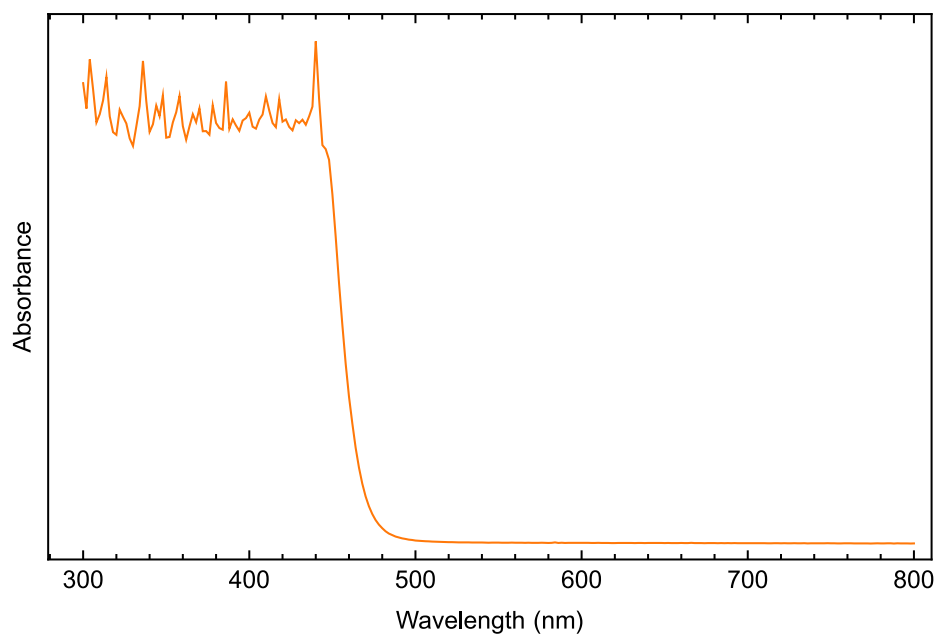


Figure S17. UV-vis of 476 band pass filter for spectral verification.

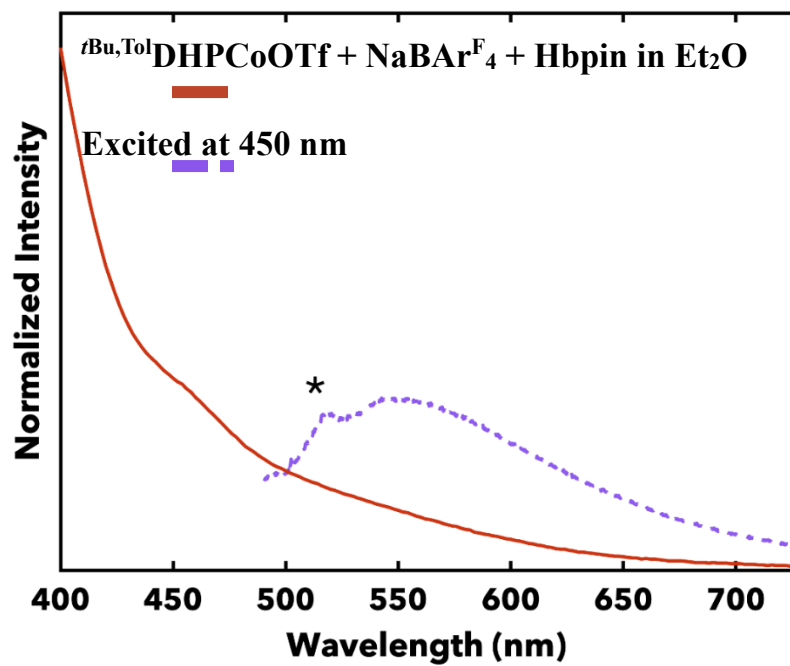


Figure S18. Absorbance and Photoluminescence Spectrum of **2-Pin** (0.14 mM) excited at 450 nm in Et<sub>2</sub>O.

## Vibrational Spectroscopy

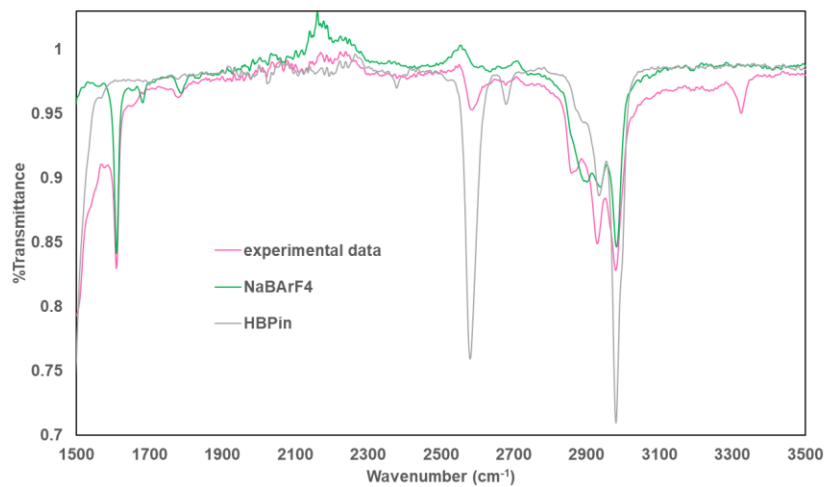


Figure S19. IR of **2-BPin** as a thin film (pink). Comparison IRs for NaBAr<sup>F</sup><sub>4</sub> and HBPIn also shown.

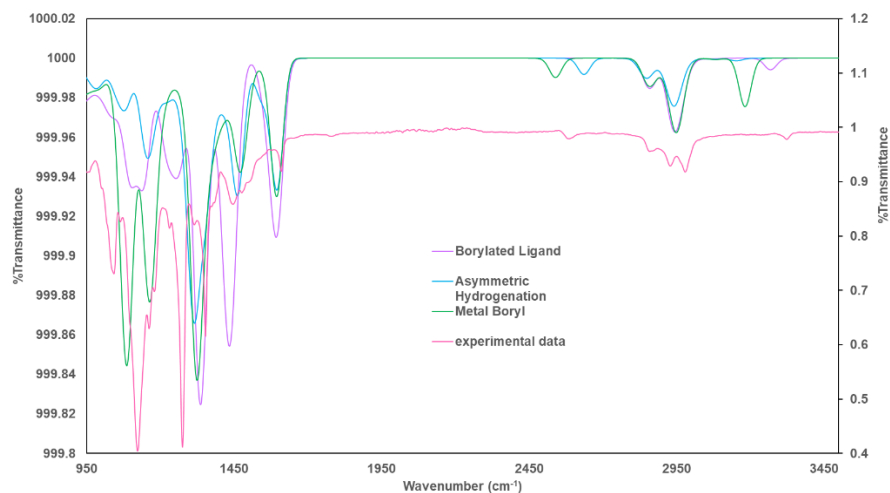


Figure S20. IR of **2-BPin** as a thin film (pink) with comparison DFT-calculated IRs for hydroborated ligand (purple), asymmetric hydrogenation of the ligand (blue), and a metal boryl species (green) shown.

## EPR Spectroscopy

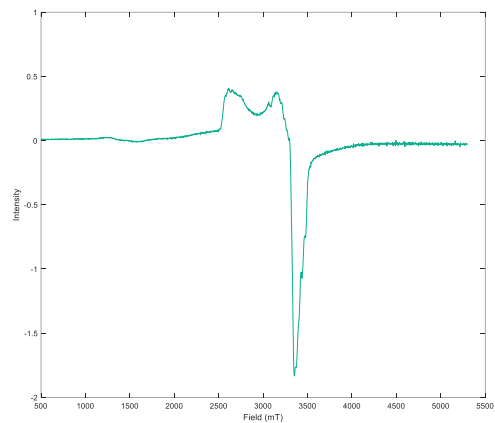


Figure S21. Full perpendicular-mode EPR spectrum of a 15 mM solution of **1** and NaBARF<sub>4</sub> in toluene at 15 K. Conditions: MW frequency, 9.639 GHz; MW power, 2.0 mW.

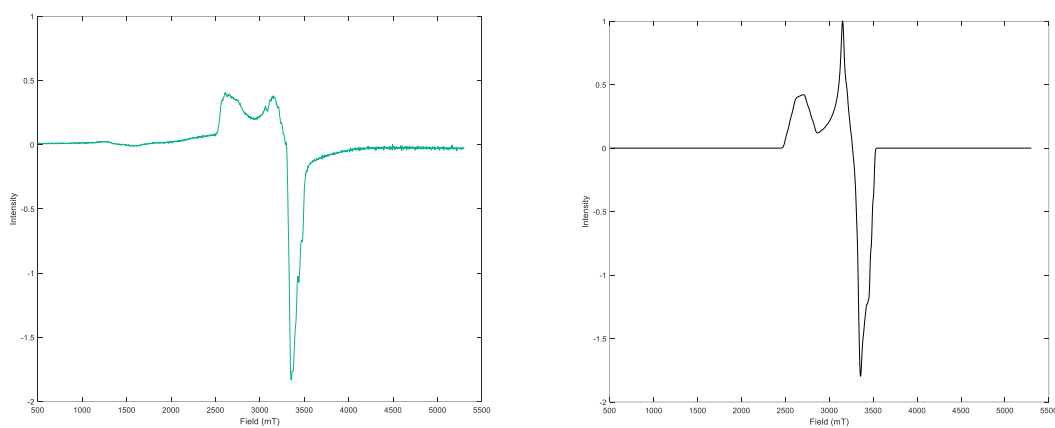


Figure S22. Perpendicular-mode EPR spectrum (left) and simulated spectrum (right) of a 15 mM solution of **1** in toluene at 15 K. Conditions: MW frequency, 9.631 GHz; MW power, 2.0 mW.

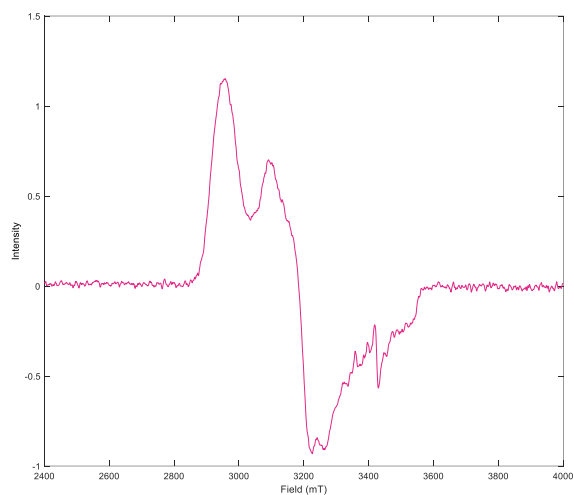


Figure S23. Full perpendicular-mode EPR spectrum of a 15 mM solution of **2-Pin** in toluene at 127 K. Conditions: MW frequency, 9.639 GHz; MW power, 2.0 mW.

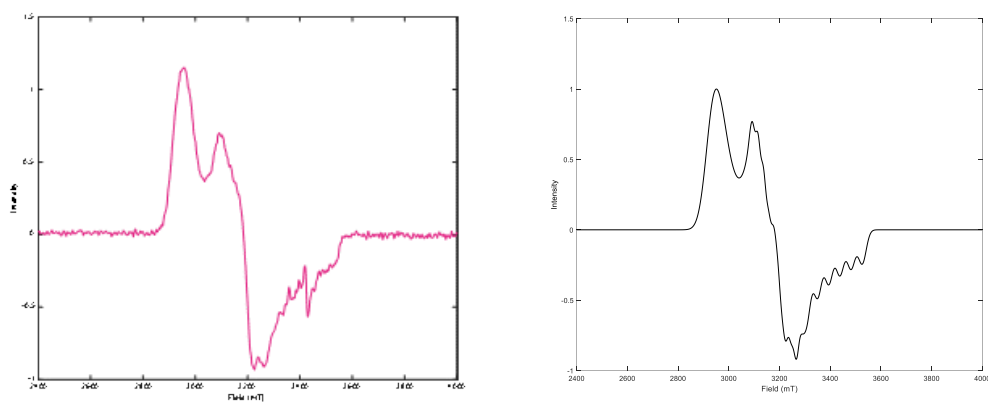


Figure S24. Perpendicular-mode EPR spectrum (left) and simulated spectrum (right) of a 15 mM solution of **2-Pin** in toluene at 127 K. Conditions: MW frequency, 9.631 GHz; MW power, 2.0 mW.

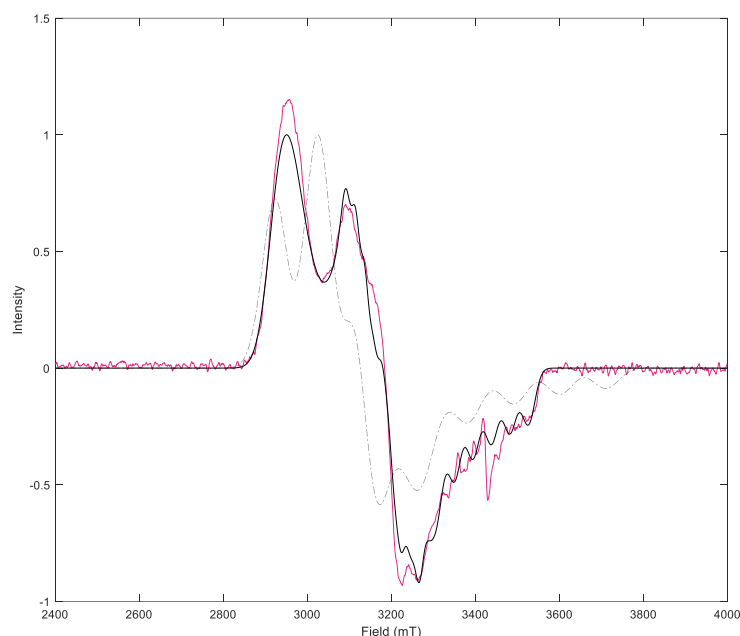


Figure S25. Perpendicular-mode EPR spectrum of a 15 mM solution of **2-Pin** in toluene at 127 K. DFT simulated spectrum plotted in gray. Conditions: MW frequency, 9.639 GHz; MW power, 2.0 mW.

Table S1. *g*-values for EPR

	<i>g</i> (x,y,z)	<i>Co-A</i>	<i>N-A</i>	<i>H-strain</i>
<b>1 + NaBAr<sup>F</sup><sub>4</sub></b>	(2.0206, 2.1183, 2.5842)	(56.160, 73.591, 108.487)	(73.543, 12.715, 172.354)	(57.187, 88.006, 159.753)
<b>1<sup>+</sup> DFT</b>	(2.0163, 2.2359, 2.3907)	(374.27, 290.83, 628.51)	(19.24, 16.95, 21.30)	N/A
<b>2-Pin</b>	(2.0417, 2.1581, 2.3282)	(124.816, 58.346, 29.917)	(4.642, 71.640, 15.488)	(99.750, 60.978, 214.930)
<b>2-Pin (DFT)</b>	(2.0740, 2.1465, 2.3390)	(73.88, 72.91, 234.46)	(20.27, 16.10, 10.36)	N/A

Due to the challenge of simulating EPR spectra with DFT that properly reflects the proportion of radical character on supporting ligands, we investigated a number of basis-sets and functionals for the DFT simulated spectra. Here we present a table of our findings, inspired by previous work in this area.<sup>1</sup> The basis-set and functional we found most reflected our experimental findings was B3LYP, with an IGLO-III functional. The best fits are highlighted in blue, with the

worst fits in red. We found that ECPs on Co led to worse results, and that B3LYP functional + CP(PPP) basis set on Co/IGLO-III basis sets on boron/carbon/nitrogen/oxygen led to the best match for experimental values. All other parameters for the EPR calculations were consistent with standard DFT methods described below, though the CPCM solvent was toluene for these calculations. We would like to note that even the best fits still overestimate the amount of spin-density residing on Co, leading to consistently higher A-values than are appropriate to fit spectra for that nucleus.

Table S2. Various DFT fits for EPR parameters—fitting *g*-values.

Experimental Fit	<b>2.3282</b>	ABS(Calc-Exp)	<b>2.1581</b>	ABS(Calc-Exp)	<b>2.0417</b>	ABS(Calc-Exp)	Average difference
PBE0, TZVP, ECP	2.251835	0.076365	2.16755	0.00945	2.068525	0.0268247	0.037546567
EPR-II, TZVP, ECP	2.251362	0.076838	2.161593	0.0034933	2.066075	0.024375	0.0349021
EPR-II, TZVP	2.338912	0.010712	2.174714	0.016614	2.082008	0.040308	0.022544667
TPSS, IGLO-III, ECP	2.1426	0.1856	2.0843	0.0738	2.0412	0.0005	0.086633333
TPSS, IGLO-III	2.1739	0.1543	2.087	0.0711	2.0444	0.0027	0.076033333
TPSSh, IGLO-III, ECP	2.1581	0.1701	2.1048	0.0533	2.0449	0.0032	0.075533333
TPSSh, IGLO-III	2.1976	0.1306	2.1044	0.0537	2.0503	0.0086	0.0643
B3LYP, IGLO-III, ECP	2.2304	0.0978	2.1242	0.0339	2.0592	0.0175	0.049733333
B3LYP, IGLO-III	2.339	0.0108	2.1465	0.0116	2.074	0.0323	0.018233333
BP86, IGLO-III, ECP	2.1634	0.1648	2.0886	0.0695	2.0451	0.0034	0.079233333
BP86, IGLO-III	2.2358	0.0924	2.1067	0.0514	2.0544	0.0127	0.052166667
M06L, IGLO-III	2.1257	0.2025	2.0754	0.0827	2.0298	0.0119	0.099033333
PBE0, IGLO-III, ECP	2.2371	0.0911	2.1675	0.0094	2.0642	0.0225	0.041
PBE0, IGLO-III	2.3446	0.0164	2.1744	0.0163	2.0795	0.0378	0.0235

Table S3. Various DFT fits for EPR parameters—fitting *A*-values.

Experi mental Fit	29.9 2	ABS(Cal c-Exp)	58.3 46	ABS(Cal c-Exp)	124. 82	ABS(Cal c-Exp)	15.4 847	ABS(Cal c-Exp)	71.6 401	ABS(Cal c-Exp)	4.64 18	ABS(Cal c-Exp)	Average difference
PBE0, TZVP, ECP	6.14	23.78	43.1 8	15.166	315. 83	191.01	26.1 8	10.6953	31.2 9	40.3501	18.7 7	14.1282	49.18827

EPR-II, TZVP, ECP	5.77	24.15	43.9 4	14.406	314. 59	189.77	26.0 5	10.5653	31.5 2	40.1201	18.6 7	14.0282	48.83993
EPR-II, TZVP	309. 4	279.48	325. 04	266.694	586. 77	461.95	25.2 7	9.7853	21.0 9	50.5501	15.5 6	10.9182	179.8963
TPSS, IGLO- III, ECP	121. 45	91.53	59.7 3	1.384	232. 75	107.93	25.9	10.4153	18.1 7	53.4701	10.2 7	5.6282	45.0596
TPSS, IGLO- III	163. 85	133.93	78.0 9	19.744	200. 04	75.22	17.4 4	1.9553	12.3 8	59.2601	4.67	0.0282	48.35627
TPSSh, IGLO- III, ECP	61.7 7	31.85	0.15	58.196	262. 13	137.31	30.0 5	14.5653	22.8	48.8401	15.6 1	10.9682	50.28827
TPSSh, IGLO- III	112. 19	82.27	50.9 2	7.426	228. 42	103.6	9.84	5.6447	16.6 6	54.9801	21.6 5	17.0082	45.15483
B3LYP, IGLO- III, ECP	42.1 1	12.19	53.9 9	4.356	296. 4	171.58	21.0 1	5.5253	25.9 9	45.6501	14.9 4	10.2982	41.59993
B3LYP, IGLO- III	73.8 8	43.96	72.9 1	14.564	234. 46	109.64	20.2 7	4.7853	16.1	55.5401	10.3 6	5.7182	39.0346
BP86, IGLO- III, ECP	132. 5	102.58	89.6 6	31.314	237. 92	113.1	22.2 8	6.7953	15.6 8	55.9601	8.2	3.5582	52.21793
BP86, IGLO- III	190. 29	160.37	89.4 3	31.084	173. 35	48.53	14.3 3	1.1547	10.2 9	61.3501	1.46	3.1818	50.9451
M06L, IGLO- III	141. 93	112.01	68.1 9	9.844	240. 28	115.46	26.2 7	10.7853	19.9 3	51.7101	13.8	9.1582	51.4946
PBE0, IGLO- III, ECP	55.7 2	25.8	51.5 9	6.756	324. 89	200.07	30.8 6	15.3753	26.0 7	45.5701	19.3 4	14.6982	51.37827
PBE0, IGLO- III	14.8 6	15.06	26.9 7	31.376	271. 37	146.55	24.7 8	9.2953	20.6 8	50.9601	14.7 4	10.0982	43.88993

## Code to generate simulations of EPR Spectra.

*I:*

```
Exp1.mwFreq=9.63913;
```

```
Sys1.lw = 1
```

```
Exp1.Range = [50 530]
```

```
Sys1.lw = 1;
```

```
Exp1.nPoints = 4096;
```

```
Sys1.g = [2.58417 2.11831 2.0206];
```

```
Sys1.Nucs = 'Co, N';
```

```
Sys1.A = [108.487 73.5911 56.1602; 172.354 12.7151 73.5425];
```

```
Sys1.HStrain = [159.753 88.0059 57.1865];
```

```
Vary1.g = [0.02 0.02 0.02];
```

```
Vary1.HStrain = [50 50 50];
```

```
Vary1.A = [10 10 10; 10 10 10];
```

```
plot(B6mod_old,(I6mod_old)/8*max(I6mod_old),B6mod_old,pepper(Sys1,Exp1)/max(pepper(Sys1,Exp1)))
```

### *2-Pin (Sys2) and 2-Pin Simulation (Sys3):*

```
Exp2.mwFreq=9.63913;
```

```
Sys2.lw = 1
```

```
Exp2.Range = [240 400]
```

```
Sys2.g = [2.32823, 2.15809, 2.04171]
```

```
Exp2.nPoints = 2048
```

```
Sys2.Nucs = 'Co, N';
```

```

Sys2.A = [29.9166 58.3457 124.816;15.4847 71.6401 4.64181];
Sys2.HStrain = [214.93 60.9784 99.7497];
Sys3.lw = 1
Sys3.g = [2.251835, 2.1617550, 2.0685247]
Sys3.Nucs = 'Co, N';
Sys3.A = [-6.14 43.18 315.83;-26.18 -31.29 -18.77];
Sys3.HStrain = [250 200 200];
Vary2.g = [0.01 0.01 0.01];
Vary2.HStrain = [20 20 20];
Vary2.A = [10 10 15; 12 12 15];
plot(Bavg, pepper(Sys3,Exp2)/max(pepper(Sys3,Exp2)),Bavg,((Iavg)/max(Iavg))-(-
0.0000540804*Bavg+0.007711),Bavg,pepper(Sys2,Exp2)/max(pepper(Sys2,Exp2)))

```

### X-ray Absorption Spectroscopy

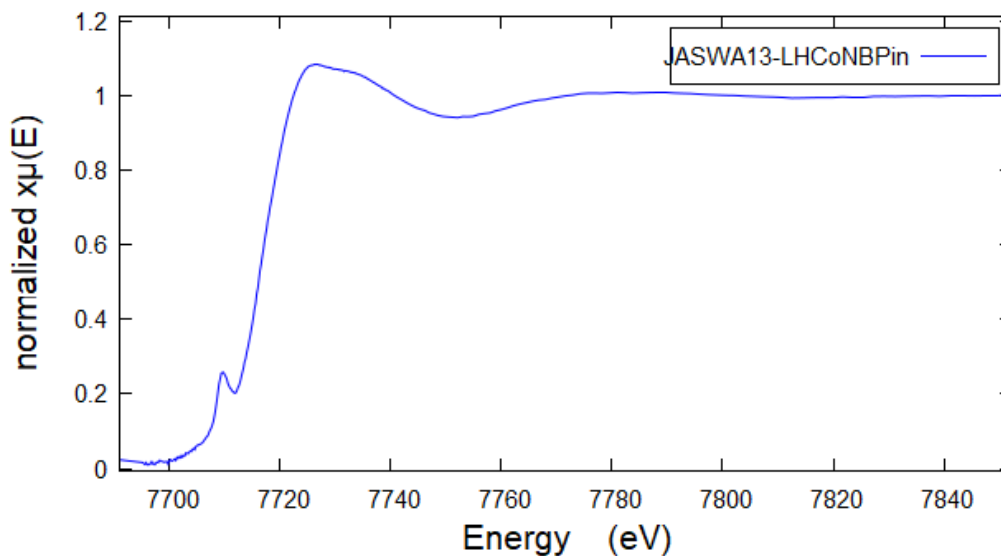


Figure S26. X-ray absorption spectra of **2-Pin** with a pre-edge feature at 7709.4 eV. This was collected as a frozen solution at 8 K in toluene.

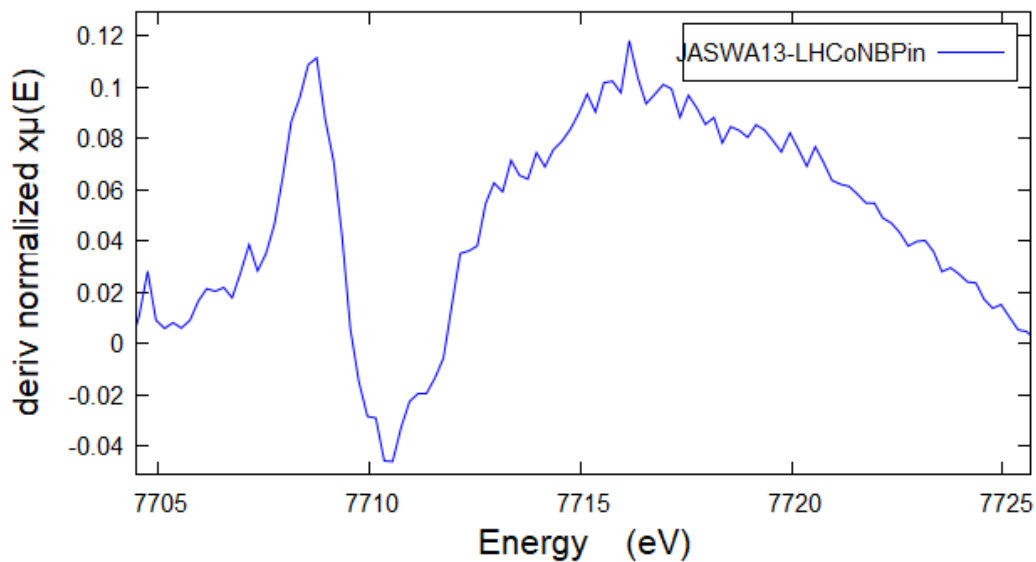


Figure S27. Derivative of X-ray absorption spectra of **2-Pin** (blue).

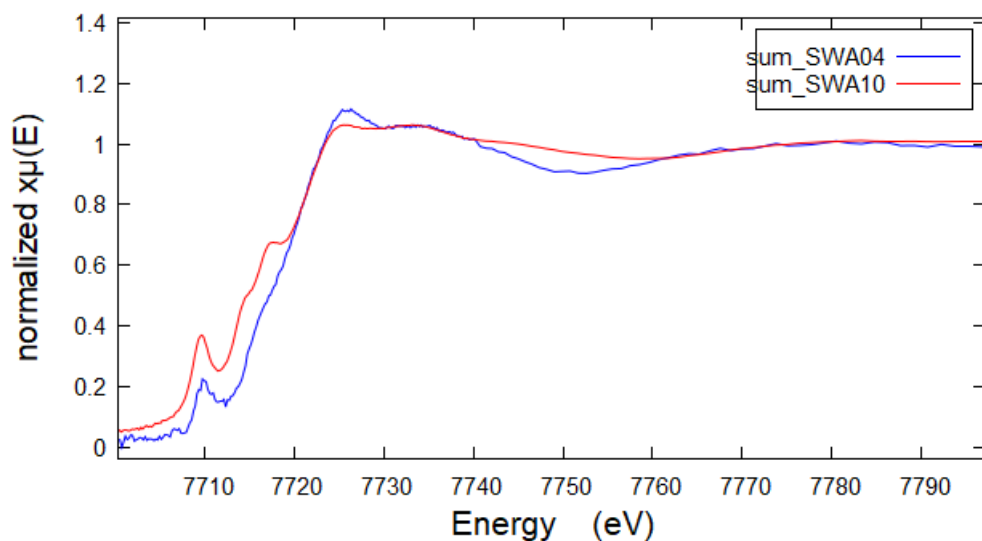
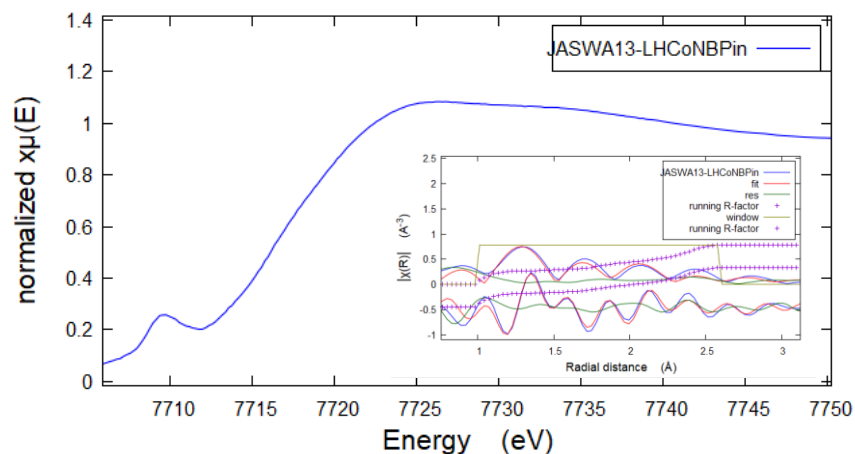


Figure S28. X-ray absorption spectra of **1** (blue) and **1-MeCN** (red) with pre-edge features at 7709.61 and 7709.53 respectively. These were all collected as frozen solutions at 83 K, with **1** in toluene and **1-MeCN** in acetonitrile.



Path	N	R(Å)
Co-N	1.00	1.8171
Co-N	2.00	1.9852
Co-O	1.00	2.0432
Co-B	1.00	2.3355

Figure S30. EXAFS (X-ray Absorption Fine Structure) Fit of **2-Pin**, which supports our assignments first of a Co(II) center, with an EXAFS spectrum not inconsistent with the proposed scatterers

**Table S2. Fityk Fits for XAS spectra.**

Compound	Center	Height	Area	FWHM
LHCoNBpin	7709.381018	0.540121	0.162475	3.15871
LHCoNBpin	7721.714586	7.13272	0.528676	12.8194
LHCoNBpin	7735.243384	26.4	1.02644	24.4384
LCoOTf (MeCN)	7709.53	0.339379	2.37475	3.41121
LCoOTf (MeCN)	7714.23	0.245007	2.02167	3.86664
LCoOTf (MeCN)	7716.84	0.394192	3.46274	5.22512
LCoOTf (MeCN)	7726.38	1.01009	7.87787	12.5776
LCoOTf	7709.61	0.140479	0.232199	1.82256
LCoOTf	7715.94	0.115077	0.41852	4.01014
LCoOTf	7726.51	1.1147	16.0353	15.8618

### Density Functional Theory (DFT): Single Point Energies

#### Calculation Details

Geometry optimization calculations and single point energy calculations were performed with ORCA<sup>2</sup> software suite using density functional theory (DFT). Geometries were fully optimized starting from coordinates generated from finalized cifs of the compound crystal structures when possible. The O3LYP functional in ORCA 5 was used for geometry optimizations, spin density plot calculations, reaction coordinates, frequency calculations, and transition state optimization on all relevant compounds for this work. For the O3LYP calculations, def2-TZVPP was used on Co, N, S, O, and F, and def2-TZVP on C and H atoms. PBE0 was utilized for TDDFT calculations, and EPR calculations were performed with a variety of functionals and basis sets, described in more detail at the conclusion of this section. Structures and energies of **1** and some related compounds also calculated using the standard conditions can be found in previously published work, but are repeated here for completion.

Notation: LS: low spin, HS: high spin

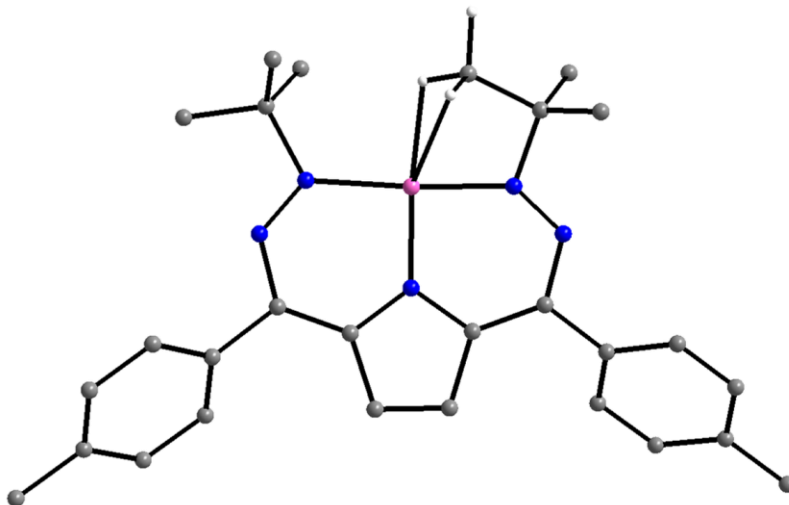


Figure S31. Calculated structure of **1**<sup>+</sup>. All C–H hydrogen atoms have been removed for clarity.

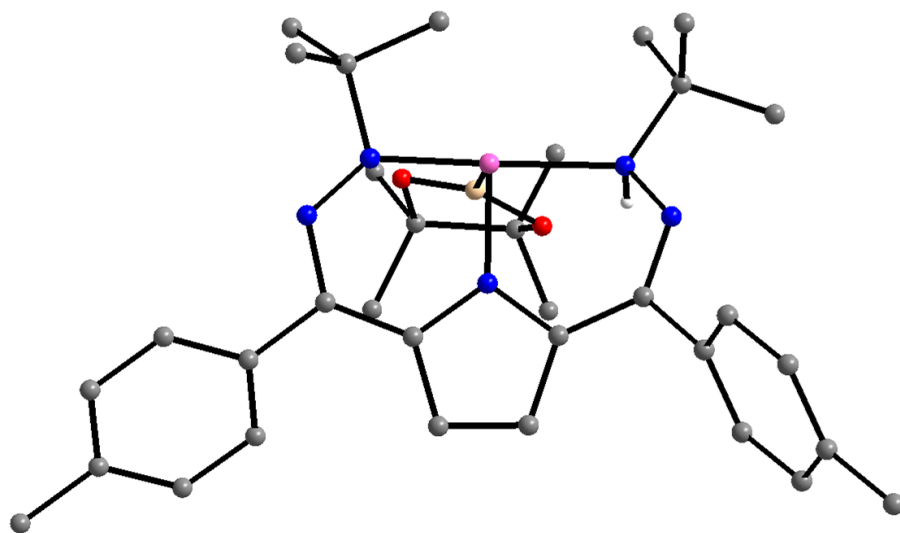


Figure S32. Calculated structure of  $[(t\text{Bu, TolDHP-H)Co-BPin}]^+$  (LS). All C–H hydrogen atoms have been removed for clarity.

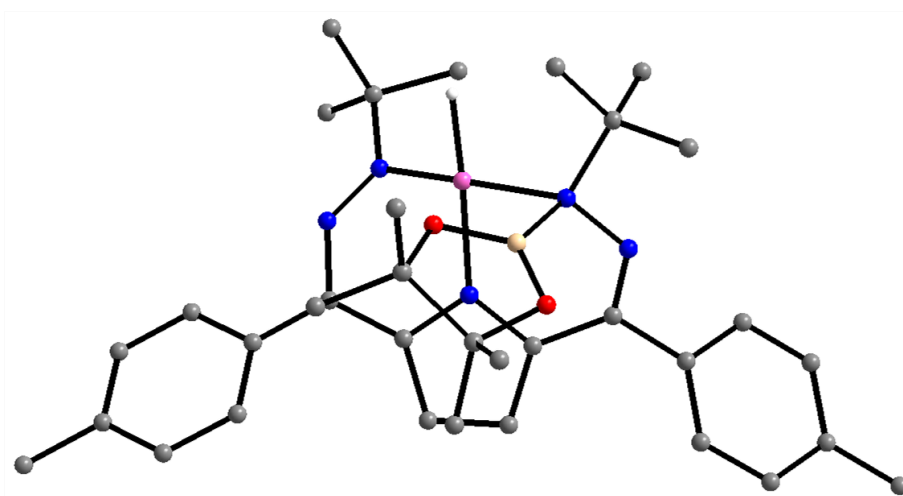


Figure S33. Calculated structure of  $[(t\text{Bu, TolDHP-BPin)Co-H}]^+$  (LS). All C–H hydrogen atoms have been removed for clarity.

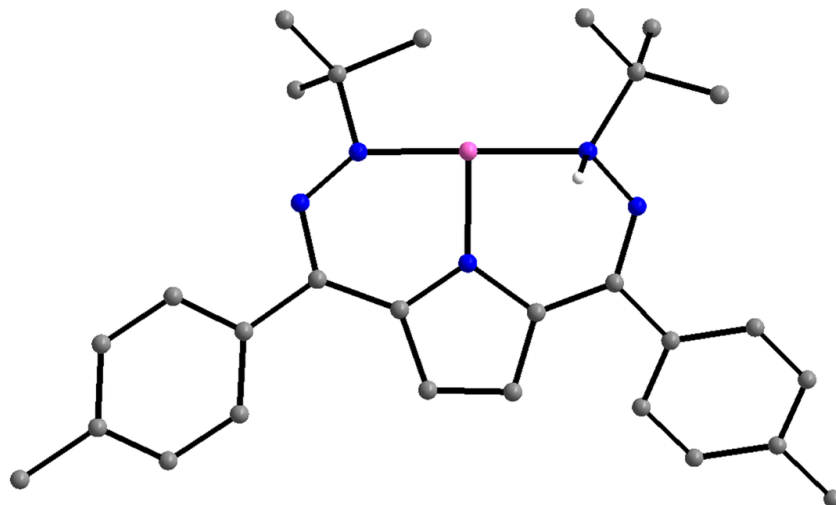


Figure S34. Calculated structure of  $[(t\text{Bu, TolDHP-H)Co}]^+$  (HS). All C–H hydrogen atoms have been removed for clarity.

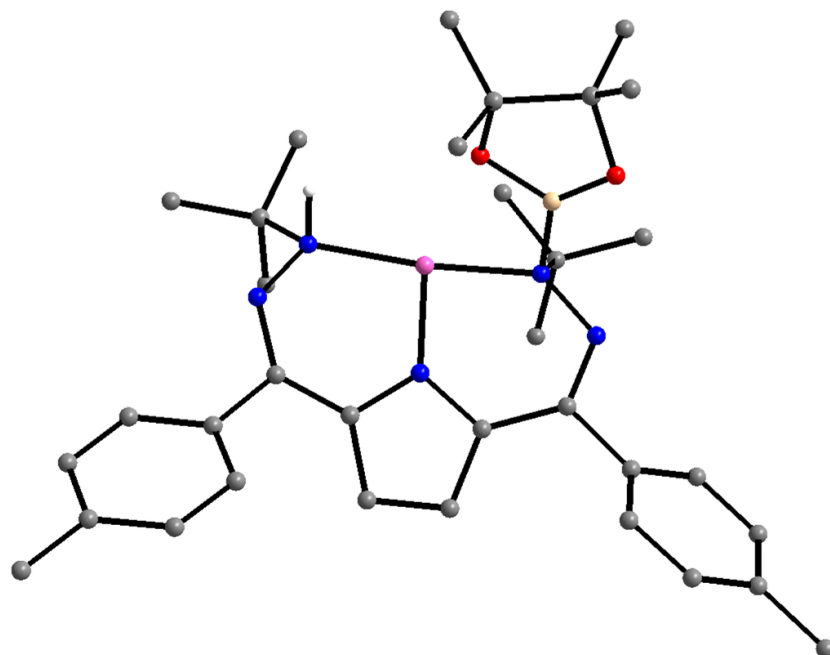


Figure S35. Calculated structure of  $[(t\text{Bu, TolDHP-HBPIn)Co}]^+$  (LS). All C–H hydrogen atoms have been removed for clarity.

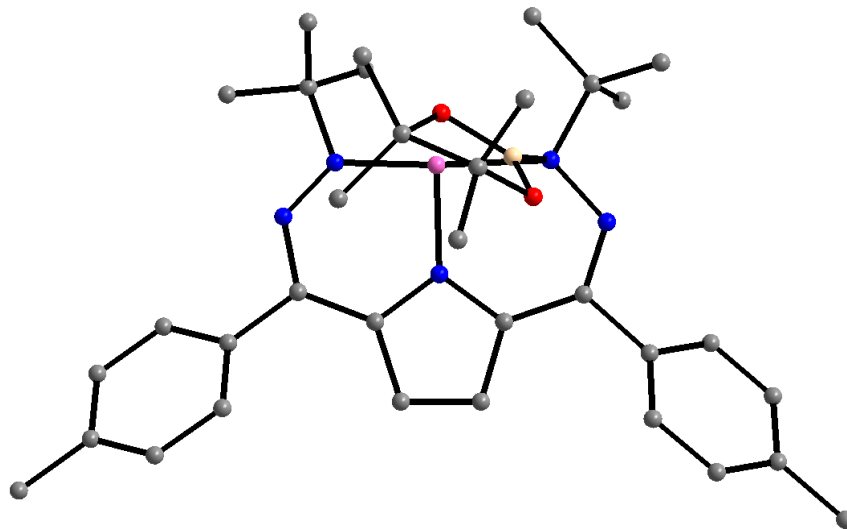


Figure S36. Calculated structure of  $[(t^{\text{Bu}}, \text{Tol})\text{DHP-BPin})\text{Co}]^+$  (LS). All C–H hydrogen atoms have been removed for clarity.

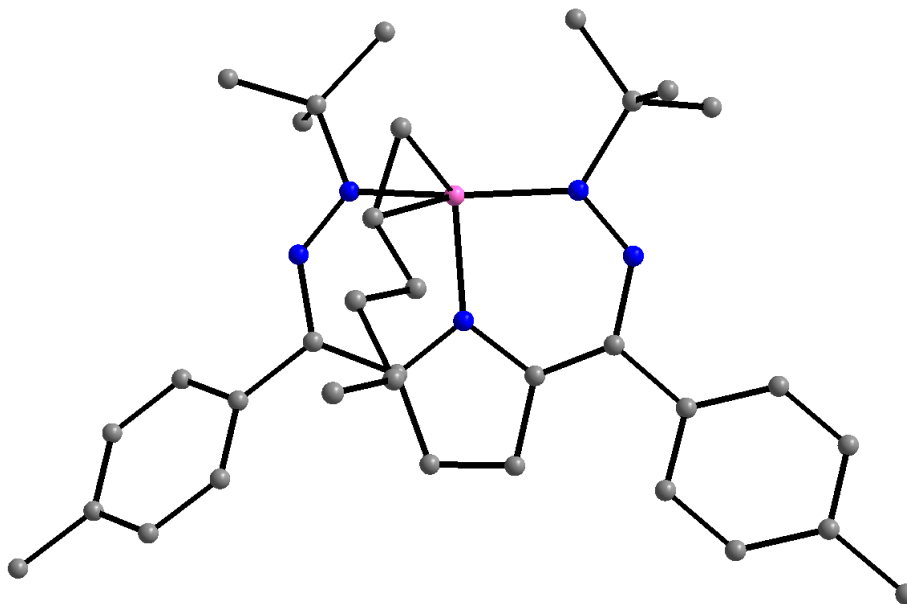


Figure S37. Calculated structure of  $[(t^{\text{Bu}}, \text{Tol})\text{DHP})\text{Co}(\text{1-hexene})]^+$  (LS). All C–H hydrogen atoms have been removed for clarity.

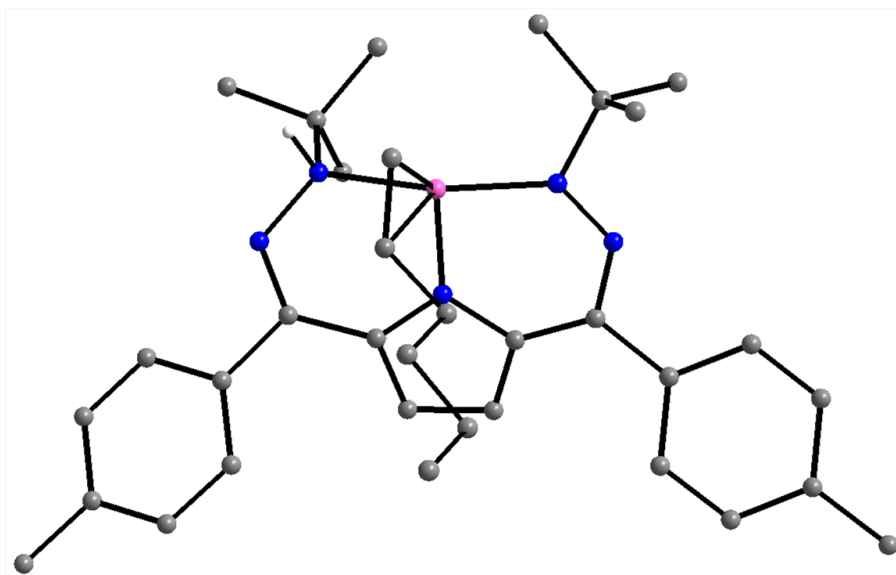


Figure S38. Calculated structure of  $[(t\text{Bu, TolDHP-H})\text{Co}(1\text{-hexene})]^+$  (LS). All C–H hydrogen atoms have been removed for clarity.

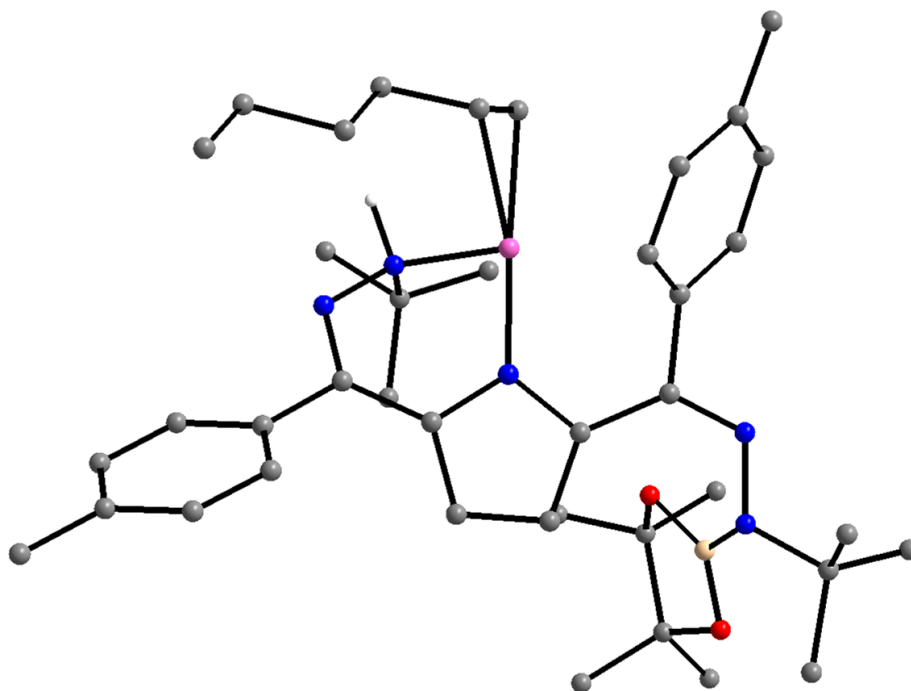


Figure S39. Calculated structure of  $[(t\text{Bu, TolDHP-HBPin})\text{Co}(1\text{-hexene})]^+$  (LS). All C–H hydrogen atoms have been removed for clarity.

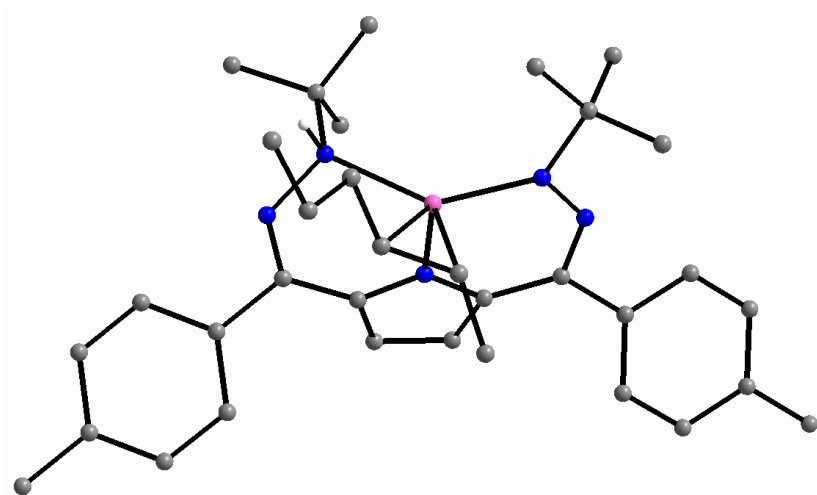


Figure S40. Calculated structure of  $[(t\text{Bu, TolDHP-H)Co(trans-2-hexene)]^+$  (LS). All C–H hydrogen atoms have been removed for clarity.

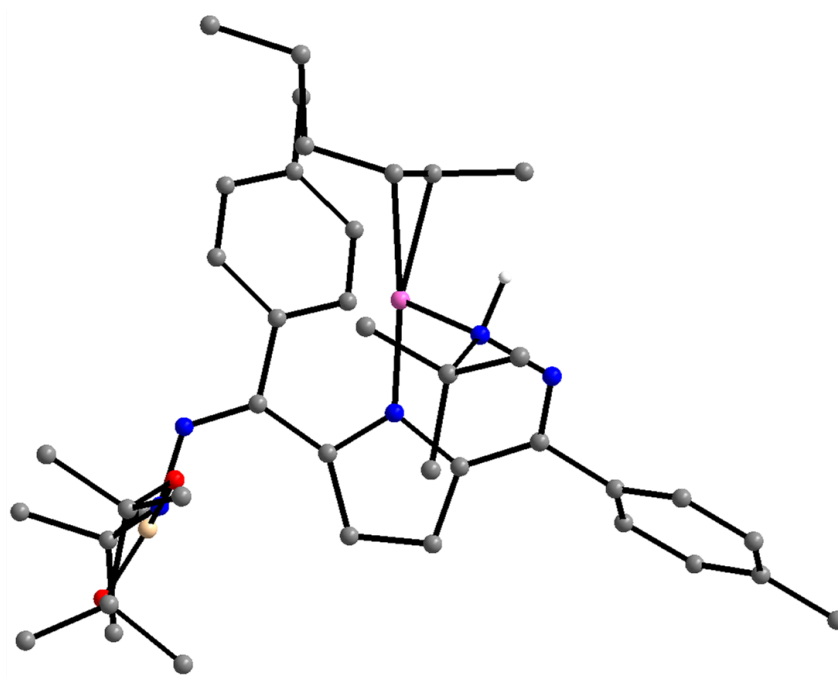


Figure S41. Calculated structure of  $[(t\text{Bu, TolDHP-HBPIn)Co(trans-2-hexene)]^+$  (LS). All C–H hydrogen atoms have been removed for clarity.

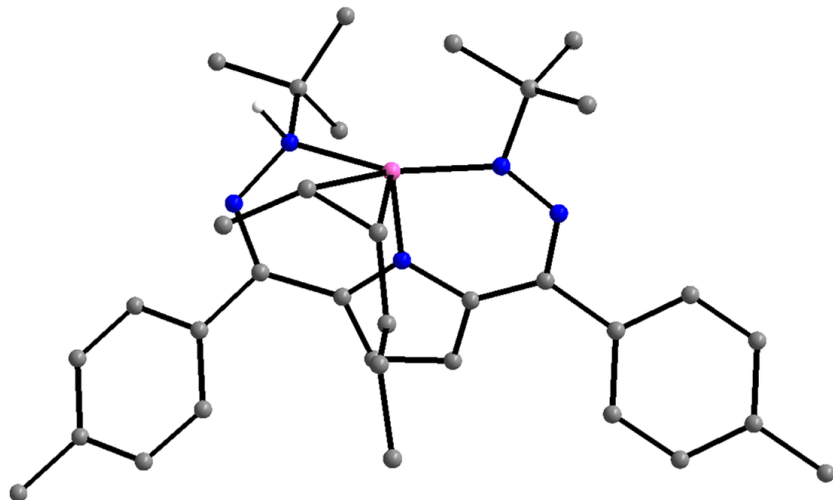


Figure S42. Calculated structure of  $[(t^{\text{Bu}}, \text{Tol})\text{DHP-H}]\text{Co}(\text{cis-2-hexene})^+$  (LS). All C–H hydrogen atoms have been removed for clarity.

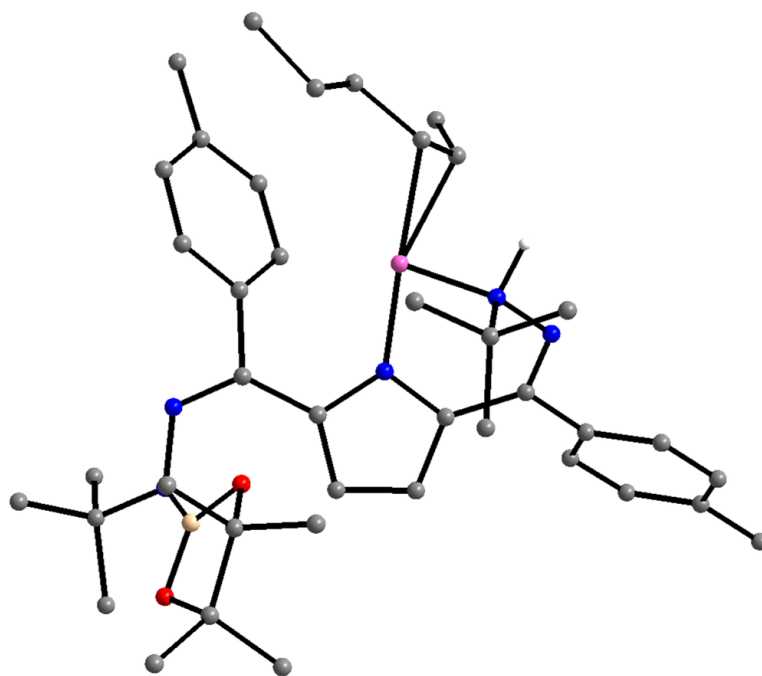


Figure S43. Calculated structure of  $[(t^{\text{Bu}}, \text{Tol})\text{DHP-HBPin}]\text{Co}(\text{cis-2-hexene})^+$  (LS). All C–H hydrogen atoms have been removed for clarity.

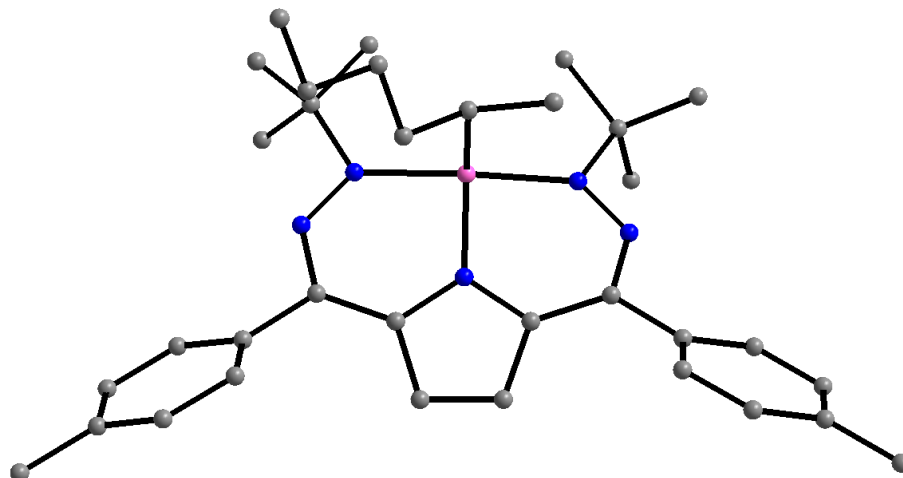


Figure S44. Calculated structure of  $[(t\text{Bu, Tol})\text{DHP})\text{Co}(\text{hexyl})]^+$  (LS). All C–H hydrogen atoms have been removed for clarity.

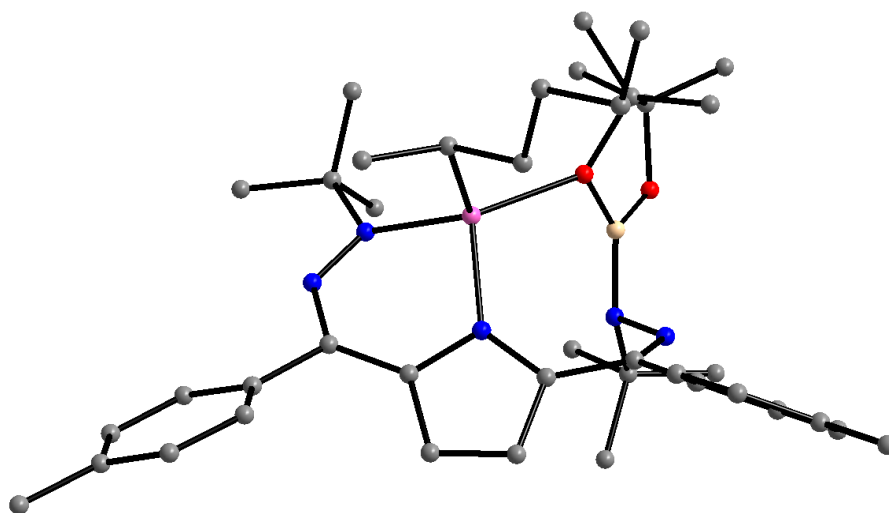


Figure S45. Calculated structure of  $[(t\text{Bu, Tol})\text{DHP-BPin})\text{Co}(\text{hexyl})]^+$  (HS). All C–H hydrogen atoms have been removed for clarity.

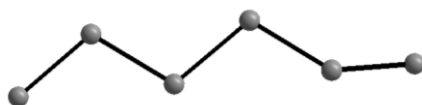


Figure S46. Calculated structure of **1-hexene**. All C–H hydrogen atoms have been removed for clarity.

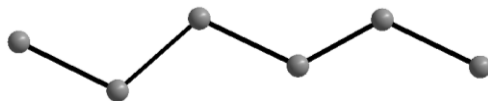


Figure S47. Calculated structure of **trans-2-hexene**. All C–H hydrogen atoms have been removed for clarity.



Figure S48. Calculated structure of **cis-2-hexene**. All C–H hydrogen atoms have been removed for clarity.

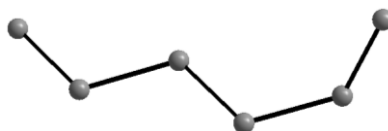


Figure S49. Calculated structure of **secondary hexyl radical**. All C–H hydrogen atoms have been removed for clarity.

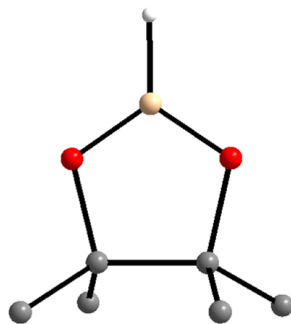


Figure S50. Calculated structure of **HBPIn**. All C–H hydrogen atoms have been removed for clarity.

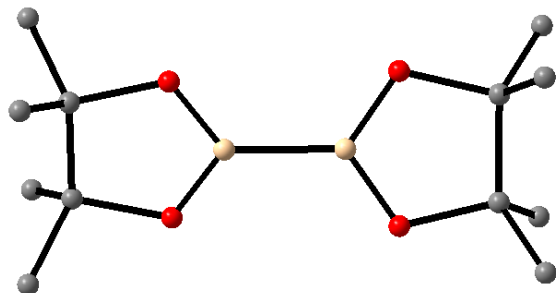


Figure S51. Calculated structure of **(BPin)<sub>2</sub>**. All C–H hydrogen atoms have been removed for clarity.

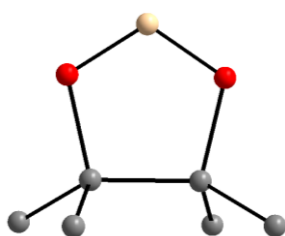


Figure S52. Calculated structure of **BPin radical**. All C–H hydrogen atoms have been removed for clarity.

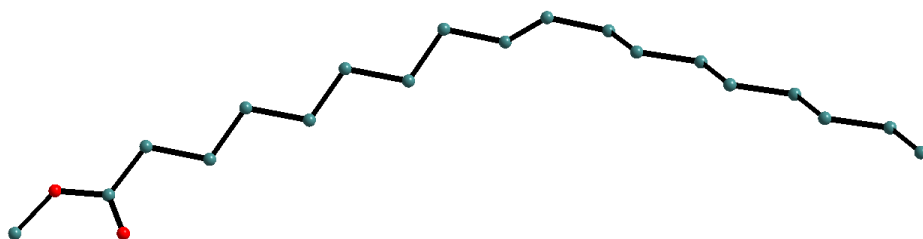


Figure S53. Calculated structure of **Methyl Elaidate**. All C–H hydrogen atoms have been removed for clarity.

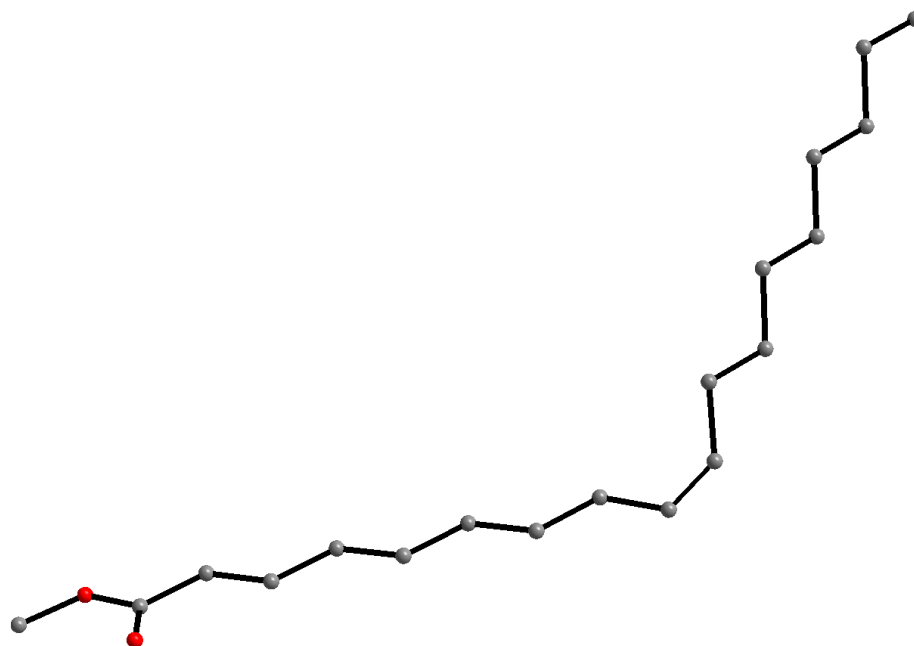


Figure S54. Calculated structure of **Methyl Oleate**. All C–H hydrogen atoms have been removed for clarity.

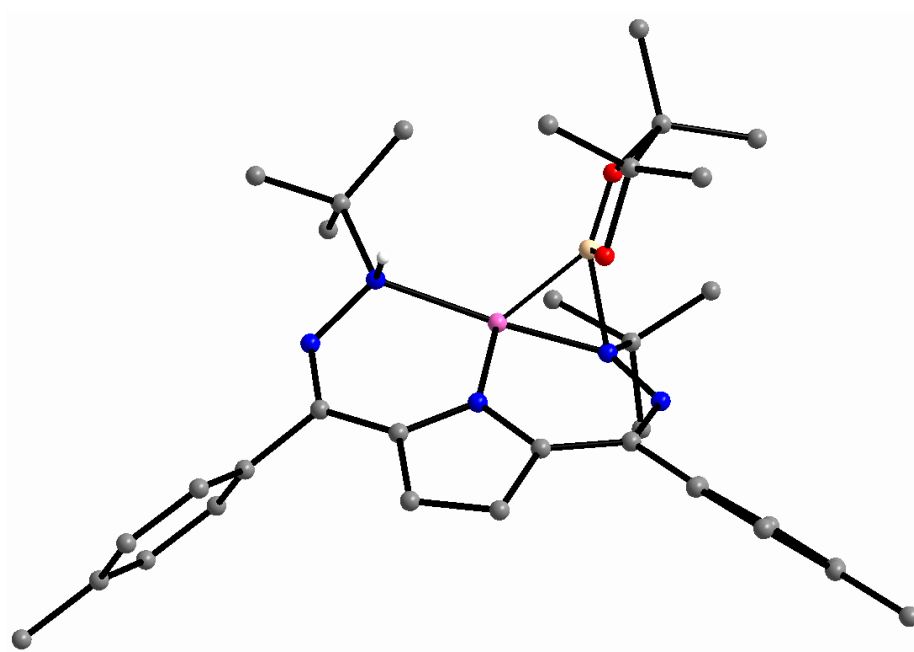


Figure S55. Calculated transition state structure between  $[(^t\text{Bu}, \text{TolDHP-H})\text{Co}(\text{BPin})]^+$  and  $[(^t\text{Bu}, \text{TolDHP-HBPin})\text{Co}]^+$  (LS). All C–H hydrogen atoms have been removed for clarity.

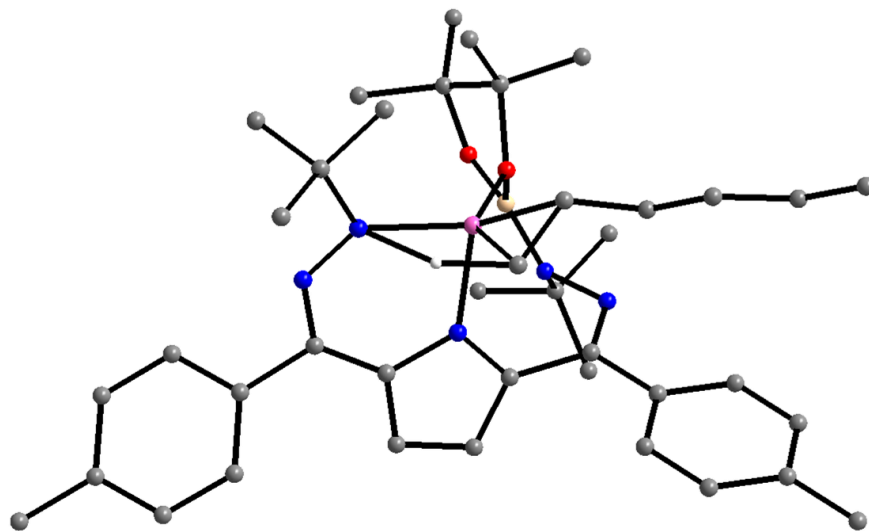


Figure S56. Calculated transition state structure between  $[(^{t}\text{Bu}, \text{TolDHP-HBPin})\text{Co}(1\text{-hexene})]^+$  and  $[(^{t}\text{Bu}, \text{TolDHP-BPin})\text{Co}(\text{alkyl})]^+$  (HS). All C–H hydrogen atoms have been removed for clarity.

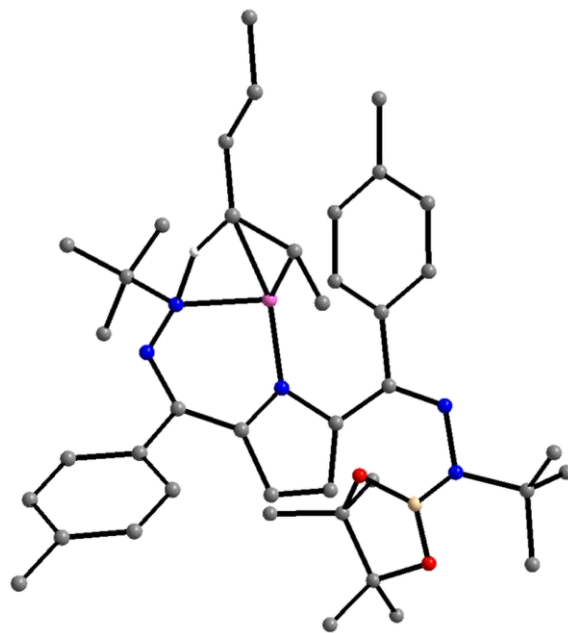


Figure S57. Calculated transition state structure between  $[(^{t}\text{Bu}, \text{TolDHP-BPin})\text{Co}(\text{alkyl})]^+$  and  $[(^{t}\text{Bu}, \text{TolDHP-HBPin})\text{Co}(\text{trans-2-hexene})]^+$  (LS). All C–H hydrogen atoms have been removed for clarity.

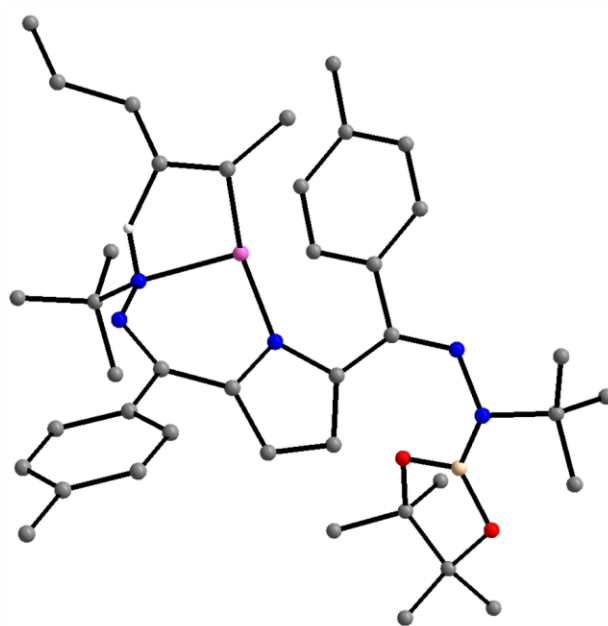


Figure S58. Calculated transition state structure between  $[(t\text{Bu, TolDHP-BPin)Co(alkyl)}]^+$  and  $[(t\text{Bu, TolDHP-HBPin)Co(cis-2-hexene)}]^+$  (LS). All C–H hydrogen atoms have been removed for clarity.

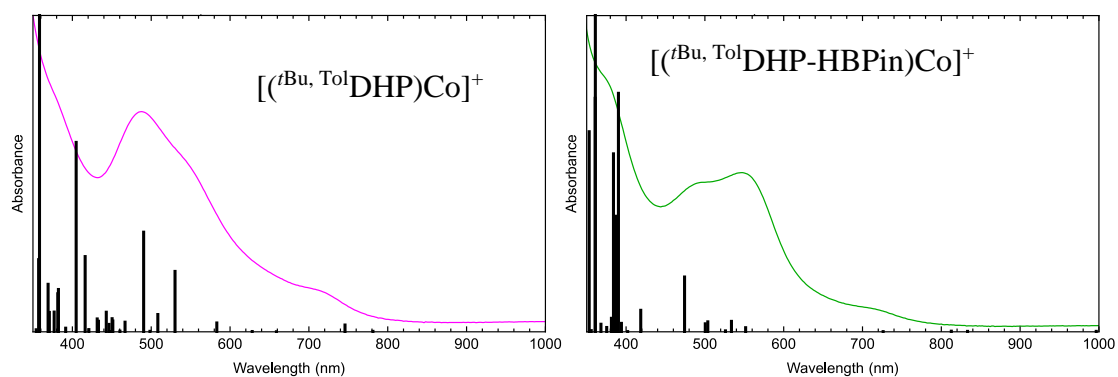


Figure S59. Calculated TD-DFT for relevant structures using PBE0 using def2-SV(P) basis sets for all atoms but Co. For Co def2-TZPP was used.

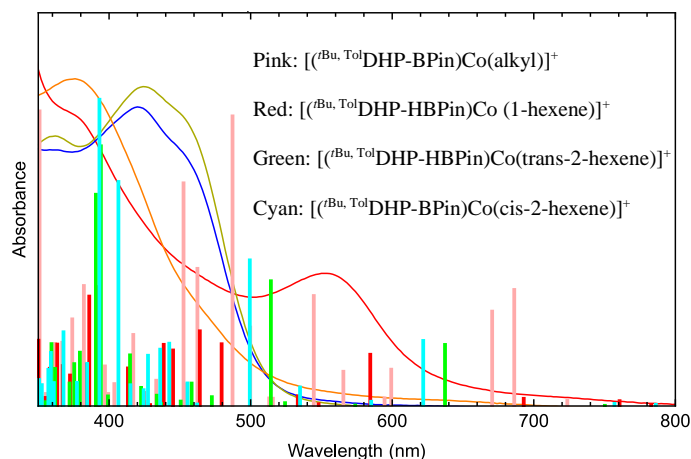


Figure S60. Calculated TD-DFT shown in Figure S48 plotted against the intermediates observed by UV-Vis.

Note that TD-DFT typically underestimates the energies of transitions and a shift to match experimental data of 50-75 nm is common in related Co-, Ni- and Fe-DHP complexes.

Table S2. Energies of Methyl elaidate and Methyl oleate Without Accounting for Entropic Contributions.

All values given in Eh	Methyl Elaidate	Methyl Oleate
S=0	-894.3184	-894.3162

Table S3. Energies of Isolable or Organic Intermediates to Form **2-BPin** (or non-borylated intermediate) From **1** Without Accounting for Entropic Contributions.

All values given in Eh	tBu, TolDHPCo+ (1)	[tBu, TolDHP-HBPin]Co+ (2-Pin)	[tBu, TolDHP-H]Co(BPin) +	[tBu, TolDHP-BPin]Co(H)+	HBPIn	[tBu, TolDHP-H]Co+	BPIn <sub>2</sub>	BPIn Radical
LS- S=1/2	-2741.14	-3152.22	-3152.19	-3152.18	N/A	-2741.72	N/A	-410.41
S=0	N/A	N/A	N/A	N/A	-411.08	N/A	-820.99	N/A

Table S4. Energies of Relevant Organic Olefin Derivatives with Entropic Contributions

All values given in Eh	1-hexene	Trans-2-hexene	Cis-2-hexene	Secondary Hexyl Radical
S=0	-235.1755	-235.1782	-235.1784	-235.725

Table S5. Compared Energies of Cobalt Intermediates to Form **2-PIN** (or non-borylated intermediate) From **1<sup>+</sup>** With Entropic Contributions.

All values given in Eh	[tBu, TolDHP-HBPin]Co+ (2-Pin)	[tBu, TolDHP-HBPin]Co(1-hexene)+	[tBu, TolDHP-H]Co+	[tBu, TolDHP-H]Co(1-hexene)+	[tBu, TolDHP]Co+	[tBu, TolDHP]Co(1-hexene)+	BPin2	<i>Bpin radical</i>
HS- <i>S</i> =1	N/A	N/A	-2741.21	-2976.37	N/A	-2976.37	N/A	N/A
LS- <i>S</i> =1/2	-3151.53	-3386.69	N/A	N/A	-2740.64	N/A	N/A	-410.24
<i>S</i> =0	N/A	N/A	N/A	N/A	N/A	N/A	-820.63	N/A

Table S6. Compared Energies of Cobalt Intermediates to Form **2-hexene from 1-hexene** with **1<sup>+</sup>** as Catalyst With Entropic Contributions.

All values given in Eh	[tBu, TolDHP-BPin]Co(hexyl)+	[tBu, TolDHP-HBPin]Co(trans-2-hexene)+	[tBu, TolDHP-HBPin]Co(cis-2-hexene)+	[tBu, TolDHP-BPin]Co+	[tBu, TolDHP]Co(hexyl)+	[tBu, TolDHP-H]Co(trans-2-hexene)+	[tBu, TolDHP-H]Co(cis-2-hexene)+
HS- <i>S</i> =3/2	-3386.688	N/A	N/A	N/A	N/A	-2976.377	N/A
HS- <i>S</i> =1	N/A	N/A	N/A	N/A	N/A	N/A	N/A
LS- <i>S</i> =1/2	N/A	N/A	N/A	N/A	-2976.376	-3778.39	-2976.356
<i>S</i> =0	N/A	-3386.684	-3386.679	-3150.937	N/A	N/A	N/A

Table S7. Compared Energies of Cobalt Transition States to Form **2-hexene from 1-hexene** with **1<sup>+</sup>** as Catalyst With Entropic Contributions.

All values given in Eh	TS between [tBu, TolDHP-H]Co(BPin)+ and [tBu, TolDHP-HBPin]Co+	TS between [tBu, TolDHP-HBPin]Co(1-hexene)+ and [tBu, TolDHP-HBPin]Co(hexyl)+	TS between [tBu, TolDHP-HBPin]Co(hexyl)+ and [tBu, TolDHP-HBPin]Co(trans-2-hexene)+	TS between [tBu, TolDHP-HBPin]Co(hexyl)+ and [tBu, TolDHP-HBPin]Co(cis-2-hexene)+
HS- <i>S</i> =3/2	N/A	N/A	N/A	-3386.682
HS- <i>S</i> =1	N/A	-3386.670	N/A	N/A
LS- <i>S</i> =1/2	-3151.499	N/A	-3386.659	N/A





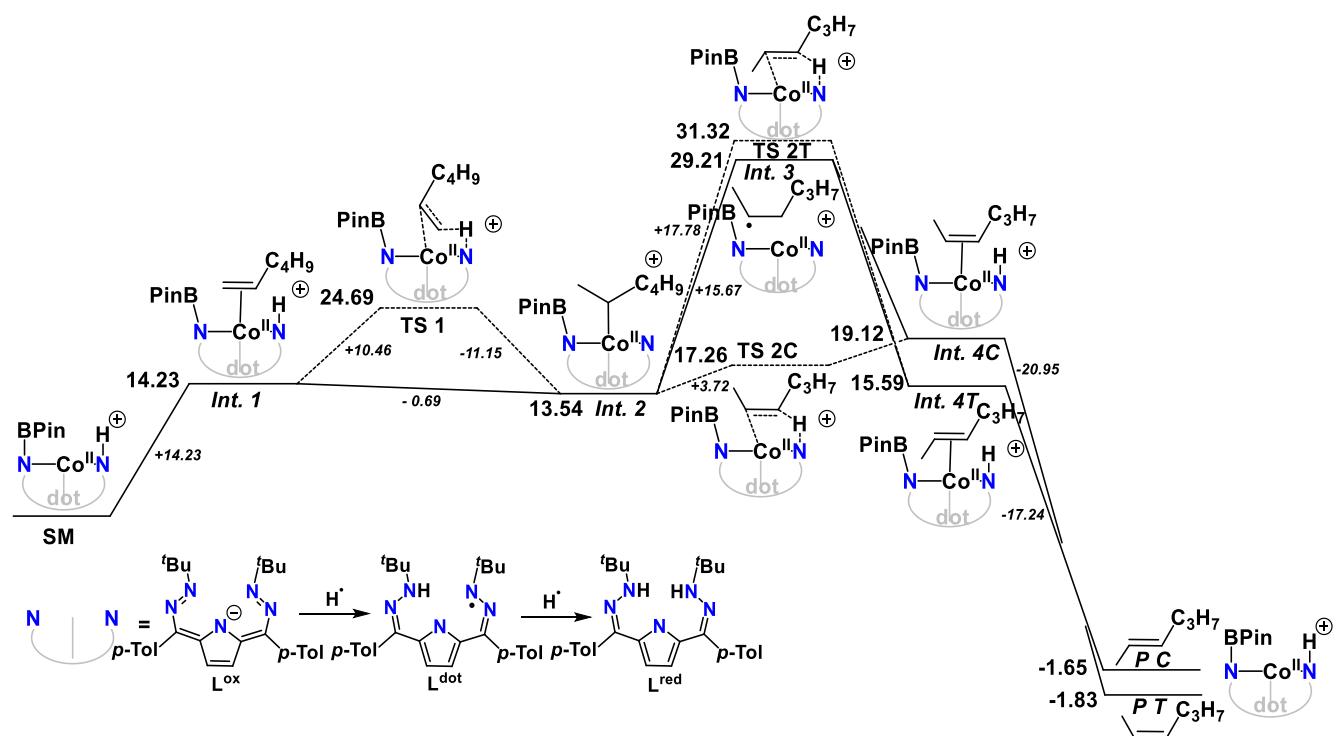


Figure S65. Reaction Coordinate: Olefin isomerization with **2** (accounting for entropic contributions).

Table S8. Calculated vs. experimental values.

	N-H <sup>a</sup>
experimental value	3327
theoretical value	3388 ( <b>2-Pin</b> ) or 2732 (non-borylated)
Scaling Factor for B3LYP/TZVP <sup>3</sup>	0.9654
Scaled theoretical value	3271 ( <b>2-Pin</b> ) or 2637 (non-borylated)
Theor./Exp.	
Ratio	0.983 ( <b>2-Pin</b> ) or 0.793 (non-borylated)

<sup>a</sup> units of cm<sup>-1</sup>

The theoretical stretching frequencies were determined from the O3LYP DFT calculation for the structure of **2-Pin**. Note: the NIST database does not list the scaling factor for O3LYP, so the factor for B3LYP was utilized.

### **General Catalytic Isomerization Procedures and Products**

#### **Procedure for 1% loading, thermal reactivity:**

In a nitrogen-filled glovebox, a standard borosilicate NMR tube was charged with unsaturated substrate (0.077 mmol, 100 eq.), **1** (0.0005 g, 0.0008 mmol), NaBAr<sup>F</sup><sub>4</sub> (0.0007 g, 0.0008 mmol, 1 eq.), borane of choice (0.0008 mmol, 1 eq.), mesitylene (0.001 mL, 0.007 mmol) (internal standard), and benzene-d<sub>6</sub> (0.6 mL). This NMR tube was heated for 3 hours under inert atmosphere in the glovebox at 65°C. The dark red-purple solution could be observed to redden immediately after borane addition, and slowly progress towards orange, then yellow over the course of the three hours. After 3 hr, the tube was analyzed by <sup>1</sup>H, <sup>11</sup>B, and <sup>19</sup>F NMR, then filtered over alumina (to remove metal-containing complexes and salts) and re-analyzed by NMR for isolated yields.

Note: for BH<sub>3</sub>SMe<sub>2</sub>, using excess will result in primarily hydrogenation reactivity. Other boranes are less sensitive to stoichiometry, and still result in isomerization.

#### **Procedure for 2.5% loading, thermal reactivity:**

The general method described above was implemented with 0.031 mmol, 40 equiv. of unsaturated substrate used.

#### **Procedure for 2.5% loading, photochemical reactivity:**

In a darkened, nitrogen-filled glovebox, a standard borosilicate J-Young NMR tube was charged with unsaturated substrate (0.077 mmol, 100 eq.), **1** (0.0005 g, 0.0008 mmol), NaBAr<sup>F</sup><sub>4</sub> (0.0007 g, 0.0008 mmol, 1 eq.), borane of choice (0.0008 mmol, 1 eq.), mesitylene (0.001 mL, 0.007 mmol) (internal standard), and benzene-d<sub>6</sub> (0.6 mL). This NMR tube was removed from the glovebox and

under dark conditions set up for illumination using the Sciencetech solar simulator SLB150B with a 476 long pass colored glass filter. This was illuminated overnight for 18 hours. The dark red-purple solution could be observed to redden immediately after borane addition, and immediately turn a golden glowing color. After 18 hr, the tube was analyzed by  $^1\text{H}$ ,  $^{11}\text{B}$ , and  $^{19}\text{F}$  NMR, then filtered over alumina (to remove metal-containing complexes and salts) and re-analyzed by NMR for isolated yields.

Note: for  $\text{BH}_3\text{SMe}_2$ , using excess will result in primarily hydrogenation reactivity. Other boranes are less sensitive to stoichiometry, and still result in isomerization.

#### **Procedure for 2.5% loading, ambient light illumination:**

The general method described above was implemented on the morning of a sunny day, with the J-Young tube rotated in the sunshine.

#### **NMR Characterization for Starting Materials and Products:**

*When not otherwise stated, HBPin is the borane in use.*

*1-Hexene:* The title compound was purchased from TCI Chemicals and dried according to the general procedure for olefin preparations. The spectral data collected matched those previously reported.<sup>4</sup>  $^1\text{H}$  NMR (400 MHz,  $\text{C}_6\text{D}_6$ ):  $\delta$  0.83 (t, 3H,  $\text{CH}_3$ ), 1.25 (m, 4H,  $\text{CH}_2\text{CH}_2\text{CH}_3$ ), 1.96 (m, 2H,  $\text{CHCH}_2$ ), 4.98 (m, 2H,  $\text{CH}=\text{CH}_2$ ), 5.75 (m, 1H,  $\text{CH}=\text{CH}_2$ ).

*2-Hexene:* Isomerization of 1-hexene by the general procedure for 1% or 2.5% cat. loading or of trans-3-hexene by the general photochemical procedure for 2.5% cat. loading yielded trans-2-hexene as follows:

$\Delta$  from 1-hexene

HBPin (1 mol% loading): (94.0, 96.0, 99.2) 96(3)% yield 2-hexene and E:Z ratio of (4.1:1, 3.2:1, 4.1:1) 3.8(5):1.

HBCat (2.5 mol% loading): 3% yield 2-hexene and E:Z ratio of 1: 2.

Na[BEt<sub>3</sub>H] (2.5 mol% loading): 50% yield 2-hexene and E:Z ratio of 1:4.

BH<sub>3</sub>SMe<sub>2</sub> (2.5 mol% loading): 70% yield 2-hexene and E:Z ratio of 1:1.3

hν from trans-3-hexene

HBPIn: (47.7, 41.1, 45.4) 44(3)% yield, E:Z ratio of (0.91:1, 0.70:1, 0.83:1) 0.8(1)

HBCyD: (30.5, 31.4, 23.1) 28(5)% yield, E:Z ratio of (0.44:1, 0.46:1, 0.30:1) 0.40(9)

*Trans-2-Hexene*: The spectral data collected matched those previously reported.<sup>5</sup> <sup>1</sup>H NMR (400 MHz, C<sub>6</sub>D<sub>6</sub>): δ = 5.41 (m, 2 H), 1.94 (m, 2H), 1.59 (d, 3H), 1.33 (sextet, 2H), 0.86 (t, 3H). For contra-thermal isomerizations, this olefin was also purchased from Thermo Scientific and dried according to the general procedure for olefin preparations.

*Cis-2-Hexene*: Isomerization of trans-2-hexene or trans-3-hexene by the general photochemical procedure for 2.5% cat. loading yielded cis-2-hexene as follows (isomerizations thermally from 1-hexene are listed above):

hν

Trans-2-hexene:

HBPIn: (37.0, 41.2, 37.3, 42.6) 40(3)% yield, (3.0, 2.9, 6.0, 1.7) 3(2)% 1-hexene byproduct

HBCyD: (49.8, 50.7, 56.5, 41.8) 50(6)% yield, (2.5, 1.9, 1.3, 7.9) 3(3)% 1-hexene byproduct

BH<sub>3</sub>SMe<sub>2</sub>: (31.1, 28.8, 36.6) 32(4)% isolated yields, (3.1, 2.9, 2.6) 2.9(3)% 1-hexene byproduct

HBCamph: (21.1, 19.1, 16.1) 19(3)% isolated yields, (3.6, 5.2, 2.7) 4(1)% 1-hexene byproduct

Trans-3-hexene:

HBPIn: (52.2, 58.8, 54.5) 55(3)% yield, E:Z ratio of (0.91:1, 0.70:1, 0.83:1) 0.8(1), and (2.2, 3.3, 1.3) 2(1)% 1-hexene byproduct

HBCyD: (69.4, 68.5, 76.8) 72(5)% yield, E:Z ratio of (0.44:1, 0.46:1, 0.30:1) 0.40(9), and (2.1, 2.1, 1.3) 1.8(5)% 1-hexene byproduct

The spectral data collected matched those previously reported.<sup>4</sup> <sup>1</sup>H NMR (400 MHz, C<sub>6</sub>D<sub>6</sub>):  $\delta$  = 5.44 (m, 2 H), 1.97 (m, 2H), 1.54 (d, 3H), 1.32 (sextet, 2H), 0.87 (t, 3H).

*Trans-3-Hexene*: For contra-thermal isomerizations, this olefin was also purchased from Fluka and dried according to the general procedure for olefin preparations. The spectral data collected matched those previously reported.<sup>6</sup> <sup>1</sup>H NMR (400 MHz, C<sub>6</sub>D<sub>6</sub>):  $\delta$  = 0.92 (t, <sup>3</sup>J(H,H)=7.3 Hz, 6 H; CH<sub>3</sub>), 1.52 (d, <sup>3</sup>J(H,H)=5.5 Hz, 4 H; CH<sub>2</sub>), 5.39 ppm (m, 2 H; CH).

*1-Dodecene*: The title compound was purchased from Sigma Aldrich and dried according to the general procedure for olefin preparations. The spectral data collected matched those previously reported.<sup>7</sup> <sup>1</sup>H NMR (400 MHz, C<sub>6</sub>D<sub>6</sub>):  $\delta$  5.80 (m, 1H), 5.03 (m, 2H), 2.00 (q, 3 H), 1.31 (m, 2H), 1.27(10 H), 0.91 (3 H).

*2-Dodecene*: Isomerization of 1-dodecene by the general thermal procedure for 1% cat. loading yielded the title compound as follows: (96.0, 98.1, 97.0) 97(1)% yield and E:Z ratio of (1.8:1, 2.2:1, 2.1:1) 2.0(2):1. The spectral data collected matched those previously reported.<sup>8</sup> <sup>1</sup>H NMR (400 MHz, C<sub>6</sub>D<sub>6</sub>):  $\delta$  = 5.46 (m, 2 H), 2.02 (m, 3H), 1.63 (E, d, 3H), 1.58 (Z, d, 3H), 1.36 (m, 2 H), 1.27 (m, 11 H), 0.91 (t, 3 H).

*Undec-1-enoate methyl ester*: The title compound was synthesized according to literature procedures<sup>9</sup> and dried according to the general procedure for olefin preparations. The spectral data collected matched those previously reported:<sup>10</sup> <sup>1</sup>H NMR (400 MHz, C<sub>6</sub>D<sub>6</sub>):  $\delta$  = 5.78 (m, 1H), 5.02 (m, 2H), 3.36 (s, 3H), 2.04 (m, 2H), 1.99 (m, 2H), 1.50 (m, 4H), 1.29 (m, 4H), 1.16 (m, 6H).

*Undec-2-enoate methyl ester*: Isomerization of undec-1-enoate methyl ester by the general thermal procedure for 2.5% cat. loading yielded the title compound as follows: (97.5, 97.8, 95.0) 97(2)%

yield and E:Z ratio of (0.96:1, 0.82:1, 0.68:1) 0.8(1):1. The spectral data collected matched those previously reported.<sup>11</sup> <sup>1</sup>H NMR (400 MHz, C<sub>6</sub>D<sub>6</sub>):  $\delta$  = 5.43 (m, 2H), 3.36 (s, 3H), 2.09 (m, 2H), 1.96 (m, 2H), 1.62 (m, 2H), 1.54 (s, 3H), 1.29 (m, 4H), 1.16 (m, 6H).

*Phenyl Acetylene*: The title compound was purchased from Aldrich and dried according to the general procedure for olefin preparations. The spectral data collected matched those previously reported.<sup>12,13</sup> <sup>1</sup>H NMR (400 MHz, C<sub>6</sub>D<sub>6</sub>):  $\delta$  7.40 (d, 2H), 6.92 (m, 3 H), 2.72 (s, 1 H).

*Triphenylbenzene*: Isomerization of phenyl acetylene by the general thermal procedure for 2.5% cat. loading yielded 1,2,4-triphenylbenzene as follows: (89.1, 89.1, 86.8) 88(1)% yield and 1,3,5-triphenylbenzene with (10.0, 8.7, 9.4) 9.4(7)% yield. The spectral data collected matched those previously reported.<sup>14,15</sup> 1,2,4-triphenylbenzene: <sup>1</sup>H NMR (400 MHz, C<sub>6</sub>D<sub>6</sub>):  $\delta$  = 7.55-7.65 (br m, 4H), 7.25-7.48 (m, 4H), 7.10-7.18 (br m 10 H). 1,3,5-triphenylbenzene: <sup>1</sup>H NMR (400 MHz, C<sub>6</sub>D<sub>6</sub>):  $\delta$  = 7.78 (3H), 7.53 (d, 6 H), 7.26 (6 H), 7.19 (3H).

*Vinylcyclohexane*: The title compound was purchased from Ambeed and dried according to the general procedure for olefin preparations. The spectral data collected matched those previously reported.<sup>16</sup> <sup>1</sup>H NMR (400 MHz, C<sub>6</sub>D<sub>6</sub>):  $\delta$  5.74 (q, 1 H), 4.88 (m, 2 H), 1.95 (m, 1H), 1.70 (m, 5H), 1.28-1.10 (m, 5H).

*Ethylidenecyclohexane*: Isomerization of vinylcyclohexane by the general thermal procedure for 2.5% cat. loading yielded the title compound as follows: (87.7, 74.4, 90.4) 84(9)% yield. The spectral data collected matched those previously reported.<sup>15</sup> <sup>1</sup>H NMR (400 MHz, C<sub>6</sub>D<sub>6</sub>):  $\delta$  = 5.04 (q, 1H), 2.08 (m, 3H), 2.00 (m, 4H), 1.50 (m, 6H).

*1-ethylcyclohex-1-ene*: Isomerization of vinylcyclohexane by the general thermal procedure for 2.5% cat. loading yielded the title compound as follows: (6.1,4.5, 4.8) 5.1(9)% yield. The spectral

data collected matched those previously reported.<sup>15</sup> <sup>1</sup>H NMR (400 MHz, C<sub>6</sub>D<sub>6</sub>): δ = 5.31 (m, 1 H), 2.0 (m, 6H), 1.48 (m, 4H), 0.92 (t, 3 H).

*(1S)-(1)-beta-Pinene*: The title compound was purchased from TCI America and dried according to the general procedure for olefin preparations. The spectral data collected matched those previously reported.<sup>17</sup> <sup>1</sup>H NMR (400 MHz, C<sub>6</sub>D<sub>6</sub>): δ = 0.74 (s, 3H), 1.15 (s, 3H), 1.36 (d, J = 9.95 Hz, 1H), 1.7 (m, 2H), 1.84 (m, 1H), 2.17 (m, 2H), 2.46 (m, 2H), 4.7 (m, 1H), 4.74 (m, 1H) ppm.

*(1S)-(1)-alpha/gamma-Pinene*: Isomerization of (1S)-(1)-beta-Pinene by the general thermal procedure for 2.5% cat. loading yielded alpha-pinene styrene as follows: (62.1, 60.4, 57.6) 60(2)% yield and gamma-pinene with (6.2, 7.9, 6.9) 7.0(9)% yield. The spectral data collected matched those previously reported.<sup>16</sup> <sup>1</sup>H NMR (400 MHz, C<sub>6</sub>D<sub>6</sub>): δ = 0.91 (s, 3H), 1.24 (s, 3H), 1.26 (d, J = 8.54 Hz, 1H), 1.64 (m, 3H), 1.9 (td, J 1 = 5.54 Hz, J 2 = 1.52, 1H), 2.03 (m, 1H), 2.18 (m, 1H), 2.2 (m, 1H), 2.3 (m, 1H), 5.2(m, 1H, CH=CCH<sub>3</sub>) ppm.

*4-phenyl-but-1-ene*: The title compound was purchased from TCI Chemicals and dried according to the general procedure for olefin preparations. The spectral data collected matched those previously reported.<sup>15</sup> <sup>1</sup>H NMR (400 MHz, C<sub>6</sub>D<sub>6</sub>): δ 7.17 (m, 5 H), 5.85 (m, 1 H), 5.00 (m, 2H), 2.68 (t, 2H), 2.36 (q, 2 H).

*4-phenyl-but-2-ene*: Isomerization of 1-allyl-4-methylbenzene by the general thermal procedure for 2.5% cat. loading yielded the title compound as follows: (68.1, 73.4, 72.8) 71(3)% yield and E:Z ratio of (1.6:1, 1.7:1, 3.7:1) 2(1):1. The spectral data collected matched those previously reported.<sup>15</sup> <sup>1</sup>H NMR (400 MHz, C<sub>6</sub>D<sub>6</sub>): δ =7.23-7.08 (m, 5H), 5.49 (m, 2H), 3.23 (d, 2 H), 1.59 (d, 3H).

*4-phenyl-but-3-ene*: Isomerization of 1-allyl-4-methylbenzene by the general thermal procedure for 2.5% cat. loading yielded the title compound as follows: (25.5, 18.0, 22.5) 22(4)% yield and

E:Z ratio of (4.5:1, 3.8:1, 3.6:1) 4.0(5):1. The spectral data collected matched those previously reported.<sup>4</sup> <sup>1</sup>H NMR (400 MHz, C<sub>6</sub>D<sub>6</sub>):  $\delta$  = 7.16-7.05 (m, 5H), 6.31 (E, d, J = 15.8 Hz, 1H), 6.11 (E, dd, J = 22.4, 6.5 Hz, 1H), 5.57 – 5.48 (Z, d, J = 15.8 Hz, 1H), 5.41 – 5.34 (Z, dd, J = 22.4, 6.5 Hz, 1H), 2.08 – 2.02 (m, 2H), 0.96 (t, J = 7.5 Hz, 3H)

*Allylbenzene*: The title compound was purchased from Thermo Scientific and dried according to the general procedure for olefin preparations. The spectral data collected matched those previously reported.<sup>8</sup> <sup>1</sup>H NMR (400 MHz, C<sub>6</sub>D<sub>6</sub>):  $\delta$  7.02 (m, 5H), 5.85 (m, 1H), 4.98 (m, 2H), 3.18 (d, 2H).

*Beta-methyl styrene*: Isomerization of allyl benzene by the general thermal procedure for 2.5% cat. loading yielded beta-methyl styrene as follows: (74.3, 74.8, 72.75) 74(1)% yield with an E:Z ratio of (8.46:1, 5.65:1, 2.5:1) 6(3):1. The spectral data collected matched those previously reported.<sup>8</sup> <sup>1</sup>H NMR (400 MHz, C<sub>6</sub>D<sub>6</sub>)  $\delta$  7.05-7.29 (m, peaks overlapped with allylbenzene peaks), 6.45 (Z, dd, 1H, J = 11.5, 1.6 Hz), 6.33 (E, dd, 1H, J = 15.8, 1.4 Hz), 6.02-6.11 (E, m, 1H), 5.63- 5.71 (Z, m, 1H), 1.74 (Z, dd, 3H, J = 7.3, 1.8 Hz), 1.68 (E, dd, 3H, J = 6.6, 1.7 Hz) ppm.

*1-allyl-4-methylbenzene*: The title compound was purchased from AstaTech and dried according to the general procedure for olefin preparations. The spectral data collected matched those previously reported.<sup>18</sup> <sup>1</sup>H NMR (400 MHz, C<sub>6</sub>D<sub>6</sub>):  $\delta$  7.12-7.07 (m, 4H), 6.01-5.90 (m, 1H), 5.09-5.03 (m, 2H), 3.35 (d, J = 6.8 Hz, 2H), 2.32 (s, 3H).

*E/Z-1-methyl-4-(prop-1-en-1-yl)benzene*: Isomerization of 1-allyl-4-methylbenzene by the general thermal procedure for 2.5% cat. loading yielded the title compound as follows: (52.4, 44.5, 48.7) 49(4)% yield and E:Z ratio of (3.3:1, 3.9:1, 3.8:1) 3.7(3):1. The spectral data collected matched those previously reported.<sup>4</sup> <sup>1</sup>H NMR (400 MHz, C<sub>6</sub>D<sub>6</sub>):  $\delta$   $\delta$ =7.18 (t, J = 9.0 Hz, 2H), 6.98 (d, J = 7.9 Hz, 2H), 6.33 (d, J = 16.5 Hz, 1H), 6.04 (dd, J = 15.7, 6.6 Hz, 1H), 2.13 (s, 3H), 1.76 (Z, dd, J = 6.6 Hz, 3H), 1.68 (E, dd, J = 6.6 Hz, 3H).

*1-allyl-4-trifluoromethylbenzene*: The title compound was purchased from Combi-Blocks and dried according to the general procedure for olefin preparations. The spectral data collected matched those previously reported.<sup>19</sup> <sup>1</sup>H NMR (400 MHz, C<sub>6</sub>D<sub>6</sub>):  $\delta$  7.58 (d, J = 8.1 Hz, 2H), 7.33 (d, J = 8.0 Hz, 2H), 5.88 (m, 1H), 5.29 – 4.84 (m, 2H), 2.81 (t, J = 7.8 Hz, 2H), 2.60 – 2.25 (m, 2H).

*E/Z-1-trifluoromethyl-4-(prop-1-en-1-yl)benzene*: Isomerization of 1-allyl-4-trifluoromethylbenzene by the general thermal procedure for 2.5% cat. loading yielded the title compound as follows: (14.8, 12.7, 13.0) 14(1)% yield and E:Z ratio of (3.5:1, 4.8:1, 6.5:1) 5(2):1. The spectral data collected matched those previously reported.<sup>20</sup> <sup>1</sup>H NMR (400 MHz, C<sub>6</sub>D<sub>6</sub>):  $\delta$  = 7.53 (d, J = 8.1 Hz, 2H), 7.41 (d, J = 8.2 Hz, 2H), 6.47 – 6.40 (m, 1H), 6.35 (dq, J = 15.8, 6.2 Hz, 1H), 1.92 (dd, J = 6.3, 1.3 Hz, 3H).

*4-allyl-anisole*: The title compound was purchased from Thermo Fisher and dried according to the general procedure for olefin preparations. The spectral data collected matched those previously reported.<sup>8</sup> <sup>1</sup>H NMR (400 MHz, C<sub>6</sub>D<sub>6</sub>):  $\delta$  = 7.00 (d, 2H), 6.80 (d, 2H), 5.89 (m, 1 H), 5.00 (m, 2H), 3.32 (s, 3H), 3.19 (d, 2H).

*E/Z-1-methoxy-4-(prop-1-en-1-yl)benzene*: Isomerization of 1-allyl-anisole by the general thermal procedure for 2.5% cat. loading yielded the title compound as follows: (189.0, 67.2, 69.2) 80(10)% yield and E:Z ratio of (4.8:1, 3.3:1, 3.0:1) 4(1):1. The spectral data collected matched those previously reported.<sup>8</sup> <sup>1</sup>H NMR (400 MHz, C<sub>6</sub>D<sub>6</sub>)  $\delta$  7.19 (d, 2H, J = 8.7 Hz, peak overlapped with C<sub>6</sub>D<sub>6</sub>), 6.78 (d, 2H, J = 8.5 Hz), 6.42 (Z, dd, 1H, J = 11.7, 1.2 Hz), 6.31 (E, dd, 1H, J = 15.7, 1.0 Hz), 5.91-6.00 (E, m, 1H), 5.58-5.66 (Z, m, 1H), 3.33 (s, 3H), 1.77 (Z, dd, 3H, J = 7.2, 1.6 Hz), 1.70 (E, dd, 3H, J = 6.5, 1.4 Hz) ppm.

*1,5-cyclooctadiene*: The title compound was purchased from Sigma Aldrich and dried according to the general procedure for olefin preparations. The spectral data collected matched those previously reported.<sup>13</sup> <sup>1</sup>H NMR (400 MHz, C<sub>6</sub>D<sub>6</sub>): δ 5.58 (4 H), 2.21 (8 H).

*1,4-cyclooctadiene*: Isomerization of 1,5-cyclooctadiene by the general thermal procedure for 2.5% cat. loading yielded the title compound as follows: (33.6, 34.7, 31.2) 33(2)% yield. The spectral data collected matched those previously reported.<sup>21</sup> <sup>1</sup>H NMR (400 MHz, C<sub>6</sub>D<sub>6</sub>): δ = 5.66 (dt, 2 H), 5.40 (dd, 2H), 2.27 (q, 4H), 2.67 (t, 2H), 1.41 (quintet, 2H).

*1,3-cyclooctadiene*: Isomerization of 1,5-cyclooctadiene by the general thermal procedure for 2.5% cat. loading yielded the title compound as follows: (26.1, 29.2, 28.1) 28(2)% yield. The spectral data collected matched those previously reported.<sup>4</sup> <sup>1</sup>H NMR (400 MHz, C<sub>6</sub>D<sub>6</sub>): δ 5.86 (d, J = 10.4 Hz, 2H), 5.55 (dd, J = 17.6, 7.3 Hz, 2H), 2.12 (s, 4H), 1.41 (dd, J = 5.6, 2.7 Hz, 4H).

*(2-methylprop-1-en-1-yl)benzene*: Isomerization of (2-methylallyl)benzene by the general thermal procedure for 2.5% cat. loading yielded *(2-methylprop-1-en-1-yl)benzene* as follows:

Δ

HBPIn: (51.69, 74.07, 41.7, 42.1, 41.2) 50(10)% isolated yields

HBCyd: (42.2, 27.0, 22.7) 30(10)% isolated yields

The spectral data collected matched those previously reported.<sup>22</sup> <sup>1</sup>H NMR (400 MHz, C<sub>6</sub>D<sub>6</sub>): δ = 7.35-6.79 (m, 5H), 6.27 (s, 1H, CH=C), 1.72 (s, 3H, Me), 1.69 (s, 3H, Me). For contra-thermal isomerizations, this olefin was also purchased from Ambeed and dried according to the general procedure for olefin preparations.

*(2-methylallyl)benzene*: Isomerization of (2-methylprop-1-en-1-yl)benzene by the general photochemical procedure for 2.5% cat. loading yielded (2-methylallyl)benzene as follows:

hν

HBPIn: (13.8, 4.8, 5.7) 8(5)% isolated yields

HBCyd: (2.0, 2.0, 6.3) 3(2)% isolated yields

The spectral data collected matched those previously reported.<sup>21</sup> <sup>1</sup>H NMR (400 MHz, C<sub>6</sub>D<sub>6</sub>): δ = δ 7.35-6.79 (m, 5H), 4.80 (s, 1H, C=CH<sub>2</sub>), 4.75 (s, 1H, 12b C=CH<sub>2</sub>), 3.15 (s, 2H, CH<sub>2</sub>), 1.55 (s, 3H, Me). For thermal isomerizations, this olefin was also purchased from Thermo Scientific and dried according to the general procedure for olefin preparations.

*1-(((4-methylenecyclohexyl)methoxy)methyl)-4-(trifluoromethyl)benzene*: The title compound was synthesized according to modified literature procedures<sup>23</sup> and dried according to the general procedure for olefin preparations. The spectral data collected matched the predicted spectra. <sup>1</sup>H NMR (600 MHz, C<sub>6</sub>D<sub>6</sub>) δ 7.37 (d, J = 7.9 Hz, 2H), 7.07 (d, J = 7.8 Hz, 2H), 4.73 (s, 2H), 4.11 (s, 2H), 3.02 (d, J = 6.9 Hz, 2H), 2.27 (d, J = 13.3 Hz, 2H), 1.96 (t, J = 13.5 Hz, 2H), 1.79 (d, J = 12.8 Hz, 2H), 1.07 (q, J = 12.4 Hz, 2H). <sup>19</sup>F NMR (600 MHz, C<sub>6</sub>D<sub>6</sub>): δ = -62.10 <sup>13</sup>C NMR (600 MHz, C<sub>6</sub>D<sub>6</sub>): δ = 128.35, 127.47, 125.42 (q, J = 3.9 Hz), 107.64, 75.90, 72.10, 38.11, 34.57, 31.51. HRMS (EI) m/z: Ref Mass (C<sub>16</sub>H<sub>19</sub>F<sub>3</sub>O): 284.1388, Obs. Mass: 284.1387.

*1-(((4-methylcyclohex-3-en-1-yl)methoxy)methyl)-4-(trifluoromethyl)benzene*: Isomerization of *1-(((4-methylenecyclohexyl)methoxy)methyl)-4-(trifluoromethyl)benzene* by the general thermal procedure for 2.5% cat. loading yielded *1-(((4-methylcyclohex-3-en-1-yl)methoxy)methyl)-4-(trifluoromethyl)benzene* as the only product as follows:

Δ

HBPIn: (96.2, 98.0, 98.5) 98(1)% isolated yields

HBCyD: (28.8, 46.5, 36.5) 37(9)% isolated yields

HBCamph: (9.1, 4.8, 3.3) 6(3)% isolated yields

BH<sub>3</sub>SMe<sub>2</sub>: (90.1, 67.1, 69.7) 80(10)% isolated yields

The spectral data collected matched the predicted spectra.  $^1\text{H}$  NMR (600 MHz,  $\text{CDCl}_3$ ):  $\delta = 7.59$  (t,  $J = 5.2$  Hz, 2H), 7.50 – 7.41 (m, 2H), 5.37 (s, 1H), 4.56 (d,  $J = 3.4$  Hz, 2H), 3.38 (tq,  $J = 9.5$ , 5.5, 2.9 Hz, 2H), 2.11 (d,  $J = 17.6$  Hz, 1H), 2.01 (t,  $J = 14.6$  Hz, 1H), 1.94 – 1.84 (m, 3H), 1.73 (t,  $J = 13.8$  Hz, 1H), 1.32 (dt,  $J = 11.2$ , 4.9 Hz, 1H).  $^{19}\text{F}$  NMR (600 MHz,  $\text{CDCl}_3$ ):  $\delta = -62.45$ .  $^{13}\text{C}$  NMR (600 MHz,  $\text{CDCl}_3$ ):  $\delta = 143.09$ , 134.21, 127.53, 125.41 (q,  $J = 3.8$  Hz), 120.01, 75.85, 72.34, 33.95, 29.58, 28.84, 26.24, 23.72. HRMS (EI)  $m/z$ : Ref Mass ( $\text{C}_{16}\text{H}_{19}\text{F}_3\text{O}$ ): 284.1388, Obs. Mass: 284.1392.

*$\alpha$ -cyclopropyl styrene*: The title compound was synthesized according to literature procedures<sup>24</sup> and dried according to the general procedure for olefin preparations. The spectral data collected matched those previously reported<sup>25</sup>:  $^1\text{H}$  NMR (400 MHz,  $\text{C}_6\text{D}_6$ ):  $\delta = 5.25$  (1H), 4.87 (1H).  $^1\text{H}$  NMR (400 MHz,  $\text{CDCl}_3$ ):  $\delta$  7.60 (d, 2H), 7.34 (t, 2H), 7.29 (d, 1H), 5.28 (s, 1H), 4.94 (s, 1H), 1.69-1.62 (m, 1H), 0.86-0.82 (m, 2H), 0.62-0.58 (m, 2H).

*E/Z-pent-2-en-2-ylbenzene*: Isomerization of  $\alpha$ -cyclopropyl styrene by the general thermal procedure for 2.5% cat. loading yielded the title compound as follows: (22, 30, 22) 25(5)% yield. The spectral data collected matched those previously reported.<sup>26</sup>  $^1\text{H}$  NMR (400 MHz,  $\text{C}_6\text{D}_6$ ):  $\delta = 7.46 - 7.12$  (m, 5H), 5.78 (t,  $J = 7.1$  Hz, E 1H), 5.45 (t,  $J = 7.4$  Hz, Z 1H), 2.21 (pent,  $J = 7.5$  Hz, E 2H), 2.03 (s, E/Z 3H), 2.02 – 1.92 (m, Z 2H), 1.06 – 0.90 (m, E/Z 3H).

*E/Z-pent-3-en-2-ylbenzene*: Isomerization of  $\alpha$ -cyclopropyl styrene by the general thermal procedure for 2.5% cat. loading yielded the title compound as follows: (32, 39, 41) 37(5)% yield. The spectral data collected matched those previously reported.<sup>27</sup>  $^1\text{H}$  NMR (400 MHz,  $\text{C}_6\text{D}_6$ ):  $\delta = 5.67 - 5.44$  (m, E/Z, 2H), 3.90 – 3.77 (m, Z, 1H), 3.43 (p,  $J = 7.2$  Hz, 1H), 1.69 (t,  $J = 5.7$  Hz, 3H), 1.35 (d,  $J = 6.7$  Hz, 3H).

*Cyclopropylmethylbenzene*: The title compound was purchased from Ambeed and dried according to the general procedure for olefin preparations. The spectral data collected matched those previously reported.<sup>6</sup> <sup>1</sup>H NMR (400 MHz, C<sub>6</sub>D<sub>6</sub>): δ 7.05-7.24 (m, 5H), 2.36 (d, J = 7.0 Hz, 2H), 0.99 (m, 1H), 0.77-0.9 (m, 2H), 0.36 (m, 2H)

*1-Hexyne*: The title compound was purchased from Sigma Aldrich and dried according to the general procedure for olefin preparations. The spectral data collected matched those previously reported.<sup>6</sup> <sup>1</sup>H NMR (400 MHz, C<sub>6</sub>D<sub>6</sub>): δ 0.71 (t, 3H, CH<sub>3</sub>), 1.19–1.33 (m, 4H, CH<sub>2</sub>CH<sub>2</sub>), 1.77 (t, 1H, ≡CH), 1.93 (dt, 2H, ≡CHCH<sub>2</sub>).

*Methyl Elaidate*: The title compound was purchased from TCI America and dried according to the general procedure for olefin preparations. The spectral data collected matched those previously reported, however this olefin was only 67.1% methyl elaidate as purchased (the other 32.9% being methyl oleate).<sup>6</sup> <sup>1</sup>H NMR (400 MHz, C<sub>6</sub>D<sub>6</sub>): δ 5.49 (m, 2H), 3.36-3.3 (s, 3H), 2.01-1.99 (t, J = 7.5 Hz, 6H), 1.51-1.1 (m, 2H), 0.97-1.02 (m, 20H), 0.90 (t, J = 6.7 Hz, 3H).

*Methyl Oleate*: Isomerization of methyl elaidate by the general photochemical procedure for 2.5% cat. loading yielded methyl oleate as follows:

hν

HBPIn: (56.5, 58.1, 53.2, 48.5) 54(4)% yield, (23.6, 25.2, 20.3, 15.6) 21(4)% increase from starting material

HBCyD: (54.9, 61.7, 56.5, 46.9) 58(4)% yield, (22.0, 28.82, 23.6, 14.1) 25(4)% increase from starting material

The spectral data collected matched those previously reported.<sup>28</sup> <sup>1</sup>H NMR (400 MHz, C<sub>6</sub>D<sub>6</sub>): δ = 5.49 (m, 2H), 3.30-3.26 (s, 3H), 2.12-2.07 (t, J = 7.5 Hz, 6H), 1.54-1.13 (m, 2H), 0.97-1.02 (m, 20H), 0.88 (t, J = 6.7 Hz, 3H).

*2,4,4-trimethylpent-1-ene*: Isomerization of 2,4,4-trimethylpent-2-ene by the general photochemical procedure for 2.5% cat. loading yielded 2,4,4-trimethylpent-1-ene as follows:

h $\nu$

HBPIn: (84.4, 80.1, 82.7) 82(2)% isolated yields

HBCyD: (43.5, 18.4, 14.9) 30(10)% isolated yields

BH<sub>3</sub>SMe<sub>2</sub>: (2.8, 0.2, 0.3) 1(1)% isolated yields

HBCamph: (11.5, 10.1, 6.0) 9(3)% isolated yields

The spectral data collected matched those previously reported.<sup>29</sup> <sup>1</sup>H NMR (400 MHz, C<sub>6</sub>D<sub>6</sub>):  $\delta$  = 4.92 (m, 1H), 4.72 (m, 1H), 1.89 (s, 2H), 1.71 (s, 3H), 0.90 (s, 9H). For thermal isomerizations, this olefin was also purchased from Thermo Scientific and dried according to the general procedure for olefin preparations.

*2,4,4-trimethylpent-2-ene*: Isomerization of 2,4,4-trimethylpent-1-ene by the general thermal procedure for 2.5% cat. loading yielded 2,4,4-trimethylpent-2-ene as follows:

$\Delta$

HBPIn: (33.5, 32.4, 38.1) 35(3)% isolated yields

HBCyD: (13.8, 18.9, 11.4) 15(4)% isolated yields

The spectral data collected matched those previously reported.<sup>28</sup> <sup>1</sup>H NMR (400 MHz, C<sub>6</sub>D<sub>6</sub>):  $\delta$  =  $\delta$  = 5.28 (m, 1H), 1.64 (s, 6H), 0.99 (s, 9H). For contra-thermal isomerizations, this olefin was also purchased from Thermo Fisher Scientific and dried according to the general procedure for olefin preparations.

*2,4-dimethylpent-1-ene*: Isomerization of 2,4-dimethylpent-2-ene by the general photochemical procedure for 2.5% cat. loading yielded 2,4-dimethylpent-1-ene as follows:

h $\nu$

(44.6, 36.5, 32.5) 38(6)% isolated yields

The spectral data collected matched those previously reported and that collected from bought standards.  $^1\text{H}$  NMR (400 MHz,  $\text{C}_6\text{D}_6$ ):  $\delta = 4.82$  (1 H), 4.75 (1 H), 1.83 (t, 2 H), 1.60 (m, 4 H), 0.95 (d, 6 H). For thermal isomerizations, this olefin was also purchased from Thermo Scientific and dried according to the general procedure for olefin preparations.

*2,4-dimethylpent-2-ene*: Isomerization of 2,4-dimethylpent-1-ene by the general thermal procedure for 2.5% cat. loading yielded 2,4-dimethylpent-2-ene as follows:

$\Delta$

(58.1, 56.2, 57.0) 57(1)% isolated yields

The spectral data collected matched those previously reported.<sup>30</sup>  $^1\text{H}$  NMR (400 MHz,  $\text{C}_6\text{D}_6$ ):  $\delta = 5.02$  (d, 1H), 2.48 (septet, 1H), 1.64 (s, 3H), 1.54 (s, 3H), 0.99 (s, 6 H). For contra-thermal isomerizations, this olefin was also purchased from Ambeed and dried according to the general procedure for olefin preparations.

*2,4-dimethylpenta-1,3-diene*: The title compound was purchased from Thermo Scientific and dried according to the general procedure for olefin preparations. The spectral data collected matched those previously reported.<sup>31</sup>  $^1\text{H}$  NMR (400 MHz,  $\text{C}_6\text{D}_6$ ):  $\delta 5.70$  (s, 1H), 5.00 (s, 1 H), 4.88 (s, 1H), 1.78 (s, 3 H), 1.71 (s, 3 H), 1.65 (s, 3 H).

*2,4-dimethylpenta-1,4-diene*: Isomerization of 2,4-dimethylpenta-1,3-diene by the general photochemical procedure for 2.5% cat. loading yielded 2,4-dimethylpenta-1,4-diene as follows:

h $\nu$

(25.1, 25.4, 19.4) 23(3)% isolated yields

The spectral data collected matched those previously reported.<sup>32</sup>  $^1\text{H}$  NMR (400 MHz,  $\text{C}_6\text{D}_6$ ):  $\delta = 4.67$  (m, 1H, obscured by starting material), 4.53 (m, 1H, obscured by starting material), 2.63 (m, 2 H), 1.90 (s, 6H).

*2,5-dimethylhexa-2,4-diene*: Isomerization of 2,5-dimethylhexa-1,5-diene by the general thermal procedure for 2.5% cat. loading yielded 2,5-dimethylhexa-2,4-diene as follows:

$\Delta$

(21.0, 31.5, 17.4) 23(7)% yields

The spectral data collected matched those previously reported.<sup>33</sup>  $^1\text{H}$  NMR (400 MHz,  $\text{C}_6\text{D}_6$ ):  $\delta = 6.14$  (s,2 H), 1.72 (s, 6H), 1.66 (s, 6 H). For contra-thermal isomerizations, this olefin was also purchased from TCI Chemicals and dried according to the general procedure for olefin preparations.

*2,5-dimethylhexa-1,4-diene*: Isomerization of 2,5-dimethylhexa-1,5-diene by the general thermal procedure for 2.5% cat. loading or of 2,5-dimethylhexa-2,4-diene by the general photochemical procedure for 2.5% cat. loading yielded 2,5-dimethylhexa-1,4-diene as follows:

$\Delta$

(39.0, 40.9, 31.5) 37(5)% isolated yields

hν

(12.6, 3.0, 2.5) 6(6)% isolated yields

The spectral data collected matched those previously reported.<sup>35</sup> <sup>1</sup>H NMR (400 MHz, C<sub>6</sub>D<sub>6</sub>): δ = δ = 5.27 (m, 1H), 4.89-4.72 (m, 2H, obscured by starting material), 2.67 (d, 2H), 1.72 (s, 3H), 1.66 (s, 3 H), 1.62 (s, 3 H).

*2,5-dimethylhexa-1,5-diene*: Isomerization of 2,5-dimethylhexa-2,4-diene by the general photochemical procedure for 2.5% cat. loading yielded 2,5-dimethylhexa-1,5-diene as follows:

hν

(6.0, 4.9, 1.7) 4(2)% isolated yields

The spectral data collected matched those previously reported.<sup>34</sup> <sup>1</sup>H NMR (400 MHz, C<sub>6</sub>D<sub>6</sub>): δ = δ = 4.89-4.72 (m, 2H, obscured by starting material), 2.08 (s, 4 H), 1.66 (s, 6 H). For thermal isomerizations, this olefin was also purchased from Combi-Blocks and dried according to the general procedure for olefin preparations.

*2,5-dimethylhexa-1,3-diene*: Isomerization of 2,5-dimethylhexa-2,4-diene by the general photochemical procedure for 2.5% cat. loading yielded 2,5-dimethylhexa-1,3-diene as follows:

hν

(21.6, 16.6, 11.0) 16(5)% isolated yields

The spectral data collected matched those previously reported.<sup>31</sup> <sup>1</sup>H NMR (400 MHz, C<sub>6</sub>D<sub>6</sub>): δ = δ = 6.00 (d, 1 H), 5.58 (t, 1 H), 4.89-4.72 (m, 2H, obscured by starting material), 2.28 (m, 1 H), 1.72 (3 H, obscured by starting material), 0.99 (6 H, obscured by starting material).

*trielaidin*: The title compound was purchased from TCI Chemicals and dried according to the general procedure for olefin preparations. The spectral data collected matched those previously reported.<sup>35</sup>

*triolein*: Isomerization of trielaidin by the general photochemical procedure for 2.5% cat. loading yielded triolein as follows:

hν

(68.6, 65.6, 58.9) 64(5)% yields

The spectral data collected matched those previously reported.<sup>36</sup> As triolein and trielaidin overlap significantly in their NMRs, a curve fitting approach was utilized to obtain these yields, with the CH<sub>2</sub> shifts from 2.11 ppm to 1.98 ppm directly next to the olefin used as the key diagnostic functionality.

*Cyclohexane methylene methanol*: The title compound was purchased from Ambeed and dried according to the general procedure for olefin preparations. The spectral data collected matched

those previously reported<sup>37</sup>: <sup>1</sup>H NMR (400 MHz, C<sub>6</sub>D<sub>6</sub>):  $\delta$  = 4.65 (s, 2 H), 3.45 (d,  $\ll Z$  = 6 Hz, 2 H), 2.4-0.9 (m, 9 H).

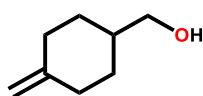
*(4-methylcyclohex-3-en-1-yl)methanol*: Isomerization of cyclohexane methylene methanol by the general thermal procedure for 2.5% cat. loading yielded the title compound as follows: 17.3% yield with HBCyD and 8.7% yield with HBPIn. The spectral data collected matched those previously reported.<sup>38</sup> <sup>1</sup>H NMR (400 MHz, C<sub>6</sub>D<sub>6</sub>):  $\delta$  = 5.34 (s, 1 H), 3.49 (t, J = 6.4 Hz, 2 H), 1.66 – 2.09 (m, 7 H), 1.62 (s, 3 H), 1.21-1.29 (m, 1 H)

*Undec-1-enoic acid*: The title compound was purchased from Sigma Aldrich and dried according to the general procedure for olefin preparations. The spectral data collected matched those previously reported<sup>39</sup>: <sup>1</sup>H NMR (400 MHz, C<sub>6</sub>D<sub>6</sub>):  $\delta$  = 5.91 – 5.75 (m, 2H), 5.01 – 4.90 (m, 2H), 2.35 (t, J = 7.2 Hz 2H), 2.05 – 1.97 (m, 2H), 1.66 – 1.61 (m, 2H), 1.36 – 1.30 (m, 10H).

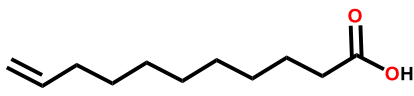
*Undec-2-enoic acid*: Isomerization of undec-1-enoic acid by the general thermal procedure for 2.5% cat. loading yielded the title compound as follows: 7.0% yield. The spectral data collected matched those previously reported.<sup>40</sup> <sup>1</sup>H NMR (400 MHz, C<sub>6</sub>D<sub>6</sub>):  $\delta$  =  $\delta$  11.97 (s, 1H), 5.48 – 5.33 (m, 2H), 2.20 (t, J = 7.3 Hz, 2H), 2.06-1.98 (m, 2H), 1.58 (d, J = 5.5 Hz, 3H), 1.56 – 1.44 (m, 2H), 1.37 – 1.25 (m, 8H).

## Controls

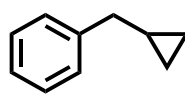
Standard 2.5 mol% loading, thermal conditions  
1 + NaBARF<sub>4</sub> + borane  
65°C, C<sub>6</sub>D<sub>6</sub>



R = CyD, 17.3% yield  
R = Pin, 8.7% yield



R = Pin, 7.0% yield  
(notable color changes pre-borane)



R = Pin, No yield

Figure S66. Unreactive or Side-Reacting Substrates. Reactivity was limited in the presence of alcohols, and distinctive side reactivity could be seen in the presence of carboxylic acids. Cyclopropyl groups alone also did not react.

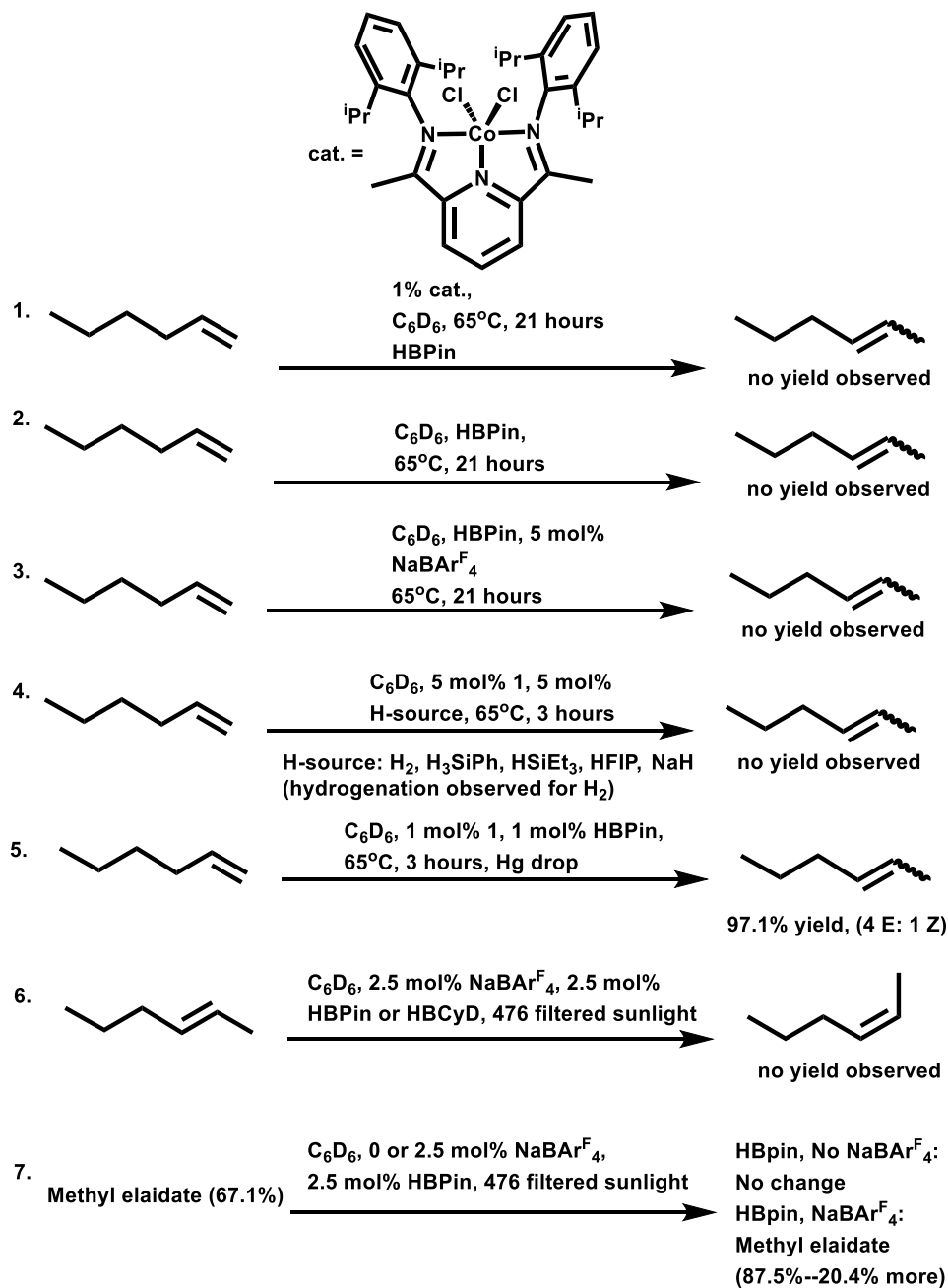


Figure S67. Controls (1) with alternative cobalt catalyst,<sup>41</sup> (4) with alternative hydride/proton/H-atom sources, (5) with a Hg drop to test for nanoparticles, and (2-3, 6-7) with no cobalt-containing species.

No yield is observed from the alternative catalyst, no yields are observed for the alternative H-sources, and no yields are observed for the majority of reactivity without cobalt. There is bond transposition to form more trans-product in the methyl elaidate control with borane and NaBAr<sup>F</sup><sub>4</sub>, however this is the opposite direction from our observed catalysis. The Hg drop control is within the error for that catalysis, so we conclude nanoparticles are unlikely to be playing a role in this reactivity.

### NMR data of New Compounds and Isomerizations: Figures S68-102

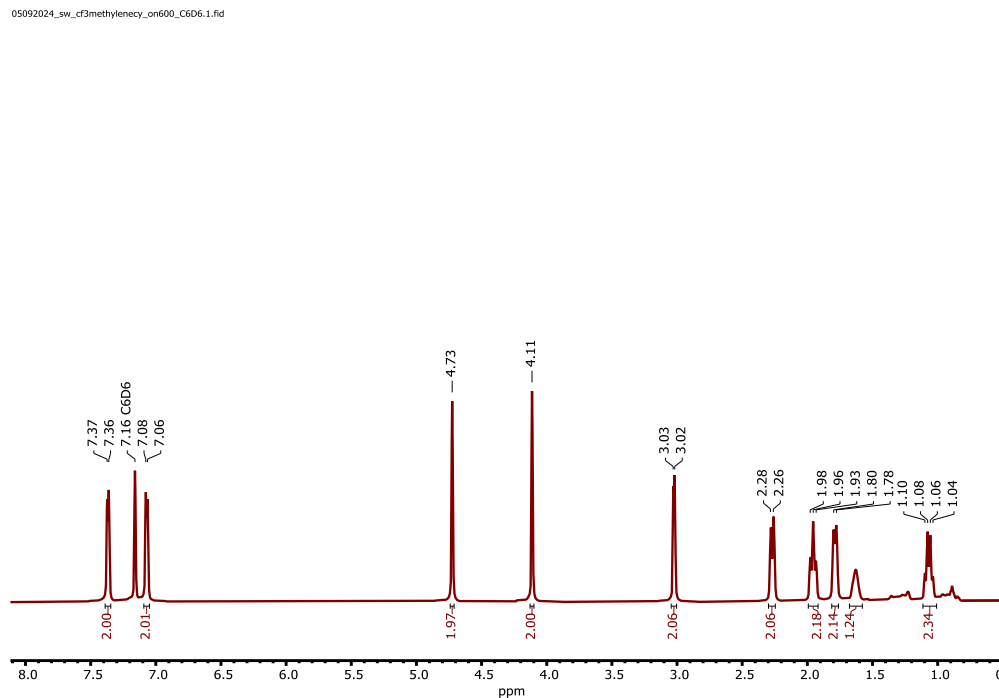


Figure S68. <sup>1</sup>H NMR of 1-(((4-methylenecyclohexyl)methoxy)methyl)-4-(trifluoromethyl)benzene in C<sub>6</sub>D<sub>6</sub> on Bruker DRX 600 spectrometer.

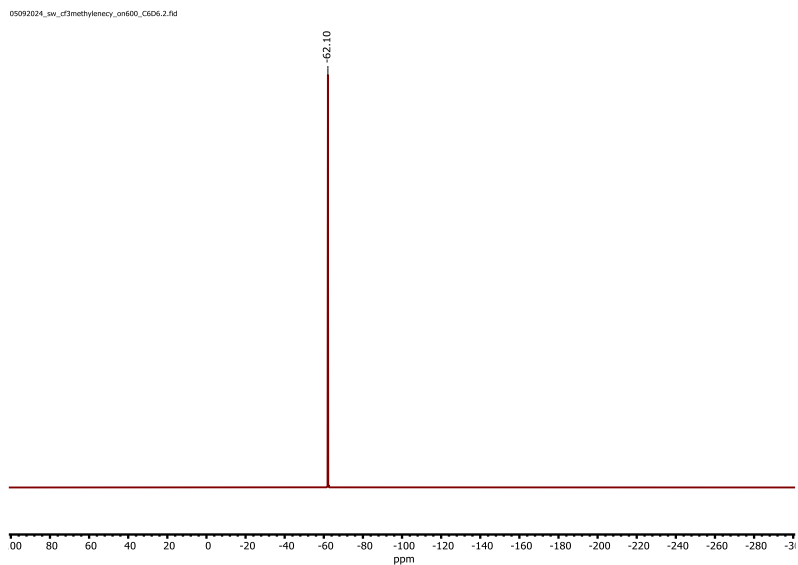


Figure S69.  $^{19}\text{F}$  NMR of 1-(((4-methylenecyclohexyl)methoxy)methyl)-4-(trifluoromethyl)benzene in  $\text{C}_6\text{D}_6$  on Bruker DRX 600 spectrometer.

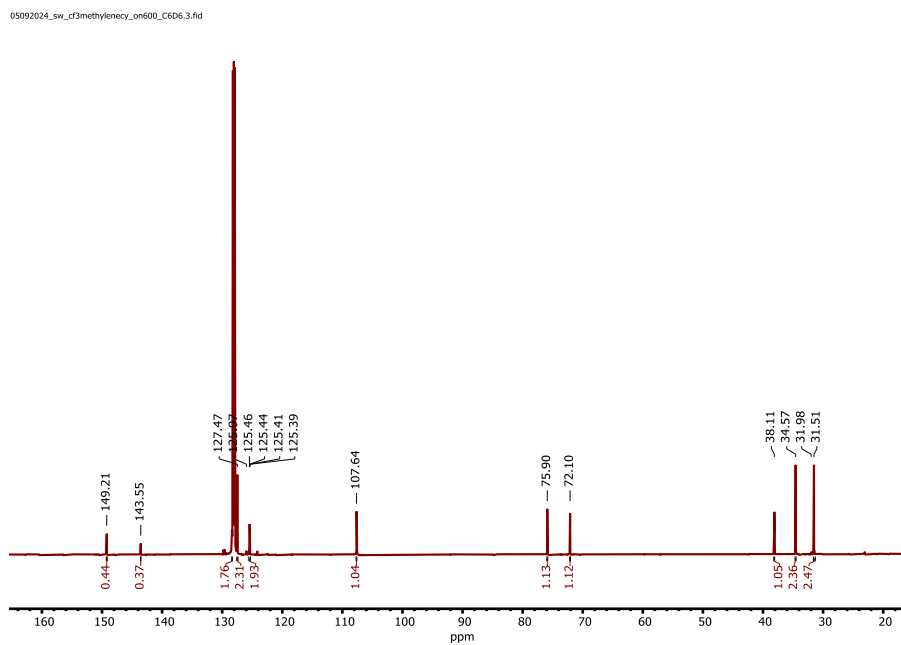


Figure S70.  $^{13}\text{C}$  NMR of 1-(((4-methylenecyclohexyl)methoxy)methyl)-4-(trifluoromethyl)benzene in  $\text{C}_6\text{D}_6$  on Bruker DRX 600 spectrometer.

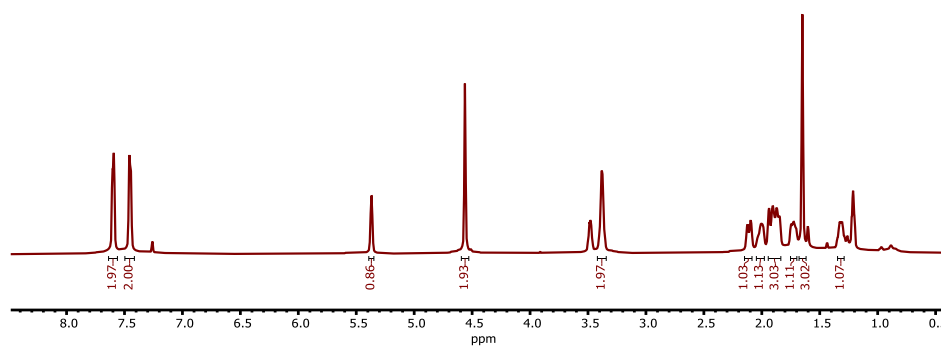


Figure S71.  $^1\text{H}$  NMR of 1-(((4-methylcyclohex-3-en-1-yl)methoxy)methyl)-4-(trifluoromethyl)benzene: in  $\text{CDCl}_3$  on Bruker DRX 600 spectrometer.

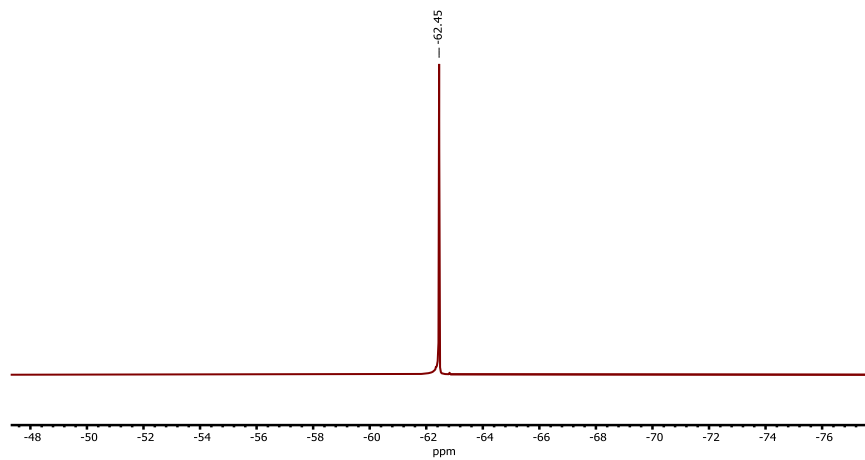


Figure S72.  $^{19}\text{F}$  NMR of 1-(((4-methylcyclohex-3-en-1-yl)methoxy)methyl)-4-(trifluoromethyl)benzene: in  $\text{CDCl}_3$  on Bruker DRX 600 spectrometer.

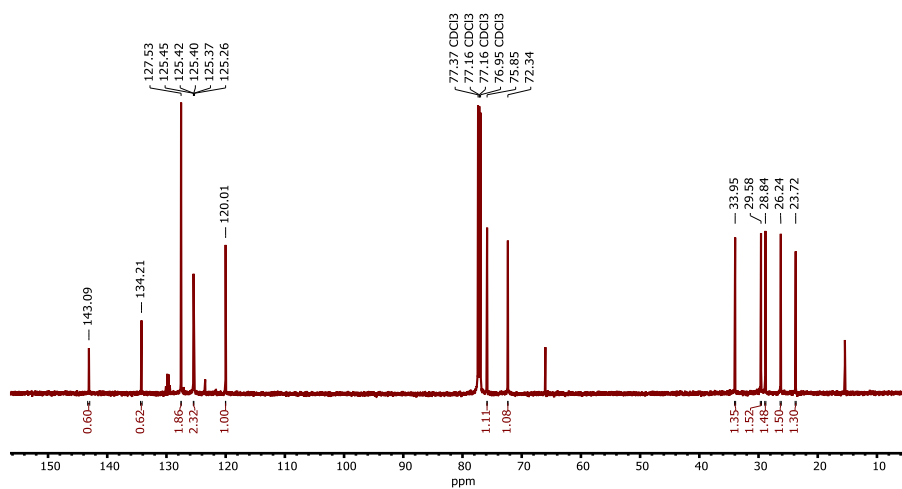


Figure S73.  $^{13}\text{C}$  NMR of 1-(((4-methylcyclohex-3-en-1-yl)methoxy)methyl)-4-(trifluoromethyl)benzene: in  $\text{CDCl}_3$  on Bruker DRX 600 spectrometer.

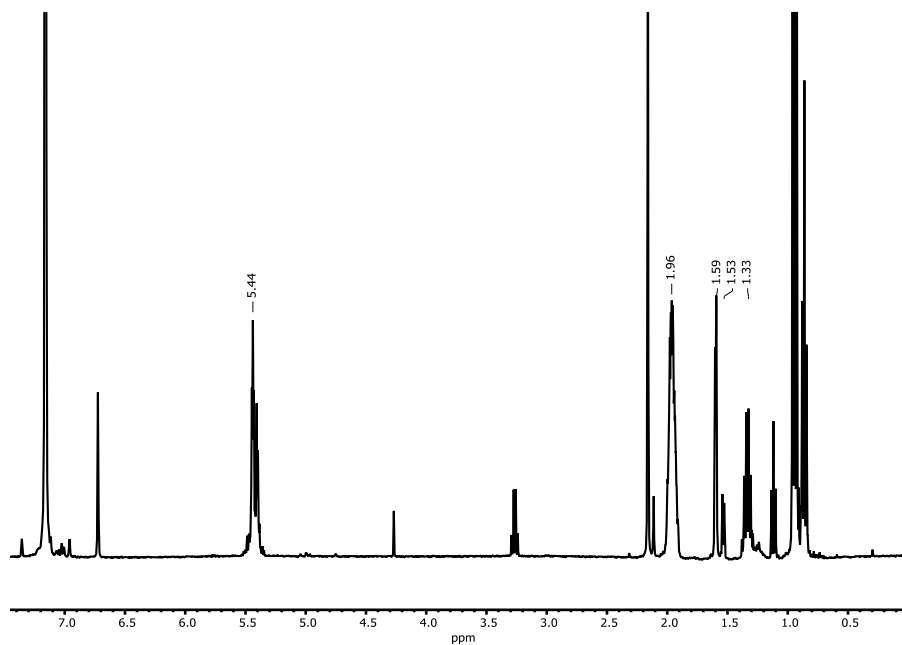


Figure S74.  $^1\text{H}$  NMR of 1 mol%: 1 isomerization of 1-hexene under standard thermal conditions in  $\text{C}_6\text{D}_6$  with 1  $\mu\text{L}$  mesitylene internal standard. Integration of various products done directly.

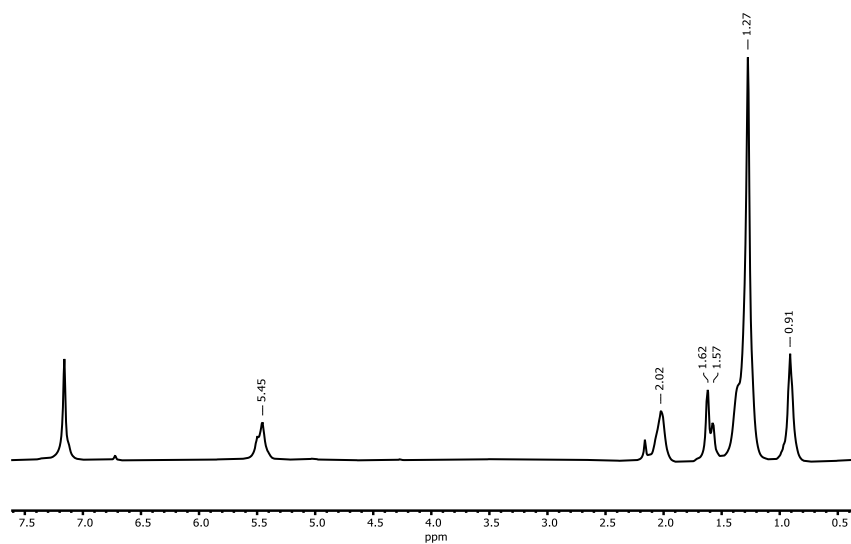


Figure S75. <sup>1</sup>H NMR of 1 mol%: 1 isomerization of 1-dodecene under standard thermal conditions in C<sub>6</sub>D<sub>6</sub> with 1 μL mesitylene internal standard. Integration of various products done directly.

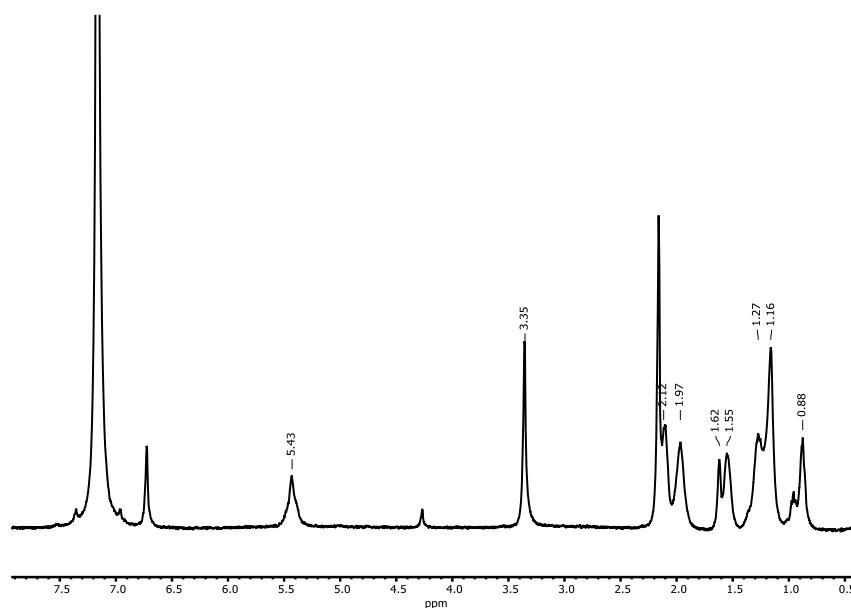


Figure S76. <sup>1</sup>H NMR of 2.5 mol%: 1 isomerization of methyl undec-1-enoate under standard thermal conditions in conditions in C<sub>6</sub>D<sub>6</sub> with 1 μL mesitylene internal standard. Integration of various products done directly.

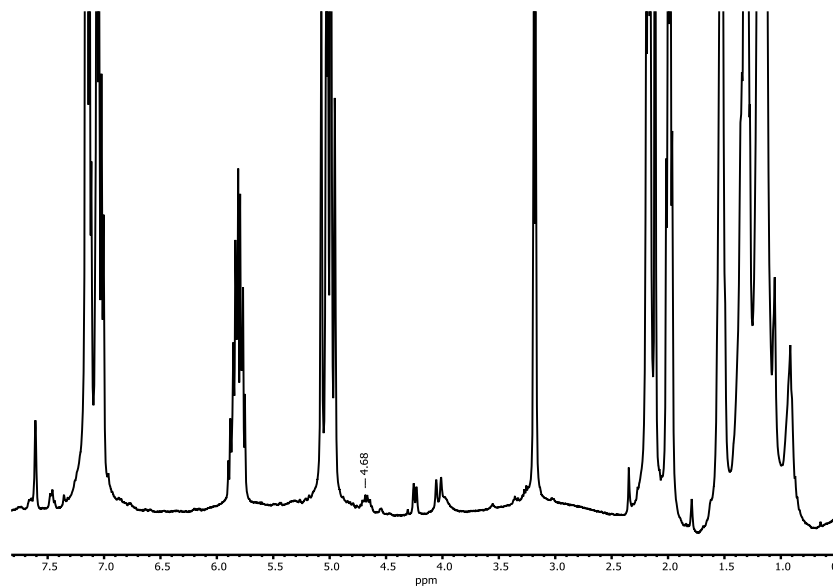


Figure S77. <sup>1</sup>H NMR of 2.5 mol%: 1 isomerization of undec-1-enoic acid under standard thermal conditions in C<sub>6</sub>D<sub>6</sub> with 1 μL mesitylene internal standard. Integration of various products done directly.

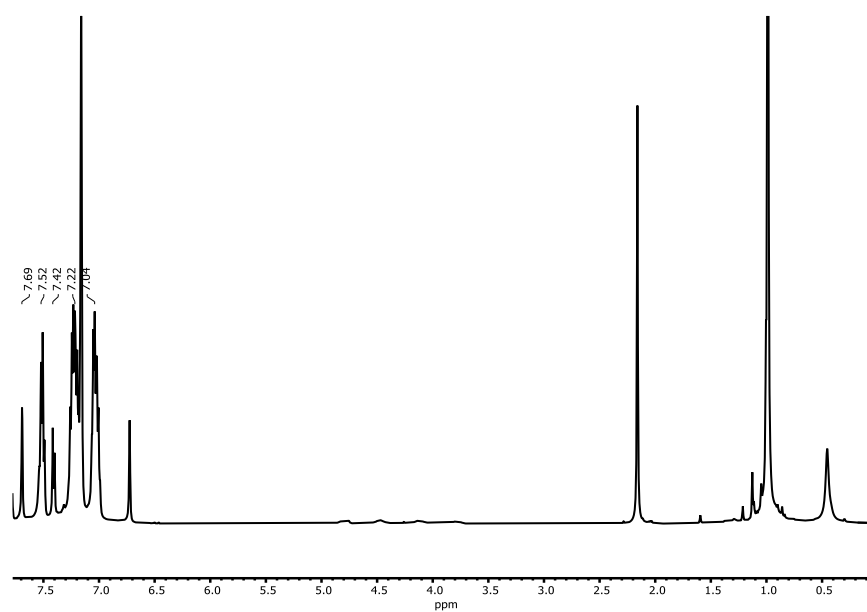


Figure S78. <sup>1</sup>H NMR of 2.5 mol%: 1 isomerization of phenyl acetylene under standard thermal conditions in C<sub>6</sub>D<sub>6</sub> with 1 μL mesitylene internal standard. Integration of various products done directly.

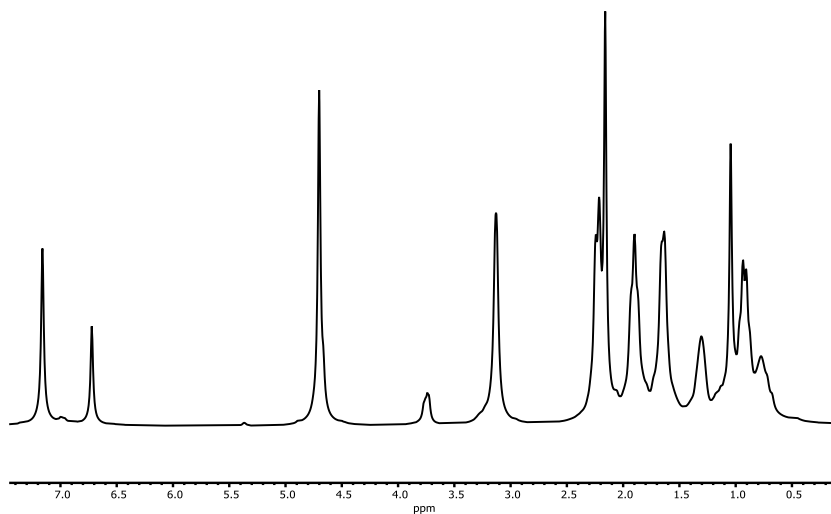


Figure S79.  $^1\text{H}$  NMR of 2.5 mol%: 1 isomerization of (4-methylenecyclohexyl)methanol under standard thermal conditions in  $\text{C}_6\text{D}_6$  with 1  $\mu\text{L}$  mesitylene internal standard. Integration of various products done directly.

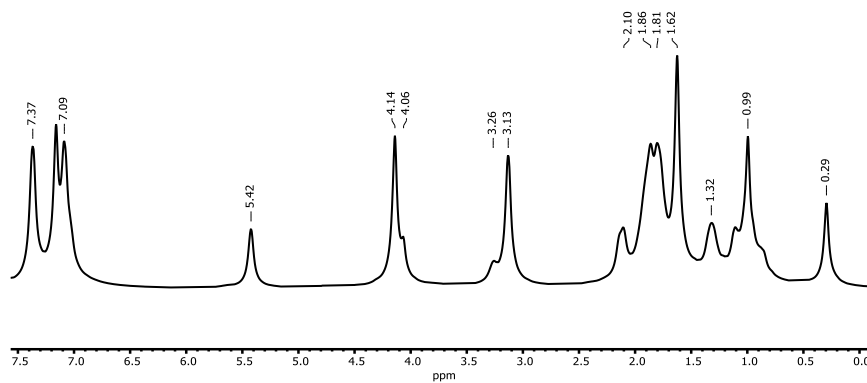


Figure S80.  $^1\text{H}$  NMR of 2.5 mol%: 1 isomerization of 1-(((4-methylenecyclohexyl)methoxy)methyl)-4-(trifluoromethyl)benzene under standard thermal conditions in  $\text{C}_6\text{D}_6$ . Integration of various products done directly.

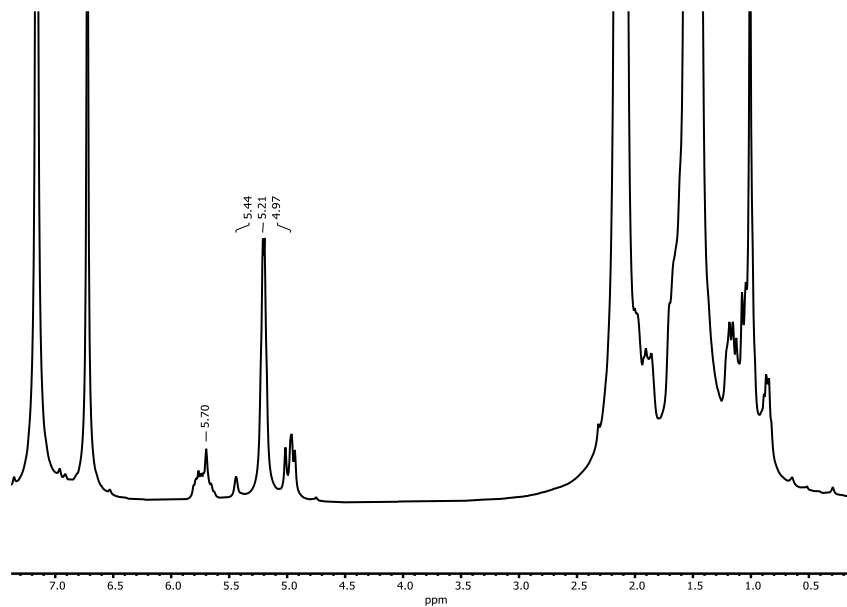


Figure S81. <sup>1</sup>H NMR of 2.5 mol%: 1 isomerization of vinyl cyclohexane under standard thermal conditions in C<sub>6</sub>D<sub>6</sub> with 1 μL mesitylene internal standard. Integration of various products done directly.

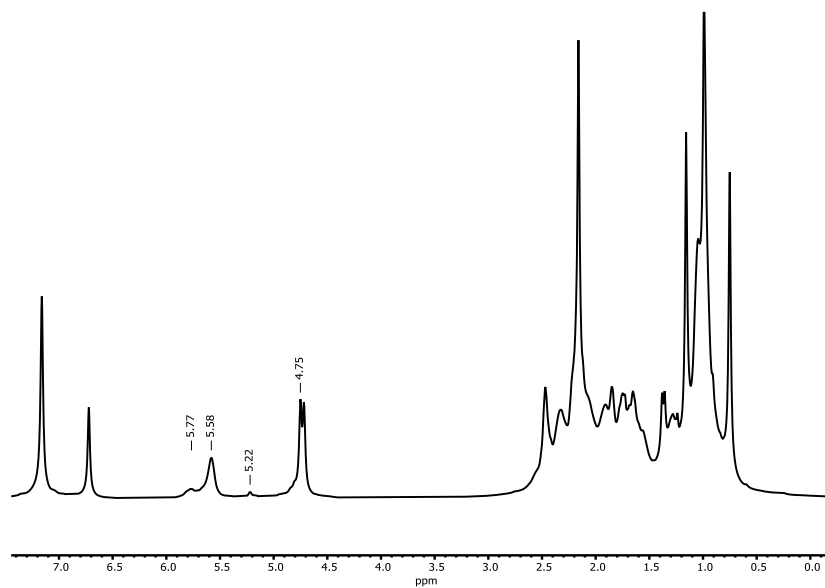


Figure S82. <sup>1</sup>H NMR of 2.5 mol%: 1 isomerization of β-pinene under standard thermal conditions in C<sub>6</sub>D<sub>6</sub> with 1 μL mesitylene internal standard. Integration of various products done directly.

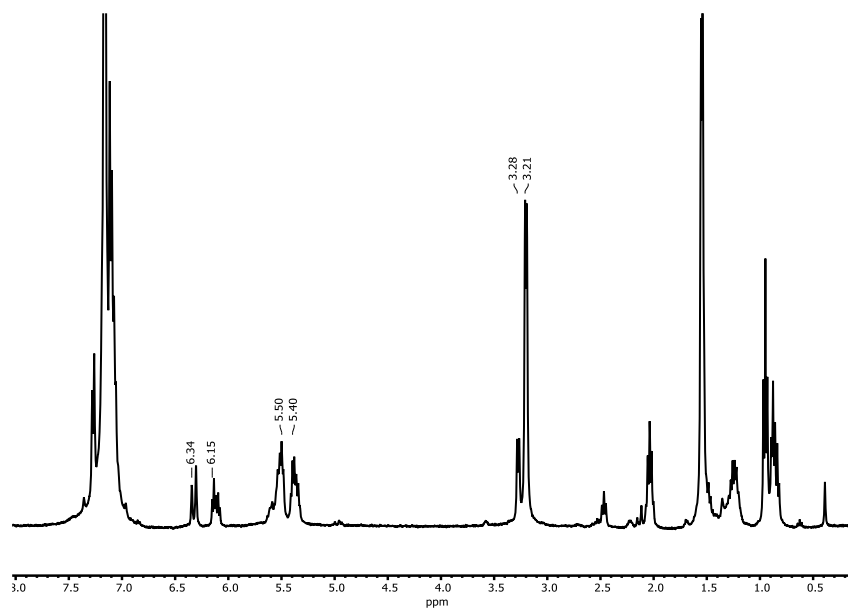


Figure S83. <sup>1</sup>H NMR of 2.5 mol%: 1 isomerization of 4-phenyl-but-1-ene under standard thermal conditions in C<sub>6</sub>D<sub>6</sub> with 1 μL mesitylene internal standard. Integration of various products done directly.

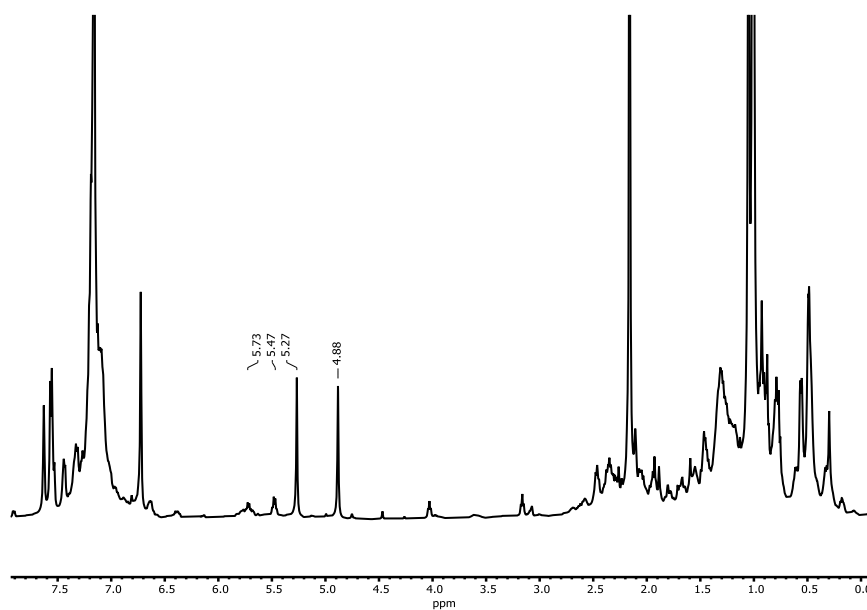


Figure S84. <sup>1</sup>H NMR of 2.5 mol%: 1 isomerization of  $\alpha$ -cyclopropylstyrene under standard thermal conditions in C<sub>6</sub>D<sub>6</sub> with 1 μL mesitylene internal standard. Integration of various products done directly.

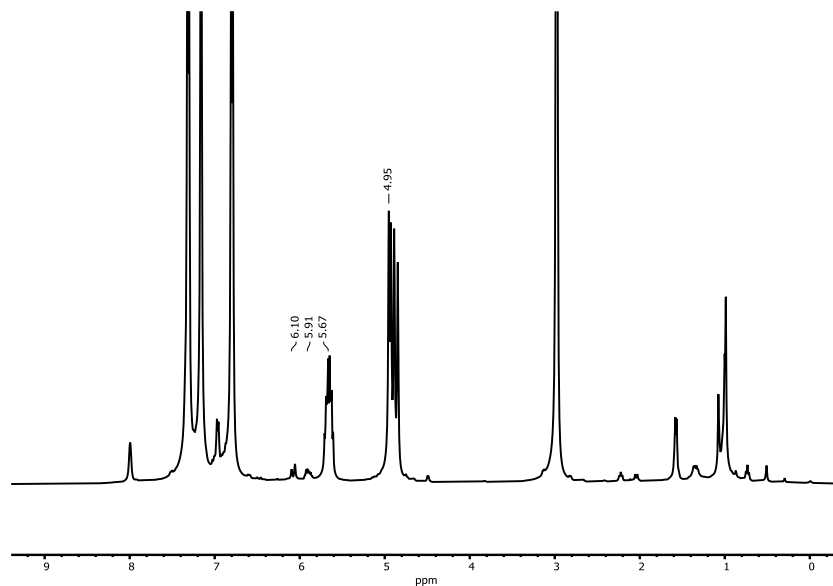


Figure S85. <sup>1</sup>H NMR of 2.5 mol%: 1 isomerization of 1-allyl-4-trifluoromethyl-benzene under standard thermal conditions in C<sub>6</sub>D<sub>6</sub> with 1 μL mesitylene internal standard. Integration of various products done directly.

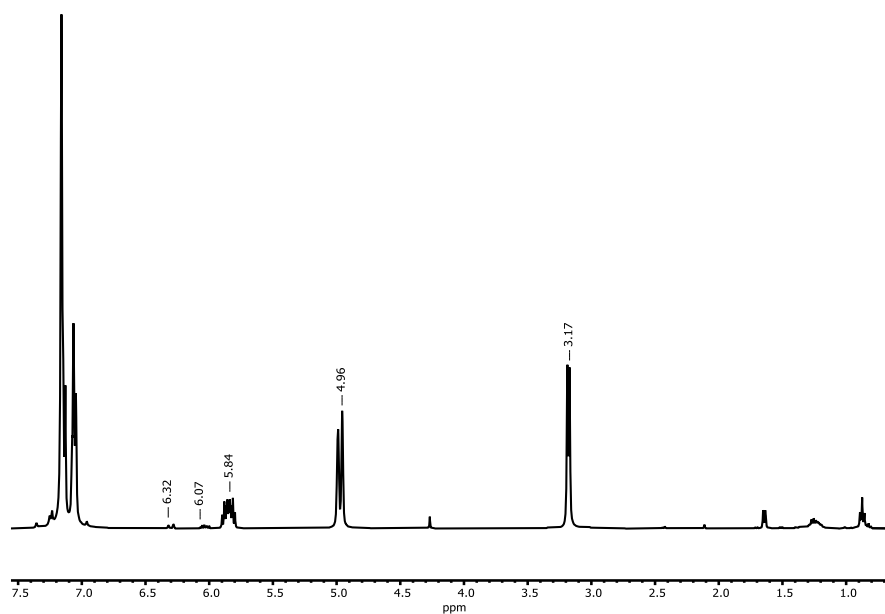


Figure S86. <sup>1</sup>H NMR of 2.5 mol%: 1 isomerization of allyl benzene under standard thermal conditions in C<sub>6</sub>D<sub>6</sub>. Integration of various products done directly.

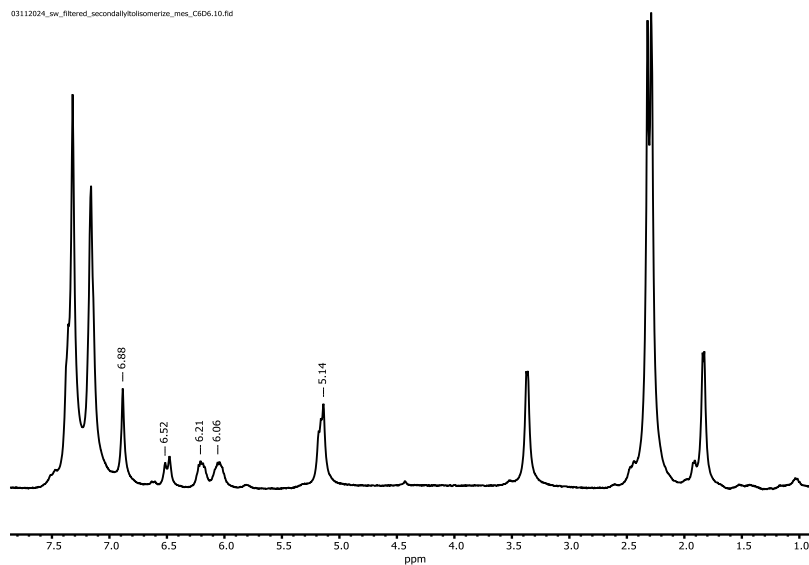


Figure S87.  $^1\text{H}$  NMR of 2.5 mol%: 1 isomerization of 1-allyl-4-methylbenzene under standard thermal conditions in  $\text{C}_6\text{D}_6$  with 1  $\mu\text{L}$  mesitylene internal standard. Integration of various products done directly.

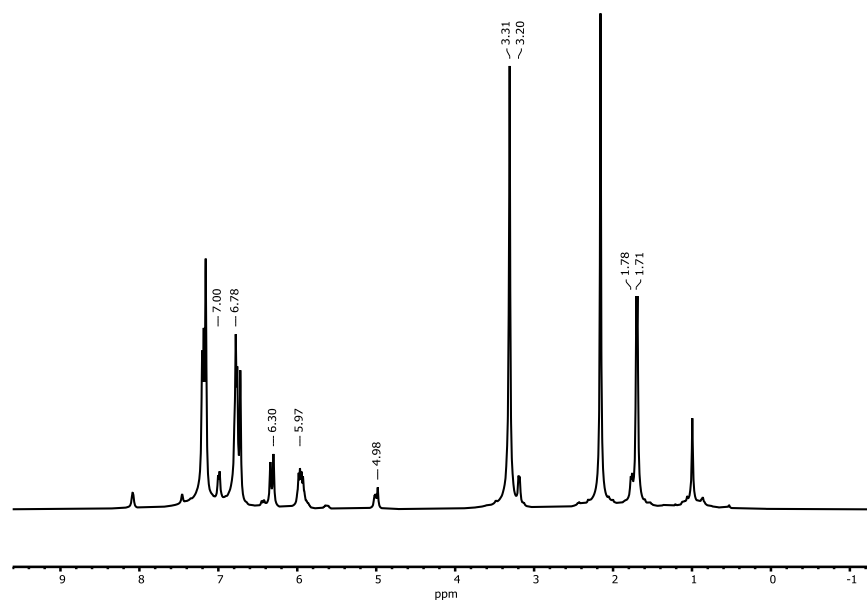


Figure S88.  $^1\text{H}$  NMR of 2.5 mol%: 1 isomerization of allyl-anisole under standard thermal conditions in  $\text{C}_6\text{D}_6$  with 1  $\mu\text{L}$  mesitylene internal standard. Integration of various products done directly.

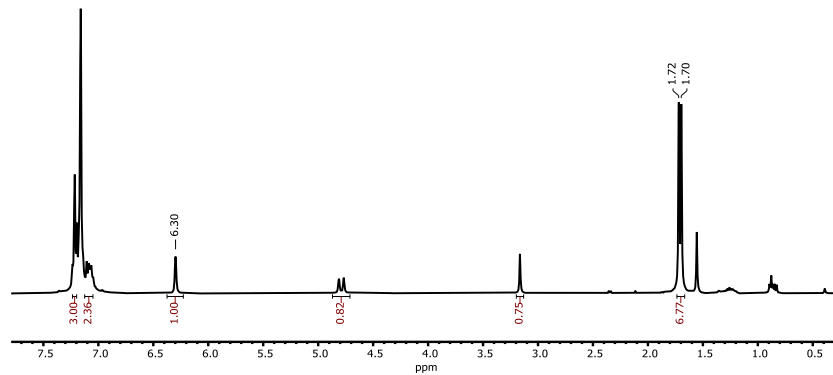


Figure S89.  $^1\text{H}$  NMR of 2.5 mol%: 1 isomerization of (2-methylallyl)benzene under standard thermal conditions in  $\text{C}_6\text{D}_6$  with 1  $\mu\text{L}$  mesitylene internal standard. Integration of various products done directly.

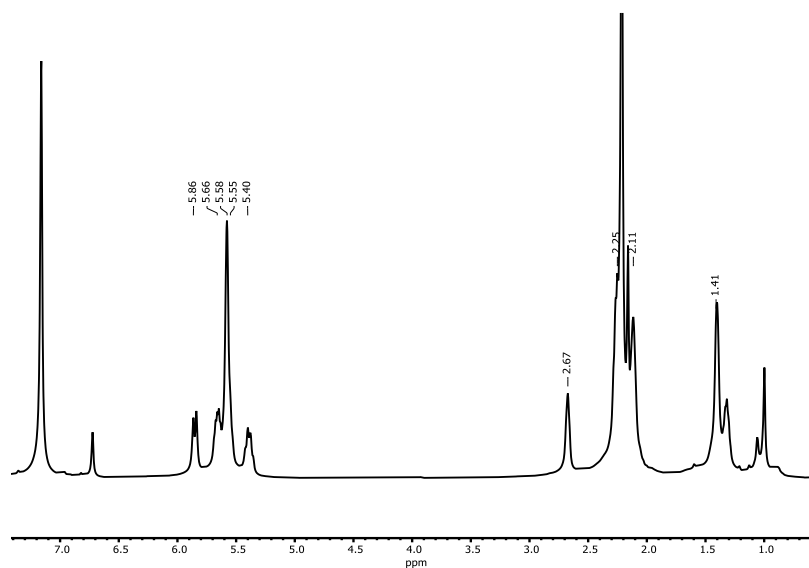


Figure S90.  $^1\text{H}$  NMR of 2.5 mol%: 1 isomerization of 1,5-cyclooctadiene under standard thermal conditions in  $\text{C}_6\text{D}_6$  with 1  $\mu\text{L}$  mesitylene internal standard. Integration of various products done directly.

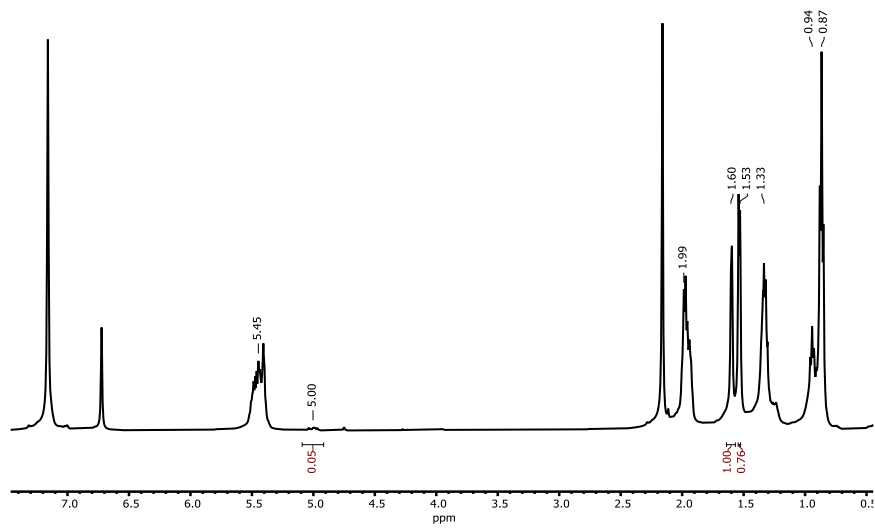


Figure S91.  $^1\text{H}$  NMR of 2.5 mol%: 1 isomerization of trans-2-hexene under standard photochemical conditions in  $\text{C}_6\text{D}_6$  with 1  $\mu\text{L}$  mesitylene internal standard. Integration of various products done directly.

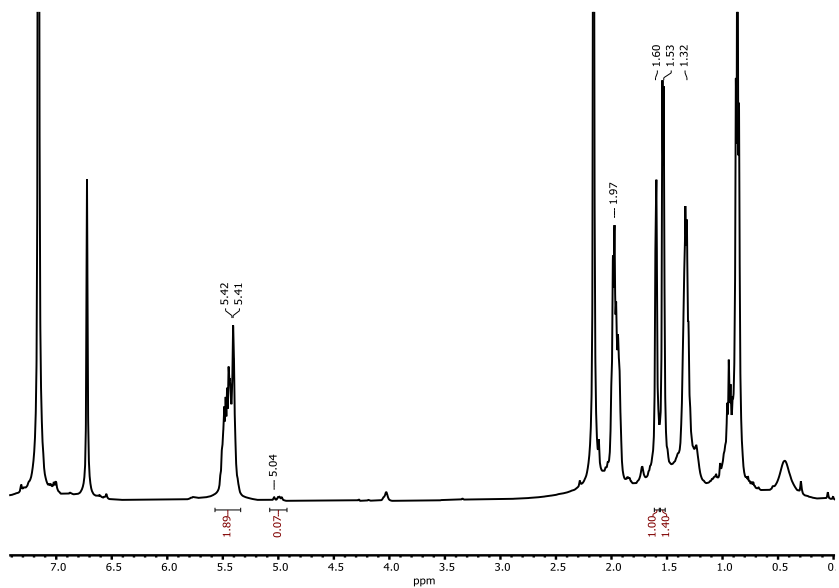


Figure S92.  $^1\text{H}$  NMR of 2.5 mol%: 1 isomerization of trans-3-hexene under standard photochemical conditions in  $\text{C}_6\text{D}_6$  with 1  $\mu\text{L}$  mesitylene internal standard. Integration of various products done directly.

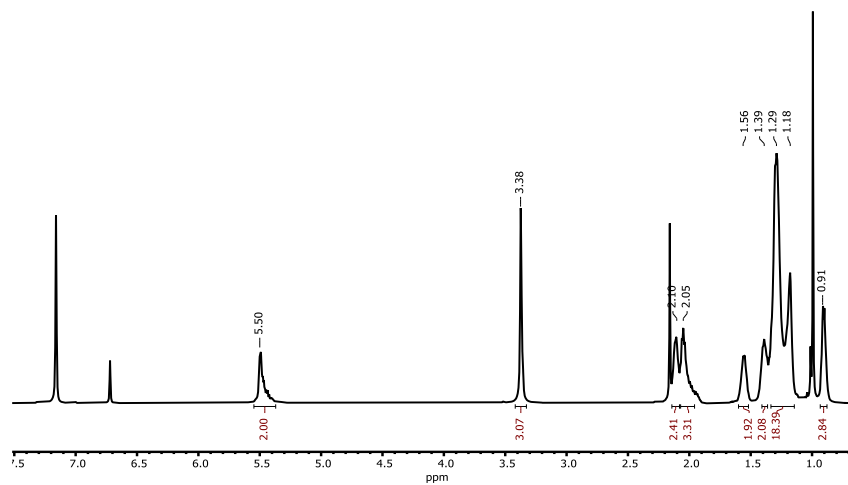


Figure S93.  $^1\text{H}$  NMR of 2.5 mol%: 1 isomerization of methyl elaidate under standard photochemical conditions in  $\text{C}_6\text{D}_6$  with 1  $\mu\text{L}$  mesitylene internal standard. Integration of various products done directly.

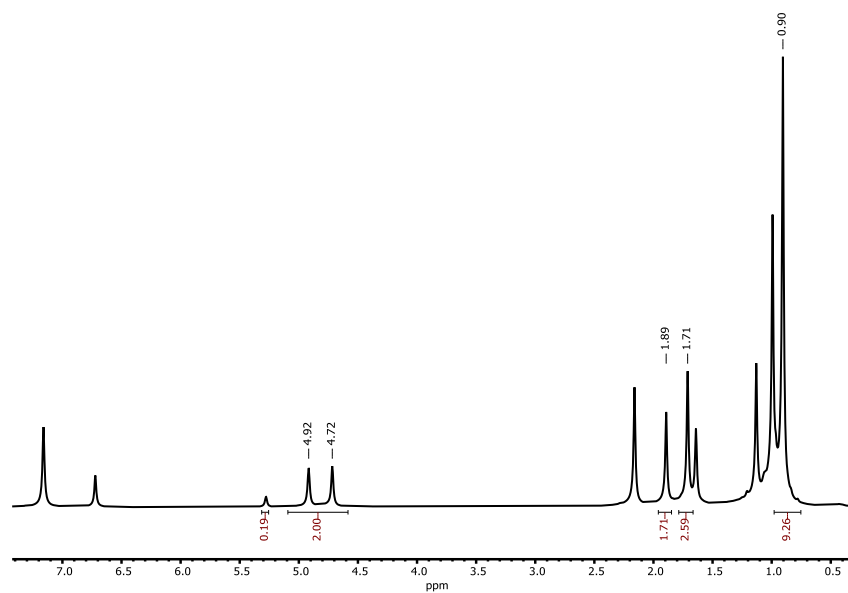


Figure S94.  $^1\text{H}$  NMR of 2.5 mol%: 1 isomerization of 2,4,4-trimethylpent-2-ene under standard photochemical conditions in  $\text{C}_6\text{D}_6$  with 1  $\mu\text{L}$  mesitylene internal standard. Integration of various products done directly.

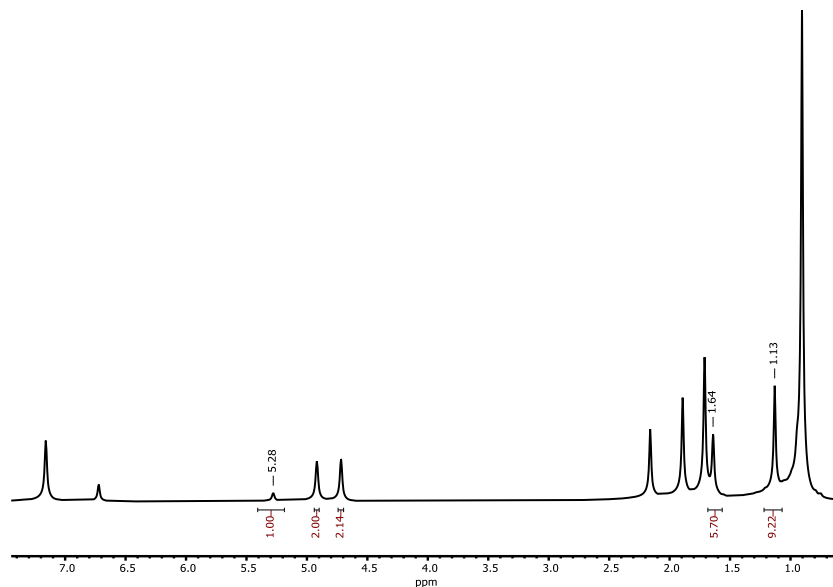


Figure S95.  $^1\text{H}$  NMR of 2.5 mol%: 1 isomerization of 2,4,4-trimethylpent-1-ene under standard thermal conditions in  $\text{C}_6\text{D}_6$  with 1  $\mu\text{L}$  mesitylene internal standard. Integration of various products done directly.

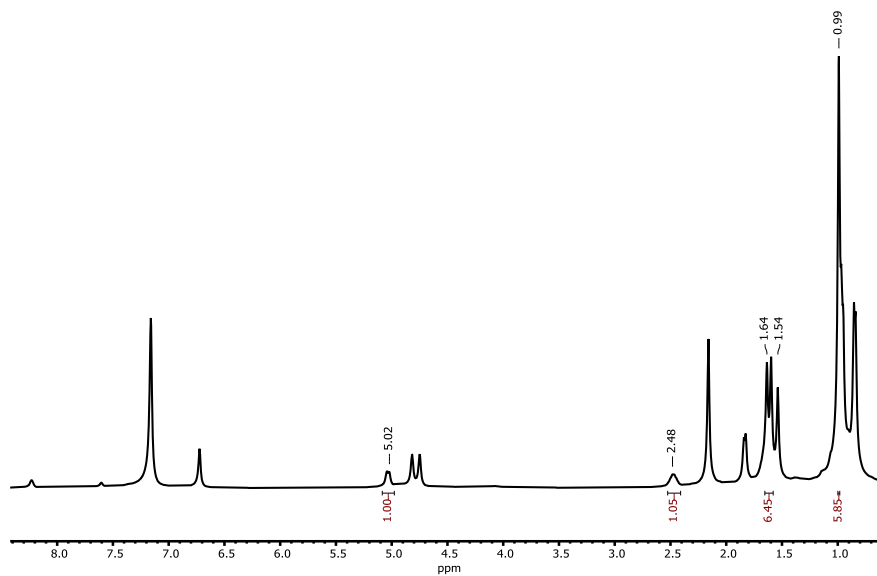


Figure S96.  $^1\text{H}$  NMR of 2.5 mol%: 1 isomerization of 2,4-dimethylpent-1-ene under standard thermal conditions in  $\text{C}_6\text{D}_6$  with 1  $\mu\text{L}$  mesitylene internal standard. Integration of various products done directly.

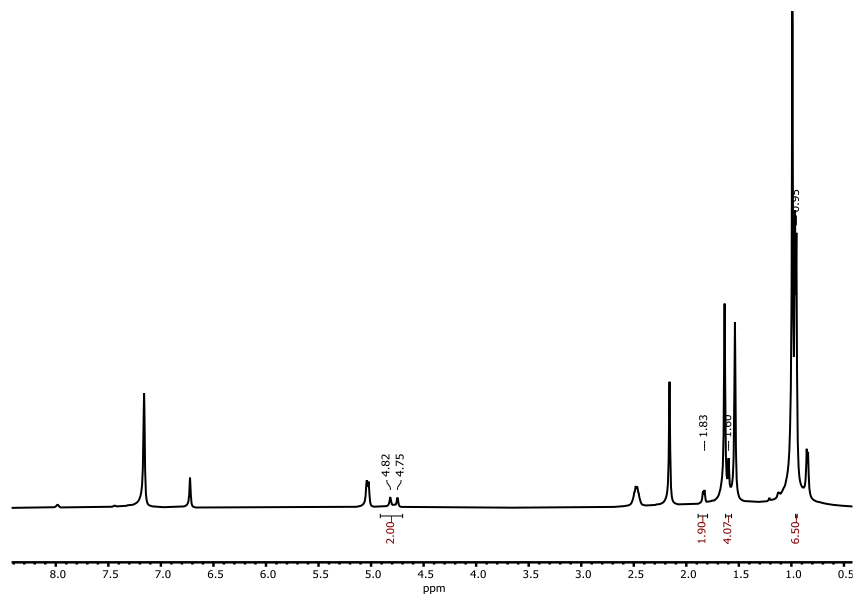


Figure S97.  $^1\text{H}$  NMR of 2.5 mol%: 1 isomerization of 2,4-dimethylpent-2-ene under standard photochemical conditions in  $\text{C}_6\text{D}_6$  with 1  $\mu\text{L}$  mesitylene internal standard. Integration of various products done directly.

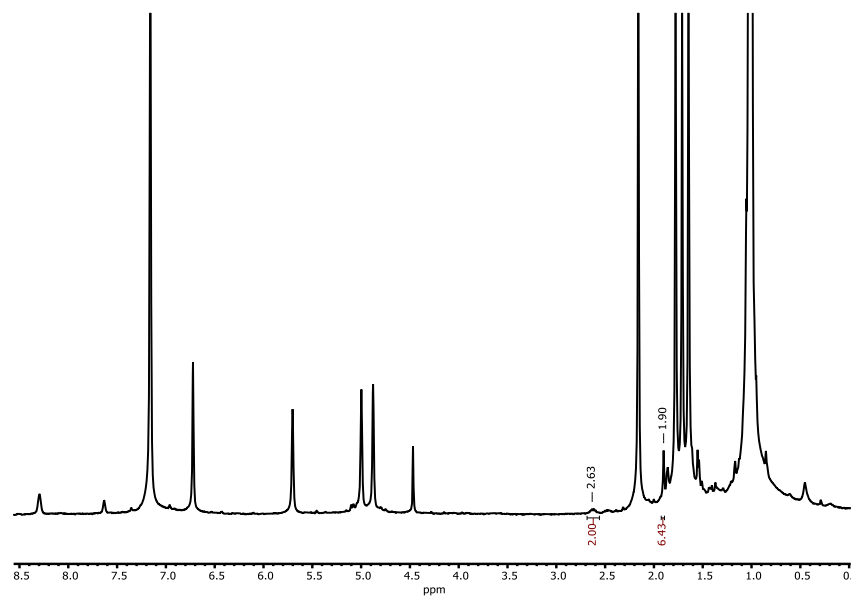


Figure S98.  $^1\text{H}$  NMR of 2.5 mol%: 1 isomerization of 2,4-dimethylpenta-1,3-diene under standard photochemical conditions in  $\text{C}_6\text{D}_6$  with 1  $\mu\text{L}$  mesitylene internal standard. Integration of various products done directly.

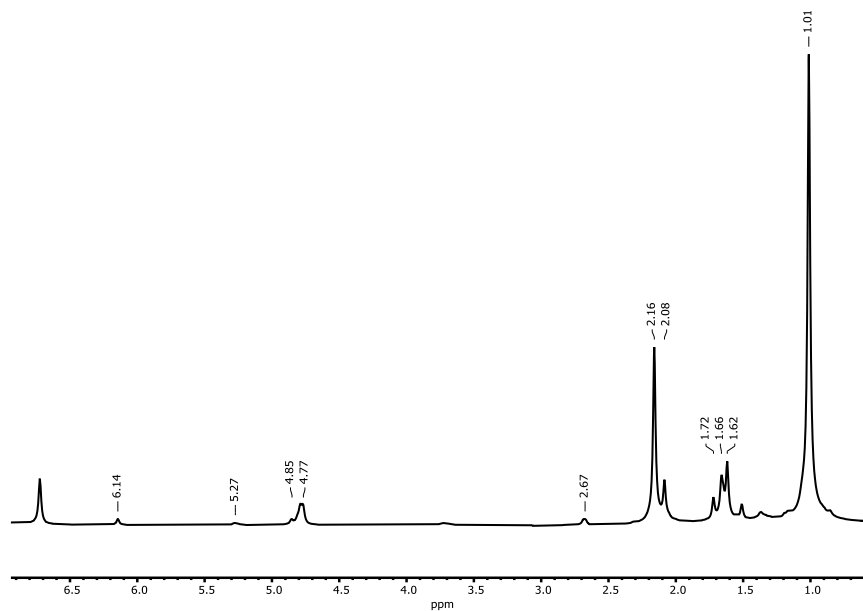


Figure S99. <sup>1</sup>H NMR of 2.5 mol%: 1 isomerization of 2,5-dimethylhexa-1,5-diene under standard thermal conditions in C<sub>6</sub>D<sub>6</sub> with 1 μL mesitylene internal standard. Integration of various products done directly.

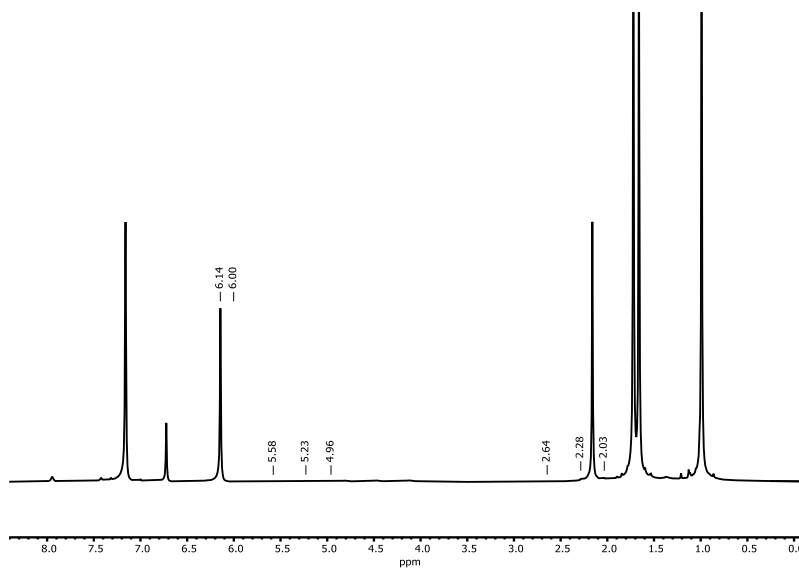


Figure S100. <sup>1</sup>H NMR of 2.5 mol%: 1 isomerization of 2,5-dimethylhexa-2,4-diene under standard photochemical conditions in C<sub>6</sub>D<sub>6</sub> with 1 μL mesitylene internal standard. Integration of various products done directly.

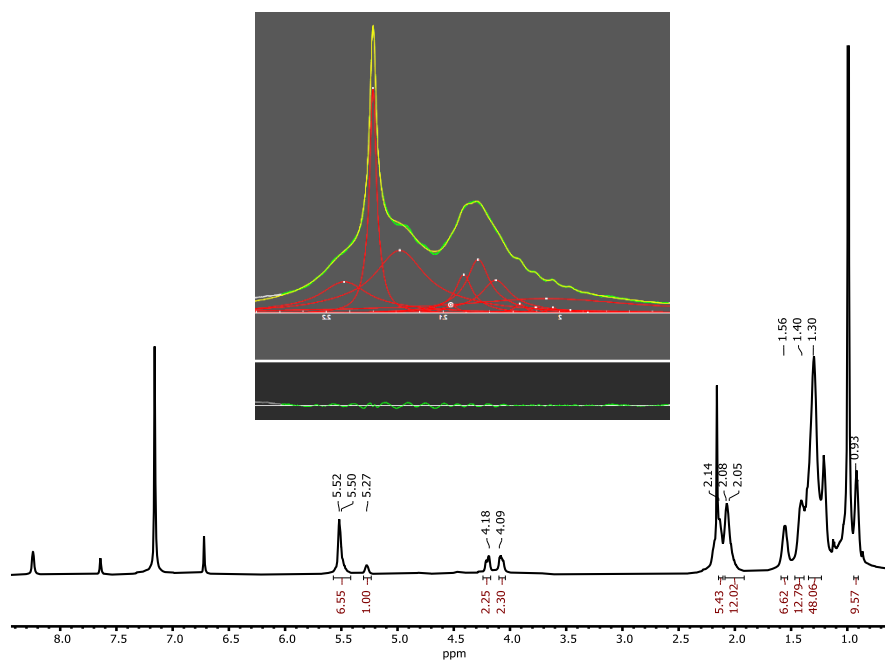


Figure S101.  $^1\text{H}$  NMR of 2.5 mol%: 1 isomerization of trielaidin under standard photochemical conditions in  $\text{C}_6\text{D}_6$  with 1  $\mu\text{L}$  mesitylene internal standard. Integration of various products done directly via curve-fitting in Fityk (inset included).

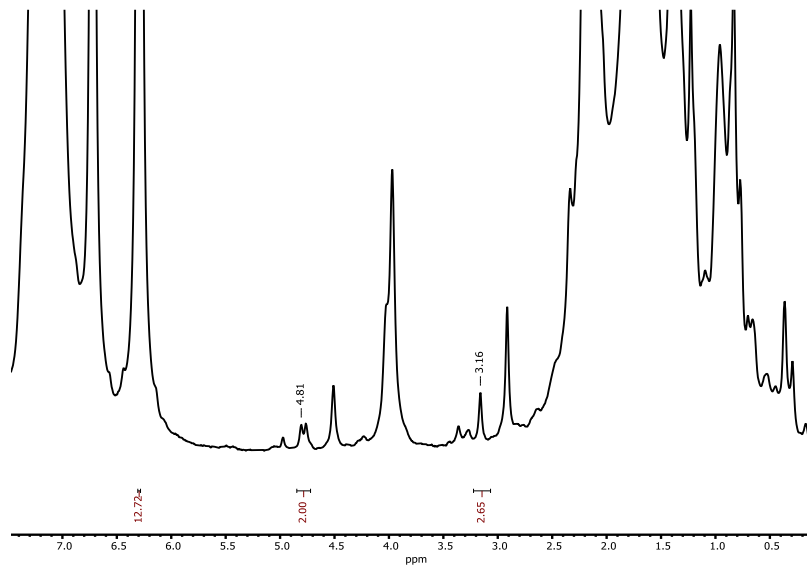
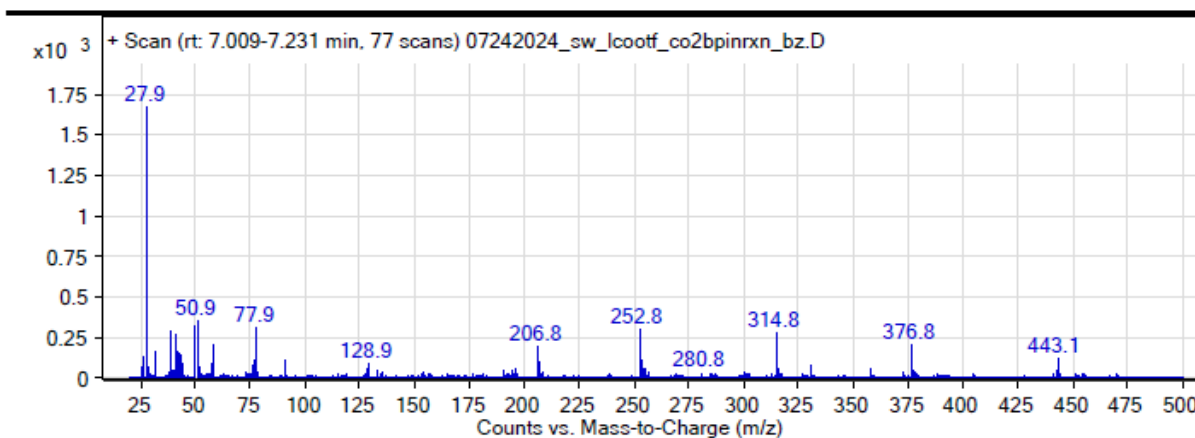
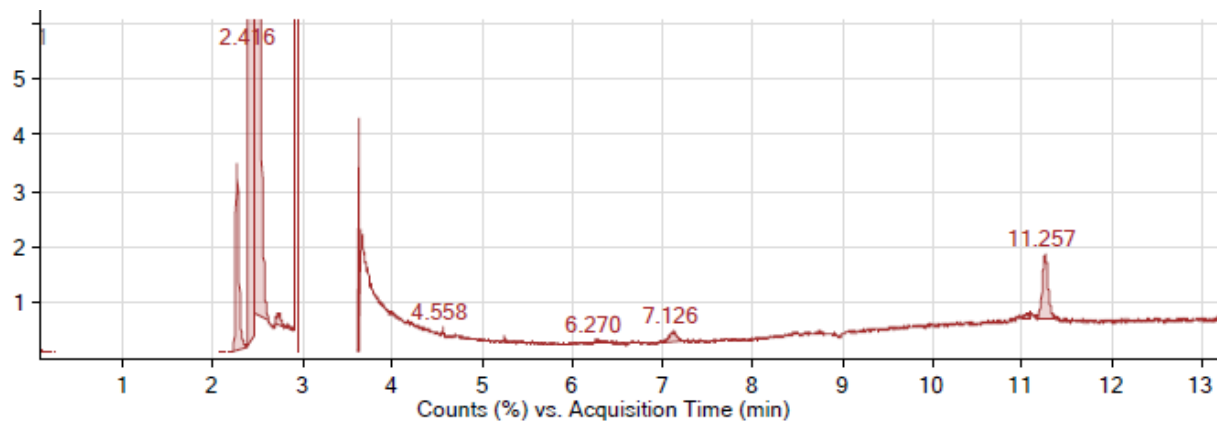


Figure S96.  $^1\text{H}$  NMR of 2.5 mol%: 1 isomerization of (2-methylprop-1-en-1-yl)benzene under standard photochemical conditions in  $\text{C}_6\text{D}_6$  with 1  $\mu\text{L}$  mesitylene internal standard. Integration of various products done directly.

## Mass Spectrometry



### Peak List

<i>m/z</i>	<i>z</i>	Abund
27.9	1	1673.8
38.9		294.5
40.9		271.48
49.9		320.82
50.9		353.12
77.9		311.71
78		203.53
252.8	1	297.66
314.8	1	277.81
376.8	1	204.26

Figure S103. GCMS of dried post-thermal isomerization reaction of 1-hexene with HBPIn.

With the olefins and other volatile residues removed, all that is observable is residual solvent peaks from the instrument below 3 minutes, a peak at 7.126 with masses corresponding to a hydroborated ligand, and a peak at 11.257 consistent with free ligand.

## References

1. Schild, D. J.; Nurdin, L.; Moret, M-E.; Oyala, P. H.; Peters, J. C. Characterization of Proposed Terminal Iron(III) Nitride Intermediate of Nitrogen Fixation Stabilized by a Trisphosphine Borane Ligand. *Angew. Chem. Int. Ed.* **2022**, *61*, 43, e202209655.
2. (a) Neese, F. "The Orca Program System" *Wiley Interdisciplinary Reviews: Computational Molecular Science* **2012**, *2*, 73-78. (b) H - Kr: A. Schaefer, H. Horn and R. Ahlrichs, *J. Chem. Phys.* **1992**, *97*, 2571. (c) Rb - Xe: A. Schaefer, C. Huber and R. Ahlrichs, *J. Chem. Phys.* **1994**, *100*, 5829.
3. NIST Computational Chemistry Comparison and Benchmark Database, NIST Standard Reference Database Number 101. Release 21, August 2020, Editor: Russell D. Johnson III
4. Schwieger, S.; Herzog, R.; Wagner, C.; Steinborn, D. Platina- $\beta$ -diketones as catalysts for hydrosilylation and their reactivity towards hydrosilanes. *J. Organomet. Chem.* **2009**, *694*, 3548-3558.
5. Wang, H.; Meng, F.; Tao, X. B(C<sub>6</sub>F<sub>5</sub>)<sub>3</sub>-catalyzed isomerization of terminal olefins. *New. Jour. Of Chem.*, **2024**, *48*, 10, 4304-4309.
6. Abinet, E.; Martin, D.; Standfuss, S.; Kulinna, H.; Spaniol, T. P.; Okuda, J. Rare-Earth Metal Allyl and Hydrido Complexes Supported by an (NNNN)-Type Macrocyclic Ligand: Synthesis, Structure, and Reactivity toward Biomass-Derived Furanics. *Chemistry - A European Journal*, **2011**, *17*, 52, 15014 – 15026.
7. Zhao, H.; McMillan, A. J.; Constantin, T.; Mykura, R. C.; Juliá, F.; Leonori, D. Merging Halogen-Atom Transfer (XAT) and Cobalt Catalysis to Override E2-Selectivity in the Elimination of Alkyl Halides: A Mild Route toward contra-Thermodynamic Olefins. *J. Am. Chem. Soc.* **2021**, *143*, 36, 14806–14813.
8. Kim, D.; Pillon, G.; Diprimio, D. J.; Holland, P. L. Highly Z-Selective Double Bond Transposition in Simple Alkenes and Allylarenes through a Spin-Accelerated Allyl Mechanism.. *J. Am. Chem. Soc.* **2021**, *143*, 8, 3070–3074.
9. Narra, N.; Kaki, S. S.; Prasad, R. B. N.; Misra, S.; Dhevendar, K.; Kontham, V.; Korlipara, P. V. Synthesis and evaluation of anti-oxidant and cytotoxic activities of novel 10-undecenoic acid methyl ester based lipoconjugates of phenolic acids. *Beilstein Journal of Organic Chemistry*, **2017**, *13*, 26 – 32.
10. MacArthur, N. S.; Wang, L.; McCarthy, B. G.; Jakobsche, C. E. Using N-Nitrosodichloroacetamides to Conveniently Convert Linear Primary Amines into Alcohols. *Synthetic Comm.* **2016**, *45*, 2014-2020.
11. Wang, Y.; Chen, W.; Lu, Z.; Hua Li, Z.; Wang, H. Metal-Free HB(C<sub>6</sub>F<sub>5</sub>)<sub>2</sub>-Catalyzed Hydrogenation of Unfunctionalized Olefins and Mechanism Study of Borane-Mediated  $\sigma$ -Bond Metathesis. *Angew. Chem. Int. Ed.*, **2013**, *29*, 7496-7499.
12. Wech, F.; Hasenbeck, M. Gellrich, U. Semihydrogenation of Alkynes Catalyzed by a Pyridone Borane Complex: Frustrated Lewis Pair Reactivity and Boron-Ligand Cooperation in Concert. *Chem. A Eur. Jour.* **2020**, *26*, 59, 13445-13450.
13. Titov, A. A.; Smol'yakov, A. F.; Chernyadyev, A. Y.; Godovikov, I. A.; Filippov, O. A.; Shubina, E. S. Pyrazolate vs. phenylethynde: direct exchange of the anionic bridging ligand in a cyclic trinuclear silver complex. *Chem. Comm.*, **2023**, *60*, 7, 847 – 850.
14. Ozerov, O. V.; Patrick, B. O.; Ladipo, F. T. Highly Regioselective [2 + 2 + 2] Cycloaddition of Terminal Alkynes Catalyzed by  $\eta^6$ -Arene Complexes of Titanium Supported by Dimethylsilyl-Bridged p-tert-Butyl Calix[4]arene Ligand. *J. Am. Chem. Soc.* **2000**, *122*, 27, 6423–643.

15. Martin, J.; Knüpfer, C.; Eyslein, J.; Färber, C.; Grams, S.; Langer, J.; Thum, K.; Wiesinger, M.; Harder, S. Highly Active Superbulky Alkaline Earth Metal Amide Catalysts for Hydrogenation of Challenging Alkenes and Aromatic Rings. *Ang. Chem. Int. Ed.* **2020**, *59*, 23, 9102-9112.
16. Tricoire, M.; Wang, D.; Rajeshkumar, T.; Maron, L.; Danoun, G.; Nocton, G. Electron Shuttle in N-Heteroaromatic Ni Catalysts for Alkene Isomerization. *JACS Au* **2022**, *2*, 8, 1881–1888.
17. Enachi, A.; Baabe, D.; Zaretzke, M-K.; Schweyen, P.; Freytag, M.; Raeder, J.; Walter, M. D. [(NHC)CoR<sub>2</sub>]: pre-catalysts for homogenous olefin and alkyne hydrogenation. *Chem. Comm.* **2018**, *54*, 13798-13801.
18. Zhang, X-T.; Tian, S-K. Palladium-catalyzed indium-mediated reductive aromatic C-H allylation of N-benzylsulfonimides with allyl esters. *Chem. Comm.* **2023**, *59*, 5075-5078.
19. Gao, M.; Gosmini, C. Co-Catalyzed Reductive Cross-Couplings of Csp<sup>3</sup>-S with Callyl-O Electrophiles to form Csp<sup>3</sup>-Csp<sup>3</sup> Bonds. *Advanced Synthesis & Catalysis.* **2023**, *365*, 21, 3597-3602.
20. Zhao, Y.; Xu, J.; Chen, H.; Xia, Y.; Hu, L. Iron-Catalyzed Oxyphosphorylation of Styrenes to Access  $\beta$ -Ketophosphonates and  $\alpha$ ,  $\beta$ -Unsaturated Ketones. *Advanced Synthesis & Catalysis.* **2023**, *365*, 19, 3290-3294.
21. Gigler, P.; Bechlars, B.; Herrmann, W. A.; Kühn, F. E. Hydrosilylation with Biscarbene Rh(I) Complexes: Experimental Evidence for a Silylene-Based Mechanism. *J. Am. Chem. Soc.* **2011**, *133*, 5, 1589-1596.
22. Slaughter, J.; Molyneux, S. A.; Peel, A. J.; Wheatley, A. E. H. Action of Organoaluminum Reagents on Esters: Alkene Production and the Degradation of Synthetic Lubricants. *Organometallics*, **2019**, *38*, 2, 395-408.
23. Kozyriev, Y. K.; Palchykov, V. A. Synthesis of challenging 6-functionalized 1-oxaspiro[3.3]heptanes – New scaffolds for drug discovery. *Tet. Lett.*, **2023**, *122*, 154515.
24. Kristensen, Steffan K.; Laursen, Simon L. R.; Taarning, Esben; Skrydstrup, Troels. Ex Situ Formation of Methanethiol: Application in the Gold (I)-Promoted Anti-Markovnikov Hydrothiolation of Olefins. *Angew. Chem. Int. Ed.*, **2018**, *57*, 42, 13887 – 13891.
25. Masnovi, J.; Samsel, E. G.; Bullock, R. M. Cyclopropylbenzyl Radical Clocks. *J. Chem. Soc., ChemComm.* **1989**, 1044–1045.
26. He, Q.; Pu, M-P.; Jiang, Z.; Wang, H.; Feng, X.; Liu, X. Asymmetric Epoxidation of Alkenes Catalyzed by a Cobalt Complex. *J. Am. Chem. Soc.* **2023**, *145*, 28, 15611–15618.
27. Bergamaschi, E.; Beltran, F.; Teskey, C. J. Visible-Light Controlled Divergent Catalysis Using a Bench-Stable Cobalt(I) Hydride Complex. *Chem. A Eur. Jour.* **2020**, *26*, 23, 5180-5184.
28. Jha, N.; Guo, W.; Kong, W-Y.; Tantillo, D. J.; Kapur, M. Regiocontrol via Electronics: Insights into a Ru-Catalyzed, Cu-Mediated Site-Selective Alkylation of Isoquinolones via a C–C Bond Activation of Cyclopropanols. *Chem. A Eur. Jour.* **2023**, *29*, 55, e202301551..
29. Land, M. A.; Bačić, G.; Robertson, K. N.; Barry, S. T. Origin of Decomposition in a Family of Molybdenum Precursor Compounds. *Inorg. Chem.* **2022**, *61*, 42, 16607–16621.
30. Ainembabazi, D.; Reid, C.; Chen, A.; An, N.; Kostal, J.; Voutchkova-Kostal, A. *J. Am. Chem. Soc.* **2020**, *142*, 2, 696–699.
31. Harris, R. K.; Ng, S.; Connelly, A. *Magnetic Resonance in Chemistry*, **1991**, *29*, 11, 1152 - 1157.
32. Zhao, K.; Knowles, R. R. *J. Am. Chem. Soc.* **2022**, *144*, 1, 137–144.
33. Lehmkuhl, H.; Tsien, Y-L. *Chemische Berichte*, **1983**, *116*, 7, 2437 – 2446.

34. Tsuji, T.; Miura, T.; Sugiura, K.; Matsumoto, Y.; Nishida, S. *J. Am. Chem. Soc.* **1993**, *115*, 2, 482–493.
35. Lie Ken Jie, Marcel S.F.; Lam. *Chemistry and Physics of Lipids*, **1995**, *77*, 2, 155 – 171.
36. Vanbésien, T.; Monflier, E.; Hapiot, F. *Green Chem.* **2017**, *19*, 1940–1948.
37. Della, E. W.; Knill, A. M.; Pigou, P. E. Synthesis of Bridgehead-Substituted Bicyclo[2.2.1]heptanes by Radical Cyclization. *J. Org. Chem.* **1993**, *58*, 2110-2114.
38. Iwasaki, K.; Wan, K. K.; Oppedisano, A.; Crossley, S. W. M.; Shenvi, R. A. Simple, Chemoselective Hydrogenation with Thermodynamic Stereocontrol. *J. Am. Chem. Soc.* **2014**, *136*, 4, 1300-1303.
39. Lu, Y.; Tan, W-Y.; Ding, Y.; Chan, W.; Zhang, H. Oxidation of Primary Alcohols and Aldehydes to Carboxylic Acids with 1-Hydroxycyclohexyl Phenyl Ketone. *J. Org. Chem.* **2023**, *88*, 13, 8114-8122.
40. Linnebank, P. R.; Ferreira, S. F.; Kluwer, A. M.; Reek, J. N. H. Regioselective Hydroformylation of Internal and Terminal Alkenes via Remote Supramolecular Control. *Chem. A Eur. Jour.* **2020**, *26*, 37, 8214-8219.
41. Britovsek, G. J. P.; Bruce, M.; Gibson, V. C.; Kimberley, B. S.; Maddox, P. J.; Mastroianni, S.; McTavish, S. J.; Redshaw, C.; Solan, G. A.; Stömberg, S.; White, A. J. P.; Williams, D. J. Iron and cobalt ethylene polymerization catalysts bearing 2, 6-bis (imino) pyridyl ligands: synthesis, structures, and polymerization studies. *J. Am. Chem. Soc.* **1999**, *121*, 38, 8728-8740.
-

## Appendix V: Chapter VI Supplementary Information

### General Methods

All chemicals were purchased from commercial suppliers and used without further purification. All manipulations were carried out under an atmosphere of N<sub>2</sub> using standard Schlenk and glovebox techniques. Glassware was dried at 180 °C for a minimum of two hours and cooled under vacuum prior to use. Solvents were dried on a solvent purification system from Pure Process Technologies and stored over 4 Å molecular sieves under N<sub>2</sub>. Tetrahydrofuran (THF) was stirred over NaK alloy and run through an additional alumina column prior to use to ensure dryness. Solvents were tested for H<sub>2</sub>O and O<sub>2</sub> using a standard solution of sodium-benzophenone ketyl radical anion. CD<sub>3</sub>CN, C<sub>6</sub>D<sub>6</sub>, and *d*<sub>8</sub>-toluene were dried over 4 Å molecular sieves under N<sub>2</sub>. <sup>1</sup>H NMR spectra were recorded on Bruker DRX 400 or 500 spectrometers. Chemical shifts are reported in ppm units referenced to residual solvent resonances for <sup>1</sup>H NMR spectra. UV-visible spectra were recorded on a Bruker Evolution 300 spectrometer and analyzed using VisionPro software. A standard 1 cm quartz cuvette with an airtight screw cap with a puncturable Teflon seal was used for all measurements. A Unisoku CoolSpek cryostat was used for low temperature measurements. IR spectra were recorded on a Bruker Tensor II spectrometer with the OPUS software suite as DCM thin films between KBr plates. Single crystal X-ray diffraction data were collected in-house using Bruker D8 Venture diffractometer equipped with Mo microfocus X-ray tube ( $\lambda = 0.71073 \text{ \AA}$ ). Electrochemical measurements were carried out using a BAS Epsilon potentiostat and using BAS Epsilon software version 1.40.67 NT. EPR spectra were recorded on an Elexsys E500 spectrometer with an Oxford ESR 900 X-band cryostat and a Bruker Cold-Edge Stinger and were simulated using the Easyspin suite in Matlab software.<sup>1</sup> Magnetic moments were determined using the Evans method.<sup>2</sup>

### *Synthesis of [<sup>t</sup>Bu,<sup>Tol</sup>DHP]CoOK (1)*

In a 20 mL vial in the glovebox, 2 mL of toluene was added to [<sup>t</sup>Bu,<sup>Tol</sup>DHP]CoOH (0.002 g, 1 eq., 0.004 mmol).<sup>3</sup> A suspension of potassium tert-butoxide (0.0022 g, 5 eq., 0.020 mmol) in toluene was added to the bright purple solution of [<sup>t</sup>Bu,<sup>Tol</sup>DHP]CoOH. After stirring for 1-2 h, or until the suspended white solids were no longer visible, the resulting green-purple solution was dried *in vacuo* and extracted into benzene. Complex **1** can then be isolated as a purple solid after crystallizations in petroleum ether. Yield: 0.0019 g, 88 %. Poor quality single crystals suitable for XRD of **1** were grown out of a cooled concentrated petroleum ether solution at -35°C. <sup>1</sup>H NMR (400 MHz, C<sub>6</sub>D<sub>6</sub>, RT): δ = 10.92 (br s), 8.44 (s), 6.67 (s), 1.88(s), 1.50(s). Magnetic Susceptibility: Evans' Method for **1** (C<sub>7</sub>D<sub>8</sub> RT, 500 MHz, μ<sub>B</sub>): μ<sub>eff</sub> = 3.62, UV-vis, nm in toluene, (ε, M<sup>-1</sup>cm<sup>-1</sup>): 2213.32. HRMS (EI) m/z: [M]<sup>+</sup> calculated for **1**: C<sub>28</sub>H<sub>34</sub>N<sub>5</sub>OKCo 554.1732 found: 554.1858.

In practice, this compound can also be obtained from [<sup>t</sup>Bu,<sup>Tol</sup>DHP]CoCl or OTf via addition of wet KO<sup>t</sup>Bu.<sup>4</sup>

### *Characterization of [<sup>t</sup>Bu,<sup>Tol</sup>DHP]Co(MeCN)*

The [<sup>t</sup>Bu,<sup>Tol</sup>DHP]Co(MeCN) has been previously reported.<sup>5</sup> In this work we report its crystal structure.

### *Preparation of UV-Vis Samples*

An aliquot of complex **1** was dissolved in toluene in a quartz cuvette in the glove box. The 1 cm quartz cuvette was equipped with an airtight screw cap. The spectrum was collected under a blanketing flow of Nitrogen.

### *Preparation of IR Samples of (1)*

Separate samples of complex **1** and [<sup>t</sup>Bu, Tol]DHP]CoOH were dissolved in dry dichloromethane to form a concentrated solution. This was dropcast onto a KBr plate, and a second plate was then placed on top. The sample was then transferred in an air-free temporary container to the spectrometer, and a spectrum was collected.

### *Electrochemical Experiments*

Experiments were performed inside the glovebox with a 1:4 MeCN:THF 0.1 M KPF<sub>6</sub> electrolyte solution at room temperature. Cyclic voltammetry measurements were made with a [Co] = 2.4 mM using a glassy carbon working electrode, platinum wire counter electrode, and silver wire pseudo reference electrode and were referenced to internal Fc/Fc<sup>+</sup> by adding ferrocene at the end of measurements. A one-compartment glass cell was filled with 4 mL of electrolyte solution. The working electrode was polished over a microcloth pad (Buehler) using alumina slurry (0.05mm EMS), followed by rinsing with deionized water and isopropyl alcohol. Reference and counter electrodes were rinsed with acetone. CVs were recorded at a scan rate of 200 mV/s scanning oxidatively.

### *Density Functional Theory (DFT) Geometry Optimizations*

Geometry optimization calculations and single point energy calculations were performed with ORCA<sup>6</sup> software suite using density functional theory (DFT). Geometries were fully optimized starting from coordinates generated from finalized cifs of the compound crystal structures when possible. The O3LYP functional was used for geometry optimizations, spin density plot calculations, and single point energy calculations. For the O3LYP calculations, def2-TZVPP was used on Co, N, S, O, and F, and def2-TZVP on C and H atoms. A CPCM solvation model for benzene was used throughout. Due to the challenge of simulating the dimeric OK complex, the calculation energies here do not include entropic contributions.

## NMR Spectroscopy

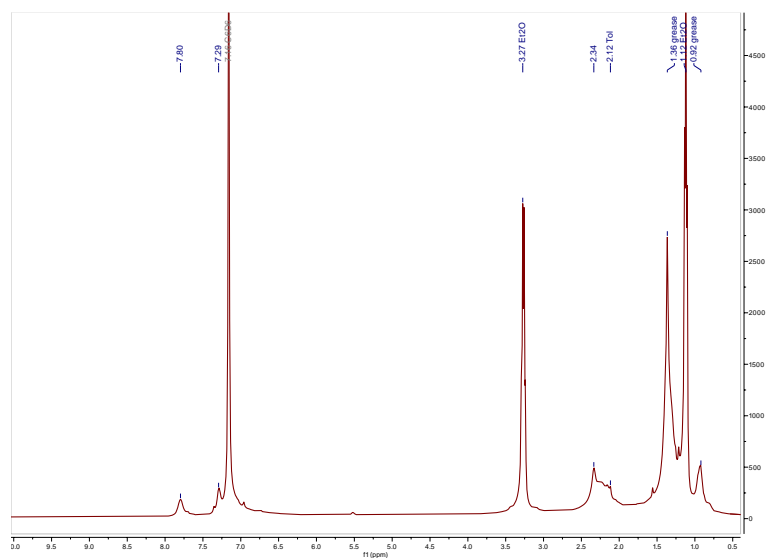


Figure S1. <sup>1</sup>H NMR of [tBu, Tol]DHP]CoOK (**1**) in C<sub>6</sub>D<sub>6</sub>.

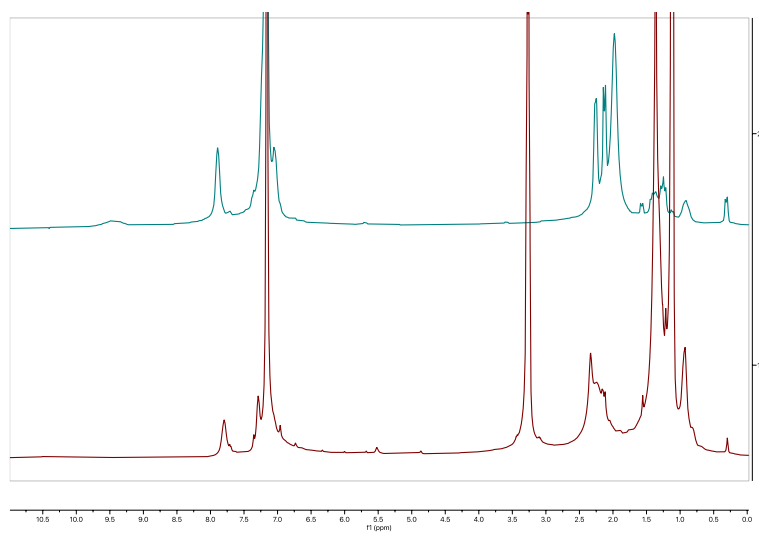


Figure S2. Comparison of <sup>1</sup>H NMR of [tBu, Tol]DHP]CoOH in C<sub>6</sub>D<sub>6</sub> (top) to <sup>1</sup>H NMR of [tBu, Tol]DHP]CoOK (**1**) in C<sub>6</sub>D<sub>6</sub> (bottom).

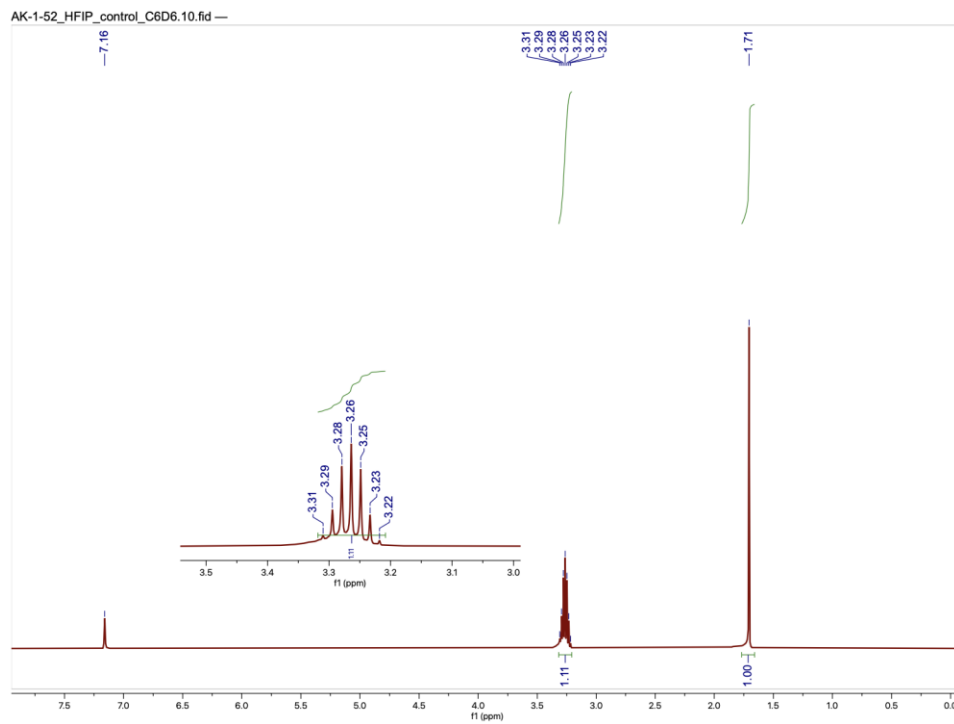


Figure S3.  $^1\text{H}$  NMR of  $(\text{CF}_3)_2\text{CHOH}$  (HFIP) in  $\text{C}_6\text{D}_6$ .

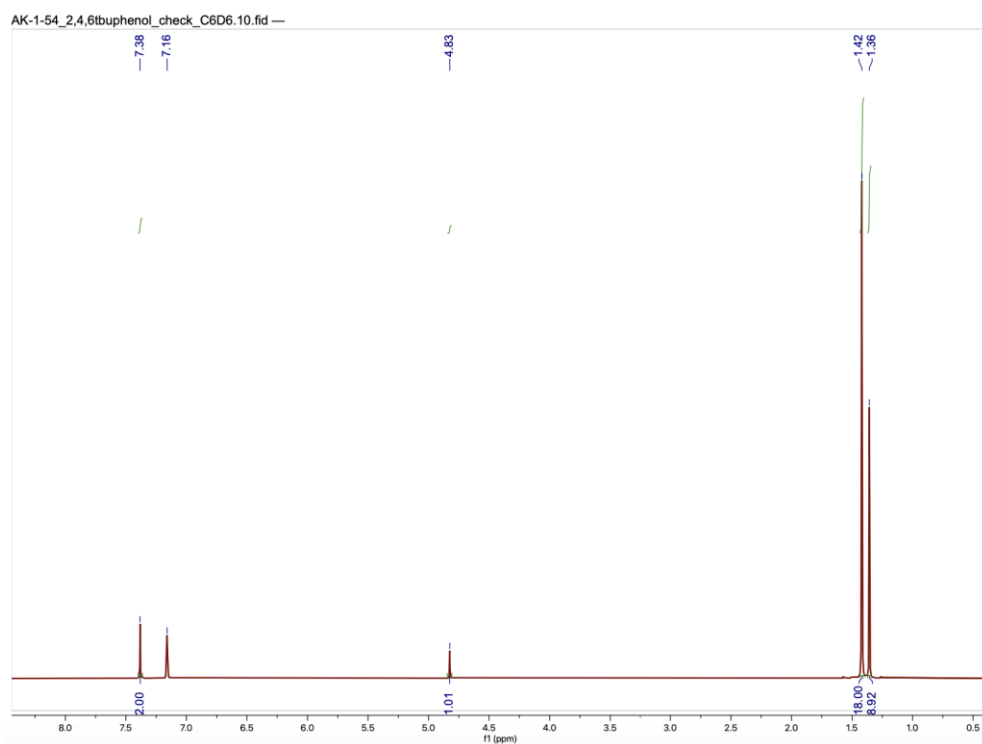


Figure S4.  $^1\text{H}$  NMR of 2,4,6-tri-tert-butylphenol (2,4,6-TTBP) in  $\text{C}_6\text{D}_6$ .

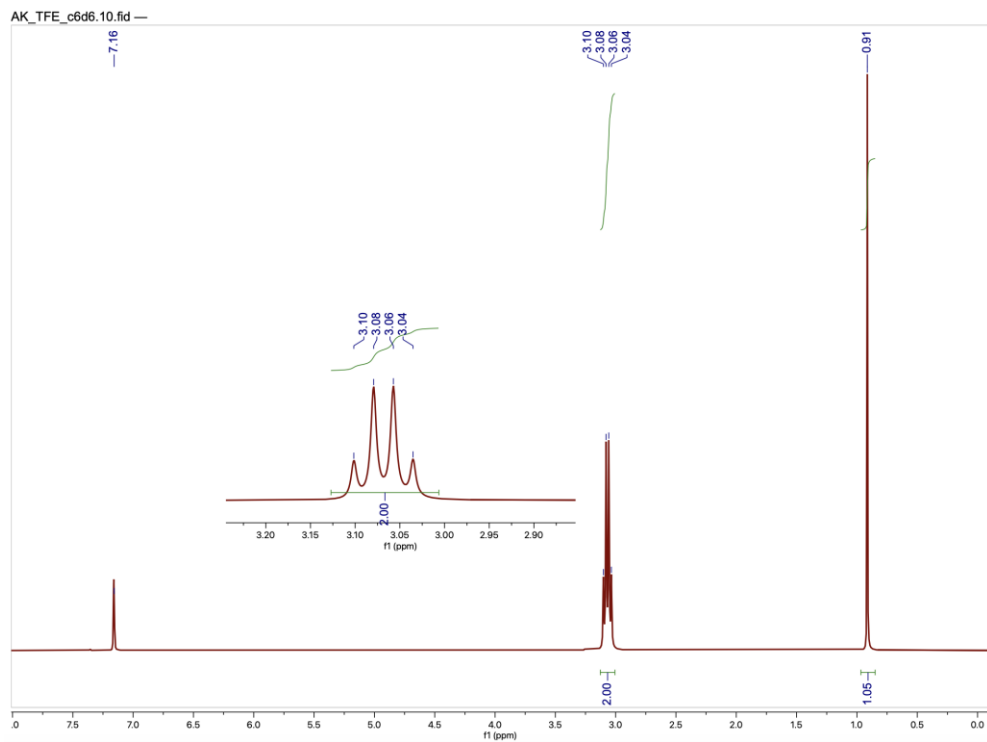


Figure S5.  $^1\text{H}$  NMR of 2,2,2-Trifluoroethanol (TFE) in  $\text{C}_6\text{D}_6$ .

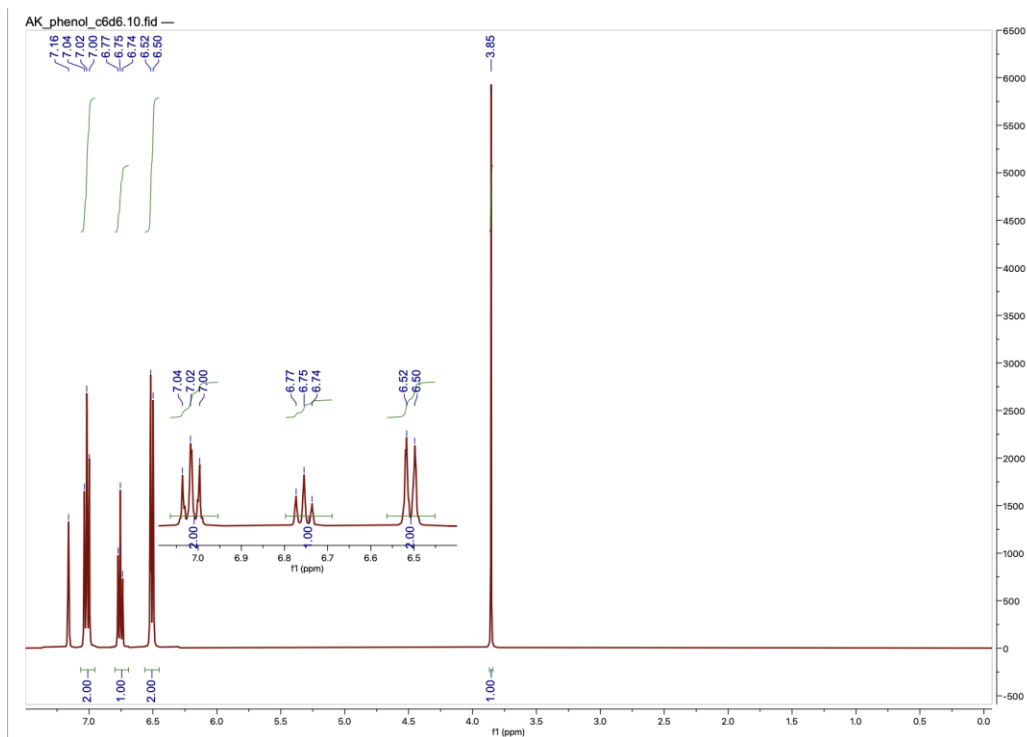


Figure S6.  $^1\text{H}$  NMR of Phenol in  $\text{C}_6\text{D}_6$ .

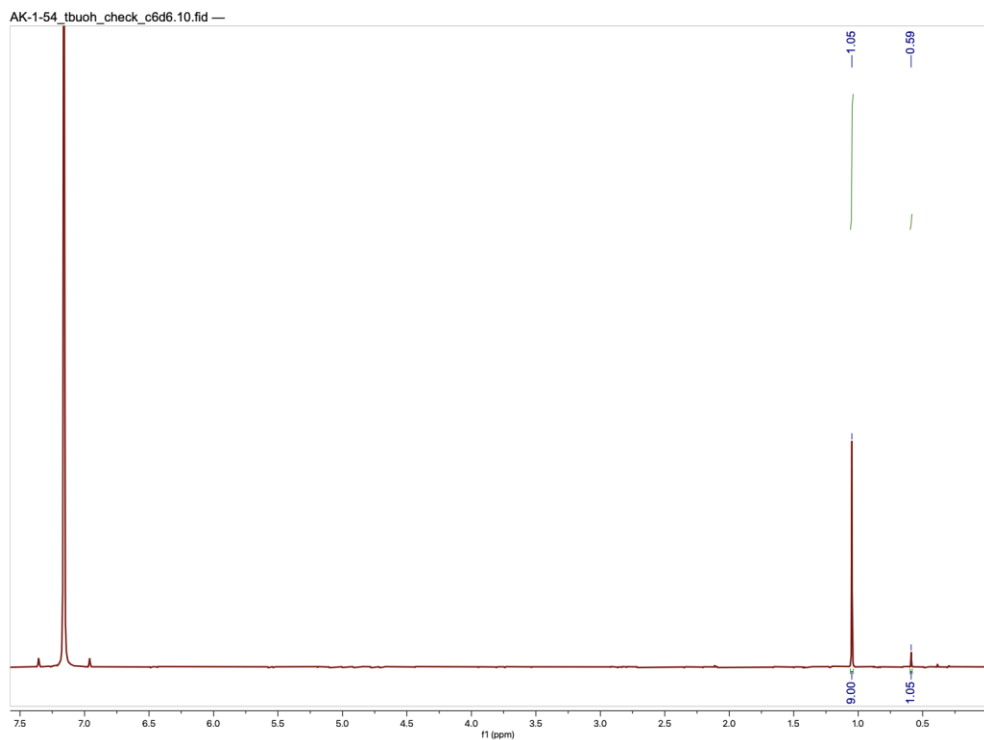


Figure S7.  $^1\text{H}$  NMR of tert-butanol in  $\text{C}_6\text{D}_6$

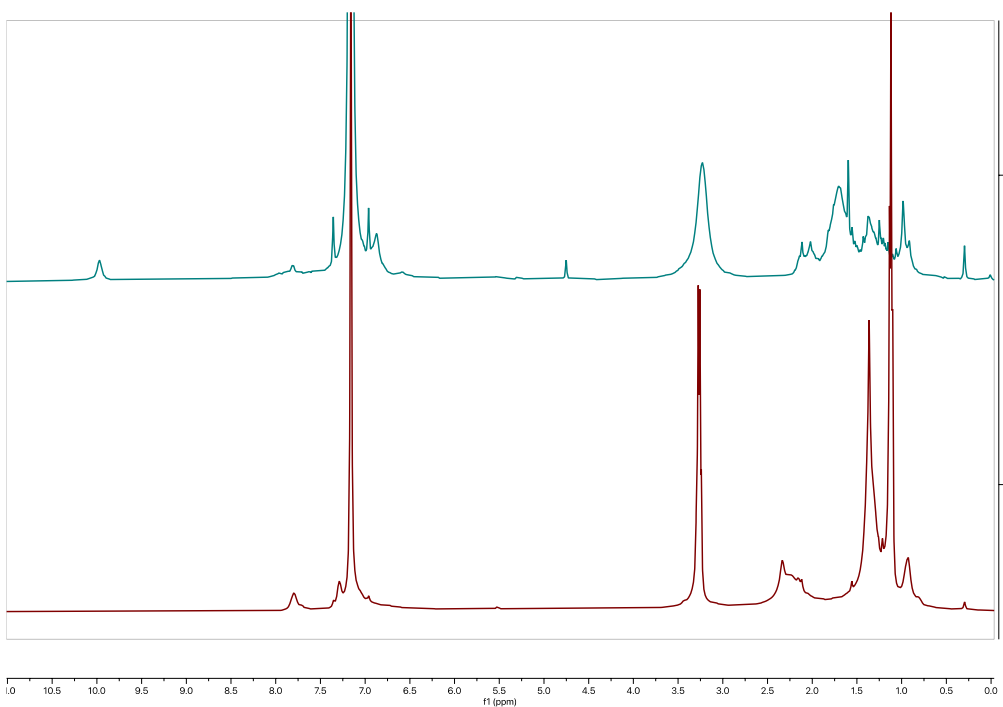


Figure S8. Comparison of  $^1\text{H}$  NMR of **1** + HFIP in  $\text{C}_6\text{D}_6$  (top) to **1** in  $\text{C}_6\text{D}_6$  (bottom)

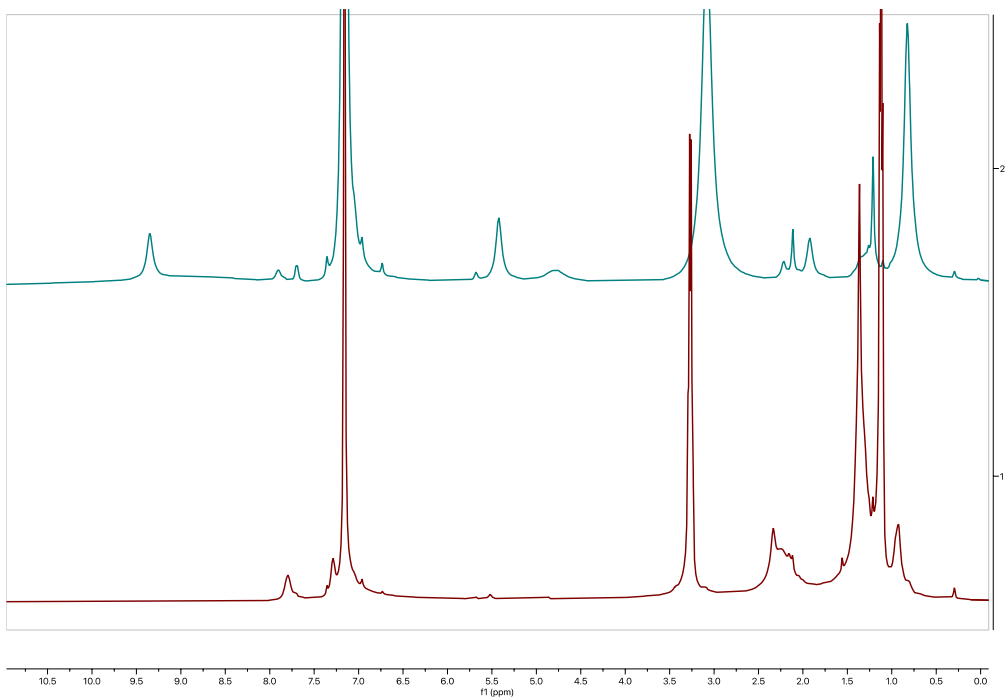


Figure S9. Comparison of  $^1\text{H}$  NMR of **1** + TFE in  $\text{C}_6\text{D}_6$  (top) to **1** in  $\text{C}_6\text{D}_6$  (bottom)

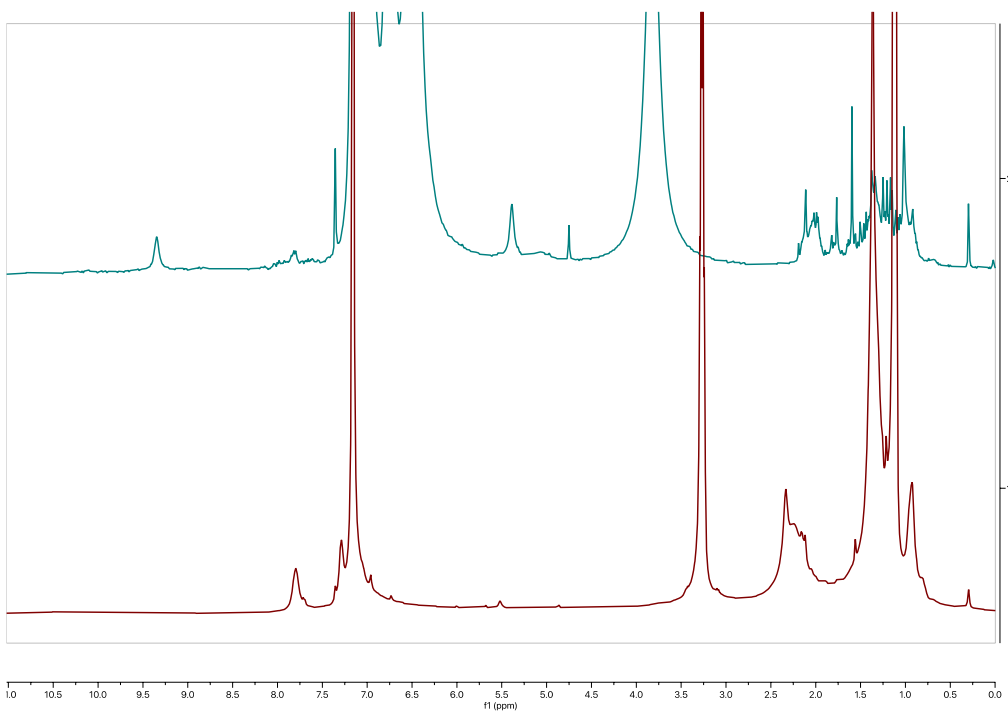


Figure S10. Comparison of  $^1\text{H}$  NMR of **1** + Phenol in  $\text{C}_6\text{D}_6$  (top) to **1** in  $\text{C}_6\text{D}_6$  (bottom)

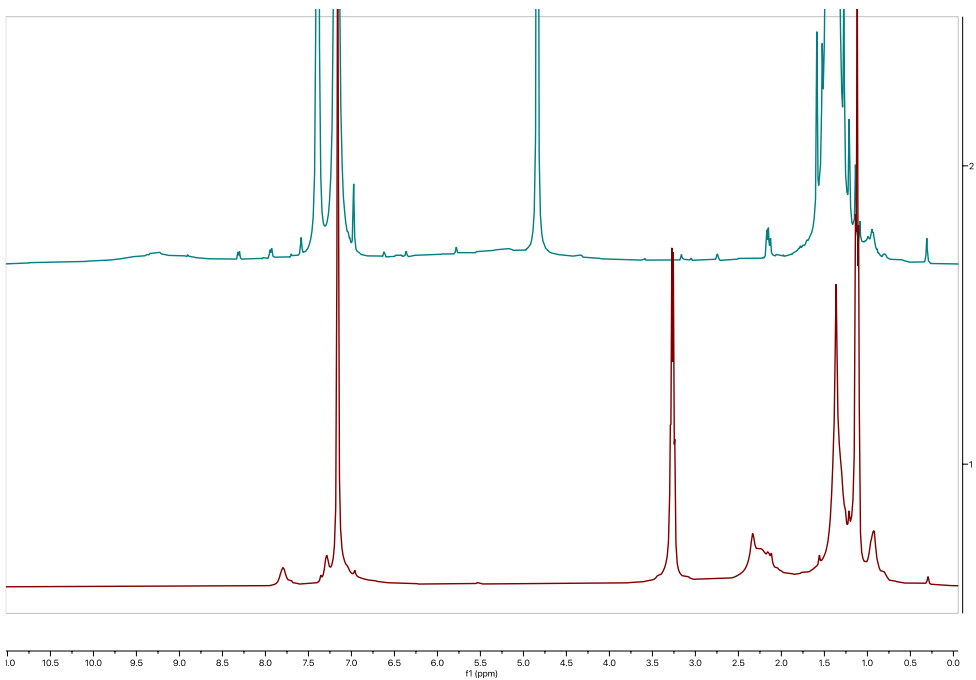


Figure S11. Comparison of  $^1\text{H}$  NMR of **1** + 2,4,6-TTBP in  $\text{C}_6\text{D}_6$  (top) to **1** in  $\text{C}_6\text{D}_6$  (bottom)

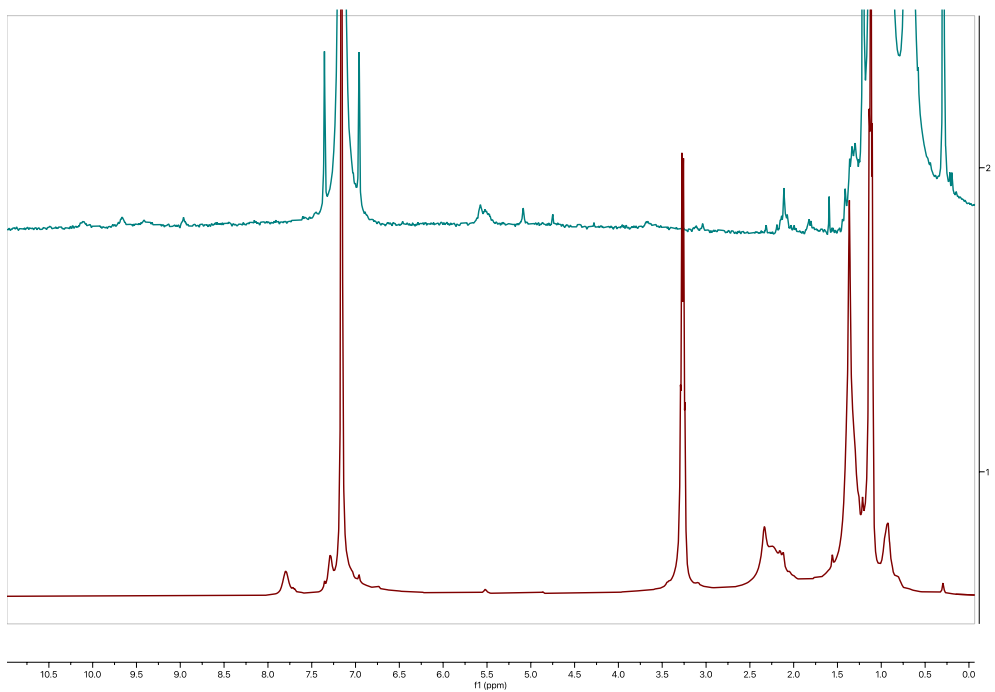


Figure S12. Comparison of  $^1\text{H}$  NMR of **1** + tert-Butanol in  $\text{C}_6\text{D}_6$  (top) to **1** in  $\text{C}_6\text{D}_6$  (bottom)

## UV-Vis Spectroscopy

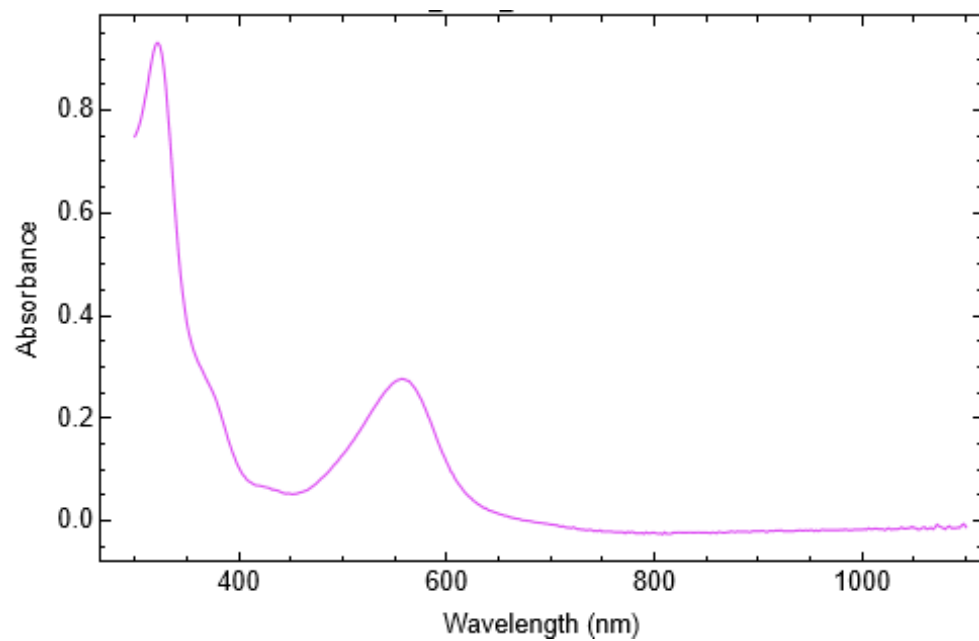


Figure S13. UV-vis of **1** from a 0.125 mM solution in toluene at room temperature.

## IR Spectroscopy

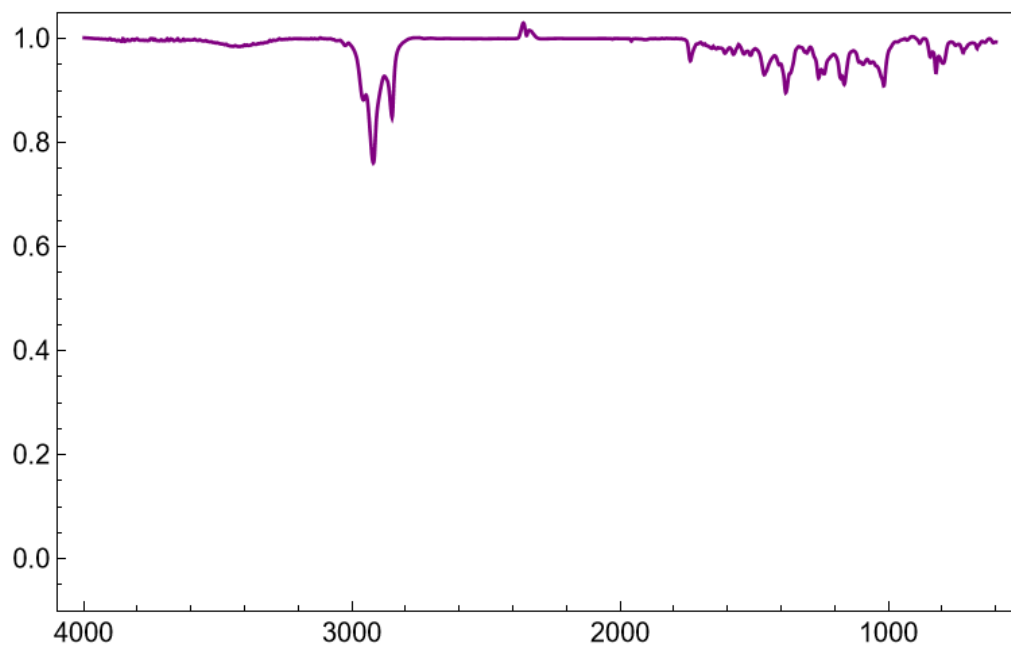


Figure S14. IR of **1** as a thin film.

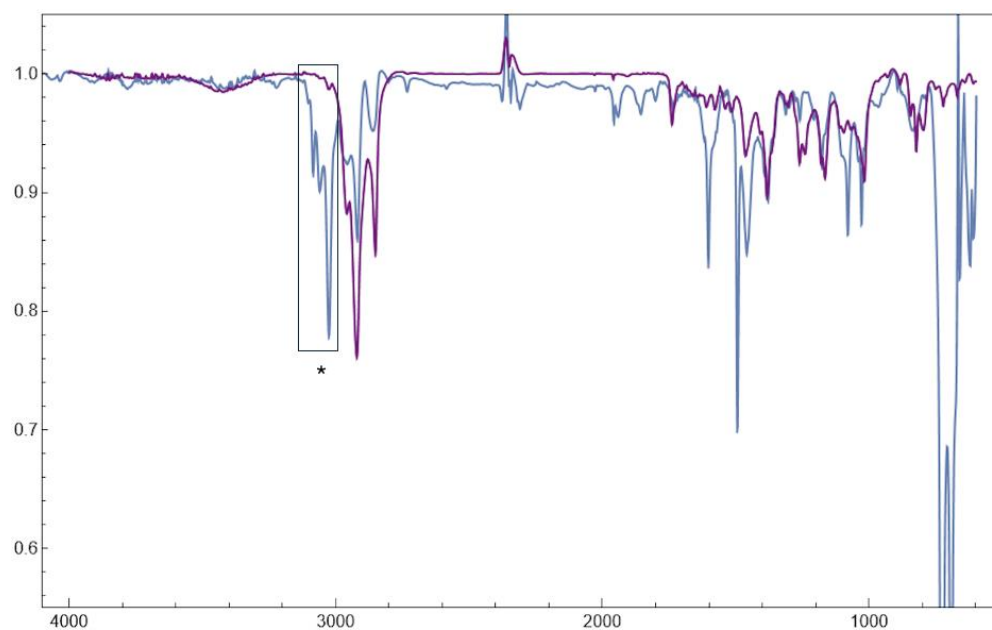


Figure S15. IR comparing IR of **1** (purple) as a thin film to IR of [*t*Bu, Tol]DHP]CoOH (blue) as a thin film.

The OH peak of [*t*Bu, Tol]DHP]CoOH is marked by an asterisk (\*) and is generally consistent with DFT calculated values.<sup>3</sup> However, we note a few overlapping stretches, presumably from C–Hs. The low frequency of this OH made arise from hydrogen bonding interactions between molecules.

## Cyclic Voltammetry

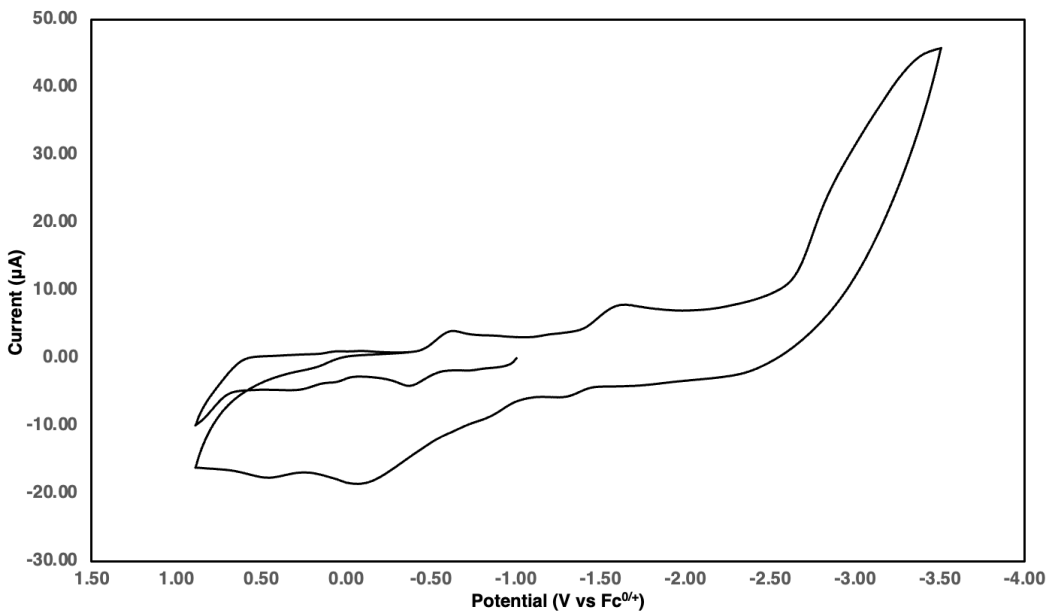


Figure S16. Cyclic Voltammogram of 2.4 mM of **1** in 0.1M KPF<sub>6</sub> electrolyte in a 1:4 MeCN:THF solution. Scan window: 1.5V to -3.5 V.

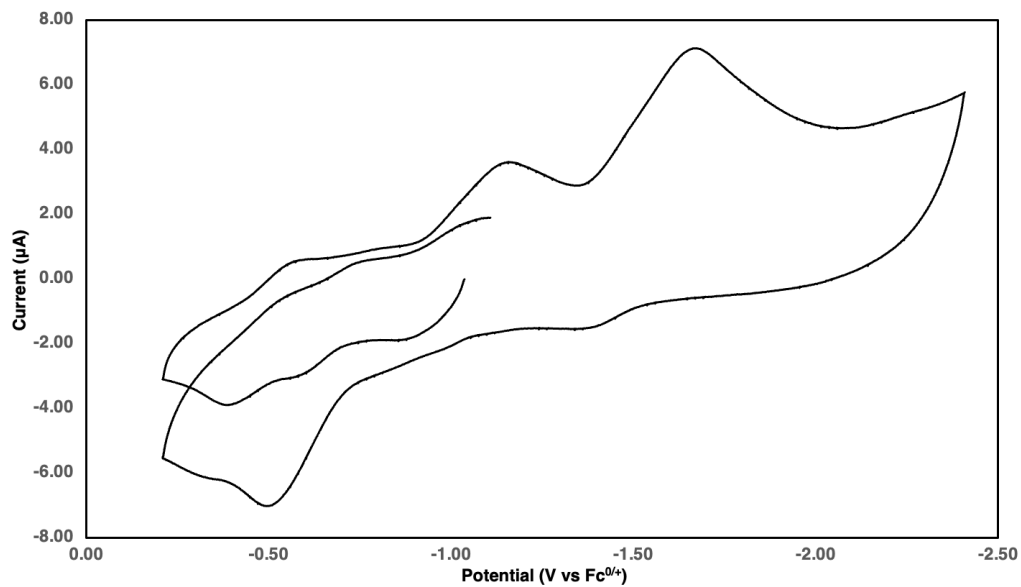


Figure S17. Cyclic Voltammogram of 2.4 mM of **1** in 0.1M KPF<sub>6</sub> electrolyte in a 1:4 MeCN:THF solution. Scan window: 0 V to -2.5 V

## Single Crystal X-ray Diffraction

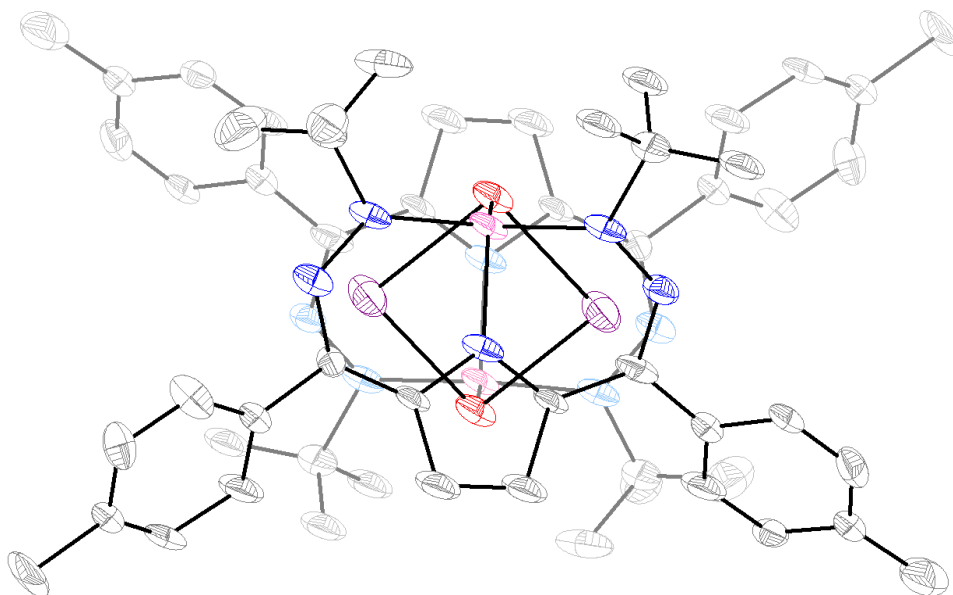


Figure S18. SXRD of **1**. Co (pink), N (blue), C (gray), O (red), K(violet). C-H H-atoms omitted.

Selected bond lengths (Å): Co-N1/N5: 1.94(1), 1.93(1); Co-N3: 1.94(1); N1-N2/N4-N5: 1.38(2), 1.32(2); Co-O: 1.96(1); N2-C5/N4-C10: 1.35(2), 1.33(2); C5-C6/C9-C10: 1.43(2), 1.41(2); C6-C7/C8-C9: 1.44(2), 1.42(2); C7-C8: 1.38(2). Selected bond angles (°): N1-M-N5: 149.4(6); N3-M-O: 107.4(5).

Table S1. SXRD of **1**.

Empirical formula	C <sub>28</sub> H <sub>34</sub> CoKN <sub>5</sub> O
Formula weight	554.63
Temperature/K	100(2)
Crystal system	triclinic
Space group	P-1
a/Å	10.153(7)
b/Å	11.686(8)

$c/\text{\AA}$	13.651(10)
$\alpha/^\circ$	89.533(19)
$\beta/^\circ$	73.197(17)
$\gamma/^\circ$	64.696(15)
Volume/ $\text{\AA}^3$	1389.1(17)
Z	2
$\rho_{\text{calc}}/\text{g/cm}^3$	1.326
$\mu/\text{mm}^{-1}$	0.797
F(000)	582.0
Crystal size/ $\text{mm}^3$	$0.242 \times 0.072 \times 0.052$
Radiation	MoK $\alpha$ ( $\lambda = 0.71073$ )
$2\Theta$ range for data collection/ $^\circ$	4.566 to 46.918
Index ranges	$-11 \leq h \leq 11, -12 \leq k \leq 13, -15 \leq l \leq 15$
Reflections collected	14083
Independent reflections	4025 [ $R_{\text{int}} = 0.2607, R_{\text{sigma}} = 0.2678$ ]
Data/restraints/parameters	4025/216/261
Goodness-of-fit on $F^2$	1.115
Final R indexes [ $I \geq 2\sigma(I)$ ]	$R_1 = 0.1435, wR_2 = 0.3264$
Final R indexes [all data]	$R_1 = 0.2880, wR_2 = 0.4058$
Largest diff. peak/hole / $e \text{\AA}^{-3}$	1.76/-0.99

Table S2. Selected bond lengths (Å) and angles (°) of **1** and related Co complexes

	<b>DHPCoOK</b>	<b>[DHP<sup>2-</sup>]Co<sup>II</sup>(MeCN)<sup>-</sup></b>	<b>[DHP<sup>1-</sup>]CoOTf</b>	<b>[DHP<sup>2-</sup>]Co<sup>III</sup>OH</b>
M—N1/M—	1.96(1)	1.936(3)	1.999(8)	1.897(3)
N5	1.92(1)	1.938(3)	2.000(8)	1.889(3)
M—N3	1.94(1)	1.938(3)	1.918(7)	1.861(3)
N1—N2/ N4—	1.38(2)	1.325(5)	1.273(10)	1.306(3)
N5	1.32(2)	1.320(5)	1.249(10)	1.302(3)
M—X(Cl/O/N)	1.96(1)	2.076(4)	2.166 2.128(6)	1.825(2)
N2—C5/ N4—	1.35(2)	1.344(6)	1.368(11)	1.350(4)
C10	1.33(2)	1.339(6)	1.383(11)	1.342(4)
C5—C6/ C9—	1.44(2)	1.402(6)	1.387(13)	1.390(4)
C10	1.42(2)	1.399(6)	1.392(13)	1.383(4)
C6—C7/ C8—	1.44(2)	1.441(6)	1.428(13)	1.439(4)
C9	1.41(2)	1.417(6)	1.445(13)	1.438(4)
C7—C8	1.39(2)	1.351(6)	1.315(13)	1.349 (4)
N1—M—N5	149.1(5)	160.51(12)	178.1(3)	162.4(1)
N3—M—X	107.4(5)	114.32(13)	113.152 105.240	143.5(1)

L = PMe<sub>3</sub> as described in the text.

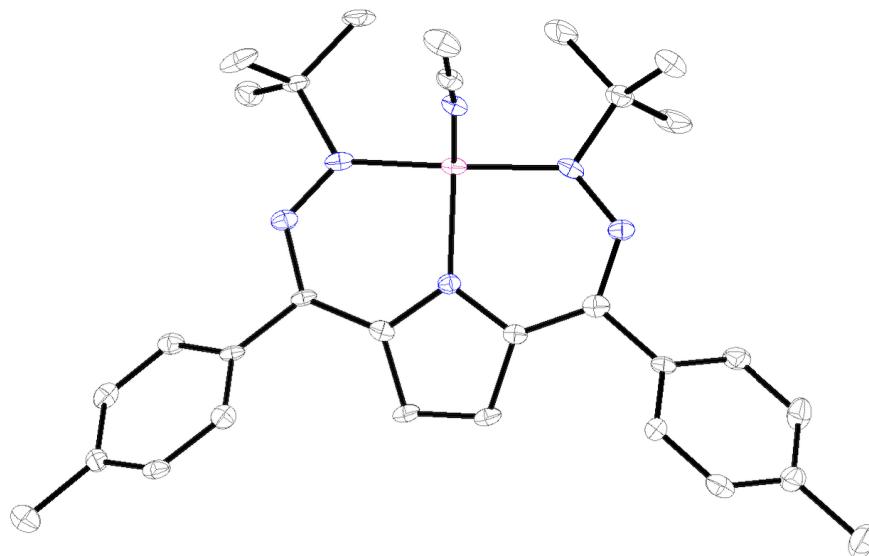


Figure S19. SXR of [ $t\text{Bu,Tol}$ DHP]Co(MeCN) . Co (pink), N (blue), C (gray), C–H H-atoms omitted for clarity.

Table S3. SXR of [ $t\text{Bu,Tol}$ DHP]Co(MeCN)

Empirical formula	$\text{C}_{30}\text{H}_{37}\text{CoN}_6$
Formula weight	540.58
Temperature/K	100(2)
Crystal system	orthorhombic
Space group	$P2_12_12_1$
a/Å	8.9652(6)
b/Å	11.2879(7)
c/Å	27.8086(17)
$\alpha/^\circ$	90
$\beta/^\circ$	90

$\gamma/^\circ$	90
Volume/ $\text{\AA}^3$	2814.2(3)
Z	4
$\rho_{\text{calc}}/\text{g/cm}^3$	1.276
$\mu/\text{mm}^{-1}$	0.639
F(000)	1144.0
Crystal size/ $\text{mm}^3$	$0.297 \times 0.122 \times 0.059$
Radiation	MoK $\alpha$ ( $\lambda = 0.71073$ )
$2\Theta$ range for data collection/ $^\circ$	4.648 to 50.264
Index ranges	$-10 \leq h \leq 10, -13 \leq k \leq 13, -33 \leq l \leq 33$
Reflections collected	54762
Independent reflections	5025 [ $R_{\text{int}} = 0.1142, R_{\text{sigma}} = 0.0647$ ]
Data/restraints/parameters	5025/0/337
Goodness-of-fit on $F^2$	1.061
Final R indexes [ $I \geq 2\sigma(I)$ ]	$R_1 = 0.0459, wR_2 = 0.0727$
Final R indexes [all data]	$R_1 = 0.0709, wR_2 = 0.0791$
Largest diff. peak/hole / $e \text{\AA}^{-3}$	0.38/-0.36

## EPR Spectroscopy

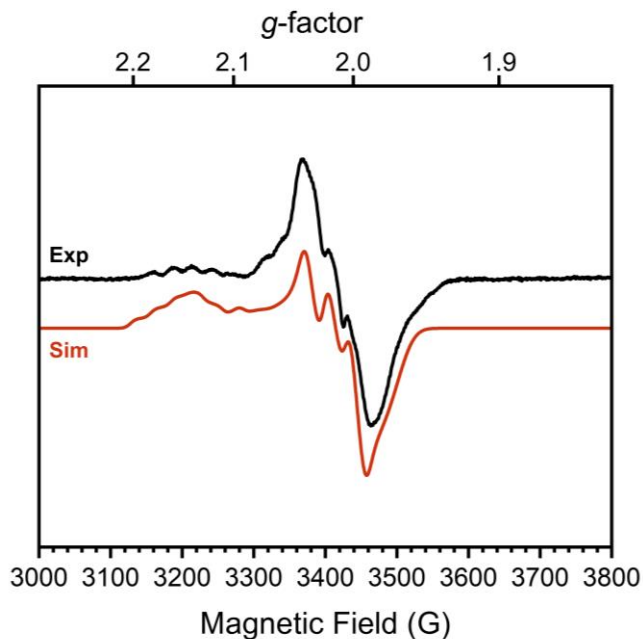


Figure S20. X-band EPR spectrum (black) and simulated spectrum (red) of a 15 mM solution of **1** (dimer) in toluene at 25 K. Conditions: MW frequency, 9.63 GHz; MW power, 2.0 mW.

Table S4. Simulated *g*-values for EPR of **1**

	<i>g</i> (x,y,z)	Co-A	N-A	H-strain
<sup><i>t</i></sup> BuDHPCoOK	(2.14553 2.015 1.98313)	(37.85 7.0606 22.664)	(85.3902 87.9404 22.6612)	(41.7975 32.2248 100)

Code to generate simulations of EPR Spectra for **1**.

```
Exp1.mwFreq=9.63;
Sys1.lw = 1
Exp1.Range = [300 380]
Exp1.nPoints = 2048
Sys1.g = [2.14553 2.015 1.98313]
Sys1.Nucs = 'Co,N';
```

```

Sys1.A = [37.85 7.0606 22.664;85.3902 87.9404 22.6612];
Sys1.HStrain = [41.7975 32.2248 100];
Vary1.g = [0.02 0.02 0.02];
Vary1.HStrain = [20 1.5 50];
Vary1.A = [10 10 10; 10 10 10];
plot(Bk,(((Ik)/max(Ik))0.225)*2,Bk,pepper(Sys1,Exp1)/(max(pepper(Sys1,Exp1))))

```

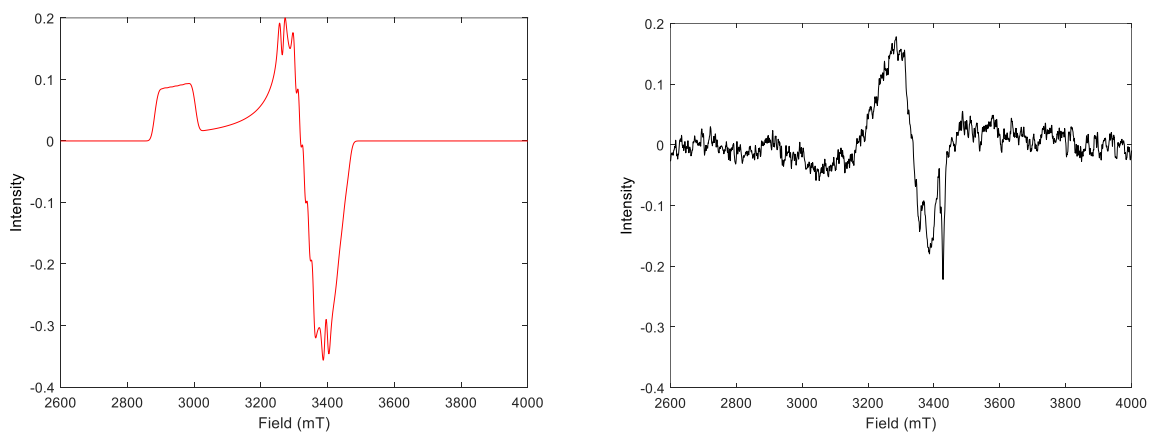


Figure S21. Small Window perpendicular-mode EPR spectrum (right) and simulated spectrum (left) of a 15 mM solution of [<sup>t</sup>Bu, Tol]DHP]CoOH in toluene at 25 K. Conditions: MW frequency, 9.63 GHz; MW power, 2.0 mW.

Code to generate simulations of EPR Spectra for [<sup>t</sup>Bu, Tol]DHP]CoOH.

```

Exp3.mwFreq=9.63913;
Sys3.lw = 1
Exp3.Range = [260 400]
Exp3.nPoints = 2048;
Sys3.g = [2.34 2.068 2.03];
Sys3.Nucs = 'Co, N';

```

```
Sys3.A = [50 40 40; 20 60 50];  
Sys3.HStrain = [50 10 50];  
Vary3.g = [0.02 0.02 0.02];  
Vary3.HStrain = [50 10 50];  
Vary3.A = [10 10 10; 10 10 10];  
plot(BOH,(IOH)/max(IOH)-(-  
0.000086*BOH+1.1044),BOH,0.2*pepper(Sys3,Exp3)/max(pepper(Sys3,Exp3)))
```

### Density Functional Theory (DFT) Calculations

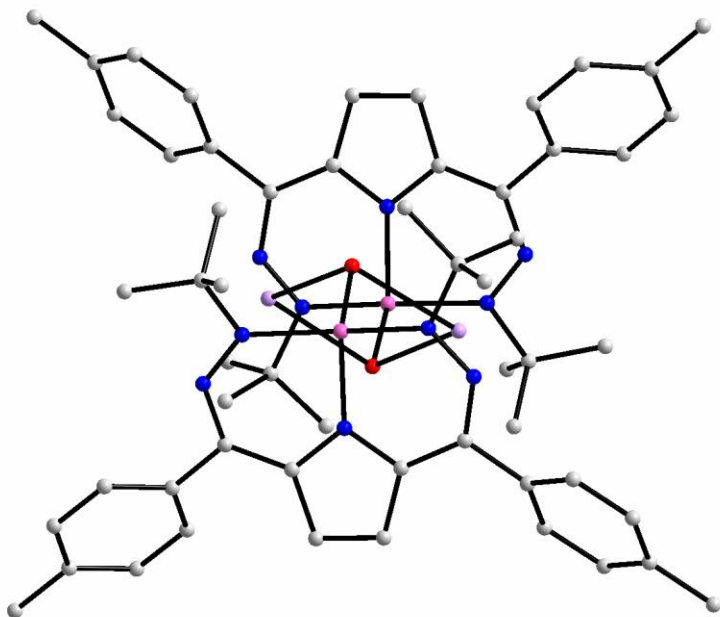


Figure S22. Calculated structure of **1**. All C–H hydrogen atoms have been removed for clarity

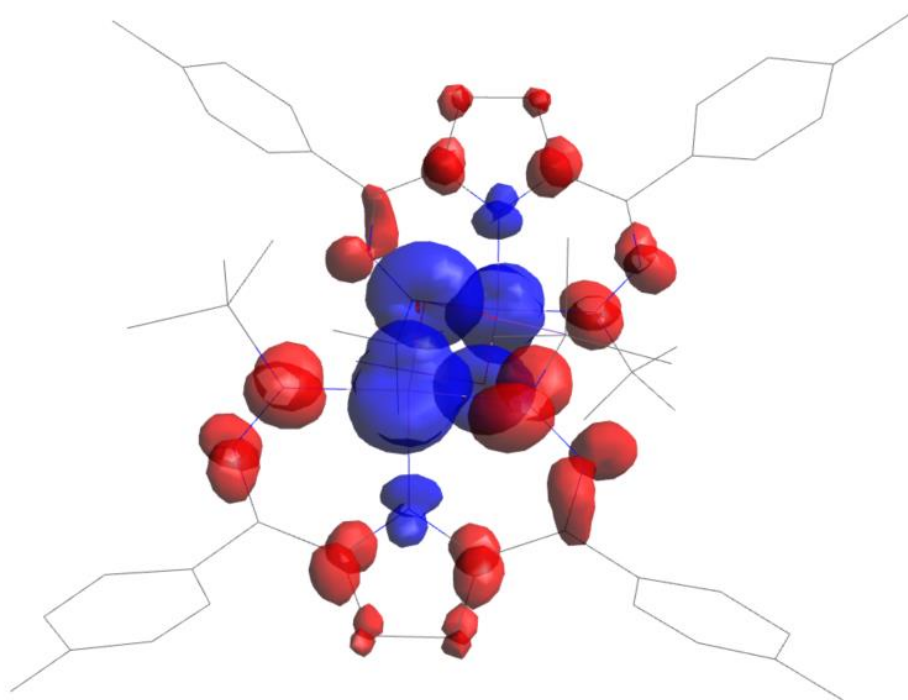


Figure S23. Spin density plot of **1** at an iso value of 0.005.

Table S5. Single Point Energy Calculations of **1** with the addition of different Acids

Dimer		LCoOK+ tbuOH	LCoOK+ CyOH	LCoOK+ IPA	LCoOK+ acetamide	LCoOK+ TFE	LCoOK+ Phenol	LCoOK+ 2,4,6- TTBP	LCoOK+ PhenSL	LCoOK+ phthalamide	LCoOK+ HFIP	LCoOK+ BzCOOH	LCoOK dimer
<i>Kcal/mol</i>	From LCoOH	-18.01	-17.82	-17.19	-7.13	-6.05	-2.98	-2.63	-1.62	-0.80	1.77	12.48	-14.75
	+												
Monomer	K[acid]	LCoOK+ tbuOH	LCoOK+ CyOH	LCoOK+ IPA	LCoOK+ acetamide	LCoOK+ TFE	LCoOK+ Phenol	LCoOK+ 2,4,6- TTBP	LCoOK+ PhenSL	LCoOK+ phthalamide	LCoOK+ HFIP	LCoOK+ BzCOOH	All single point calculations
<i>Kcal/mol</i>		-3.26	-3.07	-2.44	7.63	8.71	11.77	12.12	13.14	13.96	16.52	27.23	(no entropy)

### **pK<sub>a</sub> Values of Weak Acids**

Table S6. pK<sub>a</sub> values for acids used in pK<sub>a</sub> Bracket Study

pK <sub>a</sub>	tbuOH	2,4,6-TTBP	TFE	Phenol	HFIP
Water	16.84 <sup>7</sup>	12.19 <sup>8</sup>	12.4 <sup>9</sup>	10.0 <sup>10</sup>	9.3 <sup>11</sup>
DMSO	29.4 <sup>13</sup>	--	23.6 <sup>9</sup>	18.0 <sup>9</sup>	18.2 <sup>15</sup>
MeCN	--	--	35.8 (calc.) <sup>14</sup>	29.2 <sup>12</sup>	--

## References

1. S. Stoll and A. Schweiger, *J. Magn. Reson.*, 2006, **178**, 42–55.
2. D.F. Evans, *J. Chem. Soc.*, 1959, **0**, 2003-2005.
3. S.W. Anferov and J.S. Anderson, *J. Coord. Chem.*, 2022, **75**, 1853-1864.
4. S.W. Anferov, A.S. Filatov and J.S. Anderson, *ACS Catal.*, 2022, **12**, 9933-9943.
5. S.W. Anferov, J. Boyn, D.A. Mazziotti, J.S. Anderson, *J. Am. Chem. Soc.*, 2024, **146**, 5855-5863.
6. (a) F. Neese, *Wiley Interdis. Rev.: Comp. Mol. Sci.*, 2012, **2**, 73-78. (b) H - Kr: A. Schaefer, H. Horn and R. Ahlrichs, *J. Chem. Phys.*, 1992, **97**, 2571. (c) Rb - Xe: A.Schaefer, C. Huber and R. Ahlrichs, *J. Chem. Phys.*, 1994, **100**, 5829. (d) F. Weigend and R. Ahlrichs, *Phys. Chem. Chem. Phys.* 2005, **7**, 3297
7. A.S. Tracey, B. Galeffi and S. Mahjour, *Can. J. Chem.*, 1988, **66**, 2294 – 2298.
8. E. P. Serjeant and B. Dempsey, *Ionization Constants of Organic Acids in Solution*, IUPAC Chemical Data Series No. 23, 1979.
9. F.G. Bordwell, *Acc. Chem. Res.*, 1988, **21**, 456-463
10. M. Walton-Raaby, T. Floen, G. García-Díez, and N. Mora-Díez, *Antioxidants*, 2023, **12**, 1420.
11. B.L. Dyatkin, E.P. Mochalina, and I.L. Knunyants, *Tetrahedron*, 1965, **21**, 2991-2995.
12. A. Kütt, S. Tshepelevitsh, J. Saame, M. Lõkov, I. Kaljurand, S. Selberg, and I. Leito, *Eur. J. Org. Chem.*, 2021, **2021**, 1305–1473
13. W.N. Olmstead, Z. Margolin and F.G. Bordwell, *J. Org. Chem.*, 1980, **45**, 3295-3299.
14. Y.C. Lam, R.J. Nielsen, H.B. Gray and W.A. Goddard, *ACS Catal.*, 2015, **5**, 2521-2528.
15. D. Seebach, A.K. Beck, H. Bichsel, A. Pichota, C. Sparr, R. Wünsch and W.B. Schweizer, *Helv. Chim. Acta*, 2012, **95**, 1303-1322.

## **Appendix VI: Unpublished Work: Variable Temperature, Ligand-Promoted Metal-Ligand Spin Tautomerism**

*Where's the Electron, Miffy?*

Written for thesis, in the hopes to one day be written for more.

### **Introduction**

Changing shape, form, or size based on temperature is a commonly observed natural phenomenon, and it similarly not uncommon to observe temperature-gated color changes. These thermochromic behaviors have diverse applications—such as temperature sensing, anti-counterfeiting,<sup>1</sup> smart windows and materials,<sup>2,3</sup> and color-changing paints<sup>4</sup> or consumer products.<sup>5</sup> Transition metal complexes have potential in this area due to their distinct color changes, complex electronic structures and generally, lower color-changing temperatures.<sup>6</sup>

The mechanisms of these thermochromic systems often rely on ligand coordination, spin crossover and geometric changes.<sup>7</sup> However applicable these may be, they still remain over a limited range, as they rely on phenomena that often complete within only a relatively small temperature range, with spin crossover being one of the best strategies to obtain wider windows.<sup>8</sup> In particular, Fe-spin based crossover complexes showcase one-step “incomplete” spin crossover ranging from 80 K to 300 K.<sup>6</sup>

Here I present a ligand-gated, thermochromic cobalt complex which demonstrates one-step incomplete spin crossover from a low ( $S = 1/2$ ) spin state at low temperatures to a high ( $S = 3/2$ ) spin state at high temperatures. This behavior is observed over all temperatures we have observed—from 16 K to 358 K—and possibly beyond. Given that this range encompasses a large

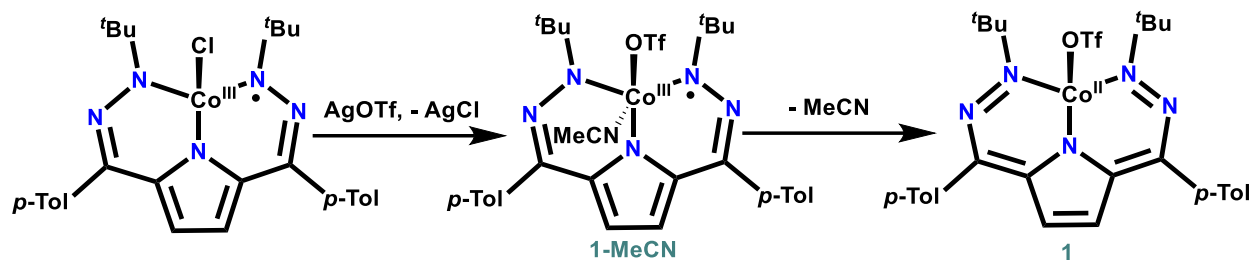


**Figure 1.** Synthesis of Complexes Discussed in this Section

amount of the reactivity and chemical endeavors that take place, this makes this compound an ideal candidate for temperature sensing.

### Synthesis and Characterization of ${}^{t\text{Bu,Tol}}\text{DHPCoOTf-MeCN}$

As previously reported,  $({}^{t\text{Bu,Tol}}\text{DHP})\text{CoCl}$  reacts with  $\text{AgOTf}$  in a mixture of benzene/acetonitrile (>2:1) to produce the maroon solid  $({}^{t\text{Bu,Tol}}\text{DHP})\text{CoOTf}$  (**1**) (**Figure 1**).<sup>9</sup> This complex is similarly paramagnetic, but not silent, and by  ${}^1\text{H}$  NMR spectroscopy appears to have a symmetric DHP environment. This complex can be crystallized suitably for SXR analysis as a very dark crystal that is five-coordinate (due to being a polymeric chain in the solid state) (Table 1). For **1**, the bond lengths within the ligand shorten distinctively, causing this complex to better resemble the oxidized ligand and the nickel-oxidized-ligand triflate complex<sup>10</sup> (Table 1).

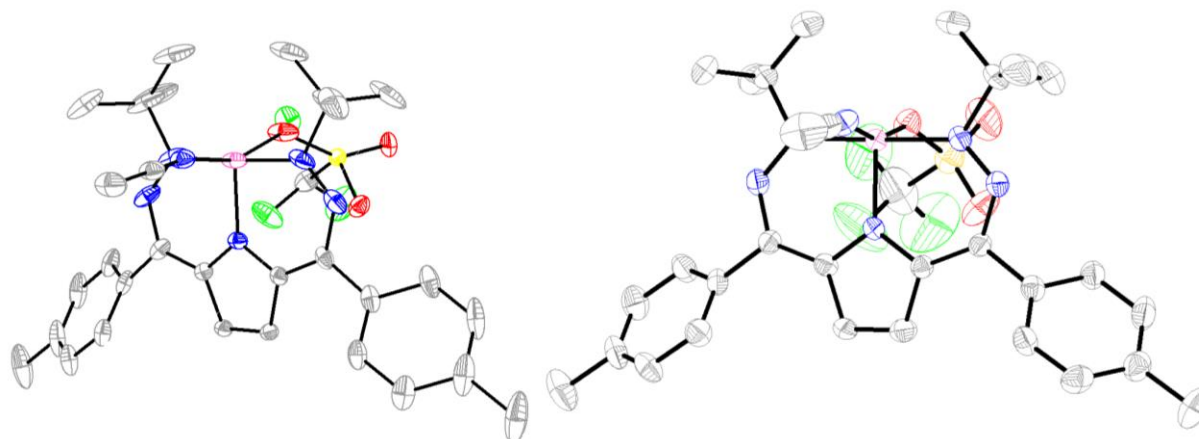


**Figure 2.** Complex **1-MeCN** at 100 K and Complex **1-MeCN** at 298 K

However, in the presence of acetonitrile, high quality dark green crystals of (*t*-Bu,*Tol*)DHP)CoOTf(MeCN) (**1-MeCN**) can also be obtained. (Figure 3, Table 1) Bound to an acetonitrile ligand, the bond lengths of this compound remain distinctly similar to the chloride complex. We have previously noted this phenomena—as shown in previous work with this complex, where water binding to form a 5-coordinate species triggered a similar spin rearrangement (both to a high spin and Co<sup>III</sup> complex).<sup>11</sup>

These rearrangements appear to not only be triggered by ligand-coordination, but also temperature sensitive. EPR shows that at low temperatures (15 K), we still observe two  $S = \frac{1}{2}$  signals—albeit with different hyperfine splittings and g-values (Figure 3). Looking at the XAS data taken in solution at 113 K or at 8 K, the K-edge shifts are still consistent with a more oxidized **1-MeCN** and a less oxidized **1**—but not by much, making the Co(II)/Co(III) designation challenging!<sup>9</sup> These complexes are then likely best described as **1**: a low spin, five-coordinate (in the solid state—four-coordinate in solution) Co(II) with a fully oxidized ligand and **1-MeCN**: a

**Table 1.** Selected bond lengths of **1**, **1-MeCN**, and related complexes (Å)

	( <i>t</i> -Bu, <i>Tol</i> )DHP)CoCl <sup>9</sup>	<b>1-MeCN</b>	<b>1-MeCN (RT)</b>	<b>1</b> * <sup>9</sup>	( <i>t</i> -Bu, <i>Tol</i> )DHP)Co(MeCN) <sup>12</sup>	( <i>t</i> -Bu, <i>Tol</i> )DHP)Co <sup>13</sup>	( <i>t</i> -Bu, <i>Tol</i> )DHP)CoOH <sup>13</sup>
<b>M-N1/</b>	1.887(6)	1.882 (2)	1.885 (4)	1.999(8)	1.938(3)	1.796(2)	1.897(3)
<b>M-N5</b>	1.893(7)	1.882 (2)	1.894 (4)	2.000(8)	1.936(3)	1.847(2)	1.889(3)
<b>M-N3</b>	1.869(6)	1.915 (2)	1.909 (4)	1.918(7)	1.938(3)	1.821(2)	1.861(3)
<b>N1-N2/</b>	1.302(9)	1.288 (3)	1.290 (5)	1.273(10)	1.325(5)	1.323 (2)	1.306(3)
<b>N4-N5</b>	1.291(9)	1.288 (3)	1.289 (5)	1.249(10)	1.320(5)	1.318(2)	1.302(3)
<b>N2-C5/</b>	1.34(1)	1.355 (3)	1.358 (6)	1.368(11)	1.344(6)	1.343(3)	1.350(4)
<b>N4-C10</b>	1.34(1)	1.355 (3)	1.347 (6)	1.383(11)	1.339(6)	1.336(3)	1.342(4)
<b>C5-C6/</b>	1.39(1)	1.388 (3)	1.386 (6)	1.387(13)	1.402(6)	1.403 (3)	1.390(4)
<b>C9-C10</b>	1.39(1)	1.388 (3)	1.386 (6)	1.392(13)	1.399(6)	1.402(3)	1.383(4)
<b>C7-C8</b>	1.352(1)	1.340 (3)	1.331(7)	1.315(13)	1.351(6)	1.353(3)	1.349(4)

\*Crystallizes as polymeric chain, monomer shown

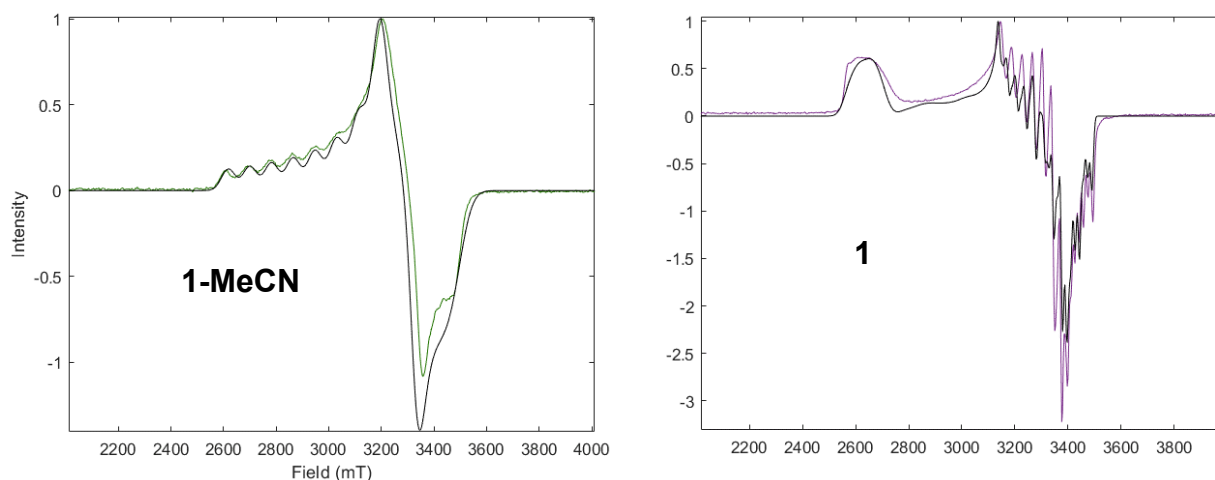


**Figure 3.** Complex **1-MeCN** (left) at 15.9 K and Complex **1** (right) at 15.9 K. **1-MeCN**:  $g = 2.0585, 2.0788, 2.1315$ ; Co-A = +15.9328, +9.9042, 57.2366 MHz, N-A = +58.4688, +19.2988, +30.0000 MHz. **1**:  $g = 2.0598, 2.0766, 2.1739$ ; Co-A = +10.8252, +22.5562, +5.6313 MHz; N-A = +31.5100, -8.0770, +30.9039 MHz. microwave frequency 9.6304 GHz, microwave power 0.2 mW.

high spin at room temperature, five-coordinate Co(III) coupled to a ligand-based-radical. **1-MeCN** appears to then undergo a high spin-low spin crossover between room temperature and 15 K, with the metal center remaining Co(III) throughout (with that rearrangement solely gated by ligand binding). Room temperature SXRD on **1-MeCN** (and (<sup>*t*</sup>Bu,<sup>*o*</sup>Tol)DHP)CoCl(MeCN) for good measure) was also collected, and though subtle shifts could be observed, this is consistent with the oxidation state rearrangements being unchanged (at least between 298 K and 100 K) (Figure ,2 Table 1).

For the spin state flip, we collected a number of pieces of data to corroborate this observation. First, integrated variable temperature EPR between 16-22 K showed the expected variation in signal for **1-MeCN** (decreased magnitude with increased temperature). We also observed via variable temperature Evans method that the high spin/low spin transition temperature was very broad, with the  $\mu_{\text{eff}}$  continuing to increase with raised temperature and decrease with

decreasing temperature. This is consistent even with the EPR, which shows even very cold, there is an effect on spin-state for this complex. SQUID measurements suggested the same thing, but were challenging to set-up reliably due to the sensitivity of **1-MeCN** to vacuum.

Visibly, distinct differences could also be observed corroboratively by UV-Vis, as the distinctive color change from purple to teal could be observed. While we were unable to go colder than  $-100^{\circ}\text{C}$ , the UV-Vis color transition had not ceased, again suggesting a very broad transition

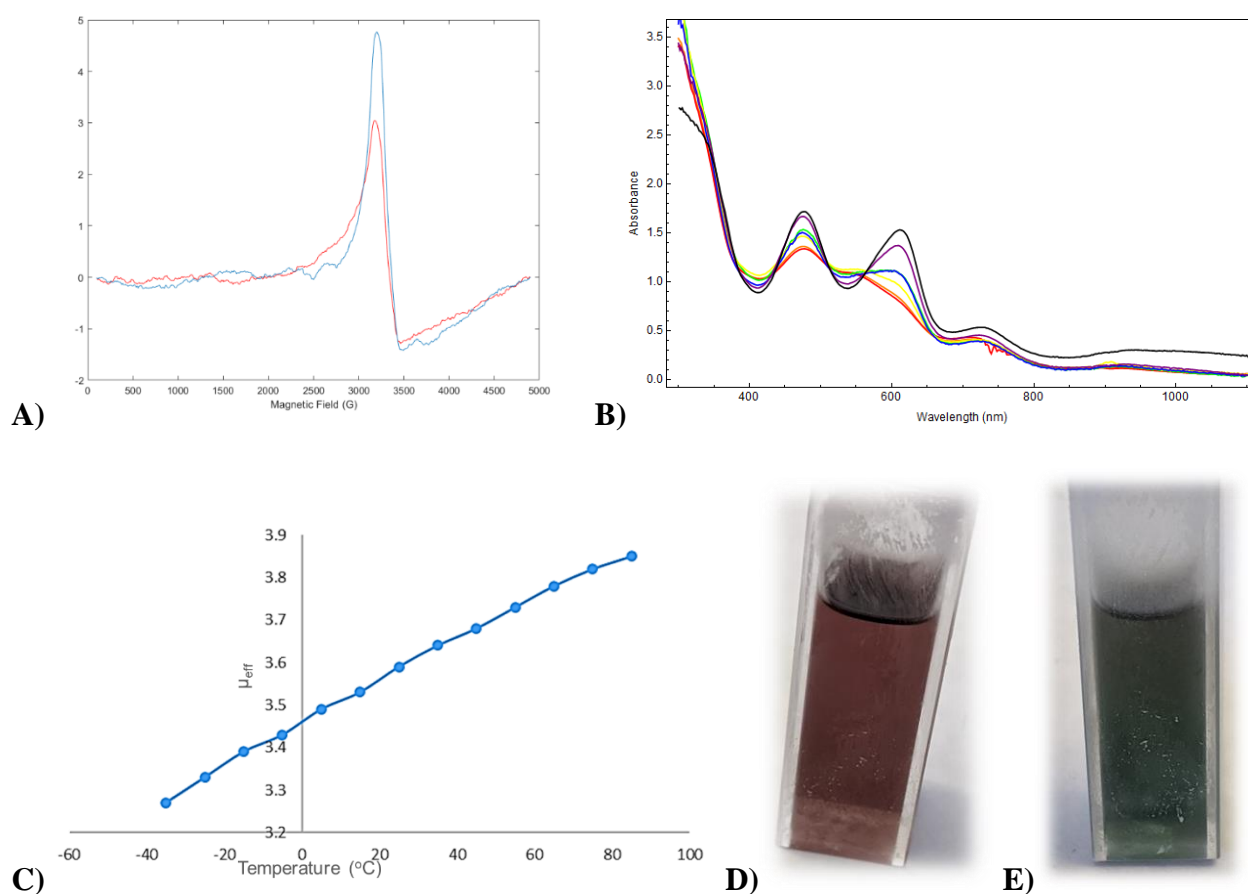


**Figure 4.** **A)** Integrated Variable Temperature EPR Spectra (16 K-22 K); **B)** 297 K to 173 K (black to red), individual scans at each temperature in 1 MeCN: 10 2-methyl THF, scan speed 1200 nm/min. **C)** Variable Temperature Evans Method in 1  $\text{CD}_3\text{CN}$ : 10  $\text{d}_8$ -toluene—358 K to 238 K. **D)** and **E)** Complex 1-MeCN at 297 K and 173 K respectively, from **B)**

temperature. We attribute this to the small energy gap between these two spin states, with the high spin state being thermally populated easily, even at relatively cool temperatures. However, it remarkably cold temperatures to fully freeze out the high spin state as evidenced by the changes occurring in the EPR even at 16-22K. We would like to additionally note, that this complex's very accessible spin states leads to unusually photo-emission properties, where the wealth of spin states available leads to visible by eye white light emission when excited.

This complex is an unusual example of first a ligand-gated redox-tautomerism from  $\text{Co}^{\text{II}}\text{DHP}^{1-}$  to  $\text{Co}^{\text{III}}\text{DHP}^2$  (as evidenced from XAS and SXRD), as well as a temperature gated high spin-low spin rearrangement (evidenced by VT Evans, UV-Vis, and EPR). It showcases the remarkable ability of this ligand to stabilize novel redox and spin states which are closely related, and therefore delicately tunable. The large temperature range for these color transitions, increased stability to air provided by acetonitrile, and the ease of distinguishing the features and colors of this complex make it also potentially viable for temperature sensing applications, with at least a working range from 358 K to 16 K, based off of the various variable temperature experiments performed. This range could well be longer, and future study will be devoted to its investigation and viability.

## References

1. Liang, L.; Xiuxian, Z.; Binbin, W.; Shuaijun, Y.; Yong, N.; Xuchuan, J. Color-changing Mechanisms and Applications of Thermochromic Transition Metal Complexes: a Review. *Materials Reports*, **2023**, 37, 4, 21010049-11.
2. Zhang, Z.; Zhang, L.; Zhou, Y.; Cui, Y.; Chen, Z.; Liu, Y.; Li, J.; Long, Y.; Gao, Y. Thermochromic Energy Efficient Windows: Fundamentals, Recent Advances, and Perspectives
3. Xiao, X.; Chen, Z-J.; Varley, R. J.; Li, C-H. Smart bistable coordination complexes. *Smart Molecules*. **2024**, e20230028.
4. Belleci, F.; Gunaratne, H. Q. N.; Licence, P.; Seddon, K. R.; Plechkova, N. V.; S'Anna, F. Ionic Liquids-Cobalt(II) Thermochromic Complexes: How the Structure Tunability Affects "Self-Contained" Systems. *ACS Sustainable Chem. Eng.* **2021**, 9, 11, 4064-4075.

5. Hakami, A.; Srinivasan, S. S.; Biswas, P. K.; Krishnegowda, A.; Wallen, S. L.; Stefanakos, E. K. Review on thermochromic materials: development, characterization, and applications. *Journal of Coatings, Technology, and Research*. **2022**, *19*, 377-402.
  6. Qamar, O. A.; Jamil, F.; Hussain, M.; Mustafa, M.; Rehman, R. U.; Inayat, A.; Habib, M. S.; Sajid, M. A review on Fe-based spin crossover complexes with synergetic conductive and fluorescent properties. *Chem. Papers*. **2023**, *77*, 7331-7359.
  7. Mehta, S.; Kushwaha, A.; Kisannagar, R. R.; Gupta, D. Fabrication of a reversible thermochromism based temperature sensor using an organic-inorganic composite system. *RSC Adv*. **2020**, *10*(36), 21270-21276.
  8. Wang, M.; Li, Z-Y.; Ishikawa, R.; Yamashita, M. Spin crossover and valence tautomerism conductors. *Coord. Chem. Rev.* **2021**, *435*, 213819.
  9. Anferov, S. W.; Filatov, A. S.; Anderson, J. S. Cobalt-Catalyzed Hydrogenation Reactions Enabled by Ligand-Based Storage of Dihydrogen. *ACS Catal.* **2022**, *12*, 16, 9933-9943.
  10. McNeece, A. J.; Jesse, K. A.; Filatov, A. S.; Schneider, J. E.; Anderson, J. S. Catalytic hydrogenation enabled by ligand-based storage of hydrogen. *Chem. Commun.* **2021**, *57*, 3869– 3872.
  11. Anferov, S. W.; Boyn, J-N.; Mazziotti, D. A.; Anderson, J. S. Selective Cobalt Mediated Formation of Hydrogen Peroxide from Water Under Mild Conditions Via Ligand Redox Non-Innocence. *J. Am. Chem. Soc.* **2024**, *146*, 9, 5855-5863.
  12. Anferov, S. W.; Krupinski, A.; Anderson, J. S. Synthesis of a Potassium Capped Terminal Cobalt Oxido. *In Preparation*.
  13. Anferov, S. W.; Anderson, J. S. A cobalt adduct of an N-hydroxy-piperidinium cation. *J. Coord. Chem.* **2022**, *75*, 11-14, 1853.
-

## Appendix VII: Unpublished Work: Oh the Crystals You'll Grow, Oh the Reactions You'll See

*Adapted from Every Yearly Report—My years in Crystals*



**Figure 1.** Attempts to make a new ligand!  $\text{BF}_3$  Catalysis on the hydrazine condensation went wrong!  $[\text{Tol},2,6\text{-Chloro-phenylDHP}]\text{B}$ , B (tan), N (blue), C (gray), Cl (dark green). C-H-atoms were omitted for clarity.

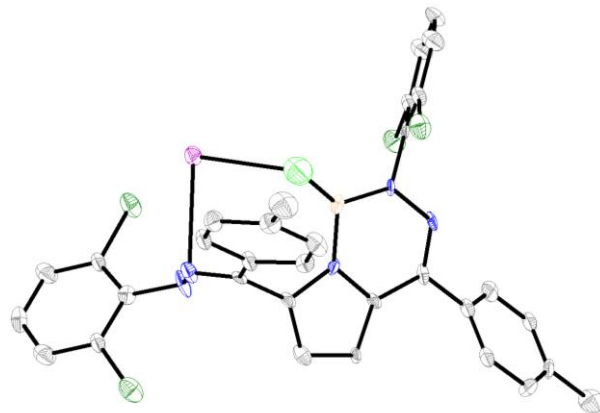


**Figure 2.** Breaking up is hard to do—trying to cleave out the boron with salts.  $[[\text{Tol},2,6\text{-Chloro-phenylDHP}]\text{BF}]\text{K}$ , B (tan), F (light green), K (purple) N (blue), C (gray), Cl (dark green). C-H-atoms were omitted for clarity.

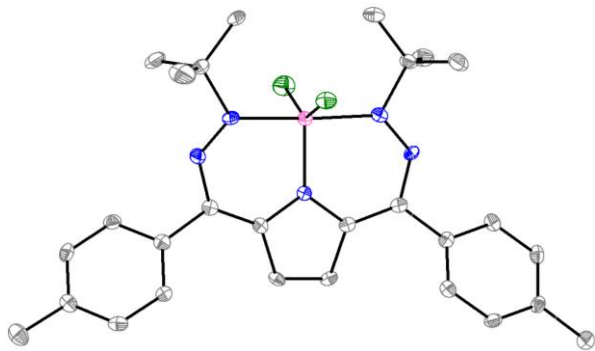


**Figure 3.** Cobalt chloride complex forms this upon reactivity with oxygen—probably some kind of disproportionation reaction.  $[\text{tBu},\text{TolDHP}]\text{CoCl}_2$ , Co (pink), N (blue), C (gray), Cl (dark green). C-H-atoms were omitted for clarity.



**Figure 4.** Cobalt chloride complex reacted with *tert*-butyl isocyanide.  $[\text{tBu},\text{TolDHP}]\text{CoCl}(\text{CN}'\text{Bu})$ , Co (pink), N (blue), C (gray), Cl (dark green). C-H-atoms were omitted for clarity.

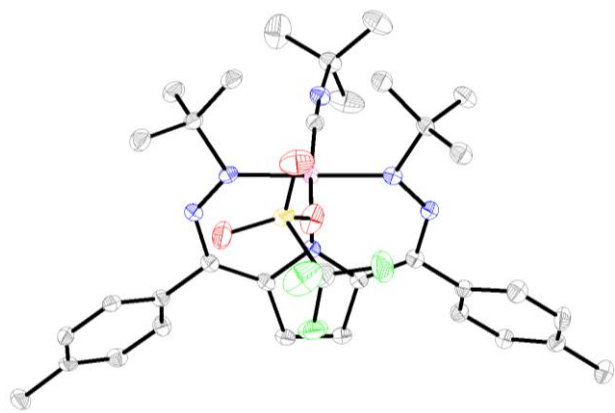


**Figure 5.** Cobalt triflate complex reacted with *tert*-butyl isocyanide.  $[\text{}^t\text{Bu,TolDHP}]\text{CoOTf}(\text{CN}^t\text{Bu})$ , Co (pink), N (blue), C (gray), Cl (dark green), O (red), S (gold), F (light green). C-H-atoms were omitted for clarity.

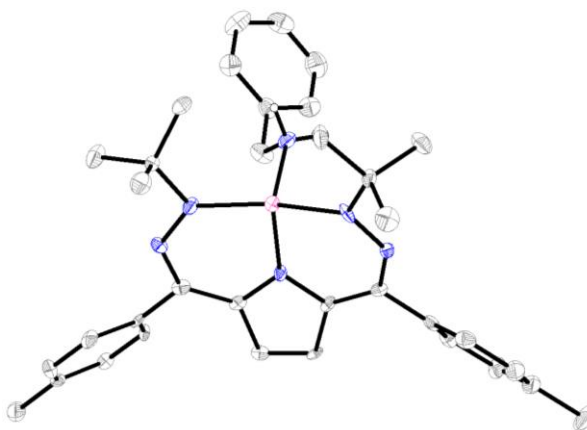


**Figure 6.** Neutral cobalt complex with benzyl amine bound.  $[\text{}^t\text{Bu,TolDHP}]\text{Co}(\text{NH}_2\text{Bz})$ , Co (pink), N (blue), C (gray). C-H-atoms were omitted for clarity.

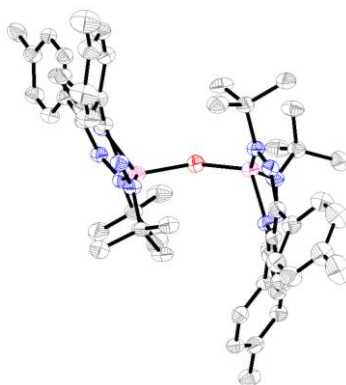
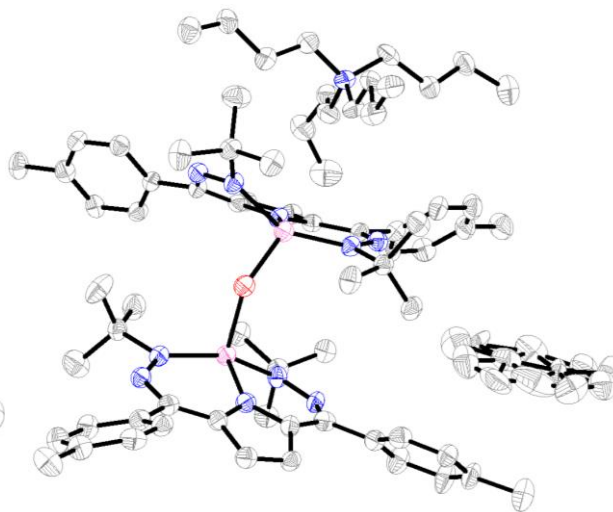
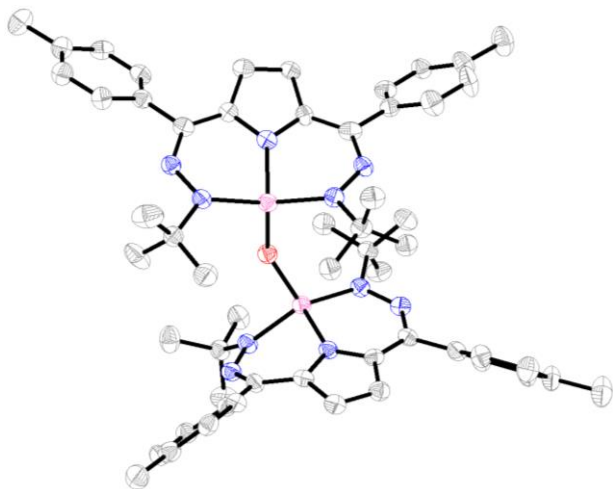


**Figure 7.** Oxo or Hydroxide bridged dimer—formed from potassium oxide cobalt complex attempt for a cyclic voltammogram in  $\text{NBu}_4\text{PF}_6$  electrolyte.  $[\text{}^t\text{Bu,TolDHP}]\text{CoO}(\text{H}?)\text{Co}[\text{}^t\text{Bu,TolDHP}](\text{NBu}_4)$ , Co (pink), N (blue), C (gray), O (red). C-H-atoms were omitted for clarity.

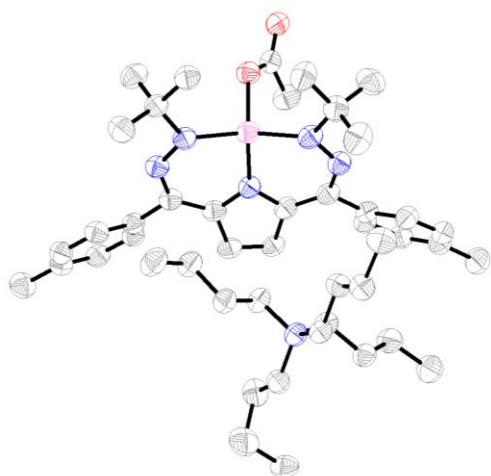


**Figure 8.** Cobalt neutral complex reacted with tetrabutyl ammonium acetate.  $[\textit{rBu,TolDHP}]\text{CoOAc}(\text{NBu}_4)$ , Co (pink), N (blue), C (gray), O (red). C-H-atoms were omitted for clarity.

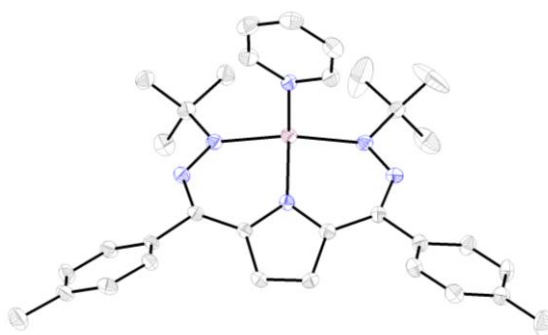


**Figure 9.** Manganese-metallated pyridine adduct.  $[\textit{rBu,TolDHP}]\text{Mn}(\text{Py})$ , Mn (purple), N (blue), C (gray). C-H-atoms were omitted for clarity.

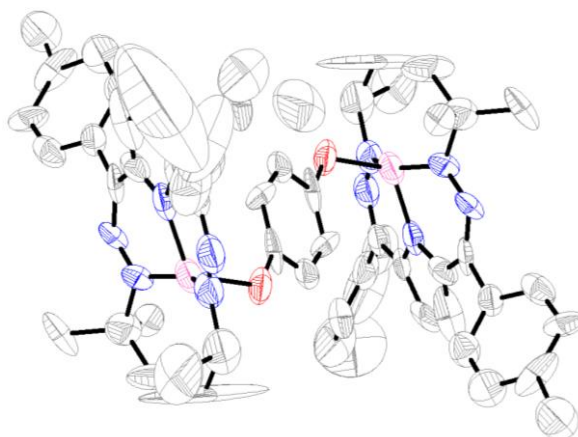
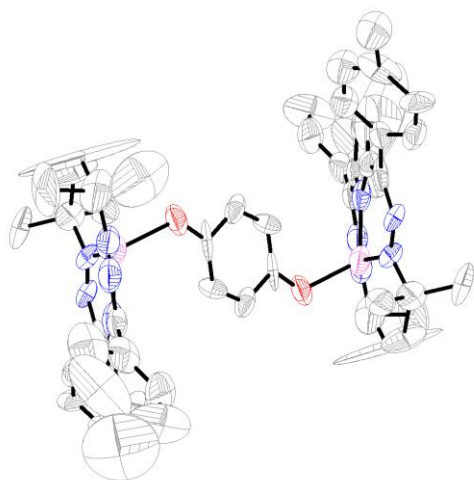


**Figure 10.** Complex formed from reduction of chloride complex with cobaltacene in the presence of hydroquinone/benzoquinone.  $[\textit{rBu,TolDHP}]\text{CoOPhOC}[\textit{rBu,TolDHP}]$ , Co (pink), N (blue), C (gray), O (red). C-H-atoms were omitted for clarity.



**Figure 11.** Cobalt homoleptic complex with phenyl analog of ligand—from an attempt to metallate!  $[\text{Ph,TolDHP-H}_2]\text{Co}[\text{Ph,TolDHP-H}]$ , Co (pink), N (blue), C (gray). C-H-atoms were omitted for clarity.

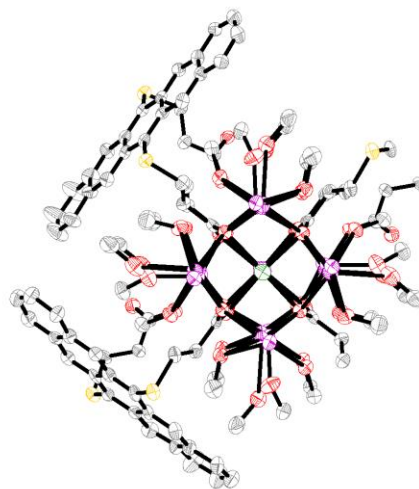


**Figure 12.** Water soluble pentacene from collaboration with L. E. McNamara and the Maurer group.  $[\text{Pentacene-(S-C}_4\text{H}_8\text{CO}_2)_2]\text{KCl}(\text{MeOH})_n$ , K (purple), S (gold), C (gray), O (red), Cl (dark green). C-H-atoms were omitted for clarity.

## Appendix VIII: Unpublished Work: Charging into Something New

*A Little something without Cobalt and with Lauren E. McNamara*

Electric fields have been suggested in enzymatic catalysis to alter product selectivity and result in orientation dependent changes in rate. Enzymes create these fields via charged polar residues or alkali metals.<sup>1,2</sup> Electric fields in oxygen double-bonded complexes (ketones, metal-oxos) often promote spin density on the oxygen atom.<sup>3</sup> Recent work even suggests that directed evolution actively works to modulate the electric field on active sites.<sup>4</sup>

Previous work on electrostatic effects in molecular compounds have largely been done with positive charges by various groups (Tolman, Kirk and Li, Lavallo, Yang, Saveant, Mayet, Borovik), but there is a dearth of anionic charge-generated electric fields. Previous work in the Anderson lab has shown the effectiveness of  $\text{BF}_3$  as an anionic functionality which is small and resembles a point charge.<sup>5</sup> Inspired by theory work that suggests the ability of an electric field on tris-bipyridine complexes to promote usually forbidden emission from even Fe analogs of these complexes (but with broadly interesting results for Fe, Ru and Os).<sup>6</sup>

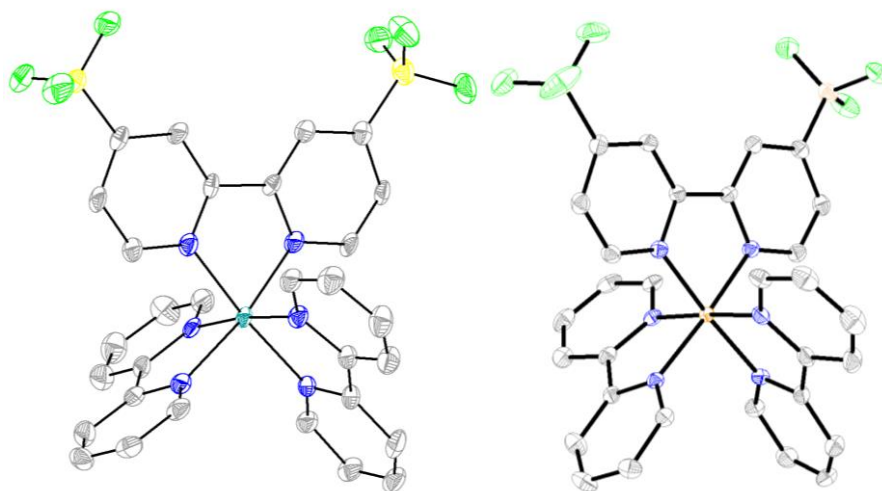


**Figure 1.** Ru and Fe analogs with two neutral bipyridine ligands and a single 4,4- $\text{BF}_3$ -bipyridine.

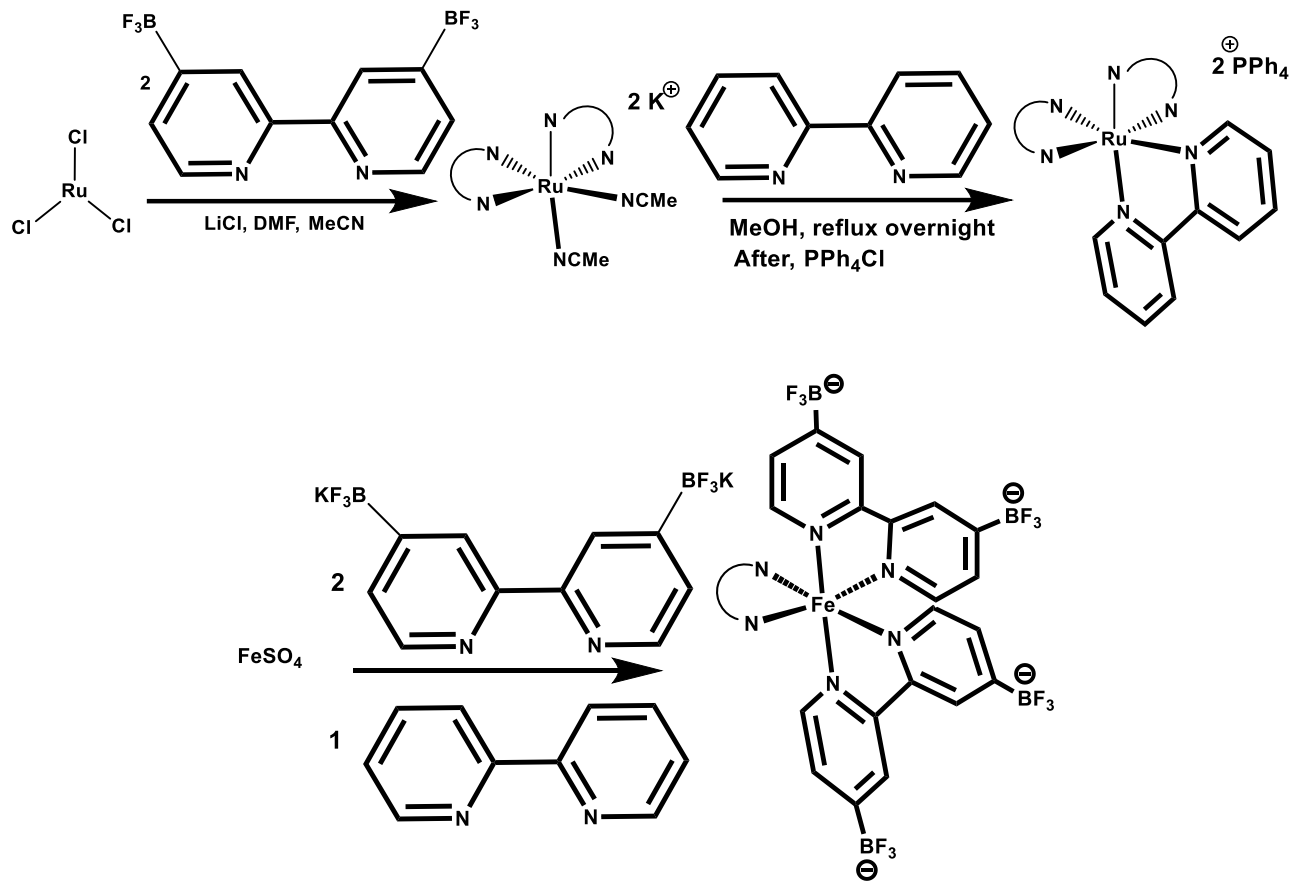


**Figure 2.** Metallations to form Ru and Fe analogs with one bipyridine ligand and two 4,4- $\text{BF}_3$ -bipyridines.

Substituting on a single bipyridine with  $\text{BF}_3$  groups in the 4,4 positions, we observe distinct differences in the spectra, but solubility limits further investigation (Figure 1). Only when multiple bipyridines are replaced by charged analogs that intriguing shifts are observed in the spectra, and the spectra readily observed in a variety of solvents (Figure 2, Figure 3).

We are still working on VT UV-Vis, DFT corroboration with Jan-Niklas Boyn, and on a collaboration with the Rovis lab on whether Fe-based photocatalysis is possible with the compounds.

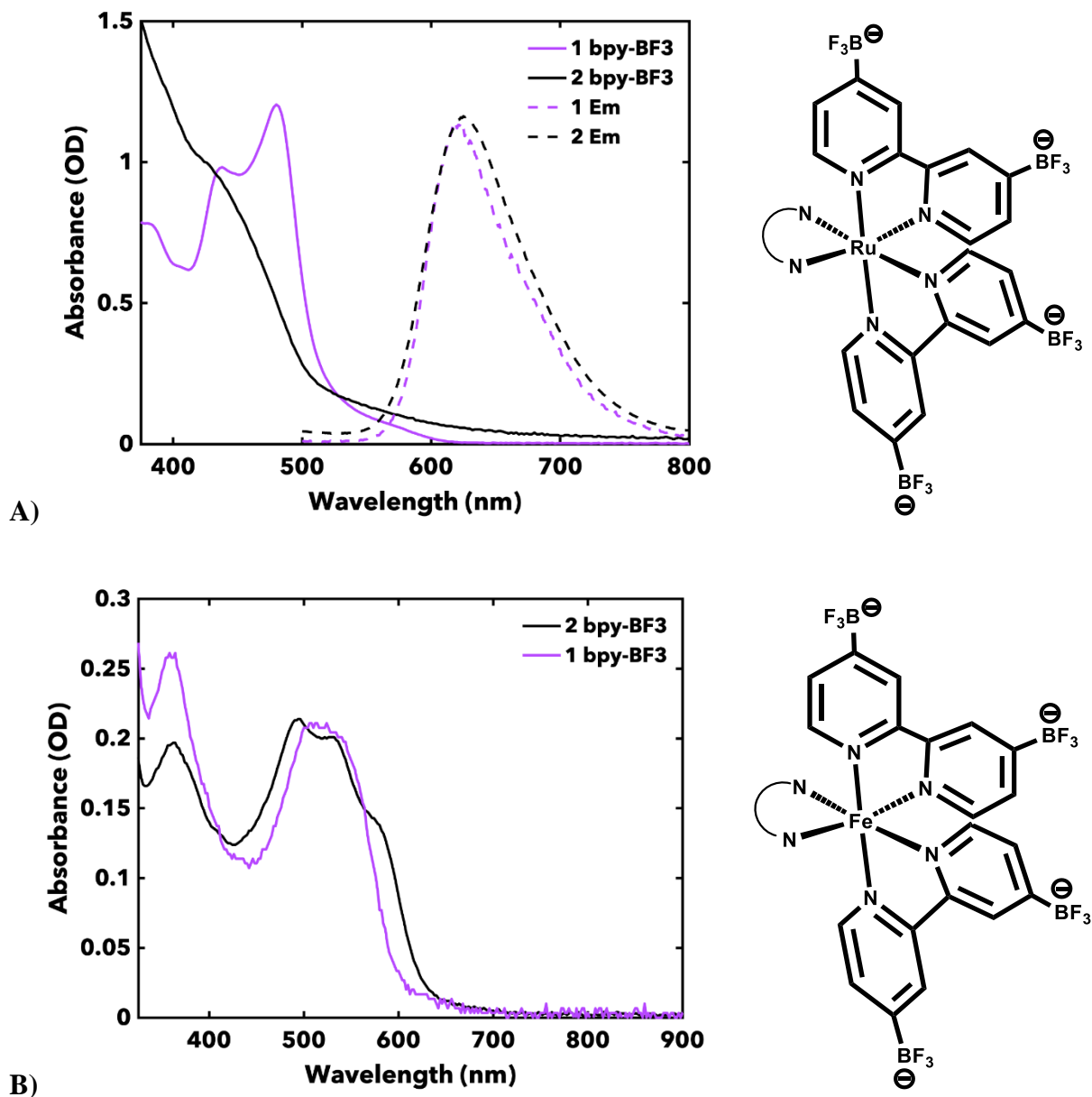


**Figure 3.** Compared UV-Vis Spectra of differently substituted Ru (A) and Fe (B) analogs.

Excitingly, the Ru spectrum changes shape dramatically and there is a shoulder at 600 nm in the Fe spectra that suggests potentially we are observing the triplet iron complex.

## References

1. Fried, Boxer *Annu. Rev. Biochem.*, **2017**, *86*, 387.
  2. Warshel *Proc. Natl. Acad. Sci.* **1978**, *75* (11), 5250.
  3. Bím, Alexandrova *ACS Catal.* **2021**, *11* (11), 6534.
  4. Chaturvedi, S. S.; Vargas, S.; Ajmera, P.; Alexandrova, A. A. *J. Am. Chem. Soc.* **2024**, ASAP.
  5. Kelty, M. L.; McNeece, A. J.; Filatov, A. S.; Anderson, J. S. *Chem. Sci.* **2022**, *13*, 4377-4387.
  6. Maurer, A. B.; Meyer, G. J. *J. Am. Chem. Soc.* **2020**, *142*, 15, 6847–6851.
-